PACIFIC EARTHQUAKE ENGINEERING RESEARCH CENTER

Toward Earthquake-Resistant Design of Concentrically Braced Steel-Frame Structures

Patxi Uriz
Exponent-Failure Analysis Associates
Menlo Park, California

Stephen A. Mahin
University of California, Berkeley

PEER 2008/08
NOVEMBER 2008

Toward Earthquake-Resistant Design of Concentrically Braced Steel-Frame Structures

Patxi Uriz
Exponent-Failure Analysis Associates
Menlo Park, California

Stephen A. Mahin
Department of Civil and Environmental Engineering
University of California, Berkeley

PEER Report 2008/08
Pacific Earthquake Engineering Research Center
College of Engineering
University of California, Berkeley

November 2008

ABSTRACT

In recent years, typical steel construction in regions of high seismic risk has shifted from moment-resisting frames to concentrically braced frames. As a result of the increased popularity of braced frames, the poor performance of some conventionally braced frames in past earthquakes, and the limited experimental data available on the inelastic response and the failure characteristics of braced-frame systems, a series of experimental and analytical investigations were initiated. The tests reported on herein contain some of the first data available on braced frames constructed in accordance with modern construction practices in the western U.S. Extensive analytical studies were undertaken to assess the analysis methods used for the research, and improved models were developed to better understand the complete range of behavior, including yielding, lateral buckling, and rupture due to low-cycle fatigue.

The primary objectives of this research are to (1) improve understanding of the behavior of this common type of structural system under cyclic inelastic deformations, (2) permit validation and improvement of computer models for predicting global and local response, and (3) improve understanding of the relation between system, member, and connection behavior.

As such, a series of investigations have been conducted, aimed at understanding and improving the seismic performance of concentrically braced steel-frame structures. Extensive analytical studies have been carried out on systems with conventional and buckling-restrained bracing. Tests on a limited number of full-scale pipe and square, hollow structural section (HSS) braces were carried out. These tests were supplemented with large-scale tests of three buckling-restrained braced-frame (BRBF) specimens and a single two-story special concentrically braced frame (SCBF). In the latter case, specimens incorporated traditional bracing elements susceptible to lateral and local buckling. These component and system test results, along with existing data, were used to develop, calibrate, and validate improved numerical models capable of realistically simulating the behavior of braced frames, including possible failure due to buckling and low-cycle fatigue. An array of numerical simulations assessed the likely performance of braced-frame structures subjected to severe earthquakes of the type expected in California. The applicability of performance-based earthquake engineering evaluation methodologies to concentrically braced frames is assessed using these results. Based on this research, recommendations are offered regarding the design, analysis, modeling, and detailing of concentrically braced frame structures.

ACKNOWLEDGMENTS

This work made use of the Earthquake Engineering Research Centers Shared Facilities supported by the National Science Foundation under award number EEC-9701568 through the Pacific Earthquake Engineering Research (PEER) Center.

Any opinions, findings, and conclusions or recommendations expressed in this material are those of the author(s) and do not necessarily reflect those of the National Science Foundation.

The research presented in this report was possible only because of the tremendous assistance of many individuals, companies, and organizations. The authors are grateful for the generous contributions of time, expertise, services, materials, and funds necessary to carry out this research.

The experimental portions of the research were conducted in the Structural Research Laboratory of the Department of Civil and Environmental Engineering at the University of California, Berkeley. The able assistance of William MacCracken, Jeffrey Higgenbotham, David Parsons, and Christopher Moy in helping to schedule the tests, set up the loading apparatus, instrument the specimens, train students, and conduct the experiments is greatly appreciated. Francis Yang, many undergraduate students, and PEER undergraduate summer interns volunteered their time and skills to help with preparation of the specimens and in conducting tests.

The buckling-restrained braced-frame (BRBF) specimens were tested as part of the design verification of the Stanley Hall Replacement Building on the Berkeley campus of the University of California. As such, the University of California provided the core funds needed to carry out the BRBF tests, in cooperation with the Pacific Earthquake Engineering Research (PEER) Center. The University's efforts were spearheaded by Edward Denton, Vice Chancellor for Facilities Services, Robert Gayle, Associate Vice Chancellor for Project Management, and Craig Comartin, the campus's consulting structural engineer. Robert Bluhm, Assistant Director for Design and Project Management, represented the campus's Capital Projects Office in overseeing the tests. The BRBF test specimens were designed by Rutherford and Chekene, the consulting structural engineers responsible for the design of the Stanley Hall Replacement Building, in conjunction with the research team, the campus's Seismic Review Panel, and others. The authors gratefully acknowledge the able assistance of Mark Saunders, Tom Lauck, Walterio Lopez, and David Gwie of Rutherford and Chekene. The fabrication of the three BRBF specimens was generously donated by Gayle Manufacturing of Woodland, California, and coordinated by David DeBlasio. Nippon Steel of Tokyo, Japan, donated the buckling-restrained braces used in the tests and provided additional financial support for the overall project. California Erectors of Benicia, California, donated their services for the BRBF specimens. Inspection services were donated by Signet Laboratories of Hayward, California.

The special concentrically braced frame (SCBF) specimen was fabricated and erected by SME Steel of West Jordan, Utah. The assistance of James Smeltzer and Mark Daniels in arranging for the donation of the material and services is greatly appreciated. Inspection services for the SCBF specimen were donated by Applied Materials and Engineering, of Oakland, California. The coordination provided by Dushyant Manmohan in scheduling the quality control and assurance inspections is acknowledged.

The tests of individual braces used to validate the analytical models of the braces were conducted by Frances Yang as part of her Master of Engineering degree requirements. The Structural Steel Education Council of Moraga, California, under the direction of Brett Manning, provided funding for these tests and arranged for the fabrication of the specimens by Herrick Corporation of Pleasanton, California.

Throughout the course of this research a number of professional engineers were unhesitant in contributing their time, advice, and expertise. Rafael Sabelli of DASSE Design, San Francisco, provided the model building designs used throughout the report, assisted in the design of the SCBF specimen, and provided advice continuously throughout the project. Eric Ko and Caroline Field of Arup Engineers, San Francisco, greatly assisted with understanding of the behavior of connections and buckling-restrained braces, and carried out independent finite element analyses of the buckling-restrained braced-frame specimens. Dr. Ian Aiken of SIE Inc., Emeryville, California, and Isao Kimura of Nippon Steel, Tokyo, provided substantial advice and data regarding buckling-restrained braces. Nippon Steel also provided a grant-in-aid to help support the overall effort. Walterio Lopez of Rutherford and Chekene, Consulting Engineers, Oakland, California, provided input to the decision-making process throughout the project and assisted in interpreting data. James Malley of Degenkolb Engineers, San Francisco, provided tremendous insight into code provisions related to steel-braced frames.

The theoretical formulation of the fiber-based, beam-column element developed for OpenSees to model the lateral buckling of braces, columns, and beams benefited significantly from numerous discussions with Prof. Filip Filippou of UC Berkeley. Dr. Frank McKenna provided valuable advice regarding development of object-oriented coding and identification of successful numerical iteration strategies. The large number of nonlinear dynamic analyses conducted as part of this research would not have been feasible without access to the Millennium Cluster of the College of Engineering, University of California, Berkeley.

Claire Johnson ably edited the final version of the report. Her patience and skill in moving this report to its final state is greatly appreciated.

This work reported on herein was conducted in partial satisfaction of the requirements for the doctor of philosophy degree by the first author under the guidance of the second author. In addition to the various financial and material contributions noted, the Byron and Elvira Nishkian Professorship in Structural Engineering provided a significant portion of the support for the first author.

The work drew heavily upon the performance-based evaluation methodologies and numerical simulation tools developed by PEER. As such, the editing and completion of the report was possible only with support from the National Science Foundation under Grant No. CMS-0600625—Robust Performance-Based Design of Concentrically Braced Steel Frame Buildings, and Grant No. 0619161—International Hybrid Simulation of Tomorrow's Braced Frame Systems.

CONTENTS

LIST OF FIGURES

LIST OF TABLES

1 Introduction

1.1 BACKGROUND

The 1994 Northridge earthquake produced unanticipated damage in special steel moment-resisting frame (SMRF) buildings (FEMA 2000a). Although no SMRF buildings collapsed, damage found in these buildings resulted in significant economic losses. One aspect of this damage was particularly alarming to many structural engineers, who had anticipated that welded steel beam-to-column connections were capable of undergoing large plastic rotations, on the order of 2% or more. In many SMRF buildings, quasi-brittle fractures had developed in and around the welded joints connecting the beam flanges to the columns. In several cases, these fractures had spread into the adjacent column and panel zone region.

As a result of this unexpected damage, the Federal Emergency Management Agency (FEMA) funded the SAC Joint Venture (comprising the Structural Engineers of Northern California, the Applied Technology Council, and the California Universities for Research in Earthquake Engineering) to investigate the problem and produce guidelines for assessing and improving the performance capabilities of existing SMRF structures and to provide recommendations for the analysis, design, and construction of new SMRF buildings. Briefly, detailed analytical studies of components, subassemblages, and complete structural systems and experimental testing of over 120 full-scale subassemblages were conducted, resulting in the following: the development of consensus-backed and cost-effective guidelines for new structures (FEMA 2000A); procedures for evaluating and modifying existing SMRF structures (FEMA 2000B); procedures for evaluating and repairing potentially damaged SMRF buildings (FEMA 2000C); and procedures for inspecting welds that are part of the lateral-load-resisting system (FEMA 2000D). A series of state-of-the-art reports were also prepared to summarize the technical background underlying the various guidelines (FEMA 2000E–J).

These new guidelines were based in part on explicit procedures for quantifying and evaluating the likely seismic performance of new, existing, retrofit, and repaired structures. This effort was among the first to apply performance-based analysis and design procedures to the development of nationally applicable guidelines for the design and evaluation of structures intended to be resistant to earthquake ground shaking. These procedures also gave building owners and engineers a tool to assess the likelihood of a steel moment-frame structure reaching a specific damage state. Although conventional prescriptive codes [e.g., International Building Code (ICC 2003) used in combination with the American Institute for Steel Construction (AISC) *Load and Resistance Factor Design* (LRFD) *Manual* (AISC 1993)] and a site-specific hazard evaluation are intended to achieve engineered structures that minimize the loss of life associated with structural collapse under rare earthquake ground shaking, no specific procedures are stipulated for assessing and quantifying the expected performance. The new FEMA guidelines provide detailed calculations that enable engineers to estimate the likelihood of collapse, partial collapse, beam-column connection failure, and other damage states for stipulated earthquake hazards. For typical new building structures, the FEMA guidelines provide simplified design procedures and default values for design parameters that when used in combination with pre-qualified connection details and stringent detailing, welding, and inspection requirements are expected to result in satisfactory performance.

Although these guidelines have helped restore the confidence that engineers and the public had in SMRF buildings prior to the Northridge earthquake, the resulting structures are subject to greater restrictions on configuration and proportioning, require more effort to design, and necessitate more stringent quality control and assurance protocols. Moreover, member sizes in SMRF systems tend to be controlled by the interstory drift limitations stipulated in modern building codes. As a consequence, member sizes are generally significantly larger than required on the basis of strength considerations alone.

1.1.1 Trends Toward Concentrically Braced Frames

The current situation has led many engineers to seek out simpler and more economical systems that promise good seismic performance with reduced interstory displacements. While some engineers have turned to eccentrically braced frames, the most dramatic shift in construction practice appears to be a substantial increase in the use of concentrically braced frames. Industry experts estimate that conventional concentrically braced frames comprise nearly 40% of the commercial steel construction market today in California (Ferch 2004), whereas this system constituted less than 10% of the market a decade ago.

Traditionally, it has been assumed that, generally, the seismic performance of steel concentrically braced frames is inferior to that of steel moment-resisting frames. Extensive damage was reported in concentrically braced frames following many recent earthquakes, including the 1985 Mexico City, 1989 Loma Prieta, 1994 Northridge, and 1995 Hyogo-ken Nanbu events (for more detailed background on past performance, see Chapter 2). The most severe damage was observed in frames where braces were proportioned to resist tension only, where connections were weaker than the braces attached to them, where braces framed into columns, and where braces were inclined principally in one direction. Since then, the seismic provisions for structural steel buildings (AISC 1997) have been updated to prohibit or restrict such conditions. Notwithstanding these improvements, the seismic performance of concentrically braced steel frames may still be less than desired. For example, conventional braces used in the United States have limited ductility capacity and are prone to fracture due to low-cycle fatigue (Lee and Goel 1987). They also tend to lose compressive strength when loaded in the inelastic range, which leads to a concentration of damage in weakened stories (Khatib et al. 1988).

Prompted by these observations, seismic design requirements for braced frames changed considerably during the 1990s, and the concept of special concentrically braced frames was introduced (AISC 1997; ICBO 1997). Additionally, researchers have undertaken a variety of investigations to develop ways to improve the performance of concentrically braced frames through:

1. The introduction of new structural configurations (Khatib 1988)
2. The use of special bracing elements, including those utilizing:
    - composite action [Liu (1988); and others]
    - metallic yielding [Chen and Lu (1990); Kamura et al. (2000); Watanabe et al. (1989); and others]
    - high-performance materials [Sweeney (1995); Ohi (2001) and others]
    - friction and viscous damping [Filiatrault and Cherry (1987); Hanson (1993); Kullmann and Cherry (1996); Aiken and Kelly (1996); and others]
3. The introduction of new behavior modes, such as uplifting foundations (Hucklebridge and Clough 1977a,b).

While several of these approaches are quite promising, many of the studies have been limited to simplified analytical simulations, or tests of individual (and frequently, reduced-scale) specimens. Very few tests of entire braced-frame systems have been performed, especially ones incorporating details representative of current practice in the United States. As such, it is difficult to quantitatively compare the various approaches suggested for improving the behavior of concentrically braced frames, and to compare the performance of concentrically braced frames with alternative framing systems.

1.1.2 Complications in Design Associated with Short-Period Force-Controlled Structures

Current building code provisions (IBC 2003) stipulate that calculations be undertaken to demonstrate that the lateral-load-resisting system meets two basic global design criteria: (1) the structure has a lateral load capacity larger than a stipulated minimum design value and (2) the frame needs to limit deflections to a specified drift for an amplified force level. For moment-resisting frames, the latter criterion often governs the proportioning of beams and columns, with member stiffness being increased to where interstory drifts fall below the stipulated limit. Because stiffer members are generally stronger as well, code-compliant moment-frame structures are often two or three times stronger than required by code. Curve A in Figure 1.1a represents a flexible structure that can achieve the minimum code lateral load requirement, but at a displacement greater than permitted. Curve B represents the same structure with members stiffened to satisfy the displacement criterion, but it is now far stronger than required.

Braced frames are inherently stiff. Thus, for the structures of the same height, braced frames will normally have a lower period than a moment frame. Given the variation of design forces with period stipulated in most building codes, and the lower response modification factor, *R,* associated with conventional concentrically braced frames, the minimum lateral design load stipulated for a concentrically braced frame is generally larger than for a moment-resisting frame. In spite of these higher forces, the inherently large lateral stiffness of braced frames is generally adequate to satisfy the lateral drift requirements in current codes without further increasing the member stiffness and strength. This is schematically illustrated by Curve C in Figure 1.1a. Because the braced frame need not have the size of its members increased to achieve the stipulated drift limit, it will likely have less overstrength compared to the moment-resisting frame, and may be susceptible to more damage than moment frames.

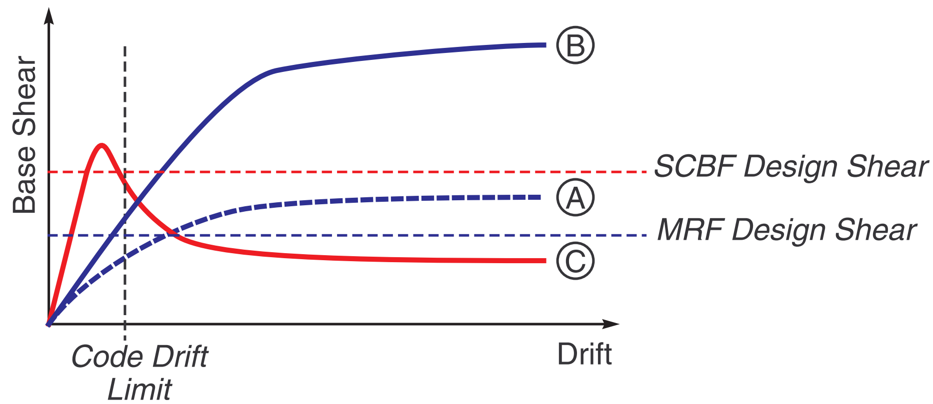

(a)

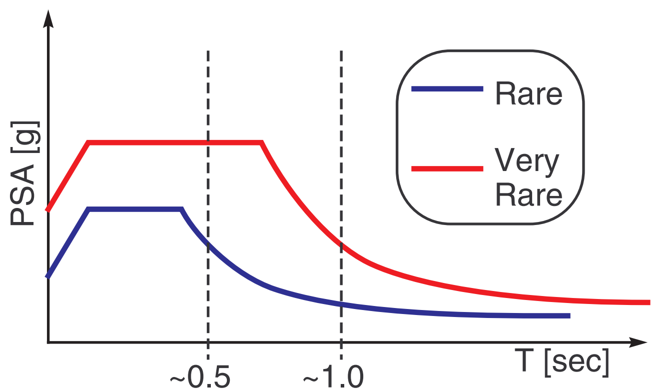

(b)

Fig. 1.1 Design issues with force-controlled short-period structures: (a) force-controlled behavior and (b) short-period effects.

It is possible that a moment frame that is stiffened to satisfy the interstory drift criterion may be as strong or even stronger than a comparable braced frame, resulting in significant accelerations and falling hazards in both structures during severe earthquake shaking.

Braced-frame structures in the range of one to four stories may also have another design consideration to contend with: they may be stiff enough to have a period where they respond in the "constant spectral acceleration" range where energy, rather than displacement, is preserved when the structure responds in the inelastic range (Chopra 1995). Most moment-resisting frames, even ones having only two or three stories, might be flexible enough to have periods sufficiently long where during severe dynamic response their peak displacements would be expected to be essentially the same as those undergone by a structure sufficiently strong to remain elastic. According to Newmark and Hall (1973), structures in the constant amplified acceleration range tend to displace more than comparable structures that respond in the elastic range. Short and stiff braced-frame structures might thus be expected to sustain more severe damage than might be suggested on the basis of a simple elastic analysis.

Figure 1.1b schematically illustrates a situation that might occur for two braced-frame structures having different periods. For occasional and rare events, the short-period (~0.5 sec) and longer-period (~1.0 sec) structures are likely to lie within the "displacement-preserved" range, or where the peak elastic and inelastic displacements are similar (Newmark and Hall 1973). For very rare events, however, the spectral properties of the ground motions in the near-fault region tend to increase in intensity and extend the constant amplified spectral acceleration range to higher periods (often greater than 1 sec) (Abrahamson and Silva 1997; ICC 2003). In these cases, structures having periods ranging from 0.3 to 1.0 sec or longer will tend to absorb the same amount of strain energy whether responding elastically or inelastically, resulting in larger displacements for the inelastically responding structure compared to estimates based on elastic analyses. Here, the ductility demands and displacements of a shorter-period braced frame designed with little overstrength may be larger than more flexible moment-frame structures.

Other researchers have noted (FEMA 2000d; Miranda and Ruiz-Garcia 2002) that the inelastic dynamic response of structures in the short-period range is more sensitive to hysteretic loop shape, whereas this shape is not as important in the displacement-preserved range. Thus, the various types of hysteretic behavior that may be exhibited by short-period braced frames may introduce complications not encountered with steel moment-resisting frames.

1.1.3 Advances in Performance-Based Evaluation and Design Methods

Because of the complexity of the factors controlling the dynamic behavior of braced steel-building systems when subjected to different types and intensities of earthquake excitation, it is essential to have a sound framework for comparing the performance of design alternatives. Performance-based evaluation criteria already established or under development by SAC (FEMA 2000a), ATC (Hamburger 2003; SEAOC 1995), the Pacific Earthquake Engineering Research Center (PEER) (Krawinkler 2002), and others contain procedures for assessing hazard, damage, and losses. Because of the extensive literature on this subject, only a brief description of some of the key aspects of this work is provided herein.

The Vision 2000 (SEAOC 1995) framework established a number of useful definitions related to performance and identified important linkages among seismic hazard, building use, and performance expectations. The SAC effort extended these basic notions for steel moment-resisting frames by introducing a probabilistic framework within which the performance of an overall system could be assessed in basic terms, such as achieving continued occupancy or collapse prevention goals. Combined efforts of PEER, FEMA, and ATC have extended these concepts even farther to incorporate additional performance criteria related to losses associated with direct structural and nonstructural damage, casualties, and disruption of services. They have also extended application to other structural materials. In the work being done by PEER, the basic theoretical and conceptual concepts and implementation methodologies have been greatly expanded, including more accurate and test-validated computer simulations and case studies, focusing on reinforced concrete buildings and bridges.

The basic PEER performance-based earthquake engineering (PBEE) process is summarized below in Figure 1.2 (Moehle 2003). This diagram illustrates the fundamental steps of PBEE starting from the location (O) of a structure and its design (D):

1. Hazard Analysis: An intensity measure (IM), such as spectral acceleration at a period of interest, is obtained through conventional probabilistic seismic hazard analysis and is expressed as a mean annual probability of exceedance, p[IM] that is specific to the location and design characteristics of the structure.
2. Structural Analysis: Engineering demand parameters (EDPs) such as peak interstory drift, floor level accelerations, plastic hinge rotations, brace axial deformations, and so on, are required to assess the performance of a structure. The relationships between these key EDPs and the IM are typically derived by performing a series of inelastic dynamic analyses using numerous ground motions representative of a particular range of Ims. Such IM-EDP relationships provide information about trends in response and the scatter (uncertainty) associated with these parameters. These relationships can be used to describe the probability of exceeding a particular value of an EDP given an IM value (p[EDP|IM]).
3. Damage Analysis: Regardless of the level of sophistication in a structural model, simplifications are introduced to achieve reasonable computational efficiency. Thus, additional relationships may be needed to identify and quantify the occurrence of damage that would detract from satisfactory performance. These damage measures (DM) may not

be directly related to the EDPs because different severities of damage may require different techniques or because the damaged component is not incorporated specifically in the numerical model. For example, increasing levels of plastic rotation may trigger progressively intrusive and expensive repair strategies (ranging from epoxy injection, local removal and restoration of concrete and reinforcing bars, to complete replacement of a segment of a member). Similarly, different relations may be needed to estimate the type and impact of damage to different types of displacement-sensitive partitions based on computed interstory drifts. Quantitative descriptions of damage for each component of interest are often expressed by one or more discrete damage states (e.g., for drywall damage, these states could be small cracks requiring painting, wide cracks requiring replacement of gypsum, and severe damage requiring partition replacement). The relationship between computed EDPs and inferred DMs is expressed as a probability of exceeding a specific damage intensity or state (p[DM|EDP]).

4. Loss Analysis: A variety of decision variables (DV) can be used to quantify the impact of local and overall damage and to judge the adequacy of the performance expected of a structure. DVs can be expressed as either monetary loss (often expressed as a function of replacement cost), likely downtime, or life safety. Thus, probabilistic functions are needed to relate the likely repair or replacement costs, downtime and casualties for various damage states (p[DV|DM]).

By integrating the impacts (DVs) of all likely damage to the structure, an estimate of overall loss can be used to assess the performance of the structure. This is schematically described by Figure 1.2, and in Equation (1.1). Performance-based earthquake engineering can provide building owners and engineers with a realistic quantitative assessment of likely seismic performance, expressed in terms of various factors (i.e., the total loss over the life of the structure, loss associated with earthquakes corresponding to a specific hazard level, or losses resulting from a specific scenario event).

$$\nu(DV) = \iiint G\langle DV \mid DM \rangle \, |dG\langle DM \mid dEDP \rangle| \, dG\langle EDP \mid IM \rangle \, | \, d\lambda(IM) \tag{1.1}$$

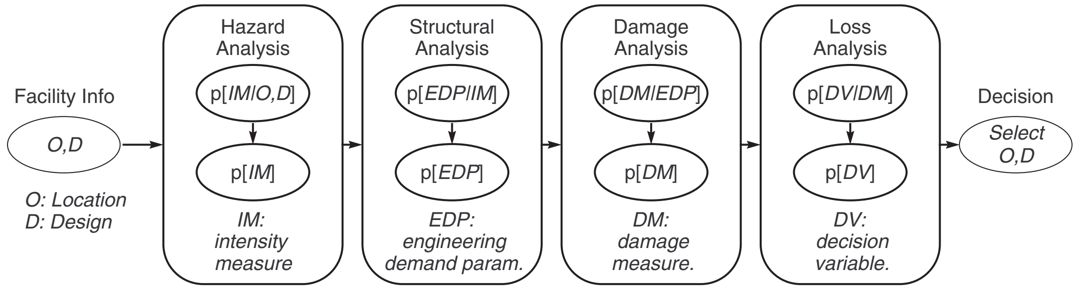

Fig. 1.2 Graphic of steps in PBEE (Moehle 2003).

The SAC PBEE methodology considered only the first three of these steps in its performance assessment of SMRF buildings and examined only the case where specific hazard levels were specified; in other words, the level of confidence one would expect regarding the ability of a structure to achieve a specified performance goal, such as collapse prevention, when the structure was subjected to earthquakes consistent with a particular hazard level (e.g., 2% probability of exceedance in 50 years). As such, the SAC procedures for performance evaluation were primarily intended to give engineers tools to assess the ability of the structure to achieve those engineering criteria associated with various types of performance. Efforts by ATC and others are extending this effort to include other non-engineering oriented performance metrics and other types of structural systems, as well as steel moment-resisting frame buildings.

To date, little work has been undertaken to extend PBEE concepts to concentrically braced steel frames. The inelastic dynamic behavior of concentrically braced frames introduce forms of behavior and failure mechanisms that have heretofore not been considered in the application of PBEE (Moehle et al. 2005). In particular, effort is needed to identify a two key definitions posed in PBEE: what engineering demand parameters (EDPs) should be used as indirect measures of global and local damage for braced-frame structures? and what key damage states (DMs) and impact losses should be monitored? To date, it is not well understood how such key demand and damage parameters are sensitive to design decisions related to the configuration and relative proportions of a braced-frame system and the strength, stiffness, and hysteretic characteristics of its members and connections. The foundation of performance-based evaluations depends on the ability to accurately predict response and damage. The ability of current analytical procedures and numerical models to predict the response of complete braced-frame systems has not been examined in depth, and as such, the absence of test-validated models to predict the behavior, including failure, of members and systems is viewed as a serious impediment to the development of PBEE methods applicable to steel-braced-frame structures.

1.2 OBJECTIVES AND SCOPE

This report explores some of the key aspects of the PBEE process and applies them to concentrically braced steel-frame structures. The thrust of this research is two-fold:

1. Assess and, where needed, improve analytical tools to predict the dynamic response and damage expected of concentrically braced steel structures during earthquakes; and
2. Conduct a preliminary investigation of the seismic performance of concentrically braced steel-frame structures.

This report considers concentrically braced frame structures incorporating conventional buckling braces and buckling-restrained braces. Assessment of analytical tools is based on comparing numerical results with existing experimental data, as well as the test results performed as part of this investigation. Studies of the likely performance of braced frames focus on the first three steps indicated in Figure 1.2, with greatest emphasis on the second of the four steps—structural analysis. This emphasis is necessary because of the reliance of the overall performance assessment on the accuracy of the numerical predictions of response and damage, and the need to improve understanding of the sensitivity of the behavior of braced-frame structures to proportioning strategies and local details. Nonetheless, the efforts undertaken herein are done within the overall context of the methodologies being developed by PEER and ATC.

1.3 ORGANIZATION OF REPORT

An extensive literature survey is provided in Chapter 2 related to (1) the performance of braced steel buildings during past earthquakes and (2) physical tests that have been conducted on steel braces and steel structures containing braces. This chapter provides background on the types of damage observed in braced frames and the data available upon which assessment of numerical models and performance can be based.

Chapter 3 presents a preliminary seismic hazard assessment of a few representative braced-frame structures. This preliminary assessment utilizes existing numerical models and follows the basic procedures for seismic performance assessment as outlined by SAC (FEMA

2000B). This chapter illustrates several major limitations of currently available approaches for analysis and performance evaluation when they are applied to concentrically braced steel frames.

The development and implementation of an analytical beam-column element able to simulate the effects of global member buckling is discussed in Chapter 4. This chapter focuses on the hysteretic behavior of compact sections (i.e., compact braces or columns) subject to significant axial loads. In addition to using past test results, new tests were performed on a series of hollow structural sections (HSS) tubular braces to assess and calibrate the improved numerical model.

Tests and field investigations indicate the importance of including the effects of low-cycle fatigue when predicting the global behavior of braced-frame structures. Chapter 5 defines, implements, and calibrates a material model, which can be incorporated in the beam-column model described in Chapter 4 to account for the deterioration and failure of members due to low-cycle fatigue. The low-cycle fatigue model is calibrated using the results of experimental studies carried out as part of this effort and elsewhere.

To assess the ability of numerical models to predict the behavior of braced-frame systems, experimental studies were undertaken, as described in Chapter 6, on several large-scale, concentrically braced steel subassemblages containing modern details and proportions. Two series of tests were performed: (1) three tests of buckling-restrained braced frames and (2) a special concentrically braced frame using conventional buckling braces. In addition to providing data to be used in the evaluation of the accuracy of structural idealizations, numerical models, and analytical procedures, the tests lead to several useful observations regarding the general behavior of braced-frame structures. At the end of this chapter, numerical models calibrated using these test results are applied to assess the likely behavior of test specimens constructed using different proportions and configurations.

In Chapter 7, a simple single-story computer model is created of a chevron-braced frame using the models developed in Chapters 4 and 5. This single-degree-of-freedom (SDOF) model represents the basic global hysteretic behavior of a braced frame having conventional buckling braces with various slenderness ratios. The results obtained with this SDOF model are compared with those for a standard bilinear hysteretic SDOF model. In this comparison, several force reduction factors , R, and periods were considered. A simple example of the PBEE framework is also conducted using these SDOF analytical models. This PBEE study provides the groundwork for subsequent analytical studies on more realistic multi-story models.

Chapter 8 presents an entire PBEE analysis of several three-story steel structures. The structures include moment-resisting frame structures, buckling-restrained braced frame structures, and conventional buckling braces with a range of configurations, braced characteristics, base plate details (i.e., uplift allowed or not), and other key details

Chapter 9 summarizes the results obtained in this investigation, identifies important conclusions and recommendations, and discusses some future research needs related to steel-braced-frame structures.

2 Literature Review

2.1 GENERAL

Considerable research has been conducted on the behavior of steel bracing elements and on connections and subassemblages from concentrically braced steel-frame structures under loading representative of strong earthquake ground shaking. Because of the rapid evolution of codes, much of this research is not necessarily consistent with modern construction detailing; however, many of the fundamental observations from these investigations are germane to an assessment of modern design and analysis procedures. Moreover, experimental data are critical to the validation and calibration of analytical models used for carrying out simulations to predict the performance of braced-frame structures. The available body of literature extends over several decades and is rapidly growing. As such, it cannot be adequately summarized in a brief chapter. Instead, an overview of major references is provided here along with useful citations to previous works that contain detailed reviews of related literature. The literature review in this chapter is separated below into two categories:

1. *Performance in Past Earthquakes:* This section examines references that describe the performance of braced steel structures in relatively modern earthquakes (1978–1995) in the United States, Mexico, and Japan.
2. *Experimental Studies:* This section discusses previous tests of brace components and concentrically braced subassemblages relevant to seismic applications.

Considerable literature also exists on numerical modeling of braces, prediction of fracture and fatigue life, behavior of various configurations of braced-frame systems, and sensitivity of behavior to various ground motion and structural characteristics. This literature will not be reviewed in this chapter, but rather distributed throughout the remainder of the report where these particular topics are considered.

2.2 STRUCTURAL PERFORMANCE IN PAST EARTHQUAKES

Previous earthquakes provide opportunities to learn important lessons regarding the behavior of engineered structures, and the adequacy of seismic design provisions. A significant number of modern concentrically braced frames have been subjected to damaging levels of ground shaking, specifically the 1978 Miyagi-ken Oki earthquake, the 1985 Michoacan earthquake, the 1994 Northridge earthquake, and the 1995 Hyogo-ken Nanbu earthquake.

2.2.1 1978 Miyagi-ken Oki earthquake (Tanaka et al. 1980 and Kato et al. 1980)

One of the earliest earthquakes that illustrated potential issues with modern braced-frame detailing and how it affected overall performance was the 1978 Miyagi-ken Oki earthquake. This earthquake had a magnitude of 7.4 and primarily affected Sendai City, the second largest city in northern Japan. Japanese investigators Tanaka, Morita, and Yamanouchi (1980) performed a detailed survey of damaged braced steel buildings in Sendai City. Because of the large increase in the number of steel buildings in this region, many of the steel buildings were relatively new and detailed according to the recent building code. At the time of the earthquake, typical bracing members consisted of double-angle braces with bolted connections to gusset plates. Tanaka, Morita, and Yamanouchi separated the damage observed into two main categories: (1) insufficient strength of connections joining braces to one another or adjacent framing and (2) inadequate consideration regarding the effects of the nonlinear response of individual braces on the behavior of braced steel frames, even under static loading.

The first category dealt with three subcategories in which damage was observed:

1. The strength of the net effective area of the bolted part of the brace was insufficient to permit overall tensile yielding. Angles with small sizes were frequently used as bracing members. These required only two or three bolts to meet code requirements. Many of these connections failed at the net reduced section and the brace was never able to yield fully in tension.
2. The strength of the fasteners was too weak. Typically, when high-strength bolts were used, they were able to develop the strength of the braces in tension. Unfortunately, many buildings used low-carbon steel bolts to attach the braces to the gusset plate, which were typically continuously threaded, so that the shear transferred by the bolts occurred in the

plane where threads existed. As a result, many of the bolted connections failed before other mechanisms (failure of the net reduced section or brace yielding).

3. The strength of the gusset plate, or its connection to the beam or column, was not sufficient to transfer ultimate loads from bracing members to the supporting framing members. Many of the gusset plates connecting the braces to the frame were welded to the beams and columns. Frequently, these connections simply did not contain enough strength to develop the forces that developed in the braces. This poor behavior was attributed to poor workmanship of some of the welds.

The second main category dealt with a basic lack of understanding of the inelastic behavior of braced-frame systems. Tanaka, Morita, and Yamanouchi noted that the distribution of the braces was important in developing the ultimate lateral load capacity of the structure, and that a distribution of braces (and brace sizes) that did not account for the likely inelastic behavior of the system prevented the system from achieving the intended capacity. Also, the effects of not being able to develop the entire tensile brace capacity were a major consideration affecting the ability of the braced frame to behave as expected.

To help characterize damage potential, Tanaka, Morita, and Yamanouchi estimated the ratio of the lateral-load-resisting capacity to the total weight of the building, as shown in Equation (2.1):

$$\alpha = \frac{Q_U}{W} \tag{2.1}$$

In this equation, Q_U is an estimate of the lateral ultimate capacity, and W the weight of the building. The strength estimate is based on nominal material properties, as-built dimensions for the brace strengths, and connection details sufficiently strong to yield the brace in tension. Heavily damaged buildings had the largest value of α, scattered in the range of 0.18–0.38. Note that the intensity of ground shaking (e.g., peak ground accelerations, distance to epicenter, etc.) was not included in this evaluation of damage potential.

Another team of Japanese researchers, Kato, Tanaka, and Yamanouchi (1980), also found similar results. Their evaluations also included a more detailed survey on other steel building types, such as moment frames. Figure 2.3 plots the observed damage with respect to the α parameter and the estimated period of the structure. Although this figure represents all types of steel buildings, the majority of steel buildings in Sendai City were braced frames, and it is reasonable to assume that shorter-period structures (i.e., 0.5 sec and below) are representative of braced structures. In this figure there appears to be little relation between damage intensity (the darker circles) and the strength parameter, α. According to the researchers, this is a result of the inability of the structure to reach its intended α value, due to one or more of the premature failure modes noted above.

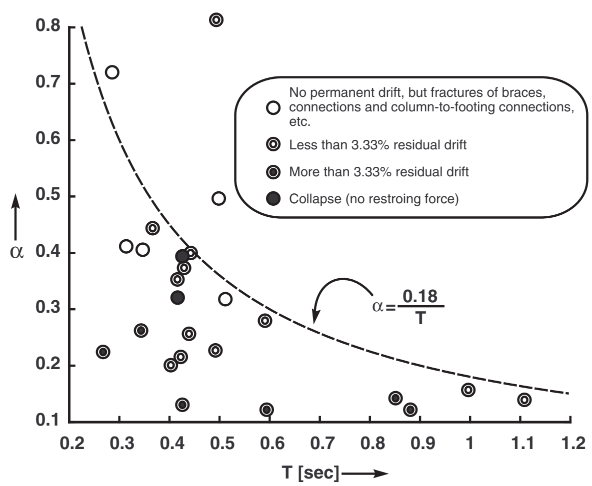

From: Kato et. al. 1980

Fig. 2.3 Relationship between period and effective strength with varying types of observed damage (Kato et al. 1980).

2.2.2 1985 Michoacan, Mexico, earthquakes (Hanson and Martin 1987; Osteraas and Krawinkler 1989)

Researchers (Hanson and Martin 1987; Osteraas and Krawinkler 1989) surveyed the performance of steel buildings in Mexico City shortly after the 1985 magnitude 8.1 and 7.5 earthquakes that occurred off the coast of Lázaro Cárdenas on September 19 and 20, respectively. This survey contained a relatively detailed review of several tall engineered steel buildings. Osteraas and Krawinkler included a brief summary of 102 steel buildings identified and surveyed by Martinez-Romero (1986). This information is condensed below in Table 2.1, which compares steel-braced-frame performance with other steel buildings. The behavior of two buildings with steel braces is described below to illustrate some specific aspects of damage.

The Atlas Edificio 21 and the Pino Suarez complex were concentrically braced steel-frame buildings that were either collapsed or irreparable after the earthquakes of September 19 and 20, 1985. Hanson and Martin (1987) reported that the Atlas building was originally constructed as a steel moment-frame building, which had been repaired and seismically strengthened with knee joints and cross bracing after a previous earthquake in 1957. This building was in the process of being demolished when the 1985 earthquake occurred; the upper seven stories of this building collapsed, along with an adjacent reinforced concrete building. It was assumed that pounding between these two buildings resulted in the collapse. The braces in the non-collapsed portion of the building appeared to have performed as intended. Little information was provided in either of the reports regarding the detailing or performance of the braces in the uncollapsed floors of the Atlas building other than that the building as a whole performed poorly.

The Pino Suarez complex consisted of five high-rise steel buildings, which were constructed on top of a subway station in the 1970s. The buildings were constructed in a row, in close proximity to one another. The row consisted of three identical 21-story buildings at the center, with identical 14-story buildings at both ends (see Fig. 2.4 for an elevation of complex). Girders in the buildings consisted of built-up trusses, and columns were fabricated from flat steel plates fillet welded into a box shape. Lateral resistance was provided by braced bays backed up by the moment-frame action of the deep truss girders welded to columns. In the longitudinal direction, two eccentrically located, full-height X-braced bays were provided. In the transverse direction, a pair of full-height, single-bay stacked chevron braces were used. Bracing consisted of built-up H sections.

Post-earthquake reconnaissance reported that one of the outer 21-story buildings fell on top of the adjacent 14-story building, leading to its collapse as well. The remaining two 21-story buildings were severely damaged, including severe column damage on the third and fourth floors, failure of the truss girder components, and failed connections where X-bracing members were spliced at their midspans.

Table 2.1 Survey of steel buildings damage (from Martinez-Romero 1986).

Type of Structure	Number of Buildings Surveyed	Summary of Damaged Observed
Moment-resisting frame	41	One building sustained severe damage, requiring partial demolition , one sustained repairable damage, and three sustained minor structural damage; the remainder were undamaged
Moment-resisting frame with braced bays	25	17 were constructed since the 1957 earthquake, of those, two collapsed totally, and one partially; four sustained varying degrees of structural damage; ten were undamaged*.
Steel frames and concrete shear walls	6	One sustained structural damage, one sustained minor structural damage, and four were undamaged.
Buildings built after 1976 (with the exception of the Pino Suarez complex)	21	One sustained structural damage, three sustained minor structural damage; 17 were undamaged.

*Note: This is biased by the Pino Suarez complex, which accounts for all three reported failures

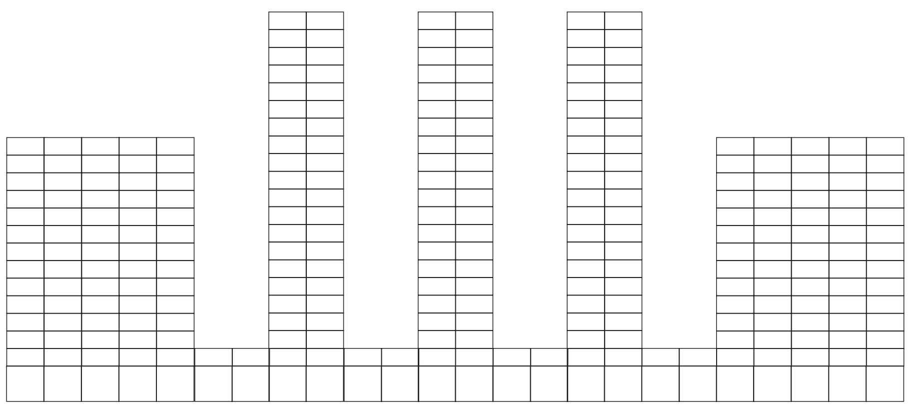

Elevation of Pino Suarez Complex

Fig. 2.4 Elevation of Pino Suarez complex (Osteraas and Krawinkler 1989).

Failures were observed in both the X-bracing and the chevron-bracing directions. X-bracing failure occurred at the midlength of the discontinuous brace at the splice plates. This damage appeared to be a result of failing to make the strength of the splice plates equal to the braces being spliced. This condition resulted in all of the tensile yielding of the discontinuous brace concentrating in the splice plates. These plates buckled when the brace was subjected to a compressive force. Low-cycle fatigue failures were observed in several of the splice plates. Connections of the braces to the beam-column connections were through fillet welded plates positioned on both sides of the brace. There was no mention of failures of these connections in either of the reports by Hanson and Martin (1987) or Osteraas and Krawinkler (1989).

The beams in the bays containing a stacked chevron consisted of truss girders. These girders suffered shear failures triggered by the vertical component of the resultant of the tension and compression forces in the braces intersecting at the midspan of the truss girder. The diagonal elements of the truss girders failed prior to the chords. Due to the large brace sizes used in the tall towers, large axial demands were induced in the columns in addition to substantial flexural and shear loading. Many of the columns buckled locally. Several of the most critically loaded columns lost axial load capacity and shortened substantially due to failure of the longitudinal fillet welds holding the section together, followed by buckling of the side plates making up the four sides of the box section.

Although there was much damage to braced steel buildings in the 1985 Michoacan earthquakes, the bracing members, connections, and lateral design forces are no longer representative of modern detailing practices in the western United States and Japan. Like the failure mechanisms evinced in buildings that were subject to the Miyagi-ken Oki earthquake, however, these cases illustrate the importance of local details and realistic estimation of the distribution of forces in the framing elements that exists when the structural system reaches its capacity.

2.2.3 1994 Northridge Earthquake (Kelly et al. 2000; Bonneville and Bartoletti 1996; WJE 1998; Naeim 1997; and Naeim 1998)

The magnitude 6.9 Northridge earthquake on January 17, 1994, caused extensive damage to steel buildings. The resulting damage found in two concentrically braced steel-frame buildings has been particularly well documented: A four-story office building located approximately 17 km southeast of the epicenter (Bonneville and Bartoletti 1996; Kelly et al. 2000), and a library at the campus of the California State University at Northridge (WJE 1998).

Kelly, Bonneville, and Bartoletti (2000) describe the damage found to a four-story office building on Lankershim Boulevard, North Hollywood. This building was designed according to the 1980 Los Angeles building code and constructed in 1986. The primary lateral system consisted of stacked chevron-braced bays. Bracing consisted of hollow steel sections (HSS), which were fillet welded to gusset plates. The gusset plates were in turn fillet welded to the beams and columns. Table 2.2 contains a summary of the brace dimensions from Kelly, Bonneville, and Bartoletti (2000), along with section slenderness ratios [the ratio shown is: (b-2t)/t; note section B.5 of the AISC (1993) permits the use of (b-3t)/t)]. As a reference, the current seismic provisions (AISC 1997) permit a value of only 16.2 for a 46 ksi nominal steel designation. Clearly, the braces on the second floor exceed this limitation by a considerable amount.

Table 2.2 Brace dimensions for HP building (from Kelly et al. 2000).

Floor Level (typ.)	Approximate ASTM Size Designation	(b-2t)/t	Area (in.^{2})
1	HSS 14x14x1/2	26	26.4
2	HSS 12x12x3/8	30	17.1
3	HSS 12x12x3/8	30	17.1
4	HSS 10x10x5/16	30	11.9

Exterior damage to this building was reported to be small, with only two broken windows and misalignment of some of the precast concrete cladding; however, the interior braced bays suffered large amounts of damage:

- beams were twisted out of plane at the beam midspan-brace connections;
- brace connections to gusset plates failed; and
- local buckling of members led to fracture of the braces at the midspan.

Brace fractures occurred either at the midspan of the brace or at the connection of the brace to the gusset plate, either at the net section or at the welded connection. Most of the damage was reported to be concentrated on the second story of this building. Considerably less damage was found on the first, third, and fourth floors. The wall partitions in the locations of the braced bays experienced noticeable cracks, with an exceptionally large bulge in the stairwell of the second floor.

Figure 2.5 shows photos taken of the building after the earthquake. Figures 2.5a–b show a complete fracture of a brace, and Figures 2.7c–d show a partial fracture at the midspan of the brace, along with severe local buckling (photos courtesy of Peter Maranian, Brandow and Associates).

This building was subsequently upgraded to meet the criteria for a special concentrically braced frame compliant with the 1994 edition of the Uniform Building Code. The retrofit scheme included using wide flange sections as braces, along with a “zipper” strut to aid in distributing the damage across several floors (Khatib and Mahin 1987).

Heavy damage was also reported at Oviatt Library at the California State University, Northridge campus (Fig. 2.6). Here, the concentrically braced frame suffered no noticeable damage with the exception of the base plates and a single brace that buckled in the east wing (WJE 1998). The lateral resisting frame consisted of X-bracing. Rather large HSS braces, not conforming to current width-to-thickness ratio requirements, were used. The columns used in the braced bays were anchored on top of a basement wall via a 4-in.-thick base plate and four to six #18 anchor bars. Bracing members were typically welded to approximately 1-in.-thick gusset plates. Figure 2.6 shows photos of damage to Oviatt Library immediately following the Northridge earthquake.

Fig. 2.5 (a) Damage photos of Lankershim Boulevard, North Hollywood, (b) complete brace fracture, (c) partial fracture at midspan, and (d) local buckling at midspan. Photos courtesy of Peter Maranian of Brandow and Associates.

(a)

(b)

(c)

Fig. 2.6 Damage photos (Finely 1999) of Oviatt Library: (a) and (b) exterior damage and (c) damage to 4-in. base plate.

Several of the anchor rods and base plates experienced significant uplift, and the authors concluded that it was very likely that the structure experienced a "rocking" mechanism during the strong ground shaking (WJE 1998). This conclusion was based on the permanent plastic elongation of the anchor rods and gaps between the bottom of the base plates and the heavily damaged mortar bed between the base plate and the top of the basement wall.

The anchor rods appeared to be designed to take only tensile forces, and large shear lugs on the bottom of the base plates were intended to transmit shear loads. It was felt that due to lack of clear detailing for the shear lugs, many of the shear lugs destroyed the mortar beds and did not allow for effective transfer of shear into the base. In most instances, brittle fractures were observed in the 3–4 in. thick base plates (Fig. 2.3c). These brittle fractures were alarming to many structural engineers, and became a landmark feature characterizing the behavior of this building by illustrating the magnitude of overturning uplift forces that may occur in braced bays and the potential brittleness of heavy welded base plates.

Only one brace was observed to have buckled laterally during the ground shaking. This brace was at the ground floor level near the base plate, and it also contained a local buckle near the gusset plate. Oviatt Library also had significant interior damage, and damage associated with loss of exterior cladding (Fig. 2.4b). The entire building was demolished after the earthquake.

Naeim (1997) and (1998) reported little to no structural damage in six instrumented braced-frame structures that experienced a modest amount of ground shaking. The responses of these buildings were recorded, and the estimates of the natural period of vibration, the change in fundamental response over time (i.e., period shift), and the estimates of roof displacement were obtained. Drifts were estimated from the integration of accelerograms, and periods were estimated using a Fourier spectrum analysis (or a moving window spectrum analysis to determine the shift in the predominant response of a structure). A description of each of these buildings is given below in Table 2.3. The approximate values of building response, and estimated fundamental periods are provided in Table 2.4 below. The values shown in this table are representative of the building response corresponding to the braced bay directions (averaged if braced bays existed in both directions).

Table 2.3 Instrumented braced frame building descriptions (from Naeim 1997).

Label	Building and Lateral Framing Description
B1	19-story office building with X-braced steel frames in the lateral direction, and moment frames in the longitudinal direction.
B2	2-story fire command building on top of base isolators
B3	3-story commercial building with unknown bracing configuration
B4	52-story office building with V braced bays around core with moment-resisting connections, along with outrigger moment frames at the perimeter
B5	6-story office building with a dual chevron and moment-resisting frame
B6	7-story university hospital with diagonally braced steel-braced frames on top of base isolators

Table 2.4 Instrumented building response (from Naeim 1997).

Label	PGA[1] (%g)	PRA[2] (%g)	Roof Drift (%)	Te[3] (sec)
B1	0.32	0.65	0.34	2.56
B2	0.2	0.77	N/A	0.2[4] / 1.14[5]
B3	0.33	0.97	0.96	0.55
B4	0.15	0.41	0.1	1.46[6]
B5	0.24	0.48	0.2	0.85
B6	0.37	0.21	N/A	0.64

[1]Peak Ground Acceleration
[2]Peak Roof Acceleration
[3]Fundamendal period from Fourier analysis of recorded data
[4]From first 15 sec of strong ground motion response
[5]From response after 15 sec
[6]It is estimated that first mode response at ~6 sec was not excited

In the 19-story office building (B1), lateral buckling of double-angle bracing was observed at the penthouse level only; the three-story commercial building (B3) experienced no noticeable structural damage, with large amounts of interior damage to nonstructural components; all other buildings had no noticeable damage. If the estimated drifts are reasonable, then it is possible that the three-story commercial building may have experienced buckling of some of its braces, as the estimated brace buckling displacement is near 0.2–0.3% for a typical braced-frame structure; however, no reports of partitions being removed for inspection were included the report by Naeim.

All other buildings appear to have responded within the elastic limit, or with little inelastic behavior, further evidenced by lack of period shift in the moving window FFT analysis of these buildings (with the exception of the base-isolated buildings).

2.2.4 1995 Hyogo-ken Nanbu Earthquake (Architectural Institute of Japan 1995, Tremblay et al. 1995)

The JMA magnitude 7.2 earthquake that occurred on January 17, 1995, exposed many problems in concentrically braced frame structures in and around Kobe, Japan. Tremblay et al (1995) performed a survey of damage to steel buildings shortly after the earthquake and reported that a majority of the bracing systems were of chevron- or single-story X-configuration. Numerous instances of slender “tension-only” brace configurations were found, but these were from buildings designed to earlier code provisions. The damage observed in this earthquake was similar in many respects to that observed in the 1978 Miygai-ken Oki earthquake.

Braced buildings designed to older (pre-1981) code provisions typically contained steel straps or bars as the primary lateral resisting elements. Many of the connections did not develop the capacity of the bracing member, and the ones that appeared to have yielded were left with a large amount of slack, leaving the structure with little lateral resistance under smaller displacements. Many steel-braced structures employing small bars and plates for braces collapsed or had large permanent residual drift.

Braced frames consistent with modern detailing and proportions also experienced considerable damage. A series of photographs (see Fig. 2.7) (Tremblay 1995) illustrates some of the observed damage in a seven-story X-braced-frame structure. In this structure, buckling in any one story was typically concentrated in one half of the brace (i.e., between the midspan where the braces intersected to the beam-column-brace connection). This is a result of the hysteretic behavior of the braces in compression, which reduces the load capacity of a brace once it buckles. Thus, the half of the brace that buckles first tends to continue to buckle, while the other half remains elastic under the reduced axial loads (see Fig. 2.7c). Gusset plate connections to the frame (see Fig. 2.7c) failed in many cases due to the inability of the connections to withstand the ultimate strength of the bracing member. Figure 2.7c illustrates the net reduced section failure of a wide flange section brace where it was bolted to a splice plate (net section failures were deemed typical of bolted brace to gusset plate connections).

A five-story parking structure in Kobe containing a two-story X-configuration was also heavily damaged. Figure 2.8 shows photos from this damaged building. Figure 2.8a shows the net reduced section failure of the brace at the connection. Figure 2.8b shows a similar connection; however, the connection experienced severe local buckling in this case. Figure 2.8c shows the location of the fracture of the brace at a beam midspan gusset connection. Figure 2.8d shows a similar connection with out-of-plane buckling of the gusset plate, and severe lateral torsional buckling of the beam. Figure 2.8e shows a gusset plate to frame connection failure. All of the failures observed in this building were attributed to improper detailing of the brace-to-frame connections.

(a)

(b)

(c)

Fig. 2.7 Single-story X-braced configuration frame with bolted wide flange bracing members: (a) damage concentration in single leg of brace, (b) gusset plate to column connection failure, and (c) net section failure at midspan. Photos courtesy of Professor Robert Tremblay, Ecole Polytechnique, Montreal, Canada.

(a)

(b)

(c)

(d)

(e)

Fig. 2.8 Damage to two-story X-configuration building: (a) net section failure, (b) local buckling at net section, (c) connection fracture at midspan, (d) connection failure to beam and out-of-plane buckling of connection, and (e) failed connection to frame. Photos courtesy of Professor Robert Tremblay, Ecole Polytechnique, Montreal, Canada.

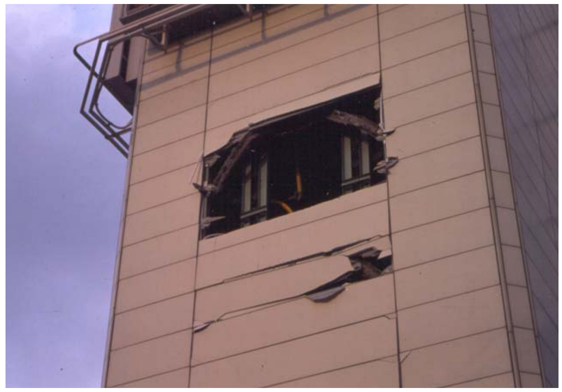

Fig. 2.9 Out-of-plane buckling and subsequent shedding of exterior cladding. Photo courtesy of Robert Tremblay, Ecole Polytechnique, Montreal, Canada.

Another issue observed with buckling of conventional braces is illustrated in Figure 2.9. In this photo, the exterior cladding from a parking structure detached from the building as a direct result of the out-of-plane buckling of the conventional bracing system, creating a potential hazard for pedestrians below.

Typical damage observed in the Ashiyahama residential complex is shown in Figure 2.10. The Ashiyahama complex is a series of 14-, 19-, 24-, or 29-story structures built on a 50-acre reclaimed section of Ashiya City. A total of 3400 high-rise apartments were built on this site. The structural system consisted of “mega-trusses,” as can be seen in Figure 2.6. During the Hyogo-ken Nanbu earthquake, widespread brittle-appearing cracks occurred throughout the complex.

The Architectural Institute of Japan Task Force that inspected the Ashiyahama complex identified three types of damage (AIJ 1995): (a) fracture in the base metal above the column splice connection (see Fig. 2.10b), (b) fracture of the column at the welded splice, and (c) fracture at the column to brace connection where the fracture extended into the column (see Fig. 2.10c). Other fractures observed by Tremblay et al. (1995) and others included failure at the brace-to-column connection where the fracture did not extend into the column.

Although the damage observed in the buildings mentioned above was significant, some properly detailed buildings performed quite well. Tremblay et al. noted that of the 452 damaged braced frames, 29 collapsed (6%), 141 had severe damage (31%), 134 sustained moderate damage (30%), and 148 (33%) had only minor damage.

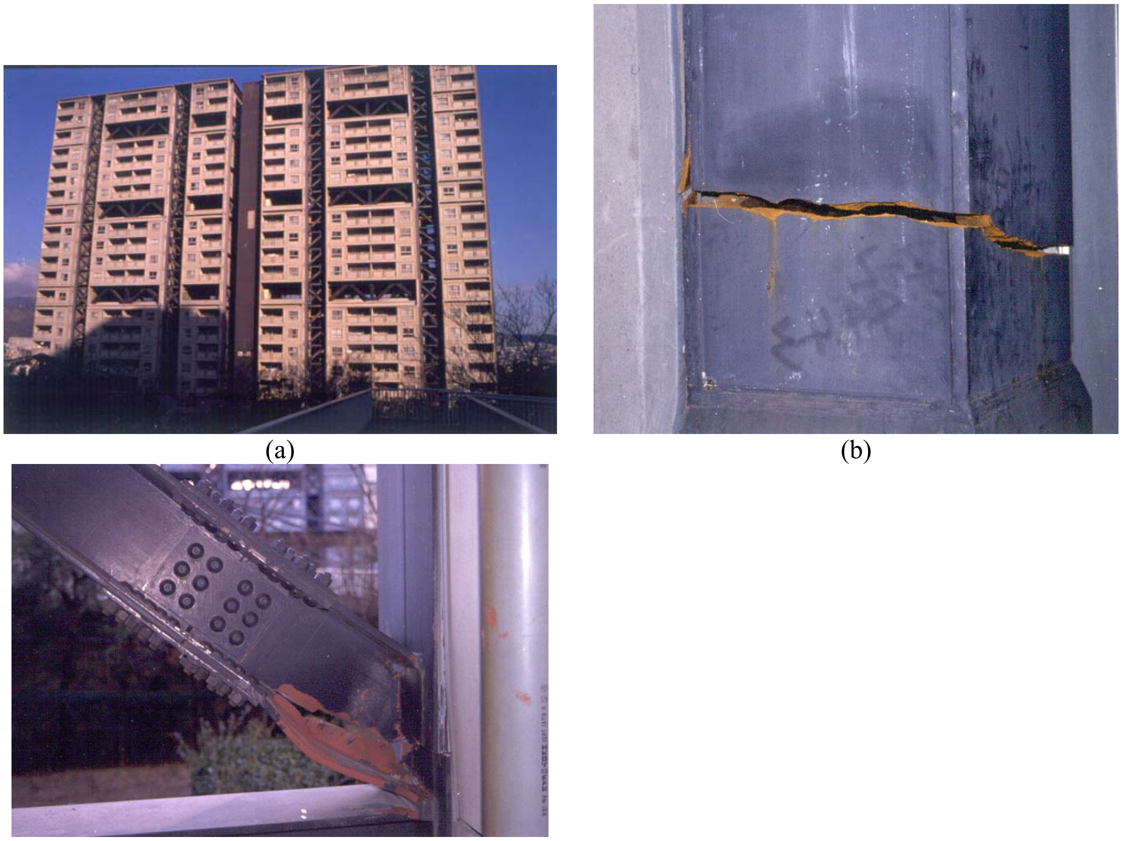

(a) (b) (c)

Fig. 2.10 Ashiyahama residential complex: (a) partial elevation, (b) typical column damage observed, and (c) typical brace-to-column connection failure. Photos courtesy of Robert Tremblay, Ecole Polytechnique, Montreal, Canada.

2.2.5 Summary

Recent earthquakes have illustrated several recurring problems associated with typical detailing and proportioning of steel-braced frames. When details were provided so that the brace could develop its full strength (both in tension or compression), it was common that out-of-plane brace buckling caused either severe damage to partitions or shedding of exterior cladding, or damage (often leading to complete or partial fracture) to braces at the midspan or at the net section. The limited number of discreet sizes available to proportion braces also appears to result in identical bracing members being used in consecutive floors, perhaps leading to a concentration of damage in the lowest story where braces with identical strength are used (e.g., the four-story braced frame in North Hollywood).

Past performance in earthquakes has also exposed what appears to be a lack of understanding of the distribution of internal forces in braced frames undergoing large lateral displacements. For example, the Oviatt Library saw large ground excitation; however, due to failure at the base of the structure, little interstory drift was observed in the braced bays (evidence of buckling was observed in only one brace). Although the braced-frame building located in North Hollywood appeared to have relatively slight exterior damage, most likely due to small interstory drifts experienced in the structure, analytical studies (Chapters 3 and 6, Khatib et al. 1988); Sabelli 2000) have predicted lateral drifts on the order of 3% for design-level ground shaking. With the increase in popularity of similar proportioning and detailing, the magnitude of potential damage is unclear in the event of a large earthquake in a large metropolitan city (i.e., San Francisco, Oakland, or Los Angeles, California), where this class of building is now more densely stocked. Greater understanding of these systems, primarily through experimental testing, are necessary to define their potential performance.

2.3 EXPERIMENTAL TEST RESULTS

Some background on experimental research pertaining to concentrically braced frames, including large- and small-scale model testing, subassemblage testing, and brace component testing is provided in this section. Recent comprehensive literature surveys have been prepared on the behavior and design of gusset plates (Astaneh-Asl 1998; Chambers and Ernst 2005), and will consequently not be discussed here.

2.3.1 Conventional Bracing

Summaries of experimental results performed on conventional braces were prepared recently by Tremblay (2002) and Lee and Bruneau (2005). Some of the earliest tests characterizing the behavior of steel braces and braced frames under cyclic loading were undertaken by Wakabayashi (Wakabayashi et al. 1977, 1971, 1973). These tests were conducted using relatively small-scale members and sometimes very short lengths; however, the effect of different slenderness ratios on hysteretic behavior was examined.

After a series of investigations on steel tubes and pipes (Sherman 1976), tentative criteria for structural applications of steel tubing and pipe were released (Sherman 1977). The commentary provided in the tentative criteria included a summary of the results from a series of compressive axial tests on round and rectangular hollow steel sections (HSS). These tests were used as the basis of design curves for hollow sections having a given yield strengths and varying slenderness ratios. This document also summarizes the effect of residual stresses typically found in HSS sections, and provides analytical expressions to derive allowable critical compressive stresses in the members accounting for these residual stresses. Along with axial behavior and characteristics of hollow sections in compression are also provisions for the allowable stress design of these members for torsion, flexure, combined loading, and even drag coefficients for wind-loading applications. It is important to note that of the tests performed, cyclic testing was not included.

Kahn and Hanson (1976) performed tests on small steel bars (1 x 0.5 in.). These tests were based on *kl/r* ratios ranging from 85 to 210. Tests of these bars were applied cyclically at both dynamic and quasi-static rates. The main thrust of these experiments was to determine the effect of dynamic loading on the axial-force axial-deformation relationship. It was determined that the dynamic and static loading cases produce nearly identical hysteretic relationships.

Jain and Goel (1978) reviewed a series of brace tests using relatively small-scale cold-formed sections that covered a wide range of effective slenderness ratios. These results were used to calibrate an analytical model for modeling the effect of brace behavior.

One of the earliest shaking table experiments on concentrically braced steel frames was conducted at the University of California, Berkeley (UCB), by Ghanaat (1980). The three-story, 3/5-scale moment-frame specimen was designed for wind loading. It provided a test-bed structure to analyze the behavior of different bracing systems: rod X-braces (*kl*/*r*=370), ¾-in. diameter pipe X-braces (*kl*/*r*=125), and double-angle X-braces (*kl*/*r*= 86). As a comparison, the moment frame without braces was also tested. This report concluded that the addition of braces designed primarily for wind can be effective in resisting intermediate-intensity earthquake-induced shaking; however, the observed drifts were quite large with substantial damage to bracing elements. It was noted that the pinched hysteretic behavior of all of the braces tested were undesirable for larger-magnitude earthquake loading, and it was conjectured that taller structures, where large P-Δ effects may be encountered, might be prone to collapse.

Tests representative of 1/6-scale tubular steel braces from a Southern California offshore platform (Zayas et al. 1980b) were performed in support of subsequent cyclic inelastic tests on two complete 1/6-scale structures (Zayas et al. 1980a). The structures consisted of two full-height X-brace stacked panels, with a final half-height panel with an inverted chevron-braced configuration. These cyclic tests were followed by a shake table test (Ghanaat and Clough 1982) and pseudo-dynamic tests (Shing and Mahin 1984) on the same structure. The brace component tests contained both fixed-ended and pin-ended configurations to bound actual boundary conditions expected in offshore platform construction. The round pipes were made of AISI 1020 mild steel tubing, which is produced using a drawing process and which changes the material properties significantly (specifically the yield strength). For this reason, four of the specimens were annealed to more closely match properties of full-scale construction material. Comparisons of D/t ratios of 33 and 48 were made.

In both D/t cases, after local buckling began, there was a rapid deterioration in the hysteretic behavior and loss of strength. It is important to note that local buckling for the more compact section initiated significantly later, leading to a significantly larger normalized energy-dissipation capacity. The members that were not annealed suffered significant damage in earlier cycles. The subsequent cyclic frame tests contained annealed pipes with D/t ratios of 33 and 48. These specimens demonstrated the great significance of the D/t ratio on the global hysteretic behavior of the specimen. As also seen in the component tests, the frame with the lower D/t ratios outperformed its less compact counterpart, resulting in better global behavior. Another important observation that was similar to observations from past earthquakes is that the damage is concentrated in one half of a brace along the full diagonal. This led to further concentration of damage in the portion of the brace that buckled during subsequent cycles.

Shake table tests of a nearly identical specimen were performed in the earthquake simulator laboratory at UCB. During the shake table tests, the buckling mechanism that formed in the upper panel of the platform caused such a large reduction in force that the lower panel did not undergo any buckling damage. This caused a concentration of drifts in the upper panel, which was not observed in the pseudo-dynamic tests. This may be due to slight differences between the specimens (material properties) or the different loading history used. Similar to the observed behavior in the pseudo-dynamic test and observations from previous earthquake reconnaissance, only one half of the X-brace acting in compression buckled in the top panel.

Researchers at UCB conducted a series of tests on the inelastic behavior of other sections that are commonly used as struts (Black et al. 1980). Twenty-four specimens were tested varying the effects of slenderness (40-120), cross-sectional shape (wide flange, double-angle, hollow square tubes, and round tubes), and end conditions. These tests chiefly demonstrated that slenderness, regardless of cross-sectional shape, dictated the basic inelastic envelope of the strut. Another important finding was the high variability in the steel material properties. Although all specimens were intended to have the same strength, the strength values at 0.2% strain offset ranged from 24 ksi to more than 80 ksi for hollow tubes and pipes.

In 1985, a series of nine full-scale specimens were tested at the University of Michigan to explore possible designs for gusset plate connections for angle and double-angle braces (Astaneh-Asl et al. 1985). The members were tested in an assembly that applied loading at a 45° incline. Each of the bracing elements was constructed of double angles, with bolted or welded stitches along the length. Connections to the gusset plate consisted of bolted or welded connections to the gusset plate. In each of the tests, three plastic hinges formed along the bracing members, one at the midspan of the brace and one at each gusset plate. It was observed that the occurrence of local buckling in the central plastic hinge led to rapid strength deterioration, and that the limiting b/t ratio for the outstanding legs of angle braces, as given by then-current specifications, was adequate. A free length beyond the brace in the gusset plate was introduced, which formed a plastic flexural hinge in the gusset plate exhibiting excellent hysteretic behavior. This gusset plate formed buckled shapes similar to those of pin-connected assemblies (i.e., $k \approx 1.0$). Design recommendations were also introduced for the design of the stitches along the length of the member.

Experimental studies at the University of Michigan (El-Tayem and Goel 1985) studied the effect of single-story X-bracing for use in seismic applications. A comparison of single-angle braces and double-angle braces was performed. In all of the tests, only one half of the total brace buckled in compression (as noted earlier from field and laboratory data for single-story X-braced configurations). This study also reported that the effect of single-angle or double-angle shape did not greatly affect the hysteresis loop; however, local buckling led to rapid degradation of the moment capacity of the connection and, subsequently, the lateral strength of the entire subassemblage. The gusset plate details used were adapted from previous studies (Astaneh-Asl et al. 1985), and these connections behaved as expected. In general, failure mechanisms occurred typically at locations of local buckling or plastic hinging in the brace, and on a few occasions, they were due to fatigue failure of gusset plates or fracture of the welds connecting the brace to the gusset plate.

Because of the tendency for failure to occur soon after local buckling occurred, a series of studies at the University of Michigan were conducted to study the effect of (1) filling hollow square tube sections with varying strengths of concrete to resist local buckling; (2) using small angles welded along each face of the HSS tube to help resist local buckling; and (3) the effect of slenderness ratios on the global hysteretic behavior (Gugerli and Goel 1980b; Lee and Goel 1987; Liu and Goel 1988). It was concluded that less slender members undergoing the same displacement history as more slender elements experienced earlier local buckling and subsequently fractured earlier during identical displacement histories. This was due to the increased rotational demands at the plastic hinges in the less slender elements. In the case of sections whose width-to-thickness ratios were approximately 30, the effect of filling hollow tubes with concrete did not considerably help the performance of tubes with identical displacement histories. It was also observed that the addition of concrete did not delay the initiation of local buckling; however, the magnitude of the local buckling was influenced by the presence of concrete in the hollow tubes.

The behavior of the braces also proved to be very sensitive to the loading history. One of the tested braces contained small angles, which were welded to the center of each of the four sides along the entire length of the brace. This angle was provided as a stiffener and was intended to limit the onset of local buckling in the section. This detail resulted in much fuller hysteretic curves and delayed the failure compared to its non-compact counterpart by several cycles. This particular detail was thought to be too costly for typical construction. In the tests conducted by Lee (1987), fractures occurred in each of the compact hollow members where maximum drifts corresponded to, on average, 1.8% drift. Corresponding concrete-filled tubes, fractured on average in loading histories that experienced maximum drifts of roughly 2.5%.

Equations predicting the fatigue life of HSS square braces and concrete-filled HSS square braces were developed on the basis of this series of tests (Lee and Goel 1987a; Liu and Goel 1988a). These relations suggested that the portion of loading excursions where the tensile forces were large was far less damaging compared to small tension forces.

In 1980, a U.S./Japan Cooperative Research Program on Earthquake Engineering Utilizing Large Scale Test Facilities was initiated between the U.S. National Science Foundation, and the Japanese Ministry of Construction and the Science and Technology Agency (Hanson 1989). The steel specimens for this research program contained both conventional concentrically and eccentrically braced framing systems. The intent of these studies was to provide large-scale tests of typical designs, and establish a relationship for reduced-scale experiments, validate and improve analytical models, and recommend provisions to adopt into code.

One-half-scale tests were conducted as prototype specimens for future full-scale tests on a chevron-configured frame (Fukuta et al. 1989). Six concentrically braced specimens were tested to observe the effect of in-plane versus out-of-plane buckling, beam versus column mode of failure for collapse, and the effect of the slenderness ratio (l/r = 70–120). Static cyclic loads were applied such that the relationship between the column axial force and the lateral shear force were maintained constant. These studies demonstrated that the compact braces [$(b\text{-}2t)/t = 6$] provided an excellent means of dissipating energy, and that the global hysteresis loops were similar to those of the moment frames. The members with slender sections [(b-2t)/t > 20] experienced severe local buckling. The experimental assemblies had difficulty in reaching the tensile capacity of the brace due to large midspan beam deflections.

Along with half-scale tests in Japan, two smaller-scale specimens were constructed in the United States, one at Lehigh University (Lee and Lu 1989), the other at Stanford University (Wallace and Krawinkler 1989). The conventionally braced-frame studies conducted at Lehigh were conducted at 0.305 scale, and all beams and columns were made as exact models of the prototype specimen. Thus, dimensionless parameters like width-to-thickness ratios were preserved. Beams and columns were manufactured from flat steel plates using a TIG welding process. Hollow tubular braces were manufactured using two flat plates that were bent to 90° angles and welded together. Lateral loads proportional to the first mode were applied to the model specimen to achieve a target displacement protocol. Early in the displacement protocol, the braces on the fourth floor fractured and were repaired for subsequent testing. The basic damage patterns observed in the subsequent full-scale tests were very similar; however, it was noted that the small-scale tests used precluded failures in the joint regions.

Similar studies to assess the veracity of small-scale tests were conducted as part of the U.S.-Japan collaboration at Stanford University (Wallace and Krawinkler 1989). A 1:12.5-scale model of a six-story braced-frame structure was created to further study scale effects, and to determine feasibility of small-scale (i.e., less expensive) testing. The tests exhibited similar performance to those reported by Fukata et al. (1989). It was concluded that the overall nonlinear dynamic response characteristics could be reproduced quite well using small-scale models; however, it was not possible to capture localized failure modes using these small models. As such, it was concluded that localized failure modes, which influence global behavior of braced buildings, could not be adequately considered in reduced-scale specimens.

Full-scale, pseudo-dynamic tests of a concentrically braced frame were conducted at the large-size testing laboratory of Building Research Institute (BRI), in Japan. A two-bay (one bay contained bracing) by two-bay six-story structure was constructed to be tested with unidirectional loading applied parallel to the direction of the braced bay. The braced bay consisted of hollow square braces connected directly to the beams and columns by means of full-penetration welds. A stacked chevron configuration was utilized for the bracing system. The construction was compliant with the U.S. code applicable at the time, and the construction process was inspected as would be done for a normal building. Gusset plates, which might have encouraged out-of-plane buckling and free rotation at the ends of the brace, were not utilized for this test structure. Instead, the connection was assumed to have fixed ends ($k \approx 0.5$). Table 2.5 contains a schedule of the brace sizes used in the tests. Because the concentrically braced frame configuration was an initial part of a larger series of tests, peak displacements were limited. Because no preferred direction of buckling was imposed by the brace end details, some lateral buckling of the braces occurred in the out-of-plane direction, and some of the buckling occurred in the in-plane direction. The first-floor braces buckled in plane and suffered significant damage at the plastic hinges, including tearing of the steel. The second-story braces buckled out-of-plane and were partially torn at the plastic hinge section. The first- and second-story braces fractured at interstory drifts slightly over 1%. The third-story braces buckled in plane and fractured at an interstory drift of roughly 0.7%. Damage to the frame other than at the braces needed to be limited. As such, the testing of the concentric frame was discontinued once the brace on the third floor ruptured (at 11.37 sec into the record). The drifts at which this test was stopped were far smaller than the maximum drifts permitted today by modern design codes (ICC 2003).

Table 2.5 U.S./Japan frame brace schedule.

Story	Brace	(b-2t)/t	kl/r (approx.)
1	6x6x1/2	10	57
2	6x6x1/4	22	34
3	6x6x1/4	22	34
4	5x5x1/4	18	49
5	4x4x3/16	19.3	61
6	4x4x3/16	19.3	61

A 0.305-scale model of the entire building tested at BRI was constructed and subjected to a single component of earthquake ground excitation on the UCB earthquake simulator (Bertero et al. 1989). This model structure contained slightly improved details at the connection to those of the full-scale specimen tested at BRI. This particular structure was designed to be a dual system with a ductile moment-resisting space frame (DMRSF) contributing to 50% of the design base shear. The input ground motion used was the north-south component of the 1978 Miyagi-ken-Oki earthquake. The largest excitation of this braced frame was this record scaled to 65% peak ground acceleration, representing a "collapse limit state" for the structure. During this test, the braces in the bottom five stories buckled either in plane or out of plane; one brace in the fifth story ruptured at the midspan at a drift of about 1.3%; one brace in the fourth story ruptured at the connection. This resulted in a maximum interstory drift of 1.9% in the fifth floor; other floors experienced drifts on the order of 1–1.5%. It was concluded that if limiting the width-to-thickness ratio of tubes was prohibited below a value of 18, then a dual system (DSMRF and concentrically braced steel frame) can effectively dissipate input seismic ground excitation provided that the DSMRF is designed for nearly 50% participation of the lateral design force. The recommended provisions at that time (ICBO 1979) required only 25% contribution from the DSMRF, which appeared to be unrealistic given the large drifts experienced on the fifth floors that were designed with a DSMRF of 50% contribution.

Researchers at the Politecnico di Milano, in Milan, Italy (Ballio and Perotti 1987) conducted a series of experiments to develop and validate analytical models for inelastic buckling braces in seismic applications. These experiments contained reduced-scale concentrically braced structures in single-diagonal and single-story X-braced configurations using either double angles or double channels placed back-to-back. The interesting observation from these tests was that the center "pin" connection used in the single-story X-configured specimens allowed for in-plane buckling of the members in a second fundamental mode shape, thus spreading damage over both halves of the brace in compression. (This novel connection would most likely not satisfy the net section criteria in current codes.) Connection detailing at the ends of the specimen was highly idealized, as were the connections of the surrounding frame.

Canadian researchers at the Ecole Polytechnique, Montreal, have more recently performed a large series of tests on concentrically braced steel frames using modern construction details similar to those found in the United States (Archambault 1995; Tremblay et al. 2003; Tremblay et al. 1995; Tremblay and Filiatrault 1996). In these tests, a series of 14 single-diagonal and 10 single-story X-configurations were tested in a single-story single-bay testing rig. The rectangular hollow section braces tested in this configuration had relatively low width-to-thickness ratios (8.9–13.8), where the width to thickness ratios are calculated by using the equation: $(b\text{-}3t)/t$. The slenderness of the braces, computed from gusset plate plastic hinge to gusset plate plastic hinge, were in the range of 100–160, and 60–110 for the single-diagonal and single-story X-braced configuration, respectively.

As evidenced in previously described tests, the single-story X-configuration concentrates buckling and related damage in only one half of the compression brace. Thus, the plastic rotation demands in the plastic hinges are increased, leading to earlier initiation of fracture. Total normalized hysteretic energy dissipated by the single-diagonal configurations was greater than those of the single-story X-bracing configurations. These results again highlight the strong correlation between fatigue life and the effective slenderness ratio of a brace. A maximum target displacement of 5 times the tension yield displacement was intended for each of the braces. Using the geometry shown in the reports results in a peak displacement drift of about 1.9%. The experiments were continued until each of the braces ruptured. It is important to note that few specimens reached drifts larger than 1.5% prior to fracture.

Uniaxial cyclic tests were performed on nine hollow structural sections that were allowed to buckle out of plane and were designed to meet the Canadian criteria for slenderness and width-to-thickness criteria (Shaback and Brown 2003). All of these tests had rectangular gusset plates with a free length from the end of the brace to the end plate that varied from 1.5 times the thickness of the gusset plate to 2 times the thickness of the gusset plate. The end plate was oriented perpendicular to the brace's longitudinal axis. All gusset plates behaved in a ductile manner, as intended. These test results were used along with other previous data to establish new, "statistically reliable" expressions to define the fatigue life of a brace, as well as the peak out-of-plane deflections as a function of the axial deformation. The proposed fatigue criteria offered a reduction of 50% in the standard deviation when compared to criteria developed earlier by Lee and Goel.

Researchers at the University of Buffalo tested ½-scale single-diagonal and single-story X-brace configurations using hollow square tubes and solid rectangular bars. These tests were performed to demonstrate the effect of using channels installed on both sides of the bracing system in the plane of the braced bay to restrain out-of-plane buckling of the members (Celik et al. 2004) . These cold-formed channels permitted second mode buckling of members when they were installed; however, the increased plastic rotation in the hollow members led to premature fracturing of the braces during earlier cycles when compared to the non-restrained members (ductility of 4 versus 6). The cold-formed channels were sized to restrain the hollow sections from buckling and, as a result, substantially strengthened and stiffened the assembly. Typical failure mechanisms for the braces involved plastic hinges, eventually leading to local buckling and rupture at the local buckle. The hollow unconstrained brace fractured at a drift of 2.8% where the constrained brace fractured at a drift of roughly 1.9%.

Yang and Mahin (2005) studied the effect of net section reinforcement, varying loading protocol, and modern connection detailing on 6 full-scale uniaxial braced specimens. The specimens consisted of a single 6 in. diameter extra-strong pipe, and 5-6×6×3/8 in. hollow structural section. The tests of the first three specimens were identical. They were of rectangular cross section and did not contain reinforcement of the net reduced section. The first specimen was loaded using a history representative of response to a near-fault motion where the brace was subjected to a moderate tension excursion followed by a large inelastic compression cycle causing lateral and local buckling at the midspan. Subsequent smaller amplitude displacement reversals led to concentration of damage at the midspan, where subsequent rupture occurred. The second and third specimens used different loading protocols. One was a near-field motion where a small compression excursion was followed by a large inelastic tension deformation. The third specimen was subjected to a more typical history where cycles were imposed having increasing amplitude with time. The loading protocol for the second and third braces induced tension failure in the net reduced section areas, resulting in less than expected ductilities at the time of fracture for these specimens. The net section reinforcement was designed and placed on otherwise identical braces. Two more braces were tested with the net reduced sections reinforced. The net section reinforcement consisted of 4 in.×3/8 in.×12 in. long A36 steel plates fillet welded to either side of the brace at the net section. The plates were designed such that the net section would pass net section criteria of the AISC (1993) provisions. The specimens were given the identical displacement loading histories as the unreinforced sections; the results showed a significant increase in energy dissipation when compared to braces without net sections.

Several other tests had previously identified potential difficulties being introduced by the net reduced area occurring at the end of the gusset plate (Archambault 1995). In some cases, wrapping the fillet weld used to connect the gusset plate to the braces around the tip of the gusset plate was sufficient to avoid fracture in the absence of special reinforcement; however, the presence of a long slot at the end of the gusset plate or poor workmanship resulted in the fracture of several these wrap-around welded connections at the net reduced section region.

Many of these tests of individual braces have been summarized by Tremblay (2002) and Lee and Bruneau (2005). Tremblay examined the effect of the slenderness ratio, the section shape, the loading history, and other properties on the initial buckling capacity of the brace; the compression strength remaining when various amounts of normalized axial shortening were imposed; the amount of lateral displacement as a function of axial shortening; the amplitude of cyclic deformation when rupture occurred; and so on. Tremblay notes that braces are often stronger than predicted using code equations, and that this difference should be accounted for in analytical studies of performance. Similarly, the larger normalized displacements reached in compression for relatively slender braces prior to rupture suggested that more stringent width-to-thickness criteria would be appropriate for stocky braces.

Lee and Bruneau (2005) used virtually the same database, but focused on the deterioration of buckling load and energy dissipation in each cycle, from cycle to cycle, as a function of the slenderness ratio, the imposed deformation history, and the section shape. They conclude that tubular braces deteriorate slower than do non-tubular sections, especially in comparison with W-sections with slenderness ratios greater than 80. Interestingly, their results suggest that while more slender braces may be able to undergo larger inelastic displacements, the strength and energy-dissipation capacities deteriorate substantially during these excursions.

2.3.2 Buckling-Restrained Braces

Because of the large amount of literature on buckling-restrained braces, the reader is referred to Uang and Nakashima (2003) for a more detailed summary on the background and history of the buckling-restrained braced frame. This section provides a brief synopsis of current experimental work in the United States, Japan, and Taiwan.

As noted in the previous section, conventional bracing and bracing details that permit lateral buckling produce asymmetric axial displacement–axial force hysteretic relationships that degrade and exhibit limited ductility capacities. For this reason, many efforts have been undertaken to restrain global buckling of seismic bracing (Watanabe et al. 1988). The fundamental concept behind buckling-restrained braces (BRBs) is to restrain global buckling modes, creating full and stable hysteretic loops under tension-compression cycling; initial buckling-restrained braces achieved this behavior by placing an unbonded ductile steel core within a concrete-filled steel tube.

Uniaxial tests on these types of systems have demonstrated smooth and stable hysteretic loops, capable of many, large, inelastic displacement cycles (Black et al. 2002; Clark et al. 1999; Merrit et al. 2003; StarSeismic 2005; Uang and Nakashima 2003; Wada et al. 1998; Wakabayashi et al. 1977; Watanabe et al. 1988). These experiments have shown the reliability of these braces when tested under uniaxial loading conditions. Typical brace to gusset plate connections include braces bolted to end connections or gusset plates, while others employ pin and clevis details (StarSeismic 2005).

Tests on simple subassemblages incorporating BRBs have shown similar brace behavior; brace hysteresis are smooth and stable, even when undergoing large rotations at brace ends; however, some undesirable behavior was reported in and around the gusset plate connections to the beam-column framing (Roeder et al. 2005; Tsai et al. 2004; Weng et al. 2005). Some tests resulted in premature failure of gusset plates in the form of out-of-plane buckling (which were subsequently retrofitted with stiffeners) (Tsai et al. 2004; Weng et al. 2005); others reported fractures at either the gusset-to-column or gusset-to-beam connection (Roeder et al. 2005).

2.4 CONCLUDING REMARKS

Reconnaissance investigations following several recent earthquakes have pointed out the relatively high rate of failure of traditional concentrically braced frames. A variety of failure modes have been noted, such as those associated with connections and details unable to develop the full tensile capacity of the braces, and local buckling and fracture of plastic hinge regions at the midspan of buckled braces. While modern codes in the United States require connections in special concentrically braced frames to develop the strength of braces, it is not clear whether current details are able to achieve this goal reliably. In addition, past tests suggest that the interstory-drift and fatigue-life capabilities of braces compliant with current SCBF requirements may not achieve demands associated with updated earthquake hazard information. Tests and post-earthquake reconnaissance investigations suggest that concentrically braced frames with relatively robust braces may be susceptible to a number of other failure modes, including fracture of the connection of the gusset plates to the supporting beams and columns, failures in columns or base plates.

Recent tests in the United States, Japan, and Taiwan demonstrate that buckling-restrained braces exhibit highly stable, ductile behavior with substantial resistance to fatigue failures. Having said that, some tests indicate that BRBFs may be susceptible to premature failures because of instability of the gusset plates or fractures in the vicinity of the gusset plate to framing member joints, and unanticipated yielding and fracture in base plates. Thus, the consequence of these various behavior modes on the performance of modern concentrically braced frames, and the efforts to mitigate the premature behavior modes that prematurely limit the capacity of the structural system need to be investigated.

3 Preliminary Seismic Performance Assessment of Concentrically Braced Steel Frames

3.1 INTRODUCTION

Few analytical studies have been carried out to assess the likelihood of concentrically braced frame systems achieving targeted performance goals, such as collapse prevention or continued occupancy, for seismic excitations representative of the total seismic hazard present at a particular site (Moehle et al. 2005). More commonly, analytical studies (Goel and Tang 1987; Jain and Goel 1979; Khatib et al. 1988; Sabelli 2000; Tang and Goel,1989; Zayas et al. 1980a) have focused on the seismic demands developed by various configurations of concentrically braced frames for relatively small ensembles of earthquake ground excitations.

Recent studies have begun to consider sets of ground motions selected to be representative of particular seismic hazard levels (i.e., 10% probability of exceedance in 50 years) at a specific site. For example, in a recent study of modern three- and six-story code-compliant concentrically braced steel frames, Sabelli (2003) used the SNAP-2D computer program (Rai et al. 1996b) to predict the response of a variety of SCBF and BRBF frames to sets of ground motions representative of metropolitan Los Angeles. These prototype structures were designed according to the 1997 *NEHRP Recommended Provisions for Seismic Regulations for New Buildings and Other Structures* (FEMA 302/303) (FEMA 1997b; FEMA 1997c) and the 1997 AISC Seismic Provisions (AISC 1997). The structures had the same basic configurations and non-seismic loading conditions as used in FEMA studies to develop guidelines for steel moment-resisting frames (MacRae 1999). A variety of SCBF and BRBF configurations were considered, including those shown in Figure 3.1.

For the SCBF systems square, hollow steel sections were employed for the braces. The SNAP-2D braced model was calibrated to mimic experimentally obtained hysteretic loops corresponding to the cross section and slenderness of the particular braces used (Black et al. 1980). A low-cycle fatigue model in SNAP-2D was used to remove braces from the model when their estimated fatigue life was exceeded. Buckling-restrained braces were represented by bilinear hysteretic springs, with properties selected to represent characteristics of BRBs observed in tests. In both cases, the braces were assumed pin ended, and the beams were idealized as being pin-connected to the columns. A simple "flagpole" column, extending over the full height of the structure, was used to represent the lateral stiffness of the remaining gravity-only framing. Viscous damping was assumed to be 5% of critical. The structural models were analyzed using suites of horizontal components of ground motions developed previously by Somerville for use in the FEMA/SAC project on steel moment-resisting frames (Somerville 1997). These suites consist of three sets of 20 pairs of horizontal ground acceleration records adjusted so that their mean spectral response matched the seismic hazard estimated by U.S. Geological Survey for downtown Los Angeles on soil type S_D corresponding to 50%, 10%, and 2% probabilities of exceedance in a 50-year period.

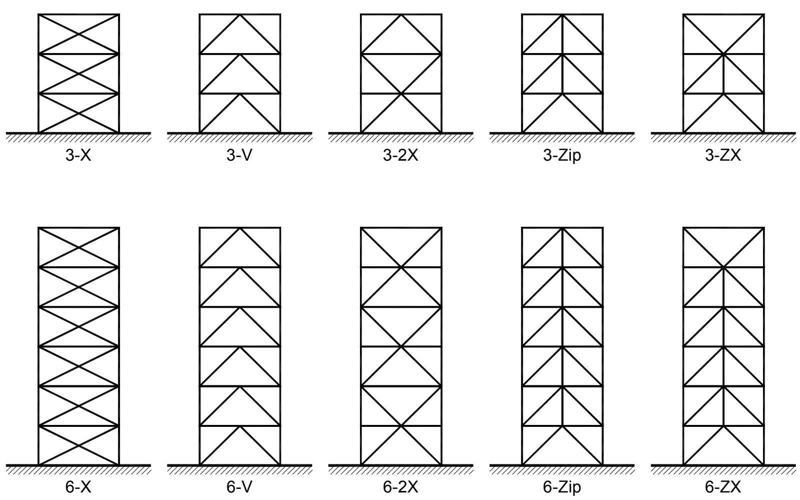

Fig. 3.1 Schematic drawing of some of 3- and 6-story SCBF frames considered (Sabelli et al. 2003).

Table 3.1 Response summary for 10% in 50-year events (Sabelli 2000).

Frame		Brace Ductility		Cumulative Brace Ductility		Interstory Drift Ratio %		Residual Interstory Drift Ratio %	
		Mean	+1σ	Mean	+1σ	Mean	+1σ	Mean	+1σ
6	BRBF	10.7	14.5	83	135	1.6	2.2	0.7	1.1
	SCBF	Braces fracture for 6 out of 20 records				1.8	2.6	0.4	0.7
3	BRBF	9.7	13.6	39	64	1.4	2.1	0.5	1.0
	SCBF	Braces fracture for 14 out of 20 records				3.9	7.0	2.5	5.6

Table 3.1 summarizes some of the results obtained from the analyses. The interstory drift ratios presented are computed as the maximum peak value of interstory drift between two adjacent floors, at any story over time, normalized by the relevant story height. The residual interstory drift index is the largest absolute value of the differences in lateral displaced shapes at two adjacent floors computed for all stories at the end of the earthquake, normalized by the relevant story height. The ductility values for the buckling-restrained braces are qualitative indices of brace damage, and are based on the peak total axial deformation or the cumulative inelastic axial deformation of each brace normalized by the deformation of the brace at first yield in tension. Average and average plus one standard deviation results are presented based on the maximum values obtained over the height of the building for each of the earthquake records.

The results of these analyses show that ground motions representing a 10% probability of exceedance in 50 years produced in a six-story chevron-configured SCBF an average peak interstory drift index of about 1.8%, approximately 12% larger than those in a comparable frame containing buckling-restrained braces (BRBFs). When the height of the structure considered was reduced to three stories, the SCBF system developed an average drift index of 3.9%, about 180% greater than that in a comparable BRBF. In comparison, separate analyses (MacRae 1999) indicate that a comparable three-story code-compliant special moment-resisting frame would develop a median peak drift of only about 1.3% for the same ground motions. Thus, it appears that the initially stiffer and stronger BRBFs have drifts similar to moment frames at this excitation level, while those for the three-story SCBFs are significantly larger. A number of factors could lead to this behavior; for instance, the initial period of the three-story braced frames is short enough that inelastic displacements might be expected to exceed values predicted by elastic analyses on the basis of conservation of energy principles (Newmark and Hall 1973). The even larger drift demands for the SCBF might be attributed in large part to the greater deterioration and low-cycle fatigue failures of the conventional braces. By comparing the average and average plus one standard deviation results in Table 3.1, one can see that there is a tremendous scatter in predicted response, indicative of the complex nonlinear response exhibited by these systems.

These interstory drifts are typically concentrated in only a few stories (often in a single story), even for the BRBF systems (though not to the same extent as for the SCBF systems). Note that 70% of the ground motions considered in these analyses caused at least one of the braces to fracture during the simulations of the three-story SCBF building, and 30% of the records completely fractured at least one brace in the six-story SCBF. The deterioration and fracture of braces directly contributes to the localization of damage in the SCBF systems. For the comparable BRBFs, the cumulative inelastic demands in all of the braces were far less than their capacities, and none came close to failing due to fatigue. Khatib and Mahin (1987) suggested that such localization in ductile braced systems might be associated with the distribution of brace strengths over the height of the building.

The results also suggest that a significant amount of permanent lateral displacement may remain following an earthquake, especially for the SCBF system. These residual displacements may have an important impact on safety under aftershocks, and on repair costs, that should be considered.

While studies such as this one can identify vulnerabilities of particular types of structures, and compare seismic demands imposed on different systems under the same excitations, they do not directly compare demands with capacities or provide information on the confidence that can be placed on the ability of the structure to achieve targeted performance goals. Following the Northridge earthquake, the FEMA/SAC Steel Project (FEMA 2000a) extended the application of reliability methods to assess the seismic performance of steel moment-resisting frame (SMRF) buildings. Global and local deformation demands were computed for a system and compared to estimates of the capacity of the structural elements and of the system as a whole; thus, two primary performance levels were considered for a stipulated seismic hazard level (FEMA 2000a).

The primary difference between this method and earlier load and resistance factor design (LRFD) approaches was the explicit consideration of behavior at the system level. Prior LRFD methodologies generally considered structural demands member-by-member, rather than considering the ability of the structure to carry load following the failure of a single element (Lee and Foutch 2000). As such, the failure of one or more elements was not by itself considered to represent the failure of the overall structure provided the system could redistribute the required lateral and gravity forces in a stable manner. Although this performance-based earthquake engineering (PBEE) approach has proved quite useful in evaluating and improving design methods for SMRFs, its applicability to other systems, such as concentrically braced steel frames, remains to be seen.

To explore the application of a simple PBEE approach to concentrically braced frames, four preliminary case studies are considered in this chapter. These cases explore the application of the FEMA/SAC PBEE methodology to SCBFs and BRBFs. The three- and six-story chevron conventionally braced steel frames (3V and 6V, respectively) along with three- and six-story chevron buckling-restrained braced steel frames (3VB and 6VB, respectively) cited earlier are used as the basis of these studies. The intent of these studies is to examine the potential benefits and limitations of this PBEE methodology as applied to braced steel structures.

3.2 PRELIMINARY PERFORMANCE-BASED EVALUATION OF BRACED FRAMES

A recent special edition of *Earthquake Spectra* contains several articles describing the performance-based evaluation methodology used in this paper (Hamburger et al. 2003; Hooper 2003; Mahin et al. 2003; Saunders 2003). Consequently, the general details of the reliability framework will not be repeated herein; however, a brief narrative discussion is provided below.

Quantification of the confidence that a performance goal can be achieved for a particular structure and seismic hazard level is divided into several sequential and interrelated tasks (FEMA 2000): site-specific hazard assessment, structural demand estimation, structural capacity evaluation, estimation of the degree of uncertainty and randomness in response estimates, and calculation of the confidence that a performance goal will be achieved. As discussed in Chapter 1, and subsequently in Chapter 7, more refined methods for PBEE have been developed since the development of the FEMA/SAC methodology.

The basic FEMA/SAC methodology considers several performance levels, and typically involves the assessment of several criteria at each performance level (such as global lateral or vertical instability and local failure of certain critical members). The primary focus of the procedures in the FEMA 350 standard (FEMA 2000a) is on the collapse prevention performance goal. While specification of the seismic hazard level and acceptance criteria are left to the owner or relevant regulatory officials, several recommendations are offered. Because of (a) the high consequences of violating this goal; (b) the realistic nonlinear dynamic analysis methods used to predict response (with little built-in conservatism); (c) the numerous assumptions made (e.g., only one component of horizontal excitation was considered); and (d) the lack of history in implementing this methodology, a high confidence of achieving the collapse prevention goal and a high seismic hazard level (2% probability of exceedance in 50 years) were recommended. A 90% confidence level was recommended for response modes associated with global collapse mechanisms (lateral collapse represented by large peak interstory drifts and compression buckling of a column), while a more moderate 50% confidence was cited for more localized failure modes (local loss of vertical load capacity of beam-to-column connections and tension failures of columns). These confidence levels were found to be consistent with the behavior of ductile SMRF structures designed according to the 1997 NEHRP provisions (Lee and Foutch 2000), and, thus, did not require any significant changes to these provisions to achieve the desired confidence level (beyond the use of ductile connections).

In this chapter, the FEMA/SAC methodology will be applied to concentrically braced frames, considering that the collapse prevention limit state for seismic events represents a 2% in 50-year probability of exceedance. In this chapter, therefore, the median peak interstory drift demands are computed for an ensemble of earthquake records representative of the 2% probability of exceedance seismic hazard level; a broader range of nonlinear dynamic analyses is carried out to estimate interstory drift capacities; and various types of aleatoric and epistemic errors are estimated based on the results of calculations and values used previously in the FEMA/SAC project for moment-resisting frames.

The FEMA/SAC methodology approaches the evaluation problem in probabilistic terms by comparing the probable peak drift demand ($\gamma\gamma_a D$) with a dependable drift capacity (φC) and assumes lognormal probability distribution functions to estimate the probability that the capacity is not exceeded. According to the FEMA/SAC methodology, a confidence parameter, λ, can be determined from Equation (3.1), with values for undefined parameters listed in Table 3.2.

$$\lambda = \frac{\gamma\gamma_a D}{\varphi C} \tag{3.1}$$

The confidence parameter λ is associated with the probability of a specific performance goal being met, given a specific hazard level (Lee and Foutch 2000). The steps undertaken to estimate the various terms in Equation (3.1) for each of the four structures mentioned above are described in the following subsections. Because of the lack of supporting test and numerical data, several significant assumptions were made to complete this work. As such, the resulting confidence values computed are only approximate, but the computations illustrate the process and help identify areas requiring further data or refinement.

3.2.1 Site-Specific Probabilistic Hazard Assessment

For these studies, the same geological conditions and seismic hazards were assumed as those used previously in the FEMA/SAC studies of moment frames located in Los Angeles (Somerville 1997), as well as in the studies of SCBF and BRBF by Sabelli (Sabelli 2000). These records were adjusted to correspond to firm soil conditions. The underlying hazard estimates were based on 1997 NEHRP provisions (FEMA 1997a). Twenty ground motions from the FEMA/SAC database were used in the analyses, corresponding to the 2% in 50-year probability of exceedance. For more information regarding development of the ground motions, the reader is referred to Somerville (1997).

Table 3.2 Definition of parameters in Equation (3.1).

Parameter	Definition
D	Median calculated demand on the structure, obtained from a structural analysis.
C	Median estimate of the capacity of the structure.
γ	Demand variability factor which accounts for the variability inherent in the prediction of demand related to assumptions made in structural modeling and prediction of the character of ground shaking.
γ_a	Analysis uncertainty factor that accounts for the bias and uncertainty associated with the specific analytical procedure used to estimate structural demand as a function of grand shaking intensity.
φ	Resistance factor that accounts for the uncertainty and variability inherent in the prediction of structural capacity as a function of ground shaking capacity.
λ	Confidence index parameter from which a level of confidence can be obtained.

3.2.2 Structural Demand Assessment

Two-dimensional analysis models were developed and are schematically shown in Figure 3.2. These models are identical to those used previously by Sabelli (2000). The story height for SCBF and BRBF structures is 13 ft for all stories, and the braced bay width is 30 ft. As noted before, an ancillary “flagpole” column, which is not shown in the figure, was used to represent the lateral stiffness, strength, and geometric nonlinearities associated with gravity-load framing elements.

Each structure was assumed to have sufficient braced bays that the redundancy factor, ρ, contained in the 1997 NEHRP could be taken as unity. For the analyses of the braced bay, an appropriate tributary reactive mass was attributed to the computer model. For the design, the response modification coefficient, *R*, that accounts for the nonlinear behavior of the system for the SCBF and BRBF system was taken to be 6. The resulting structural designs resulted in three-story SCBF and BRBF systems with a fundamental period of about 0.5 sec and about 0.9 sec for the six-story buildings. More detailed information about the model and design assumptions can be found in Sabelli (2000).

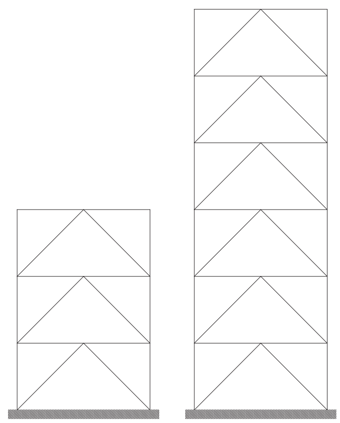

(a) 3-story frame (b) 6-story frame

Fig. 3.2 Configurations of SCBF and BRBF frames considered.

Nonlinear dynamic analyses identical to those undertaken by Sabelli (2000) were used to estimate the maximum peak interstory drifts developed for each structure for each ground motion record. Interstory drift (normalized by the height of each story) is used in this preliminary study as a parameter to characterize global damage. Interstory drift is expected to be related to the maximum plastic deformations in structural components, the degree of displacement-sensitive nonstructural damage, and the tendency for the structure to develop global instabilities due to P-Δ effects. Additional studies are required to assess the validity of this assumption (for example, it may be necessary to monitor more closely local damage in connections, gusset plates, braces, etc., and more rigorously check for buckling or fracture of the column elements). For this preliminary study, the peak interstory drift predicted in any story over the height of a building is used to characterize damage to that building for a specific ground motion. Assuming a ideal lognormal probability distribution of these results (Hamburger 2003), median values and standard deviations are computed for the peak median interstory values, expressed in logarithmic form, for the suite of ground motions.

Seismic demands were characterized by extracting the peak normalized interstory drift from the analysis results computed for each of the twenty 2% in 50-year events. The median value of these demands is taken as the parameter *D* in Equation (3.2). The variability (uncertainty) of dynamic response for this hazard level is represented by the standard deviation of the natural logarithms of the peak drift demands (β_{DR}). β_{DR} is used in conjunction with parameters characterizing the variability of ground motion intensity at the site for the stipulated seismic hazard to compute the demand variability factor, γ, used in Equation (3.2). Based on the FEMA/SAC methodology this variability parameter is shown in Equation (3.2), with definition of the values for this equation shown in Table 3.3.

$$\gamma = e^{\frac{k}{2b}\beta_{D_R}^2} \tag{3.2}$$

Table 3.4 summarizes the demands and demand factors calculated from the nonlinear dynamic analyses. Figure 3.3 illustrates the tremendous scatter in inelastic drift demands for the four structural models considered. Note that the median drifts have all increased considerably, compared to average values reported previously by Sabelli (2000) for 10% in 50-year events. Similarly, the median peak interstory drift indices computed for the SCBF frames are 44% and 48% higher than for the BRBFs. For the SCBF systems, the coefficient of variation is on the order of one for these ground motions; several ground motions develop interstory drifts in the structures of more than 10% of the story height. The coefficients of variation computed for the BRBF systems are still large, but less than half of those for the SCBF systems.

Table 3.3 Definition of parameters in Equation (3.2).

Parameter	Definition
k	Logarithmic slope of the hazard curve (here taken as 3, for the Pacific Northwest, California and Alaska),
b	Coefficient representing the amount that the demand increases as a function of hazard. For flexible moment-resisting frames, this value is normally taken as unity, but for shorter-period braced frames a value greater than 1 might be expected based conservation of energy principles (Chopra 1995; Newmark and Hall 1973).

Table 3.4 Demand results and parameters.

	Median Drift Demand (in/in)	Median Plus 1 Standard Deviation (in/in)	β_{DR}	γ
3V	0.056	0.119	0.70	2.08
6V	0.046	0.081	0.63	1.81
3VB	0.039	0.059	0.55	1.57
6VB	0.031	0.046	0.41	1.28

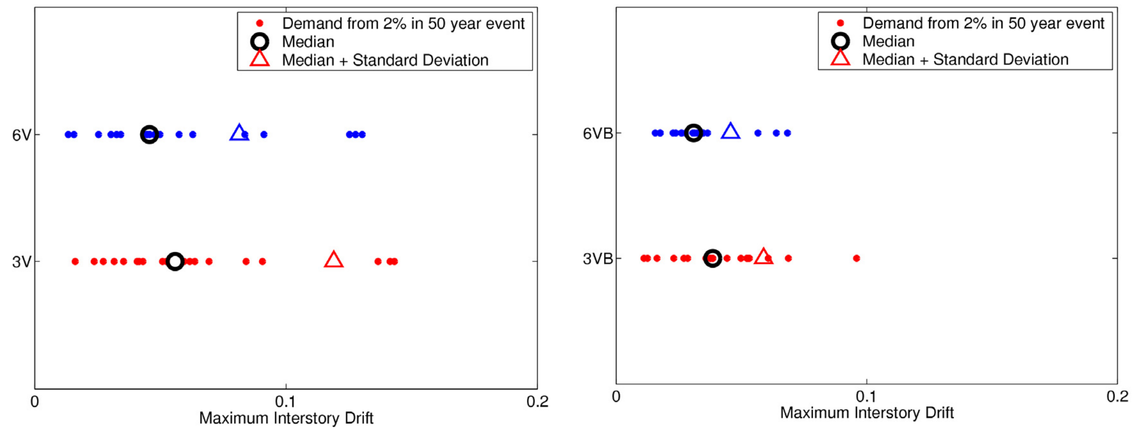

(a) SCBF systems (b) BRBF systems

Fig. 3.3 Peak interstory drift indices for 2% in 50-year events.

The analytical models and procedures used also introduce uncertainties (epistemic errors) into the response predictions. For example, a comparison of Figures 3.4–3.5 shows the significant difference between the analytical hysteretic loops used in these analyses and ones obtained experimentally (Black et al. 1980). These plots are for a representative hollow square steel strut having a slenderness ratio of 80. While the general post-buckling character of the analytical model is similar to that observed in the tests, it is clear that significant simplifications have been introduced. These differences in brace hysteretic characteristics may result in errors in predicting peak responses, or even behavior modes.

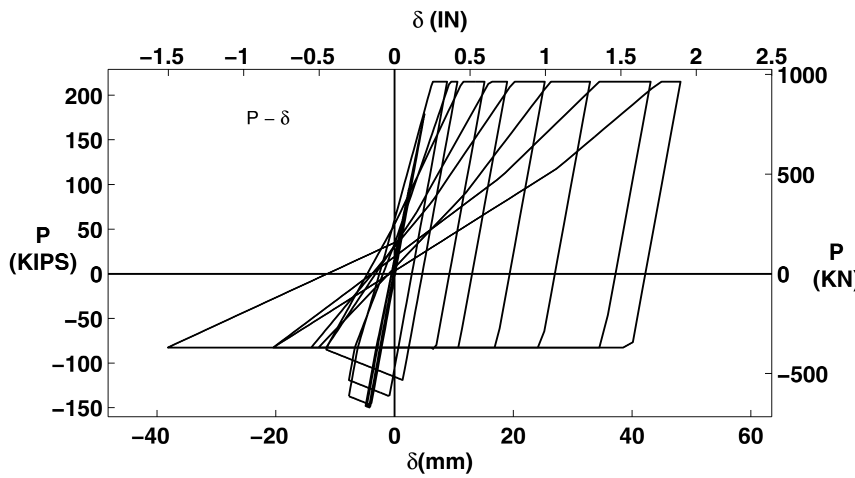

Fig. 3.4 Phenomenological numerical hysteresis model from SNAP-2DX for a strut with *kL*/*r* of 80.

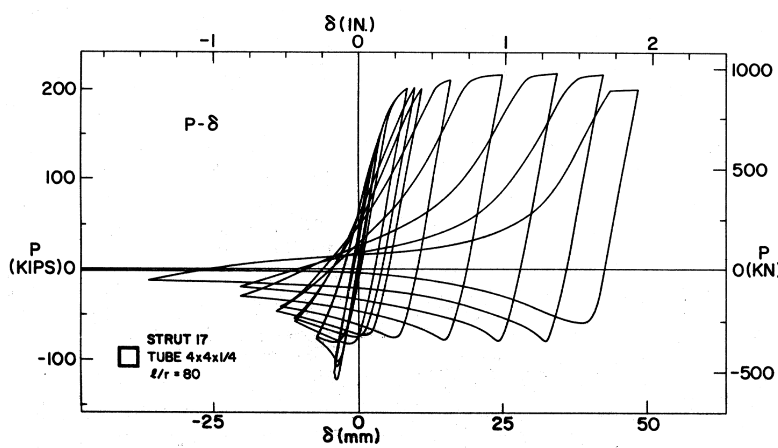

Fig. 3.5 Experimental hysteresis loops for hollow square strut with *kL*/*r* of 80 (Black et al. 1980).

Other epistemic uncertainties can arise from the inability to model accurately other structural components (e.g., gusset plates, connections, columns, base plates, etc.), characterize viscous damping, model the effects of nonstructural components and portions of the structure assumed not to contribute to the lateral load resistance of the structure; the use of 2D versus 3D models; discounting foundation flexibility; or limiting the number of components of excitation considered. Similarly, other errors can be introduced by the numerical procedures selected. For instance, the results may be sensitive to the integration time-step interval or iteration strategy selected in a nonlinear dynamic analysis, and elastic models are expected to provide less reliable predictions than ones that account for nonlinearity. Such epistemic errors can introduce bias and contribute to greater uncertainties in predictions. These analyses-related epistemic errors are characterized in this methodology by an analysis uncertainty factor, γ_a, given by Equation (3.3), with new parameter definitions given in Table 3.5.

$$\gamma_a = C_B e^{\frac{k}{2b}\beta_{D_U}^2} \tag{3.3}$$

Table 3.5 Definition of undefined parameters in Equation (3.3).

Parameter	Definition
β_{DU}	Standard deviation of the natural logarithms of the response parameters accounting for variability introduced by modeling and numerical procedures.
C_B	Bias introduced, equal to demand predicted by an "optimal" analysis model and procedure divided by the median demand predicted using the model and method employed for the evaluation (= 1.0 for nonlinear dynamic time history analysis).

Table 3.6 Analysis uncertainty parameters.

	C_B	β_{DU}	γ_a
3V	1.0	0.15	1.03
6V	1.0	0.20	1.06
3VB	1.0	0.15	1.03
6VB	1.0	0.20	1.06

This type of uncertainty can be reduced by using more refined and accurate analytical models and procedures. In the FEMA/SAC program, a large number of analyses were undertaken to characterize and quantify these errors. The values were found to depend on several factors, especially the performance goal being investigated (degree of nonlinearity), hysteretic characteristics of the connections (ductile versus brittle), analysis method used, and height of the structure. For the purposes of this preliminary performance assessment, the same values of γa recommended for moment-resisting frame structures are used for SCBF and BRBF systems. This is expected to be an unconservative assumption, as the large scatter in the results observed in the dynamic analyses suggests that the predicted response should be very sensitive to modeling and perhaps changes in the numerical procedures. Khatib et al. (1988) demonstrated that global response predictions are sensitive to modeling of the braces. Thus, eventual values predicted for confidence in achieving the collapse prevention performance level should be viewed within the context of this assumption. Table 3.6 lists the analysis uncertainty parameters that were used for the collapse prevention evaluations reported in this chapter.

3.2.3 Capacity Assessment

For estimating the seismic capacity of a SMRF, the FEMA/SAC guidelines suggest using an incremental dynamic analysis (IDA) procedure (Lee and Foutch 2000). Default values are provided based on application of this method to various model SMRF structures. These default values are not appropriate for braced-frame structures, so direct computation is necessary. The IDA method involves carrying out a sequence of nonlinear dynamic analyses, in which the intensity of the ground motion accelerograms considered are incrementally increased until a limit state "failure" is observed. In the FEMA/SAC methodology, failure is defined when the rate of increase of peak interstory drift with increasing ground motion intensity exceeds five times that associated with an elastic system (or at a prescribed maximum interstory drift ratio beyond which the reliability of the analysis is considered doubtful (e.g., 10%). This criteria is based on the concept that a disproportionate increase in response signals the onset of collapse or other unacceptable behavior. It does not identify the actual collapse of the structure (as many parameters that contribute to the collapse are not modeled). Other failure criteria have been suggested by other investigators (Vamvatsikos and Cornell 2002). For the investigations presented here, the criteria suggested in FEMA 351 (2000a) are used.

For this study, a total of 6400 nonlinear incremental dynamic analyses were computed using the U.C. Berkeley Millennium cluster (http://www.millennium.berkeley.edu) requiring approximately 20 hours to complete. Figures 3.6–3.7 plot the results of the incremental dynamic analyses.

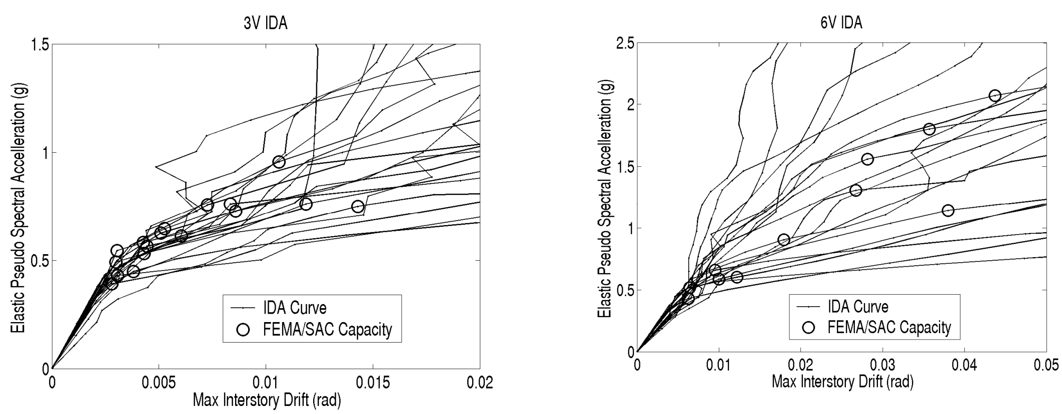

(a) 3V (b) 6V

Fig. 3.6 Incremental dynamic analysis for SCBF systems.

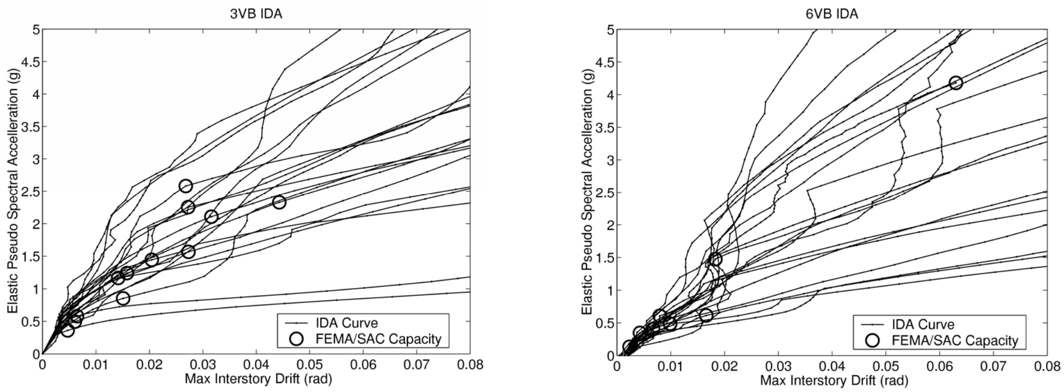

(a) 3VB (b) 6VB

Fig. 3.7 Incremental dynamic analysis for BRBF systems.

In these plots, the peak interstory drift index obtained over all levels from an inelastic analysis is plotted for a specific ground motion as a function of the intensity of the ground motion. Here, the parameter used to quantify the ground motion intensity is the pseudo-spectral acceleration of the scaled ground motion at the first mode period of the structure. Each of the curves on these plots corresponds to one of the 20 FEMA/SAC ground motions from the 2% probability of exceedance in 50-year database. The circled points on the curves correspond to the ground motion intensity (and interstory drift index) where the rate of increase in drift exceeds the criteria stated in the FEMA/SAC guidelines. Because a nonlinear dynamic analysis of the system is carried out in performing these analyses, and member yielding and failure are accounted for, these capacities are not based on the initial yielding or even failure of a single element, but rather on the situation where the rate of increase of lateral displacement of the overall system becomes excessive. As can be seen, the seismic capacity predicted in this way is different for each ground motion.

From Figures 3.6–3.7, it is clear that, in general, the structures are able to sustain considerably greater intensities of ground motion than that corresponding to the FEMA/SAC criterion. In fact, many of the BRBF frames do not achieve this criterion until after the interstory drifts exceed 10% (the upper value permitted by the FEMA/SAC methodology). As such, it is clear that the seismic capacity predicted in this manner would be sensitive to the slope of the IDA curve selected to represent the onset of failure. While these analyses include the effects of geometric nonlinearities, potential flexural yielding of beams and columns, and buckling and low-cycle fatigue failures of the braces, beam-to-column and brace-to-frame connections were assumed to be infinitely ductile, and buckling or tensile failures in columns were disregarded.

Note that several important modes of possible failure were not accounted for in these studies, and care should be taken in assuming that the structures can actually achieve the large interstory drifts suggested by these plots.

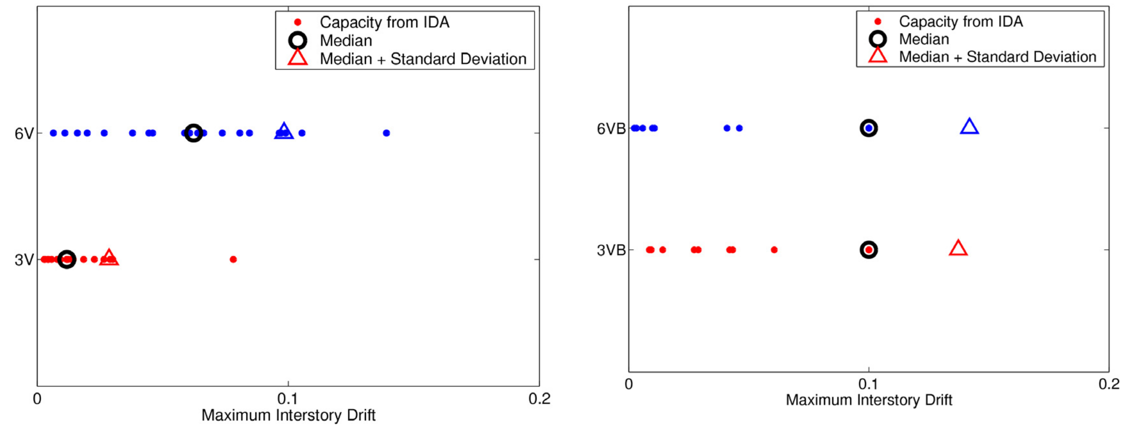

(a) SCBF Systems (b) BRBF Systems

Fig. 3.8 Seismic drift capacity results based on incremental dynamic analyses for SCBF and BRBF systems.

Figure 3.8 contains a plot of all of the analytically computed seismic capacities for the three- and six-story buildings expressed as interstory drift. The dispersion of the results obtained for different ground motions can clearly be seen in this figure. The median drift capacities, C, of the four structures are shown in these plots. Because many capacities were computed for individual records for the BRBF systems, the median capacity was obtained by sorting the results from lowest to highest, and counting from the lowest capacity until a location halfway between the 10th and 11th ranked records, or 10% drift (if this value is lower), was reached. Table 3.7 lists the median capacities as well as the logarithmic standard deviations of the computed capacities. Based on this methodology, the median capacity of both BRBF systems was taken as 0.10.

Table 3.7 Capacity results and randomness and uncertainty parameters.

	Median Drift Capacity (in/in)	Median Plus Standard Deviation (in/in)	β	φ_R	β_U	φ_U	$\varphi = \varphi_R \varphi_U$	FEMA 351 (Brittle Connections) φ
3V	0.012	0.029	0.84	0.35	0.15	0.97	0.34	0.85
6V	0.062	0.098	0.82	0.36	0.20	0.94	0.34	0.70
3VB	0.100*	0.155	0.94	0.27	0.15	0.97	0.26	0.85
6VB	0.100*	0.142	1.31	0.076	0.20	0.94	0.07	0.70

* maximum value permitted by FEMA 350

It is clear that the SCBF 3V frame has a particularly small seismic "capacity" based on this method (likely due to the larger number of cycles and higher drift demands imposed on this stiffer structure (see Table 3.4 for comparison). In fact, the predicted median capacity of the 3V frame is substantially smaller than the median demand. This does not necessarily signify that collapse or failure always occurs, due to the probabilistic distribution of demands and capacities. Consequently, a statistical interpretation of the demands and capacities is needed to assess the likelihood that the collapse prevention performance goal is violated.

To continue with the statistical interpretation, logarithmic standard deviations are needed to characterize the variation in computed capacities, β, and the epistemic uncertainties introduced by in analytical prediction of drift capacity, β_U. The FEMA/SAC guidelines suggest that β_U may be taken for moment-resisting frames as 0.15 for a three-story building and 0.2 for a six-story building. As noted previously regarding β_{DU}, the complex, deteriorating behavior of SCBFs, and the lack of data regarding braced frames at very large drifts suggest that the value of β_{DU} might be larger than for moment-resisting frames. Similar concerns arise in estimating β_U for braced frames. Nonetheless, the FEMA/SAC values for β_U are used here for the preliminary performance evaluations. The value of β_R is computed as the logarithmic standard deviation of the computed drift capacities, and used to compute a resistance factor φ_R accounting for the randomness in the computed drift capacities; i.e.,

$$\varphi_R = e^{-\frac{k}{2b}\beta^2} \tag{3.4}$$

The values of φ_R and β_U are then used to compute a resistance factor for global collapse, φ:

$$\varphi = \varphi_U \varphi_R = e^{-\frac{k}{2b}\beta_U^2} \varphi_R \tag{3.5}$$

The resulting values of β, β_U, φ_R, φ_U, and φ are presented in Table 3.7. Note that the large scatter in the computed drift capacities results in a particularly low value of the resistance factor for global stability, φ. Particularly in the case of BRBF systems, this appears to be an artifact of the IDA methodology and the default limits on drift capacity imposed by the FEMA/SAC guidelines (i.e., low maximum median drift permitted in combination with the high coefficient of variation on the actual predicted values results in very low values of φ_R). While additional study might improve this estimation, it should be recalled that the values used here for φ_U are likely to be unrealistically large. The resistance or capacity reduction factors that result from these values range from 0.7 to 0.34, substantially smaller than the default values allowed by FEMA 351 in the evaluation of moment-resisting frames containing pre–Northridge connections susceptible to brittle fracture (the values for ductile connections range between 0.9 and 0.85).

3.2.4 Confidence Assessment

At this point, all of the parameters needed to solve Equation (3.1) for λ have been determined. Once λ is determined, the standard Gaussian variate K_X can then be computed using Equation (3.6) (new parameters in this equation are defined in Table 3.8). As before, k is taken as 3.0, and b is assumed to be 1.0 in this equation.

$$K_X = \frac{k\beta_{UT}}{2b} - \frac{\ln(\lambda)}{b\beta_{UT}} \tag{3.6}$$

Because the logarithmic standard deviations used to represent uncertainty in this preliminary evaluation have been directly taken from the FEMA/SAC guidelines, the values of β_{UT} used in subsequent calculations are taken from Table 3-11 in FEMA 351, and account for various sources of uncertainty in demand, capacity, and member characterization. The results of these calculations are shown in Table 3.9. This table also includes the calculated confidence level of achieving the system-level collapse-prevention performance goal given ground motions consistent with a hazard level with a 2% in 50-year probability of exceedance. Based on this approach, the 3V structure has a particularly low confidence level, i.e., less than 2%. As noted previously, the median demand predicted for this structure is much larger than the median capacity predicted using the IDA approach. The 6V structure has a much larger confidence of meeting this performance criterion, i.e., 40%, but this value is still far smaller than the 90% confidence recommended in the assessment of new SMRF structures.

Table 3.8 Definition of new parameters in Equation (3.6).

Parameter	Definition
β_{UT}	Uncertainty measure equal to the vector sum of the logarithmic standard deviation of the variations in demand and capacity resulting from uncertainty.
K_X	Standard Gaussian variate associated with probability x of not being exceeded as a function of number of standard deviations above or below the mean found in standard probability tables.

Table 3.9 Confidence parameters for preliminary PBEE.

	λ	β_{UT}	K_X	Confidence Level
3V	11.76	0.25	-9.49	< 1.0%
6V	2.03	0.35	-1.92	2.7%
3VB	0.74	0.25	1.57	94%
6VB	0.60	0.35	2.41	99%

For FEMA 350 and 351, the recommended acceptance criterion for achieving global collapse prevention is 90%. It is clear that this preliminary evaluation suggests that both of the BRBF systems considered should be able to achieve collapse prevention with this level of confidence.

The confidence levels computed using this methodology for two examples of new code-compliant SCBF systems are alarmingly low, lower in fact than predicted by FEMA (2000c) for many older pre–Northridge moment-frame buildings. For instance, values of confidence against global collapse (2% in 50-year events) for a welded steel moment-frame building designed in Los Angeles in accordance with 1973 UBC code (with no limitations on maximum drift) were 71% and 20% for the 3- and 9-story buildings, respectively. Interestingly, confidence values for avoiding local collapse for the identical hazard and structures were 7% and 3% for the 3- and 9-story buildings, respectively.

While there are a number of assumptions and approximations introduced in applying the FEMA/SAC reliability framework to the assessment of concentrically braced steel-frame structures, the same assumptions were applied to the SCBF and BRBF. Thus, it is apparent that BRBF systems of the type considered herein are likely to be much more resistant to collapse when subjected to rare and unusual earthquake ground motions than comparable SCBF systems. It should be noted, however, that the complete FEMA/SAC evaluation has not been completed herein for either the BRBF or SCBF systems. This would require consideration of local failures in critical elements such as the braces, connections, and columns. Moreover, a number of assumptions were needed to complete the evaluation, including major ones related to modeling of uncertainties and estimating via the IDA methodology the capacity of braced systems.

The low values of computed confidence levels for SCBF systems suggest that earlier concerns regarding conventional concentrically braced frames may be warranted, and that a much more careful assessment of the seismic vulnerability of SCBF structures is needed. Even disregarding the specific confidence values computed, representative values of peak interstory drifts for the three-story SCBF frame are 3.9% and 5.7% for records consistent with a 10% and 2% probability of exceedance, respectively. As noted previously, 70% of the records considered in the 10% in 50-year hazard set caused at least one brace to fracture in the three-story SCBF frame. While the BRBF systems performed better compared to the comparable SCBF systems, the peak computed interstory drifts for the BRBF systems ranged between 3% and 4% for the 2% in 50-year events. These average (or median) values and the large scatter in response are higher than many engineers would find desirable. As a result, efforts to improve the design, proportioning, and detailing of concentrically braced steel frames appear warranted.

Nonetheless, the assumptions and limitations of these analyses and evaluations need to be recognized and considered when interpreting these results. Thus, an important aspect of any work to improve the performance of braced-framed structures would be to improve methods for numerically simulating their dynamic response and to better characterize the various sources of aleatoric and epistemic errors.

3.3 CONCLUSIONS

The preliminary studies in this chapter indicate that current approaches to the design of concentrically braced frames are likely to achieve structures that will exhibit a wide range of behavior when subjected to earthquakes capable of causing inelastic response. Conventionally braced and buckling-restrained braced frames designed to current design specifications are likely to undergo brace buckling or yielding when interstory drifts exceed approximately 0.3%–0.5%. Even the 10% in 50-year events caused widespread fracture of the braces in the SCBF systems and ductilities on the order of 10 in the buckling-restrained braces. While buckling-restrained braces are able to undergo large inelastic deformations, conventional buckling braces are not. While fractures of conventional buckling braces contribute to weak story behavior, both SCBF and BRBF systems tend to develop large interstory drifts in only a few stories. These concentrations of damage, and the relatively short period of low-rise braced-frame structures, tend to result in much larger displacements than would be predicted on the basis of conventional elastic analysis methods.

Current research on performance-based design has tended to focus on extending evaluation methods to explicitly address issues of importance to decision makers. These decision variables relate to the direct cost of damage to structural and nonstructural components (repair or replacement costs), the indirect costs associated with disruption and loss of function, and the costs of fatalities and injuries. While these topics are critical to the progress of the overall PBEE framework, it is clear from the preliminary performance evaluations presented above that there are several major issues that need to be addressed before moving on to consideration of these decision variables. These include:

1. **Improving and calibrating the reliability of numerical models and analytical procedures.** The results presented clearly show that the behavior of SCBF systems is highly nonlinear and dependent on the hysteretic models used to simulate buckling, deterioration, and failure due to low-cycle fatigue. It is assumed that the uncertainties (epistemic errors) used in the preliminary computations are low, yet improvements in modeling may lower these values, as well as reduce the scatter in the predicted results. Similarly, improving modeling of the connection regions may provide additional reserves not accounted for in these analyses. Such improvements in modeling need to be extended to accounting for low-cycle fatigue and other possible failure modes in buckling-restrained braces, connections, and beams and columns. Because of the high axial load in beams and columns, the vulnerability of these elements to lateral buckling should be evaluated as well. In general, all relevant behavior modes should be characterized. These concerns and improvements may necessitate corresponding improvements in numerical procedures.

2. **Developing appropriate methods for characterizing the capacity of braced-frame systems.** While the IDA methodology is a powerful concept related to defining the interstory capacity of a structure, its use with braced frames has raised a number of questions. Some of these may be associated with the limitations of the numerical models. For instance, the IDA results suggest that braced frames were capable of very large displacement capacities. If low-cycle fatigue and member buckling (of beams and columns) were incorporated in the models, the structures might not be able to deform under cyclic loading to such large drifts. Similarly, the relative rate of increase of displacement compared to a similar elastic system as a measure of unacceptable behavior (as used in the FEMA/SAC methodology) appears arbitrary, and small changes in this criterion are believed to have large changes in the predicted displacement capacity and in the confidence of achieving the collapse prevention performance level. In addition, it was noted that the imposition of an arbitrary upper limit for the peak interstory drift capacity had unexpected effects on the predicted confidence values.

In general, additional investigations are needed regarding the basic procedure; alternative methods might provide more reliable and useful insight into performance.

3. **Characterizing the aleatoric and epistemic errors associated with predicting the response of braced-frame systems.** In these studies, estimates of aleatoric errors were taken directly from the FEMA/SAC guidelines for moment-resisting frames. As noted previously, it is not believed that these values are applicable to concentrically braced steel frames. Thus, improved values are needed using improved numerical models. Similarly, estimates of these errors are needed for situations where simplified analysis methods are utilized.

4. **Assessing and improving the overall performance-based evaluation framework as needed for concentrically braced frame systems.** When the previous items are addressed, it will be possible to undertake a more complete performance evaluation of concentrically braced frames. It may be possible or necessary to devise an improved framework or approach compared to that developed by the FEMA/SAC project, in particular, inclusion of factors such as low-cycle fatigue, column and beam buckling, strength loss, residual displacements, etc.
5. **Examining means of improving the behavior of braced-frame structures where substantial vulnerabilities are detected.** An improved framework and numerical tools may still find that certain systems or aspects of a concentrically braced system are disproportionately vulnerable. As such, studies should then be undertaken to rectify this situation by improving the design methods, strategies for proportioning the structures, and detailing requirements. The PBEE approach will permit this to be done in a balanced manner. For instance, increased strength and stiffness might be traded off against detailing requirements, or special provisions developed to protect against various types of premature local failure.

4 Hysteretic Modeling of Steel Struts

4.1 INTRODUCTION

Because the earthquake response and performance of concentrically braced steel frames is primarily dependent on the behavior of the bracing elements, a logical starting point for any effort to improve performance assessment is to refine the ability of numerical models to simulate the hysteretic behavior of steel struts that may yield, buckle, or fail during severe seismic events. As noted in Chapter 2, the hysteretic response of small-to-moderate-scale steel braces has been the subject of numerous experimental studies (Black et al. 1980; Gugerli and Goel 1980b; Lee and Goel 1987; Liu and Goel 1988; Roeder et al. 2005; Tremblay and al. 1995; Yang and Mahin 2005), and a growing database detailing the performance of buckling-restrained braces is also developing (Clark et al. 1999; Merrit et al. 2003; StarSeismic 2005; Uang and Nakashima 2003; Wada et al. 1998; Wakabayashi et al. 1977). A wide variety of analytical models for steel braces have been proposed and used to simulate this behavior. These may be categorized into three categories: (a) phenomenological models; (b) physical-theory models; and (c) continuum finite element models. Each of these approaches has strengths and limitations.

Phenomenological Models—Phenomenological models provide the simplest and most computationally efficient approach. These numerical models are typically basic one-dimensional truss elements with hysteretic behavior that mimics experimentally observed response. The hysteretic characteristics are governed by a set of empirical rules that simply describe the shape of hysteretic loops without any substantial regard to physical phenomena that might occur within the brace. Buckling-restrained braces are often represented by bilinear hysteretic models, although piece-wise linear or curvilinear models intended to account for Baushinger effects are occasionally used. For example, a Bouc-Wen model (e.g., see Black et al. (2004) used to model

Baushinger effects in steel is shown in Figure 4.1. A simpler bilinear hysteretic representation is shown in Figure 4.2

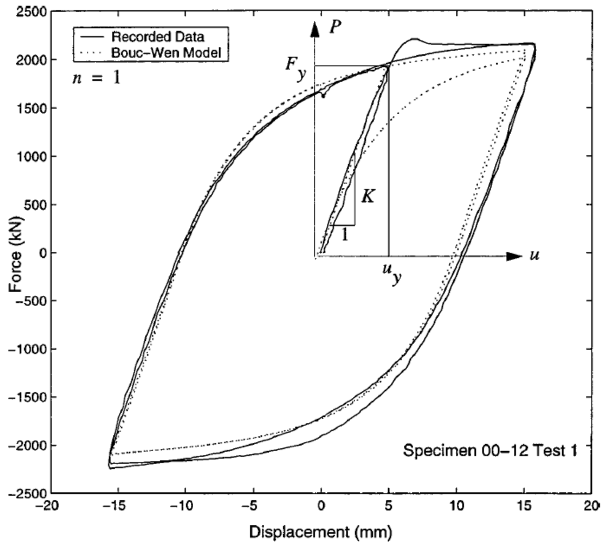

Fig. 4.1 Axial force–axial displacement hysteresis of analytical Bouc-Wen model (dotted line) and experimental testing (solid line) (from Black et al. 2004).

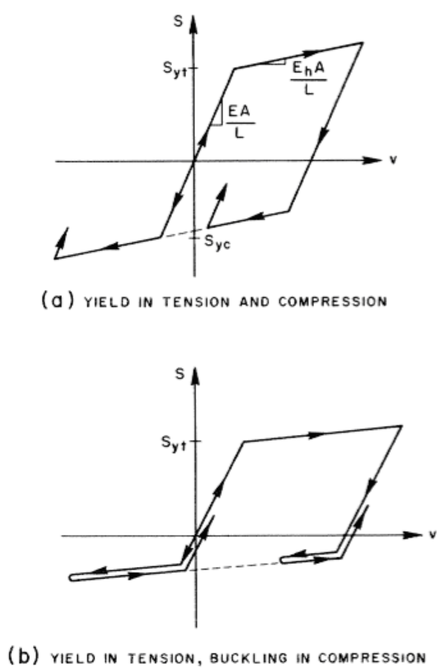

Fig. 4.2 Early braced hysteresis model (from Riahi et al. 1979).

The earliest phenomenological models of conventional buckling braces often represented buckling by mimicking bilinear nonlinear elastic behavior in compression and bilinear hysteretic behavior when the brace was in tension (Riahi et al. 1979). Such a model is shown in Figure 4.2b.

Subsequent phenomenological models incorporated the deterioration of strength that occurred under compressive shortening of the brace following buckling, the reduction of buckling capacity that is observed in tests during repeated compression excursions, and a variety of rules describing in piece-wise linear fashion the complex hysteretic shapes that occur during cycling between compression and tension states (Gates et al. 1977; Gugerli and Goel 1980b; Ikeda et al. 1984; Jain and Goel 1978; Lee and Goel 1987; Popov et al. 1976). While these models mimic the deterioration in stiffness and strength that is observed in braces, and several incorporated measures to categorize severity of damage (e.g., cumulative plastic straining or energy dissipation), very few (Jain and Goel 1978; Lee and Goel 1987; Rai et al. 1996b) included a damage model that removed the brace from the structural model once its predicted fatigue life was achieved.

Representative experimental results for a pin-ended conventional steel brace susceptible to lateral buckling are shown in Figure 4.3a (Uriz and Mahin 2004), along with the numerical results (Fig. 4.3b) obtained with a phenomenological truss model with piece-wise linear hysteretic behavior (Rai et al. 1996a). Although this model and other similar ones are able to mimic the overall behavior of such braces, at a reasonable computational expense, this approach suffers from a number of limitations:

1. Users need to specify a number of parameters used by the rules embedded in the model to control the shape of the hysteretic models. The more realistic and complex the numerical model, the greater the number of parameters that need to be specified. As such, the usefulness and accuracy of phenomenological models depend on the availability empirical information with which to determine the appropriate modeling parameters. Ikeda and Mahin (1984) surveyed numerous strut test results and recommended appropriate parameters for a model they developed, but they did not recommend failure criterion. Jain and Goel (1978) surveyed the results of another set of strut data and made recommendations for rules for modeling the brace hysteretic characteristics including failure. In both cases, very few analyses were carried out to characterize the sensitivity of overall system and local behavior to modeling uncertainties. The limited available

databases in each case require the user to significantly extrapolate modeling parameters or make simplifying assumptions when encountering cases not previously tested.

2. The hysteretic loop shapes considered by many models capture the basic overall inelastic characteristics of braces, but simplify some of the potentially important details. For instance, in Figure 4.3b, the numerical model represents the brace behavior during shortening as a horizontal line following a brief descending branch from the initial or reduced buckling load. The test results being mimicked (Fig. 4.3a) exhibit a small negative effective stiffness throughout this portion of a loop. Gupta and Krawinkler (2000) and MacRae (1994) commented on the importance of negative post-yield stiffness on stability predictions. Similarly, the numerically simulated hysteretic loops have a concave downward shape as they reload in tension from a previous compression excursion, whereas the experimental results are concaved upward. Such discrepancies are common with phenomenological models, to greater or lesser extent.

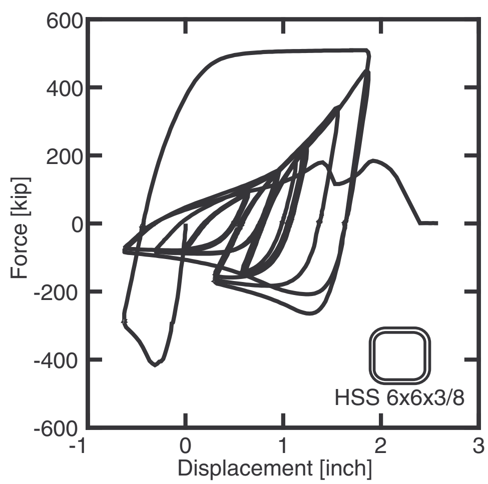

(a) Experimental behavior of steel strut (Uriz and Mahin 2004)

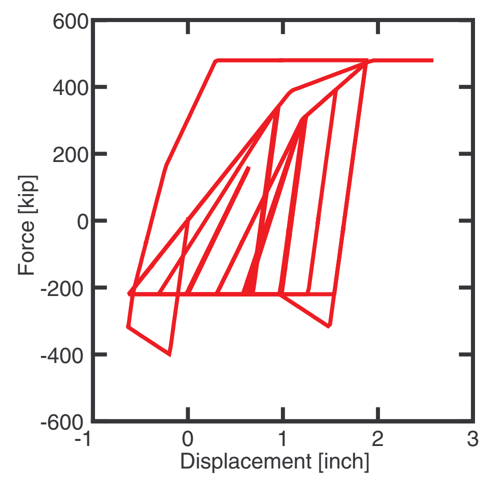

(b) multi-linear brace model (Rai et al. 1996a)

Fig. 4.3 Experimental response of steel brace and phenomenological modeling.

3. Most models represent the bracing member by a one-dimensional truss element with pin connections to the adjacent framing. As such, the in-plane bending stiffness of bracing elements is not taken into account and braces with fixed ends must be represented by pin-ended members having equivalent slenderness properties. These limitations may be acceptable in most cases, but they introduce uncertainties that need to be accounted for in making assessments of performance and do not allow extension of the element to cases where flexural members or beam-column elements may buckle.

4. In some instances, bending and other actions may result in localization of damage that cannot be accounted for simply or automatically. For example, in an X-braced-frame configuration, inelastic compression deformations tend to concentrate in only one of the braces along the compression diagonal. This has the effect of doubling the inelastic compression damage in one half of the diagonal and thereby reducing the fatigue life of the brace subsystem. Such behavior can be "seeded" in analyses based on phenomenological models, but require specialized knowledge of behavior on the part of the modeler. Fixed-ended braces can develop three plastic hinges when they buckle and the adequacy of low-cycle fatigue failure models for such cases is not known.
5. For performance-based assessment, the engineer may require information about consequential damage produced by the lateral buckling of braces. For instance, such buckling can damage nonstructural elements and interfere with the operation of adjacent mechanical components, such as elevators. One-dimensional truss models cannot provide such information directly, so that simple estimates based on kinematic or empirical relationships (Tremblay et al. 2003) between axial and transverse displacements are needed.
6. While pin-ended brace models may represent the basic behavior of the braces, the model does not attempt to simulate the complex state of stress that develops in the brace-beam-column connection region. As noted in Chapter 2, the results for experimental investigations and field reconnaissance show that the gusset plate to beam-column connection region is susceptible to considerable damage and failure.

Regardless of these limitations, phenomenological models have been used with success in numerous studies of braced-frame response (Ikeda et al. 1984; Khatib et al. 1988; Zayas et al. 1980b).

Physical-Theory Models—Significant effort to date has been expended to develop so-called "physical theory models." Most of these models are based on a linear elastic beam-column element with inelastic hinges concentrated at the element ends and midspan (Giberson 1967), or in the case of pin-ended braces with two collinear elastic beam-columns separated by a generalized plastic hinge at the midlength. This formulation has been used to help understand the basic mechanical properties of braces undergoing cyclic inelastic buckling by solving it in closed form using a plasticity-based representation of the inelastic axial load-bending moment relationship of the plastic hinge region at the midspan of the brace (Hassan and Goel 1991; Higginbotham 1973).

A similar element, but somewhat simplified, generalized plastic hinge model was developed by Ikeda and Mahin (1984) for introduction to a general-purpose 2D dynamic analysis software package. In both cases, geometric nonlinearities relative to the element's basic coordinate system were taken into account explicitly in the formulation of the model. Several computer analysis programs permit beam or beam-columns to have sections defined by fibers. The cross-sectional shape can vary along the length of an element, and each fiber can have different constitutive characteristics. The earliest of these attempts utilized the large displacement analysis capabilities of the software to explicitly account for buckling of braces, beams, and columns (Powell and Campbell 1994). Hall and Challa (1995) have used a fiber discretization of the cross section and a form of the corotational formulation (Crisfield 1991) for the element to describe the inelastic hysteretic response of steel members, but their correlations with the experimental results were limited to a single specimen. More recently, Jin and El-Tawil (2003) have used a distributed inelasticity element with a bounding plasticity model of force-resultants for the interaction between bending moment and axial force. A geometric stiffness matrix was added to the member material property related stiffness. Correlations with experimental evidence were reasonable in the tensile stress range, but were not as accurate under compression.

Physical theory models overcome some of the limitations of phenomenological models; in particular, they are theoretically less dependent on empirical parameters. In concept, the user simply needs to input information about the geometry of the brace, the distribution and characteristics of fibers at various critical sections, and the material properties to be considered.

In general, such models can account for the combined effects of bending and axial load. These advantages are at the cost of increased computational effort. On the other hand, Ideda and Mahin (1984) found it still necessary to introduce a number of empirical parameters into their formulation to improve fidelity with the experimental results. A number of factors are not accounted for in many physical theory representations, such as unknown and often disregarded initial stresses, initial geometric imperfections, changes to the shape of the cross section that occur during loading, imperfect representation of material properties, plane sections not remaining plane due to the multi-axial states of stress developed in the plastic hinge region, onset of local buckling, lack of a validated failure model for the materials, etc. While some of these issues can be overcome via improvements in physical theory modeling, few of these models are implemented in generally available, open-source computer programs.

Continuum Finite Element Models—Many of the remaining modeling limitations can be overcome using general purpose finite element programs capable of large displacement analysis (HKS 2002; LSTC 1999), and representing brace components and their connection to the adjacent framing by small-sized shell or solid elements, and using appropriately selected multidirectional material models. Several studies of this type have been carried out recently (Field 2003). Because of their inherent complexity, the difficulty in preparing input files and the computational expense of running them, such detailed finite element models remain relatively uncommon in structural engineering practice or research.

Based on the above discussion, it appears that a good starting point for improving brace models would be to implement a modern physical theory model capable of automatically representing braces having a variety of cross-sectional shapes and boundary conditions. By restraining lateral deformations, these models can be used to represent buckling-restrained braces. For braces that are allowed to buckle, they allow the user to specify initial imperfections where this is desirable, and provide the user with information related to the lateral displacements that occur during earthquake shaking.

Thus, this chapter will examine the capability of a physical theory brace model implemented using features of the open-source, computational framework Open System for Earthquake Engineering Simulation (OpenSees) (McKenna 1997; http://opensees.berkeley.edu). The object-oriented framework of this software permits a wide variety of material, section, member and structure level characteristics to be combined to achieve a versatile physical theory representation of various members, including simple braces, and more general three-dimensional beam-columns. Recommendations for formulating the model for conventional buckling braces are developed, and the model is validated, by means of an extensive set of correlation studies with steel braces having different types of cross section. Issues related to low-cycle fatigue related failure of braces are deferred until Chapter 5.

4.2 MODELING OF BUCKLING-RESTRAINED BRACES

Numerical modeling of buckling-restrained braces where issues related to lateral buckling can be disregarded is generally accomplished by representing the strut as a simple, one-dimensional, pin-ended truss element having the appropriate effective uniaxial force-displacement properties. In many practical cases, the materials are represented by standard bilinear hysteretic models, while in more refined cases, multilinear and curvilinear models are employed. For instance, the experimental and numerical results for a large-scale buckling-restrained brace reported by Clark et al. (1999) are compared in Figure 4.4 for the case where the materials in the buckling-restrained brace are represented by a standard Mennegato-Pinto (1973) model available in OpenSees (McKenna 1997). Quite good agreement is obtained using this simple approach.

In some cases, the effects of end moments or localized yielding along the length due to changes in core profile are to be considered. In such cases, one or more fiber-based beam-column elements of the type available in programs like OpenSees can be conveniently used in series provided buckling effects are adequately restrained.

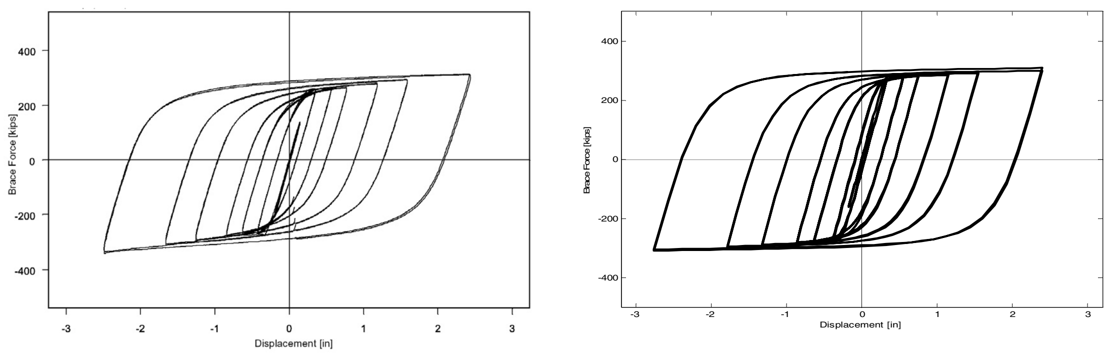

(a) (b)

Fig. 4.4 Calibration of Menegotto-Pinto steel material model for use in brace fiber model: (a) axial force–displacement hysteresis from buckling-restrained brace tests (Clark et al. 1999) and (b) OpenSees uniaxial truss with Menegotto material model.

4.3 PROPOSED STRUT AND BEAM-COLUMN NUMERICAL MODEL INCLUDING EFFECTS OF LATERAL BUCKLING

The inelastic frame element utilized herein accounts for distributed inelasticity through integration of material response over the cross section and subsequent integration of section response along the length of the element. It is based on the force formulation (Spacone et al. 1996), an approach that offers significant advantages over the more common displacement formulation: (a) the force-interpolation functions are always exact in the absence of second-order effects; (b) a single element can be used to represent the curvature distribution along the entire member with sufficient accuracy through selection of a sufficient number of integration points (monitoring sections); and (c) the formulation has proven numerically robust and reliable, even in the presence of strength softening, as is the case for buckling steel braces. This element is in extensive use in seismic response simulation studies within the OpenSees framework.

The element response in the basic system without rigid body modes is derived from small deformation theory. Nonlinear geometry under large displacements can be accounted for during the transformation of the element forces and deformations from the basic to the global reference system of the structural model, as described in Filippou and Fenves (2004) for the two-dimensional formulation; details about three-dimensional geometric transformation can be found in de Souza (2000).

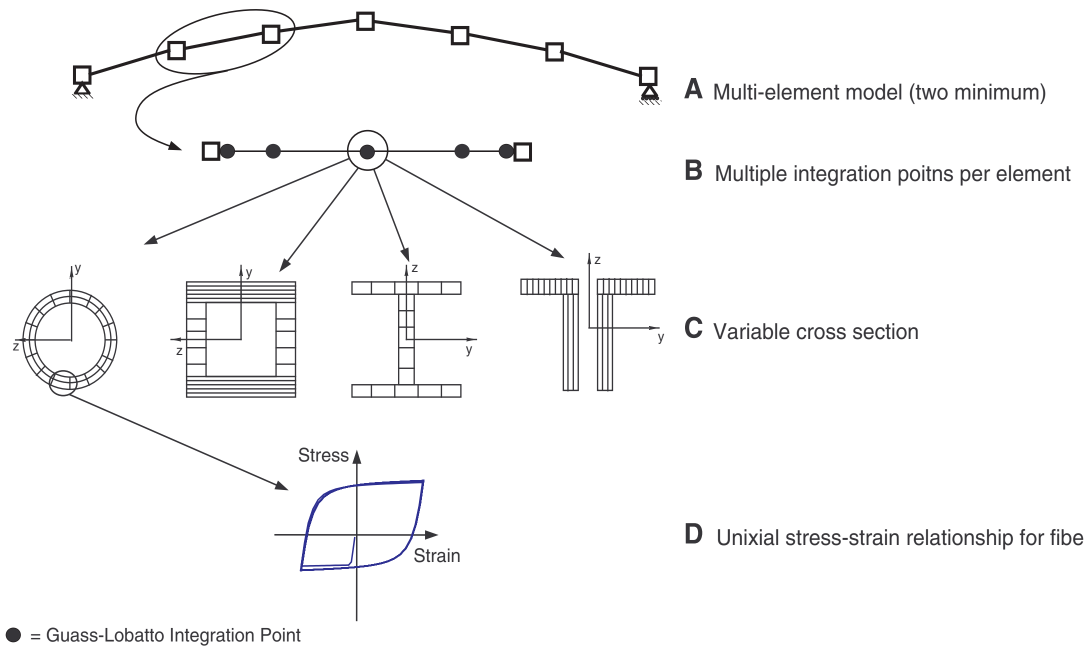

Fig. 4.5 Schematic illustration of proposed multi-element beam-column element showing (a) initial camber—exaggerated, (b) monitored integration points, (c) ability to model multiple cross sections, and (d) uniaxial material model.

The inelastic beam-column element with small deformation theory used herein relies on the corotational theory to represent the moderate to large deformation effects of inelastic buckling of the concentric brace (i.e., "large displacements and small strains"). To this end the brace needs to be subdivided into at least two elements (see Fig. 4.5), while a finer subdivision is necessary for representing accurately local deformations and, in particular, steel strains at the critical sections of the brace. The latter are very important in low-cycle fatigue studies for the prediction of the ultimate failure of the buckling braces (see Chapter 5). The issue of mesh refinement is addressed in parametric studies presented below. An inelastic frame element with moderate deformations overcomes the need for brace subdivision into more than two elements. Such an element was not publicly available at the time of this study, but details of its formulation can be found in deSouza (2000).

The inelastic beam-column element used herein accounts for the interaction of axial force and bending moment along the brace by integration of the uniaxial, hysteretic steel material model over the cross section of the brace (fiber model; see also Fig. 4.5). Shearing deformations are ignored in the numerical quadrature. The Menegotto-Pinto hysteretic model is used for the steel fibers, with extensions included for kinematic and isotropic hardening (Filippou et al. 1983). In a distributed plasticity model, section response is monitored at several points along the element axis. In the absence of geometric nonlinearities, this is not very important because the most critical internal force combinations occur at the end sections. The numerical integration method used in each beam-column element follows the optimized Gauss-Lobatto distribution (Bathe 1995), which includes, at a minimum, monitoring points at each end of the element. As will be seen later in Chapter 5, more nodes and elements may be required to improve accuracy of local response predictions.

The advantage of using a distributed plasticity beam-column element is that inelastic deformations can take place at any section along the length of the member, which is important for accurate estimation of local strains, and modeling members with variable section properties and restrained end conditions. By using a fiber representation of the section, initial stresses associated with the member fabrication and construction processes can be represented, and realistic material properties can be specified, including damage and failure of individual fibers due to low-cycle fatigue. In this investigation, all stresses in the section at the beginning of an analysis are assumed to be zero. Low-cycle fatigue-related damage is to be considered later (see Chapter 5).

The fiber model as implemented herein has several important limitations. Some of these are discussed below:

- *Cross Sections Do Not Distort During Loading*—A significant limitation of the model presented here is that plane sections are assumed to remain plane, and distortion of the cross-sectional shape is not considered (e.g., see Fig. 4.6). Considerable distortion of the cross section may occur, even prior to local buckling due to Poisson's effects and initial imperfections, especially after the formation of local buckles. In many cases the effective depth of the section is substantially reduced, resulting in a significant deterioration of the sections strength and stiffness.

- *Local Buckling Is Not Considered*—The actual strain in the vicinity of a local buckle is likely much larger than that predicted for a member where only uniaxial stresses are considered for fibers oriented parallel to the longitudinal axis of the member. Because the orientation of the principle compressive stresses within the locally buckled region may not be parallel with the longitudinal axis of the member, the effective strength and stiffness of the section would be further reduced compared to the analytical model. To delay the onset of local buckling in earthquake-resistant structures, the Seismic Provisions (AISC 1997) require compact sections, e.g., $(b - 2t)/t < 110/ Fy$ for rectangular HSS sections. Such provisions are intended to enable the member to sustain its capacity through significant but unspecified inelastic rotations. It would be expected that braces having compact sections would have a longer fatigue life compared to ones with more slender cross sections. Once local buckling occurs, the accuracy of the proposed brace model, which ignores these effects, is likely reduced. As will be seen in Chapter 5, modeling parameters can be calibrated to test results to improve fidelity.

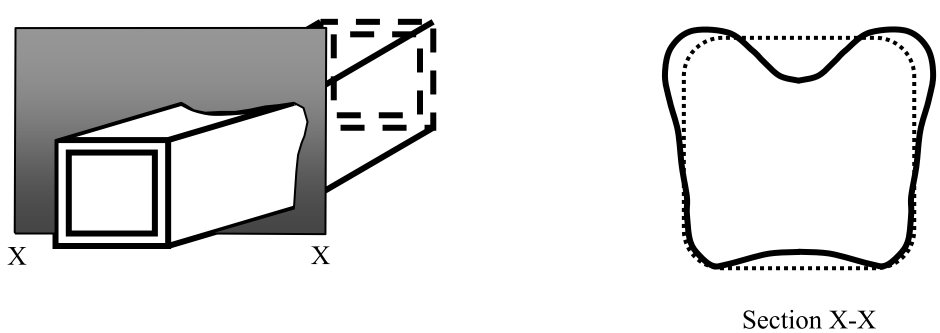

Fig. 4.6 Tubular brace member with local buckling at section x-x and detail of cross-sectional shape due to local buckling.

- Multi-axial Stress States Are Ignored—In addition to situations noted above where multi-axial stress states can develop, the assumptions that sections remain plane during deformation and that the steel responds uniaxially may result in erroneous predictions in the region of a discontinuity or stress concentration. Examples of such situations for braces include the introduction of holes or stiffeners, and especially, the region where the braces are connected to gusset plates. In the case of HSS and pipe sections, the brace is often slotted at each end so it can be slipped over and welded to the gusset plate. When the slot extends beyond the end of the gusset plate into the brace, a region of net reduced area results. This reduced area, in combination with the stress concentrations caused by welding of the brace to the gusset plate may have a pronounced effect on the hysteretic behavior, including premature rupture if this section is not adequately reinforced. The effects of these stress concentrations will be discussed in Chapter 5.

- Torsional Response Is Neglected—For the sake of simplicity, torsional stiffness for all beam models were ignored, thus neglecting loss of axial and bending stiffness from this (assumed) secondary failure mode. Lateral torsional buckling modes are consequently not considered. It is important to note that torsional stiffness may be added in parallel in the OpenSees platform.
- Initial Stress Conditions Disregarded—In these analyses the initial state of stress in the individual fibers is set equal to zero. This is not a necessary condition, and initial stresses can influence the initial yielding and buckling loads, shape of the hysteretic loops, and fatigue life. Identification of the appropriate initial state of stress to consider, accounting for the forming of the member and fabrication of the structure, is beyond the scope of this report.

Figure 4.7 illustrates representative fiber discretization of the type of cross sections considered. In each case, these are developed considering bending about the local z-axis during buckling. If more general loading is desired, a two-dimensional grid of fibers is needed. The discretizations shown in Figure 4.7 are for illustrative purposes only, and the number and size of fibers used in an analyses may differ considerably. In general, the fiber representation allows a wide variety of standard and built-up cross sections to be considered.

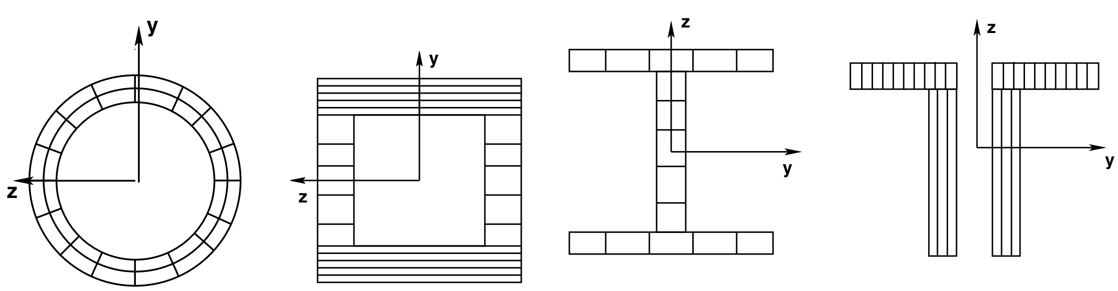

(a) Hollow circular (b) Hollow structural I wide flange (d) double angle

Fig. 4.7 Cross sections of common brace sections (buckling about local *z* axis).

4.4 PARAMETER STUDY

To demonstrate the capabilities of the proposed physical theory fiber model and its sensitivity to modeling parameters, the results of a parametric study are presented in this section based on a simple pin-ended brace. The ability of the model to simulate the strut test results is examined in the next section.

A fiber brace model was constructed in OpenSees using the fiber-based, beam-column model to mimic a previously-tested strut (Black et al. 1980). The strut selected consisted of an extra-strong 4-in. diameter steel pipe. The strut was welded to physical clevises at both ends to represent pin connections, and the distance between the centers of the clevises was 118.4 in., giving the member a slenderness (*kl*/*r*) ratio of 80. The reported yield strength of the steel was 24 ksi. This particular strut was chosen due to its cross-sectional properties, which was rather compact (i.e., D/t = 13.4; significantly less than $0.07E/F_y = 84$ for a flexurally compact circular tube section with this low F_y value). As such, the effects of local buckling (and lateral torsional buckling) can generally be ignored for these analyses. Figure 4.8 shows the experimentally obtained axial force–axial displacement hysteresis loops for this specimen.

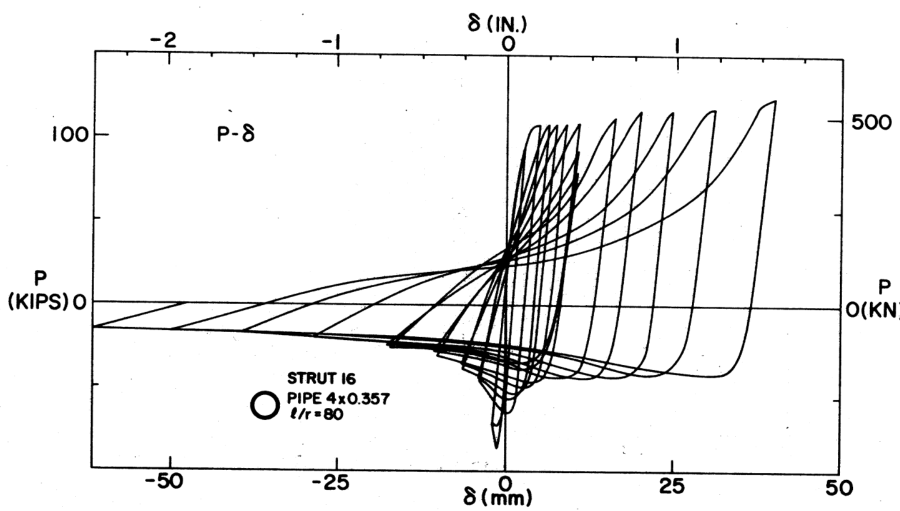

Fig. 4.8 Experimental hysteretic response of 4 in. extra-strong pipe (Black et al. 1980)

In building an OpenSees model of a brace using the approach suggested here, a number of decisions need to be made regarding the number of nonlinear beam-column line elements that the individual strut should be subdivided, the number of integration points used along each of these line elements, the initial camber (imperfection) to be assumed along the strut, the number and distribution of fibers used to represent the cross sections at the integration points, and the material property model. The sensitivity of the numerical results to such decisions is examined below.

The number of subelements from "pin-end" to "pin-end" was one of the main parameters considered for this study. The number of subelements used was 30, 10, 4, and 2. The reason for using more than two elements is an attempt to capture the complicated displaced shape of the buckled brace in the inelastic range. Each nonlinear beam-column element contains a number of integration points, which are used to interpolate polynomial displacements functions of order 2p-1 exactly, where p is the number of integration points. In actuality, these polynomial interpolates may not be physically accurate due to nonlinear material properties, which may result in distributions of deformations that are not adequately described by a few polynomials. For this reason, the number of integration points in the model was also varied in the parametric study. The number of integration points per element considered was 7, 5, 3, and 2.

A quadratic perturbation shape was used to define the initial camber. Without this initial camber, this pin-ended brace will behave as an ideal, perfectly straight uniaxial strut, with no global buckling possible. A small initial camber introduces a perturbation that triggers buckling. In a more complex model, with continuous end conditions for the brace, the flexural deformations of the brace may be sufficient to induce buckling. In order to test the sensitivity of predicted behavior to this initial camber, the value of the peak camber, δ, at the center was assumed to be 3%, 2%, 1%, and 0.01% of the total length of the brace. This is shown in Figure 4.9 below, where δ is the maximum perturbation at the center of the specimen and L is the length of the specimen. This quadratic initial camber was implemented regardless of the boundary conditions considered subsequently.

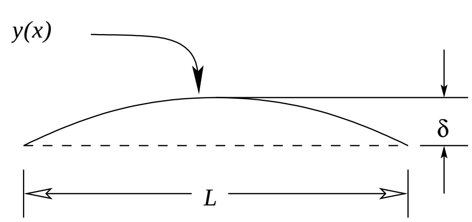

Fig. 4.9 Initial camber of specimen in undisturbed state.

The cross sections of the braces were defined by a circular fiber section shown in Figure 4.10a. This cross section was created using the circular patch command in OpenSees. A parameter study was also conducted varying the number of fibers used to describe the cross section. The number of fibers across the thickness and around the perimeter was varied. The following pairs of parameters were considered: (1, 5), (1, 10), (5, 10), (10, 60) and (2, 30), where the first term in each pair represents the number of fibers across the thickness of the tube, and the second term represents the number of fibers around the perimeter. In cases not dealing specifically with the effect of the number of fibers in the cross section, two fibers were assumed across the thickness with 30 sets of fibers around the perimeter.

The material model used was based on the Menegotto-Pinto steel model with an elastic modulus of 29,000 ksi, yield strength of 24 ksi, and a kinematic strain-hardening ratio of 0.3%. The resulting stress-strain relation for the steel is shown in Figure 4.4b above.

The length and end conditions used for the numerical model match the experimental situation described above. The strut was loaded axially with the lateral force applied by a hydraulic actuator at one end, as shown schematically in Figure 4.10b. The deformation history that was used is shown below in Figure 4.10c. This displacement history is identical to the displacement history used in the physical tests (Black et al. 1980). This history was kept constant for the entire parametric study to observe the effects of the free parameters chosen.

The model used assumes zero initial stresses. Steel members, including pipes, have significant residual stresses, often approaching the yield stress level, due to the nature of the fabrication process, which can be on the order of 40–80% of the yield strength for cold-worked and non-stress-relieved sections (Sherman 1976). These residual stresses can influence the initial buckling load, cross-sectional deformation, and local buckling.

An example tcl script for modeling and analyzing the strut is located in Figure 4.11.

4.4.1 Initial Deformation

The initial camber was varied from 3%, 2%, 1%, and 0.01% of the member length. For the strut in consideration here, this corresponds to an initial lateral offset at the midspan of $\delta = 3.5, 2.4, 1.2$, and 0.015 in., respectively. Clearly, the larger initial deformations are larger than would be permitted in practice; however, they are examined here for comparison purposes. For these analyses, the brace was subdivided into four beam-column subelements, and seven integration points were used in each subelement.

The strut was initially analyzed under monotonically decreasing axial displacements—the right node shown in Figure 4.10b was monitored until the brace shortened by 1.5 in. The axial force–axial displacement relationships predicted are shown in Figure 4.12a. This figure clearly illustrates the sensitivity of the initial buckling load to the assumed initial camber; differences in load-carrying capacity diminish as axial displacements increase. The strut reaches its maximum compression strength (and buckles) at an axial displacement of about 1/8th in. or less. For more than 0.5 in. shortening, the forces resisted for all four camber situations are found to be quite similar.

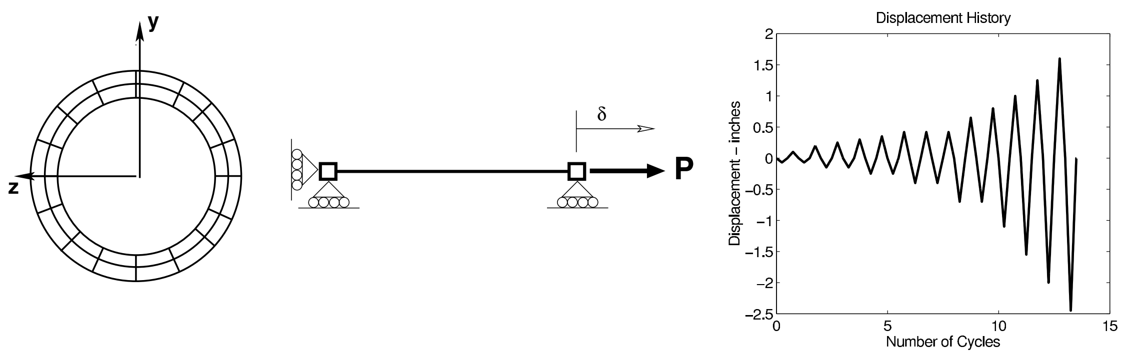

(a) (b) (c)

Fig. 4.10 Details of geometry and loading for parameter study of 4 in. extra-strong pipe specimen with pin-pin conditions. (a) hollow circular section discretization with 2 fibers in radial and 30 fibers in circumferential direction, (b) setup and loading for simulation, and (c) displacement history.

```
## Units kips-inches
model      BasicBuilder   -ndm 2        -ndf 3
## Nodes
node 1 0.0   0.0
node 2 10.0  0.0
node 3 12.0  0.0
node 4 50.0  0.5
node 5 88.0  0.0
node 6 90.0  0.0
node 7 100.0 0.0
## Mass
mass 7 1.0 0.0 0.0
#Boundary Conditions
fix 1 1 1 1
fix 7 0 1 1
## Materials
#uniaxialMaterial Steel01 1 40.0 29800.0 0.003
uniaxialMaterial Steel02 1 40.0 29800.0 0.003 20 \
    0.925 0.15 0.0005 0.01 0.0005 0.01
## Pipe Section (4" diameter, ½" wall thickness)
section fiberSec  1  {
    patch circ 1 20 4 0.0 0.0 2.0 1.5 360.0 0.0
}
## Gusset Plate Section (1" thick, 20" wide)
section fiberSec 2 {
    patch quadr 1 4 4 -10.0 0.5 -10.0 -0.5 10.0 -0.5 10.0 0.5
}
## Transformation
geomTransf Corotational 1
## Define Model
element elasticBeamColumn   1  1 2   1e3 1e8 1e6   1 ;# 'Rigid' offset
element nonlinearBeamColumn 2  2 3   3   2         1 ;# Gusset plate
element nonlinearBeamColumn 3  3 4   3   1         1 ;# Brace
element nonlinearBeamColumn 4  4 5   3   1         1 ;# Brace
element nonlinearBeamColumn 5  5 6   3   2         1 ;# Gusset plate
element elasticBeamColumn   6  6 7   1e3 1e8 1e6   1 ;# ,Rigid' offset
## Apply the nodal Load
pattern Plain 1 Linear { load 7 1.0 0.0 0.0 }
## Recorder
recorder Node –file LoadDisp.dat –time –node 7 –dof 1 disp
## Static Analysis parameters
test EnergyIncr 1.0e-8   300    0
algorithm KrylovNewton
system UmfPack
numberer RCM
constraints Plain
analysis Static
set peaks [ list 0.25 0.5 1.0 1.5 2.0 2.5 3.0 3.5 4.0 ]
for {set i 1 } { $i <= 9 } {incr i } {
    set dU [expr -1.0*pow((-1.0),$i)*[lindex $peaks [expr $i-1] ]/50.0 ]
    integrator DisplacementControl 7 1 $dU 1 $dU $dU
    analyze 50
}
```

Fig. 4.11 Example OpenSees script.

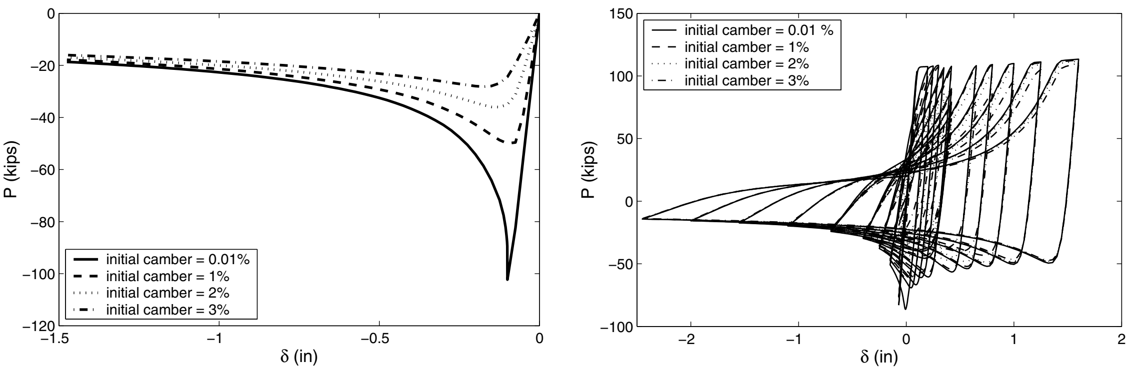

(a) monotonic response in compression (b) hysteretic response

Fig. 4.12 Effect of initial deformation on buckling and hysteretic behavior of strut; analytical model made up of 4 elements with seven integration points in each; ratio of maximum initial displacement to brace length varies from 0.01% to 3%.

Also, a comparison of Figure 4.12b and shows a striking resemblance between the test and analysis result. This gives some confidence in the approach used herein.

The sensitivity of the buckling strength to initial camber has practical implications for design and modeling. If an actual brace in a structure, or a brace in an analytical model, have initial cambers larger than expected, buckling will be reached prematurely. As a result, significantly different load distributions and inelastic deformation mechanisms may be predicted compared to those developed in the actual structure. Thus, it is important to model the initial cambers as realistically as possible.

4.4.2 Number of Nonlinear Elements per Strut

In this section, the number of nonlinear elements that make up the length of the strut is varied. The number of integration points is kept constant at seven integration points per subelement. The initial camber of the center of the strut was set to 0.05% of the strut length. Because of the relatively simple, symmetric deformed shape associated with a “pin-pin” assembly, a “fixed-pin” assembly with the same geometric and material properties was also analyzed. The latter case is expected to result in an asymmetric distribution of yielding along the member.

Figures 4.13a–b show the responses of the strut when subjected to the monotonic displacement excursion to 1.5 in. shortening for the “pin-pin” and “fixed-pin” condition, respectively. For the case of the “pin-pin” and the “fixed-pin” end conditions the buckling strength is nearly identical and relatively insensitive to the number of subelements. The shape of the post-buckling behavior does differ somewhat for the two boundary conditions (with the less slender strut losing strength at a slightly slower rate), and the number of elements selected has a small effect on the forces predicted for a given axial displacement, especially for the fixed-pinned case. Using more subelements tends to reduce the predicted force resisted by the strut in the post-buckling range.

Figures 4.14a–b show the same specimens subjected to the cyclic displacement history shown in Figure 4.10c. Again, regardless of the number of subelements used to define the strut, the responses are nearly identical. Again, trends are similar to those observed for the monotonic shortening case, in that the struts modeled with more subelements resist slightly less force in the post-buckling range.

Figures 4.15a–b show the curvature distribution along the struts at the last time-step of the cyclic hysteretic loading shown above. The curvature is plotted at each Gauss-Lobatto integration point. Although the hysteresis loops for the differing number of elements is nearly identical, the distribution of curvature is not. For instance, for the "pin-pin" condition, considering only two subelements, results in significantly higher predicted curvatures at the midspan of the strut. This increased curvature corresponds to a higher moment (based on the strain-hardening characteristics assumed for the steel), which in turn accounts for the larger predicted axial load capacity for this case.

For the "fixed-pin" boundary condition, the curvature distribution in Figure 4.15b shows that two flexural plastic hinges form: one at the left end and to the right of the midlength of the strut. As noted earlier, the effect of large displacements is accounted for in the transformation of basic forces to the global coordinate system; however, the response of each of the individual internal elements corresponds to the small deformation theory. For this reason, the internal curvature is more closely represented when more elements are modeled. Note that when two subelements are used, the location of the central plastic hinge is offset from the location inferred from all of the other cases where more subelements were used. The results obtained for four or more subelements and seven integration points are all very similar.

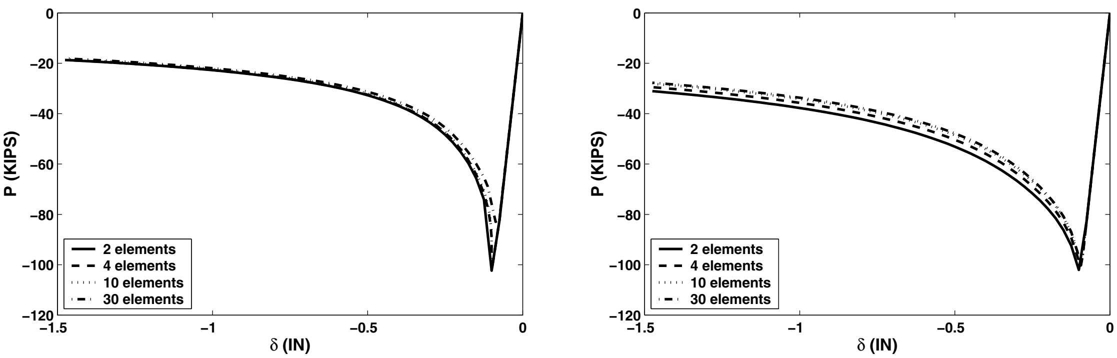

(a) pin-pin support conditions (b) pin-fixed support conditions

Fig. 4.13 Effect of number of elements on buckling response of strut with seven integration points per subelement.

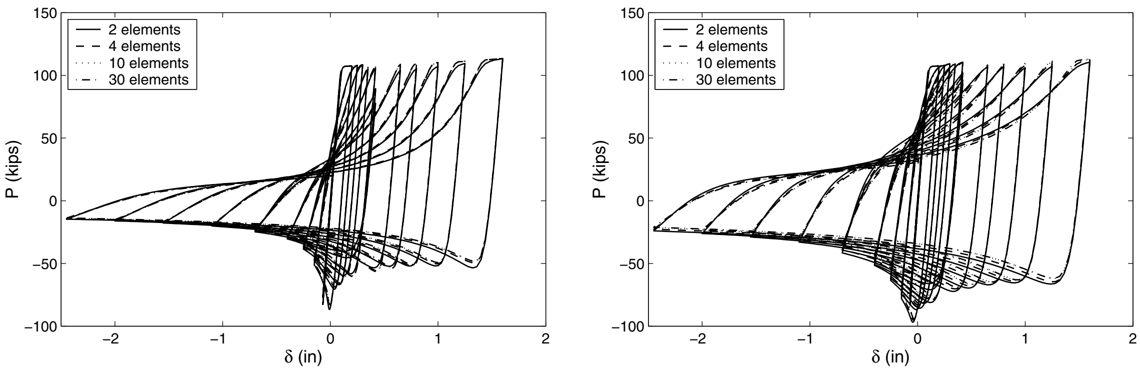

(a) pin-pin support conditions (b) pin-fixed support conditions

Fig. 4.14 Effect of number of elements on hysteretic response of strut with seven integration points per element.

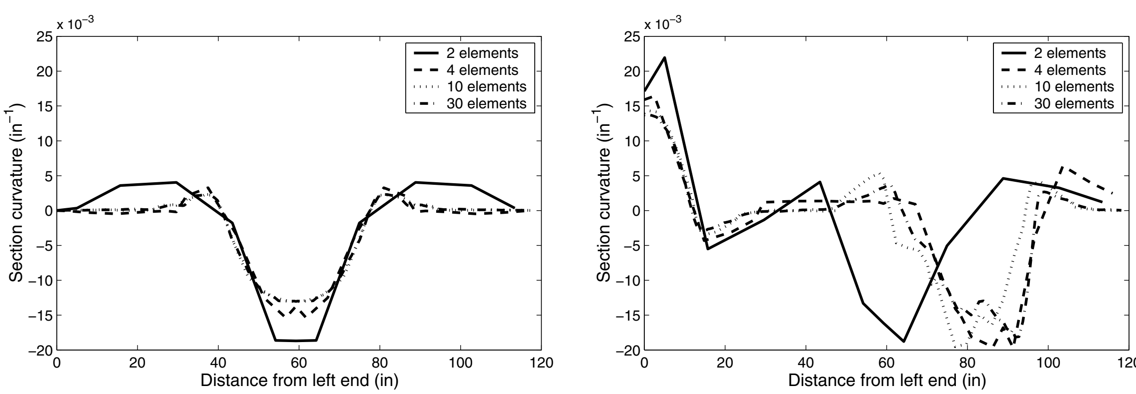

(a) pin-pin support conditions (b) pin-fixed support conditions

Fig. 4.15 Computed curvature distributions for different number of elements and seven integration points per element.

4.4.3 Number of Integration Points

In this section the number of integration points within each element is varied. For this series of analyses, the number of elements was fixed at two, as this was found to be adequate in the previous section to capture the basic hysteretic characteristics of a strut. Within each subelement, 2, 3, 5, or 7 equally spaced integration points were considered (two of these are located at the ends of the subelement). The initial displacement of the center node was set equal to 0.05% of the initial length of the strut for all of the analyses.

Figure 4.16a shows the result of a monotonic quasi-static shortening of the uniaxial strut. In this instance, the model with only two elements and two integration points per element exhibits a slightly more significant loss of compressive strength in the post-buckling regime than the cases with more integration points. This is due to an underintegration of the element. Nonetheless, underintegration of element response is not recommended, and the minimum number of integration points recommended for the inelastic beam-column element is three. The models containing three, five, and seven integration points have almost identical results under monotonic loading.

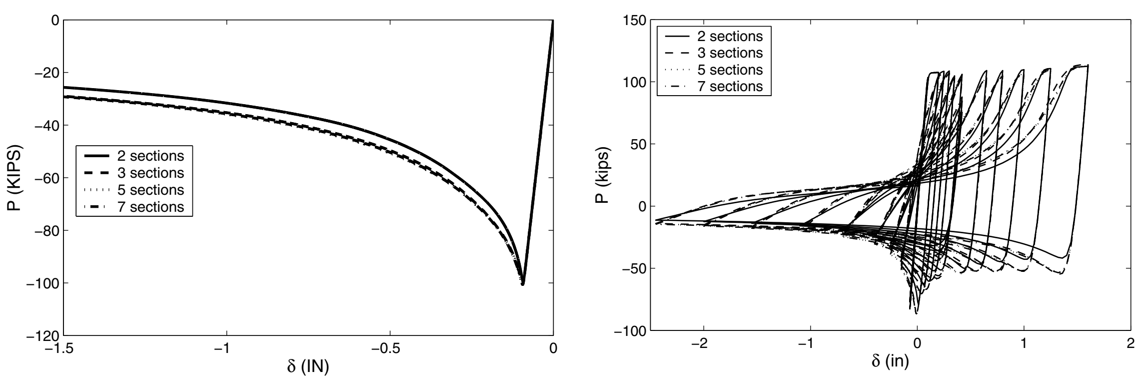

(a) monotonic response (b) hysteretic response

Fig. 4.16 Effect of number of integration points on strut response for two elements.

4.4.4 Number of Fibers

In this section, the number of fibers used at the cross-sectional level was varied. Table 4.1 lists the identification symbols used in this parametric study for the different combinations of fibers across the thickness and around the perimeter. For all these cases, the number of elements was kept at four, and the number of integration points per element was kept at three.

Figure 4.17 shows the results from the fiber parameter study. As one would expect, the monotonic and hysteretic behavior of the element that is represented by one fiber across the thickness and five fibers around the circumference does not accurately represent either the buckling load or the hysteretic behavior. This is a result of the reduced flexural stiffness and increased sensitivity to the interaction between moment and axial loads when only a few fibers are used to represent the entire cross section. Clearly, this calculation is more sensitive to the number of fibers around the perimeter than the number of fibers, as illustrated by the comparison of lines B and C and lines D and E in Figures 4.17a–b.

Table 4.1 Case identification symbols for fiber parameter study.

ID	Number of fibers across thickness	Number of Fibers around the perimeter
A	1	5
B	1	10
C	5	10
D	10	60
E	2	30

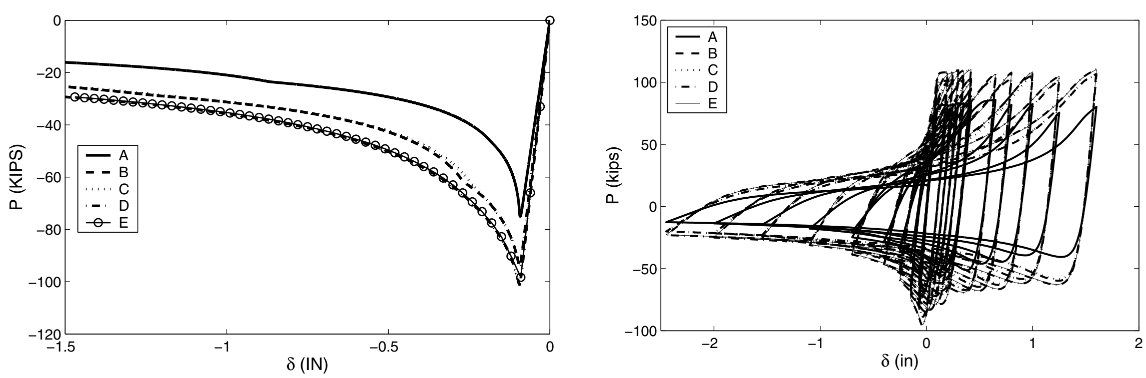

(a) monotonic response

(b) hysteretic response

Fig. 4.17 Effect of number of fibers used in cross-sectional representation. All responses are from four elements with three integration points per element.

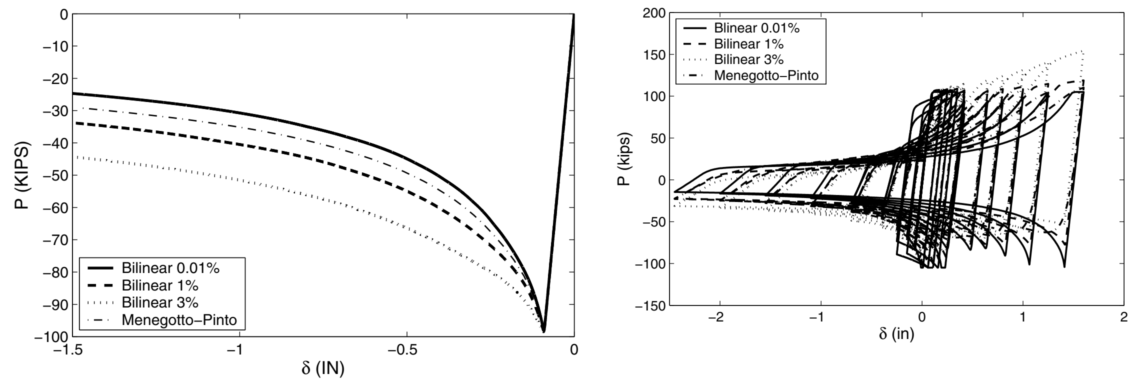

(a) monotonic response (b) hysteretic response

Fig. 4.18 Effect of nonlinear material type on hysteretic behavior of proposed element.

4.4.5 Material Model Type

This section discusses the influence of material constitutive relations on the nonlinear behavior of struts. The material models considered for this parameter study consisted of (a) the bilinear material type (Steel01) and (b) the Menegotto-Pinto material type used above. All of the material models had identical yield strength and elastic modulus. For Steel01, three values of strain-hardening ratio were considered, equal to 0.01%, 1%, and 3% of the initial modulus. The first of these values is intended to be representative of elastic-perfectly-plastic material behavior. Figure 4.20a shows a monotonic shortening of the strut for the different material models; note that the value of strain hardening does not influence the initial buckling load for monotonic shortening. It does significantly influence, however, the post-buckling behavior of the strut, with less strain hardening corresponding to a more dramatic loss of axial stiffness and strength.

Figure 4.20b shows the hysteretic behavior of these braces subjected to the cyclic loading protocol in Figure 4.10c. In the later compressive cycles, following tensile yielding of the strut, the bilinear models all exhibit sharp, well-defined buckling values, with higher buckling loads for the cases with lower strain hardening. The Menegotto-Pinto model and, to a far lesser extent, the bilinear models with relatively large strain hardening exhibited smoother buckling modes in the later cycles. This may be indicative of inelastic behavior spreading out further along the length of the strut, leading to a larger out-of-straightness (initial imperfections) in subsequent cycles. In fact, the bilinear material model with 0.01% strain hardening nearly returns to an almost perfectly straight condition when yielded in tension, causing nearly elastic-perfectly-plastic behavior when the member is loaded again in compression.

4.5 COMPARISON OF NUMERICAL AND TEST RESULTS

In this section, the ability of the OpenSees physical theory fiber model to predict experimentally observed behavior will be assessed for a variety of braces subjected to cyclically applied loads. Braces having a variety of cross sections are considered, including ones having sections constituted by wide flange; pipe; square, hollow steel shapes; and double angles. Different brace slenderness (kL/r) and compactness (b/t) ratios will be considered. It is expected that the proposed OpenSees model can more accurately capture the global behavior of steel struts with compact cross-sectional shapes.

For all of the models in this section, two elements were used, each with three integration points, to model a single strut. Each cross section was modeled to capture its hysteretic characteristics about its weak axis, as schematically shown in Figure 4.7, with six fibers across the depth of each flange and six fibers along the web for hollow structural tubes; five fibers were used for each flange and five fibers were used for the web for wide flange sections; two fibers along the thickness and 30 fibers around the perimeter for pipe sections; ten fibers in each flange and ten fibers along the length of the web for double-angle sections. As noted before, it is not expected that the results will be too sensitive to the number of fibers beyond a basic representation of the section. The material properties shown in Figure 4.4 were used to represent steel properties.

4.5.1 Struts Containing Compact Sections

The results used for comparison with numerical predictions were obtained from a series of tests by Black et al. (1980). The plots of the test results are obtained by scanning graphs from that report. More details regarding test conditions and results may be found in Black et al. (1980).

Figure 4.19a shows the experimental hysteresis loops for a W8x20 strut with a kL/r ratio of 120. This member is rather slender when compared to the pipe brace with a $kL/r = 80$ (shown in Fig. 4.8). As a consequence, the ratio of the absolute values of compression to tensile load capacities is smaller, and the ratio of reduced post-buckling compressive capacity to initial buckling capacity is larger. The loading history used in the test results is a slow ratcheting of the peak inelastic displacements tension excursions. Figure 4.19b shows the OpenSees analytical results for the same loading history. There is excellent agreement. These plots also show the experimental and analytical results for the transverse displacement of the brace at the plastic hinge. The OpenSees model predicts these transverse displacements with a high degree of accuracy. As noted previously, this out-of-plane displacement can create a hazard during earthquakes and necessitate costly repairs. The ability to model this transverse displacement accurately is helpful in assessing performance.

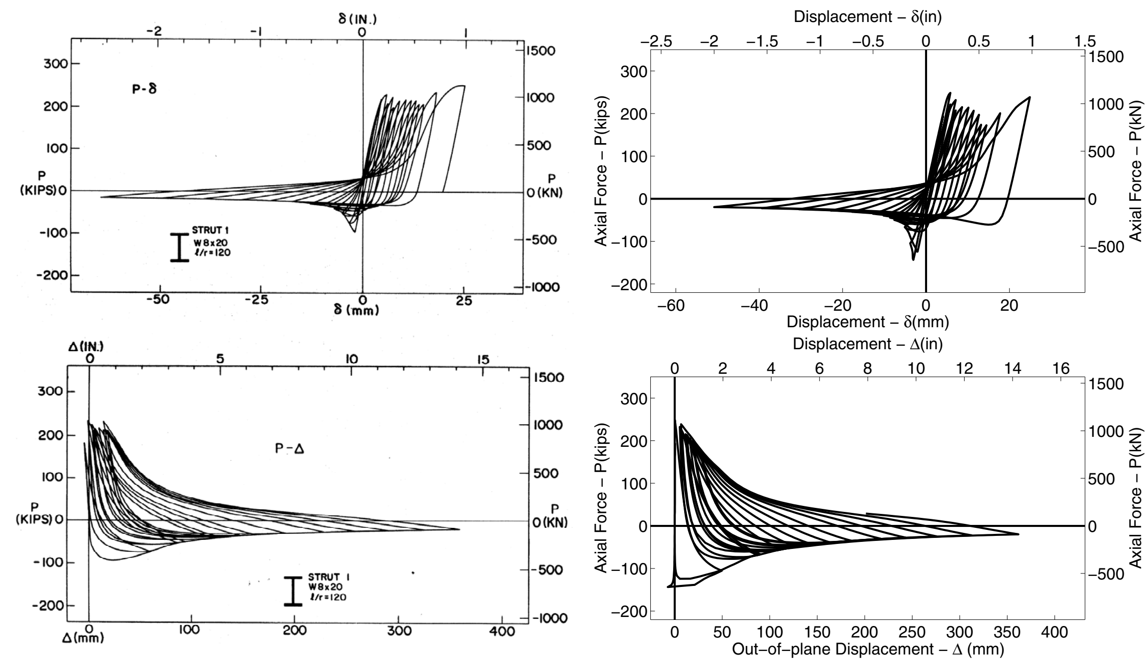

(a) experimental (b) analytical

Fig. 4.19 Correlation of hysteretic response of W8×20 strut with buckling before yielding in tension.

Figure 4.20a shows the axial force–axial displacement hysteresis of a brace similar to the one shown in Figure 4.19a. For this brace, the *kL*/*r* ratio is reduced to 80, and the sign of the loading history is reversed so that the brace undergoes a yield excursion in tension before it reaches the initial buckling condition. Because the material model includes the "Baushinger" effect, the brace model is automatically able to produce hysteresis loops similar to the experimental results.

Figure 4.21a shows the hysteretic behavior of a similar wide flange strut, but with a kL/r ratio of 40; this change "fattens" the hysteretic loops. The OpenSees model of this experiment is shown in Figure 4.21b. Again, the analytical representation is excellent. There are some discrepancies during later cycles, possibly due to local warping of the section.

Figure 4.22 depicts the hysteretic behavior of a double-angle strut and the results of a corresponding OpenSees simulation. For these tests, the double-angle struts have stitch plates at the minimum code-required spacing. This gives them an effective kL/r ratio of 80. For the analyses, the two angle sections are assumed to be part of the same section (along the entire length of the strut) with no relative movement between them (i.e., a plane section drawn across both sections in the undeformed configuration remains plane during deformation). This assumption is not good under large inelastic deformations because of the large distance between stitch plates, and formation of local buckles. As a result, the actual tests show a gradual decrease in buckling load capacity with each cycle. During the last tensile excursion, the section began to fail. Although the OpenSees model did not capture this failure, the overall fidelity of the predicted response is quite good.

Figures 4.23a–b show experimental and analytical force-displacement hysteresis loops for a HSS 4×4×1/4. The section satisfies the AISC requirement for being compact (b/t = 16). As such, the OpenSees model was able to simulate the global behavior quite well.

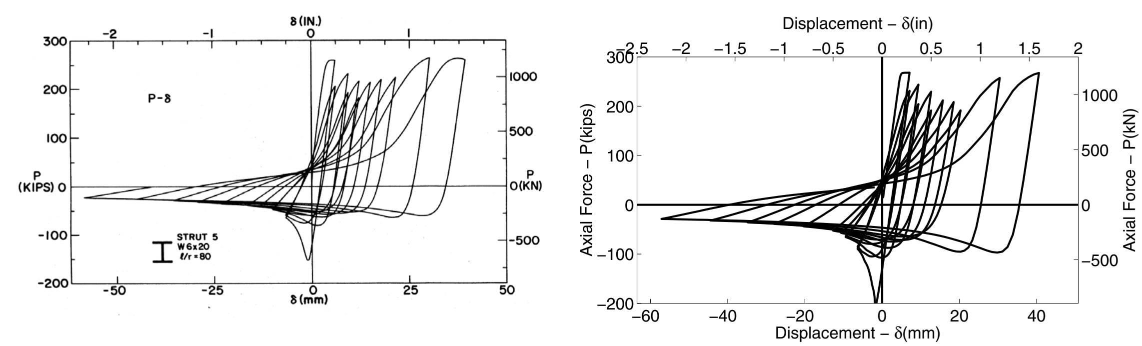

(a) experimental (b) analytical

Fig. 4.20 Correlation of hysteretic response of W6x20 strut with tension yielding before buckling.

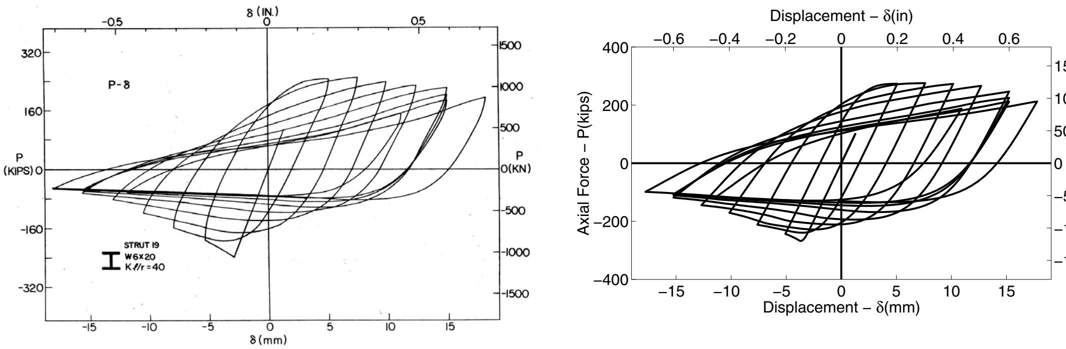

(a) experimental (b) analytical

Fig. 4.21 Correlation of hysteretic response of W6x20 strut with small slenderness ratio kl/r=40.

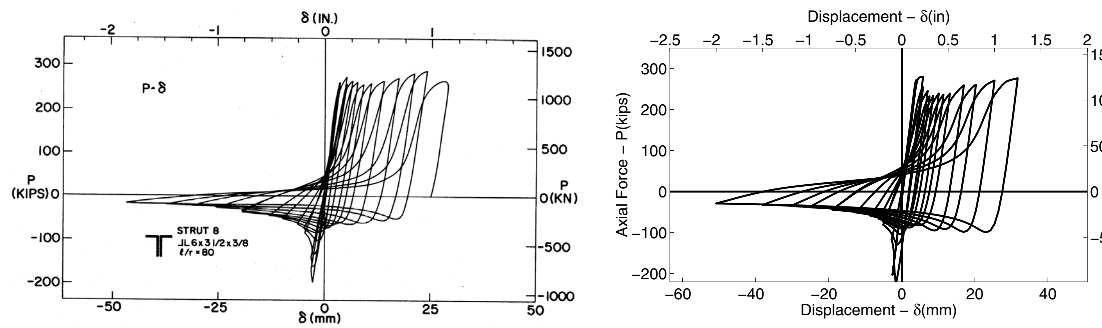

(a) experimental (b) analytical

Fig. 4.22 Correlation of hysteretic response of double L6x3½x3/8.

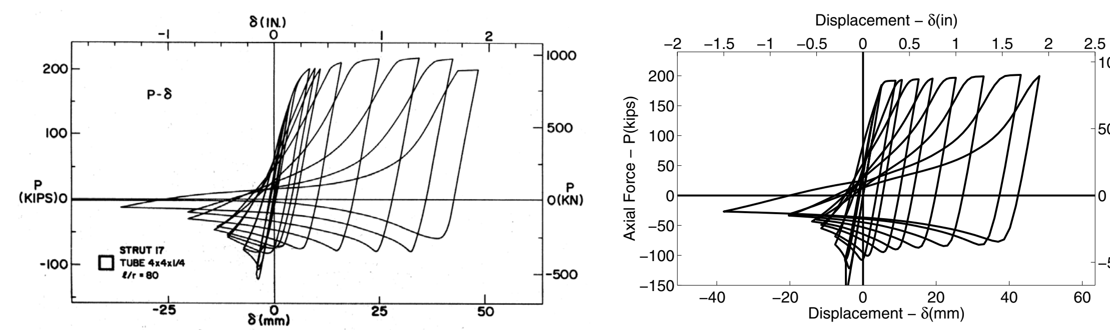

(a) experimental (b) analytical

Fig. 4.23 Correlation of hysteretic response of HSS 4x4x1/4 hollow strut.

4.5.2 Struts Containing Non-Compact Sections

To examine the ability of the proposed buckling model to simulate the response of struts having non-compact sections, two tests by Lee et al. (1987a) were analyzed. The experimental results presented in this section were scanned from the report by Lee (1987). The reader is urged to consult that report for more information regarding test conditions and findings.

Figure 4.24a shows the hysteretic behavior of a HSS 4×4×1/8 strut. The section was not compact and locally buckled. Local buckling in high non-compact members can occur at or even before the onset of global buckling. Local buckling behavior generally has an important influence on the global post-buckling and hysteretic behavior of struts. The numerical results (Fig. 4.18c) diverge from the experimental ones as the axial forces approach the buckling load during the first cycle. The rate of deterioration during the first post-buckling excursion and the degree of deterioration of the hysteretic loops on subsequent cycles are far worse for the physical specimen than predicted numerically (where the effects of local buckling are disregarded).

A number of investigators (Lee 1987; Lee and Goel 1987) have suggested that the global and local behavior of hollow steel struts with moderate width-to-thickness ratios can be improved by filling them with concrete. Figure 4.24b illustrates the modest improvement to hysteretic behavior using concrete fill (Lee and Goel 1987) for a strut with kL/r = 43 and b/t = 28. Some improvement in behavior can be seen but substantial discrepancies between the numerical and experimental results still exist (compare Figs. 4.24b and c). The concrete fill does not entirely prevent local buckling, and significant slip between the concrete and the steel shell is likely.

It is thus recognized that the modeling approach suggested herein is valid only for compact sections, and for ranges of behavior where local buckling has not occurred. The effects of local buckling may be accounted for in a number of ways: (1) use of effective material properties calibrated to particular test results; (2) modeling the local buckles at particular locations along the brace by adding nodes at these locations and sets of flexural beam-column elements and employing the corotational formulation to let these buckle locally at the same time as the member as a whole buckles (this has significant limitations as multidirectional states of stress in the material are ignored); and (3) using shell or solid elements in combination with large displacement capabilities of a general finite element analysis program.

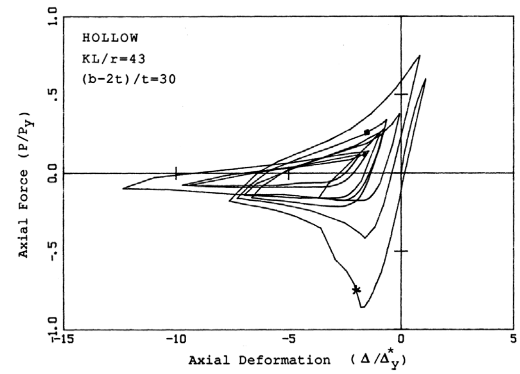

(a) Section containing slender width-to-thickness ratios (Lee and Goel,1987)

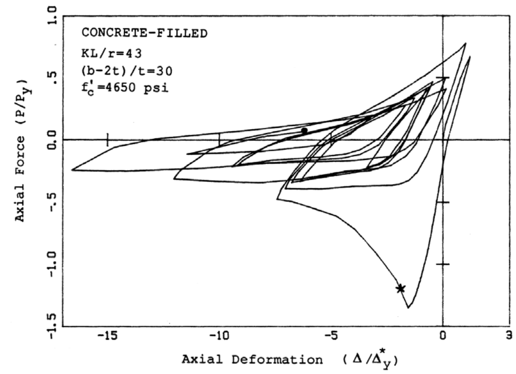

(b) Identical specimen with concrete-filled tube (Lee and Goel 1987)

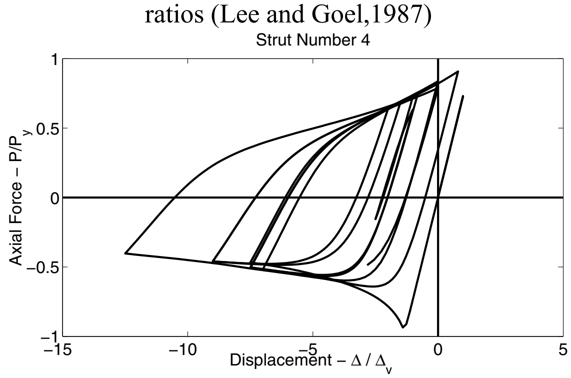

(c) analytical

Fig. 4.24 (a) HSS 4x4x1/8 sections tested as hollow members, (b) as concrete-filled, and (c) along with OpenSees predictions.

4.6 CONCLUSIONS

The chapter presents a model for the inelastic buckling behavior of steel members. The model consists of a force-based frame element with distributed inelasticity and fiber discretization of the cross section. With this approach, the response of the element can be derived by integration of the uniaxial stress-strain relation of the fibers and can account for kinematic and isotropic hardening as well as the Bauschinger effect of the material. Even though the element only accounts for small deformations in the formulation of stiffness and force quantities, large displacement geometry is included in the nonlinear transformation of the force-deformation relation of the individual element following the corotational formulation concept.

While the modeling approach proposed is applicable to beam-column elements in general, application of this concept has been limited in this chapter to simple bracing members or struts. Correlation studies with available experimental evidence of the hysteretic axial force–axial displacement response of steel struts demonstrate the ability of the proposed model to represent realistically the buckling strength, the post-buckling behavior, the tensile strength, out-of-plane deformations, and overall hysteretic behavior of struts with various types of compact cross-section. The parametric studies carried out related to the hysteretic behavior of a tubular brace result in the following modeling recommendations:

1. The brace member is subdivided into two inelastic beam-column elements (this increases to three or four, if asymmetric buckling of the member is likely).
2. An initial camber of 0.05–0.1% of the brace length is specified at the brace midspan.
3. Ten to fifteen layers across the depth of the cross section generally suffice for the accurate representation of the spread of yielding and the estimation of inelastic strains at the critical sections of a brace. Of these, five layers are used near the tension and compression most edges (i.e., in the flanges) and the rest are distributed across the web of the cross section.

For struts with compact sections, the effect of local buckling on the global hysteretic behavior is not very significant throughout most of the life of the brace. Local buckling is, however, important for the estimation of inelastic strains at critical sections of the brace. The accuracy of this estimation greatly impacts the analyst's ability to predict the brace fracture due to low-cycle fatigue. Clearly, local buckling and related effects have a very significant effect on the overall hysteretic behavior and failure of braces with non-compact cross sections. For this reason, it is important in future research to examine the means of simulating the effects of local buckling and related phenomena. In the next chapter, an empirical approach to simulating low-cycle fatigue related failures in braces susceptible to local buckling is explored and adapted to the OpenSees fiber-based beam-column model.

As noted previously, this approach to modeling struts is equally applicable to axially loaded beams and beam-columns; however, remaining to be carried out are correlation studies to assess the accuracy of the proposed model for beams and columns under generalized loading.

5 Modeling the Effects of Low-Cycle Fatigue

5.1 BACKGROUND

Uniaxial struts that buckle, either in plane or out of plane, typically form plastic hinges that experience very large rotational demands and consequently undergo very large strain deformation histories (Jain and Goel 1978; Lee and Goel 1987; Shaback and Brown 2003; Stojadinović 2003; Tremblay et al. 2003). These strain histories can cause local rupture due to low-cycle fatigue. Local buckling within the plastic hinge can substantially increase local strain demands and further reduce fatigue life. Once fracture initiates, the strength and stiffness of the entire element deteriorate quite rapidly (Gugerli and Goel 1980b; Ikeda and Mahin 1986). Where braces are rigidly connected (rather than pin-connected by gusset plates) to the adjacent framing, plastic hinging and low-cycle fatigue are issues of concern at the two ends as well as at the middle.

As stated previously, the performance of braced frame structures is very sensitive to the performance of its braces. Fracturing of the braces creates a sudden loss of strength and stiffness, necessitates the development of a new and possibly unanticipated load path, and can fundamentally change the behavior mode exhibited by the structure. All of these can have a dramatic effect on the maximum displacement and structural integrity of a braced-frame structure during a strong earthquake (Ikeda and Mahin 1986). Because the effect of low-cycle fatigue is an essential consideration in modeling steel-braced frames, this chapter focuses on developing and calibrating a low-cycle fatigue model for use with the OpenSees fiber-based beam-column buckling model presented in Chapter 4. Due to the fundamental limitations of the fiber modeling approach used, several simplifications are necessary. In particular, no attempt is made to model the actual local buckling phenomena that may occur or to account for principles of fracture mechanics to predict potentially brittle behavior that might occur at stress concentrations or discontinuities. As such, the phenomenological low-cycle fatigue damage model developed needs to be calibrated using relevant test data.

Methods used for predicting the low-cycle fatigue life of a material or component must be viewed as approximate. Considerable scatter is apparent in the observed low-cycle fatigue life measured using virtually identical specimens, and the results can be very sensitive to apparently small changes in detailing or loading conditions. To illustrate this point, Figure 5.1 shows axial load–axial displacement hysteretic loops for two identical uniaxial brace specimens; specimen 01 was tested by Yang (Yang and Mahin 2005) and specimen 07 was later tested by Uriz. Both were subjected to identical axial displacement histories (following a compression-dominated, near-fault protocol). Although specimen 01 did not reinforce the net reduced section, both specimens 01 and 07 failed at the midspan plastic hinge region.

Figure 5.1 shows that the initial fracture of specimen 01 was a whole cycle earlier than for specimen 07, even though the localized yielding and damage near the net reduced sections at the ends of specimen 01 might be expected to reduce the strain demands in the central plastic hinge region for this specimen. Uniaxial cyclic tests on reinforcing bars (Brown and Kunnath 2000) along with many cyclic tests on wide flange sections (Ballio and Castiglioni 1995; Bertero and Popov 1965; Fisher et al. 1997; Krawinkler et al. 1983; Popov and Pinkey 1969; Stojadinović 2003) have also shown similar differences in the fatigue life achieved by specimens with similar configurations and loading histories. As such, it should be anticipated that the methods used in this section to simulate the effects of low-cycle fatigue can be reasonably accurate to only within a few cycles. Even with such a large anticipated scatter of experimental data, the models developed in the past and in this section provide the analyst with an essential tool in the assessment of the performance of structures where low-cycle fatigue is of concern. Uncertainty with respect to modeling fatigue life may be an important issue to consider in assessing the overall performance of braced-frame structures.

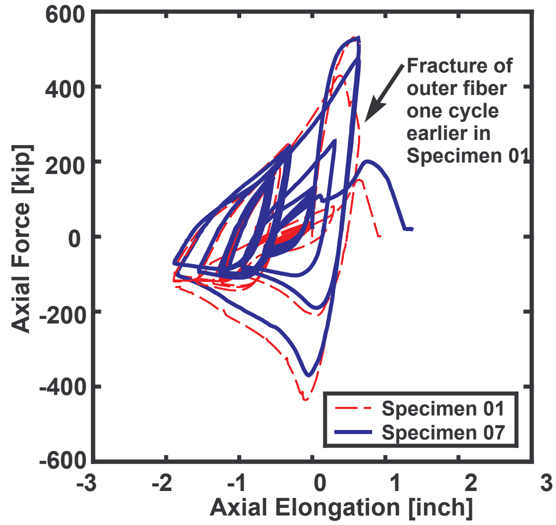

Fig. 5.1 Comparison of two uniaxial specimens with identical loading history and location of fatigue fracture.

The effects of low-cycle fatigue may be important for elements other than braces, of concern in regions of steel members and connections where large inelastic strains may occur, especially in conjunction with local buckling. These include low-cycle fatigue of the yielding portions beams, beam-columns, fully- and partially-restrained beam-to-column connections, and column-to-base-plate connections (and reinforcing bars in reinforced concrete structures). To be able to treat such general situations, the numerical modeling tools developed in this chapter focus on conditions where low-cycle fatigue can be represented consistent with limitations imposed by fiber modeling. As such, the model would not be applicable to situations where plane sections may not remain plane, where the section is susceptible to considerable distortion (e.g., non-compact sections) and where the local region in question is subject to multiple components of stress (e.g., near stress concentrations). In addition, application of such a numerical model requires using relevant experimental data to identify the empirical coefficients required by the model. Based on these considerations, this chapter will focus primarily on effects of low-cycle fatigue on the plastic hinge regions of steel bracing members and steel beam-columns.

Typically, uniaxial constant amplitude tests are performed to determine the fracture life characteristics of a particular detail fabricated from a specific material; however, loading sequences due to earthquake-induced loading are rarely constant in amplitude. For this reason, several counting schemes have been introduced to determine the number of equivalent cycles withstood under a variable deformation history (Amzallag et al. 1994; Anthes 1997; ASTM

2003; Downing and Socie 1982; Glinka and Kam 1987; Nagode and Hack 2004). The simplest and most popular method of defining equivalent cycles, and counting the number and amplitude of these cycles, is the "rainflow" method, or a variation thereof. The damage associated with each cycle is then determined using a fatigue life versus deformation amplitude relation, and damage occurring over all cycles is obtained by accumulating damage resulting from each equivalent cycle. This accumulated damage is used to predict the onset of rupture of a uniaxially loaded material (Ballio and Castiglioni 1995; Brown and Kunnath 2000; Fisher et al. 1997; Krawinkler et al. 1983; Shaback and Brown 2003; Stojadinović 2003).

Because typical phenomenological element models do not track local strains, cycle counting algorithms for these elements are based on the overall strut axial force–axial displacement hysteresis loops, rather than on local stress–strain relationships. Several investigators have used this approach, and identified the various empirical parameters needed to implement the model based on the results from several experimental studies of struts (Tang 1987). While these models have provided good predictions of the onset of rupture in pin-ended uniaxial struts (when calibrated using data for braces with the appropriate kl/r and b/t ratios), they are difficult to use with fiber models (since the entire strut would need to be removed when its fatigue life was exceeded) and are difficult to extend to other situations where fiber models can be effectively utilized (e.g., struts with fixed ends, beams and beam-columns).

When fiber models are used to represent structural uniaxial material properties, strains are explicitly tracked in each fiber. Thus, cycle counting can be based on the strain histories within each fiber across a section and at each section along the member length. Consequently, a fiber-based low-cycle fatigue model would predict rupture within individual fibers, and a gradual, partial or complete failure of the sections would be modeled automatically. Given that, this approach does not account for (a) fracture mechanics related phenomena that might lead to rapid propagation of a crack that initiates in a cross section due the local rupture of the material due to low-cycle fatigue or (b) the effect of local buckling and strain localization that may occur in a plastic hinge region.

Typically, rainflow counting methods for characterizing the number and amplitude of the cycles imposed are typically employed after loading of the member in question has stopped. For this reason, a slightly modified version of the standard rainflow cycle counting method is implemented herein with an "on-the-fly" damage monitoring capability. With this capability, as the strain history progresses during the structural response, individual uniaxial fibers are monitored and removed from the fiber element conglomeration when their fatigue life is exceeded. This approach, in conjunction with properly calibrated low-cycle fatigue failure criteria, should permit reasonable extrapolation to situations where fiber models are used to represent plastic hinge behavior.

This chapter briefly describes current empirical methods for modeling the effects of rupture in buckling struts based on phenomenological and fiber-based elements. A modified rainflow counting rule is first defined and then implemented as a material model within OpenSees. Data for uniaxially loaded struts and bending of wide flange beams are used to identify the appropriate parameters for predicting fatigue life. The numerical results obtained using this approach are compared to test data for several struts. The results are also compared to predictions made with existing fatigue models based on brace axial load–axial displacement relationships (e.g., as implemented in SNAP-2DX, and used in the preliminary analyses presented in Chapter 3).

5.2 MODELING THE EFFECTS OF FATIGUE USING PHENOMENOLOGICAL MODELS

Due to the nature of most phenomenological models, previous successful methods for modeling the effects of low-cycle fatigue for struts have been implemented at the element level rather than at the material level. Cycle counting was based on the strut's axial displacement history, and fracture criteria were empirically derived accounting for material properties, cross-sectional shape, and local and global slenderness (kl/r and b/t) ratios.

A popular fatigue model of this type was developed by Tang (Tang and Goel 1989), and subsequently refined by Lee and Goel (1991) using additional experimental results by Hassan and Goel (Lee and Goel 1987). Because of the extensive data set used for calibration, this method provides considerable confidence in the predictions of brace rupture due to low-cycle fatigue.

The fatigue model refined by Lee and Goel (Lee and Goel 1987) was based on a normalized axial force–displacement hysteretic curve, as shown in Figure 5.2. Fatigue life prediction was based on the cumulative deformation that a brace can withstand prior to cross-sectional failure. In this model, more importance is placed on the portion of a tension excursion that occurs after the member has substantially straightened, rather than the portion while the member is beginning to straighten. For example, in Figure 5.2, the tension excursion A to C is divided into two portions, Δ_1, and Δ_2; Δ_1 extends from A to B, and Δ_2 extends from B to C. The point B on the excursion is characterized by the deformation where the load reaches 1/3 of P_y.

The cycle counting is weighted considering this definition, as shown in Equation (5.1). This definition is applied to all cycles to aggregate the total weighted deformation imposed on the brace. The cumulative deformation to failure (Δ_f) is then calculated for rectangular HSS sections using Equation (5.2), where C_S is a numerical constant obtained by statistical analysis of the experimental results, b is the width of the hollow tube, d is the depth of the hollow tube, and F_y (in ksi) is the actual strength of the steel.

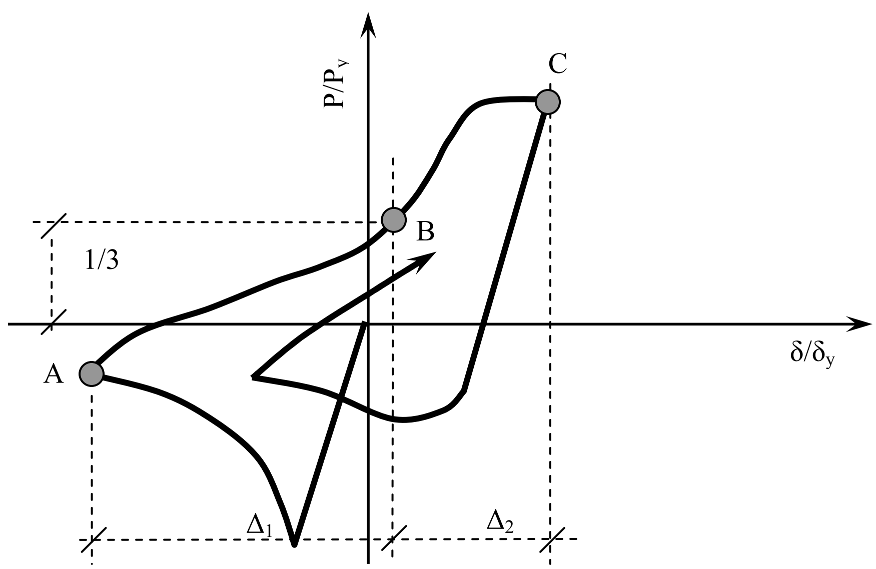

Fig. 5.2 Normalized hysteretic curve used for calculating fatigue life (Lee and Goel 1987).

$$\Delta_f = \sum \left[0.1\Delta_1 + \Delta_2\right] \tag{5.1}$$

$$\Delta_f = C_S \frac{(46/F_y)^{1.2}}{\left[(b-2t)/t\right]^{1.6}} \left(\frac{4b/d+1}{5}\right) \tag{5.2}$$

This approach to fatigue life prediction was later refined by studies in Canada by Archambault et al. (2003) and by Shaback and Brown (2003). Although the weighting method defined in Equation (5.1) was still used in these studies, they improved the “statistical reliability” of the approach by modifying Equation (5.2) and calibrating the model to a more extensive set of uniaxial strut tests. The resulting empirical relation is shown in Equations (5.3)–(5.4) (shown for SI units). According to Shaback and Brown (2003), this equation produces a 50% reduction in the standard deviation over previous models.

$$\Delta_f = C_S \frac{\left(350 / F_y\right)^{-3.5}}{\left[(b-2t)/t\right]^{1.2}} \left(\frac{4(b/d) - 0.5}{5} \right)^{0.55} (70)^2 \text{ for } \frac{KL}{r} < 70 \tag{5.3}$$

$$\Delta_f = C_S \frac{\left(350 / F_y\right)^{-3.5}}{\left[(b-2t)/t\right]^{1.2}} \left(\frac{4(b/d) - 0.5}{5} \right)^{0.55} \left(\frac{KL}{r} \right)^2 \text{ for } \frac{KL}{r} \geq 70 \tag{5.4}$$

The criteria in Equations (5.2)–(5.4) are applicable to low-cycle fatigue of HSS struts. Similar equations can be developed for any section provided enough experimental data are available for meaningful statistical analysis to determine the needed coefficients.

5.3 MODELING THE EFFECTS OF LOW-CYCLE FATIGUE USING OPENSEES FIBER MODEL

5.3.1 Background

In classical approaches to modeling low-cycle fatigue, a linear relationship is assumed between the log of the number of constant amplitude cycles to failure N_f and the log of the strain amplitude ε_i experienced in each cycle. This is often referred to as the Coffin-Manson relationship, and is represented below by Equation (5.5) (ASTM 2003; Fisher et al. 1997; Glinka and Kam 1987). In this equation, ε_0 is a material (or component) parameter that roughly indicates the strain amplitude at which one complete cycle on a virgin material will cause failure, and m is another material (or component) parameter that describes the sensitivity of the log of the total strain amplitude to the log of the number of cycles to failure. In this model, a cycle is simply an incremental strain or displacement excursion, which begins at a trough, continues to a peak, and returns to another trough (see Fig. 5.3).

In contrast to the damage model represented by Equation (5.1), where an excursion twice as large causes twice the damage, the logarithmic nature of Equation (5.5) generally results in disproportionate damage occurring in larger cycles. Generally, empirical parameters determined for Equation (5.5) differ for low-cycle fatigue (where significant inelastic deformations occur in each cycle) and for high-cycle fatigue (where the element in question is generally loaded in the elastic range).

$$\varepsilon_i = \varepsilon_0 \left(N_f\right)^m \tag{5.5}$$

During seismic response, it is unlikely that a component will be subjected to constant amplitude cycling. As such, the amplitude of each cyclic excursion in deformation history and the number of cycles at each amplitude identified is often computed using a rainflow cycle counting method (ASTM 2003; Fisher et al. 1997). Damage for each amplitude of cycling is estimated by dividing the number of cycles at that amplitude (ni) by the number of constant amplitude cycles at that amplitude (Nfi) necessary to cause failure, and overall damage due to low-cycle fatigue is estimated by linearly summing the damage for all of the amplitudes of deformation cycles considered (ε_i). Known as Miner's rule, this form of damage accumulation is shown in Equation (5.6), and it has the important implication that the sequence of each cycle during the overall response has no effect on the fatigue life. In Equation (5.6), *DI* is a parameter that varies from 0 (in the virgin undamaged state) to 1 (at failure) and represents an accumulated damage index.

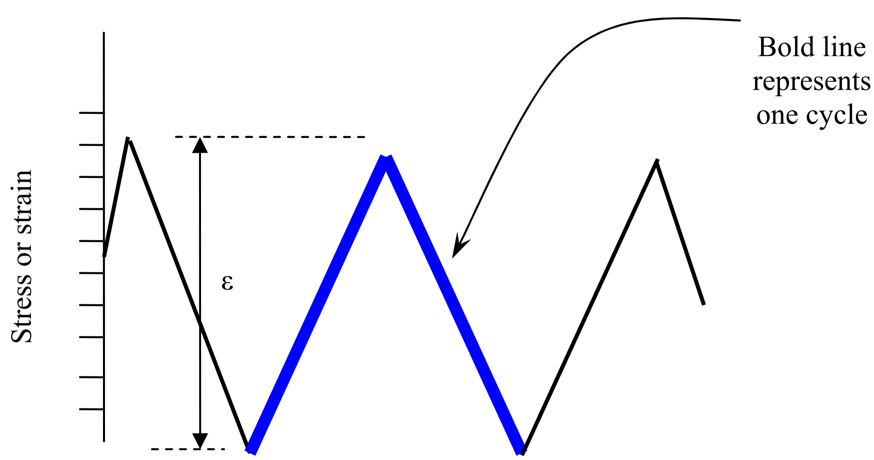

Fig. 5.3 Illustration of a cycle and its corresponding strain, ε.

$$DI = \sum \frac{n_i}{N_{fi}} \tag{5.6}$$

As an example, if one is to take one cycle at strain amplitude of ε_i, then the equivalent damage due to this complete cycle would be:

$$DI_i = \frac{n_i}{N_{fi}} = \frac{1}{10^{m^{-1}\log\left(\varepsilon_i/\varepsilon_0\right)}} \tag{5.7}$$

For a one-half cycle at strain ε_i, (i.e., a monotonic strain from value ε to value $\varepsilon+\varepsilon_i$), the damage due to this strain would simply be:

$$DI_i = \frac{n_i}{N_{fi}} = \frac{(1/2)}{10^{m^{-1}\log\left(\varepsilon_i/\varepsilon_0\right)}} \tag{5.8}$$

When calibrated, research has shown that such a model can be used to successfully predict low-cycle fatigue failure of concrete reinforcement and wide flange components (Ballio and Castiglioni 1995; Bertero and Popov 1965; Fisher et al. 1997; Krawinkler et al. 1983; Popov and Pinkey 1969; Stojadinović 2003). Note, however, that many other models exist to accumulate damage (e.g., Amzallag et al. 1994; Brown and Kunnath 2000; Chai et al. 1995; Fisher et al. 1997; Glinka and Kam 1987; Lehman 1998).

5.3.2 Modified Cycle Counting

There are several alternative methods to count equivalent constant amplitude cycles (ASTM 2003). The American Society of Testing and Materials (ASTM) has standardized some of the most common methods for cycle counting and has included them as part of an active standard (ASTM 2003). A common feature of these methods is that they analyze the entire strain history of interest to identify and count cycles. To monitor whether a fiber has reached its fatigue life, this standard approach would necessitate examination of the entire time strain history for each fiber at each time-step, since the strain history changes as each increment of strain occurs. Because of the computational effort involved in this approach, a modified procedure is proposed that utilizes the traditional rainflow cycle counting method to accumulate damage, but does so by analyzing only a relatively short moving window of recent strain history.

Based on experience with analysis of strain histories associated with earthquake response, the modified method keeps track of only the four most recent peaks (strain reversals) at any given time. This makes memory allocation much simpler when programming a material model to consider the accumulation of low-cycle fatigue-related damage. This simplification contains some other minor differences from the standard cycle counting procedures, as will be shown below through an example. It should be noted that commonly accepted rainflow cycle counting procedures (ASTM 1987) do not all result in identical values for the number of equivalent cycles and their corresponding amplitudes for a given strain history. While the new model proposed below does not track strain amplitudes exactly as would be done in a traditional rainflow method for all cases, the number of cycles and the corresponding amplitudes are in many cases identical.

Table 5.1 lists definitions of several parameters needed to understand the cycle counting method implemented here.

Table 5.1 Parameters used in cycle counting.

Parameter	Definition
Peak	Location in strain history were the slope of the strain history reverses sign
X	Absolute value of strain range (from peak-to-peak), under consideration
Y	Absolute value of previous strain range (from peak-to-peak)
A,B,C,D	Peak labels, D is the most recent peak under consideration, and A is the oldest.

5.3.3 Modified Cycle Counting Method and Peak Counting

A narrative explanation of the process used to accumulate damage in individual fibers is described below, which describes how and when damage is accumulated. In the narrative, Miner's rule is used to accumulate damage; however, other accumulation rules could be used. If at any point damage index *DI* become larger than unity, then the corresponding fiber in the cross section has its stress and stiffness reduced to zero. While the effective stiffness and strength of the fiber could be gradually reduced as a function of *DI*, this was not done herein.

An illustrative example of how cycles are counted in the modified rainflow method is presented in Figure 5.4. A fictitious strain history is assumed for the example, and the modified rainflow cycle counting procedure is used to keep track of the number of cycles, and their corresponding strain range. In this graphic example, the method used to accumulate damage is not described.

1. Start of history
   a. Begin with zero damage
   b. First point is considered a peak, peak A.
   c. Small cycle counter (SSC) is zero, SSC=0.
2. Continue along strain history until two subsequent peaks, peaks B and C, have been identified.
3. Calculate range Y as |B-A|, and range X as |C-B|,
   a. if X>Y;
      i. count Y as ½ cycle,
      ii. accumulate damage; $DI = DI + \dfrac{(1/2)}{10^{m^{-1}\log\left(Y/\varepsilon_0\right)}}$
      iii. discard peak A, and peaks B, and C, become peak A, and B. respectively.
      iv. Continue until a new peak, C, is reached,
      v. go to step 3.
   b. if Y>=X;
      i. SSC=SSC+1
      ii. continue until peak D is reached
      iii. go to step 4
4. Calculate range Y as |C-B|, and range X as |D-C|,
   a. if X>Y;
      i. count one full cycle at Y
      ii. accumulate damage; $DI = DI + \dfrac{1}{10^{m^{-1}\log\left(Y/\varepsilon_0\right)}}$
      iii. discard peaks B and C, peak D becomes peak B
      iv. continue until a new peak C is found
      v. set SSC = 0
      vi. go to step 3
   b. if Y>=X
      i. SSC=SSC+1
      ii. go to step 5

5. If SSC = 2
    a. count one full cycle at range X
    b. accumulate damage: $DI = DI + \dfrac{1}{10^{m^{-1}\log\left(X/\varepsilon_0\right)}}$
    c. discard peaks C and D
    d. SSC = 0
    e. continue until new peak C is determined
    f. go to step 3
6. If at the last point in the history (can be considered a peak)
    a. The last point is B (i.e., peaks C and D do not exist):
        i. X = |B-A|
        ii. one half cycle at X is counted
        iii. accumulate damage: $DI = DI + \dfrac{(1/2)}{10^{m^{-1}\log\left(X/\varepsilon_0\right)}}$
    b. The last point is C (i.e., D does not exist)
        i. X = |C-B|, Y=|B-A|
            (a) if X>Y
                (i) count one full cycle at Y, and one-half cycle at X
                (ii) accumulate damage: $DI = DI + \dfrac{(1/2)}{10^{m^{-1}\log\left(X/\varepsilon_0\right)}} + \dfrac{1}{10^{m^{-1}\log\left(Y/\varepsilon_0\right)}}$
            (b) if Y>=X;
                (i) count one full cycle at X, and one-half cycle at Y
                (ii) accumulate damage: $DI = DI + \dfrac{1}{10^{m^{-1}\log\left(X/\varepsilon_0\right)}} + \dfrac{(1/2)}{10^{m^{-1}\log\left(Y/\varepsilon_0\right)}}$
    c. If the last point is D,
        i. if |D-A| > |A-B|
            (a) X = |D-A|; Y= |B-C|
            (b) count one full cycle at Y, and one-half cycle at X
            (c) accumulate damage: $DI = DI + \dfrac{1}{10^{m^{-1}\log\left(Y/\varepsilon_0\right)}} + \dfrac{(1/2)}{10^{m^{-1}\log\left(X/\varepsilon_0\right)}}$

ii. if |D-A| < |A-B|

(a) X = |B-A|; Y= |D-C|

(b) count one full cycle at Y and one-half cycle at X=|B-A|

(c) accumulate damage: $DI = DI + \dfrac{1}{10^{m^{-1}\log\left(Y/\varepsilon_0\right)}} + \dfrac{(1/2)}{10^{m^{-1}\log\left(X/\varepsilon_0\right)}}$

During an analytical simulation, the fatigue life of a fiber may be exhausted before a peak is reached. Thus, step 6 in the above narrative needs to be computed at each converged point in the strain history. For the damage accumulation, we remove damage index *DI* on the left-hand side of the accumulation equation and replace it with a temporary index representing the last damage index, *DL*. If *DL* is larger than unity, the fatigue life is flagged as being exhausted, and the material fiber is removed from the cross section by reducing its stress and strain to zero. If *DL* is less than unity, *DL* is discarded and the analysis proceeds to the next step.

Step 1

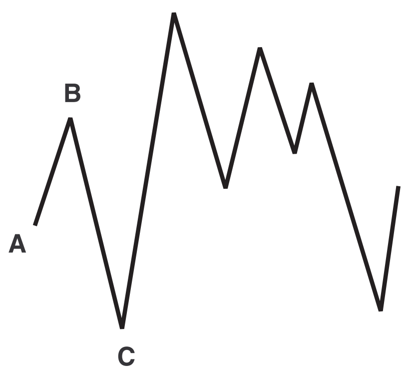

Point A is considered the starting point. Point A will always be the left-most of the last four points considered. Since a minimum of two excursions are required, we continue along the history until we gather two more peaks, B and C, and compute their strain ranges.

Y = |B-A|

- X = |C-B|

X ≥ Y:

Because A is at start, count one-half cycle as Y=|B-A|

discard point A, peak B becomes point C, peak C becomes peak B

go to next peak

It is assumed that each intermediate point (not shown here) is assumed to be the last data point along the way to a peak; damage is then calculated; if the fatigue life has been exceeded, then the material is assumed to be fractured. In this case if the last data point were to be before point B, e.g., B′, then one cycle at Y=|B′-A| is counted. If the last data point is just before point C, say C′, then one half cycle at Y=|B-A| is counted along with one-half cycle at X=|C′-A|

Step 2

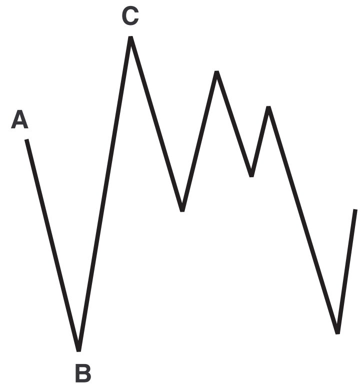

Now that we have acquired the next peak, analyze the strain ranges

$$Y = |B-A|$$
$$X = |C-B|$$
$$X \geq Y:$$

Because A is at start, count one-half cycle as

$$Y=|B-A|$$

discard point A, peak B becomes point C, peak C becomes peak B

go to next peak

(Note: this is identical to standard rainflow cycle counting procedure until this point)

If the last peak were somewhere before peak C, say C′, then one-half cycle at $Y=|B-A|$ is counted along with one-half cycle at

$$X = |C'-B|$$

Step 3

$$Y = |B-A|$$
$$X= |C-B|$$
$$X < Y:$$

increment small cycle counter

$(0+1 = 1)$

go to next peak

Again, if the final point was before point C, say C′, one cycle at $Y=|B-A|$ is counted along with one-half cycle at $X = |C'-B|$

Step 4

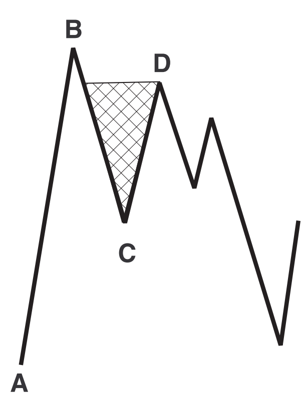

$$Y=|C-B|$$
$$X=|D-C|$$
$$X < Y:$$

increment small cycle counter

$(1+1=2)$

because small cycle counter = 2, count one full cycle at $Y = |D-C|$

clear small cycle counter

discard points D and C

go to next peak

Here, if the last data point is before point D, say D′, then one half cycle at $Y=|D'-A|$ is counted along with one full cycle at

$$X = |B-C|$$

Step 5

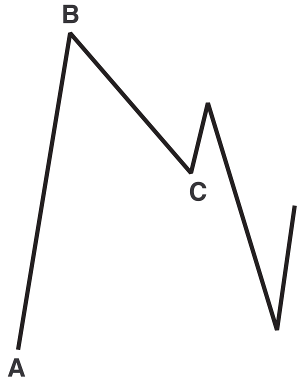

Y=|B-A|
X=|C-B|
X < Y :
increment small cycle counter
(0+1=1)
move to next peak

Again, if the final point was before point C, say C′, one cycle at Y=|B-A| is counted along with one half cycle at

X = |C-B|

Step 6

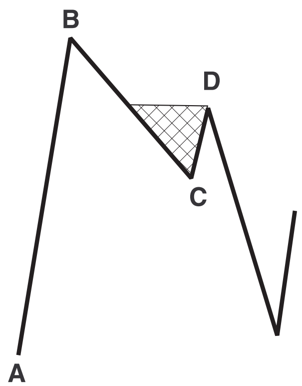

Y = |B-C|
X= |D-C|
X < Y :
increment small cycle counter
(1+1=2)
Because small cycle counter = 2, count one cycle at Y = |D-C|
clear small cycle counter
discard points D and C
go to next peak

Here, if the last data point is before point D, say D′, then one half cycle at Y=|D′-A| is counted along with one full cycle at X = |B-C|

Step 7

Y=|B-A|
X=|C-B|
X < Y :
increment small cycle counter
(0+1=1)
move to next peak

Again if the final point was before point C, C′, one cycle at Y=|B-A| is counted along with one half cycle at X = |C′-B|

Step 8

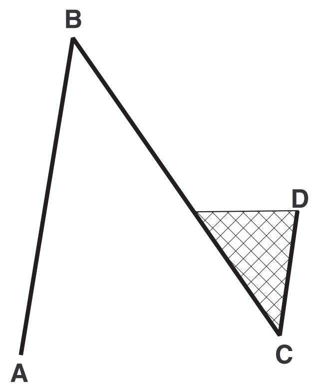

Y=|C-B|
X=|D-C|
X < Y :
increment small cycle counter
(1+1=2)
Because small cycle counter = 2, count one cycle
at Y = |D-C|
clear small cycle counter

Because this method is designed to be streamlined peak D is not considered the "last point", therefore we count only: one cycle at
X=|D-C|
Here if the last data point is before point D, say D′, then one half cycle at Y=|D′-A| is counted along with one full cycle at
X = |B-C|

Fig. 5.4 Graphic description of cycle counting method.

The above description of the fatigue model was implemented in OpenSees as a material wrapper. That is to say, the fatigue material can wrap any uniaxial material where strains (or deformations) are monitored. For all of the examples herein, the material is represented by the Menegotto-Pinto material model. The way the material is implemented in OpenSees, however, it can be extended (with no additional effort) to nonlinear springs for zero-length beam-column rotations (nonlinear springs representing shear links in beam-column members, concrete reinforcement, and any other material where the parameters m and ε_0 are known for the relationship being modeled). Appendix A contains the OpenSees C++ code used for the fatigue analysis presented above.

5.3.4 Calibration of OpenSees Fatigue Model Using Previous Test Results

Ballio and Castiglioni (1995) conducted several constant amplitude, low-cycle fatigue tests on cantilever columns with cross sections representing HEB, HEA, and IPE sections (see Table 5.2). In these tests, a pre-defined displacement history was applied in a cyclic fashion at 1.4 meters away from the fixed base of the cantilever. Some of the prescribed displacements caused severe local buckling at the base of the cantilever, while some of the tests were conducted at displacement levels just beyond yield so numerous cycles were imposed prior to failure. Ballio and Castiglioni reported that the number of cycles to failure seemed to follow the Coffin-Manson relationship shown in Equation (5.5), regardless of the amplitude of the cycles. Subsequently, when variable amplitude histories were applied to the specimens a linear accumulation model for damage (Eq. 5.6) adequately predicted the onset of fracture on variable amplitude tests, when combined with an appropriate cycle counting scheme (e.g., rainflow cycle counting). For this reason, the Ballio and Castiglioni data provide a useful starting point for calibrating the modified low-cycle fatigue model.

Table 5.2 Geometric properties used in low-cycle fatigue study (Ballio and Castiglioni 1995).

Shape	Area (cm^2)	Flange (mm)			Web (mm)		
		b	t	b/t	h	t_w	h/t_w
HE220A	64.3	220	11.0	20.0	188.0	7.0	26.8
HE220B	91.0	220	16.0	13.8	188.0	9.5	19.8
IPE300	53.8	150	10.7	14.0	278.6	7.1	39.2

A two-dimensional OpenSees model was created to mimic the Ballio and Castiglioni experimental setup. This model contained a nonlinear, force-based beam-column element with multiple fiber cross sections representing the HEA, HEB, and IPE sections tested. Each cross section contained four fibers distributed over the height of each flange, and four fibers distributed over the height of the web. Three integration points were specified for the element. The material model used for the specimen was the Menegotto-Pinto material. The value for yield strength for all of these models was identical and set to be the nominal value for yield strength for the European material properties, as specified for these specimens. The prescribed amplitudes and number of cycles from physical tests were imposed on the analytical model using a displacement control static analysis algorithm in OpenSees. Uniaxial strain histories were then extracted from the most heavily strained (outermost) fibers for the cross section at the fixed base. A constant displacement history applied at the top of the beam results in a strain history at the outer fiber at the base section where the first cycle may have a strain amplitude slightly larger than the second (can differ by roughly 2–5%), and the third cycle may be slightly less than the second (see Fig. 5.5). After about two or three cycles, depending on the displacement amplitude applied at the cantilever tip, the strain amplitude is nearly constant. Thus, in this study, the strain amplitude of all cycles of the outer fiber strain history are averaged, and is referred to, interchangeably, as the average strain amplitude, or simply the strain amplitude. For the sake of consistency, this is continued throughout this study; however it is perfectly reasonable to use any strain amplitude from any of the cycles to be representative of the strain amplitude due to the extreme similarity in magnitude.

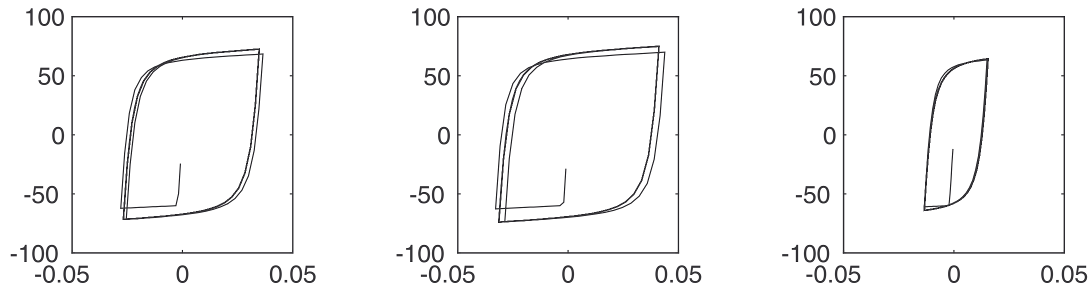

Fig. 5.5 Stress-strain histories extracted from outermost fiber of base cross section, showing very small difference in strain amplitude in first few cycles. Note similarity of strain histories in all cycles.

The averaged strain amplitude from the fiber's hysteresis was then assumed to be the strain amplitude, corresponding to the number of cycles to failure observed in the outermost fiber of the experiment. A log-log plot of the number of cycles to failure and the average strain amplitude extracted from the outer fiber of the analytical model is presented in Figure 5.6. Also shown in this figure is a least-squares linear regression of the data (solid line). It is clear from the figure that the Coffin-Manson relationship is valid. It is important to recognize that while local buckling occurred in many of the specimens, the analytical model used to predict strain amplitudes did not account for this phenomenon. As such, the computed strains do not represent the actual strains in the member, but parameters used in the model are "calibrated" to the data in order to compensate for this fact. Figure 5.6 also suggests that the relationship may be relatively independent of the member cross section.

The slope of the solid line shown in the log-log plot in Figure 5.6 is -0.458. This is the coefficient m in Equation (5.5) and relates the sensitivity of the total strain to the number of cycles to failure. The corresponding value of the coefficient ε_0 was determined to be 0.190, representing (approximately) the strain range at which one complete cycle will cause low-cycle fatigue failure. These parameters can be used in conjunction with Equation (5.6) and the cycle counting algorithm to predict when fatigue failure is to occur during other loading histories.

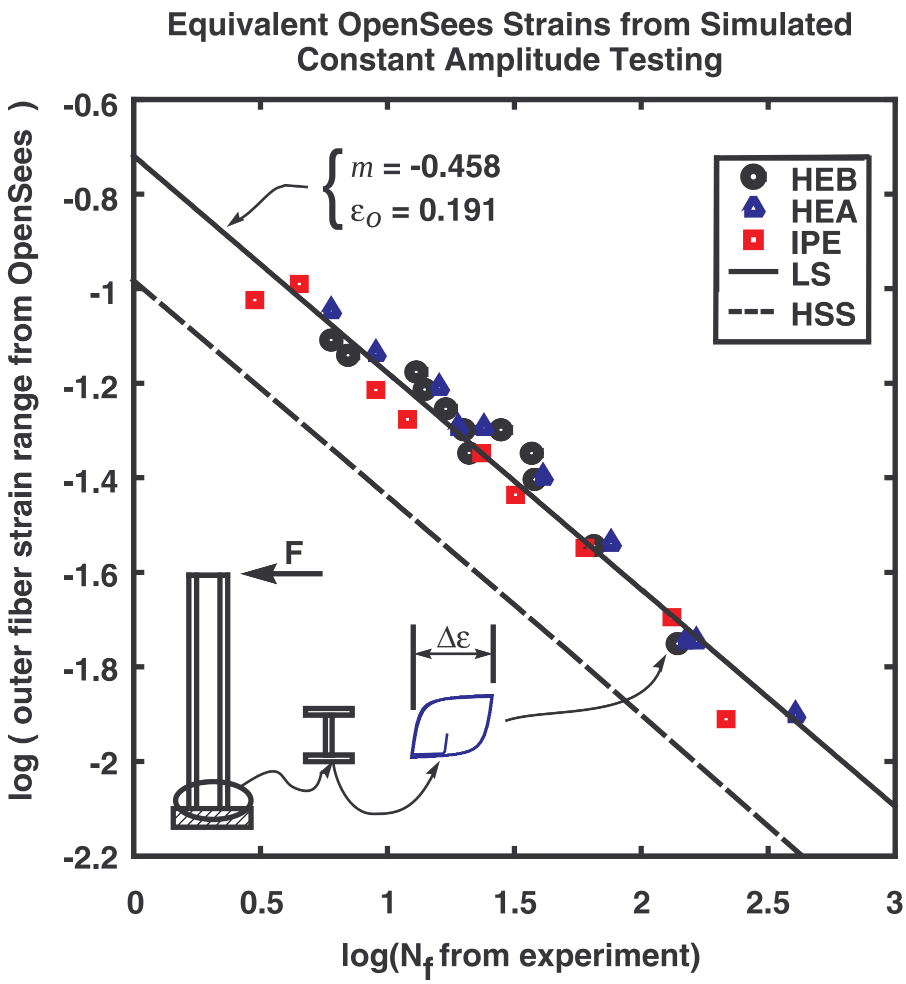

Fig. 5.6 Constant amplitude cyclic tests of HEA, HEB, and IPE sections and equivalent strain amplitude from OpenSees simulation. Solid black line represents least squares fit of simulated strains and dashed line represents assumed strain-cycle relationship for HSS sections.

5.3.5 Calibration of OpenSees Low-Cycle Fatigue Model Using HSS Strut Data

5.3.5.1 General

The results of the series of tests of simple HSS struts by Yang and Mahin (2005) described in Chapter 4 were supplemented herein to calibrate the low-cycle fatigue model in OpenSees for use with braces of typical proportions and connection details. Each experiment was continued until failure. All of the specimens, fabricated from 6×6×3/8 HSS tubes, had identical details. Of the HSS specimens tested, specimens 01, 02, and 03 did not contain net section reinforcement, and consequently, the failure of specimens 02 and 03 occurred at the net section. specimen 01, however, fractured at the midspan as a result of damage caused by a large initial compressive cycle. The reduced net areas were reinforced in the remaining five specimens, and failure occurred in all of this at the midspan.

Two constant amplitude tests were also performed to refine the calibration for fatigue parameters ε_0 and m. The constant amplitude experiments were identical to those carried out by Yang and Mahin, but the specimens were subjected to a series of constant amplitude cycles until they failed. In one of the specimens, the peak displacement imposed corresponded to a normalized displacement of 4 (specimen 8) and, in the other, to a normalized displacement of 2 (specimen 9). For these specimens, the peak strut elongation and shortening during each cycle were the same. The normalized displacement, μ, is defined here as the strut axial displacement divided by the elastic axial displacement corresponding to theoretical buckling load provided by AISC (2000).

The calibration of the OpenSees fatigue model was performed for these tests in a fashion similar to those mentioned above, where an analytical model of the test specimen is created, and then the strain history was extracted from the location where the failure was observed. Once the strain hysteresis record is extracted, the average strain amplitude was calculated for the outermost compression fiber at the midspan cross section of the brace. Next, the strain amplitude versus number of cycles to failure data were computed and plotted on log-log scale to make a best-fit line for a Coffin-Manson curve. During this process, two interesting analytical discoveries were made: (1) the number of nonlinear, large displacement beam-column elements needed to accurately and consistently measure local strains is quite large and (2) the stress-strain hysteresis extracted from the outermost fiber of the critical section does not have a constant amplitude for the specimens subjected to axial constant amplitude displacement cycles.

A series of nonlinear quasi-static analyses of a single buckling strut was modeled by subdividing its length into 2, 4, 10, 16, 20, 30, 40, and 100 nonlinear force-based beam-column elements in OpenSees. Similar to the WF section fatigue calibration, the strain history was extracted from the outermost fiber of the critical (center) section of the brace element. Figure 5.7 illustrates this process and shows the strain histories from each of the varying number of element cases; one can infer that the number of elements needed to appropriately capture the strain history of the element is between 16 and 60 elements. Note that the most radical difference in strain history occurs when comparing the strains extracted from the model with two elements versus the model with four elements.

In Chapter 4 it was shown that global force-displacement behavior can be captured accurately with as few as two elements; using only two elements the local strains are not accurately modeled. Because the strain history used in the calibration of the fatigue parameters is sensitive to the assumed performance of the brace, a minimum of 20 elements are needed to accurately describe the strains in the brace element model for fatigue calibration. In an analytical study, the number of elements was subdivided into equal length elements for modeling simplicity; however, a region of many small elements near the plastic hinge would also be appropriate, assuming that most nonlinearity of material and displacement occurs in this region.

Along with the interesting discovery made regarding the number of elements, it was determined that the constant amplitude tests did not result in constant amplitude strains in the analytical model, as was desired for these tests. Figure 5.8 shows the extracted stress-strain history for an analytical model for both the outer fiber at the midspan of the brace (Fig. 5.8a) and that at the base section for one of the IPE sections mentioned above (Fig. 5.8b). The analytical strain extracted from the OpenSees analysis contains a very large strain excursion in the first half cycle (during brace buckling), which is more than twice the average strain amplitude (~3.3%). Thus, the constant displacement amplitude tests do not result in constant strain amplitude cycles, especially for large values of normalized displacement (i.e., 4 or greater). Thus, these constant displacement amplitude brace tests do not provide the preferred information on constant strain amplitude cycles as was possible for the cantilever beams tested by Ballio and Castiglioni.

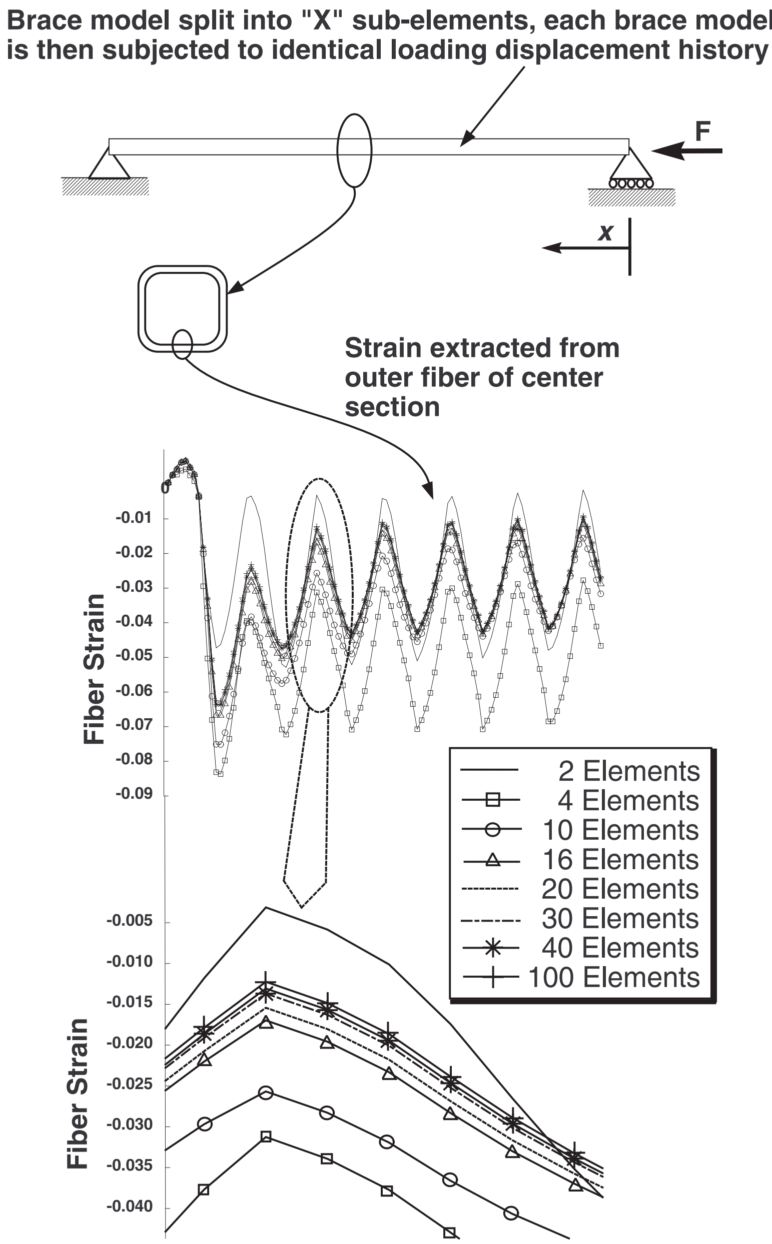

Fig. 5.7 Strain histories extracted from midspan of HSS buckling member. Consistent solution is reached when using nearly 100 elements.

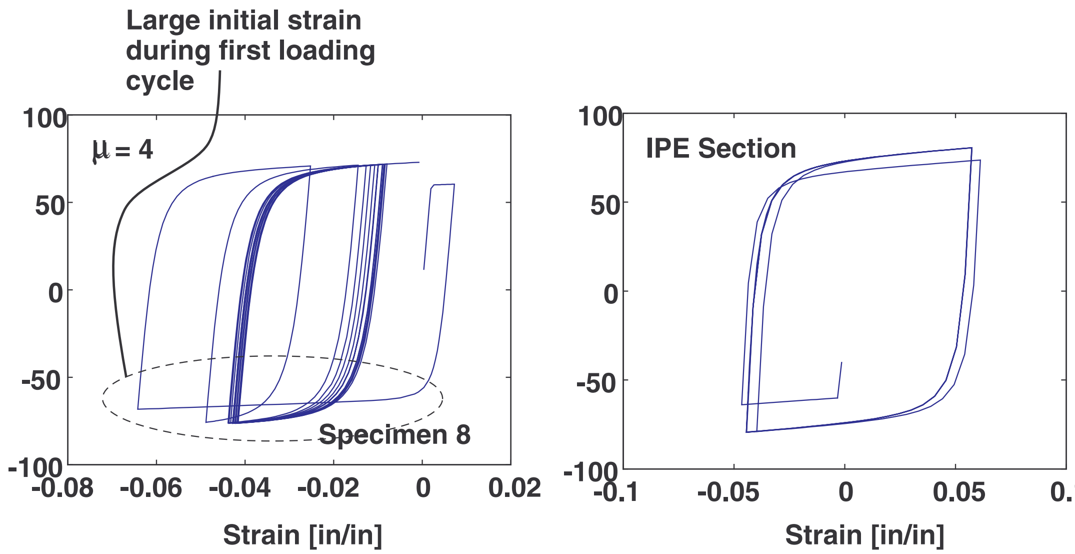

(a) (b)

Fig. 5.8 Strain histories extracted from (a) midspan of HSS buckling member (10^{th} element of 20), and base of IPE model. Note very large initial stress, which occurs in HSS element, which is roughly equivalent to 2 times amplitude of smaller strains. Thus constant amplitude brace tests do not necessarily result in "constant amplitude" strain cycles.

5.3.5.2 Parameter Calibration for Models of Braces Having Reinforced Net Reduced Area Sections

Because the strain histories from the constant amplitude tests did not allow for a constant amplitude calibration, values of *m* and *ε0* were evaluated to determine their appropriateness for use with braces. Values for *m* and *ε0* of -0.5 and 0.095, respectively, were found to predict failure due to low-cycle fatigue within one cycle of the observed result for the 6×6×3/8 braces tested that had their reduced net area regions reinforced. Figure 5.9 shows the hysteresis of the OpenSees elements incorporating this fracture model and the experimental hysteresis for the fatigue model parameters cited above. Figure 5.10 plots four displacement histories, indicating both the location at which failure was observed in the outer fiber (solid black dot) of the actual test specimen and the location in the displacement history when analytical failure is predicted (solid grey dot). With the exception of specimen 5, the parameters accurately predict the onset of fracture in the same cycle. The model of specimen 5 conservatively predicts fracture one cycle earlier than observed.

Figure 5.10 also plots predicted failure of the same displacement history using the model proposed by Lee and Goel (1987). The model by Lee and Goel does not trigger fracture for specimens 4 or 7 at all, and predicts complete fracture during the same cycle as was observed in specimen 5, and within two cycles for specimen 8. Interestingly, the model removes the element in its entirety once fracture is reached; thus there is no degradation in the model.

Figure 5.11 shows an overlay of the experimental hysteresis with the model by Goel et al.

5.3.5.3 Parameter Calibration of Models of Braces That Do Not Have Reinforcement Applied To Regions of Net Reduced Area

As mentioned before, three of the uniaxial strut tests did not have reinforcement applied to the net reduced area section that occurs at the end of the slot in a brace where it attaches to the gusset plate. As such, failure occurred in the net section in specimens 2 and 3. Although specimen 1 did not contain net section reinforcement, the large initial shortening imposed by the prescribed loading history resulted in significant lateral and local buckling at the midspan, causing serious degradation of brace tensile strength for the displacement history imposed. This relieved the net section of large tensile stresses in subsequent loading cycles when damage concentrated at the midspan.

An OpenSees model was created that explicitly modeled the net section. Because of a simplification used in fiber-element theory, the effects of strain concentrations were not accounted for when using nonlinear beam-column elements. Thus, a net section was created that assumed (for the sake of simplicity) a length of four times the thickness of the gusset plate, and fibers were removed from the area corresponding to the width of the gusset plate. Thus, in tension, the material model would undergo significant strains due to the concentration of yielding over such a small region, whereas in compression, once global buckling begins, the global forces relax considerably, and the net section is relieved from yielding. Figure 5.12 contains a simple cartoon illustrating how the net section was modeled in OpenSees. In the OpenSees model, the net section is placed directly after the element used to model the gusset plate. A total of 20 nonlinear elements (not including the gusset plate and net section elements) were used to calibrate these parameters.

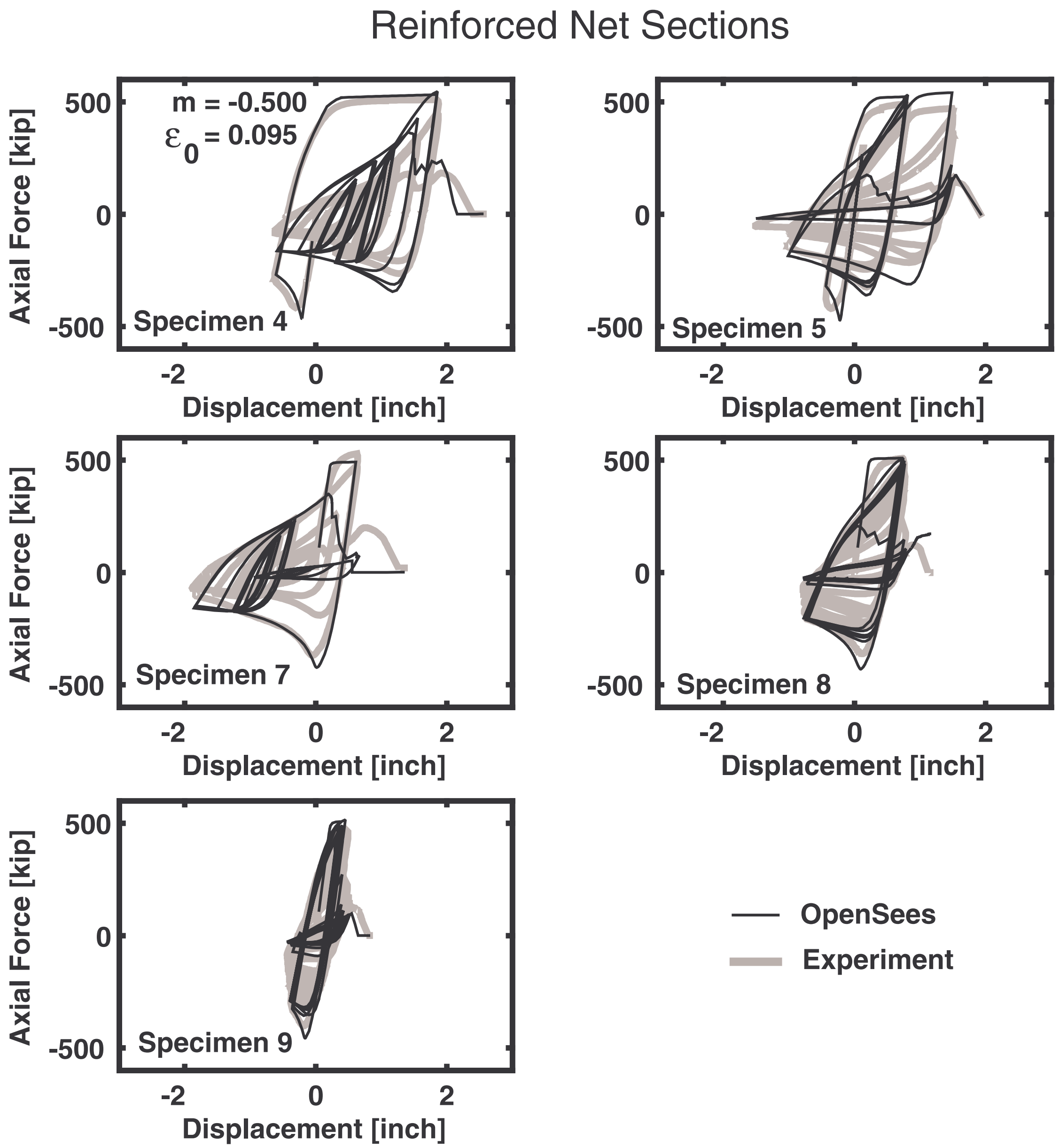

Fig. 5.9 Calibrated parameters and force-displacement hysteresis from experiments. All OpenSees models predict failure within one cycle to that observed except for specimen 9 (where negligable amounts of local buckling was observed). *m* =-0.5, ε_0 = 0.095.

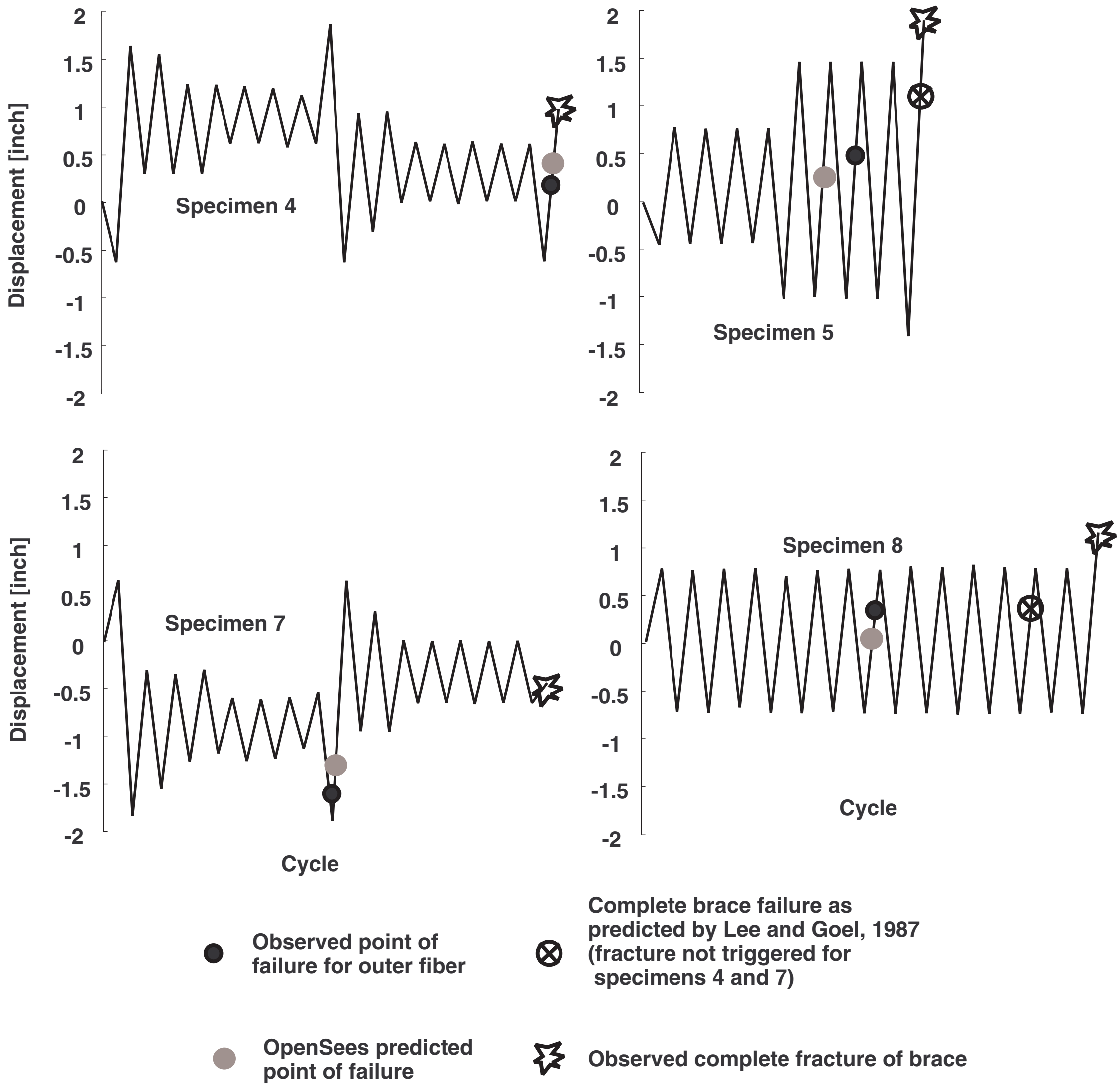

Fig. 5.10 Location of observed and analytical failure in reinforced net sections. *m* =-0.5, ε_0 = 0.095.

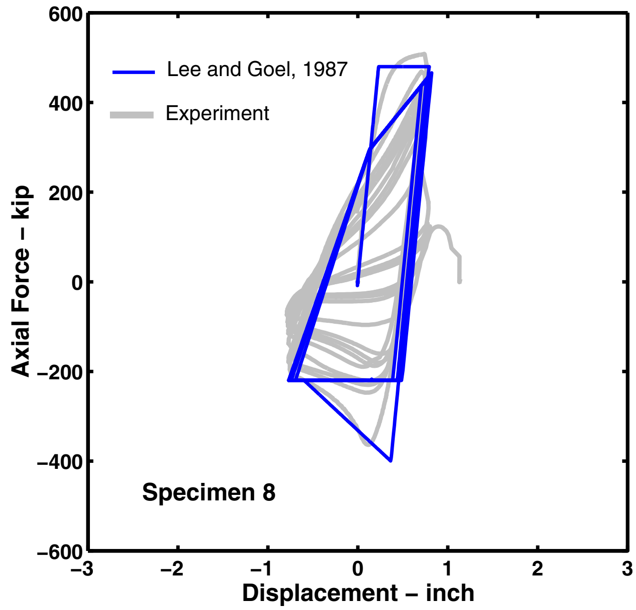

Fig. 5.11 Specimen 8 overlaid with Lee and Goel (1987) fracture model. Note no degradation observed after first buckling in numerical results until final failure.

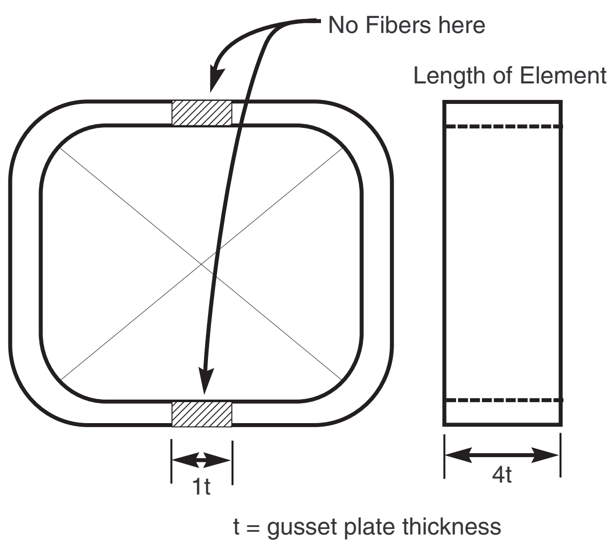

Fig. 5.12 Schematic illustrating net section modeling used in OpenSees.

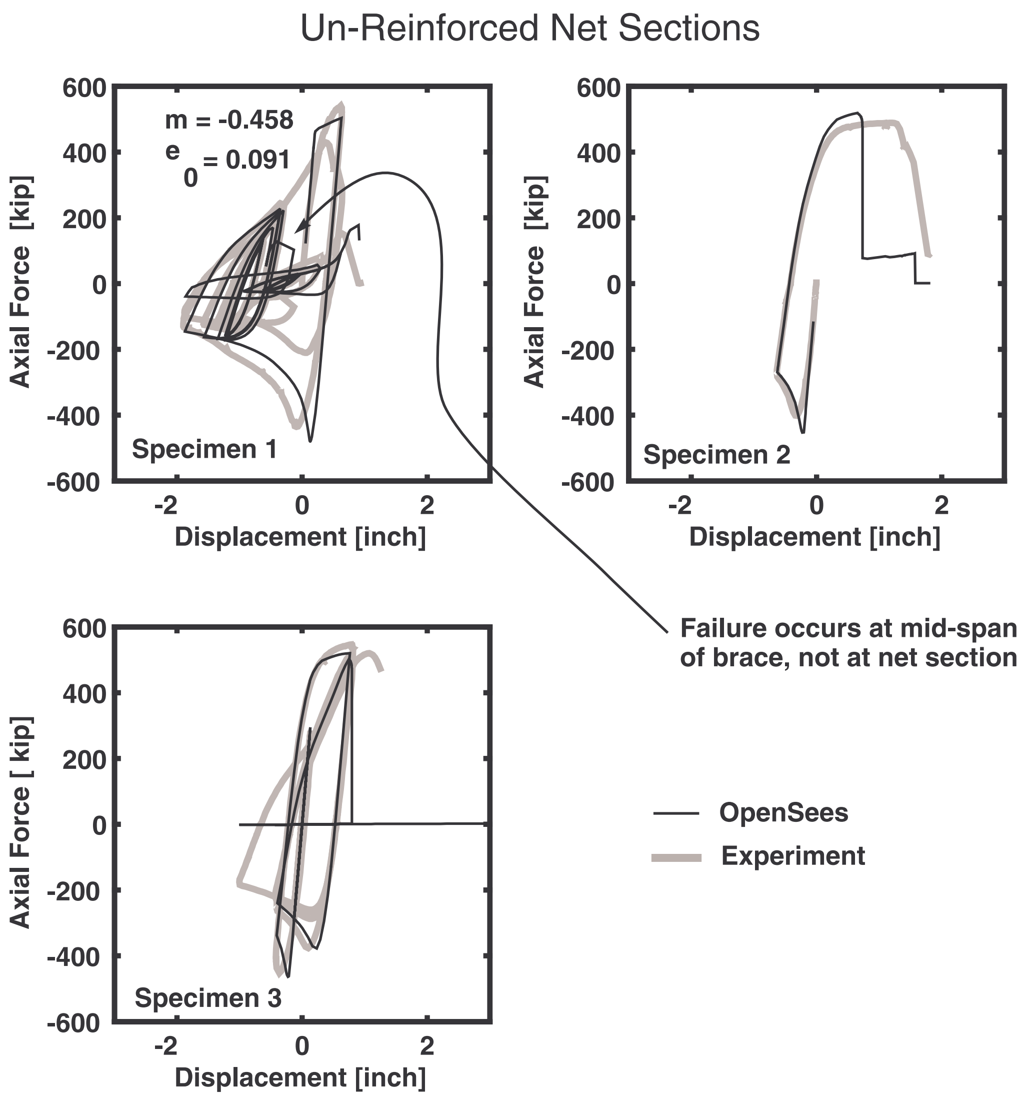

Fig. 5.13 Hysteresis comparing OpenSees analysis of braces with sections having net reduced areas with experimentally observed values.

The limited number of tests available made it difficult to completely calibrate the model, so a simplifying assumption was made that the *m* parameter was similar to the wide flange sections listed above (-0.458). This parameter was selected because the net reduced section did not experience the large local buckling and cross-sectional distortion as observed at the midspan of the braces. Thus, ε_0 was the sole parameter sought, such that the failure of specimen 1 occurred at the midspan of the brace, and at the net section for specimens 2 and 3. The value for the parameter ε_0 that best fit this description was found to be 0.091. Figure 5.13 shows the resulting axial force−axial displacement hysteresis of the OpenSees model and the experimental values. Interestingly, for specimen 1, the OpenSees model predicts fracture at the midspan of the brace at the same time fracture was observed at the midspan during testing. For both specimens 2 and 3, the OpenSees model conservatively predicts the failure mechanism at the net section. Given the limitations of the fiber model to mimic the complex stress concentrations at the net reduced area section, and the limited available data, this degree of accuracy is considered sufficient.

5.4 COMPARISON OF LOW-CYCLE FATIGUE PARAMETERS FOR DIFFERENT CROSS SECTIONS

A comparison of the parameters used to define the low-cycle fatigue model can most easily be done by preparing Coffin-Manson plots for four different sections: wide flange sections, HSS members, BRB members, and reinforcing bars. These lines are plotted below in Figure 5.14. The values for the reinforcing bars are obtained from the results by Brown and Kunnath (2000), and those for the BRB elements are estimated using simple procedures described below. A brief narrative comparison of the plots follows:

- Wide flange beams: These parameters are obtained using the OpenSees model of the tests by Ballio and Castiglioni described above. The calibration compensates for the fact that the OpenSees model disregards the change in shape of the cross section associated with local buckling. Care should be exercised in extrapolating these data to members with different boundary conditions, lengths, b/t ratios, and material properties. For the range of parameters considered, the WF sections have the largest fatigue life of the members considered here. (m =-0.458, ε_0 = 0.191) Note that these tests were conducted under cyclic flexural loading in the absence of axial load.
- HSS braces: These values were determined using the process described above that resulted in parameters that best described the observed behavior for the uniaxially tested specimens. Only one size specimen was considered, but several loading histories were considered (m =-0.5, ε_0 = 0.095). For the brace without reinforcement of the net area, the parameters were m = -0.458, and ε_0 = 0.091 in the net section. These results suggest HSS sections are more vulnerable to fatigue than WF sections, but the loading conditions imposed differed.

- BRB element (conventional method): The typical code method for specifying the energy-dissipation capacity of buckling-restrained braces is in terms of the cumulative inelastic deformations that a brace undergoes. Typically, braces are expected to withstand a total cumulative plastic deformation at least 300 times larger than the nominal yield displacement. Assuming symmetric displacement cycles, the number of cycles to failure can be estimated for a given constant amplitude of cyclic deformation. Thus, the number of cycles to failure at a constant amplitude of 4.0 times the yield displacement can be computed as 300/(4*(4-1)) = 25. Each complete cycle at a peak normalized displacement of 4 results in a cumulative normalized displacement demand of 4*(4-1) = 12. This method can be repeated for other amplitudes to determine the corresponding number of cycles to failure. This approach does not yield a linear Coffin-Manson relationship, as shown below in Figure 5.14. This plot suggests that BRBs may be more resistant to fatigue than HSS or WF sections when large amplitudes of strain are imposed but less so when small cyclic amplitudes are applied. In tests of buckling-restrained braces, cumulative normalized displacements generally exceed 300, often by factors of 2, 3 or even more; however, in these tests the loading history is rarely of constant amplitude, and generally the history consists of small-amplitude cycles followed by cycles with increasing amplitudes.
- BRB element (using one constant-amplitude displacement test): Few BRB tests have been carried out to the point of failure of the brace, but rather simply stop when a project or code criterion for minimum cumulative normalized inelastic displacement is reached. For subsequent comparative analyses of BRBF and SCBF systems, it would be useful to have an estimate of the actual fatigue model parameters for BRBs. To do this, the same procedures as used before for WF and HSS sections were used. Assuming that the value for m is similar to those for HSS and wide flange sections, a value of m equal to 0.458 was assumed. Based on the results of an OpenSees analysis of a single uniaxial test of a BRB at constant amplitude that was tested until failure (Black et al. 2002), the strain history was extracted, and the value of the parameter, ε_0, was selected such that it resulted in the correct number of cycles to failure as was observed (m =-0.458, ε_0 = 0.12). Note in Figure 5.14 that the fatigue life of the steel in a BRB is similar to that in a HSS; however, the strain demands in a HSS buckling brace would be expected to be far greater than

those in a BRB. Clearly, additional test results to failure are needed to improve understanding of the fatigue life of BRB elements.

- Concrete reinforcing bar: These values are taken directly from Brown and Kunnath (2000), and are thought to be representative of typical reinforcing bar parameters for grade 60 steel, assuming no buckling (m = -0.43, ε_0 = 0.081). The reader is referred to the literature for more information regarding the test methods used.

Coffin-Manson curves for the above parameters are plotted below in Figure 5.14. Note that most of the material models have a very similar value for the parameter, m, when these are determined independently. The main exception is for the conventional method to specify the cumulative normalized inelastic displacement capacity of a BRB. Similar discrepancies between methods based on cumulative energy and classical fatigue-based models have been noted by Chai and Romstad (1995). The value of ε_0 varies significantly, however, from section type to section type. From this plot we can see that the material that is the least susceptible to strain-induced low-cycle fatigue failure is that of the wide flange section, whereas the reinforcing bar is the most sensitive to strain at large strain amplitudes, and the HSS material is the most sensitive to fatigue at moderate strain values. One of the observations from this plot is that the cumulative plastic deformation fatigue model used for buckling restrained braces does not fit the linear Coffin-Manson model (as evidenced by the thin dotted line); in the 2–8 cycle to failure range, the model appears to fit well.

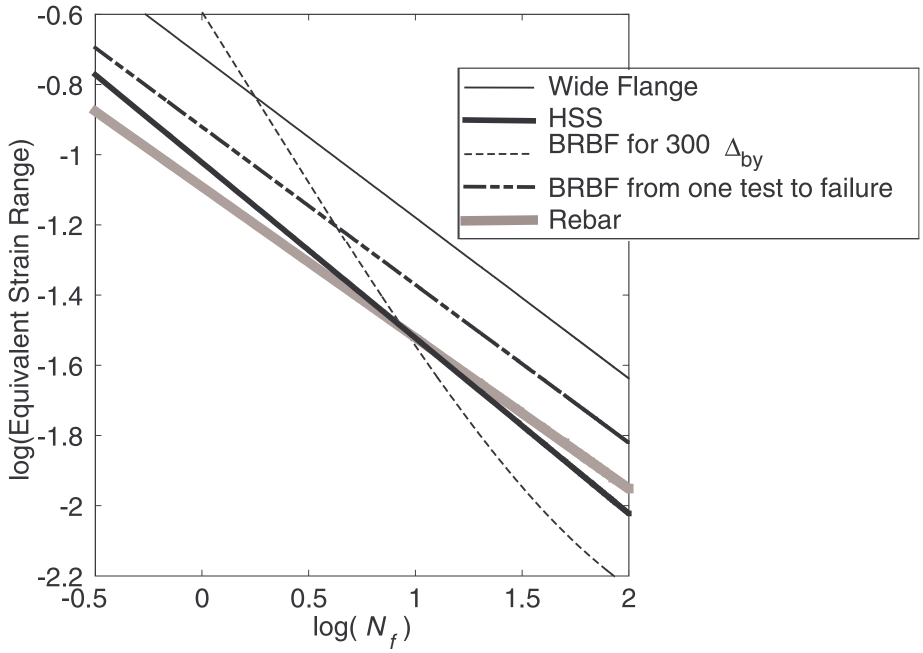

Fig. 5.14 Comparison of parameters used for various steel materials.

Moreover, since fiber models track local behavior by means of stress-strain hysteresis in each fiber, fatigue models based on overall axial force–axial displacement relations are difficult to implement. As seen in this chapter, it is possible to implement in OpenSees a fiber-based low-cycle fatigue model incorporating a classical damage mechanics approach based on rainflow cycle counting, a Coffin-Mansion relation between the amplitude of inelastic cycles to the number of cycles at that amplitude to failure, and Minor's rule for cumulating damage associated with different cycles. A modified method to keep track of cycles and their equivalent amplitude during a computer analysis was developed and described in this chapter, and parameters that define the fatigue life for WF members in flexure, HSS members in axial cycling, BRB, and bar sections were estimated based on limited experimental data. It was shown that numerical models for buckling braces need, at a minimum, 20 nonlinear elements along their lengths to consistently compute the strain history. The modeling parameters developed for HSS sections permit quite accurate prediction of the fatigue life of the braces considered. The conventional method used to determine the fatigue life expectancy of a buckling-restrained brace member is based on cumulated plastic strain; while simple, this model predicts trends inconsistent with those observed for other steel sections.

A detailed study of the fatigue relationships of Lee and Goel clearly show that the fiber model is a more conservative estimate of the time to fracture for the analytical model for both the time to initial fracture and the time to complete fracture as observed by modeling the 6×6×3/8 specimens. The phenomenological member approach model still offers relatively good accuracy, considering the required computational effort; however, the phenomenological models have been calibrated only for uniaxial braces that buckle with pinned ends. Thus, their accuracy for more complex loading or boundary conditions is uncertain.

The proposed cycle counting model is similar to that of the traditional rainflow counting method with only minor differences, which allow for "on-the-fly" cycle counting. This method has been successfully used herein for bracing elements to model the effects of fracture due to low-cycle fatigue.

6 Comparison of Experimental and Analytical Predictions of Braced-Frame Behavior

6.1 INTRODUCTION

This chapter presents the experimental results on simple BRBF and SCBF specimens, and these results will be used to (1) improve understanding of the cyclic inelastic behavior of braced steel frames; (2) assess the relation between individual tests of braces and those of a complete system; (3) evaluate the ability of conventional computer models, as well as more refined ones like those developed in Chapters 4 and 5, to predict observed behavior; and (4) devise recommendations for the analysis and modeling of steel-braced frames. The calibrated analytical models developed are subsequently used in Chapter 7 to assess the response and performance of a variety of steel-braced frame systems.

In formulating the experimental program, it was desired that test specimens be representative of modern code-compliant construction, be fabricated at or near full scale, incorporate at least one story and realistic boundary conditions, and be subjected to loading histories representative of intense earthquake ground motions. To facilitate comparison of experimental and analytical results and results for different tests, a similar displacement history was quasi-statically imposed on all specimens. In the case of BRBF frames, three one-bay wide, two-story planar specimens were tested. For these specimens, the upper story was simplified and strengthened so that inelastic deformations concentrated in the lower story. Both inverted-V (chevron) and single-diagonal configurations were considered. For the SCBF specimen, a single one-bay, two-story specimen was tested with HSS square tubular braces arranged in an inverted-V (chevron) configuration. To achieve the desired level of realism, all specimens were designed by registered professional engineers, and fabricated, erected, and inspected by commercial firms experienced in seismic-resistant construction. Because of practical, economic, and other considerations, a number of important simplifications were introduced in the experiments: e.g., all specimens were tested with the plane of the braced frame oriented in the horizontal direction, no gravity loads were considered, and only a single lateral load was applied at the top floor of the specimens. Given the objectives of these tests, and the relative small amplitude of gravity loads compared to the seismic loads expected in the critical members, these simplifications were considered acceptable.

Section 6.2 describes the details of the experiments on the BRBF specimens, and comparisons with the analytical results are presented in Section 6.3. Comparable information on the SCBF test specimen is presented in Sections 6.4 and 6.5. For the BRBF and SCBF tests, a variety of elastic and nonlinear numerical procedures were used to predict the observed behavior, including ones incorporating modeling assumptions ranging from those commonly used in design to ones that were intended to reflect more realistically the observed behavior. Particular attention was placed on assessing the ability of the models to predict the global mechanical characteristics of the specimens (e.g., stiffness, strength, ultimate deformability, etc.) and key engineering demand parameters: (1) peak interstory drifts; (2) onset of lateral buckling, peak lateral displacement, loss of load-carrying capacity, and fracture of conventional buckling braces (and if observed, in the case of buckling-restrained braces); and (3) formation of plastic hinges and other inelastic behavior modes in beams, columns, and connections. Overall observations regarding the behavior of the test specimens and recommendations regarding modeling of braced frames are offered in Section 6.6.

6.2 TESTS OF BRBF SPECIMENS

A total of three BRBF specimens were designed, constructed, and tested as part of a construction project on the University of California, Berkeley campus (López et al. 2004). Because of project specific requirements, the test sequence represented a lower story in a taller structure. The test specimens were intended to provide information needed to validate assumptions regarding BRBs acting as part of a frame, various local connection details, and numerical modeling. For economic and practical reasons, the specimens were one-bay wide, and included the entire bottom story and those portions of the second story needed to distribute forces realistically to the lower story. Consistent with the project requirements, a welded moment-resisting connection was provided between the beam and the columns, and “Unbonded Braces” (manufactured by

Nippon Steel) were used for the buckling-restrained braces. These braces were bolted to gusset plates by means of high-strength bolts and splice plates.

The moderate amount of damage expected in the framing members suggested that only the buckling-restrained braces (and their connecting gusset plates) needed to be changed from test to test. Thus, the same beams, columns, beam-to-column connections, upper-level braces and loading head (as shown in Fig. 6.1) were used in all three tests. Three different sets of BRBs were added to this subassemblage, as illustrated in Figures 6.2–6.4. Because the second story of the specimen was intended to remain elastic, several simplifications were introduced, including the use of relatively strong, wide flange braces. Preliminary analyses of the test specimen indicated that the beam and columns in the upper level could be deleted with little effect on the behavior of the lower story. This allowed the specimen to be constructed in the test setup at slightly larger scale and reduced specimen construction costs. The resulting specimen consisted of a single story containing buckling-restrained braces, which supported an elastic "top hat" bracing system to transfer loads from the actuator to the lower story of the specimen.

Table 6.1 contains a list of the specimens that were tested and a brief description of each. The first specimen (BRBF-1) consisted of BRBs in the lower story arranged in a chevron configuration, whereas the second and third specimen (BRBF-2 and BRBF-3, respectively) consisted of a single BRB positioned along the diagonal of the bay. A structural drawing of the specimen frame without the bracing is shown in Figure 6.1. As can be seen in this figure, the specimens are all 20′-0′ wide from center to center of the columns. The first story is 10′-10″ from the base to the center of the lower beam, whereas the second story is approximately 9′-6″ tall to the centerline of the actuator. Figure 6.2 shows a structural drawing of the BRBF-1 configuration, and Figure 6.3 shows an overhead photo of the BRBF-1 after testing. Figure 6.4 shows a structural drawing of test specimens BRBF-2 and BRBF-3. Figure 6.5 shows a photo of specimen BRBF-3 after testing.

Information regarding the project-specific design assumptions and proportioning can be found in López (2004), and is for this reason not included herein. The test setup, construction and instrumentation are outlined in Section 6.2.1, and the loading protocol employed is described in Section 6.2.2. The experimental results are provided in Section 6.2.3, while discussion of behavior is presented in Section 6.2.4. The analytical studies comparing the results of computer modeling with the test results are presented in Section 6.3.

Table 6.1 BRBF Specimen labels and descriptions of lower level in specimen.

Specimen Label	Description
BRBF-1	One-story (130.5 in. high), one-bay (240 in. wide) frame with inverted-V concentrically braced configuration. Each brace cross section ~6 in^2.
BRBF-2	One-story (130.5 in. high), one-bay (240 in. wide) frame with single concentric diagonally braced configuration. Brace cross section ~ 6 in^2.
BRBF-3	One-story (130.5 in. high), one-bay (240 in. wide) frame with single concentric diagonally braced configuration. Brace cross section ~ 11.5 in^2.

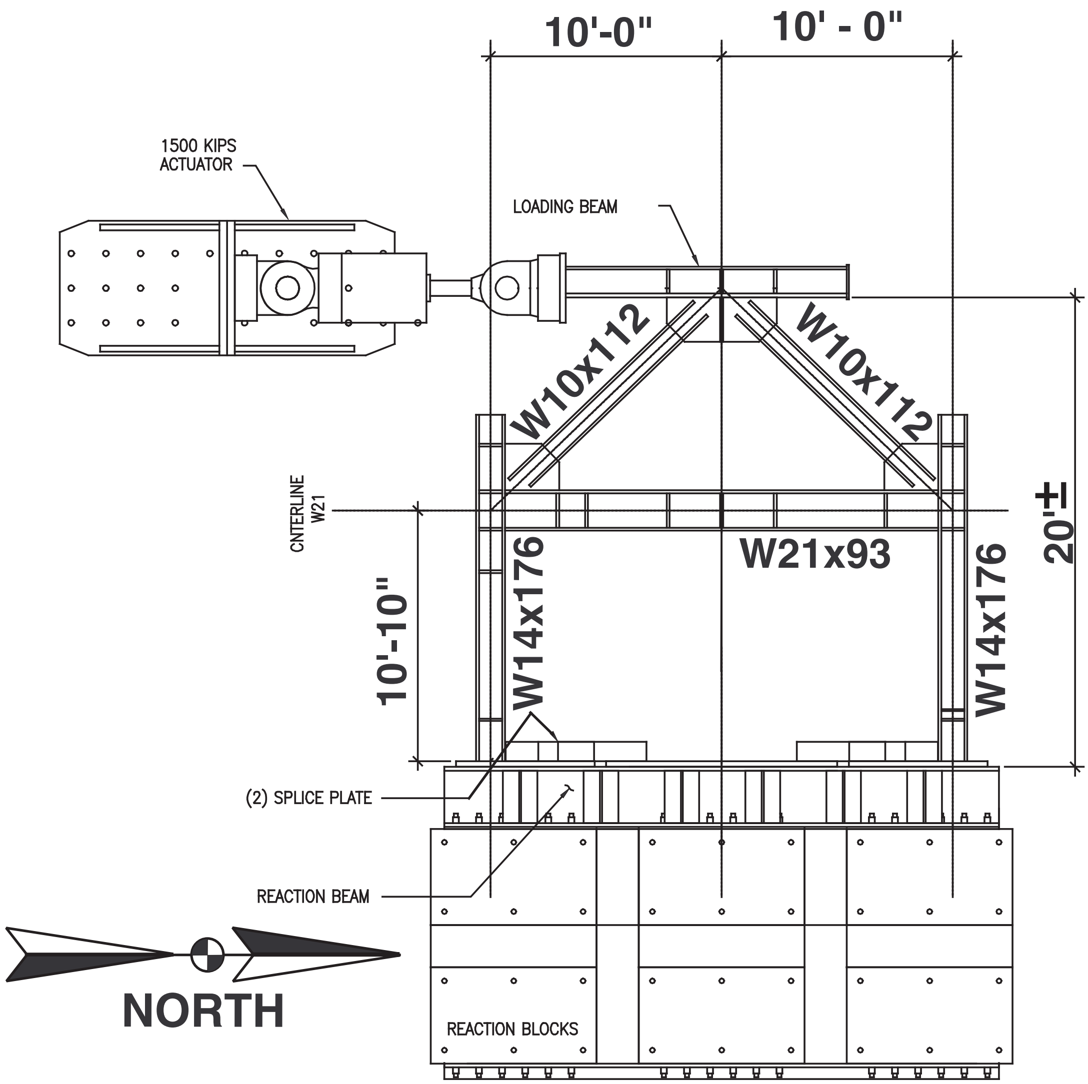

Fig. 6.1 BRBF bare frame.

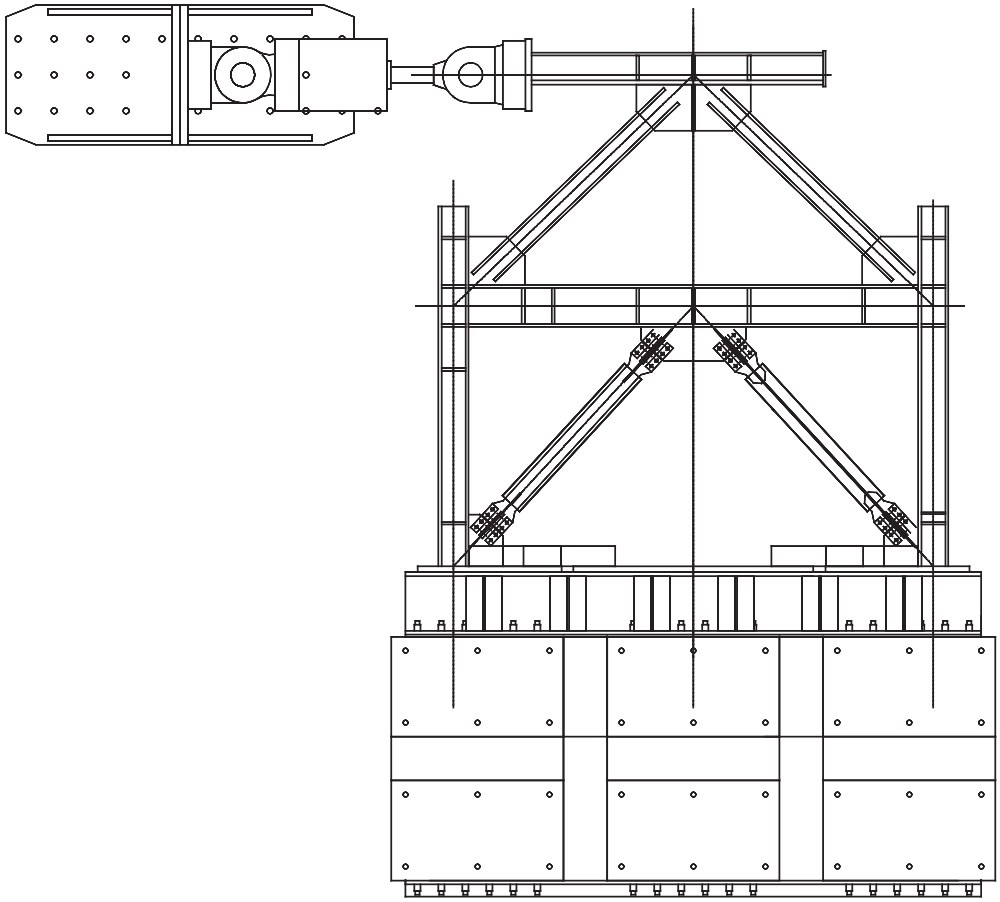

Fig. 6.2 BRBF-1 test setup.

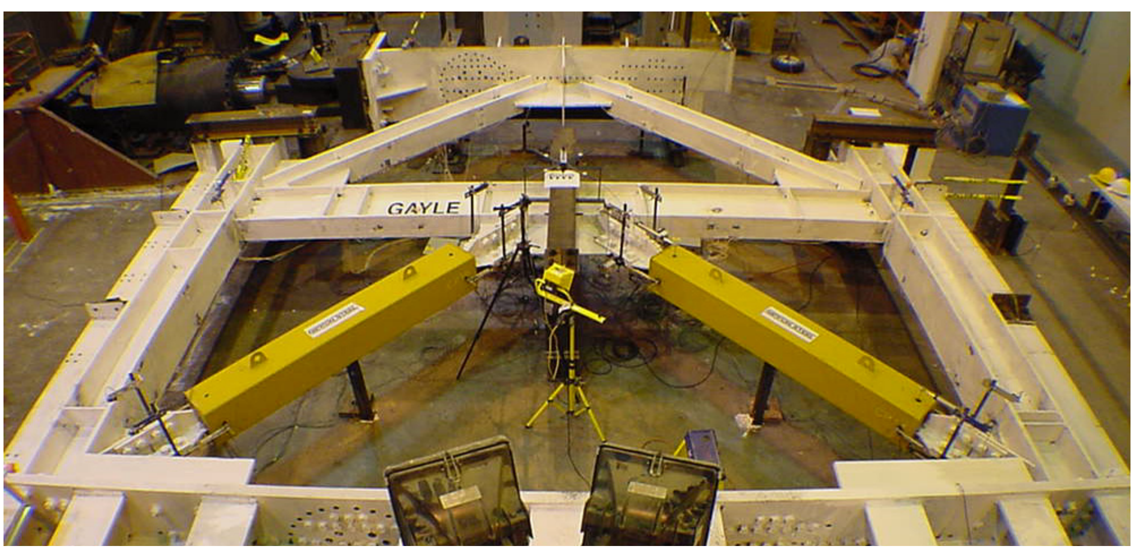

Fig. 6.3 BRBF-1 specimen after test.

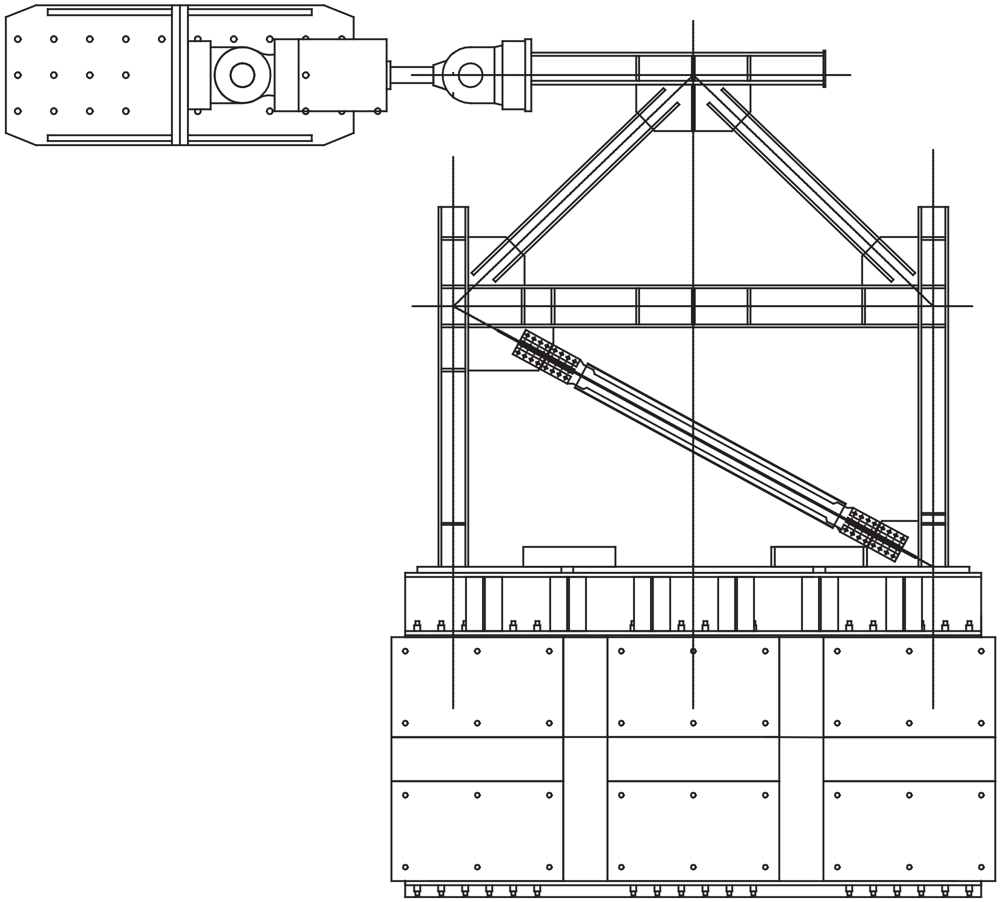

Fig. 6.4 BRBF-2 and BRBF-3 setup.

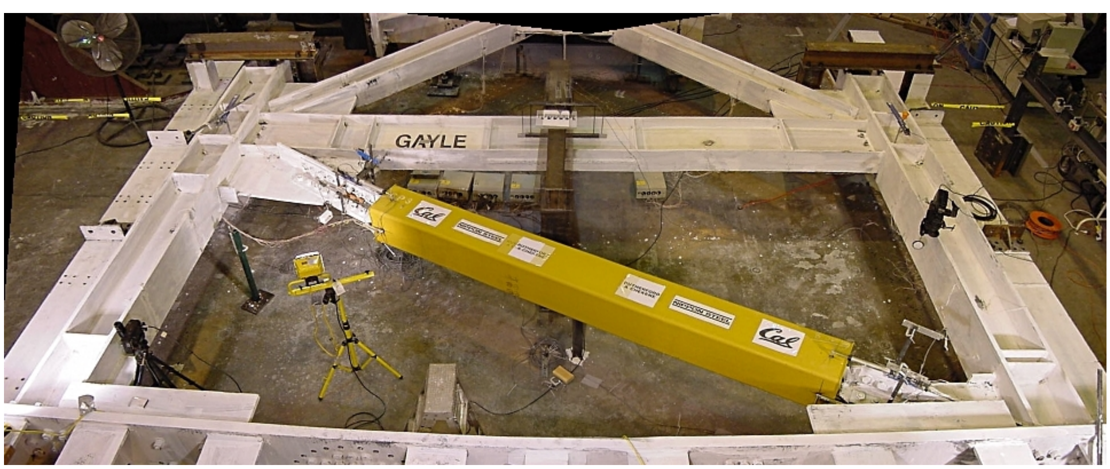

Fig. 6.5 BRBF-3 specimen after test.

6.2.1 Specimen Construction, Test Setup, and Instrumentation

All specimens were tested in the horizontal position. Figures 6.2–6.4 show the plan configuration for all three tests. The actuator reaction frame was stressed to the laboratory strong floor using twenty 250 kip capacity Williamson prestress rods. The 1.7 million pound capacity servo-controlled actuator had a clevis at each end. One clevis was attached to the reaction frame and the other was attached to a heavy built-up steel loading head that transferred loads from the actuator to the test specimen.

The base of the columns in the test subassemblage was attached by means of complete joint penetration welds to base plates. The base plates were bolted to another large steel built-up section, which in turn was prestressed to an existing system of large concrete reaction blocks attached to the laboratory strong floor. To help transfer the base shear from the specimen to the foundation beam, a steel "drag" plate was bolted to the foundation beam between the column base plates. Pairs of stiffeners were used to connect each base plate to the drag plate. The base or "foundation" beam was adequately attached to the reinforced concrete reaction blocks to resist the anticipated base shear and the compressive axial column reactions; however, the tensile capacity of the connections of the foundation beam to the reaction blocks was deemed only marginally adequate. Because of the limited number and size of holes in the anchorage blocks, it was not possible to simply increase the number and tensile capacity of the anchor rods connecting the foundation beam to the reaction block. Consequently, two large jumbo sections were installed parallel to, and slightly outboard of the specimen's columns (these can be seen in Figs. 6.3 and 6.5). These were shimmed against the top of the foundation beam, and grouted and stressed to the laboratory strong floor to increase the tensile resistance of the foundation beam. The jumbo beams were placed about 6 in. outboard of the columns, to permit unimpeded lateral movement of the specimen for the displacements expected during the tests.

Care was taken to have the lower portion of the specimen constructed consistent with procedures anticipated in the field. As such, the fabricator delivered pre-assembled members to the laboratory with base plates, stiffeners, shear tabs, and the gusset plates welded to the columns, and with the central gusset plate and various stiffeners welded to the beams. Holes used for attaching the buckling-restrained braces to the gusset plates were pre-drilled in the gusset plates, as they would be in an actual building. The subassemblage consisting of the columns, lower-level beam and buckling-restrained braces used in the first specimen was assembled on the lab floor in the vertical orientation as shown in Figure 6.6. This orientation permitted the welding materials, procedure, and positions used to connect the beam, columns, and gusset plates to be identical to those used in actual buildings. Certified welders performed the welding and special inspection was provided during the fabrication and erection as stipulated by code. This included visual inspection of all fit-ups and completed welds, "continuous" visual inspection of all complete joint penetration welding, and ultrasonic testing of all complete joint penetration welds. All welding inspection was performed in accordance to AWS specifications and was performed by a certified independent inspection agency (see Fig. 6.7). All welds were made with notch tough filler metal.

Once the lower story was erected, it was tilted into a horizontal position. A series of supports at the top of the columns and midspan of the beam, and the location of the boltholes in the foundation beam, supported the centerline of the specimen 36 in. above the laboratory floor. The specimen supports consisted of small frames constructed from W8 sections and positioned perpendicular to the center of the lower column and the tops of both columns. As part of these supports, a set of horizontal beams was located directly under the specimen and another set was bolted over the specimen to prevent out-of-plane or torsional movement at these locations. These frames were stressed to the laboratory strong floor. A set of pipes or rods were welded to the W8 sections and greased to minimize frictional resistance between the supports and the specimen (e.g., see Fig. 6.8). The dimensions of the support frames were selected to provide adequate in-plane movement of the specimen.

The column base plates and drag plate were also connected at this stage to the foundation beam using over 30, A490, 1.25-in. diameter bolts that were tightened utilizing direct tension indicating (DTI) washers. The base plates and the drag plate were connected by means of full-penetration welds to two pairs of shear transfer plates (see Fig. 6.9).

Fig. 6.6 Frame being welded in vertical position.

Fig. 6.7 Magnetic particle testing of beam-column connection.

Fig. 6.8 Out-of-plane restraint at top of south column (north column restraint is similar).

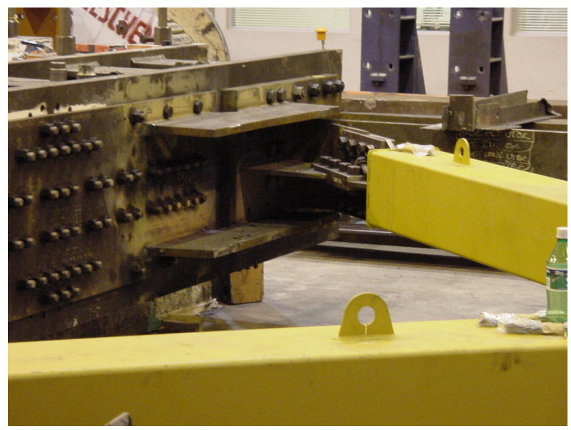

Fig. 6.9 Southern base place connection showing drag plates and large number of bolts to ensure rigid connection.

The remainder of the test subassemblage was erected in the horizontal position. This consisted of a pair of W10x112 braces oriented in a chevron configuration (Fig. 6.10). Each brace was connected by means of complete joint penetration welds to a central stiffened gusset plate at the top of the specimen, and to stiffened gusset plates at the top of the connection of the lower beam to the columns. The gusset plates were all 1-in. thick, and the stiffeners were sized and positioned to match the configuration of the wide flange section used. The central gusset plate at the top of the specimen was directly welded to the loading head attached to the actuator. The existing loading head was built up from several heavy steel sections and was mechanically restrained so it would not permit significant out-of-plane or torsional movement of the top of the specimen (see Fig. 6.11).

Fig. 6.10 Welding of W10 section to loading arms.

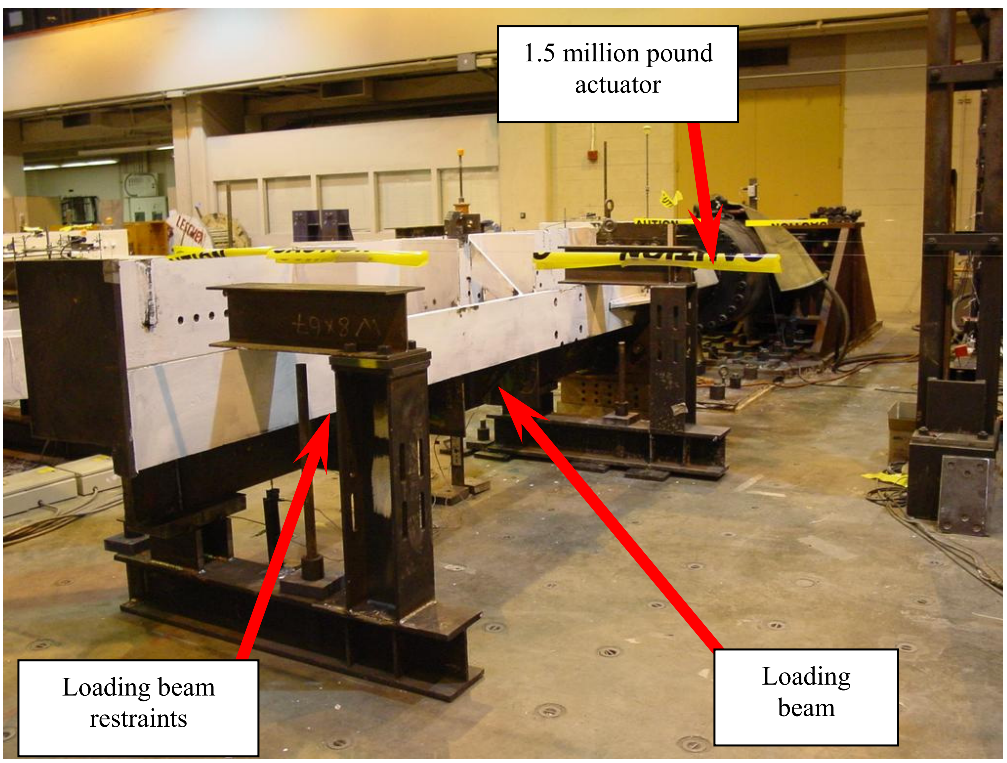

Fig. 6.11 Photo of loading beam, restraints, and actuator.

The subassemblage frame was kept in place for all three tests. The details of the test setups, member, and BRB properties are described following.

6.2.1.1 BRBF-1 Setup

Figure 6.3 above shows the installed configuration after the first test. The cross section of the interior core of each buckling-restrained brace consisted of a flat plate; one of the braces was installed such that one core plate was placed perpendicular to the laboratory floor, while the other was placed parallel to the laboratory floor. Although the central cores of the BRBs in this specimen were flat plates, each end had a transition to a cruciform section to facilitate bolting at each end to the gusset plates. Four pairs of splice plates were thus used to connect each end of the BRBs to the gusset plate. Each gusset plate had a single stiffener on each side that aligned with the end fin on the BRBF. Although the BRBF connections in the prototype structure did not specify a specific faying surface, the specimen was designed having a slip-critical connection with a class A faying surface with an assumed coefficient of friction of 0.33. Each end of each buckling-restrained brace was bolted to the gusset plate using a total of 16, 1.25-in Power A490 bolts with DTI washers; normal-sized holes were specified. A special inspection was provided to ensure that the proper torque was applied to the bolts. No difficulties were encountered in the fit-up of the bolted connections.

The specimen was whitewashed with a light coating of lime, facilitating identification of locations in the specimen where yielding occurred (i.e., the mill scale and attached whitewash tended to flake off at these locations).

6.2.1.2 BRBF-2 Setup

After the completion of BRBF-1 testing, the specimen was re-centered using the hydraulic loading actuator, and the buckling-restrained braces and their gusset plates were removed. The removal process consisted of flame cutting the gusset plates from the beams and columns in the lower story, and cleaning the protruding surfaces by air-arc gouging and grinding the remaining surface smooth. The configuration of specimen BRBF-2 is shown in Figure 6.4 The area of the core used in the BRB was the same as that used for specimen BRBF-1. New gusset plates were installed for the single-diagonal BRB used in the BRBF-2 specimen. Because the specimen was oriented in the horizontal position, single-bevel, full-penetration welds were utilized to attach the gusset plates to the framing. Backing bars were used to help position the gusset plates and were left in place during testing. Once the gusset plates were installed, the buckling-restrained brace was attached to the specimen in a manner similar to BRBF-1. That is, four pairs of splice plates, and DTI washers and sixteen 1.25-in. Power A490 bolts were used at each end of the brace. Because the brace was bolted into place approximately 45 minutes to one hour after the welding was completed, a small initial stress may have developed in the buckling-restrained brace as the welds cooled. Lastly, the stiffeners located at the exterior bases of the columns were repaired by air-arc gouging the weld and base material along a crack that developed there during the testing of BRBF-1. New fillet welds were installed in these locations.

6.2.1.3 BRBF-3 Setup

Figure 6.5 shows the installed configuration for BRBF-3 (photo taken after testing was completed). The core of the buckling-restrained brace had a cruciform shape and had an area twice that of the braces used in specimens BRBF-1 and BRBF-2 (Fig. 6.13).

The loading actuator was used to straighten the bare moment frame such that it would be plumb with zero load on the actuator. Damage to gusset plates during testing of BRBF-2 warranted installment of new gusset plates for BRBF-3. As before, the existing gusset plates from BRBF-2 were removed by flame cutting, and the surfaces were prepared for future welding by air-arc gouging and grinding. The braces were first fastened (and fully tensioned) to the gusset plates such that the brace and gusset plate assembly was lowered into position via an overhead crane. Backing bars were used to position the gusset plates for welding. The gusset plates were full-penetration welded in the down-hand position. The backing bar was left in place and a reinforcing fillet was placed (overhead welding) on the backing bar between the column (or beam) and backing bar. Sixty-four (32 at each end), 1-in. A490 bolts were taken to appropriate pre-stress values using an impact wrench and DTI washers.

The gusset plate detail for BRBF-3 contained an extra stiffener plate attached to the column and the end of the upper gusset plate. This stiffener was not on the original construction documents, but was added in response to damage observed in specimen BRBF-2. Figure 6.12 shows a close-up of this gusset plate stiffener.

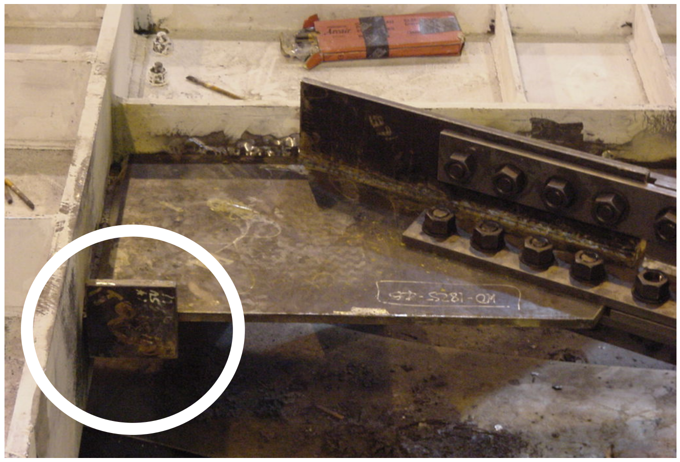

Fig. 6.12 Gusset plate stiffener.

The whitewash from previous testing was brushed off with a steel brush, and a new coat of whitewash was applied. This process may have loosened and removed much of the mill scale remaining on the specimen. This reduced the effectiveness of the whitewash in visual detection of yielding during testing of specimen BRBF-3.

6.2.1.4 Section Properties

The properties of the frame and braces for all three tests are described below. The properties described are for the specimen prior to the testing.

6.2.1.5 Frame Properties

All of the rolled shapes and plate material met requirements for ASTM A572–Gr 50. The mill certificates from these indicate that the uniaxial yield strength averaged around 55 ksi, with ultimate uniaxial strength ranging from 72 to 76 ksi. More detailed frame material properties are shown in Table 6.2.

Table 6.2 Frame material properties.

Member	Size	Grade	Yield Strength (Ksi)	Ultimate Strength (Ksi)
Column	W14x176	ASTM A572–Gr 50	55	73
Beam	W21x93	ASTM A572–Gr 50	54	72
Loading Brace	W10x112	ASTM A572–Gr 50	55	76
Plate Steel	Varies	ASTM A572–Gr 50	~55**	~70**

**Varies

6.2.1.6 Brace Properties

Tables 6.3 and 6.4 describe the geometry of the braces, including material properties and section properties, respectively, for all three specimens. The braces were manufactured by Nippon Steel Corporation, Japan (i.e., unbonded braces). The steel material designation shown in the tables is therefore Japanese, and there is no equivalent ASTM standard.

Figure 6.13 illustrates the dimensions of the core sections listed in Table 6.4. Two different styles of brace interior cross sections were used in the tests. The BRB cross section for both specimens BRBF-1 and BRBF-2 consisted of a flat plate. For the first test, where two braces were present, each of the interior plates were oriented perpendicular to each other in order to assess the effect of this parameter on response. For BRBF-2, the core was oriented parallel to the plane of the test specimen. The BRBF-3 brace contained a cruciform cross section with dimensions shown in Table 6.4

Table 6.3 Global brace properties.

Member	Grade	Yield Strength (Ksi)	Ultimate Strength (Ksi)	Yield Length (in)	Overall Length (in)	Yield Area (in^2)
CP-1A	JIS*-SN400B	40.9	62.2	93.1	118	6.33
CP-1B	JIS*-SN400B	40.9	62.2	93.1	118	6.33
CP-2	JIS*-SN400B	40.9	62.2	157.8	185.9	6.33
CP-3	JIS*-SN400B	40.9	62.2	134.2	185.9	11.69

*Japanese Industrial Steel

Table 6.4 Brace section properties.

Member	Specimen	t_1 (in)	w_1 (in)	t_2 (in)	w_2 (in)	Core Orientation Relative to Lab Floor
CP-1A	1	0.75	8.5	N/A	N/A	—
CP-1B	1	0.75	8.5	N/A	N/A	|
CP-2	2	0.75	8.5	N/A	N/A	—
CP-3	3	0.75	8.5	0.75	8.5	+

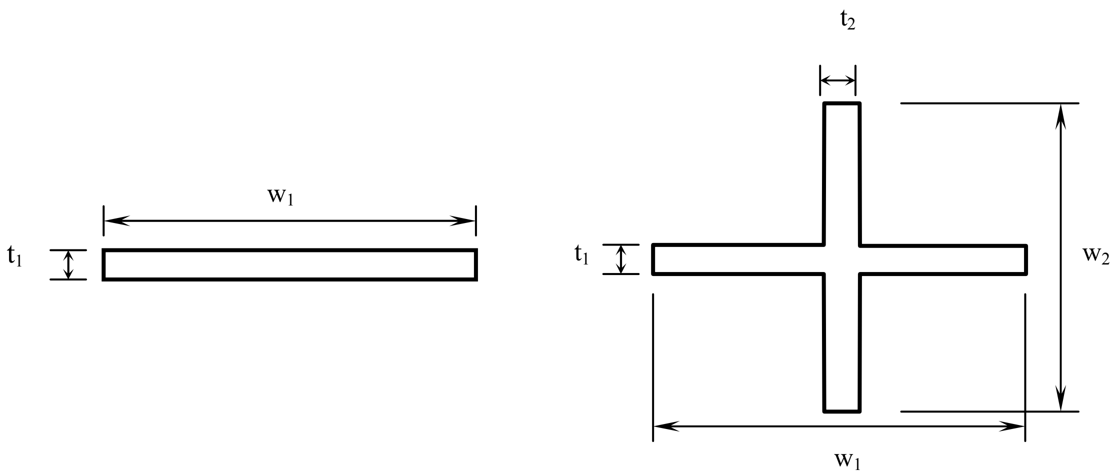

Fig. 6.13 Core sections.

6.2.1.7 Data Acquisition and Control System

The AUTONET software computer package was used for data acquisition and hydraulic control of the tests. The AUTONET system ran on a Canadian UNIX™ platform with a real time display of processed data. Instrumentation consisted of a total of 195 channels for the first test and 176 channels for the second and third test. The data from all of the instrumentation were collected with a NEFF system set to sample data approximately 35 times per ramp cycle (140 times per complete cycle).

6.2.1.8 Instrumentation

Instrumentation was classified into four different categories: global displacement instrumentation, strain-gage instrumentation, buckling-restrained brace displacement instrumentation, and load cell instrumentation. Sufficient instrumentation existed to ensure redundancy in the data collected. Other instrumentation was also included to monitor the boundary conditions on the lab floor. For example, a total of 10 channels were devoted to monitoring the potential slip of the reaction block, and two channels to monitor the potential slip of the hydraulic actuator. No noticeable movement was observed in the reaction block to strong floor assembly, or in the actuator-to-strong floor assembly. The actuator force was measured through the use of a pre-calibrated load cell, which was calibrated by a third party to 1,500,000 pounds.

Global Frame Displacement Instrumentation

Figures 6.14–6.15 describe approximate locations selected for global displacement monitoring. All displacement instrumentation was calibrated prior to testing using the AUTONET system. The arrows in Figures 6.14–6.15 show the direction for which displacements were recorded, and Table 6.5 gives a brief description of what the instrumentation was recording.

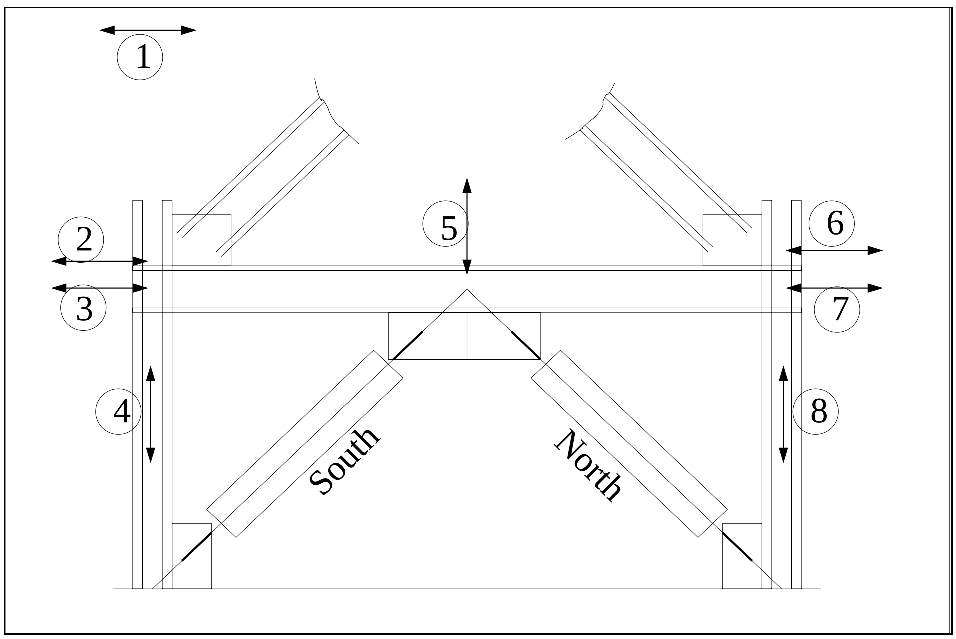

Fig. 6.14 Displacement instrumentation for specimen BRBF-1.

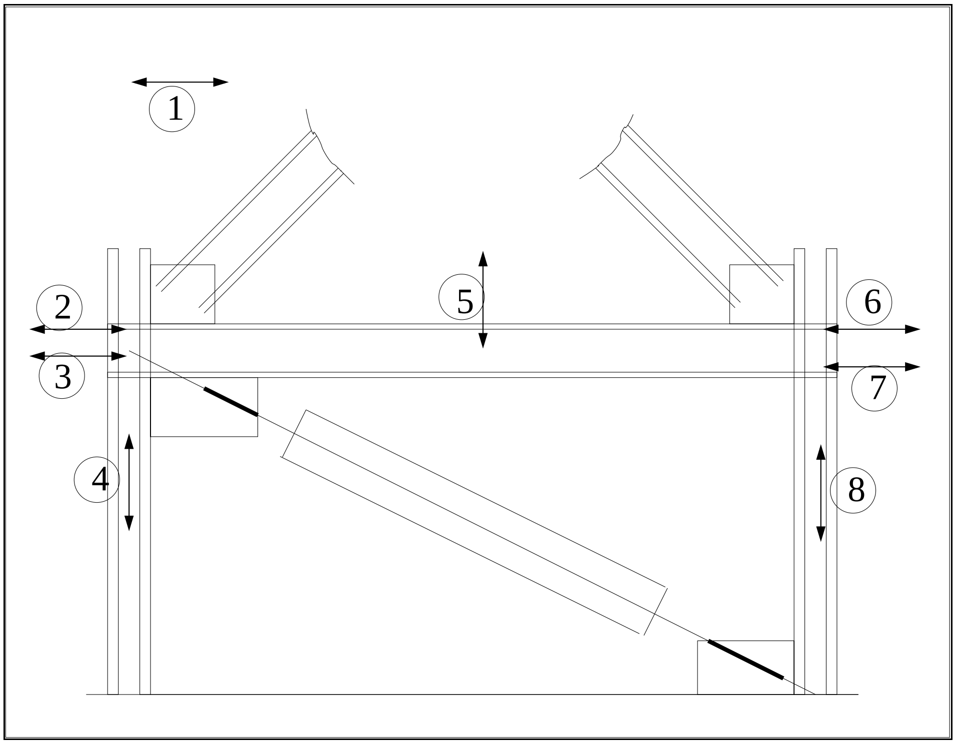

Fig. 6.15 Displacement instrumentation for specimens BRBF-2 and BRBF-3.

Table 6.5 Description of instrumentation.

Location	Instrumentation	Stroke (+/- in.)	Description
1	Wire Potentiometer	15	Actuator Displacement
2	Wire Potentiometer	7.5	Panel Zone Rotation
3	Wire Potentiometer	7.5	Beam Displacement
4	Stick Potentiometer	0.5	South Column Axial Disp.
5	Stick Potentiometer	0.5	'Vertical' Beam Disp.
6	Wire Potentiometer	7.5	Panel Zone Rotation
7	Wire Potentiometer	7.5	Beam Displacement
8	Stick Potentiometer	0.5	North Column Axial Disp.

Strain-Gage Instrumentation

Strain gages and strain rosettes were placed throughout the frame. The majority of the strain gages were purchased from Tokyo Sokki Kenkyujo Corporation, Japan, and some from the Micro Measurement Group, Inc. The gages placed on the BRB core plates (16 on each brace) were installed by the manufacturer in Japan, prior to shipment to the United States.

For BRBF-1, a total of 116 strain-gage channels were located on the specimen, both on the steel frame and on the buckling-restrained braces. For BRBF-2 and BRBF-3, a total of 103 strain gages were installed and monitored during testing. The strain gages were placed on the frame using the installation procedures suggested by the manufacturer.

Low-level tests were performed prior to each experiment to check that the strain gages were functioning appropriately. In some instances, some of the gages needed to be replaced, especially if they were in regions of high heat from welding or air-arc gouging. Figures 6.16–6.17 illustrate the approximate locations of the strain gages for both test configurations. The locations and configurations of the strain gages on the moment frame for BRBF-2 and BRBF-3 were identical to those on BRBF-1.

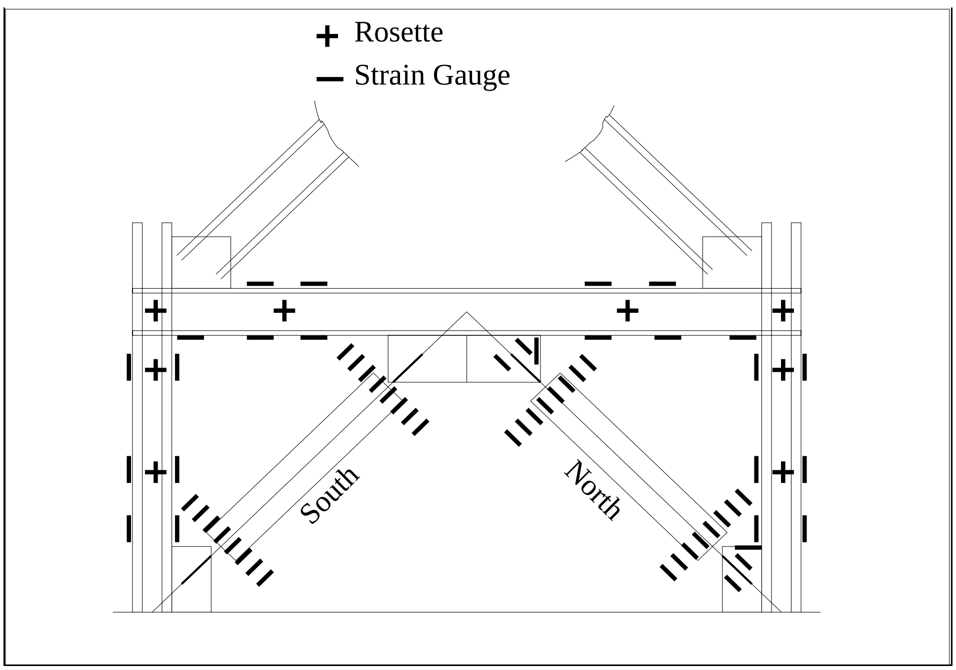

Fig. 6.16 Strain-gage instrumentation for specimen BRBF-1.

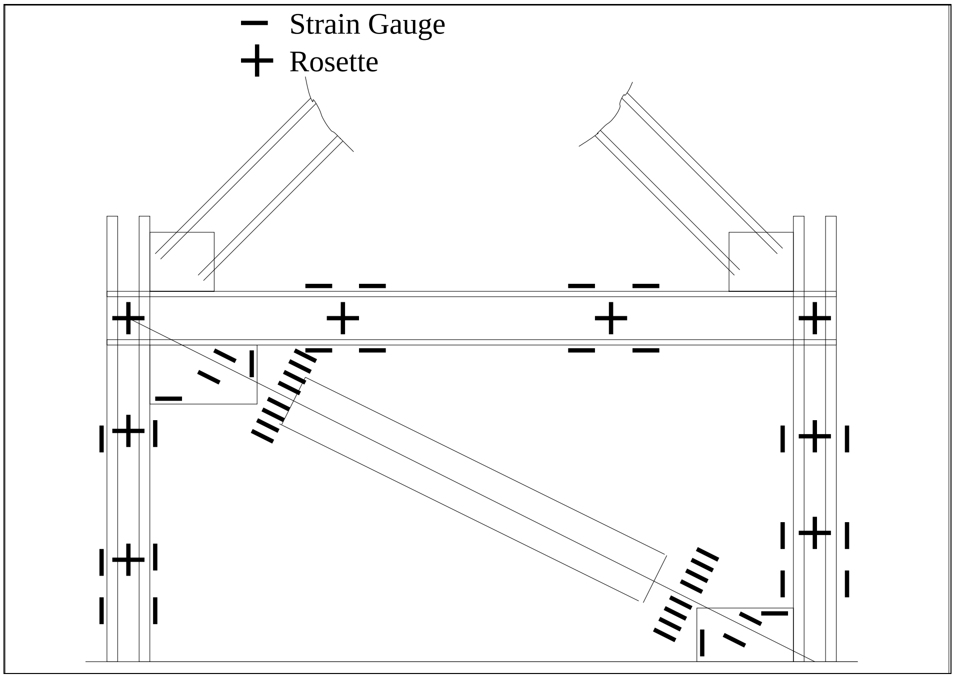

Fig. 6.17 Strain-gage instrumentation for specimens BRBF-2 and BRBF-3.

Buckling-Restrained Brace Displacement Instrumentation

Two wire potentiometers were installed on mounting stands attached to the specimen to measure the axial deformation and in-plane rotation occurring from one end of the brace to the other. The two wires pots were placed on either side of the brace and ran parallel to the brace. For BRBF-1, only the northern brace was so instrumented, as the displacement of the southern brace could be determined by geometry.

In addition to measuring the overall deformations of the braces, the axial deformation and rotation of the end attachments for the BRBs were measured relative to the work point and to the steel tubes encasing the BRB core. The steel tube, which encases the BRB core, is expected to develop negligible axial stress during hysteretic loading, thus the total extension of the brace core was measured at each end of the brace, relative to steel tube, with high precision. Previous tests have concluded this to be a reasonable assumption (AISC 1997; Clark et al. 1999). Each end of the buckling-restrained braces had a total of four displacement potentiometers (pots), which simultaneously measured extension and end rotation. Similar instruments were used between the attachments to the work points. Figures 6.18–6.20 illustrate their relative locations.

For BRBF-1, only the northern brace was instrumented extensively. Only potentiometers measuring in-plane relative displacement quantities were provided on the southern brace.

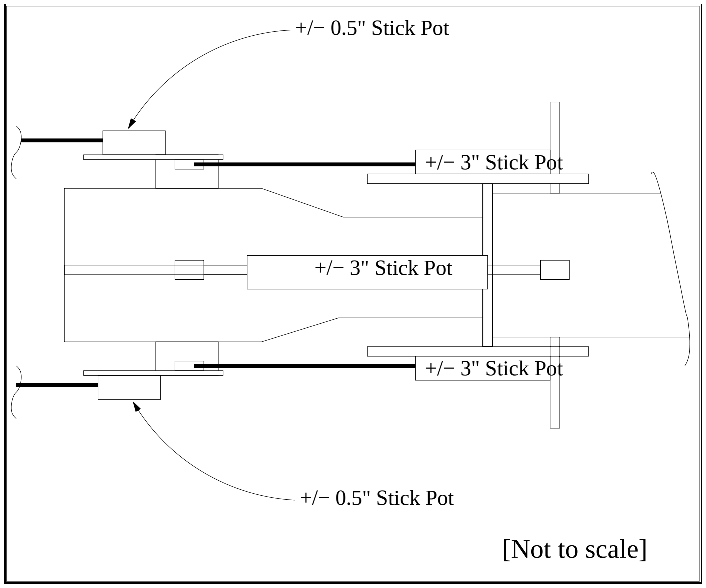

Fig. 6.18 Buckling-restrained brace end instrumentation plan.

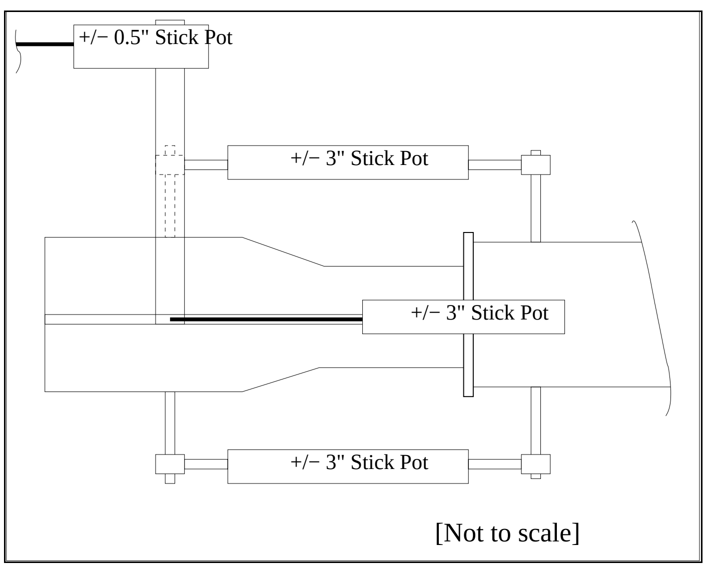

Fig. 6.19 Buckling-restrained brace end instrumentation elevation.

Fig. 6.20 Buckling-restrained brace instrumentation at beam midspan, also showing out-of-plane restraint at midspan.

Estimation of Axial Loads in Braces

It was not feasible to place a load cell in between the brace and the gusset plate. As such, the axial force in the brace was estimated by subtracting column shear forces from the actuator load, and resolving the resulting force into the axial component of the brace(s). For specimen BRBF-1, this resultant component was divided by two, which assumes that each brace contributed equally to the lateral resistance of the structure. The column shears were calculated assuming that plane sections remain plane. The strain gages used to record the strains in the column were located in sections that were expected to remain elastic during the loading. Because of the large shear forces in the columns, the column webs yielded in all three tests; therefore, the Bernoulli assumption of plane sections remaining plane is not necessarily a good approximation at larger deformations, and the estimates of column forces may not be correct. The brace forces that are shown in the subsequent sections are therefore only estimates of the brace force. Note that the estimates are relatively accurate at lower displacement levels.

6.2.2 Loading Protocol

The loading protocol used followed the loading protocol provisions outlined in the AISC/SEAOC *Recommended Buckling-Restrained Brace Frame Provisions* (AISC 1997). Brief definitions used in the calculation of target displacements for cyclic loading are provided in Table 6.6. Table 6.7 shows the numerical values of drift used for all three specimens. The control node for all three specimens was located at the work point of the southern column panel zone at the end of the lower-level beam.

The loading protocol in the AISC/SEAOC provisions suggests that 6 cycles be performed at a displacement corresponding to $\Delta_b = \Delta_{by}$ (or the displacement that corresponds to first yield of the BRB); four cycles applied corresponding to $\Delta_b = 0.5\Delta_{bm}$ (where Δ_{bm} is the estimated analytical target displacement taken for a specific site hazard); four cycles imposed corresponding to $\Delta_b = 1.0\ \Delta_{bm}$; and four cycles applied corresponding to $\Delta_b = 1.5\Delta_{bm}$. The number of the cycles corresponding to 1.5 Δ_{bm} was reduced to two, in an attempt to limit damage to the moment frame that was to be re-used.

Figures 6.21–6.22 contain a graphic illustration for the loading protocol generated for BRBF-1 and BRBF-2, respectively. The loading protocol for BRBF-3 was identical to the loading protocol for BRBF-2. Modifications were subsequently made to the loading protocol for BRBF-3 and will be described below.

Table 6.6 Loading protocol definitions.

Symbol	Definition
Δ_b	Deformation quantity used to control loading of the test specimen (total brace end rotation for the subassemblage test specimen: total brace axial deformation for the brace test specimen)
Δ_{bm}	Value of deformation quantity, corresponding to the design story drift.
Δ_{by}	Value of deformation quantity, at first significant yield of test specimen

Table 6.7 Deformation values for testing.

Specimen	Δ_{by} (in)	Δ_{bm} (in)
BRBF-1	0.37	1.75
BRBF-2	0.39	2.25
BRBF-3	0.33	2.25

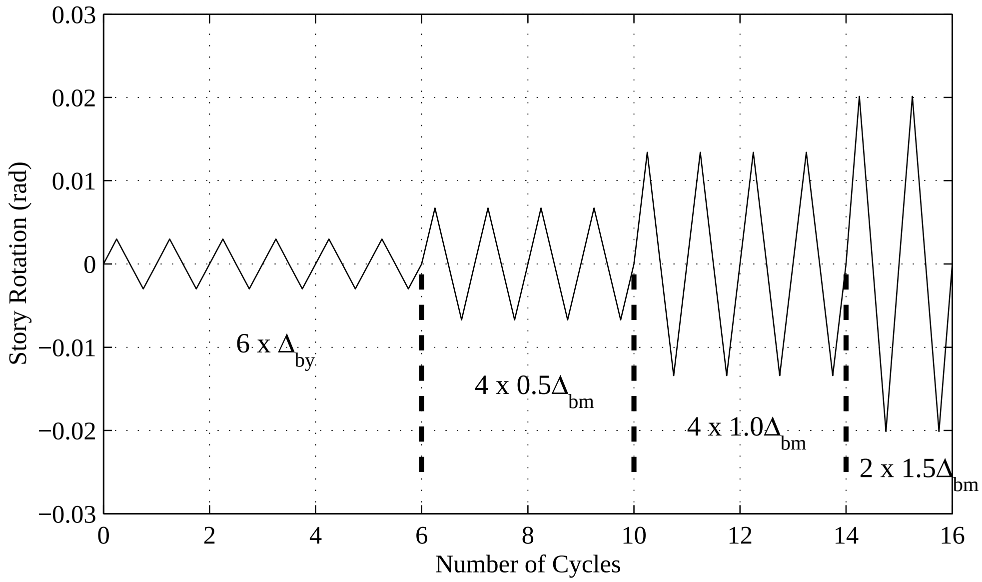

Fig. 6.21 Loading protocol for specimen BRBF-1.

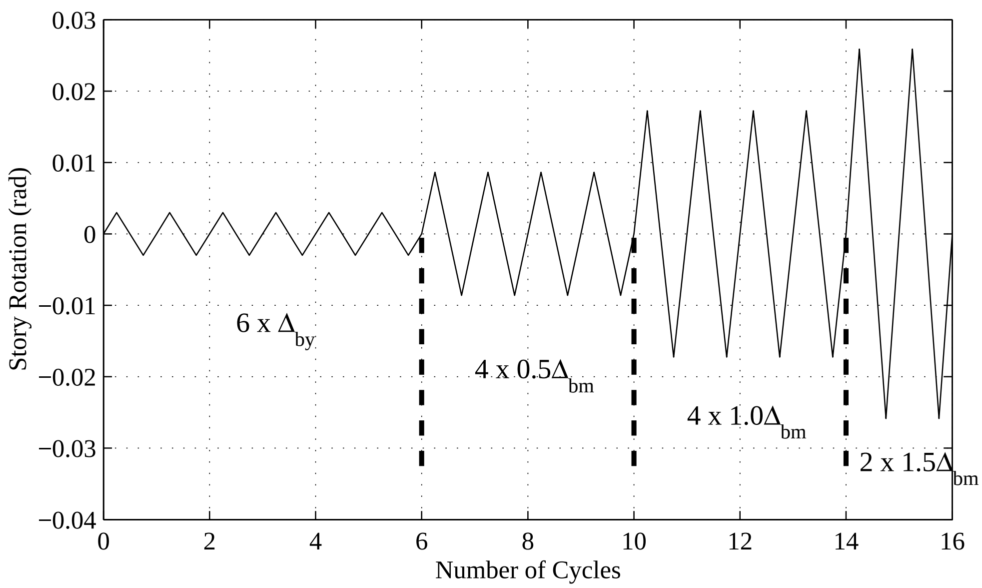

Fig. 6.22 Loading protocol for specimens BRBF-2 and BRBF-3.

6.2.3 Experimental Results

6.2.3.1 BRBF-1 Results

The testing of BRBF-1 was conducted over the course of one entire day, on Wednesday, January 9, 2002. Testing began at approximately 10:00 a.m. and continued until approximately 5:00 p.m. with an hour lunch break. The test was displacement controlled and run statically with pauses to take photos after peak displacements were reached. Real-time plots were shown on a monitor that overlooked the structural bay. A total of four video cameras captured all loading events. The temperature of the structural lab remained approximately constant near 70° for the entire day.

Key Observations

The experiment is broken up into four sets of cycles: 6 x $\Delta_b = \Delta_{by}$, 4 x $\Delta_b = 0.5\Delta_{bm}$, 4 x $\Delta_b = 1.0\Delta_{bm}$, and 2 x $\Delta_b = 1.5\Delta_{bm}$. Detailed information about each of these cycles is provided below.

$\Delta_b = \Delta_{by}$

During the first cycle, frame yielding was observed (flaking of whitewash) at several locations in the subassemblage. Yielding began at the column base just above the stiffener plates. Some yielding also occurred at the stiffener plate locations in the lower beam. "Popping" noises were heard from the base of the specimen near the bolted connection to the base plate; however, there was no noticeable slipping of the base plate, nor was any slipping detected from instrument readings. Some yielding was also observed on one of the reaction beam stiffener plates.

$\Delta_b = 0.5\Delta_{bm}$

In the locations where previous yielding was observed, a noticeable increase in the intensity and distribution of yielding was observed. Yielding was now observed in both the north and south panel zones. Signs of yielding in the column web were observed toward the base of the both columns. This yielding began at the ends of the columns and propagated toward the midheight as the number of cycles increased. The gusset plates showed signs of significant yielding at both the north and south column to base connections. The yielding began just outside of the full-penetration weld and tended to run parallel to the weld along the column.

Initial flexural yielding was observed in the columns near the base gusset plates and near the top of the base column stiffeners (see Fig. 6.23). The column stiffeners at the base of the column also began to yield just above the base plate.

The buckling-restrained brace began to display small, yet noticeable rotation of the attachment region relative to the confining steel tube, while the extension/compression cycles did not appear to be hindered. The bond preventing material found in the brace core became exposed during each cycle, signifying visible axial extension and compression of the braces.

No noticeable yielding was observed in the gusset plate connecting both braces to the bottom of the lower beam. Both moment connections also failed to show any signs of yielding in either the beam or column at this level of drift, although yielding was apparent in the panel zone.

(a) (b)

Fig. 6.23 (a) column stiffener plate and (b) north gusset plate at $\Delta_b = 0.5\Delta_{bm.}$

$\Delta_b = 1.0\Delta_{bm}$

Yielding was observed in the beam-column connections near the bottom flange of the beams. There was an increase in the amount of panel zone yielding. Increased yielding in the column web was observed at the base of the column. Yielding just below the beam-column connection increased in length to roughly 4 in. This yielding propagated toward the center of the column and along the length of the column. An increase in yielding was observed in the gusset plate at the base of the columns. No yielding was observed in the gusset plate connected to the BRBs at the center of the lower beam.

At this stage, the central gusset plate stiffener located on the gusset plate connecting the braces to the lower beam began making contact with the out-of-plane lateral support, indicative of out-of-plane beam rotation during testing. Because of a construction error, the clearance provided at this location was very small. Testing was paused and the out-of-plane restraint was ground to allow for greater clearance. The out-of-plane stiffener was ground down approximately ¼ in. and no further contact was observed. A displacement potentiometer measuring connection slip was damaged during one of the cycles when the center gusset plate stiffener became stuck on the out-of-plane support. This channel was not replaced.

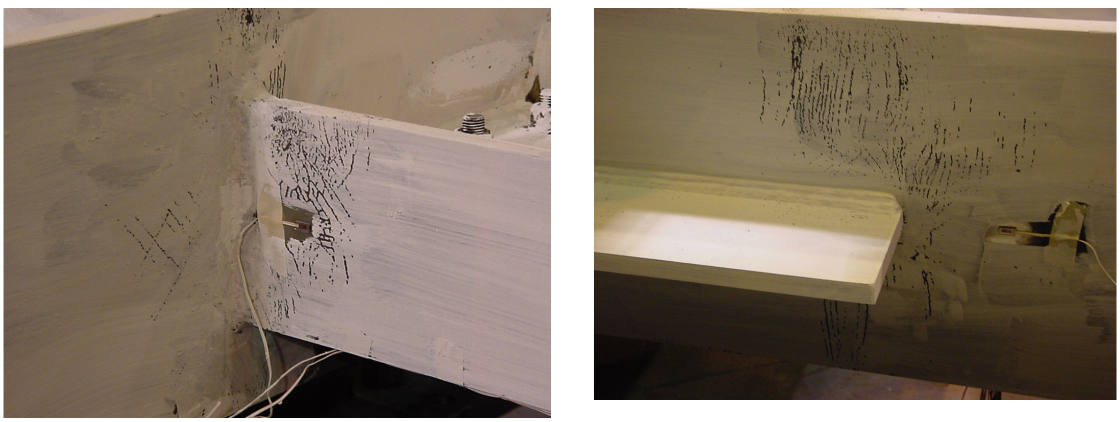

(a) (b)

Fig. 6.24 (a) beam-column connection and (b) north column base at $\Delta_b = 1.0\Delta_{bm.}$

$\Delta_b = 1.5\Delta_{bm}$

Yielding in the column webs continued to increase and propagated along the entire length of the column web (see Fig. 6.25d) during these cycles. The yielding of the gusset plates at the column bases spread over most of the gusset plate surface. Severe yielding was observed just above the gusset plates at the base of the specimen, indicating a plastic hinge formed (see Fig. 6.25a).

No noticeable bolt slip was observed in the connection of the brace to the gusset plate during these or previous cycles. The gusset plates at the base, however, suffered a substantial amount of yielding (see Fig. 6.25c); however, there was no evidence of any cracks or buckling in any of the base gusset plates. The gusset plate located at the midspan of the beam did not have any evidence of yielding at this displacement level.

The north buckling-restrained brace dropped out of plane slightly more than 0.5 in. during this large excursion but returned to its initial position when the specimen was returned to zero lateral displacement. The column stiffener at the exterior base of both columns fractured. The fractures propagated along the weld to the base plate toward the column and stopped just at the face of the column flange.

No damage, including yielding, was detected in the upper story of the specimen throughout the testing.

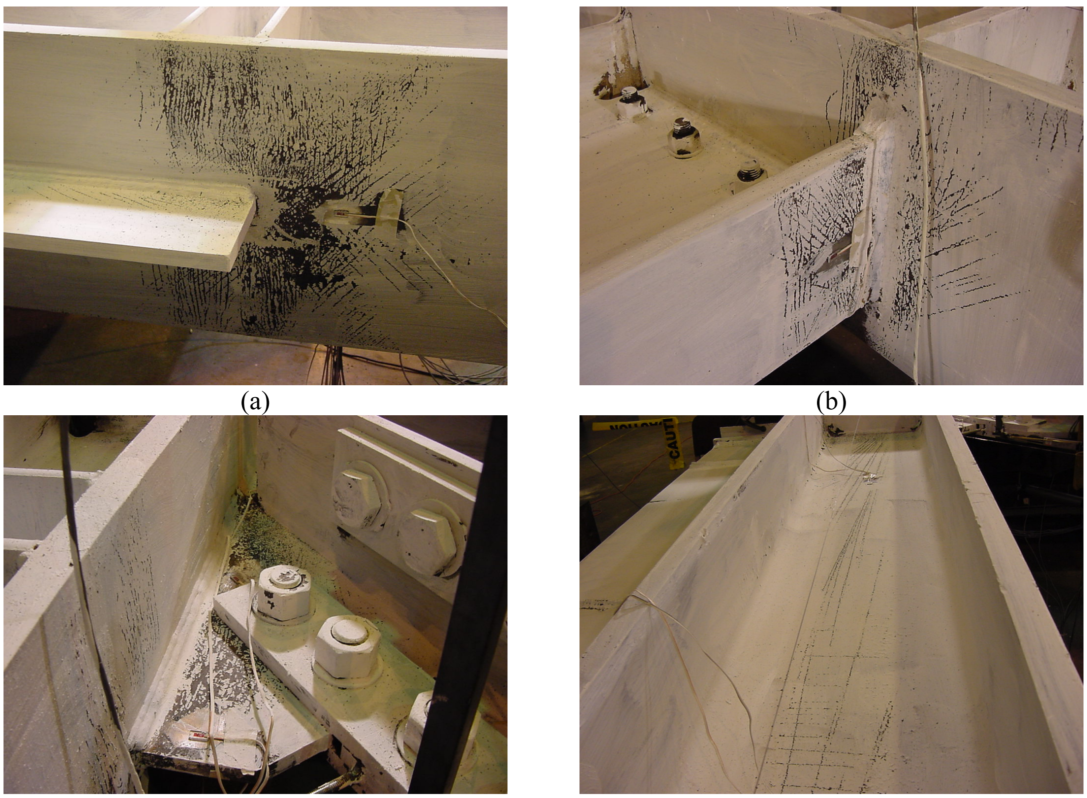

(a) (b) (c) (d)

Fig. 6.25 Damage to specimen BRBR-1 at $\Delta_b = 1.5\Delta_{bm}$: (a) North base of column, (b) north beam-column connection, (c) north base gusset plate, and (d) web (shear) yielding in column.

6.2.3.2 BRBF-1 Response Quantities

A summary of some important response quantities is shown in Table 6.8. The global hysteresis during the displacement-controlled testing is shown in Figure 6.26. The figure plots the actuator force versus the lower-story drift.

It is important to remember that the brace forces are only estimates of the actual force. As noted before, yielding of the column webs prevented an accurate determination of the column shears, although it is felt that the estimates provided are reasonable up to and including the 1.0 Δ_{bm} cycles. The forces in the two braces were further assumed to be of equal amplitude but opposite in sign (Clark et al. 1999). Figure 6.27 plots the relationship between the axial deformations of the north brace versus its estimated axial force during all 16 cycles of testing.

Figures 6.28–6.29 illustrate the buckling-restrained brace in-plane rotation versus story-drift rotation. This rotation is measured from the instrumentation at the end of the encasing tube to the work point of either end of each brace. The relationship for these braces is approximately one-to-one. That is, for a unit rotation of the story there is approximately a unit rotation at the end of the brace. Although significant yielding was observed in the gusset plates, rotations were consistent with drifts; therefore the yielding mechanism is thought to be primarily an axial one. The ratio of brace end rotation to interstory drift is somewhat smaller than one at the top of the braces, suggesting that the local and global rotation of the beam reduces the end rotation demands on the braces away from the base of the structure.

Figure 6.30 shows the vertical displacement (east-west displacement) at the midspan of the main beam during the loading history. The peak displacement amplitude is approximately 0.1 in. (upward), which occurs mainly in the first cycle during which the braces yield; variations of the vertical displacement of the beam during subsequent (and even larger) cycles of lateral displacement are much smaller. The small displacement would indicate that the difference in tension and compression forces in the braces remain nearly a constant (i.e., a small net vertical force on the beam during reversing cycles), and that this difference in force is more or less locked in once the buckling-restrained braces yield.

Although the gusset plates were designed to remain elastic during the tests, there was significant inelastic action in the lower gusset plates, as described above. Figure 6.31 plots the recorded gusset plate displacements in the direction of the brace centerline, plotted against the lower-story lateral displacement. Because one of the displacement transducers was shaken loose on the upper end of northern brace, the results in Figure 6.31b are only approximate in the later cycles. From these plots, it can be seen that the permanent axial deformation of the gusset plates was on the order of 0.3 in. per brace, which is roughly 10–20% of the brace elongation from work-point to work-point, suggesting that the gusset plate yielding played an important part in the overall yield mechanism for the specimen.

Table 6.9 shows the cumulative inelastic axial deformation estimated for each of the buckling-restrained braces during the test. Because the test was displacement controlled (and the out of balance force in the two braces was small), the axial deformation for both braces in each of the cycles were very similar. Therefore, an average brace extension is shown to simplify the calculations. The values in Table 6.9 are calculated assuming mill certificate values for yield strength. Yield lengths were assumed from drawings provided by Nippon Steel Corporation. The resulting cumulative plastic deformation ($257\Delta_{by}$) satisfies the AISC/SEAOC (2001) guidelines for buckling-restrained brace tests ($140\Delta_{by}$), although this criterion is not required for subassemblage tests.

After removal from the specimen, the buckling-restrained braces were shipped to Japan and subsequently tested by Nippon Corporation until failure. However, those test results are not currently available.

Table 6.8 Detailed response quantities.

Quantity		Minima	Maxima
Peak Actuator Force (kips)	Set 1: Δ_{by}	480	485
	Set 2: 0.5 Δ_{bm}	685	682
	Set 3: 1.0 Δ_{bm}	1011	979
	Set 4: 1.5 Δ_{bm}	1168	1129
Peak Lateral Drift (in.)	Set 1: Δ_{by}	0.39	0.39
	Set 2: 0.5 Δ_{bm}	0.86	0.86
	Set 3: 1.0 Δ_{bm}	1.75	1.75
	Set 4: 1.5 Δ_{bm}	2.63	2.63
Brace Yield Force (kips)	(From mill certs.)	259	259
Brace Yield Displacement (in.)		0.13	0.13
Brace Max Force (kips)	Set 1: Δ_{by}	259	246
- estimated -	Set 2: 0.5 Δ_{bm}	275	272
	Set 3: 1.0 Δ_{bm}	318	320
	Set 4: 1.5 Δ_{bm}	370	380
Brace Max Extension	Set 1: Δ_{by}	0.21	0.19
(in.)	Set 2: 0.5 Δ_{bm}	0.5	0.48
	Set 3: 1.0 Δ_{bm}	0.95	1.05
	Set 4: 1.5 Δ_{bm}	1.43	1.65

Table 6.9 Cumulative inelastic axial deformation.

Set	μ_p ***per peak***	$\Sigma\mu_p$
6 X Δ_{by} .	0.57	13.6
4 X 0.5 Δ_{bm}	2.84	45.4
4 X 1.0 Δ_{bm}	6.83	109.3
2 X 1.5 Δ_{bm}	11.06	88.5
Total		256.9

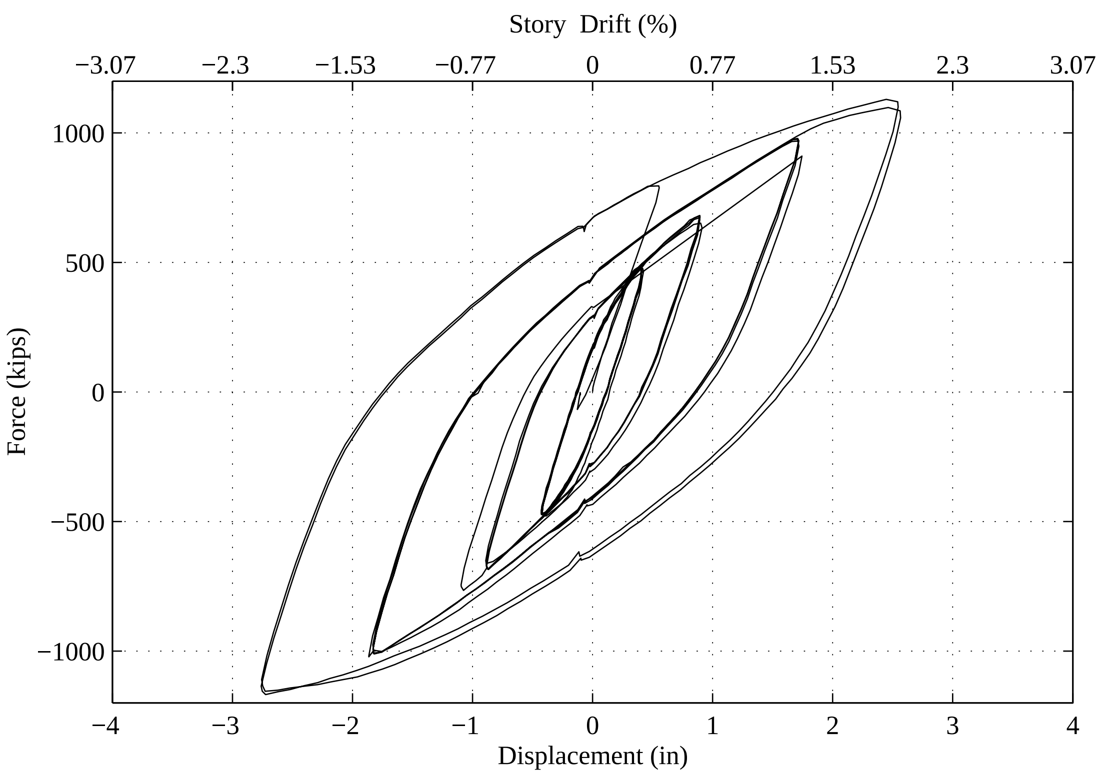

Fig. 6.26 Base shear versus lateral displacement in ground story.

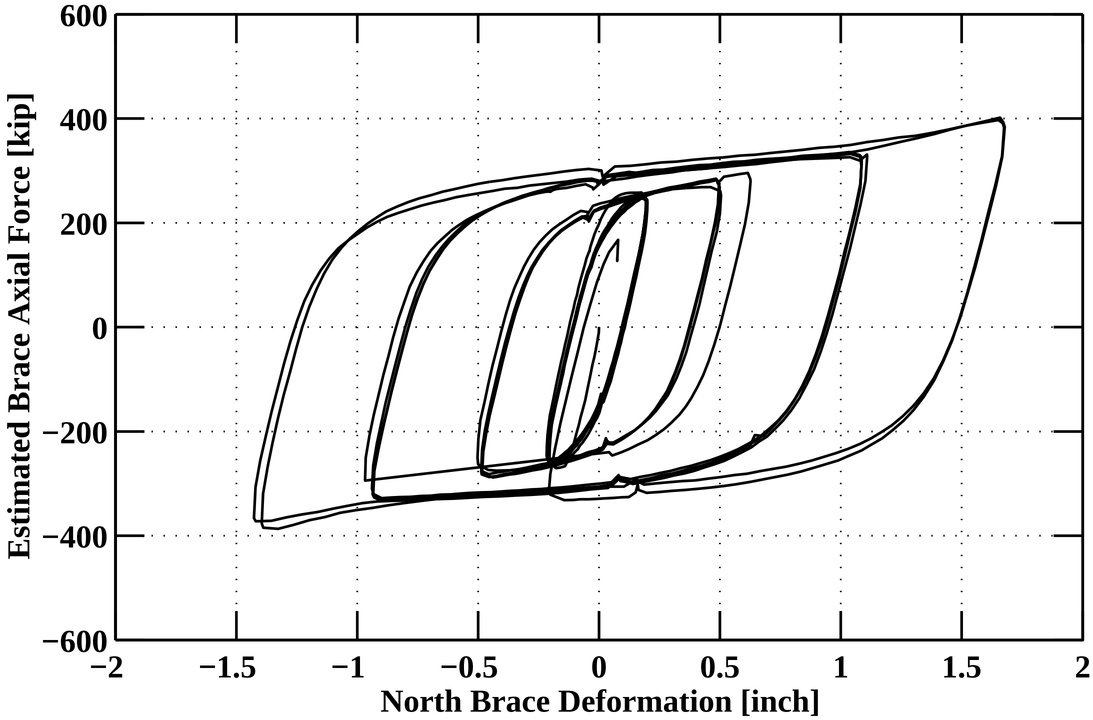

Fig. 6.27 Estimated buckling-restrained brace hysteresis (north brace).

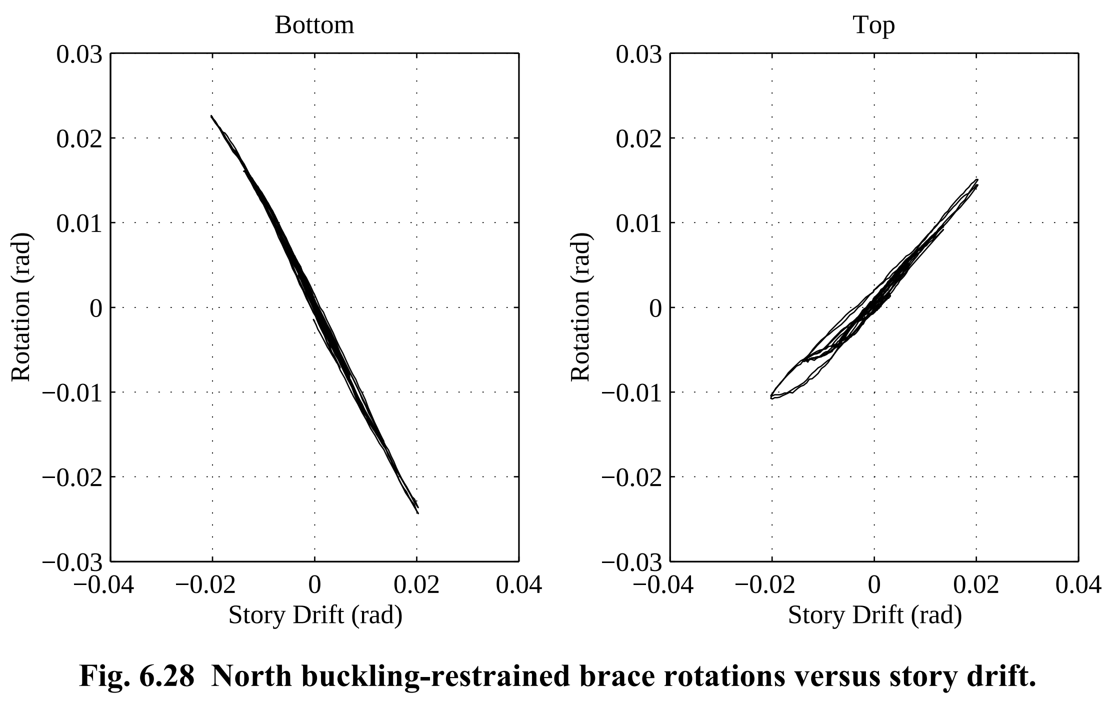

Fig. 6.28 North buckling-restrained brace rotations versus story drift.

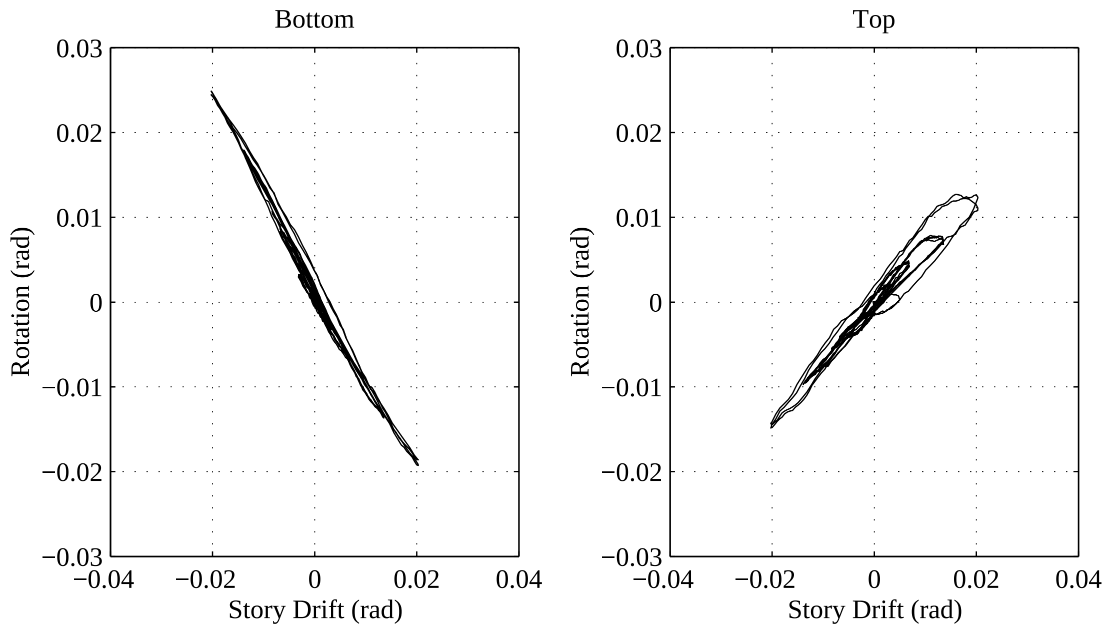

Fig. 6.29 South buckling-restrained brace rotation versus story drift.

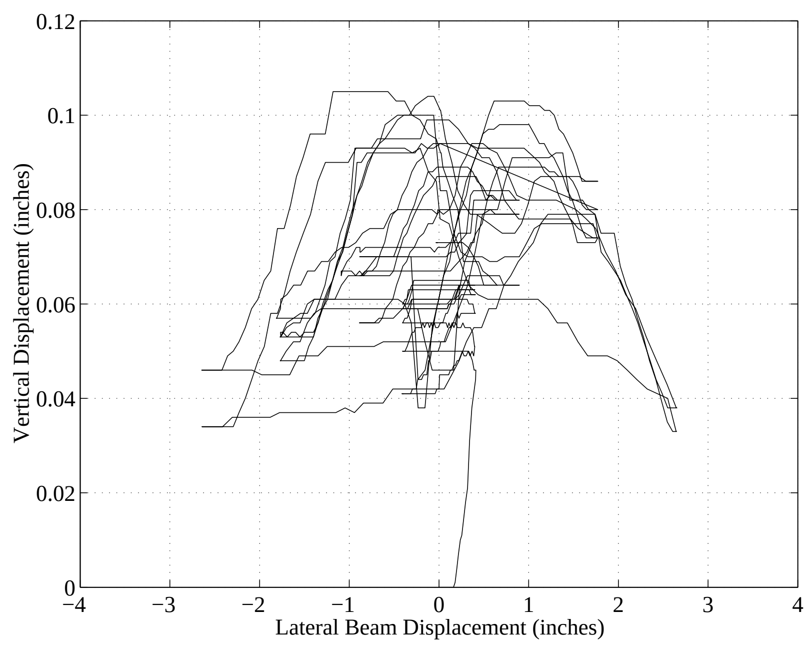

Fig. 6.30 Vertical displacement of midspan versus lateral displacement of beam.

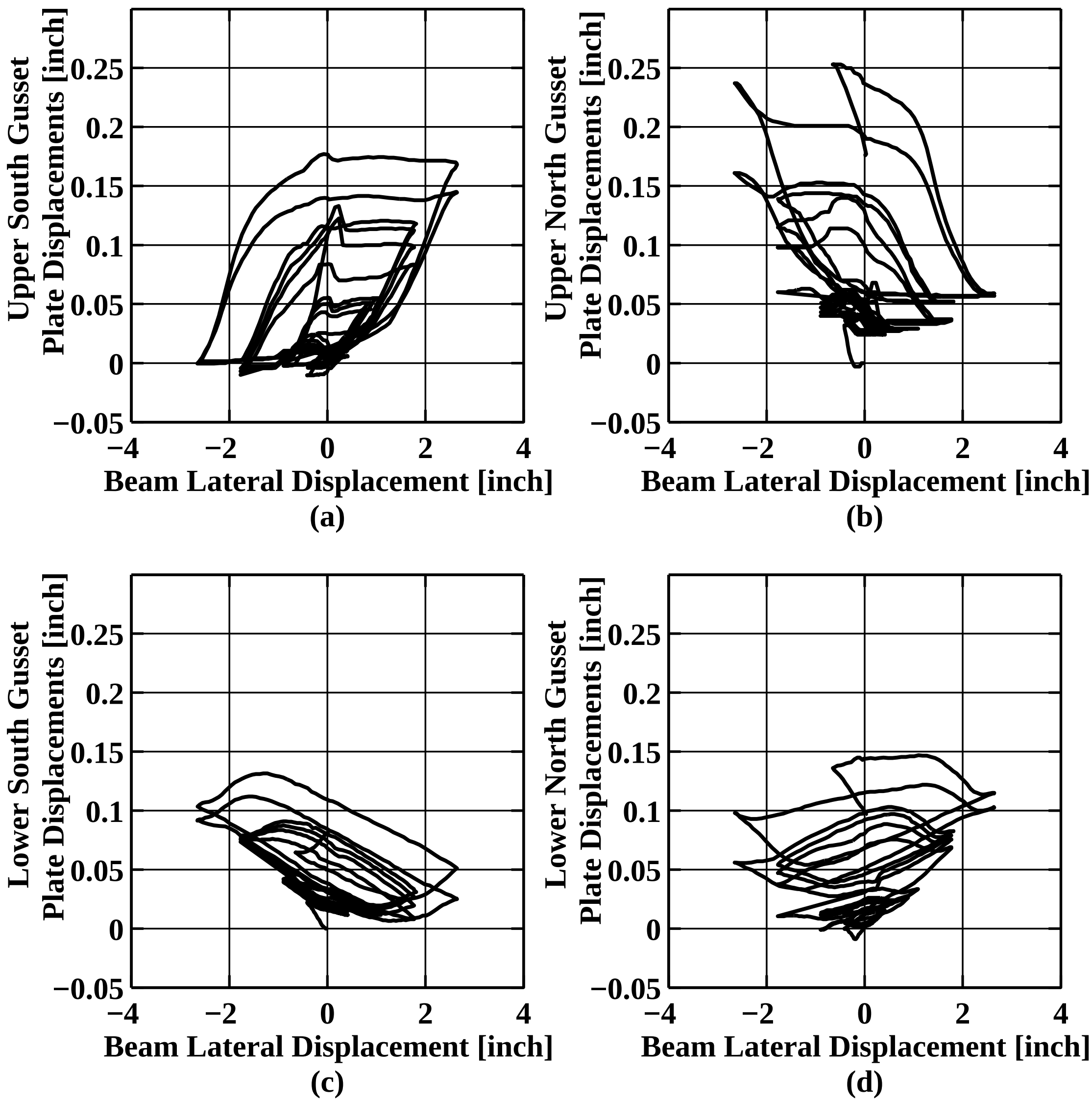

Fig. 6.31 Observed gusset plate elongations for south brace (a) and (c), for north brace (b) and (d).

6.2.3.3 BRBF-2 Results

BRBF-2 was conducted over the course of two days, the first day being Friday, February 1, 2002, and Monday, February 4, 2002. The first six cycles of this test were performed on the February 1, while the remaining cycles were performed on February 4. The instrumentation was left in place over the weekend and data acquisition was started again on Monday. The data show that the instrumentation was recording the same values on Friday afternoon as they were on

Monday morning; thus no shifting (or drift) of instrument values was recorded. For both days, four video cameras recorded the entire test in progress.

Key Observations

The experiment is broken up into four sets of cycles: 6 x $\Delta_b = \Delta_{by}$, 4 x $\Delta_b = 0.5\Delta_{bm}$, 4 x $\Delta_b = 1.0\Delta_{bm}$, and 2 x $\Delta_b = 1.5\Delta_{bm}$. Detailed information about each of these cycles is provided below.

$\Delta_b = \Delta_{by}$

There was no indication of any noticeable yielding at these levels of drift anywhere in the frame or on any of the gusset plates. No noticeable distortion of the columns or brace was observed.

$\Delta_b = 0.5\Delta_{bm}$

Yielding was observed in the gusset plate attached to the upper end of the BRB near the full-penetration welding to the column. Figure 6.32 shows the initial stages of yielding during this stage of loading. Small popping-like noises were also heard coming from stiffener plates near the south column base. Yielding was also observed throughout the stiffener plates at the bottoms of the north and south columns.

Fig. 6.32 South gusset plate yielding near beam-column connection.

$\Delta_b = 1.0\Delta_{bm}$

Yielding in the column webs, indicative of shear yielding, was again observed. Similar to the BRBF-1, the yield lines began at the column base and continued to spread toward the midheight of the column. Distortion of the columns at this displacement was clearly visible to the eye at these cycles, and had the appearance of “shear” deformation, rather than a flexural type of distortion.

During the first couple of cycles at this amplitude level, the gusset plate yielding began to spread further into both gusset plates along the weld interface to the column. Yield lines began forming on the column exterior near each base plate and also near each panel zone, indicating the presence of flexural yielding in the columns. More concentrated yielding was observed in the column flange at the free end of the gusset plate to column connection, at both ends of the brace, and in the beam at the free end of the gusset plate to beam connection on the south column.

During the last two cycles at this amplitude, cracks began forming at the free end of gusset plate-to-column connection on both the north and south gusset plates. Cracks formed in the weld and propagated toward the work point about 1 in. on each gusset plate by the end of the four cycles at this amplitude (see Fig. 6.33c).

The bottom of the gusset plate at the southern beam-column connection was noticeably warped at the peak displacement associated with the brace in tension. The gusset plate buckled upward (out of the plane of the frame). This gusset plate buckling appears to be associated with the “closing” of the moment connection, rather than the axial forces in the brace (the axial forces were tensile when these buckles were observed). During the peak displacements at this amplitude, associated with the brace in compression, there was no noticeable buckling in the gusset plate. The framing action acted in this case to opening of the moment connection.

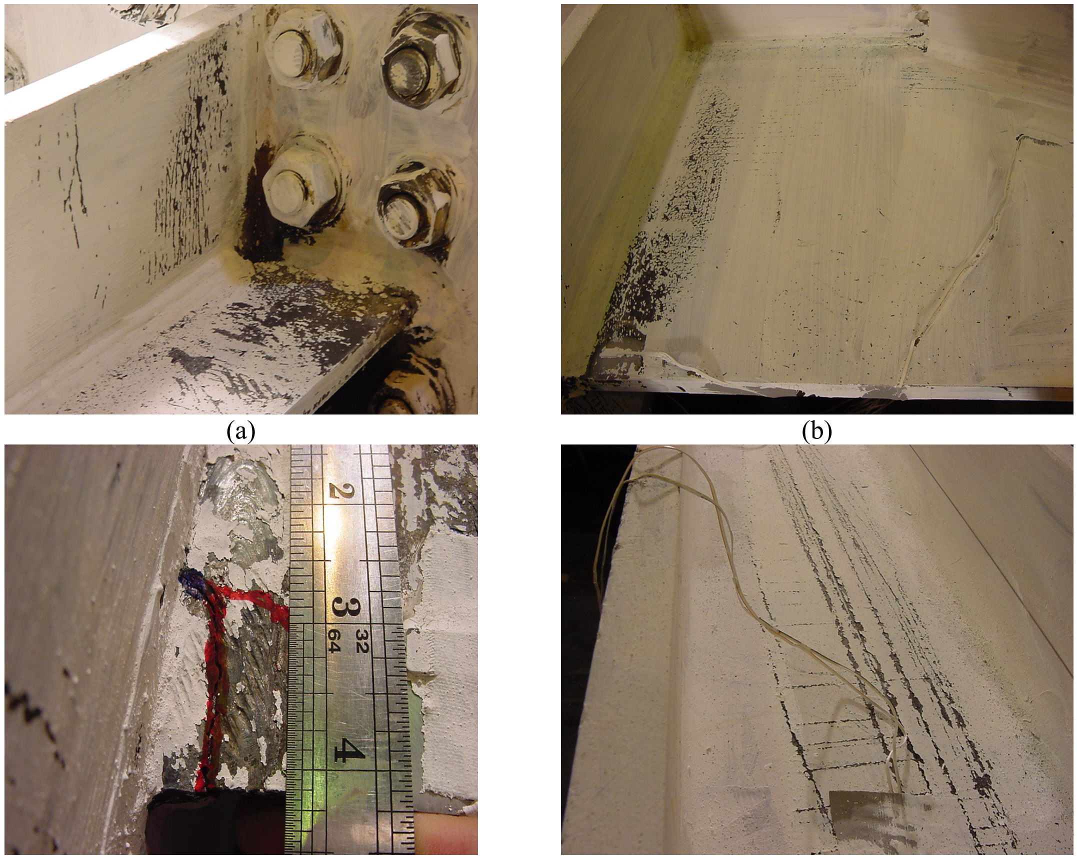

(a) (b) (c) (d)

Fig. 6.33 Damage observed in BRBF-2 at $\Delta_b = 1.0\Delta_{bm}$: (a) column stiffener plate yielding, (b) initial yielding in south gusset plate, (c) eventual crack formation, and (d) column web yield lines.

$\Delta_b = 1.5\Delta_{bm}$

Cracks continued to propagate toward the work points on the gusset plate to column connections. When the brace was in tension, buckling of the south gusset plate became quite noticeable (see Fig. 6.34b). The south gusset plate buckles laterally a total of approximately ½ in. over a 12-in. length. Flexural yielding was observed on column exteriors near the base and near the beam-column connections.

The south column stiffener plate connection to the base plate fractured during these cycles; however, the crack did not propagate into the column. Yielding in this region was significant, as shown in Figure 6.34d, and propagated past the region of the stiffener plate toward the base of the connection.

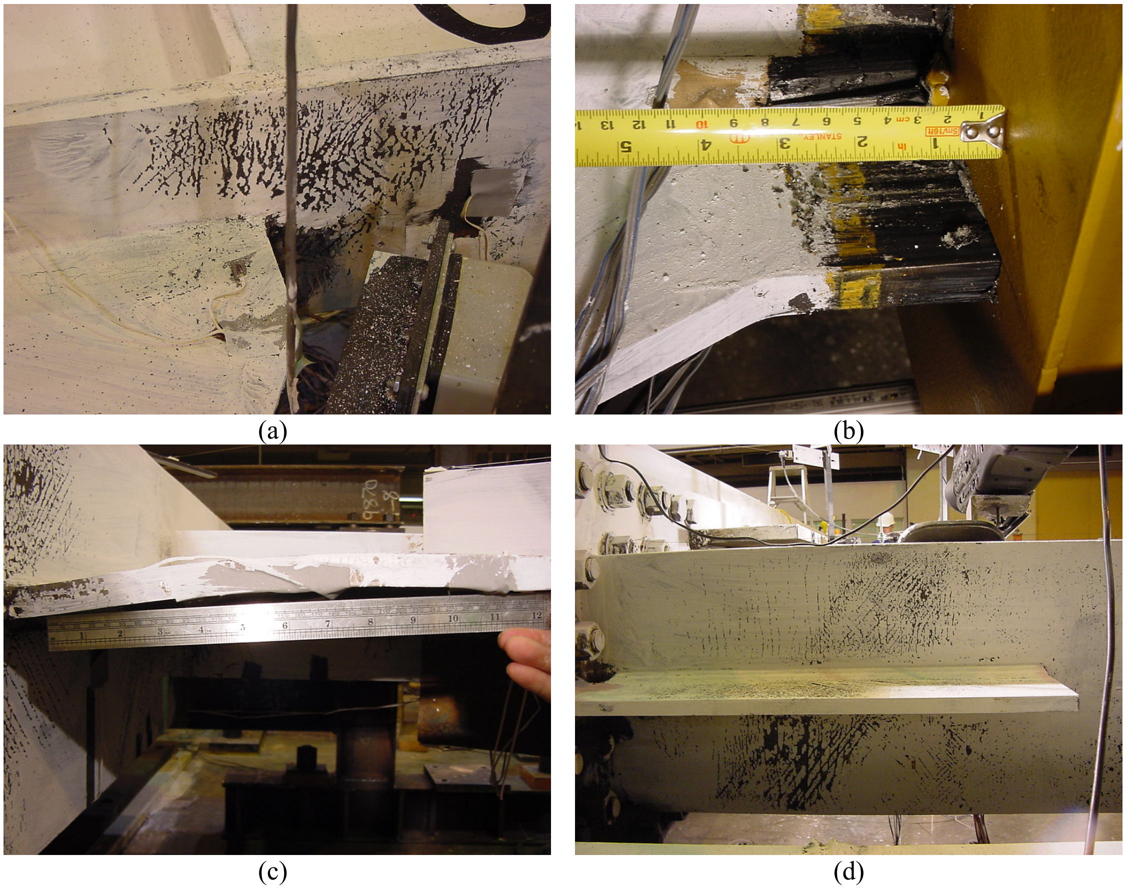

Fig. 6.34 Damage to BRBF-2 at $\Delta_b = 1.5\Delta_{bm}$: (a) Beam yielding, (b) buckling-restrained brace extension, (c) gusset plate buckling, and (d) south column base yielding.

Yielding was observed in the main beam near the gusset plate, indicating flexural yielding in the beam (see Fig. 6.34a). Noticeable yield lines were also found on the bottom flange of the beam at the beam-column connection.

Brace extension and rotation was visible to the eye with no noticeable slip in the bolted connections to the gusset plates.

6.2.3.4 BRBF-2 Response Quantities

A summary of some important response quantities is shown in Table 6.10. The global hysteresis during the displacement-controlled testing is shown in Figure 6.35. The figure plots the actuator force versus the lower-story drift. Figure 6.36 shows the buckling-restrained brace hysteresis during all 16 cycles of testing. As noted before, the forces in the brace are estimates because of yielding in the column web. Both hysteretic loops are full and stable throughout the entire loading history, in spite of local buckles and fractures in the gusset plates.

Figure 6.37 illustrates the buckling-restrained brace in-plane rotation versus story-drift rotation. There is clear hysteresis with respect to the rotation behavior, implying that there was significant in-plane rotation demand on the gusset plates. The initial cycles report similar behavior as to the observed behavior in BRBF-1; in later cycles, this degradation becomes more apparent.

Table 6.11 shows the cumulative inelastic axial deformation that was observed for the test. Because the test was displacement controlled, the axial deformation for the brace in each of the cycles were very similar. Therefore, an average brace extension was computed to simplify the calculations. The values in Table 6.11 are calculated assuming mill certificate values for yield strength. Yield lengths were assumed from drawings provided by Nippon Steel Corporation.

Figure 6.38 plots the vertical deflection of the beam at the midspan. Interestingly, this plot indicates larger vertical displacements compared to BRBF-1, where the two braces were connected at this location. Thus, deflections from bending are larger than those for the unbalanced load at the center of the brace.

Table 6.10 Detailed response quantities.

Quantity		Minima	Maxima
Peak Actuator Force (kips)	Set 1: Δ_{by}	380	410
	Set 2: 0.5 Δ_{bm}	680	687
	Set 3: 1.0 Δ_{bm}	964	929
	Set 4: 1.5 Δ_{bm}	1047	1000
Peak Lateral Drift (in.)	Set 1: Δ_{by}	0.39	0.39
	Set 2: 0.5 Δ_{bm}	1.13	1.13
	Set 3: 1.0 Δ_{bm}	2.25	2.25
	Set 4: 1.5 Δ_{bm}	3.38	3.38
Brace Yield Force (kips)	(From mill certs.)	259	259
Brace Yield Displacement (in.)		0.221	0.221
Brace Max Force (kips)	Set 1: Δ_{by}	235	295
- estimated -	Set 2: 0.5 Δ_{bm}	262	317
	Set 3: 1.0 Δ_{bm}	288	376
	Set 4: 1.5 Δ_{bm}	264	413
Brace Max Extension	Set 1: Δ_{by}	0.32	0.32
(in.)	Set 2: 0.5 Δ_{bm}	0.88	0.87
	Set 3: 1.0 Δ_{bm}	1.81	1.76
	Set 4: 1.5 Δ_{bm}	2.75	2.65

Table 6.11 Cumulative inelastic axial deformation.

Set	μ_p per peak	$\Sigma\mu_p$
6 X Δ_{by} .	0.45	10.8
4 X 0.5 Δ_{bm}	2.99	47.8
4 X 1.0 Δ_{bm}	7.11	113.8
2 X 1.5 Δ_{bm}	11.23	89.9
Total		262.2

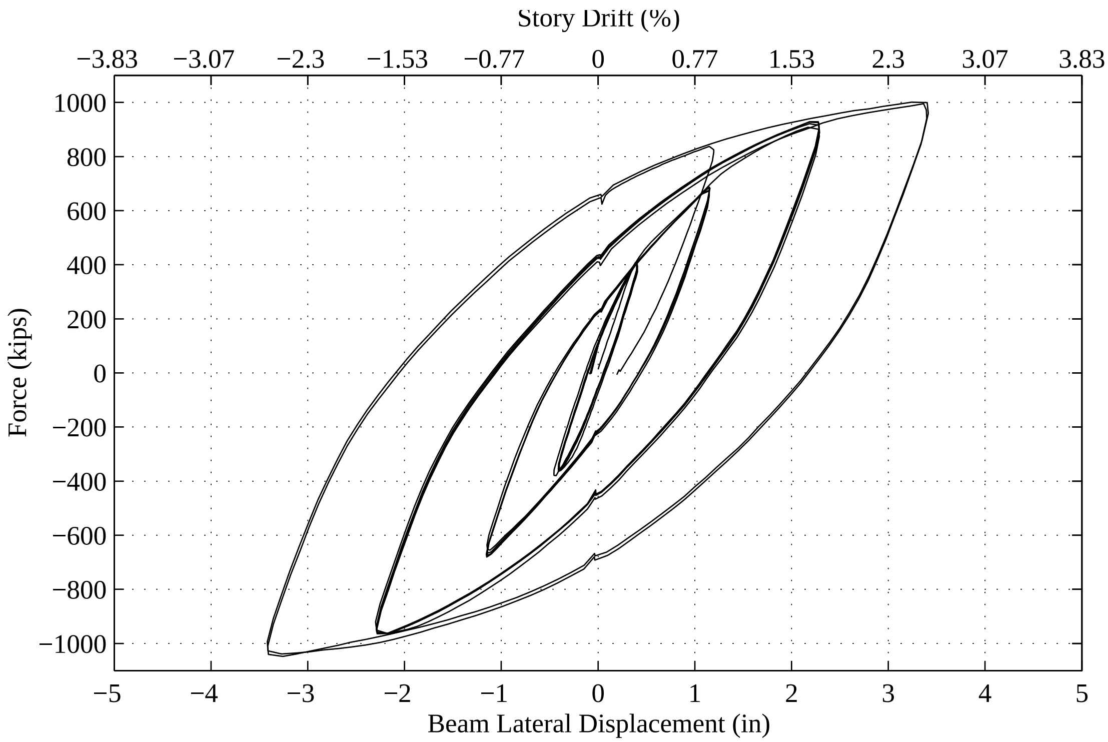

Fig. 6.35 Lateral beam displacement versus base shear.

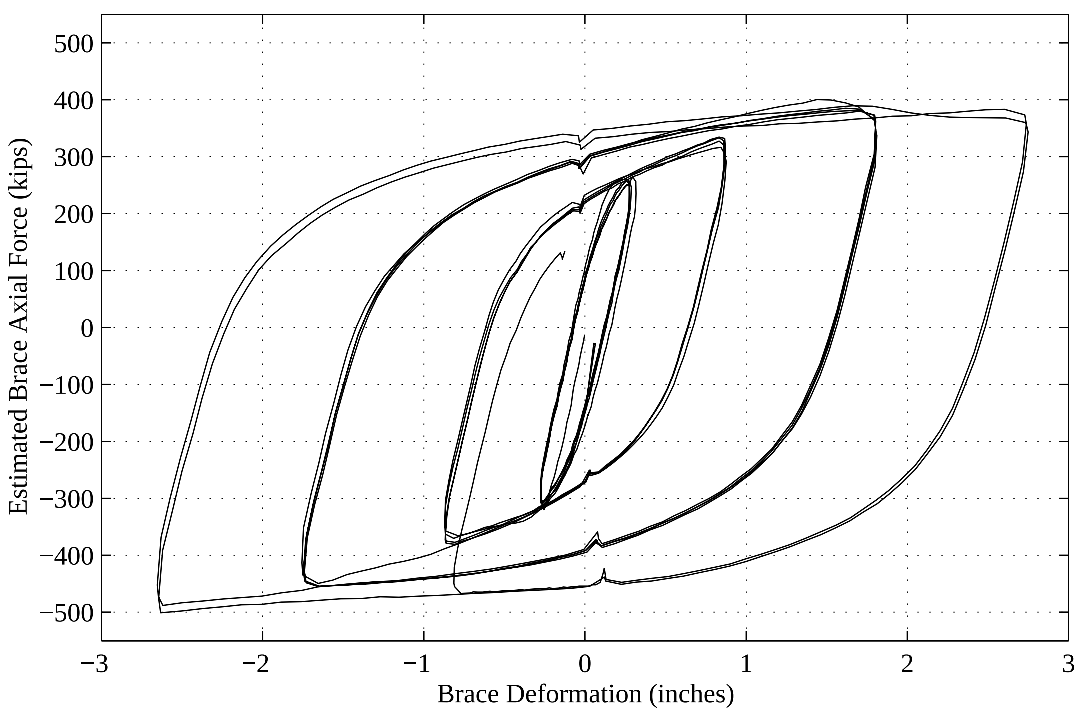

Fig. 6.36 Estimated buckling-restrained brace hysteresis.

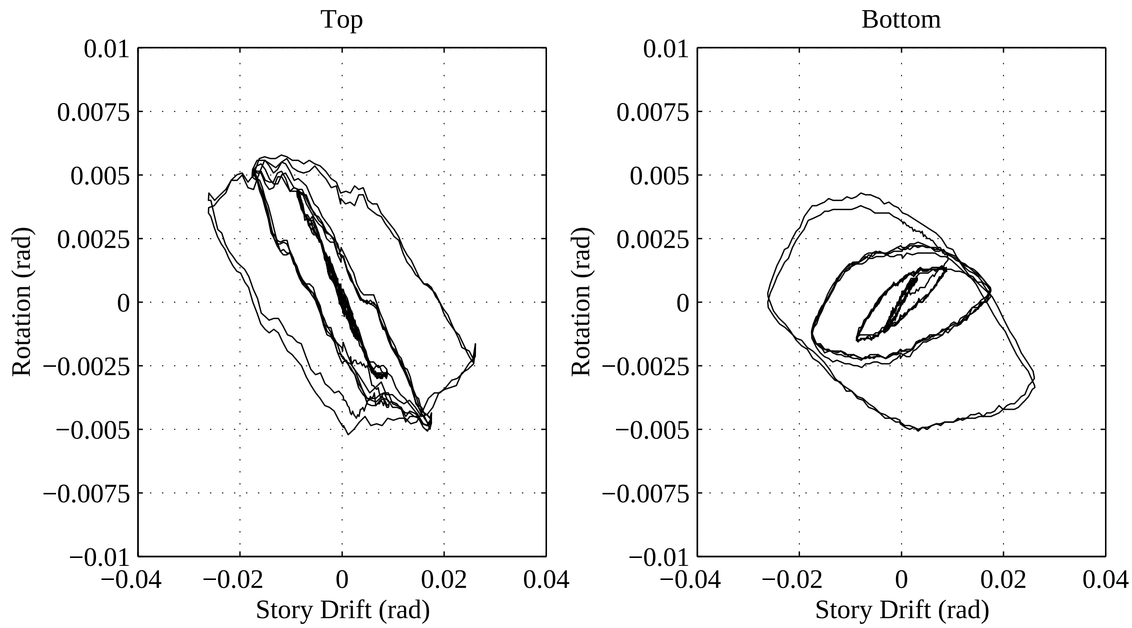

Fig. 6.37 Buckling-restrained brace rotations versus story drift.

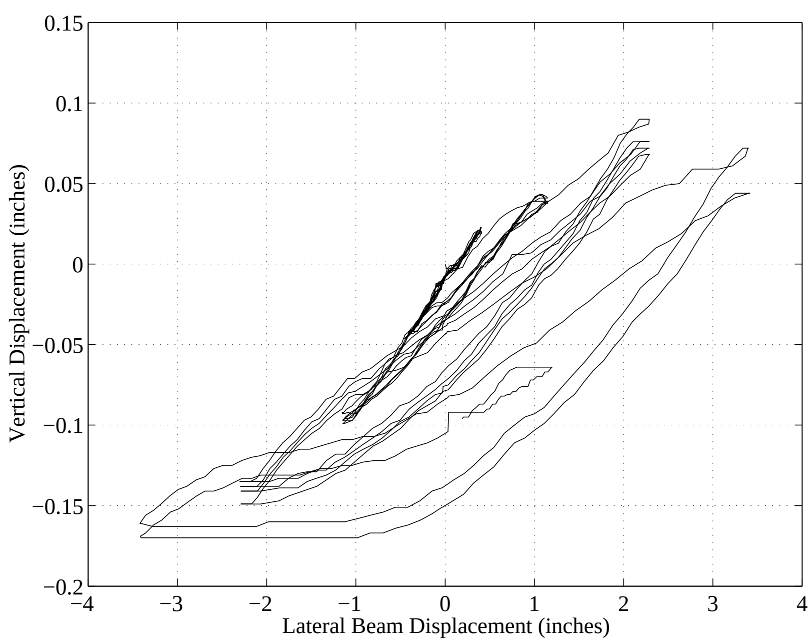

Fig. 6.38 Vertical displacement at midspan of beam during testing.

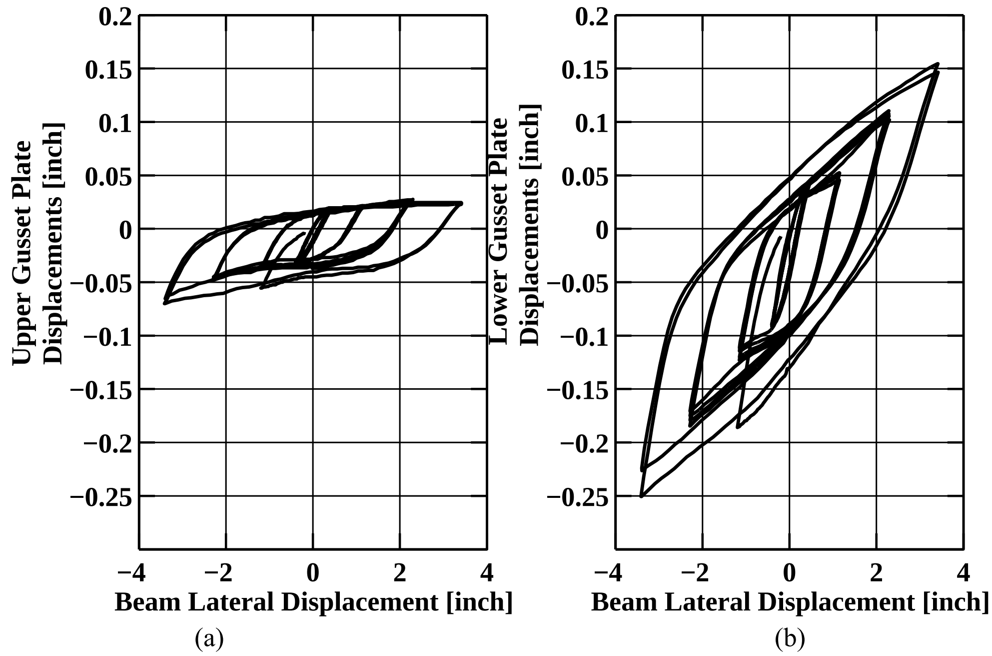

Fig. 6.39 Gusset plate elongation along brace centerline for (a) upper gusset plate and (b) lower gusset plate.

6.2.3.5 BRBF-3 Results

The test of BRBF-3 was conducted over the course of two days, the first day being Tuesday March 12, 2002, the second Wednesday, March 13, 2002. The first ten cycles of the test were performed on March 12, while the remaining cycles were performed on March 13. The quasi-static tests were performed in a similar fashion as to the two previous tests, and the loading protocol is identical to the one shown in the previous section for BRBF-2. The instrumentation was left in place over night and data acquisition was started again on Wednesday. The data show that the instrumentation was recording the same values on Tuesday afternoon as on Wednesday morning. For both days, four video cameras recorded the entire test in progress.

The original intent of this test was to load the specimen as per the previous loading protocol, then continue loading at +0.5 in. increments in peak amplitude until the limits of the testing facility was reached or it was no longer safe to continue. Because of events described below, the loading protocol was modified. The final loading protocol is shown in Figure 6.40.

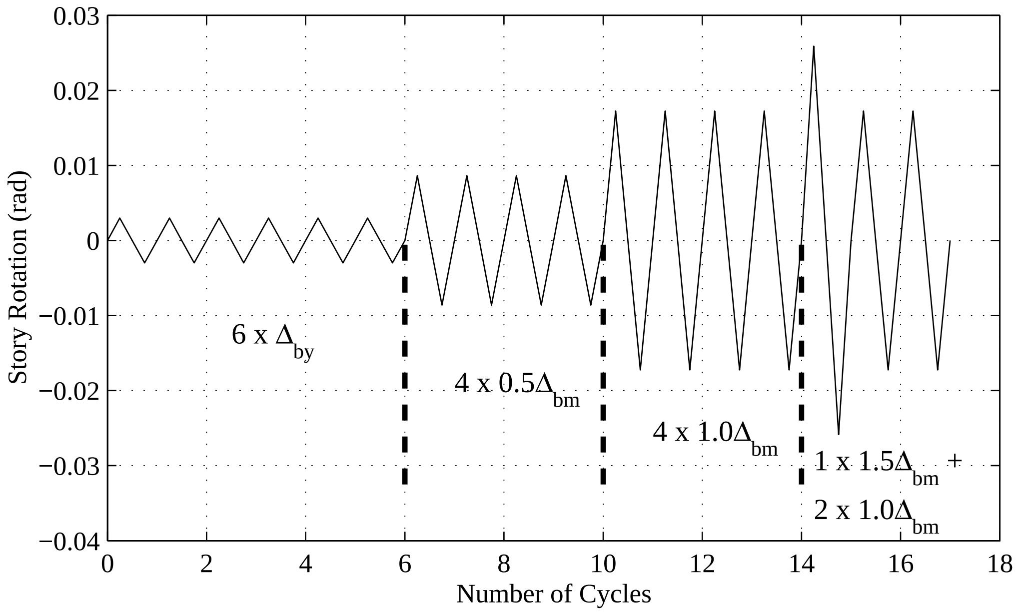

Fig. 6.40 Modified loading protocol for test of specimen BRBF-3.

Key Observations

The experiment is broken up into four sets of cycles: $6 \times \Delta_b = \Delta_{by}$, $4 \times \Delta_b = 0.5\Delta_{bm}$, $4 \times \Delta_b = 1.0\Delta_{bm}$, and the last cycle was augmented as described above. Detailed information about each of these cycles is provided below.

$\Delta_b = \Delta by$

The frame had softened as a result of the yielding that occurred in the previous tests, therefore, the lateral displacement of the lower beam corresponding to Δ_{by} was determined experimentally, rather than on the basis of calculations. During the first excursion, the axial deformation in the buckling-restrained brace was monitored, and the lateral displacement on the specimen was increased until the brace axial displacement reached its computed axial yield displacement. The lateral drift of the bottom story when the beam reached this displacement was found to be 0.33 in. This was then the value set for Δ_{by} for the subsequent five cycles.

No noticeable yielding was observed during these excursions. Many popping noises were heard for specimens BRBF-1 and BRBF-2, but negligible yielding was visible during these cycles and the specimen was “quiet.” This may be in part to the wire brushing and installation of a new coat of whitewash. Instrumentation did not pick up any yielding either.

$\Delta_b = 0.5\Delta_{bm}$

At peak displacements during these cycles, the column shear distortion was noticeable to the naked eye; however, the yield lines were not as pronounced as in previous tests. This may in part be due to the new coat of whitewash on the specimen.

There was no noticeable significant yielding anywhere in the test specimen. The gusset plates had no visible signs of yielding near the full-penetration welds. This was a common location for yield lines in previous tests.

The buckling-restrained brace displacement was, however, quite noticeable, and real-time hysteretic plots during the testing were showing evidence of structural nonlinearity. Thus, damage appeared to be concentrated in the brace.

$\Delta_b = 1.0\Delta_{bm}$

During the first cycle at Δ_{bm}, yield lines became clearly visible in the south column near the interior stiffener plate located at the bottom edge of the gusset plate. There was some indication of yielding at the new gusset plate stiffener that was added adjacent to this interior stiffener for these tests. Noticeable yielding was also found in the lower beam near the gusset plate to beam connection, indicating the formation of a flexural hinge in the beam. This yielding is shown in Figure 6.41a–b. Small cracks in the full-penetration weld of the gusset plate to the beam were detected visually. The cracks began at the free end of the gusset plate and progressed less than 1 in. toward the work point of the beam-to-column connection. The south column exterior stiffener rib plate fractured at the base of the column.

The bottom flange of the beam at the beam-to-column moment connection at the north end of the specimen had a visible crack in the heat-affected zone, which had an apparent crack width of about 1–2 mm. The crack is shown in Figure 6.41c. The crack ran along the entire width of the flange. During peak excursions to the north (i.e., when the bottom flange was in compression), the crack was not noticeable. The south column base also evinced some yielding near the region that contained the stiffener rib plate.

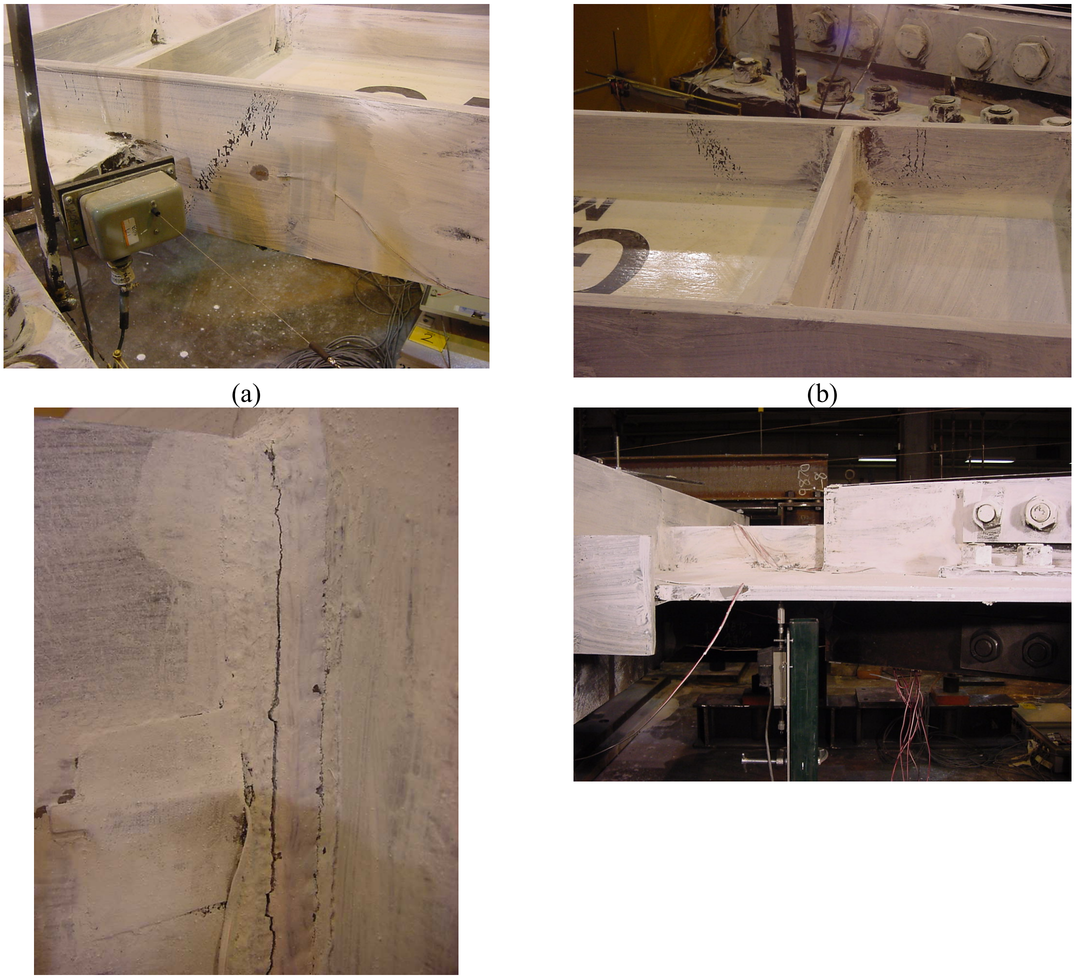

(a) (b)

(c) (d)

Fig. 6.41 Damage in specimen BRBF-3 at $\Delta_b = 1.0\Delta_{bm}$: (a) yielding in beam near gusset plate viewed from bottom, (b) yielding in beam near gusset plate viewed from top, (c) fracture in weld heat affected zone at bottom of flange of north beam-column moment connection, and (d) gusset plate under compressive frame action.

$\Delta_b = 1.5\Delta_{bm}$

Originally, there were to be two cycles at $1.5\Delta_{bm}$ as done for the previous specimens; however, only one full cycle was completed at this amplitude, and two additional cycles were completed at the $1.0\Delta_{bm}$ level.

Before reaching the maximum lateral displacement toward the north (a target displacement at the first-story beam of 3.375 in.), a loud noise was heard at a displacement of about 2.2 in. The testing was momentarily paused so that the source of the noise could be located. A large crack had fractured the entire bottom flange of the lower-level beam near the tip of the south gusset plate connection (see Fig. 6.42a). This occurred during an excursion when the brace was in compression. At this instance, the bottom flange of the beam at the tip of the gusset plate was in tension. The fracture, before reaching the peak of the first cycle at $1.5\Delta_{bm}$, had propagated into the web of the beam about 2.5 in. Yielding was observed at this time in the south side wide-flange brace in the upper level. This brace was directly above the connection that fractured. The fracture in the beam resulted in the bottom flange of the lower-level beam displacing out of plane. The loss of continuity of the lower-level beam flange resulted in a loss of lateral restraint for the flange, which was connected to the brace that was loaded in compression at this point. This lateral displacement of the bottom flange and gusset plate resulted in the buckling-restrained brace buckling out of plane. This buckling was associated with out-of-plane rotation of the gusset plate and inelastic bending deformations at the end of the concrete-filled steel tube intended to restrain midspan buckling of the brace.

The load excursion at $1.5\Delta_{bm}$ was then continued. At the peak excursion for this cycle, it was also noticed that the entire lower-level beam flange-to-column column moment connection on the north end of the beam was fractured. The fracture propagated through the entire flange and completely separated the bottom flange from the full-penetration weld that was there (see Fig. 6.42b).

At the peak excursion to the north, the buckling-restrained brace buckled out of plane considerably. Figure 6.42e shows the large out-of-plane rotation seen. Out-of-plane lateral displacements as large as 12 in. were measured approximately 36 in. away from the beam-to-column connection at the maximum frame displacement to the north. The brace partially "straightened" during excursions toward the south, where as little as 3 in. of lateral displacement was observed at the same location. This was the general trend for the last two cycles imposed at $1.0\Delta_{bm}$. These cycles demonstrated a tremendous cyclic plastic rotation capacity of the end regions of the buckling-restrained brace where it enters the restraining tube.

During the last two cycles at $1.0\Delta_{bm}$, the crack in the beam web propagated further into the web. Figure 6.42 shows the beam fracture after the final cycle. The full-penetration weld between the gusset plate and beam also began to fracture along the length of the weld. The weld fracture continued almost the entire length of the gusset plate. This may have been associated in part with the out-of-plane bending of the gusset plate to beam connection during the buckling of the brace. The extensive buckling of the gusset plate caused a fracture at the end of the gusset plate stiffener that was included for the brace connection. Figures 6.42c–d show the gusset plate and the stiffener at the largest amplitude displacement to the north. The gusset plate at the base of the north column suffered little damage during these final cycles.

6.2.3.6 BRBF-3 Response Quantities

A summary of some important response quantities is shown in Table 6.12. The reader is reminded again that the brace force is an estimate. The global hysteresis of the lower story of the specimen during the displacement-controlled testing is shown in Figure 6.43. It can be seen that after the beam fracture, the maximum global force of the entire system is reduced to roughly 70% of the peak load during the Δ_{bm} cycles. Figure 6.44 plots the relationship between the axial deformations of the brace versus an estimate of axial force during all 16 cycles of testing. These hysteretic plots are full and stable through the cycle during which the beam fractured. After the beam fracture, the stiffness and strength of the specimen are both reduced. In particular, once the bottom flange of the beam fractures and there rotational restraint of the end of the brace is lost, the hysteretic loop estimate for the buckling-restrained brace takes on the appearance of a brace that buckles. The brace is nonetheless able to develop significant inelastic action, similar to that of a moderately slender brace that does not fail due to low-cycle fatigue.

Fig. 6.42 Damage observed in specimen BRBF-3 at 1.5Δ_{bm}+: (a) beam flange fracture, (b) beam-column connection fracture, (c) base column gusset plate, (d) north gusset plate after beam fracture, and (e) brace rotation at peak displacement toward north.

Figure 6.45 illustrates the buckling-restrained brace in-plane rotation versus story-drift rotation. The earlier cycles indicate a relatively rigid connection showing similar behavior to BRBF-1 gusset plates; however, at later cycles, considerable rotational inelastic demand is placed on both the gusset plates. By comparing performance with that of BRBF-2, the stiffener apparently had relatively little effect on the rotational stiffness of the gusset plate, in both cases reaching a rotation of nearly 0.5%. This would indicate that the combined axial and flexural demands on the gusset are significant when confined as detailed for these tests.

Figure 6.46 shows the vertical displacement at the midspan of the main beam during the loading. This movement is generally associated with the bending of the beam along its length, but some comes from the axial extension of the columns.

Table 6.13 shows the cumulative inelastic axial deformation that was observed for the test. Because the test was displacement controlled, the axial deformation for the brace in each of the cycles was very similar. Therefore, an average brace extension was then used to simplify the calculations. The values in Table 6.13 are calculated assuming mill certificate values for yield strength. Yield lengths were assumed from drawings provided by Nippon Steel Corporation. Because of the fracture at the beam flange, the value of the cumulative plastic deformation was not computed after 75% of a cycle at the maximum displacement (the beam failed at this point). The total cumulative displacement of the frame was 219Δ_y, which exceeds the requirement imposed on individual braces by the AISC/SEAOC guidelines (140 Δ_y).

Table 6.12 Detailed response quantities.

Quantity		Minima	Maxima
Peak Actuator Force (kips)	Set 1: Δ_{by}	497	520
	Set 2: 0.5 Δ_{bm}	846	908
	Set 3: 1.0 Δ_{bm}	1185	1140
	Set 4: 1.5 Δ_{bm}	1270	1150
Peak Lateral Drift (in.)	Set 1: Δ_{by}	0.33	0.33
	Set 2: 0.5 Δ_{bm}	1.13	1.13
	Set 3: 1.0 Δ_{bm}	2.25	2.25
	Set 4: 1.5 Δ_{bm}	3.42	3.44
Brace Yield Force (kips)	(From mill certs.)	477.8	477.8
Brace Yield Displacement (in.)		0.184	0.184
Brace Max Force (kips)	Set 1: Δ_{by}	440	424
- estimated -	Set 2: 0.5 Δ_{bm}	538	493
	Set 3: 1.0 Δ_{bm}	610	542
	Set 4: 1.5 Δ_{bm}	630	590
Brace Max Extension	Set 1: Δ_{by}	0.2	0.16
(in.)	Set 2: 0.5 Δ_{bm}	0.8	0.8
	Set 3: 1.0 Δ_{bm}	1.67	1.68
	Set 4: 1.5 Δ_{bm}	2.19	2.53

Table 6.13 Cumulative inelastic axial deformation.

Set	μ_p per peak	$\Sigma\mu_p$
6 X Δ_{by} .	0	0
4 X 0.5 Δ_{bm}	3.35	53.6
4 X 1.0 Δ_{bm}	8.08	129.2
1 X 0.75 Δ_{bm}	12.04	36.1
Total		218.9

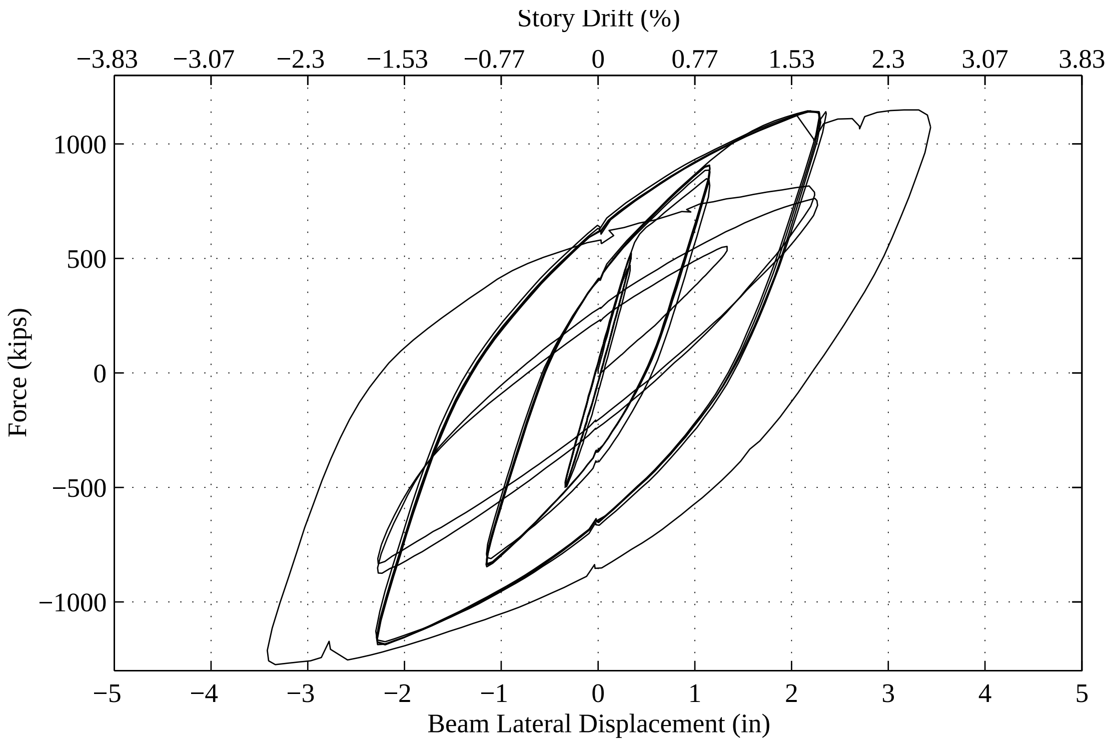

Fig. 6.43 Lateral beam displacement versus base shear.

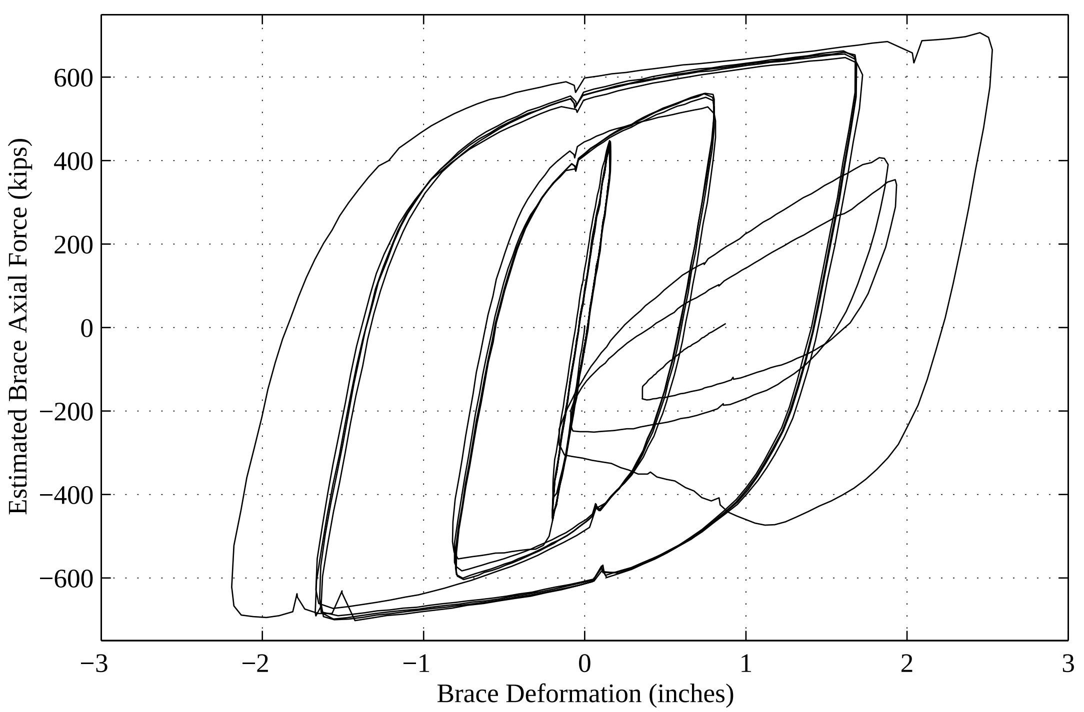

Fig. 6.44 Estimated buckling-restrained brace hysteresis.

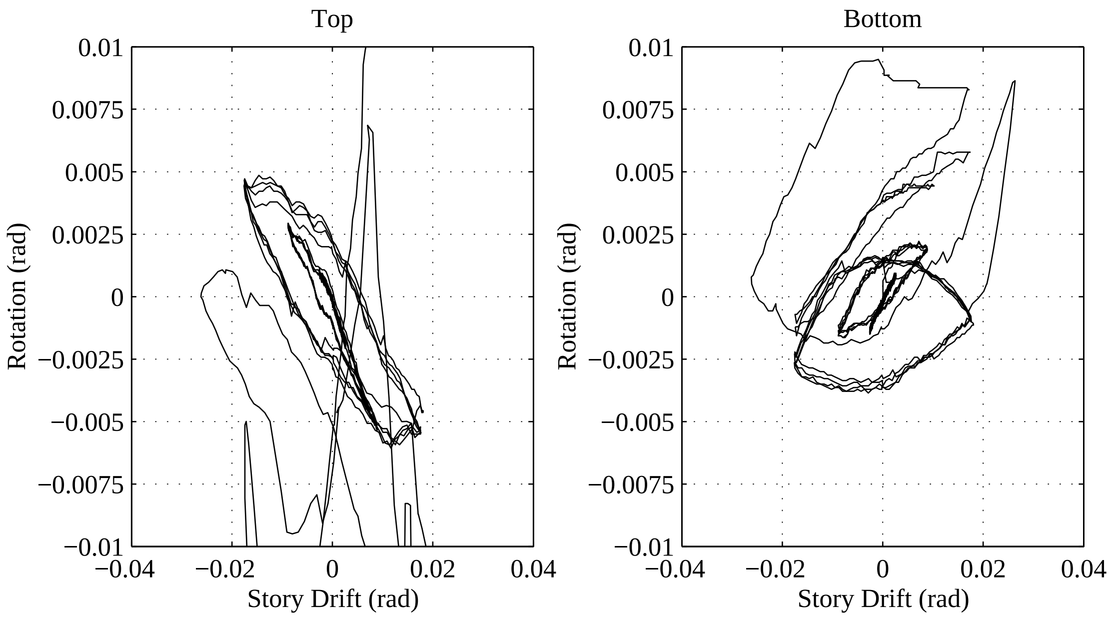

Fig. 6.45 Buckling-restrained brace rotations versus story drift.

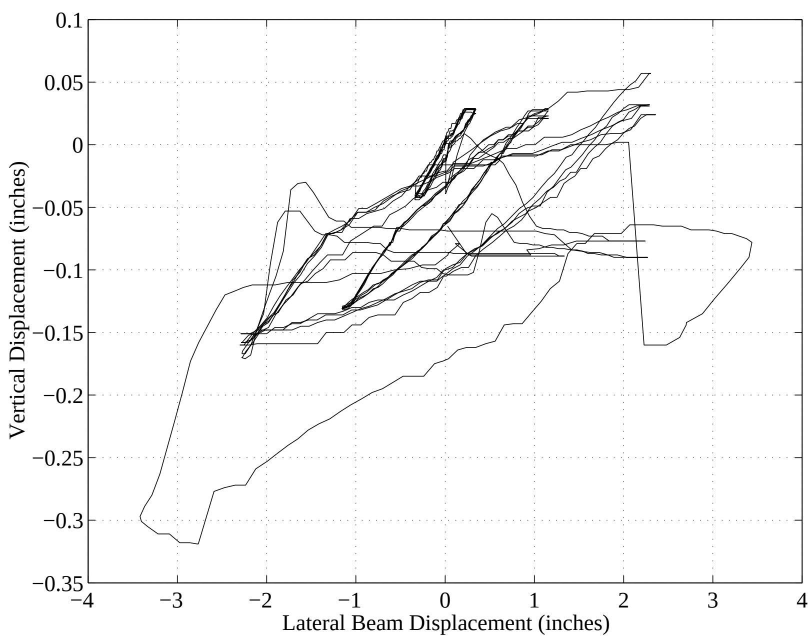

Fig. 6.46 Midspan vertical displacement versus beam lateral drift.

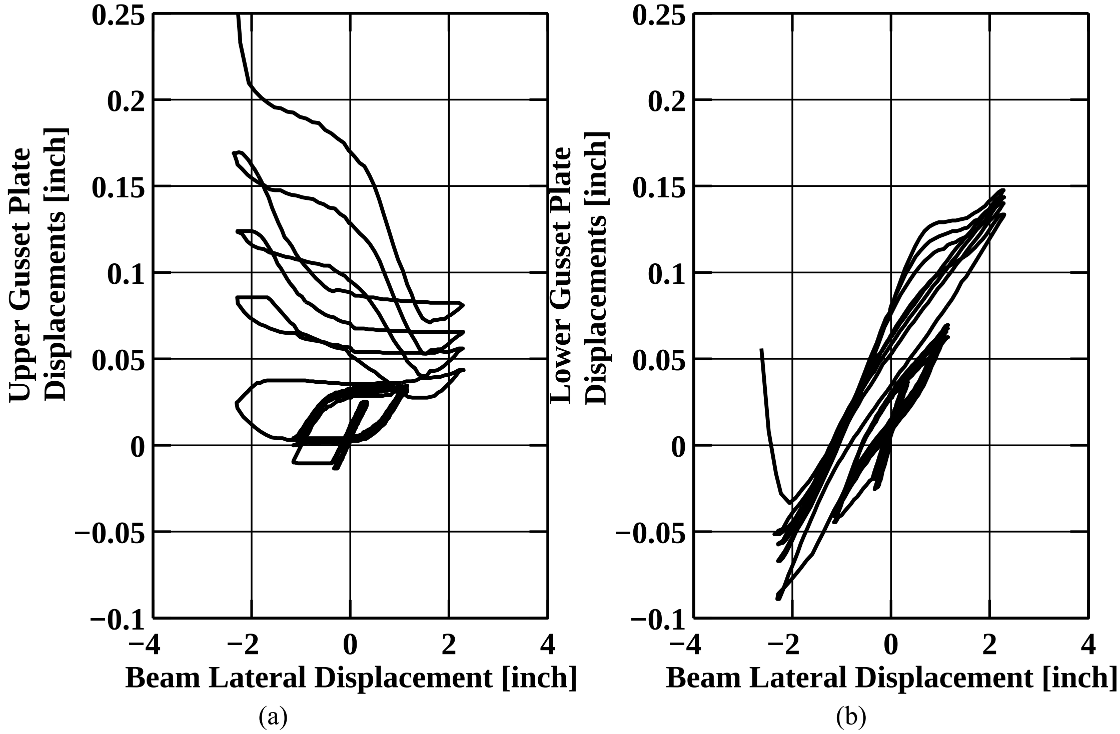

Fig. 6.47 Gusset plate extensions for (a) upper gusset plate and (b) lower gusset until just after fracture of main beam.

6.2.4 Discussion of BRBF Behavior

6.2.4.1 BRBF-1

The beam-column connections in all of the test specimens were detailed as full ductile moment connections. As a result, there was yielding at these connections and frame action contributed significantly to the strength and stiffness of the overall specimen. A well-balanced distribution of damage was observed in the frame: yielding occurring at the end of the gusset plate, in the panel zone region and on the bottom of the beam at the face of the column, as well as shear yielding in the columns.

Unexpected behavior was witnessed in the columns. Because of the combined effect of large flexural moments at the ends of the columns and significant axial loads, larger than expected shear developed in the columns. As a result, there was substantial shear yielding in the column webs. This created no adverse effects on the overall behavior of the braced frames, but this behavior was not expected during the original design of the specimen. For the design of the specimen, the designer assumed that the beams were pin connected to the columns, as is common in practice, but a rigid moment connection was provided as a backup system.

In general, due to the widespread yielding observed, the frame behaved in a very ductile manner. The braces behaved as predicted with the absence of any slip in the bolted connections. The upper gusset plate seemed to have fared very well with only a small tendency to buckle laterally, but there was extensive yielding in the lower gusset plate (however, not in the out-of-plane buckling mode associated with conventional braces).

The steel tube, which encased the north buckling-restrained brace, experienced some "walking" as the tests progressed; thus, the total extension was not equally distributed at each end of the brace. During the last couple of cycles, the core at the top of the north brace began to extend more than the core at the lower end of the same brace. This resulted in about a 0.5 in. relative unbalance in the location of the buckling-restrained brace encasement tube.

The vertical stiffener provided on the exterior face of the column proved to be unnecessary, and fractured repeatedly in all of the specimen tests.

6.2.4.2 BRBF-2

Global behavior of this specimen was stable and repeatable. As seen in the previous test, the damage was well distributed and there were no detrimental or strength degrading mechanisms that formed during testing.

Both columns experienced well-distributed shear yielding due to a combination of high axial loads and relatively rigid end conditions. Both columns also suffered from a large amount of distributed flexural yielding at south beam-column connections, the north and south column base, and at the north beam-column connections at larger displacements.

Fractures occurred at both BRB gusset plate connections due to frame action. Fractures began to propagate from the tip of the gusset-column connection toward the work points. The gusset plate connections were full-penetration welded, but the backing bar was left in place, this may have acted as a crack initiator. The cracks on both gusset plates propagated along the length of the column weld approximately 2 in. from the edge of the gusset plate toward the work point. Because the tearing of the weld was due to frame action, the brace was at full compressive capacity when the fractures began to propagate, this may have hindered the crack propagation.

The fractures did not appear to hinder the performance of the frame in a detrimental way globally. Gusset plates for this type of connection are typically fillet welded on site.

During the negative displacement excursions (i.e., with the specimen traveling south), the top gusset plate experienced local buckling at its bottom free edge. The lack of disturbance to the whitewash on the gusset plate suggests that the buckling observed was predominately elastic. During these excursions, there was also yielding noticed on the bottom side of the beam. Most of the damage of the southern gusset plate occurred at the tips of the gusset plate on the beam and column. The buckling-restrained brace behaved well, no unexpected behavior was observed. The braces were able to withstand the rotational displacements without any adverse effect to the axial capacity or performance. The brace was near its compressive displacement capacity during the larger lateral excursions, but did not contact the steel casement with its flared extruding connectors. No bolt slip was witnessed at all, even at full excursions.

The beam seemed to have experienced very little inelastic flexural demand. The beam appeared to remain elastic during all cycles and only minor yielding was found near the edge of the beam gusset plate. The stiffener rib at the south column base fractured at its connection to the base plate. This connection fractured during the previous test and was re-welded prior to testing of BRBF-2. The crack did not propagate into the column. Due to the lack of the gusset plate at the base of the south column, this base experienced a large rotational demand.

6.2.4.3 BRBF-3

The fracture at the gusset plate and beam connection raises concern about the detailing provided for this specimen; however, preliminary analysis might indicate that the cause of the fracture propagation may be due, in part, to the extensive heat treatment and fatigue that the beam flange experienced in the previous testing and re-welding of the new gusset plate. The fracture initiation point at the tip of the weld of the gusset plate to the beam may have been defective. Another explanation for the sudden fracture of the beam flange is that when the beam begins to form a plastic hinge at this location, the material at the tip of the gusset plate is subjected to a high biaxial tensile stress condition in the plane of the beam flange, as well as high out-of-plane constraint (by the gusset plate and beam web).

Prior to the fracture of the beam, the specimen experienced, smooth, stable, hysteretic performance with no strength degrading mechanisms like local buckling, etc. The additional stiffeners on the gusset plates minimized the buckling behavior of the gusset plate during compressive frame action. As seen in the two previous specimens, the stiffener ribs at the base of the south column fractured at the connection to the base plate. The northern column base was more likely to yield in flexure due to the additional rigidity.

The pre-qualified WUF-W type moment connection on the northern column saw many cycles of inelastic rotation by the time the bottom beam flange to column weld fractured. The cause of the fracture is still unknown. Because of cost considerations, metallurgical tests were not performed to determine if the fracture was due to low-cycle fatigue or other factors. While the connections saw the cumulative effects of three braced-frame tests, the lateral displacements in these tests are considerably smaller than those that would have been expected in a test of a moment-resisting frame, which was the basis for this connection detailing.

Although it was not intended to rotate out of plane as much as it did, the buckling-restrained brace witnessed very large inelastic rotations and was still able to maintain a large percentage of its axial capacity in compression, ~30%. The brace connection had completed nearly 90° of cumulative inelastic rotation by the time that the specimen had completed the last cycle. There were no indications that the buckling-restrained brace failed along the interior of the core plate; however, this was not verified due to inability to access the interior core plate.

6.3 COMPARISON OF EXPERIMENTAL AND ANALYTICAL RESULTS FOR BRBF SPECIMENS

Accurate analytical models can provide insight into structural behavior for not only assemblies that are tested, but also for those with *reasonable* variations of member proportions and details. The usefulness of physical testing can not be underestimated, as was highlighted with the unexpected column shear yielding observed in all of the specimens, buckling of the gusset plate in BRBF-2 due to frame action, and fracture of the beam for BRBF-3. This section provides insights into some of the experimental testing using classic plastic analysis, along with OpenSees analysis of an analytical representation of all three BRBF specimens. The OpenSees models validated in this section will be used for performance-based analyses of buckling-restrained braced frames presented in subsequent chapters.

6.3.1 Column Web Yielding

An approximation to the yield capacity of the column based on Von Mises yield criteria was used to determine the capacity at which the column would begin to yield in shear (Bruneau and Mahin 1991). Equation (6.1) shows the result of such an approximate analysis, and Equation (6.2) shows the approximate value of shear stress in the web, where w is the thickness of the web, and h is the height of the web from inside flange to inside flange (see Fig. 6.48).

$$\tau_w = \frac{1}{\sqrt{3}}\sqrt{{\sigma_y}^2 - {\sigma_w}^2} \tag{6.1}$$

where

$$\tau_w \approx \frac{V}{wh} \tag{6.2}$$

where σ_w is the axial stress in the column web (P/A_{web}). With the axial force equal to zero, the maximum value of allowable shear stress becomes:

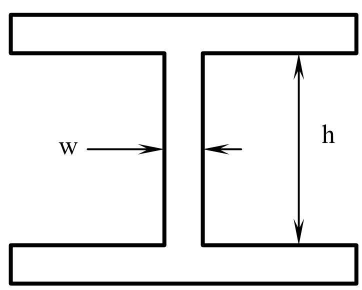

Fig. 6.48 Column cross section.

$$\tau_w = \frac{1}{\sqrt{3}}\sqrt{(55\,Ksi)^2 - 0} = \boldsymbol{31.75\ Ksi} \tag{6.3}$$

For specimen BRBF-1, the length of the column from the base of the stiffener to the bottom side of the flange is approximately 97 in. Following simple statics, the shear force in the column can be calculated when end moments are known. Figure 6.49 illustrates the column forces that are present when the column has formed two plastic hinges on each end and no axial load.

For simplicity, if we ignore the axial force in the column, we can estimate the values of M_p, and from there calculate the value of V_{max}. Equation (6.4) below shows this value:

$$V = \frac{2M_p}{L} = \frac{2Zf_y}{L} = \frac{2(320)(55)}{97} = 362.88\,Kips \tag{6.4}$$

Using Equation (6.4) as the value of the shear force in the web, the following is the maximum applied shear stress:

$$\tau_w \approx \frac{V}{wh} = \frac{362.88}{(0.830)(11.25)} = \boldsymbol{38.9\ Ksi} \tag{6.5}$$

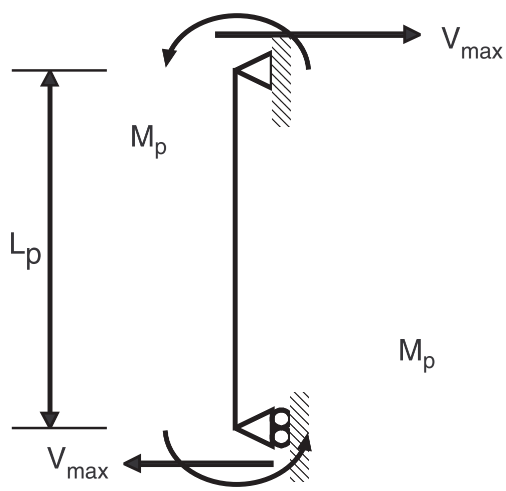

Fig. 6.49 Idealized column forces.

We can see by comparing Equations (1.3) and (6.5) that the applied stress in the web when a plastic mechanism has formed is going to cause the column web to yield. This causes larger than expected deformations in an analytical model where elastic or inelastic deformations due to shear are often neglected.

6.3.2 OpenSees Modeling

OpenSees models were created representing each of the three BRBF specimens. Although there appeared to be some panel zone yielding, panel zone shear deformations were not modeled in this analysis for the sake of simplicity. Figures 6.50–6.51 are schematic representations of the analytical models used in this study for BRBF-1 and BRBF-2 and 3, respectively. Each beam and column element was modeled as a discreet fiber element with cross-sectional properties to match those given in Table 6.2. The buckling-restrained brace members were modeled as simple inelastic truss elements using a Menegotto-Pinto steel material model, calibrated to previous uniaxial tests of buckling-restrained braces (Clark et al. 1999), as shown in Figure 6.52. Boundary conditions were assumed to be fixed out of plane and rigid boundary conditions were taken at the base of the models. The thick black lines in these figures are representative of members that are modeled as elastic elements with similar flexural stiffness properties to the connection elements, and are thought to be representative of the behavior of the column in flexure in locations of stiffening elements. These effects are assumed to be the result of gusset plates or external stiffeners. The thick black lines on the bracing elements are modeled as rigid end offsets representing the elastic portion of the buckling-restrained braced frame. Overall dimensions for the model are taken from as-built geometry and are located in Figures 6.1–6.2, and 6.4.

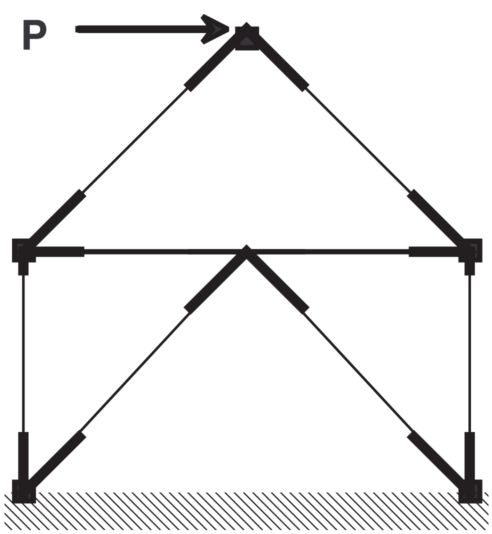

Fig. 6.50 Illustration of OpenSees model for BRBF-1.

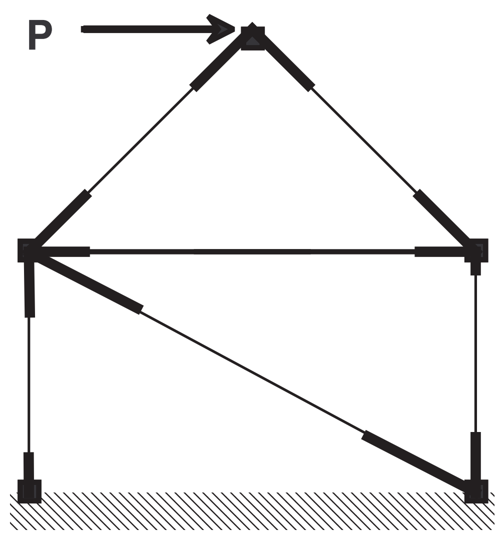

Fig. 6.51 Illustration of OpenSees model for BRBF-2 and -3.

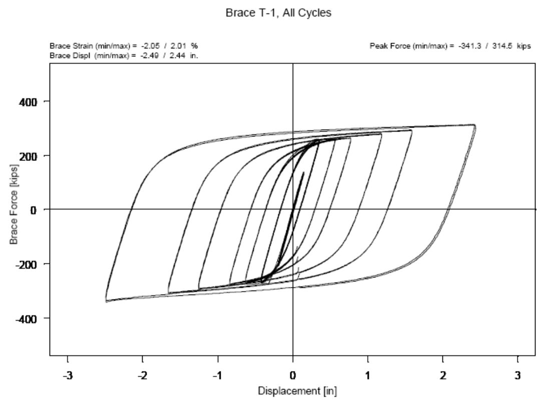

Fig. 6.52 Axial force axial deformation hysteresis from Clark et al. (1999).

6.3.2.1 Results

To analytically replicate the test results numerically, a displacement-controlled, quasi-static algorithm was applied in OpenSees to the analytical models described above. The control node used in these analyses corresponded to the control node that was used during the experiments, and the displacement history corresponded to the displacement history shown in Figure 6.21, 6.22, and 6.40 for BRBF-1, -2, -3, respectively.

Figure 6.53 shows the results for the analytical model of BRBF-1 overlaid on top of the data extracted from the experiment. Figure 6.53a shows the applied lateral load–beam displacement relationship of the bottom story. The analytical model predicts the global behavior quite closely, in terms of initial “elastic” stiffness, strength and hysteretic loop shape.

The discrepancies in the results may be associated with the shearing deformations in the beam-to-column connections and in the columns, which are not modeled in this analysis. For the analysis results presented, only flexural and axial deformations are considered.

Figures 6.53b–c show the analytical values of the brace elongation versus brace force. In both of these plots, the analytical model predicts larger displacements than those observed in the test. The experimental values plotted show the elongation of the brace itself and do not include the elongation that occurs in the gusset plate, either inelastic or elastic. The analytical model assumes that these regions are rigid. As such, all of the computed inelasticity is located in the brace truss element, whereas considerable yielding is noted in the gusset plates during the tests. From these plots we can see that roughly 10–15% of the overall “brace” displacement may have occurred in the gusset plates. As verified in Figure 6.31, the gusset plates had non-negligible elastic extension, primarily while the brace was loaded in tension. Figure 6.53d plots the moment at the base of the southern column plotted against the story drift. Although the analytical model in this subfigure is stiffer due to assumed infinitely rigid boundary conditions, the maximum forces and general behavior are similar. Because the member forces obtained from the tests are only approximate, especially for the later cycles, the correlation of the numerical and experimental results is believed to be satisfactory.

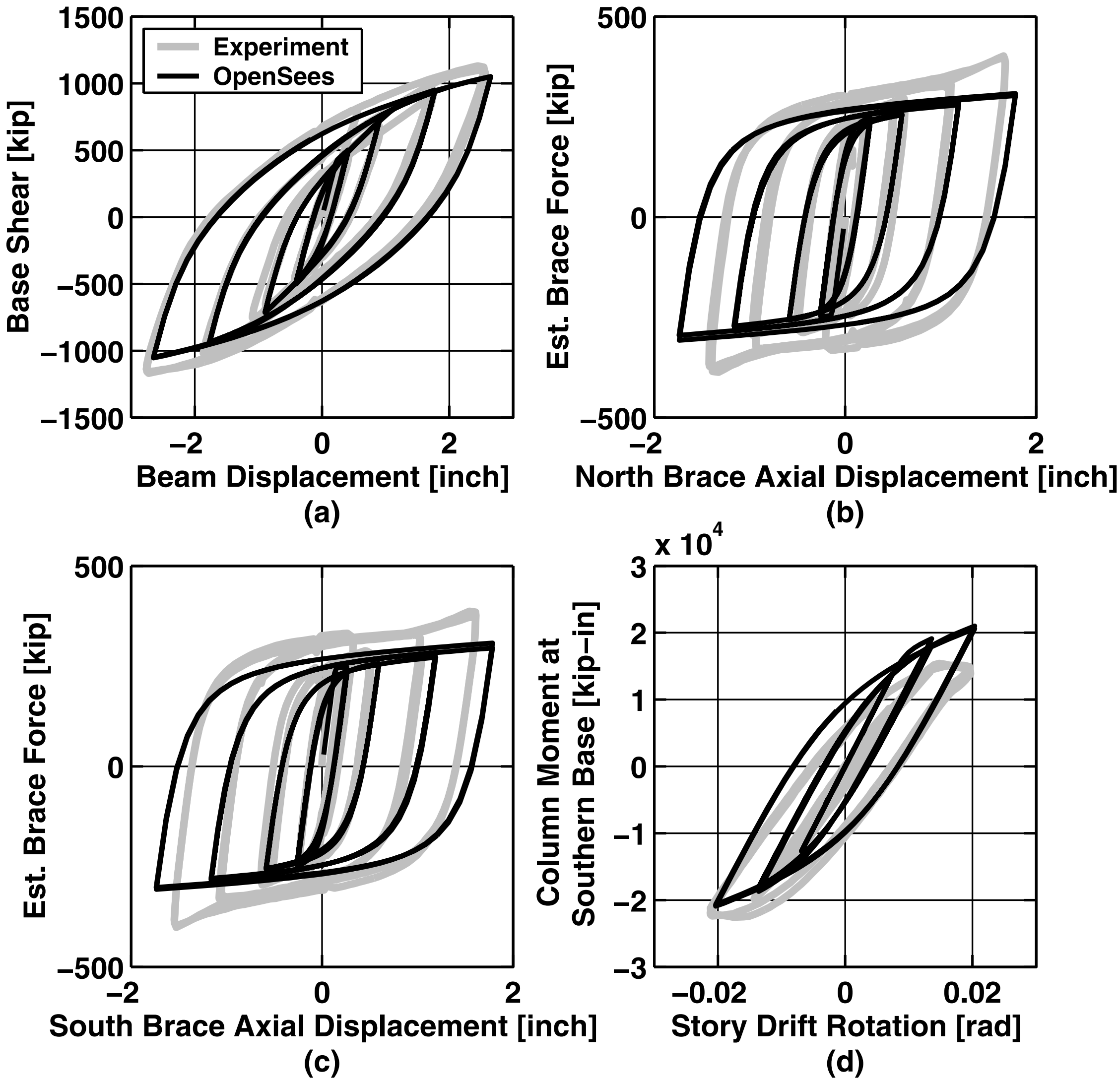

Fig. 6.53 Comparison of BRBF-1 results with OpenSees analysis.

Figure 6.54 shows similar analytical response quantities along with recorded response quantities from BRBF-2. Figure 6.54a shows an excellent agreement between the analytical prediction and the observed results for the global behavior. Figure 6.54b plots the brace axial force axial displacement relationship for the brace. It is important to note that the experimental brace force is extracted from estimates of the column moments. Due to extensive column shear yielding (see Fig. 6.33), this estimate of column moments may be inaccurate, and it is thought to be the source of the larger compressive axial force (~100 kips larger) predicted in the brace for the test results, and the corresponding discrepancy in the column moment. Because the approximated experimental results are consistently unsymmetrical with respect to the origin (in contrast to the analysis model) and because the global hysteretic characteristics are well predicted by the analysis, it is believed that this difference is due to the difficulties in estimating the column shears. Figure 6.54c shows the moment at the base of the southern column just above the gusset plate plotted against the story drift. The data extracted from the experiment show unsymmetrical behavior which is likely attributed to the shear yielding in the column.

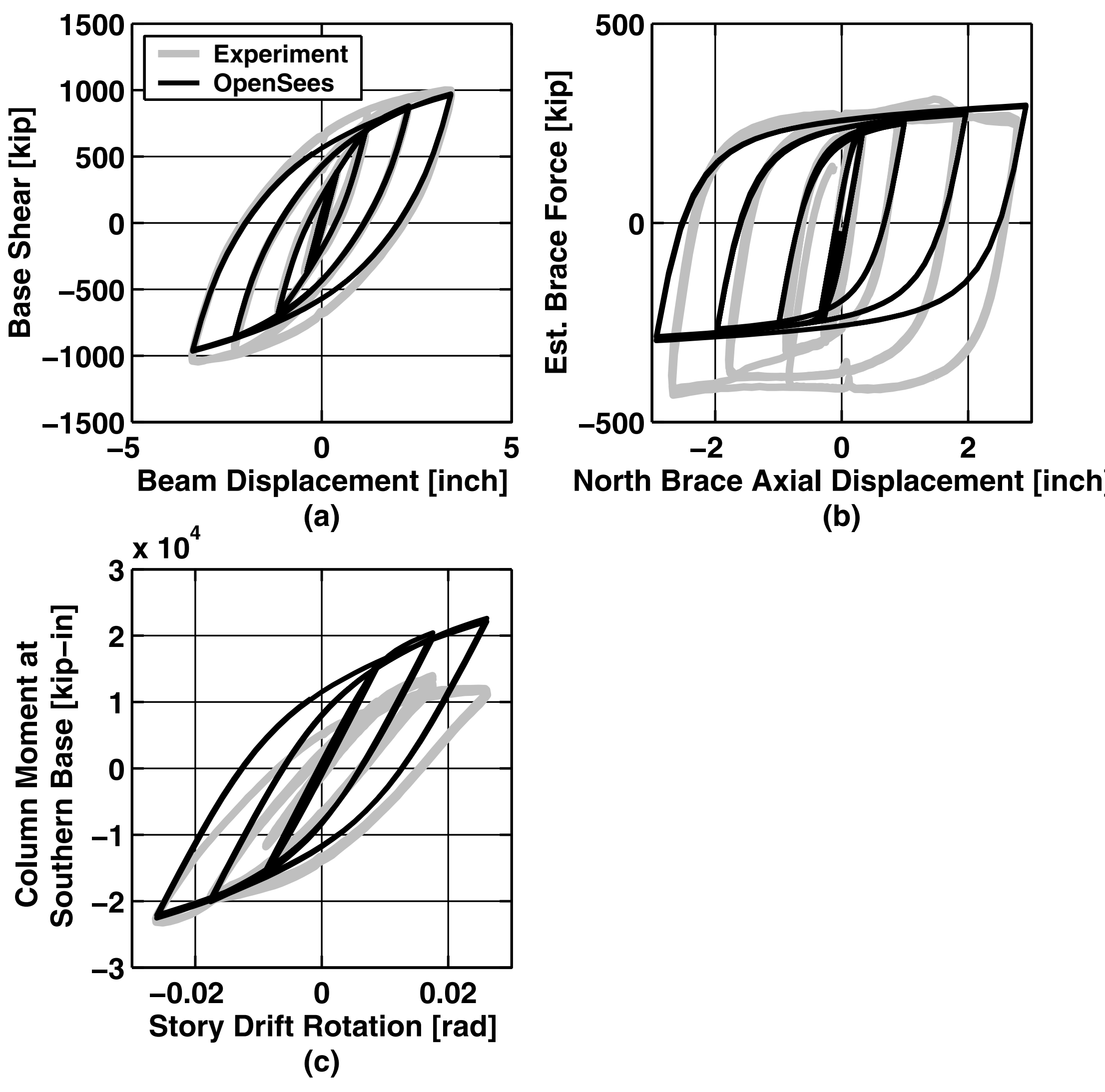

Fig. 6.54 Comparison of BRBF-2 results with OpenSees analysis.

Figure 6.55 shows the results of analytical modeling compared with data extracted from BRBF-3. As with BRBF-1 and BRBF-2, Figure 6.55a shows excellent agreement between the analytical model and experiment related to the global lateral force-lateral drift relationship up until the point of fracture of the beam. Figure 6.55b shows an offset in the compressive forces (~100 kips larger compressive force than tension) similar to that shown in Figure 6.54b. Again, this offset is thought to be indicative of the shear yielding in the southern column during the compressive cycles. Figure 6.54c shows the moment at the base of the southern column just above the stiffener plotted against the story-drift rotation. Here, the analytical prediction is only slightly stiffer and stronger than the observed estimate of column moment.

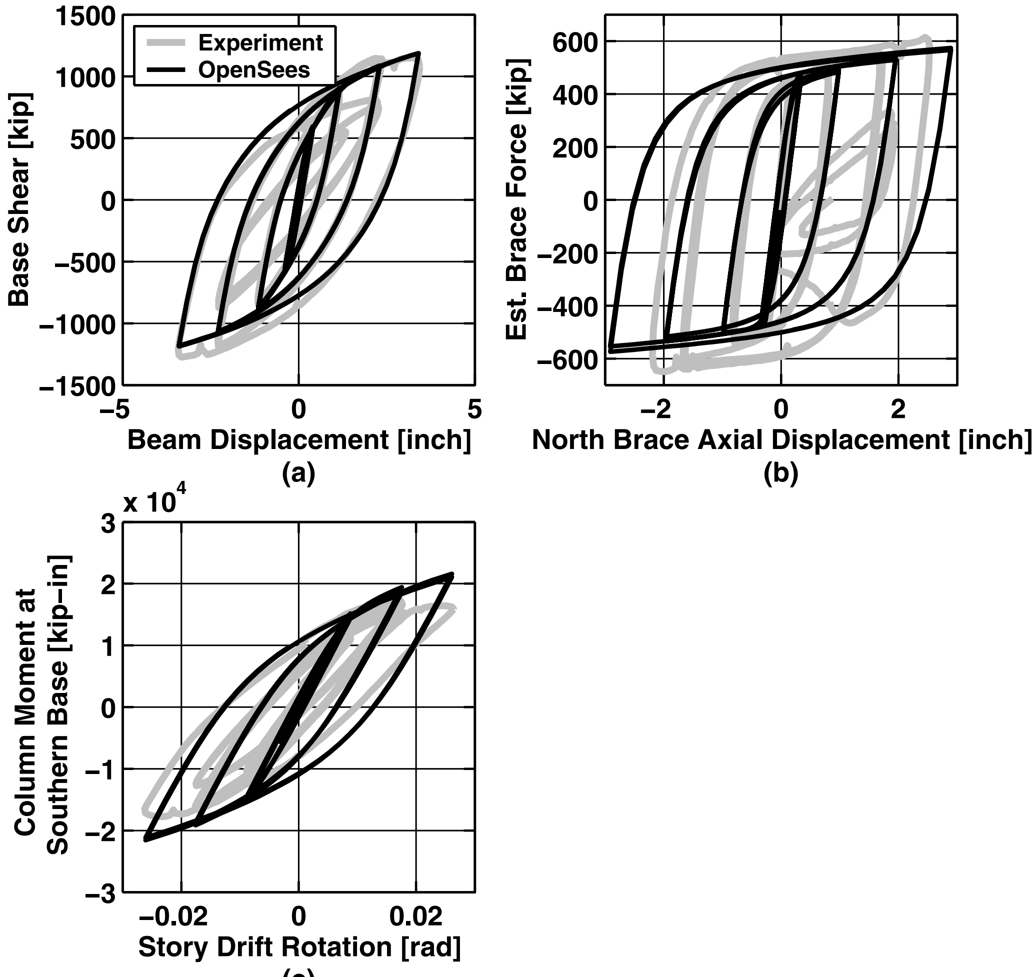

Fig. 6.55 Comparison of BRBF-3 results with OpenSees analysis.

6.3.2.2 Summary and Conclusions

The OpenSees models used in this section utilized simple nonlinear truss elements to mimic the observed behavior of previously tested uniaxial specimens. This assumption implies that the flexural component of the brace element has a negligible contribution to the global behavior, which proved to be a reasonable approximation of the observed behavior as shown in Figures 6.53a, 6.54a, and 6.55a.

Beam-column forces were found to be sensitive to the boundary conditions that were assumed. For the models described above, the beam-column boundaries are modeled as elastic elements with similar flexural stiffness to those of the beam or column. Rigid offsets yielded in large estimates of stiffness for not only the beam-columns, but also in global estimates of initial stiffness.

In conclusion, the OpenSees model was able to reasonably capture the local and global behavior of the BRBF-1, BRBF-2, and BRBF-3 (prior to fracture of the main beam). No attempt was made to model the onset of fracture of the beam in specimen BRBF-3, or its post-fracture behavior.

6.4 TESTS OF SCBF SPECIMEN

Because SCBFs are expected to be vulnerable to the formation of weak stories following the onset of brace buckling, it was thought desirable to include two full stories in the test model. In this manner, the transition from a regular distribution of interstory drifts over the height of the specimen to one where drifts might be concentrated in one story could be investigated. This would also provide a good opportunity to assess the abilities of the analytical models to capture this behavior. As such, the SCBF specimen was designed to represent a two-story building, rather than the lower story of a taller structure.

To facilitate comparison between the results obtained for the SCBF and BRBF specimens, the configuration of the SCBF specimen was chosen to be similar to that of BRBF-1, and the buckling capacity of the diagonal braces in the lower story of the SCBF specimen was set approximately equal to the strength of the buckling-restrained brace used in BRBF-1. Thus, specimen SCBF-1 had similar overall dimensions as BRBF-1, the braces were arranged in an inverted-V (chevron) configuration, and the average interstory drift history imposed on SCBF-1 was essentially the same as that imposed on the lower story of BRBF-1. Thus, the specimen was not designed considering the dynamic characteristics of a particular prototype structure, but rather to have fundamental proportions and details consistent with a low-rise SCBF with braces having strength equal to the buckling-restrained brace in BRBF-1.

The details of the design and construction of SCBF-1 are presented in Section 6.4.1. The test setup and instrumentation are outlined in Section 6.4.2, and the loading protocol employed is described in Section 6.4.3. Overall aspects of the response are presented in Section 6.4.4, while local behavior is detailed in Section 6.4.5. Discussion and concluding observations are included in Section 6.4.6. The analytical studies comparing the results of different computer models and analysis procedures with the test results are presented in Section 6.5.

6.4.1 Specimen Design and Construction

Test specimen (SCBF-1) consists of a two-story, one-bay, chevron-braced frame detailed in compliance with criteria for special concentric braced frames (SCBF) contained in the 1997 AISC Seismic Design Provisions (AISC 1997) and the 1993 load and resistance factor design (AISC 1993). The specimen is nearly full scale, with the lower story being 10 ft tall and the upper floor 9 ft tall; the columns were spaced 20 ft apart on center (see Fig. 6.56). The braces were fabricated from square, hollow structural sections (HSS) conforming to the specification for ASTM A500 grade B, to be representative of modern concentrically braced frame construction. Wide flange sections conforming to dual certification for ASTM 992 and ASTM 572, Grade 50, were used for the beams and columns. Unlike, the BRBF specimens, the beams were designed assuming they were “pin” connected to the columns, as this was believed to be a typical assumption for low-rise concentrically braced frames, and would allow study of the inadvertent frame action that may occur in SCBF systems designed in this fashion.

A structural drawing of the specimen is shown in Figure 6.56, and a photograph in the assembled configuration in Figure 6.57. Detailed structural drawings are provided in Appendix B.

The lower-story brace was selected to have an unfactored critical buckling load capacity similar to the tensile strength of the buckling-restrained brace in BRBF-1. This resulted in the HSS 6x6x3/8 (ASTM A 500 Grade B) strut test specimen described in Section 5.1.4. Other members and connections in the test specimen were designed according to current code provisions (AISC 1993; AISC 1997), considering the nominal properties of the brace selected.

For instance, the lower-story beam was designed assuming pin connections at its ends to the columns, and axial loads, bending moments, and shears associated with the unbalanced load at the beam midlength resulting from the full yield capacity of the tensile brace and a degraded buckling capacity of the compression brace, as stipulated in AISC seismic design provisions (AISC 1997). Because the beams in test specimens were not to be attached to a floor slab, the out-of-plane unbraced length of the lower-story beam was taken as 10 ft–0 in. (the beam was to be laterally braced in the test setup at its midspan and near its ends). Thus, the resulting W24×117 wide flange beam employed was slightly stiffer and stronger (larger) than might be expected in a more typical design with continuous lateral bracing provided by the floor slab. Because the same lateral forces were applied to both stories by the single actuator acting at the top floor, the same size braces and beams were used for the top and bottom stories.

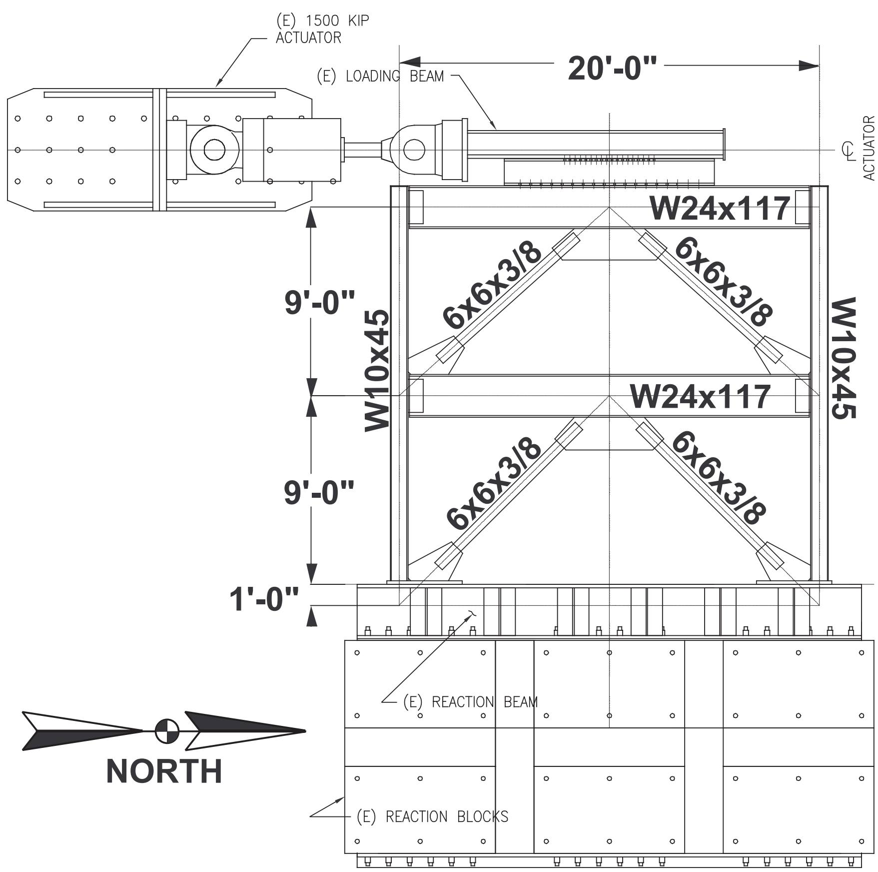

Fig. 6.56 Test setup.

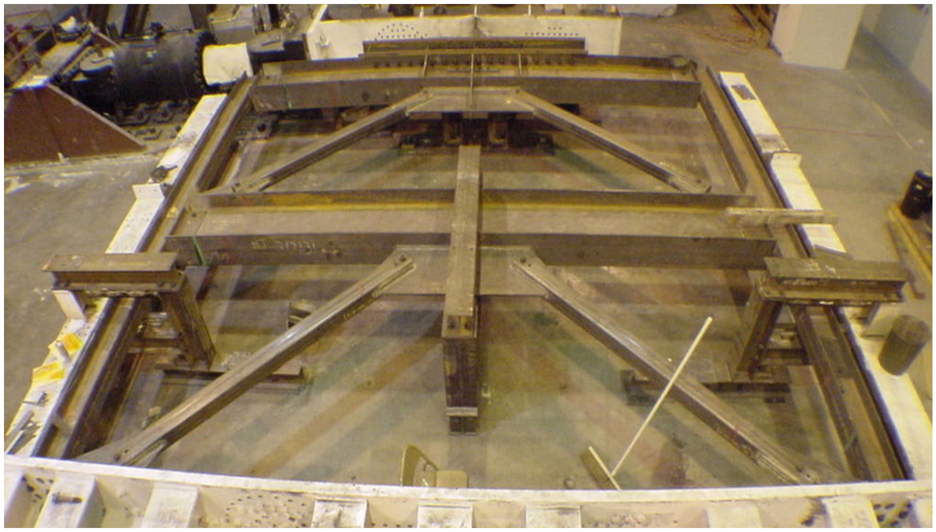

Fig. 6.57 Specimen SCBF-1 before test.

The gusset plate connection dimensions and proportions were determined using the uniform force method described in the second volume of the 1993 load and resistance factor design (AISC 1993). The shape of the gusset plate allowed for a fold line region, twice the thickness of the gusset plate in length, perpendicular to the brace. This enabled the brace to buckle out of plane of the frame during compressive cycles. The resulting gusset plates were tapered, and fabricated from 7/8-in. thick ASTM A572, Grade 50 steel plate. Pairs of fillet welds were used to attach the gusset plate to the beam and column, and were sized such that the capacity of the gusset plate would be developed prior to weld fracture. The resulting fillet welds were ¾ in. thick.

The braces were slotted at each end to facilitate their connection to the gusset plates. The ends of the 1 in. wide slots were drilled to help avoid stress concentrations in this region. The length of the slot was based on the distance required for four 3/8 in. fillet welds to transfer a tension load equal to $R_y F_y A_g$ from the brace to the gusset plate. The reduced net area region in the brace at the end of the gusset plate was reinforced with pairs of 4×3/8×12-in. plates (ASTM A36) attached to the faces of the brace parallel to the plane of the gusset plate. The reinforcing plates were attached to the brace using ¼ in. fillet welds, sized to develop the full capacity of the plate over half the length of the reinforcing plate. The effectiveness of such reinforcement in preventing premature fractures at the reduced net area region was demonstrated in Chapter 2 (Yang and Mahin 2005) and Chapter 5.

The single-plate shear tab used to connect the web of the beam to the column was designed to resist both the horizontal and vertical loads predicted using the uniform force method. The shear tabs were welded in the shop to the column flanges using pairs of 5/8 in. fillet welds (one on each face of the tab). They were attached during erection to the beam web via nominal erection bolts and 3/8 in. fillet welds placed on the remaining three edges of the tab.

Because the specimen was to be tested in the horizontal position, in-plane forces associated with gravity loads would not be represented in the columns, beams, and other elements. To have a similar state of stress in the columns (and beams) as they would have in a specimen where gravity loads were imposed during testing, gravity loads were not directly considered in the design of the columns or beams. Thus, the columns were designed to resist lateral loading on the frame corresponding to Ω_0 (the overstrength factor) times the nominal ultimate design load for the frame. The design lateral load was taken as twice the horizontal component of the force acting in a single brace. The overstrength factor (Ω_0) was taken to be 2 (AISC 1997). The resulting size of the wide flange column was W10×45 (dual certified ASTM 992 and 572, Grade 50). The column base flanges were full-penetration welded to a 2 in. thick steel plate (ASTM A572, Grade 50). Cope holes were cut into the web near the area of welding in order to position a backing bar for the welding of the flanges to the base plate. The backing bar remained in place after the welding was complete. The column web was welded to the base plate using a pair of ½ in. fillet welds. Each of the base plates were in turn bolted to the foundation reaction beam by sixteen 1-1/8 in. diameter, A490 bolts.

More detailed section properties are listed in Table 6.14. Mill certificate values are presented in Table 6.15. All welds were executed using the FCAW process, and all consumables for fabrication and erection were designated to be notch tough filler material suitable for seismic applications. All welds were inspected and weld materials were verified by a certified inspection agency during fabrication and erection, thus confirming the adequacy of all welding materials and details.

Table 6.14 Section properties.

Member	A (in^2)	Ixx (in^4)	Zx (in^3)	r_y (in)	Material
Column (W10x45)	13.3	248	54.9	2.01	A992/A572, Gr. 50
Beam (W24x117)	34.4	3540	327	2.94	A992/A572, Gr. 50
Brace (HSS 6x6x3/8)	8.08	41.6	16.8	2.27	A500 Gr. B
Plate material	n/a	n/a	n/a	n/a	A572 Gr. 50
Net Section Reinforcing Plate	n/a	n/a	n/a	n/a	A36

Table 6.15 Material properties from mill certificates.

Member	Average Fy (ksi)	Average Fu (ksi)	% elongation
Column (W10x45)	55.8	73.7	23.9
Beam (W24x117)	58	74.5	26
Brace (HSS 6x6x3/8)	60.6	65.9	36.0
Base Plate material	55	81	17
Gusset Plate Material	56	78	20
Net Section Reinforcing Plate	48	69	33.5

Shop fabrication was done such that the beams were shipped to the laboratory with the gusset plates and stiffeners welded to the beam. The columns were fabricated with the shear tabs for the upper and lower beams welded to the column, and with the base plate and bottom gusset plate welded to the base of the column. All holes were pre-drilled in the shop. Slots in the braces were also made in the shop.

The specimen was fabricated in the laboratory in the test fixture in early November 2004. This differs from BRBF-1, which was fabricated in the upright position. It was believed that this more economical approach was acceptable since the erection of SCBF-1, unlike BRBF-1, did not include any CJP welds. The columns were loosely bolted to the foundation reaction beam followed by positioning of the two beams using erection bolts. The top beam was then fitted to the out-of-plane restraining system and actuator loading headpiece using the adapter beam (Appendix B, Fig. B.6). The braces were then positioned between the gusset plates using temporary erection bolts. The specimen was then squared, followed by tightening of bolts and welding of the braces to the gusset plates. Because the reinforcement plates used at the net reduced areas were not installed as part of the original fabrication, they were installed as the last step in the erection process. No issues were identified during the inspection process.

6.4.2 Test Setup and Instrumentation

The specimen was tested with the plane of the frame oriented horizontally (see Figs. 6.56–6.57) in the same test setup as used for the BRBFs. Similar to the BRBF specimens, the column base plates were bolted to the large steel beam attached to the concrete reaction blocks. Because the entire top story of the specimen was included in SCBF-1, the actuator loading head was attached to the top of the top floor beam by means of a W14×176 spacer beam (see Fig. 6.56). Eighteen 1-1/8 in. A490 bolts were used to attach the top and bottom flanges of the spacer beam to the loading head and to the top flange of the upper-story beam in the specimen. This beam added considerable stiffness and strength to the top beam in the specimen. Given the substantial strength and stiffness this beam is required to resist by code (associated with the potential unbalance of forces in the fully yielded tension brace and degraded compression brace intersecting at its midspan), preliminary nonlinear analyses suggested that the added stiffness of the spacer beam/loading head would not significantly change the overall response of the specimen.

Ideally, out-of-plane restraint for the columns should have been provided near the top of the beams (where they would likely be attached to a floor slab in an actual building); however, this restraint would have interfered with the placement of instrumentation needed to measure brace and connection movements, so out-of-plane restraint was provided for the column about two feet below the bottom of the lower beam (see Fig. 6.58). Analysis suggested that this configuration was adequate. As noted previously, the midspans of both beams were restrained from moving out of plane. At the lower level, a detail similar to that used for the columns was used (see Fig. 6.59). Because of the location of the loading head, this configuration was not possible for the upper beam, and an alternative detail was used, where an out-of-plane restraint was added between the lab floor and the mid-depth of the beam web (see Appendix B). During the tests, the loading apparatus and restraining system operated satisfactorily, with no indication of unanticipated movement or localized yielding.

More than 150 channels of instrumentation are installed on the specimen, including strain gages, displacement transducers, load cells, and so on. Detailed drawings indicating the placement of instrumentation may be found in Appendix C, and a complete channel listing is contained in Appendix D.

Control of the data acquisition and hydraulic actuator subsystems was again done using an AutoNet™ software computer package, in combination with a NEFF data acquisition system (sampling data approximately 140 times per cycle), and a MTS 406/407 control subsystem.

Fig. 6.58 Column out-of-plane restraint.

Fig. 6.59 Beam out-of-plane restraint.

Instrumentation was installed to measure applied forces, global and local deformations, and strains. Numerous strain gages were installed in locations expected to remain elastic to allow the distributions of internal forces to be estimated. A detailed description of the displacement instrumentation and strain-gage locations can be found in Appendix C. Figures 6.60–6.61 contain photos showing a partially assembled instrumentation support stand on the northern beam-column connection and the locations of the strain gages prior to painting the surfaces, respectively.

Three video cameras were used to web cast the results during tests, and five high-resolution networked video cameras were used to archive the behavior of the specimen. The high-resolution cameras were located (1) high above the experimental setup for an overhead view of the specimen; (2) above the northern brace on the lower story; (3) directly above the northern beam-column connection; (4) directly above the southern base plate; and (5) aimed horizontally across the lower story. Numerous digital photographs were also taken to record the progression of damage.

Once the entire specimen was assembled, a coat of lime (whitewash) was applied to the steel to enhance the visibility of mill-scale flaking during loading. This is an indication of locations where yielding occurs. These areas appear as dark (black) regions in photographs.

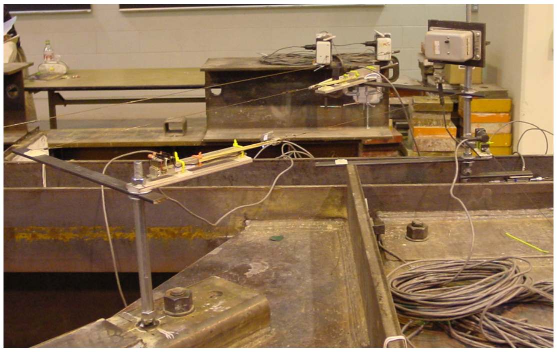

Fig. 6.60 Photo of instrumentation during construction.

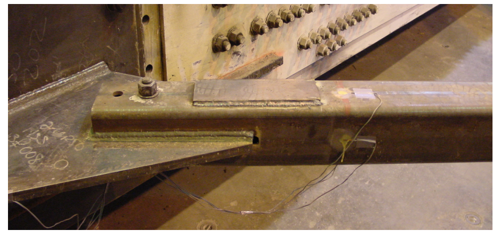

Fig. 6.61 Photo of some strain-gage locations prior to testing on bottom end of lower-story northern brace.

6.4.3 Loading Protocol

The same history of target interstory drift as applied to BRBF-1 was applied to SCBF-1. This history was based on the AISC/SEAOC protocol developed for testing buckling-restrained braced frames. The use of the same loading protocol was intended to facilitate comparison of the behavior of SCBF-1 and BRBF-1. In the case of BRBF-1, the target drifts were imposed on the lower story because the specimen had only one level of BRBs and BRBFs were not expected to concentrate disproportionate amounts of drift in one level. In the case of SCBF-1, the target drifts were imposed at the top floor beam. In effect, the average drift over two stories is specified, rather than the peak drift occurring in any one story. As such, if damage concentrates in one level, the peak interstory drift ratios developed will be larger than those imposed on BRBF-1. The target average interstory drift history was converted to a target roof level, lateral displacement history. During the test of SCBF-1, the displacement of the top beam was monitored and controlled. The distribution of displacements between the two stories was not controlled, and depended entirely on the evolution of damage in the specimen during the test.

The resulting roof displacement history (Fig. 6.62) consisted of six cycles at a roof drift expected when the braces reached their nominal buckling capacity (Δ_{by}, or an overall drift ratio of about 0.15%), four cycles at a roof drift equal to half of the benchmark displacement (about 0.67% drift), four cycles at a roof drift equal to the benchmark displacement (Δ_{bm}) for the structure (about 1.34%), and two more at a roof drift equal to 150% of the benchmark displacement (2%). The structure was then pushed to the south until the displacement capacity of the test setup was reached (about 10 in. of roof displacement). Because of an error, the last excursion to the north at the 0.5Δbm level was not imposed.

The 2005 AISC Seismic Provisions became available after the testing of the BRBF specimens. These modify the test protocol for BRBF subassemblages , with only two cycles at the Δ_{by}, $0.5\Delta_{bm}$, and $1.0\ \Delta_{bm}$ levels. However, it adds two cycles at the $2.0\Delta_{bm}$ level, stipulating that Δ_{bm} should not be taken less than 1% interstory drift. For individual braces, it mandates that cycles at $1.5\ \Delta_{bm}$ be continued until a cumulative inelastic deformation at least equal to 200 times the yield displacement. The acceptance criteria require that the specimen exhibit repeatable and stable hysteretic behavior without any fracture of the braces or their end connections under this test protocol. While the updated 2005 protocol could have been used for SCBF-1, it was decided to use the same protocol as used for the BRBF-1 specimens so a more realistic comparison could be made with respect to their behavior.

It is interesting to note from the preliminary assessment of demands on SCBF frames (Chapter 3) that a three-story tall 1997 NEHRP-compliant SCBF structure designed for the Los Angeles area would be expected to develop a median peak interstory drift of 2% for ground motions consistent with a 10% probability of exceedance in 50 years, but that the median peak interstory drift demand increases to 4.5% for a seismic hazard corresponding to a 2% probability of exceedance in 50 years. An earlier study, by Sabelli, Mahin, and Chang (2003), that used simpler numerical models to represent brace behavior estimated that the average peak interstory drift for the same three-story braced frame was 3.9% for ground motions scaled to correspond to a seismic hazard with a 10% probability of exceedance in 50 years.

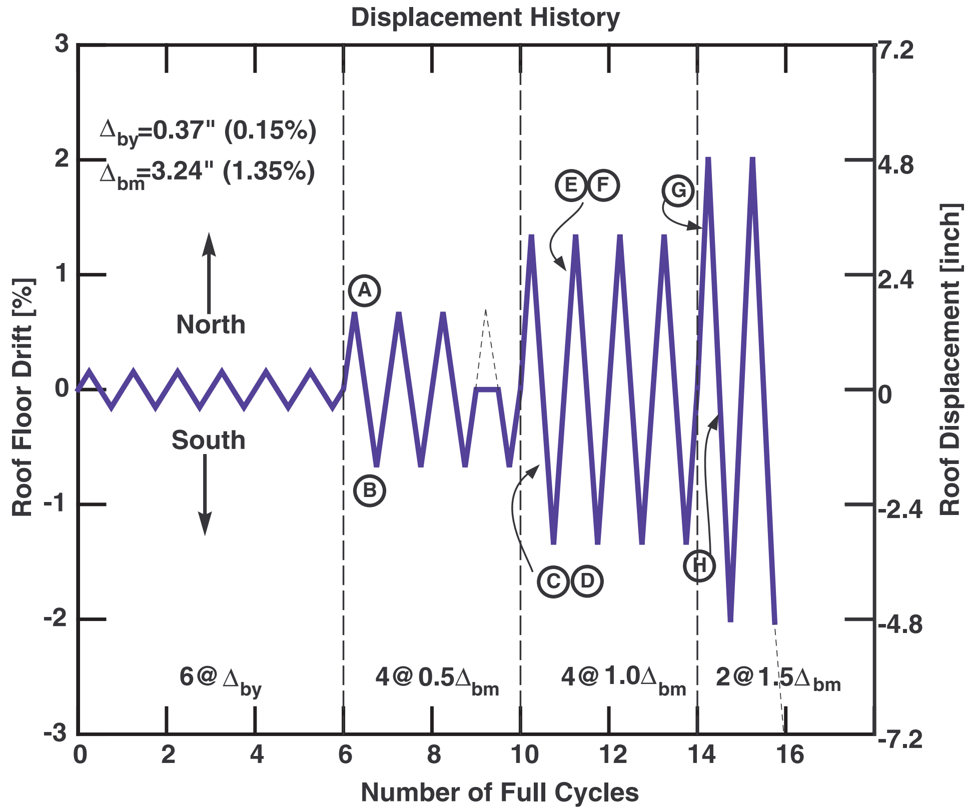

Fig. 6.62 Overall target displacement history at top floor level.

6.4.4 Overview of Experimental Results

The specimen developed a peak lateral load capacity of 635 kips prior to buckling of any brace, about 135% of the nominal design capacity (i.e., taken as twice the horizontal component of the computed brace buckling load). Because of the specimen's high lateral stiffness, the measured roof drift index at the onset of lateral brace buckling was relatively low (0.45%). Prior to buckling, the interstory drifts observed in each story were nearly identical. Once buckling occurred, the overall response of the specimen was dominated by out-of-plane lateral buckling of the braces in the lower level, followed by a concentration of drift demands and eventual fracture of the braces and columns in this story.

Hysteretic loops showing the overall relation between the lateral displacement at the top beam and base shear are shown in Figure 6.63. Similar loops relating the interstory drift between the base and the lower beam and the base shear are plotted in Figure 6.64. The evolution of peak lateral load developed by the specimen with cycle is shown in Figure 6.65. The floor displacement for each story (and the percentage contribution of each story to the total roof displacement of the specimen) is shown in Figure 6.66.

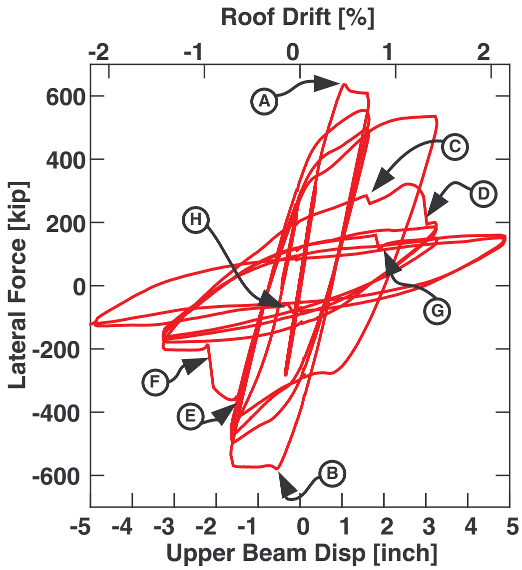

Fig. 6.63 Roof displacement versus base shear plot.

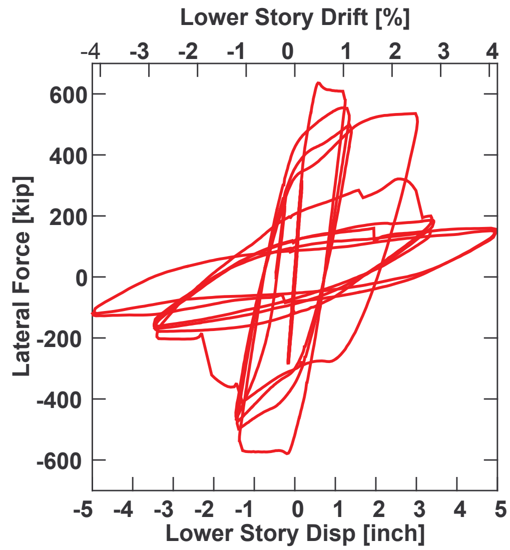

Fig. 6.64 Lower-story drift versus base shear plot.

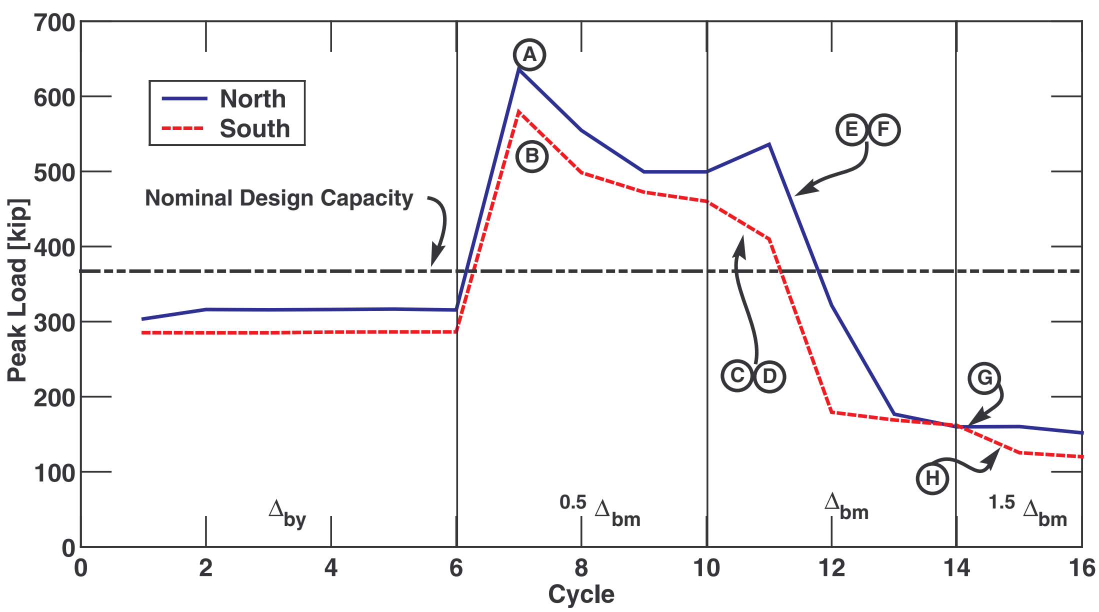

Fig. 6.65 Peak load measured during each cycle.

Buckling commenced during the first compression excursion for each brace in the lower story at a target roof displacement of $0.5\Delta_{bm}$ (see points A and B in Figs. 6.62–6.64). Noticeable yielding (evinced by flaking of whitewash) occurred during the compression portions of these cycles at the midlength of the braces and to a lesser extent in the gusset plates at the ends of these braces. Even though the in-plane axial shortening of the braces is relatively small during these cycles (slightly more than 1 in.), the transverse out-of-plane displacements of the braces were quite large (greater than 4 in.). During each of the subsequent $0.5\Delta_{bm}$ cycles, local buckles formed and re-straightened near the midlength of the lower-level braces and partial thickness fractures (i.e., they did not extend all the way through the thickness of the tube) developed. From Figures 6.63–64, it is clear that the specimen's load capacity is slightly asymmetric, with inelastic excursions in one direction reducing the capacity during the subsequent excursion at the same displacement amplitude in the opposite direction. Moreover, the capacity can be seen to drop significantly from cycle to cycle during the $0.5\Delta_{bm}$ target roof displacement excursions (1.62 in.).

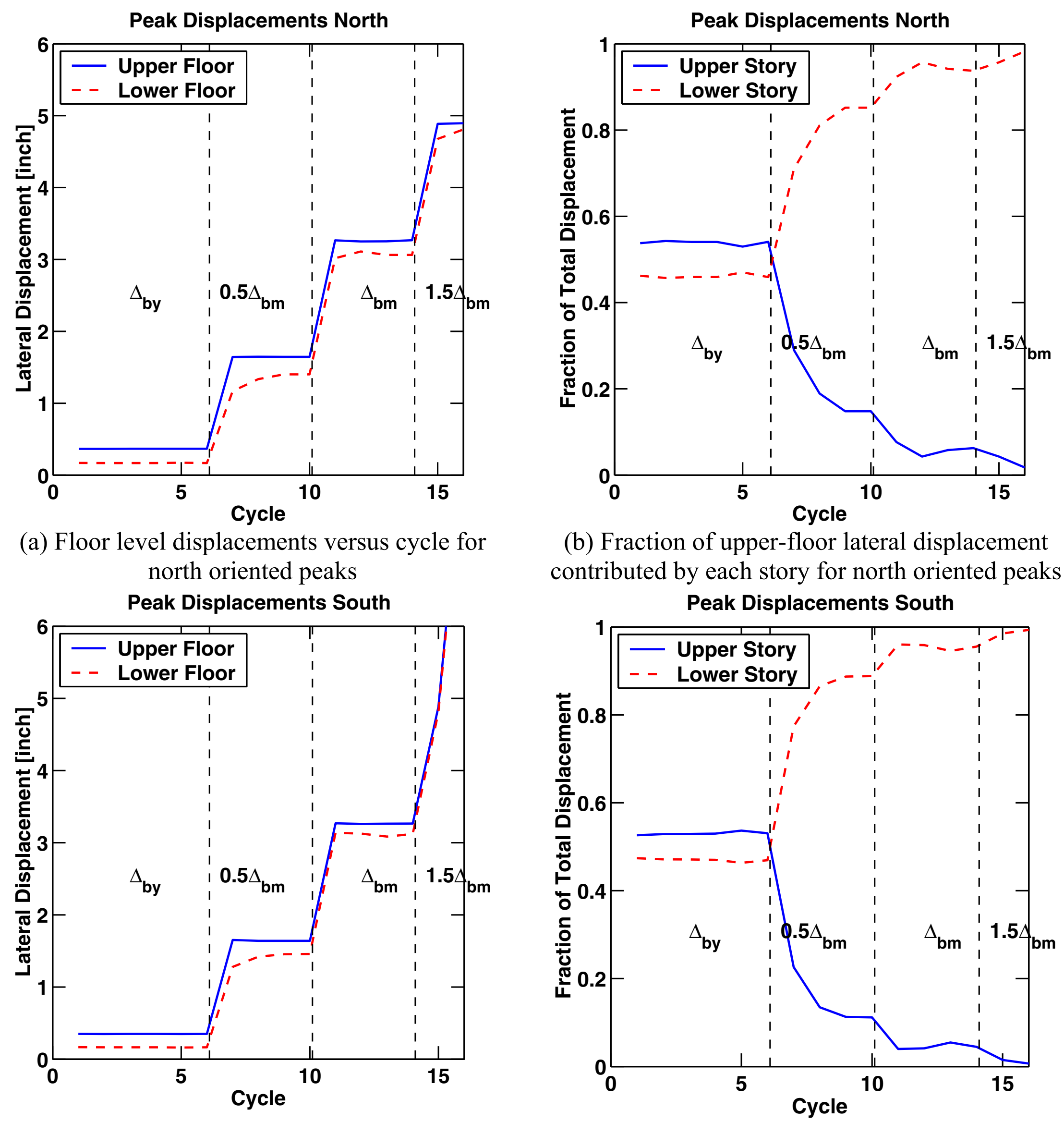

(a) Floor level displacements versus cycle for north oriented peaks

(b) Fraction of upper-floor lateral displacement contributed by each story for north oriented peaks

(c) Floor level displacements versus cycle for south oriented peaks

(d) Fraction of upper-floor lateral displacement contributed by each story for south oriented peaks

Fig. 6.66 Distribution of drift at each cycle.

Displacements also concentrated in the lower story, so that by the third cycle at $0.5\Delta_{bm}$, about 85% of the roof displacement had concentrated in the lower level (see Fig. 6.64). During these cycles, the out-of-plane displacements of the midspan of the braces exceeded 6.5 in., about 4.5 times greater than the longitudinal shortening of the braces.

The specimen regains some of its strength during the first excursion to $1.0\Delta_{bm}$ (3.24 in. roof displacement), but is only able to sustain the first half of the first cycle at this drift level before fracturing the north brace in the lower story during the second half of the cycle (specimen moving toward the south). This tension fracture is detectable in the hysteretic loops (e.g., Fig. 6.63) as two rapid changes in frame load capacity; the first (point C) occurs when the side of the tube that had previously undergone the most compression deformation (due to local buckling) fractured, and the second (point D) when the entire cross section fractured. The southern brace at the lower level completely fractured during the first half of the second cycle to $1.0\Delta_{bm}$ as the specimen is moving toward the north (points E and F on Figs. 6.62–6.64). Because an earlier half cycle of the displacement history to the north at a drift of $0.5\Delta_{bm}$ had been accidentally omitted, the south brace could have failed earlier had this cycle been included.

In contrast with the lower level of the specimen, there were no visible signs of damage or flaking of whitewash in the upper level throughout the entire loading history. Strain-gage data revealed, however, that a very small amount of yielding occurred in the braces near the connection to the gusset plates. Displacement instrumentation placed on either side of the gusset plates indicated that the out-of-plane rotation of the upper gusset plates—presumably along the fold-line—was quite small (approximately 0.005 rad. *upward*), whereas the rotation of the lower-story gusset plates was more than 40 times larger (about 0.2 rad. *downward*).

Once fracture occurred in the lower-level level braces, the overall lateral stiffness and strength of the system diminished considerably, and frame action was relied on to provide lateral resistance. As noted in Figures 6.66a–d, more than 90% of the roof lateral displacement during the third $1.0\Delta_{bm}$ was due to drifts in the lower level. This illustrates the tendency of conventional braced frames to localize damage during inelastic cycling. As noted previously, the computed median peak drift for a similar three-story SCBF in Los Angeles would be expected to range between 2–3.9% for a 10% in 50-year seismic hazard, and on the order of 4.5% for a 2% in 50-year seismic hazard. The capacity of the specimen following fracture of both braces was approximately 175 kips, or 28% of the peak strength developed by the specimen. This corresponds to 120% of $4M_p/L_c$ where M_p is taken as $R_y Z_c F_y$ and L_c is the distance from the top of the gusset plate on the base plate to the bottom of the shear tab for the lower-level level beam.

During the first half of the fourth cycle to $1.0\Delta_{bm}$, the top of the south column suddenly (and loudly) fractured just below the shear tab connecting the lower beam to the column. The fracture extended completely though the flange adjacent to the shear tab and crossed about one-quarter the width of the column web. During the second half of the first cycle at $1.5\Delta_{bm}$, the northern column fractured in a similar manner. The occurrences of these column fractures are noted in Figures 6.62, 6.63, and 6.65 as points G and H. The lateral strength and stiffness of the structure decreased additionally after the fractures occurred. The cracks in both column webs extended somewhat during the subsequent cycles. The specimen was finally pulled toward the south to the maximum displacement permitted by the test setup. Although existing damage intensified, no new types of damage were noted (for example, at the bases of the columns or in the upper story) during this final excursion.

An estimated hysteretic loop for the lower-story north-side brace is shown in Figure 6.68. Consistent with the test results shown in Chapter 3, the brace looses compression strength rapidly following the onset of buckling, and from one cycle to the next.

It is interesting to note that the brace does not yield or elongate significantly in tension (until after it fractures). This is in large part due to the flexibility of the beam. While the beam is designed to be strong enough to avoid yielding when the vertical component of difference between the tensile capacity of one brace and the reduced compression capacity of the other brace is applied to its midspan, no restriction is placed on the acceptable vertical displacement of the beam under this condition. In this case, the beam deflects downward in the plane of the frame nearly 1 in. during the $0.5\Delta_{bm}$ cycles (see Fig. 6.67), thereby reducing the tensile elongation (and force) that needs to be developed in the brace. Thus, the brace hysteretic loops are asymmetric with respect to displacement, shortening far more than they elongate.

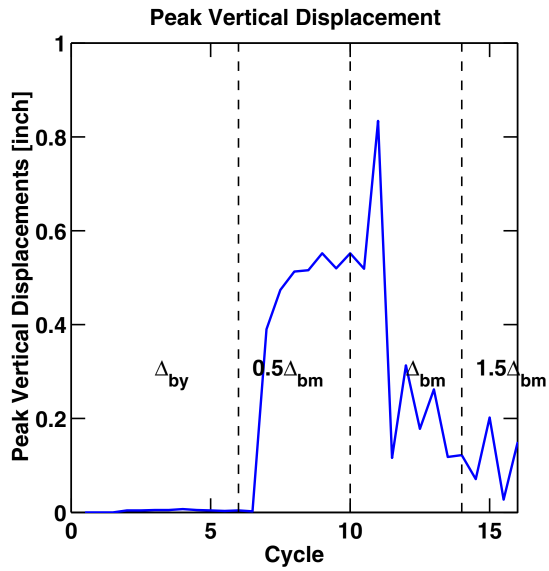

Fig. 6.67 Peak vertical displacements of beam midspan.

Once the brace fractures, it can no longer develop force in tension, but it is able to develop a very small compression load when the displacement history brings the two sides of the fractured brace back into contact again. Because the transverse, out-of-plane displacement of the braces at this stage is very large when contact is re-established, the in-plane resistance of the brace is small even when the gap is closed. This behavior during gap closing is shown in Figure 6.68.

While the upper-story braces did not exhibit any visible signs of yielding, Figure 6.70 shows that the upper-level braces did experience small permanent plastic deformations during cycles corresponding to 0.5Δbm. The displacements for this figure were taken from the average strain from the strain gages located near each end of the brace, multiplied by the length of the brace, thus assuming uniform distribution of these strains. The magnitude of this permanent plastic deformation is on the order of 0.1 in., which is roughly one half of the predicted tensile yield displacement. Similar observations were found for the northern brace in the upper story (not shown here).

Significant yielding was observed at the exterior side of the base of each column and above the gusset plate on the inside of the column. Damage was observed in the connections beginning on the cycles corresponding to 0.5Δbm. Figure 6.69 shows the yielding pattern observed at the $0.5\Delta_{bm}$ cycle at the southern base.

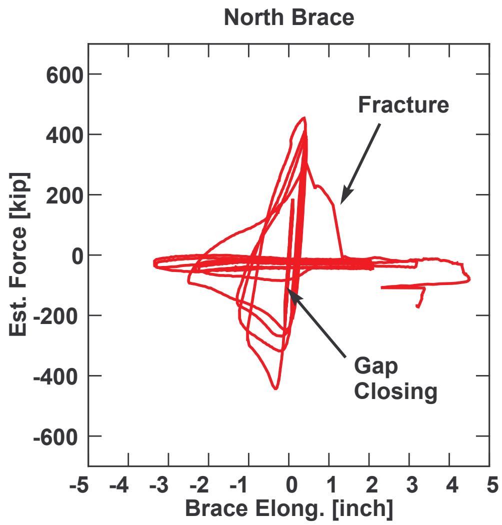

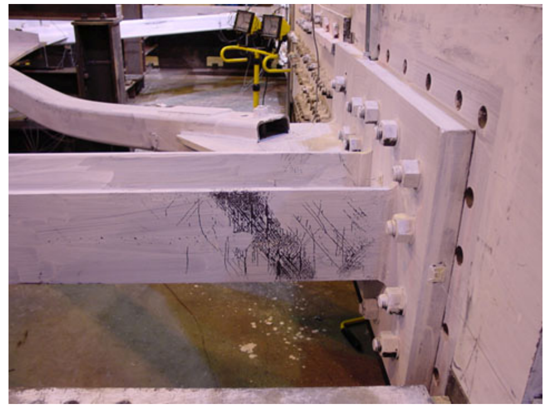

Fig. 6.68 Axial force-axial displacement relation estimated for lower-story, north brace.

Fig. 6.69 Yielding of column base and buckled brace at third 0.5Δbm cycle.

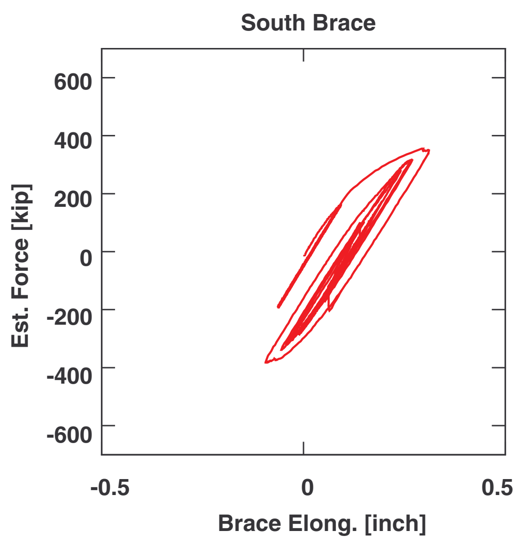

Fig. 6.70 Axial force–axial displacement relation estimated for upper-story, south brace.

Figures 6.71–6.72 show approximate moment-rotation relationships for the columns just below the lower-level beam shear tab. The instrumentation located in the panel zone to record in-plane joint rotations was unfortunately unreliable at larger displacements. As such, the rotation in these plots is taken as the lateral displacement in the second floor divided by the floor height (giving an upper bound on the actual rotations). Of particular interest, Figure 6.72 illustrates the effects of compression-flexure interaction on column behavior during the first cycle at $1.0\Delta_{bm}$. This interaction resulted in pronounced column yielding in flexure at approximately two-thirds of the nominal plastic capacity (shown as the dotted lines). In subsequent cycles, the reduced axial load in the columns (due to the fracture of lower-story braces reducing the lateral strength of the specimen) relieved the columns of the high axial loads and the moment-rotation observed is similar to what may be expected for a lightly loaded column. The increased axial loads during the $1.0\Delta_{bm}$ cycles are from not only larger axial loads from braces in the upper floors, but also unbalanced loads from the beam.

Figures 6.73 and 6.74 show the interaction curves for the beam-column connection of the south and north beam-column connections, respectively. The interaction surface shown is the theoretical interaction surface associated with the initial yielding of the beam-column by axial and flexural forces. The presence of the unbalanced load shows an unsymmetrical bias, represented by the large loops at roughly a 45° angle. This presence of axial load from the unbalanced load is verified by the large vertical displacement in the large W24 beam, as shown in Figure 6.64.

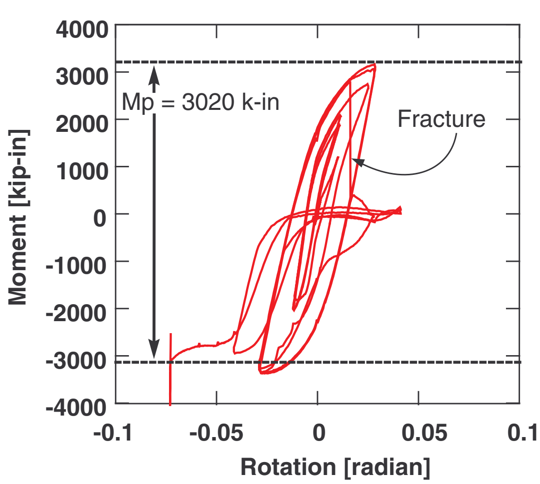

Fig. 6.71 Moment-rotation of southern beam-column connection.

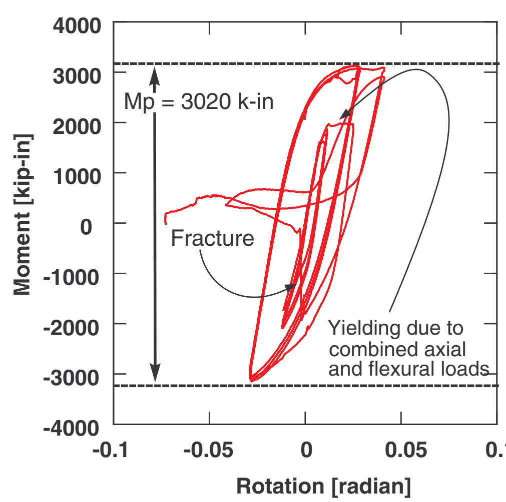

Fig. 6.72 Moment-rotation of northern beam-column connection.

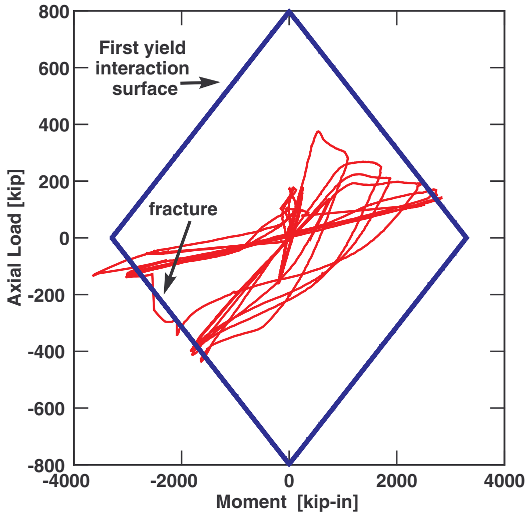

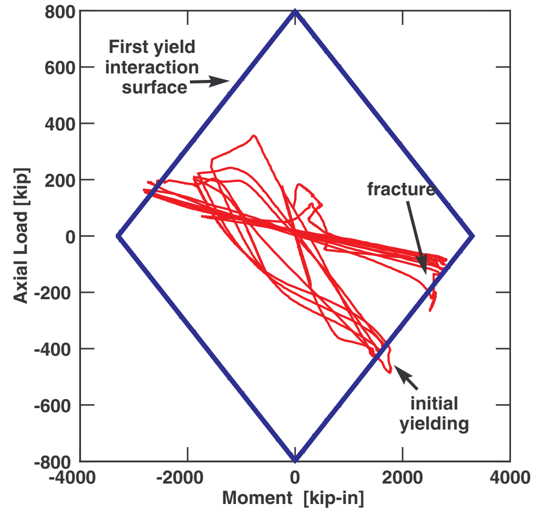

Fig. 6.73 Axial load–bending moment interaction of south column near beam-column connection.

Fig. 6.74 Axial load–bending moment interaction of north column near beam-column connection.

The bolted base plate connections were designed using the 1993 load and resistance factor design. A total base slip of nearly 1/8 in. was observed at both the North and South column base plates. Some more detailed observations and photographs are provided below regarding damage at different target roof drifts.

6.4.5 Detailed Local Observations

6.4.5.1 Cycles at Δ_{by}

Interstory drifts are nearly equally distributed between the upper and lower levels at this stage. Little yielding is detected by flaking of whitewash except near the base plates (especially near the interior weld access hole, which does not significantly intensify in later cycles, suggesting that its early onset may be associated with residual stresses introduced during fabrication). This minor yielding on the interior flange of the column can be detected in Figure 6.75. Minor yielding was also observed in the base of the southern base and is shown in Figure 6.76.

At this level, which is just below the expected buckling capacity of the braces, there was no visual indication of out-of-plane motion of the braces. The instrumentation located above and below both ends of the lower-story brace indicates less than 0.5% out-of-plane rotation.

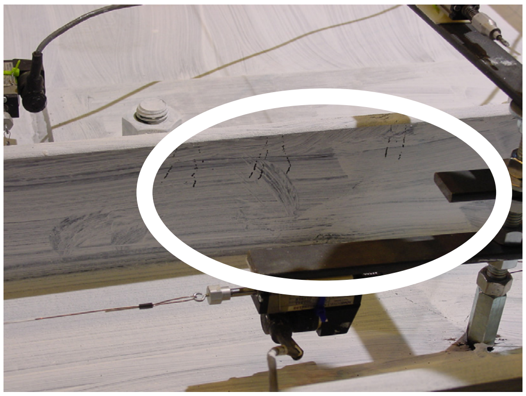

Fig. 6.75 Initial yielding on inside flange of lower, northern beam-column connection.

Fig. 6.76 Initial yielding shown at inside southern base of column.

In-plane moments deduced from strain gages indicate that moments approached roughly 4% of the nominal plastic in-plane moment capacity of the brace.

6.4.5.2 Cycles at $0.5\Delta_{bm}$

Buckling of the lower-story braces was observed during the first excursion at this level when compression buckling loads developed in the braces during the first cycle (see Figs. 6.77–6.78). Because overall lateral forces dropped once buckling occurred in the lower level, out-of-plane movement and total axial elongations were reduced in subsequent cycles for the braces in the upper level. The lower-level level braces almost fully re-straighten during these cycles when the displacement direction reversed and tension is applied (see Figs. 6.77– 6.80).

Local buckling initiated in each brace and increased during each subsequent cycle at this level (see Fig. 6.79). Significant tears in the base metal were seen in the locally buckled regions, especially near the corners of the tubes on the compression-most side (Fig. 6.81). Very minor yielding was noted in the cover plates installed to reinforce the sections with reduced net areas (Fig. 6.82).

Instrumentation placed above and below the end of each of the lower-story braces recorded roughly 0.10 radian out-of-plane rotation with no signs of cracking or other distress due to this large rotational demand (Fig. 6.83). Upper-story braces had no significant out-of-plane rotations at these drift cycles.

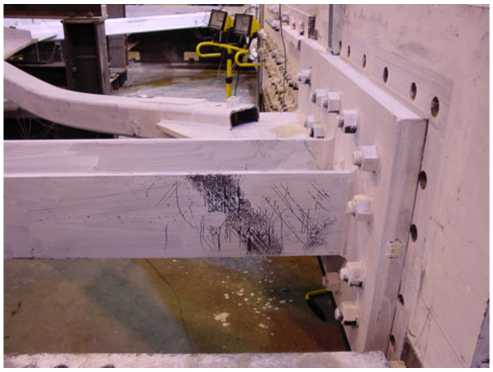

Fig. 6.77 Buckling of compression (near) brace and yielding of column.

Fig. 6.78 Flexural yielding of gusset plate due to out-of-plane rotations from buckling.

Fig. 6.79 Buckled and re-straightened brace in lower level–0.5Δbm cycles.

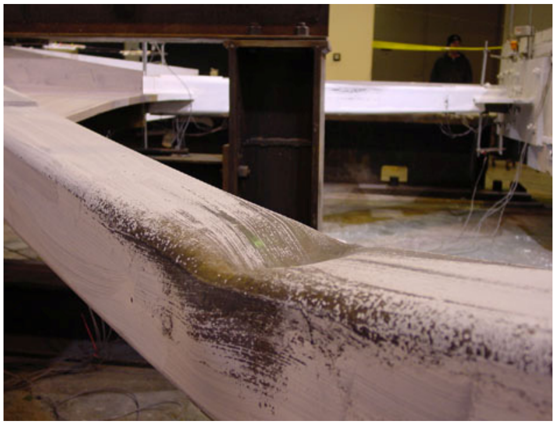

Fig. 6.80 Local buckle in lower-level level brace–during later 0.5Δbm cycle.

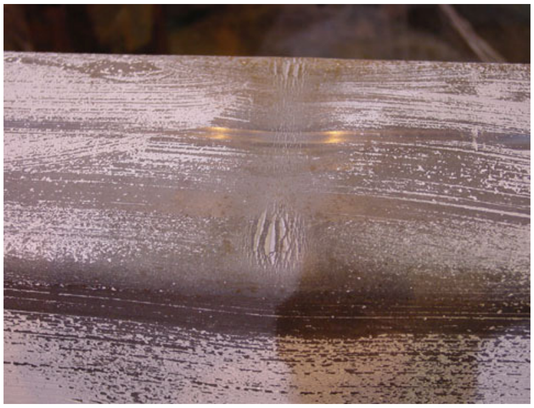

Fig. 6.81 Initial tears form at corner of brace–0.5Δbm cycles.

Fig. 6.82 Local yielding of reinforcing cover plates at section with reduced net area.

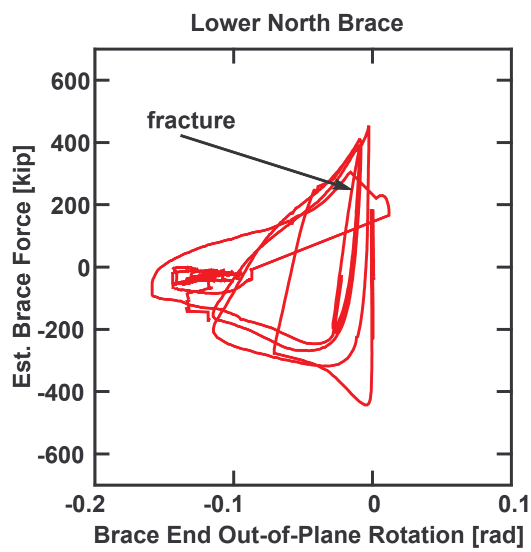

Fig. 6.83 Out-of-plane rotation of lower north brace taken near base plate.

6.4.5.3 Cycles at 1.0Δ_{bm}

During the first half of the first cycle (as the frame was moving to the north), the lower-story brace on the south side was in tension. It was noted visually that the brace had rotated plastically in plane just below the gusset plate attached to the lower beam (Fig. 6.84). The yielded region appeared to occur at the end of the reinforcing cover plate on the side that would be expected to elongate under frame bending action. Distress was also noticed at the tips of the fillet welds used to connect the brace to the gusset plates (this occurred gradually throughout the test and was present to varying degrees at the ends of both braces). Whitewash was found to be flaking at the welds connecting the brace to the gusset plate, near the slot in the brace, next to the net reduced section. There was little indication of yielding at the end of the weld away from the center of the brace. At the same stage, the north brace had buckled severely (Fig. 6.85).

During the second half of the first cycle at this drift level, the north brace re-straightened (Fig. 6.86) and completely fractured at its midlength. The south brace fractured in a similar fashion during the northward excursion of the second cycle at a target roof drift of $1.0\Delta_{bm}$. It is apparent that the tension fractures of the braces occurred in four stages: (1) gradual tearing of the corners of the tubes perpendicular to the longitudinal axis of the brace at a location where the crest of major local buckle had previously formed on the most compressed side of the brace; (2) sudden merging of the corner tears across the entire side of the brace; (3) gradual growth of this crack across the depth of the section; and (4) sudden rupture of the entire section. This process is illustrated in Figures 6.87–6.89. A photo of the frame during the last 1.0Δbm cycle with both lower-level level braces fractured is shown in Figure 6.90. The lack of damage in the upper story can be noted in the photo.

During the cycles at a target roof displacement of $1.0\Delta_{bm}$, considerable distress also occurred in both lower beam-to-column connections. Generally, the beam, shear tab and weld from the shear tab to beam web exhibited little evidence of yielding. There was considerable yielding of the column web near the bottom edge of the shear tab, however, and warping of the column flange below the shear tab (Fig. 6.91). A small under-bead crack was noticed at the bottom end of the fillet welds used to connect the shear tab to the column flange (Fig. 6.92). This small crack remained stable during the first three $1.0\Delta_{bm}$ cycles.

The yield line patterns in the column flange and web near the connection are complex. Interestingly, it appears that the column web very near the shear tab does not yield on the surface toward the viewer in Figure 6.91 (as evinced by flaking of whitewash) even though there is considerable evidence of yielding and out-of-plane buckling of the web nearby. It should be noted that the center plane of the shear tab is offset from the centerline of the column, introducing an eccentricity in the load transfer path. The central portion of the column web near the shear tab has yield lines oriented vertically as well as at a 45° orientation (an *x*-pattern). There was considerable visual evidence during these cycles that the column web was being elongated and shortened (crushed) transverse to the column longitudinal axis in the plane of the column web near the bottom of the shear tab. The local buckles that formed in the column flange near the bottom of the shear tab appeared to be symmetric in shape with respect to the column web, suggesting they might be associated with the transverse inelastic deformations in the column web, rather than only with column flexure. Horizontally oriented yield lines were also evident in the column just below the shear tab, consistent with flexure of the column.

During the $1.0\Delta_{bm}$ cycles, noticeable twisting was observed of the columns in the lower level about their longitudinal axes. The columns were restrained from out-of-plane motion and twisting at a location about 2 ft below the bottom of the beam. This did not fully prevent rotation or transverse displacement, allowing approximately 3/8-in. displacement out of plane. The rotation in the column was sufficient for the restraints to come fully into contact with the column flanges.

During the fourth cycle at the $1.0\Delta_{bm}$ target roof drift level, the interior flange of the south column fractured suddenly and loudly. The fracture extended completely through the column flange and part way across the column web (Fig. 6.93). During the first cycle to $1.5\Delta_{bm}$ roof drift, the north column fractured in a similar manner (Fig. 6.94). The fractures propagated from the previously noted cracks at the bottom ends of the fillet welds used to connect the shear tab to the column. These fractures in the column webs continued to extend during subsequent cycles until they reached about half way across the section. No fracture was detected in the exterior column flanges. While the interior flange could not take tension loads, the fractures in the locally buckled flanges re-closed when the displacement of the specimen was applied in a direction that would tend to produce compression in the interior flanges.

The damage during cycles to $1.0\Delta_{bm}$ target roof drift resulted in a dramatic loss of lateral-load-carrying capacity as shown in Figure 6.63. For instance, the lateral load drops to nearly 30% of the peak load as a result of brace buckling and fracture. The fractures in the columns reduce the strength of the specimen to nearly 20% of the peak load. As a comparison, BRBF-1 had no loss of lateral carrying capacity through this level of cycling, and in actuality, continued to increase its capacity during subsequent cycles.

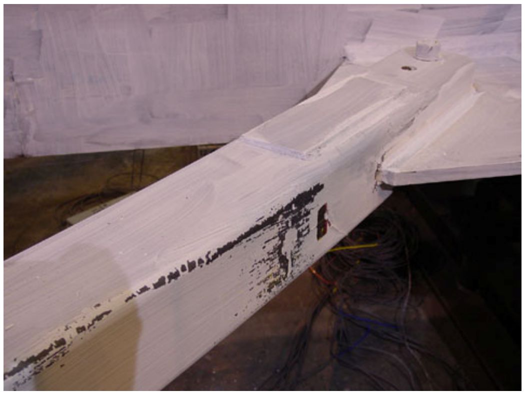

Fig. 6.84 In-plane rotation of south brace during northward excursion of first 1.0Δ_{bm} cycle.

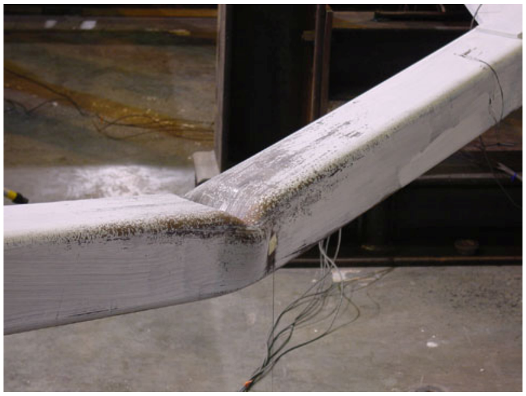

Fig. 6.85 Out-of-plane buckling of north brace during northward excursion of first 1.0Δ_{bm} cycle.

Fig. 6.86 North brace just before fracture initiation during first 1.0Δ_{bm} cycle.

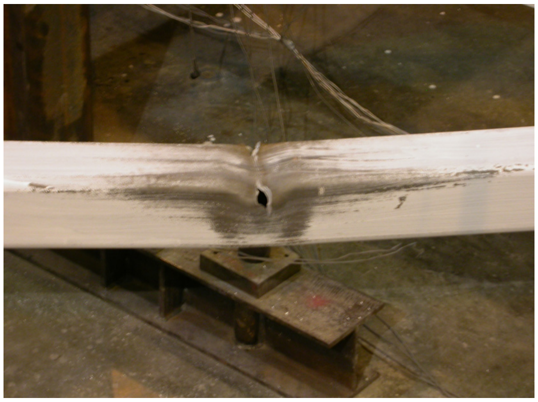

Fig. 6.87 Fractured corners on south brace during first 1.0Δ_{bm} cycle.

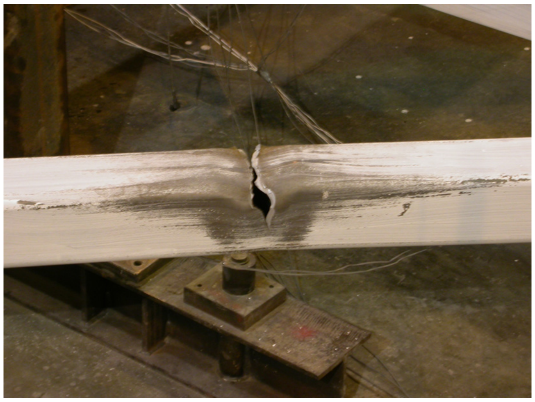

Fig. 6.88 Sudden fracture of one face of south brace and gradual propagation of fracture across cross section during first cycle at 1.0$\Delta_{bm.}$

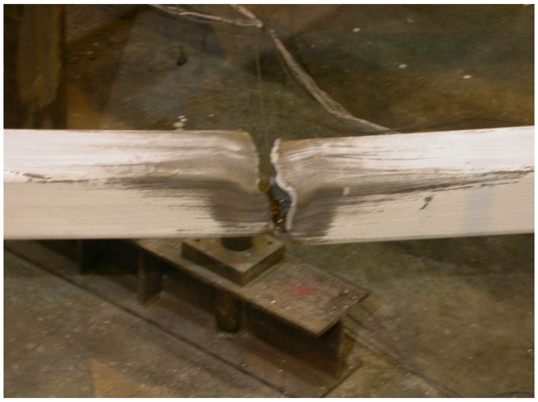

Fig. 6.89 Complete fracture of south brace during first cycle at 1.0$\Delta_{bm.}$

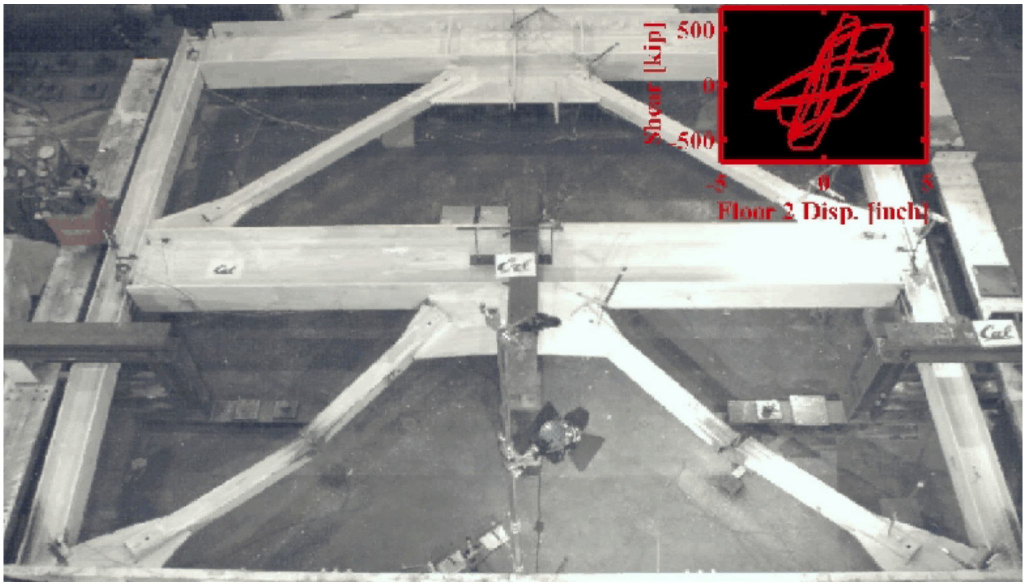

Fig. 6.90 Photo of SCBF-1 during last 1.0Δ_{bm} cycle.

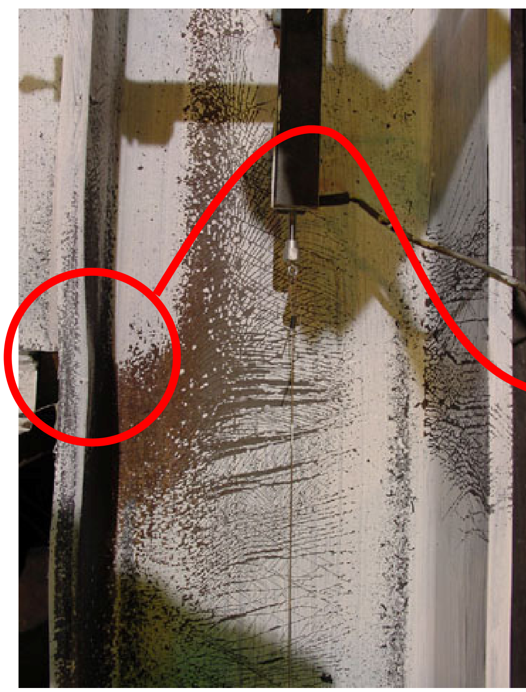

Fig. 6.91 Yield lines in column web and distortion of interior column flange during 1.0Δ_{bm} cycles– north column shown (south column similar).

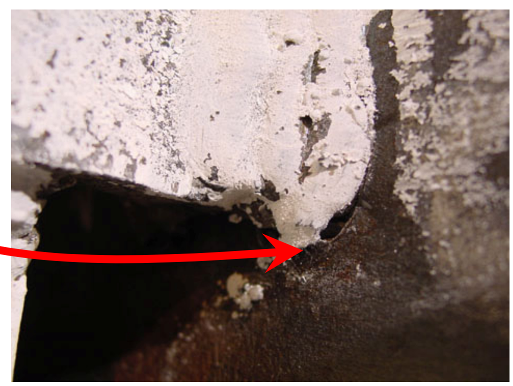

Fig. 6.92 Crack initiation in column flange along heat affected zone at tips of fillet welds attaching shear tab to column during 1.0Δ_{bm} cycles.

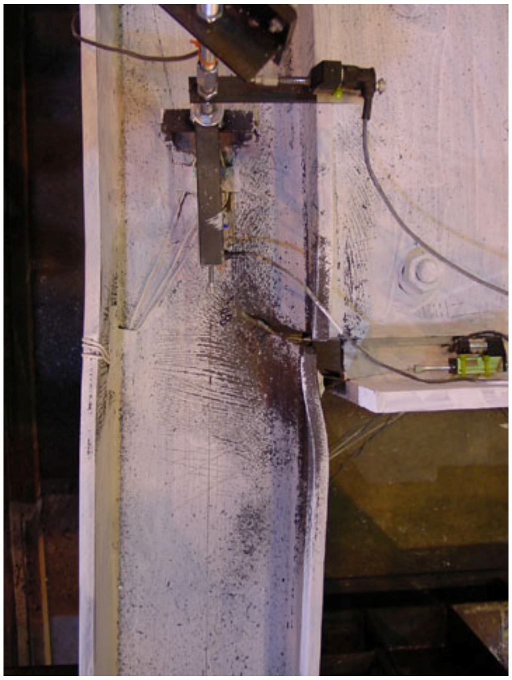

Fig. 6.93 Fracture of south beam-column connection at last $1.0\Delta b_m$ cycle.

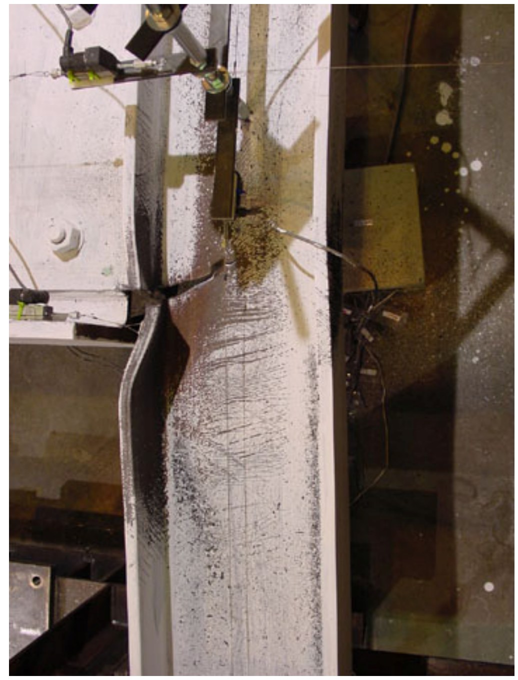

Fig. 6.94 Fracture of south beam-column connection early in first $1.5\Delta_{bm}$ cycle.

6.4.5.4 Cycles at $1.5\Delta_{bm}$ and Beyond

During the first cycle of the frame to a target roof displacement of $1.5\Delta_{bm}$, the interior flange of the north column fractured, as noted previously. The lower portion of the columns exhibited considerable yielding, as can be seen in Figure 6.95. The plastified region is relatively long on the exterior face of the column, but quite short on the interior face (starting at the top of the gusset plate).

A small crack was noticed following the Δ_{by} cycles in the weld of the exterior flange of the north column to the base plate. This was observed at the tip of the column flange and extended along the heat-affected zone (HAZ) between the bevel in the flange base metal and the complete joint penetration (CJP) weld. The crack appeared to open the space between the column flange and the backing bar (left in place on the interior face of the column flange during fabrication). This crack, which was watched closely, opened slightly and extended very gradually throughout the test, but unstable crack growth (fracture) of this section did not occur. The state of the crack at the end of the experiment is shown in Figure 6.96.

Following the $1.5\Delta_{bm}$ cycles, the specimen was pushed toward the south until the capacity of the loading setup was reached (about 10 in.). No new types of damage were detected during this excursion.

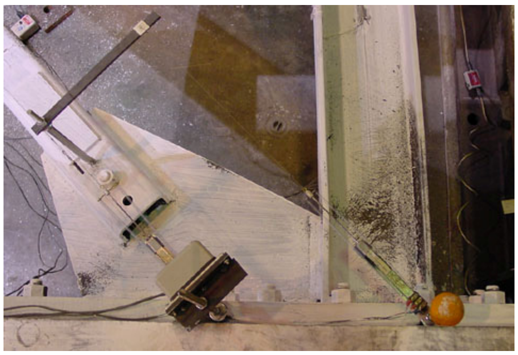

Fig. 6.95 Yield pattern in north column base region at end of test.

Fig. 6.96 Fracture in base plate following heat-affected zone along bevel in exterior column flange—crack propagated slowly from $1.0\Delta_y$ cycles to end of test.

6.4.6 Discussion and Concluding Observations

A brief summary of observations from the experiment on SCBF-1 is provided below:

1. The basic behavior of the braces in the specimen was similar to that observed in tests of individual braces (see Chapter 4). The braces bucked out of plane at loads consistent with their predicted capacities. Although the slenderness ratio of the braces used (kL/r = 54) was well within the range permitted (AISC 1997), the compression load capacity decreased rapidly following lateral buckling and from cycle to cycle. Local buckling occurred at midspan soon after the initial onset of lateral buckling (the section used satisfies AISC Seismic Provisions (AISC 1997) requirements for b/t ratios, but would exceed the criteria by about 14% if RyFy were used in place of Fy). Both lower-level level braces fractured completely at the midspan region within two cycles of displacement at a target roof drift index of $1.0\Delta bm$.

2. Once lateral buckling of the braces occurred, interstory drift and all subsequent damage concentrated in the level that first buckled. In this specimen, both levels had similar lateral load capacity and the same applied loading. Nonetheless, the initial buckling in the lower level resulted in a weak first-story response. It was noted that out-of-plane displacements of buckled braces were often five times greater than the axial shortening, creating potential life safety or economic impacts.
3. The beam was strong enough to avoid yielding, but was sufficiently flexible so that the braces did not reach their yield capacity or sustain significant net elongation when loaded in tension.
4. Even when the braces were reinforced to avoid premature fractures due to reduced net reduced area problems, complete fractures of the braces occurred during the first and second cycle to a target roof drift of 1.0Δbm. Because of concentration of damage in the lower story, the interstory drift in the lower story was 2.8% at the last cycle at this displacement amplitude, 97% larger than the imposed average overall drift of 1.4% that was imposed at the roof. It is important to note that at a reduced lateral capacity of 150 kips (Fig. 6.65) the elastic drift in the upper story is less than 0.2 in. during these cycles. While the interstory drift demands in the lower level are substantially higher than the average demand targeted for the specimen, they are far smaller than median demands that have been predicted for 2% in 50-year earthquake hazard levels for low-rise SCBF structures (Sabelli 2000; Uriz and Dreger 2003; Uriz and Mahin 2003). The severity of the concentration of damage might be ameliorated in actual buildings to a small degree by the gravity-only framing.
5. The beam-to-column connections and base plates were assumed in design to be pin-ended connections. Nonetheless, the uniform force method and other design and detailing requirements resulted in substantial connections, which resulted in considerable frame behavior in the specimen.
   a. Once the braces buckled, framing action of the beams and columns began to contribute significantly to the lateral load resistance of the specimen. This inadvertent framing action was not able to compensate for the loss in brace compression capacity that occurred following initial buckling. Substantial flexural yielding was noted at the tops and bottoms of the lower-story columns that was not considered in the original

design. Following fracture of the lower-story braces, the beam and column framing developed about 30% of the peak lateral load previously developed by the specimen.

b. The beam-to-column connections exhibited complex local behavior when unintentionally called upon to transfer moment from a column to the adjacent beam and brace, and ultimately this led to premature fracture of both columns (one during the last cycle associated with $1.0\Delta_{bm}$ and the other during the next cycle (at $1.5\Delta_{bm}$).

c. The lateral restraint on these connections did not match that which would likely be present in an actual building. Thus, certain behavior modes observed in these tests (e.g., twisting of the column about a vertical axis) may have been restrained, if a floor diaphragm were provided.

d. Had the upper-level braces buckled, rather than the lower-level level braces, even larger eccentric forces could have been applied to beam-to-column connection. The behavior in this situation was not investigated by this test.

6. Although there were significant differences in member proportions and details, the previous buckling-restrained braced frame (BRBF-1) was able to go through the entire loading history (through $1.5\Delta_{bm}$) without fracture of the braces or framing elements.

Based on these experimental results and observations, additional consideration is needed to:

1. Carry out numerical analyses to evaluate the adequacy of analytical models to predict the inelastic behavior of SCBF systems.
2. Assess experimentally or analytically the impact of:
   a. Improving the resistance of braces to post-buckling loss of compression capacity of the braces (lower or higher kl/r ratios),
   b. Improving resistance to local buckling and low-cycle fatigue (e.g., by using different section shapes [pipes and wide-flange sections or concrete-filled steel tubes (Lee and Goel 1987)],
   c. Mobilizing the tensile capacity of the braces better by using stiffer beams, or by using two-story x-braced configurations.
   d. Utilizing more robust beam-to-column (and base plate) connections (e.g., employing moment-resisting connections rather than pin-ended connections, using alternative methods to proportion gusset plates, including floor slabs or other rotational restraints

for the column at the floor level, improved welding, adding stiffeners or continuity plates, etc.).

e. Employing more economical or efficient gusset plate connections. In lieu of the tapered gusset plates used in the current specimen, consideration might be given to more common rectangular-shaped gusset plates, details that do not include a straight yield zone in the gusset plate perpendicular to the brace equal to twice the thickness of the gusset plate, details intended to provide a fixed boundary conditions for the braces, and gusset plates bolted to the beams and columns, etc.
f. Utilizing other brace configurations, such as single-diagonal bracing, single-story and double-story X-bracing, zipper frames, uplifting foundations, and so on.
g. Simulating more realistic boundary conditions, such as those associated with floor slabs, adjacent gravity-only framing, three-dimensional loading, orthogonal braced frames that intersect at a common column, nonstructural components that interact with braces during buckling, etc.
h. Improving the displacement loading protocols for the assessment of SCBF frames. Appropriate protocols may differ for systems designed for different *R* values (e.g., 6, 3, or 1), for different height (period) structures, and for sites with different seismic hazards (western versus eastern U.S.). This may also include use of hybrid (pseudo-dynamic) simulation methods to better represent actual loading conditions in large-scale tests.

Several of these issues will be addressed in the next section.

6.5 MODELING AND ANALYSIS OF SPECIMEN SCBF-1

This section focuses on the ability of various numerical modeling procedures, of the type that could be used to assess or evaluate seismic performance, to simulate the behavior of the specimen SCBF-1. All of the analytical models assumed boundary conditions at the base plate as fixed beam-column connections were considered fixed with rigid-end offsets, and rigid beams were assumed where the loading arm was bolted to the frame. In the next section, analyses will be presented considering the effect of assuming pin connections between the beams and the columns. Subsequently, the analysis model will be modified slightly to assess possible specimen behavior in the event of modest changes in the structural configuration.

Four models are considered in this section to determine the effect of the modeling method on the prediction of the behavior of specimen SCBF-1. The models ranged from complex to simple as follows:

1. A nonlinear three-dimensional model with fiber sections, large displacements, and a calibrated fatigue model (see Fig. 6.97)—**FWF**.
2. A nonlinear three-dimensional model with fiber sections and large displacements with no fatigue modeling implemented—**FNF**.
3. A nonlinear two-dimensional model using parameters from FEMA 356 (FEMA 2000d) to define brace and moment-frame parameters—**FEMA 356**.
4. An elastic two-dimensional model—**EL**.

All of the models were implemented and run using OpenSees. For the three-dimensional models (FWF and FNF), all of the beams, columns, and braces were modeled as force-based fiber elements. Torsional stiffness was implemented as an uncoupled spring using stiffness values computed from elastic section properties. The steel fibers were modeled using a Menegotto-Pinto formulation using mill certificates values of yield strength. Out-of-plane restraints were included in the model at locations where restraints were located during physical testing. A cartoon of these conditions with some geometric properties is shown in Figure 6.98. Fatigue parameters for the brace material for model FWF were set to have m = -0.5. The value ε_0 was taken to be 0.095, which was the average of the values of ε_0 found from the four uniaxial tests with net reduced area section reinforcement shown in Chapter 5.

Table 6.16 Fatigue parameters for FWF model.

Element	m	ε_0
Beam and Column	-0.458	0.191
Brace	-0.5	0.095

Beam and column fiber materials contained low-cycle fatigue parameters as identified in Chapter 5 from previous findings of other researchers. A summary of the fatigue parameters employed herein are given in Table 6.16. Model FNF was identical to FWF, only that the fiber material was not allowed to fail due to low-cycle fatigue or from large tensile strain.

The FEMA 356 model consisted of a two-dimensional model, which used FEMA 356 as a guideline to model the inelastic behavior of the beams, columns, and braces. It was implemented in OpenSees assuming all nonlinear behavior occurred in zero-length elements.

This results in a model representative of static nonlinear pushover models that might be used in practice. Figure 6.99 shows the typical force-displacement relationship used in the modeling of the zero-length sections, where the vertical axis is the force (Q), and the horizontal axis represents the deformation (θ or Δ). Points B, C, and D on this graph represent the force and deformation where yielding, significant loss of load-carrying capacity, and failure occur, respectively. Table 5-6 of FEMA 356 was used to select the values for B, C, and D and these values are shown in Table 6.17 for all of the elements modeled. FEMA 356 and FEMA 273 (FEMA 1997) encourage use of more refined values based on test results, but the default values are used here. The default values from FEMA 356 Table 5-6 are not allowed when nonlinear dynamic analyses are to be performed. The brace elements were assumed to be pin-ended trusses with an axial plastic region at the center of the brace having properties consistent with the values shown in Table 6.16. The beam and column elements were assumed elastic with plastic hinges located at each end of the element.

Model EL assumed elastic behavior and consisted of a simple two-dimensional model with identical boundary conditions as used in the FWF, FNF, and FEMA 356 models. Bracing elements were assumed to be pin-ended, and beams and columns were assumed to have the same rigid end offsets as described in other models.

Each of the models provides a different level of sophistication, each with relatively specific goals in mind. In this case, each level of sophistication is thought to increase accuracy at an increase computational cost. A summary of capabilities and features of the modeling is shown in Table 6.18.

Table 6.17 FEMA 356 computed parameters for nonlinear behavior of SCBF.

Element	Point	Q	θ or Δ
Beam	B	17,985 kip-in	0.0028 rad
	C	22,571 kip-in	0.0266 rad
	D	10,791 kip-in	0.0322 rad
Column	B	2,751 kip-in	0.0052 rad
	C	3,185 kip-in	0.0352 rad
	D	543 kip-in	0.0512 rad
Brace (Compression)	B	307 kip	0.154 in.
	C	307 kip	0.231 in.
	D	111 kip	1.230 in.
Brace (Tension)	B	484 kip	0.183 in.
	C	644 kip	2.200 in.
	D	387 kip	2.750 in.

Table 6.18 Modeling properties.

Model	Fatigue	Brace Bucking	Column Buckling
FWF	Yes	Yes (implicit)	Yes (implicit)
FNF	No	Yes (implicit)	Yes (implicit)
FEMA 356	No	Yes (explicit)	No
EL	No	No	No

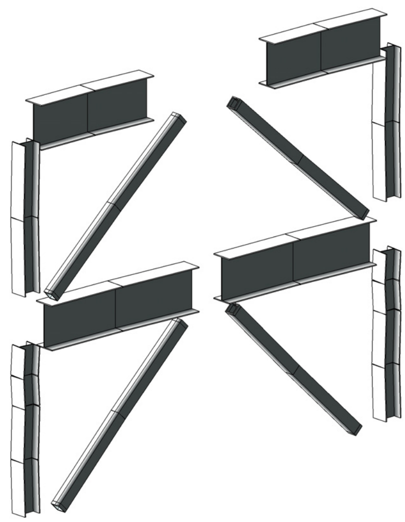

Fig. 6.97 Extruded graphic of OpenSees model.

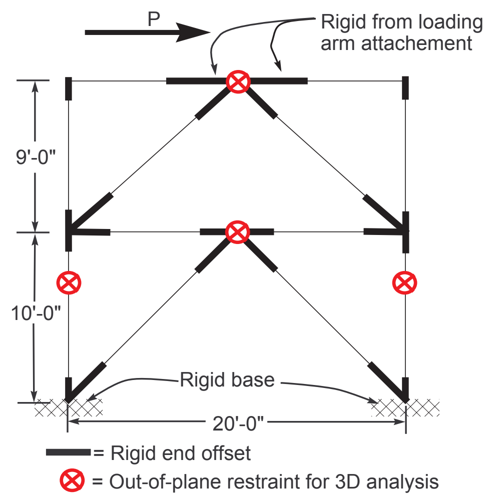

Fig. 6.98 Modeling geometry and boundary conditions.

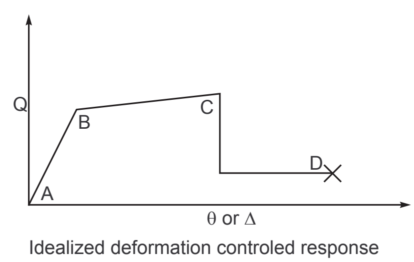

Fig. 6.99 Idealized load deformation quantities (from FEMA 2000d).

Monotonic Push

A static pushover using each of the four different models was performed in a displacement-controlled fashion. The target node displacement in this case was the lateral displacement of the center node of the top beam.

Figure 6.100 is a plot comparing the upper-beam lateral displacement versus lateral load. Although all four models provide an accurate estimate of the initial tangent stiffness of the structure in the elastic range, it is clear that the pushover methods are unable to account for the effect of low-cycle fatigue experienced by the specimen on overall frame strength and displacement capacity. The FEMA 356 model provides a reasonable estimate of the initial trend for strength reduction, even though the pushover is not cyclic, but overestimates the deformation capacity of the specimen by a substantial margin. In the FEMA 356 model, the rotations predicted in the beam and columns trigger a loss in the strength of these members, which causes the lower south brace to unload rather than reaching its deformation capacity as lateral displacements increase. The large loss of lateral strength in the FEMA 356 model is achieved when the beam on the lower floor reaches its flexural deformation capacity and fails in flexure. Note that prior to this large loss of lateral strength, the analytical model predicts that the beam-column connection suffers significant damage and that the north connection reaches its ultimate deformation capacity. Thus, the force-displacement relationship predicted by the FEMA 356 model is similar to that observed for the specimen, but the failure mode is wrong. The behavior predicted by the FWF and FNF models is similar to the test results, but the models do not predict the deterioration of behavior associated with cycling.

A comparison of the analytical behavior of the lower braces is shown in Figure 6.101. All of the models predict the initial axial stiffness quite well. The FEMA 356 model is fairly conservative with regards to the brace behavior in compression (lower-north brace). Note that FEMA 356 allows a 3% strain hardening during the tensile yield excursion, which appears to be too large with respect to the observed behavior. In the FWF and FNF models, the peak and envelope of compressive brace loads, along with envelope tensile behavior, is predicted well. The buckling model predicts a steeper loss of load at the first compressive peak; at subsequent cycles of 0.5Δbm, the FWF and FNF pushover envelope predicts a slightly larger force. Thus, the average behavior is predicted in this pushover model.

Figure 6.102 plots a comparison of the projected column moments in the lower-story columns just below the shear tab for the FWF, FNF, and FEMA 365 models. The FWF and FNF models predict a relatively low yield strength for the northern column. This is most likely due to the sharper than actual loss of compressive force in the lower north brace (as seen in Fig. 6.101), creating a larger axial and flexural demand in the column. The FWF and FNF models predict with reasonable accuracy the coupled flexural and axial behavior of the southern beam-column connections. The flexural strength of the column in the FEMA 356 model is constant and based on the estimated axial load in the column at the target lateral displacement. As such, it does not account for the higher axial loads that occur prior to brace buckling, nor does it account for the reduced rotational stiffness for small rotations when parts of the section have yielded. For this reason, the initial yield moment in the northern column is not captured correctly. Although the moment-rotation at initial yield is inaccurate, the predicted reduced yield moment of 2751 kip-in. (see Table 6.17) very closely approximates the envelope behavior of the beam-column connection at later cycles.

The behavior of the upper-level braces is not shown here; however, the FEMA 356 model predicts buckling in the upper north brace at an upper-beam lateral displacement of roughly 0.5 in. Once the upper north brace looses its compressive strength, the residual strength in the upper floor remains stronger than in the lower floor, and thus the displacements concentrate on the bottom floor during the pushover, as was observed during testing.

The EL model does not provide much insight into the post-buckling behavior of the two-story assembly. The initial tangent stiffness of brace members and members are provided as observed. Thus, this model may prove to be worthy for analysis with negligible amounts of inelastic inactivity.

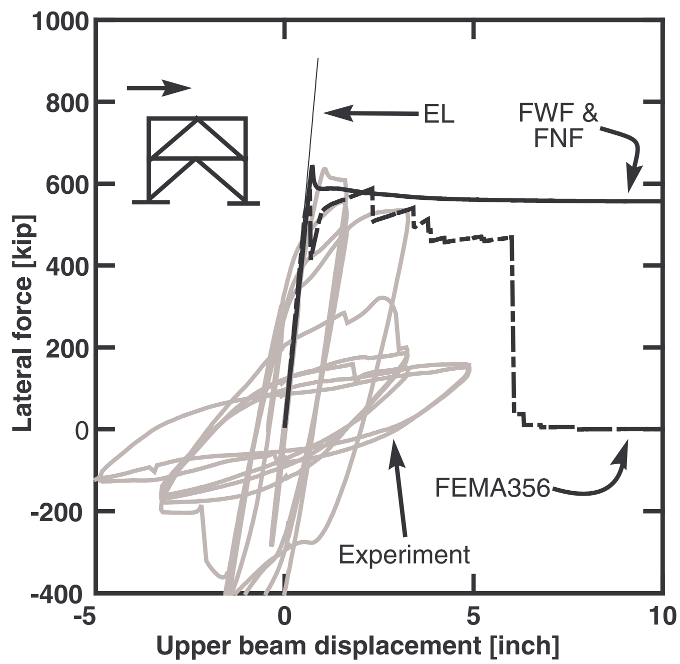

Fig. 6.100 Pushover comparison of global behavior.

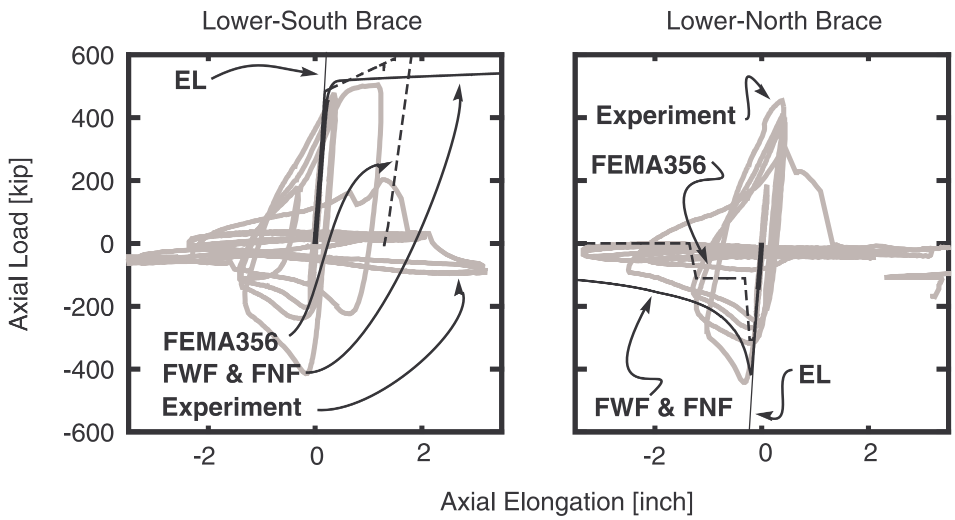

Fig. 6.101 Pushover comparison of lower braces.

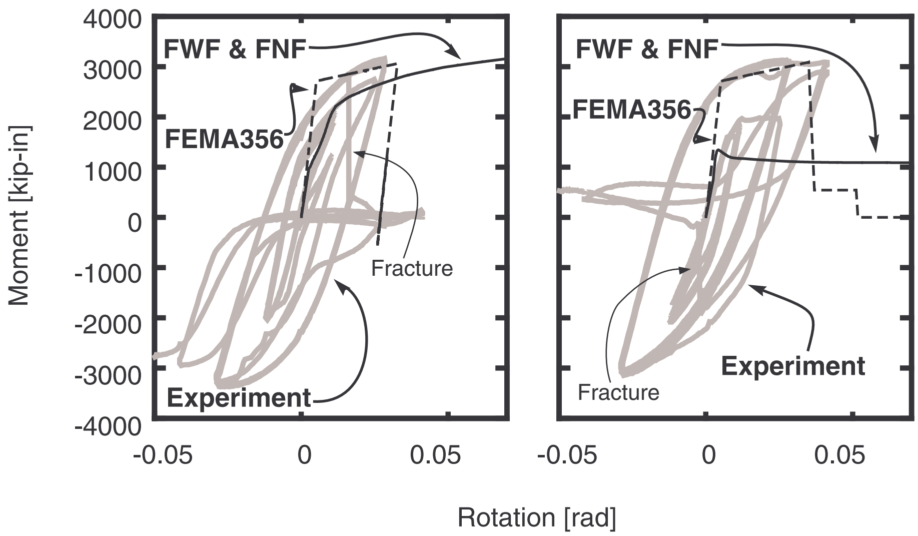

Fig. 6.102 Pushover comparison of beam-column connection behavior at top of lower-level level columns; south column on left, and north column on right.

Hysteretic Cycling

The FEMA 356 model is not an acceptable means of analysis for nonlinear dynamic procedures. The intent of the FEMA model is to capture the reduction of forces through backbone curves that represent the effects of cyclic strain history (Section 2.13.3, FEMA 273, 1997a). Thus monotonic "pushovers" incorporating realistic backbones from cyclic tests representative of earthquake-induced cyclic displacements should produce reasonable estimates of damage at a target roof displacements. For this reason, the analyses in this section will examine the difference in the behavior obtained only with the FWF and FNF models. The EL model offers no additional information from hysteretic loading, and for this reason is not shown here.

A static, cyclic, displacement-controlled algorithm was imposed on the FWF and FNF models using the displacement history from the data acquisition system of the upper-beam lateral displacement. Figure 6.103 contains a comparison of the global behavior of the FWF and FNF models. Point A on the figure shows the location where the first fracture due to fatigue occurs in the FWF model. This analytical failure occurs approximately one cycle prior to the witnessed failure; however, at this cycle the brace in specimen SCBF-1 had many initial tears at the tube corners. Point B on the same figure indicates where the FWF model predicts the failure of the lower north brace. This coincides exactly with the observed behavior, and the hysteretic loops match well up until this point. Points C and D in Figure 6.103 indicated where the lower north column base and south column base fracture in the FWF model, respectively. During the experiment, the column connection to the base did contain evidence of small amounts of fracture, as shown in the previous section. Because the column fractured dramatically near the lower beam-to-column connections, however, the strains at the bases of the columns were reduced compared to the analytical model. Thus, if the beam-to-column connections did not fail, it is likely that SCBF-1 connections at the base would have failed due to low-cycle fatigue.

In Chapter 5 we demonstrated that the proposed fatigue model would be able to predict fracture within a cycle of the actual failure of an individual brace. This is consistent with the results obtained for the analysis of a complete system. Because of the complex behavior and stress concentrations in the beam-to-column connections used in specimen SCBF-1, the strain histories obtained in the analytical model using the simple fiber representation of the connection are not representative of those actually occurring. The plane sections remain plane assumption of the numerical model would represent this connection more as having the beam flanges fully welded to the column flanges rather than having the shear tab to column connection actually employed. As such, it is not unusual that the model was unable to predict the severity of the fracture of the beam-to-column connection.

The FNF model illustrates the ideal performance of the SCBF frame, where there is much less strength and stiffness deterioration than observed in the specimen and in model FWF. The pinched hysteretic loops predicted capacities in the later 1.5 Δ_{bm} cycles result in base shears that correspond to roughly 85% of those observed at the initial buckling load, illustrating the importance of modeling fracture due to low-cycle fatigue.

Figure 6.104 shows the brace behavior predicted with the FWF and FNF models. Because of the large accumulation of local buckling damage in the first four 0.5 Δ_{bm} cycles, and the inability of the OpenSees fiber model to account for local buckling, the maximum computed brace hysteretic forces are larger than those observed. Point A points to the location of the predicted failure of the brace. This is the point where the FWF and FNF models diverge. Because of the analytical modeling assumptions, the element force-deformation relationship "flat-lines" at the point of fracture (the fibers are entirely removed from the model), and there is no "gap closing" type behavior when the two halves of a fractured brace come in contact during subsequent cycles. Because of the large permanent lateral displacements of the braces at this point, the post-fracture contribution of the braces is generally small. The FNF model shows very little tensile yielding in the braces, a result of strain growth and degradation of the lower beam in flexure. As such, the hysteretic loops of "ideal" compact braces with code-compliant slenderness are very highly pinched.

Figure 6.105 shows the FWF and FNF models of the lower beam-to-column connections. In both models the initial elastic stiffness is very similar to the observed stiffness; however, unloading and reloading stiffness differ from those observed at larger cycles, with the FWF and FNF models predicting larger stiffness values. This indicates that the rigid-end assumption is not entirely accurate at this stage (note that the next section will explore the results when this connection is assumed to be pinned). The results show that the assumed stiffness of the beam-column connection is initially well-represented using a fixed assumption, but that the yielding, buckling and fracture observed in the actual connection results in a local and global degradation of strength and stiffness, and a substantial change in the distribution of internal forces and damage. Because there is no brace fracture in the FNF model, the combined axial and flexural loads in the column continue to cause premature flexural failure due to axial and flexural interaction, as can be seen in the hysteretic loops. In the FWF model, the reduction axial load in the columns, the moment capacity is considerably larger.

The behavior of the upper-level braces is not shown here; however, both FWF and FNF models predict the observed essentially elastic behavior of these braces.

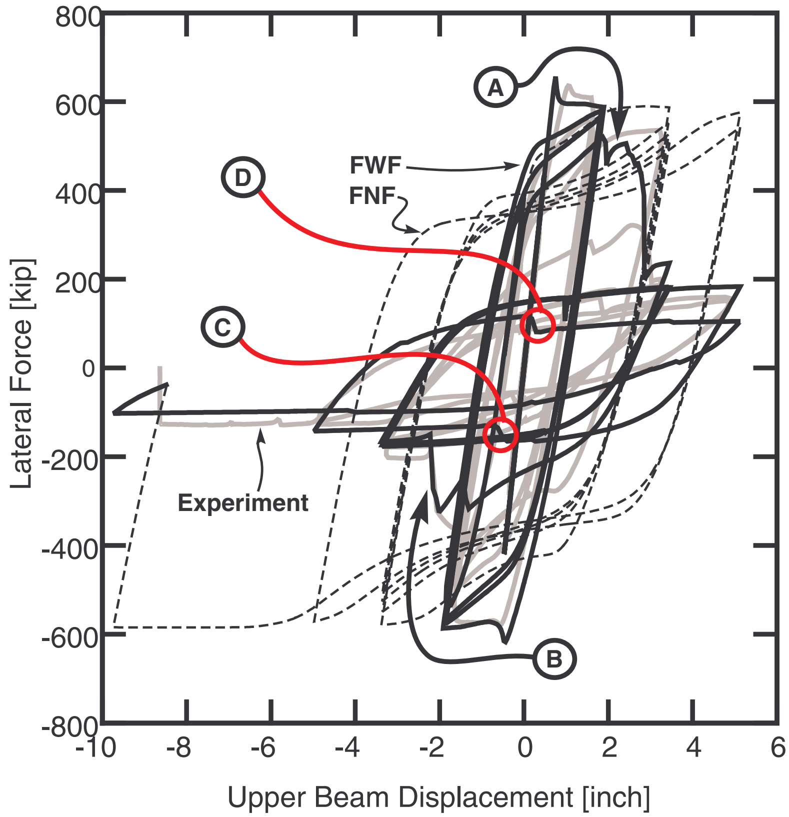

Fig. 6.103 Global hysteretic cyclic modeling of FWF and FNF models.

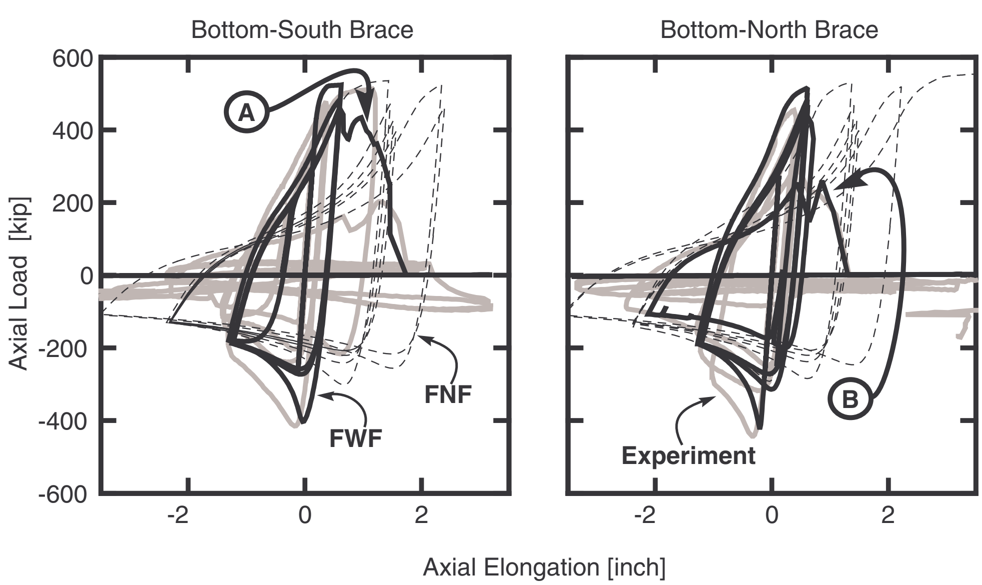

Fig. 6.104 Hysteretic cyclic modeling of lower braces for FWF and FNF models.

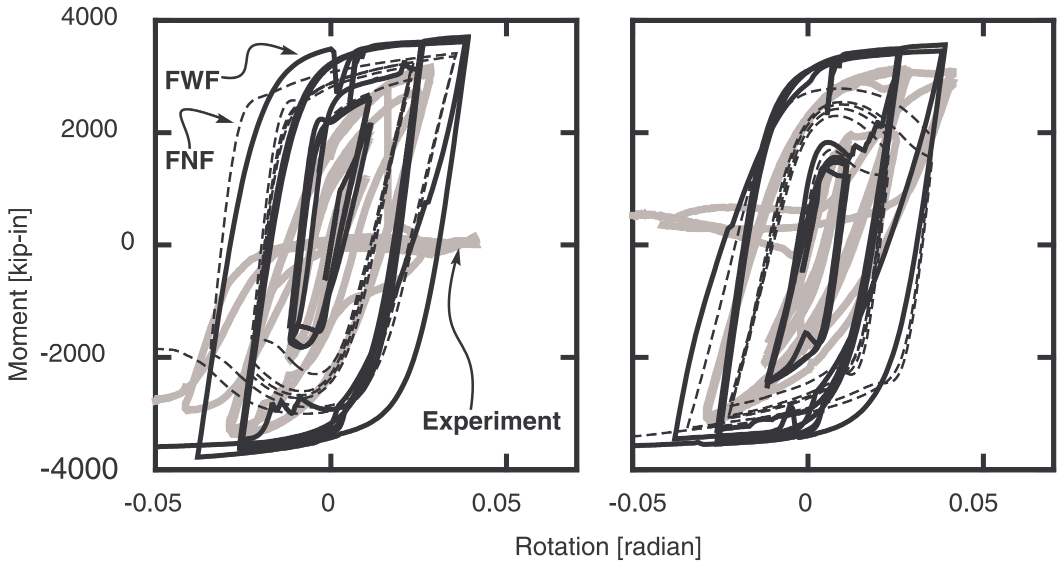

Fig. 6.105 Hysteretic cyclic modeling of lower columns for FWF and FNF models.

6.5.1 Effect of Boundary Conditions on Modeling Overall Behavior

The design of a SCBF frame often assumes pin-ended connections between the beam and column. Although this assumption is considered conservative for the sizing of the braces and the beam that spans between the two column, this may not necessarily be a conservative assumption for the design of the column. In this section, additional analyses are provided to assess the effect that a pin-ended beam assumption would have on numerical predictions of the behavior of specimen SCBF-1 and to explore the consequences of assumptions used to design SCBF structures on behavior.

For the analyses in this section, all four analytical models presented in the previous section are re-created with beam-to-column connections assumed to be ideally pinned; column bases are still assumed to be fixed for this exercise. Rigid end offsets were assumed, as in previous models. For the FWF and FNF models, the gusset plate was still modeled by a rigid offset as done in the previous section. A quasi-static pushover analysis will be performed for all of the models, as will a cyclic loading history analysis, using a displacement-controlled algorithm that imposes the controlling lateral displacement at the upper-level beam.

Monotonic Pushover Analysis

Figure 6.106 shows the results of a monotonic pushover analysis of all four analytical models along with the experimentally observed behavior. With the pinned analytical assumptions used here, the expected peak lateral strength of all of the nonlinear models is reduced. This is to be expected, as the pin-ended beam-to-column connections do not allow the frame to contribute to the system strength and stiffness. The columns are continuous and fixed base so that they will provide some lateral stiffness and strength, especially once the braces begin to buckle or yield.

The FWF and FNF models both predict a similar peak lateral strength, as expected. In both of these models the upper-level braces are predicted to remain elastic, as observed during testing of the subassembly. The lower-level brace axial force–axial displacement and beam-column moment-rotation are very similar to that of the model with fixed boundary conditions, with the exception that the rotational stiffness is substantially reduced (as would be expected). Because the column fiber element explicitly accounts for axial load-bending moment interaction, the bending induced in the column as a result of the lower braces responding inelastically and the upper braces remaining elastic causes the north column to yield. This is even in spite of the fact that the pin connection releases the beam-column connection from moments associated with the beam.

The general behavior and sequence of nonlinear events are superficially similar for the FEMA 356 models with pinned and fixed connections. Two major exceptions are the distribution of damage and the moment in the column at the beam-column connection. In the pushover analysis of the pin-ended beams, the upper-floor brace experiences large compression deformation; it is important to note that the upper floor of the physical specimen did not exhibit any appreciable damage.. The large drop of force in Figure 6.108 comes from the pin-ended beam on the first floor reaching its flexural deformation capacity in bending; again it is important to note that no appreciable flexural yielding was observed at the lower-level beam midspan during physical, cyclic testing. Figure 6.108 shows the moment-rotation of the lower-story columns just below the beam-column connection, where the rotation is as defined previously. In this pushover analysis, the beam-column interaction is elastic until the large loss of lateral load associated with the lower-level beam failure at the midspan, at which point the sense of the moment switches to negative after the top floor is reduced in strength. Thus, the assumption of pin-pin does not accurately predict the expected flexural force and deformation in the beam-column connection, potentially leading to an underdesigned column in flexure.

The EL model predicts with reasonable accuracy the initial lateral stiffness of the entire specimen. This is reasonable considering the lateral stiffness of the frame at this stage is essentially due completely to the axial stiffness of the braces, beams, and columns. As seen in the experiment, the loss of lateral strength of the brace led to the loss of more than 80% of the lateral strength and stiffness.

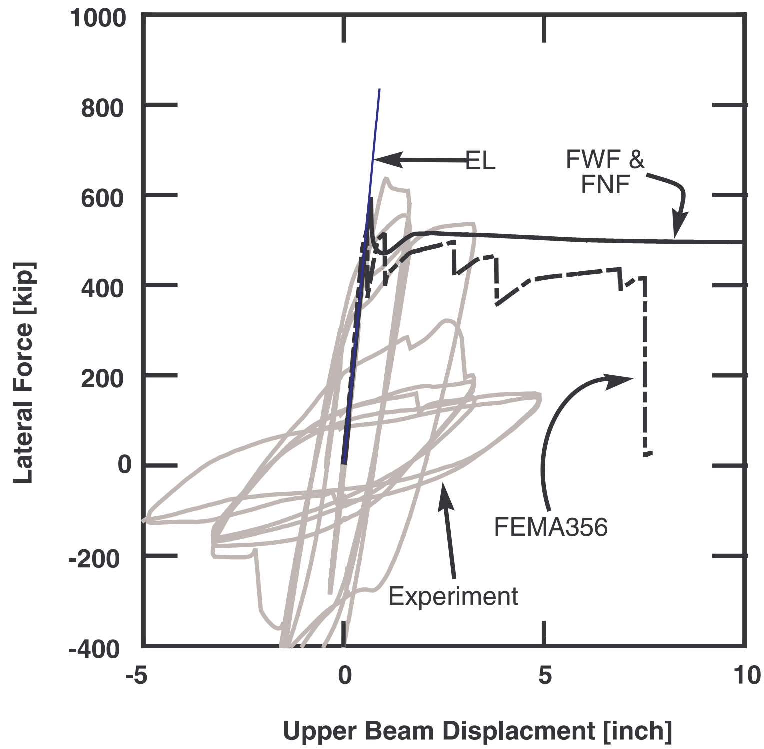

Fig. 6.106 Pushover comparison of global behavior of pin-connected assembly.

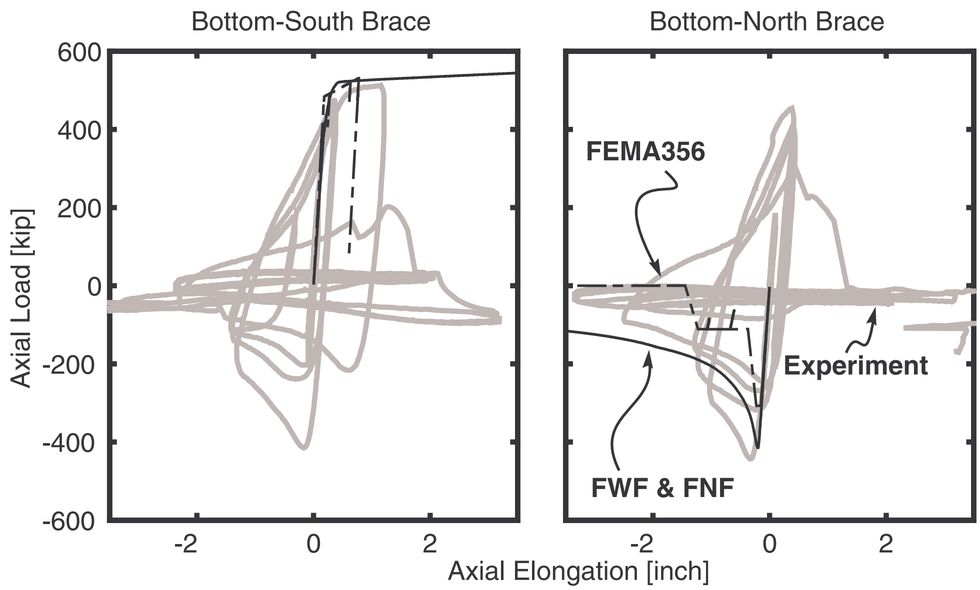

Fig. 6.107 Pushover comparison of lower braces using pin-ended model.

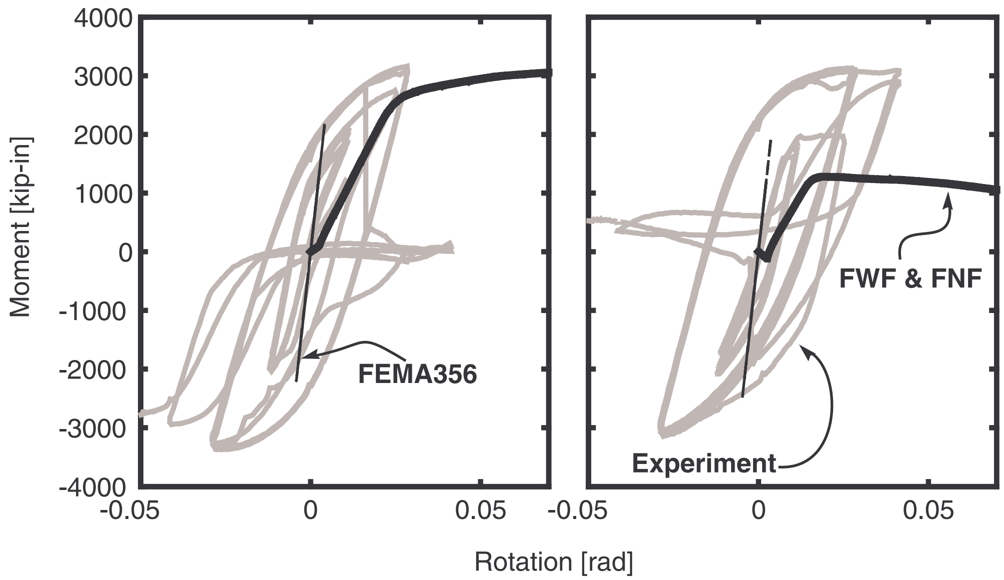

Fig. 6.108 Pushover comparison of beam-column connection behavior using pin-ended model (column moment shown).

Hysteretic Cycling

As before, a displacement-controlled algorithm was applied to the pin-ended analytical model to impose the lateral displacement history from the test specimen at the top loading beam. The FEMA 356 model was not used for the cyclic analyses as explained previously. The computed results from this hysteretic cycling are shown in Figure 6.109. As in the pushover analysis, the FNF and FWF analytical models predict a slightly smaller yield force and more rapid degradation of initial stiffness than observed in the test. The small difference in strength demonstrates that the frame contributes little at this stage. Using model FWF, the cycles at which both the north and south lower braces fail are similar to those predicted in the fixed-ended model (see Fig. 6.119). Note that both the FNF and FWF models have global buckling failures in the bottom floor only.

Figure 6.111 illustrates the behavior beam-to-column connection. The behavior is similar to that assumed from the fixed-ended model; however, the loading and unloading stiffness is substantially less than that of the observed stiffness. The large disparity in the predicted analytical stiffness (compared to the relatively slight disparity with the fixed-ended model) implies that the fixed-ended assumption is “more correct” than the pin-ended model. Although this is not a surprise, this graph illustrates the relative accuracy of the fixed- and pin-ended models. Note that in the FNF model, the beam-column connection is predicted to fail in flexure due to large axial loading.

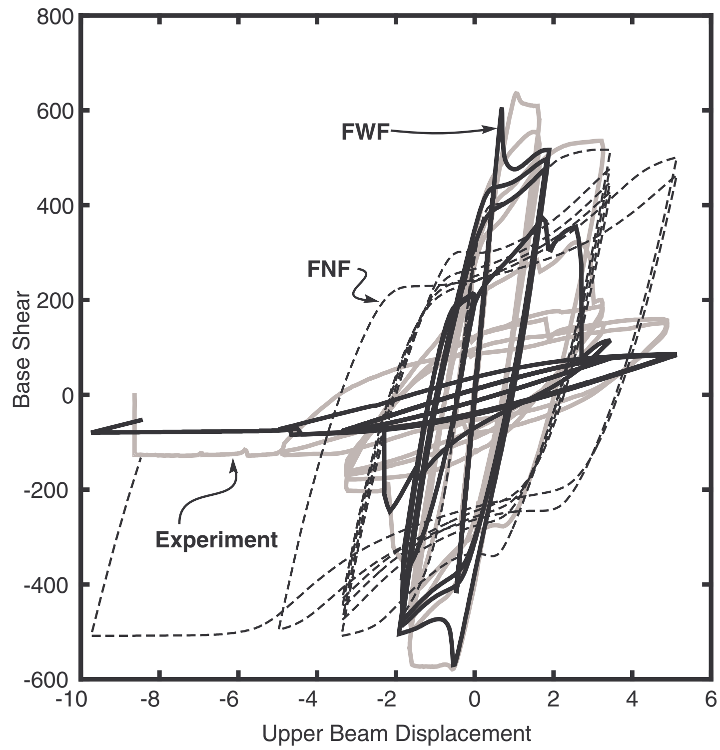

Fig. 6.109 Global hysteretic cyclic modeling of FWF and FNF pin-ended models.

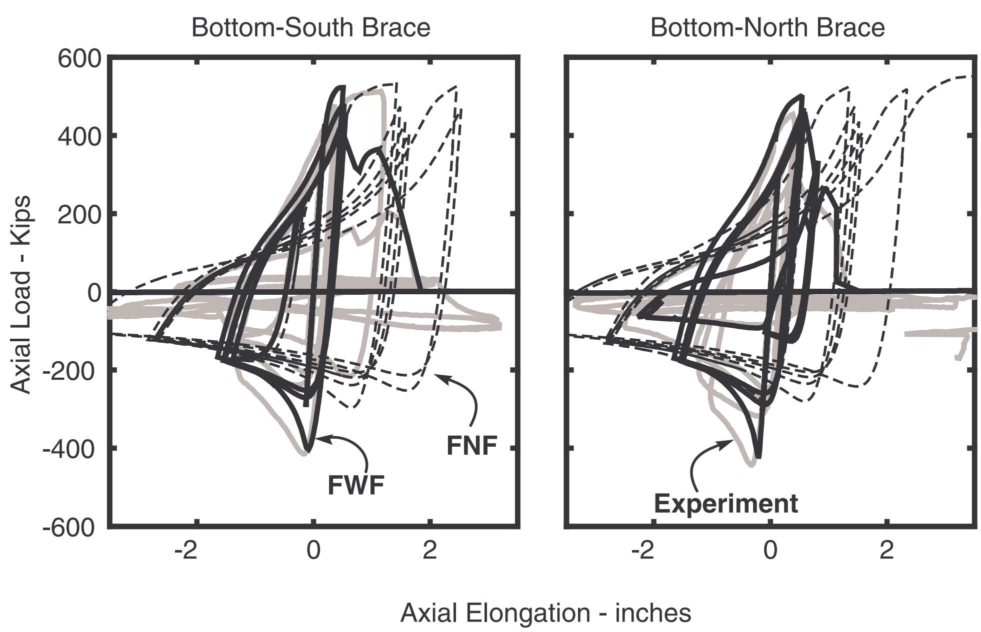

Fig. 6.110 Hysteretic cyclic modeling of lower braces for FWF and FNF pin-ended models.

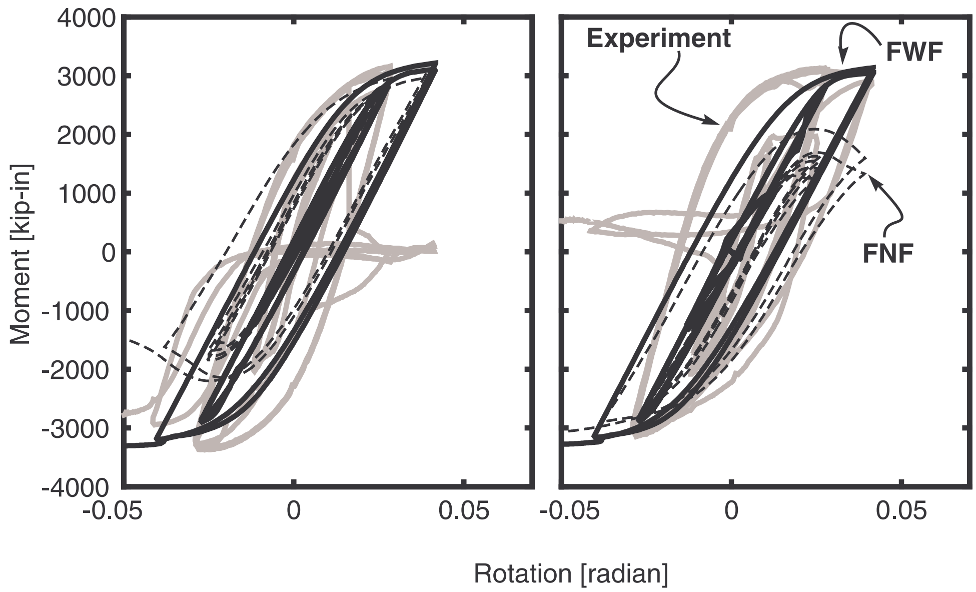

Fig. 6.111 Hysteretic cyclic modeling of lower columns for FWF and FNF pin-ended models.

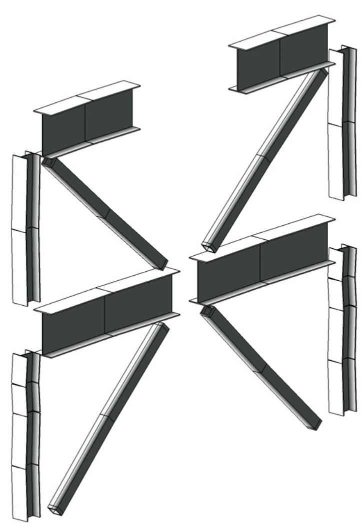

Fig. 6.112 Extruded graphic of OpenSees model with alternative, two-story X, configuration.

6.5.2 Alternative Configuration

Using the calibrated fatigue model, the effect of using an alternative configuration is explored in this section. Because the braces in the lower story did not sustain significant tensile elongations once the braces buckled, a specimen with a stiffer and stronger beam might be considered desirable. Because the beam is already quite large, it was more economical to achieve the same goal by inverting the braces in the upper story, resulting in a so-called two-story X-braced configuration. This configuration is likely more economical than the standard chevron configuration, as the size of the beam can be substantially reduced. By reducing the beam size, the unbalanced vertical component of brace load that the beam must be designed for is eliminated or substantially reduced. Many engineers also believe that this configuration may avoid problems associated with weak stories. A new FWF model was formulated based on the same member sizes as used in SCBF-1 (i.e., for simplicity, the beam size was not reduced for this analysis).

Only the cyclic lateral displacement history was applied to the altered specimen using the FWF model. Figure 6.112 is an extruded graphic of the OpenSees model showing the assumed configuration. All of the boundary conditions and constraints were assumed to be identical to those of the fixed-ended FWF model from above.

Figure 6.113 shows the hysteretic lateral force–roof displacement history of the analytical two-story X-configuration. Buckling is predicted to occur only in the lower-story braces. Moreover, the cyclic force–displacement behavior of the braces tends to dominate the response, so the additional stiffness of the beam provided by the upper-story braces does not increase the performance of the lower-story braces. The failure of the north and south lower-story braces are predicted to occur at the same cycle as for the standard chevron configuration. There is a small difference in the immediate post-buckling behavior of the brace (Fig. 6.114) that is attributed mainly to the additional stiffness of the beam; however, this additional stiffness does not appear to help the overall behavior of the brace. In fact, the global behavior seems to be almost identical to the previous fixed-ended stacked-chevron FWF model.

Figure 6.115 shows the anticipated behavior of the beam-column moment-rotation connection. With this configuration there is a larger demand placed on the lower-story column. As such, the southern beam-column connection is predicted to fracture during the first excursion at 1.5Δbm due to low-cycle fatigue. This fracture places an even larger demand on the northern beam-column connection, yet the connection is not predicted to fail due to low-cycle fatigue. As in the observed case, however, it is thought that the detailing may cause a strain concentration that may lead to a low-cycle fatigue failure that can not be captured by the fiber-modeling techniques used here.

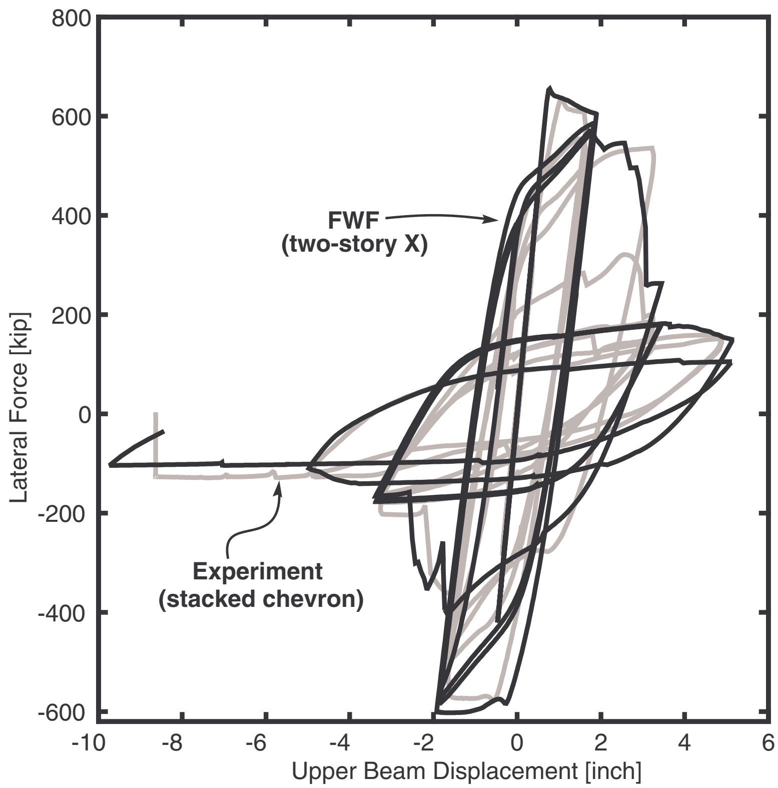

Fig. 6.113 Global behavior comparison of stacked chevron configuration (tested) and two-story X-configuration (analytical).

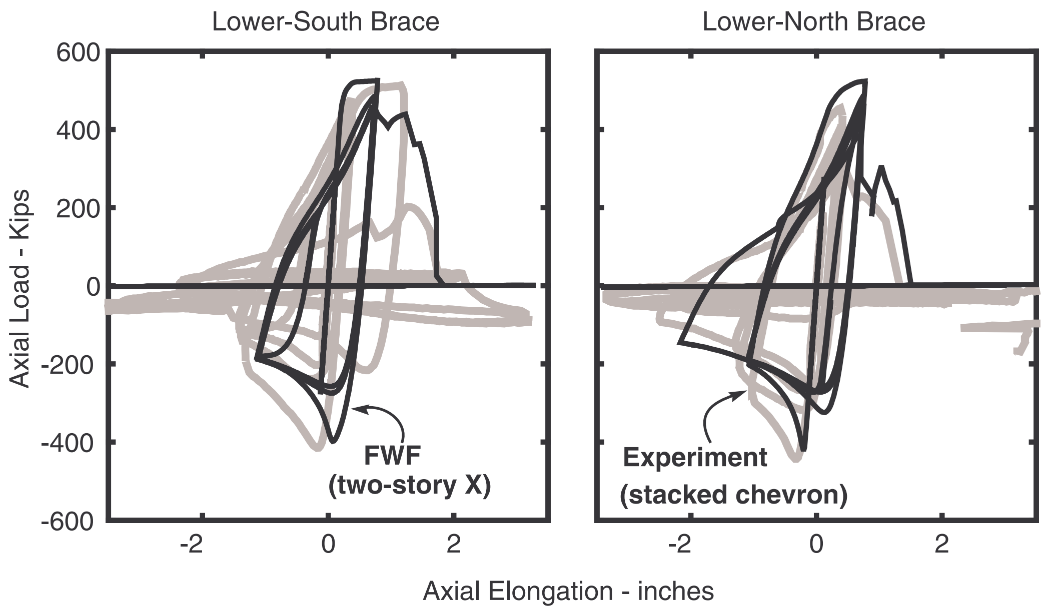

Fig. 6.114 Expected brace behavior at lower story for two-story X-configuration.

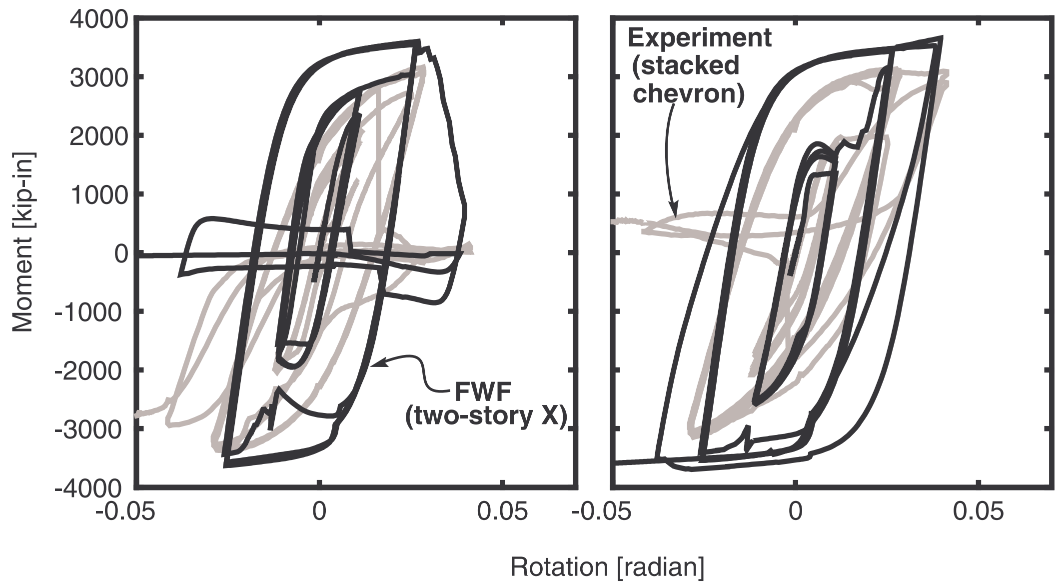

Fig. 6.115 Expected moment rotation at beam column just below beam-column connection.

6.5.3 Summary and Conclusions

All of the analytical models considered here provide a reasonable estimate of initial stiffness. All of the nonlinear models predict the initial buckling loads and location of first buckling (lower story) with a similarly reasonable estimate. This is regardless of the assumptions made about beam and column end fixity, or even configuration.

The FEMA 356 model also provides a reasonable prediction of global strength degradation in the pushover analyses, which is intended to be representative of cyclic deformations. Note that the FEMA 356 model significantly overestimates the deformation capacity of the specimen and fails to identify properly the members that fail.

The interaction of flexural demands and axial demands played a significant role in the initial yielding and subsequent performance of the beam-column connection region. As such, modeling beam-column connection restraint is important. The fixity can lead to an incorrect conclusion that the columns may remain elastic, as shown in the FEMA 356 models. Because the fiber models (FWF and FNF) both take advantage of an explicit calculation of the interaction of axial load and flexural interaction, the end rigidity seems to be less sensitive to end restraint assumptions for these models.

The calibrated fatigue model predicted to a high degree of precision the cycle at which the brace would fail and produced a realistic progression of failure as fibers are removed from the specimen. The fatigue model was able to only approximately suggest the onset for fracture in the gusset plate-shear tab to column connection detail used in the test specimen.

The damage in the entire test specimen was completely concentrated on the lower story. As such, the analytical models should reflect this concentration of damage, in either a cyclic or static pushover analysis. This concentration is sensitive to the analytical modeling assumptions of the beam-column connection, as illustrated with the FEMA 356 model containing pin-ended beam-column connections. In this model, the top-story compression brace buckles along with those in the lower story.

In general, all analytical assumptions used predicted the weak-story behavior and rapid deterioration of strength and stiffness of the SCBF frame. It is seen that a low-cycle fatigue model is essential to properly capture the deterioration of the system. The basic results shown in this chapter are consistent with the previous numerical results. This suggests that SCBF structures may be particularly vulnerable to seismic excitations that lead to even modest numbers and amplitudes of inelastic displacement excursions.

6.6 COMPARISON OF BRBF AND SCBF SPECIMENS

Although the BRBF test specimens were intended to be part of a larger structure than that considered for the SCBF specimen, the braces in specimen SCBF-1 were designed such that the design axial force would match the strength of the buckling-restrained brace in specimen BRBF-1. Story dimensions in both of these tests were very similar, and both specimens contained a chevron configuration. The columns in specimen BRBF-1 were significantly larger than those in SCBF-1, and fully welded connections were used in BRBF-1. As such, the results of these two specimens can be compared, but the difference between the specimens must be fully realized when making these comparisons.

Figure 6.116 plots the estimated contribution to the base shear by the buckling-restrained braces from BRBF-1 along with the estimated base shear contribution of the conventional braces in SCBF-1. This plot removes from the comparison the direct contribution of the framing to the lateral load resistance of the two specimens. Interestingly, related to the design procedures used, the lateral forces and stiffness are similar until 0.5 Δ_{bm}. At this point, the BRBF-1 braces continue to strain harden and increase resistance with increasing deformation, compared to severe strength degradation in the SCBF-1 frame. Target drift was calculated through nonlinear pushover of a model containing fully restrained beam-column connections.

Figure 6.117 shows the same hysteresis loops as Figure 6.116 but also includes the brace contribution to base shear for the FNF analytical model of SCBF-1. The FNF hysteretic loop does not contain the effects of low-cycle fatigue and can be interpreted as the “ideal” behavior of the braced-frame structure. The FNF prediction provides a great deal of added hysteretic energy dissipation when compared to the observed SCBF-1 behavior. Although the improvement is substantial, the FNF model still does not attain the energy dissipation and overall performance of BRBF-1.

The buckling capacity of the brace in SCBF-1 was intended to match the strength capacity of the BRBF brace. Code compliant design for an SCBF will typically contain a design *R* value that is smaller than that for a BRBF brace (i.e., R = 6.4 for SCBF systems versus R = 8.0 for BRBF systems (IBC 2003). Although increasing member sizes accordingly will increase for the same displacement history the hysteretic energy dissipated in the FWF and FNF models of the SCBF system, it has been shown that short-period structures are very sensitive to hysteretic shape during dynamic excitation (Khatib et al. 1988; Miranda and Bertero 1994) and that this added energy dissipation under simple cyclic loading does not guarantee improved dynamic performance.

Regardless of the differences in detailing, it is clear from the figures that the hysteretic shape is drastically different for the BRBF and SCBF specimens. After completing the loading protocol for the BRBF-1, as a result of strain hardening the capacity of the structure has actually increased, whereas for the SCBF-1 specimen, the lateral capacity is reduced to less than 10% of its original strength.

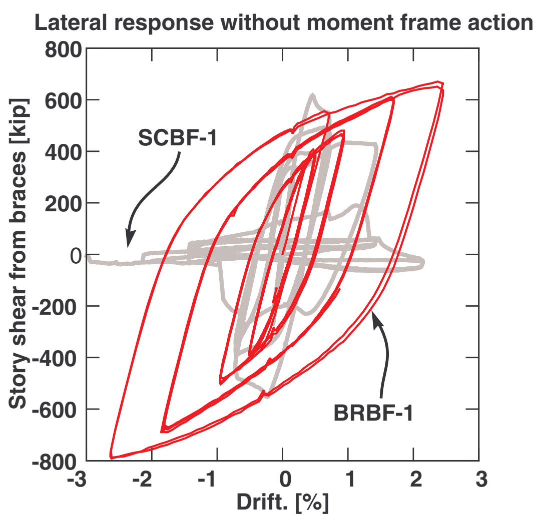

Fig. 6.116 Global behavior comparison of SCBF-1 and BRBF-1.

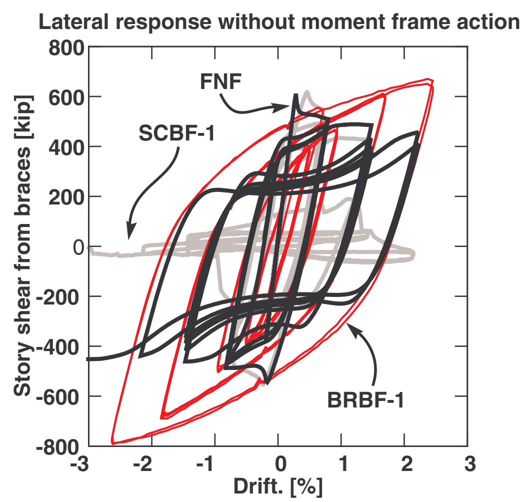

Fig. 6.117 Global behavior comparison of SCBF-1, BRBF-1 and FNF numerical model.

7 Simple Performance-Based Hazard Analysis of SDOF Systems

7.1 GENERAL

A computationally and conceptually efficient way of understanding the inelastic dynamic response of complex multi-degree-of-freedom systems is to study the nonlinear dynamic response of simplified single-degree-of-freedom systems (SDOF) that incorporate many of the general global hysteretic characteristics of the more complex system. These SDOF models also provide, in a very general sense, the ability to compare the performance potential of many different types of structures. Thus, there is the opportunity to explore quickly various performance criteria and their likelihood of exceedance given seismic hazard levels or environments. Such studies can help develop an intuitive feeling for the sensitivity of behavior to various basic parameters, but they disregard the contributions of higher mode effects, formation of weak stories, and do not provide any specific insights into the effects of detailing or proportioning of members. Nonetheless, such analytical studies are believed to be very useful.

Many SDOF studies have been performed in the past on simplified nonlinear oscillators, several of which are summarized in a paper by Miranda and Bertero (1994). These previous studies explored the effects on response of multiple parameters, which characterize the nonlinear behavior of SDOF systems.

The intent of this chapter is to perform a simple study of SDOF models representative of braced-frame systems, accounting for the effects of buckling. OpenSees fiber-based buckling elements, described in Chapter 4, will be used to construct the SDOF model. The effects of low-cycle fatigue will not be considered in this chapter. The objectives of these studies are two-fold:

1. Study the effect of the response modification factor, R, used in design on the displacement demands of simplified, conventional buckling systems for a range of brace slenderness ratios.
2. Use the simple SDOF model to perform a simple performance-based hazard assessment comparing different systems using a single performance criterion; i.e., maximum lateral displacement (ductility).

7.2 COMPARATIVE RESPONSE OF A SDOF SYSTEM REPRESENTING A CONVENTIONAL BRACED FRAME WITH BUCKLING BRACES

7.2.1 Analytical Model

An OpenSees analytical model was created to simulate the basic inelastic dynamic response of a simple conventional buckling frame. For this study, the behavior of the simplified system was assumed to be akin to a simple, two-bay system with idealized pin connections and axially rigid beams and columns (see Fig. 7.1). Thus, only two braces are included in the model. A cartoon representation of the OpenSees analytical model is shown in Figure 7.2. This simplified model has four nonlinear beam-column elements configured so that when one brace is extending, the other brace is shortening. This is done by constraining the lateral translational degree of freedom of nodes 3 and 4 to be identical, as represented in Figure 1.2 by the thick black line.

To trigger buckling in the braces, an initial imperfection was introduced using the following technique. An initial lateral displacement was imposed on the SDOF model equivalent to 0.5% of the length prior to running nonlinear analysis. The corotational formulation in OpenSees has the ability to “straighten” SDOF systems such that this initial imperfection is numerically zero. As such, the system was straightened, resulting in an initial out-of-plane load at nodes 2 and 5. The load was applied such that it developed 5% of the yield moment of the brace element. This lateral displacement and load would help trigger lateral buckling during the subsequent dynamic analyses.

The brace element itself was a solid rectangular cross section with ten fibers in the local y-axis. The material used for each of the uniaxial fiber materials was a Menegotto-Pinto material with a yield strength of 60 ksi and an initial tangent stiffness of 29,800 ksi. The post-elastic strain hardening was set at 0.3% of the initial stiffness.

For the investigations presented in this section, the "yield" force of the conventional buckling system was defined as the load at which AISC (1993) predicts buckling to occur; this is shown below in Equations (7.1a–c). This was chosen over the calculated Euler buckling loads because this method was found to be relatively accurate for a range of slenderness ratios, as shown in Figure 7.3. To calculate both the exact buckling load and determine the appropriate dimensions for a specific force reduction factor*, R,* would have added several iterations of nonlinear dynamic time-history analysis. In Figure 7.3, the buckling stress, $F_{CR},$ is calculated by taking the peak buckling load and dividing by the area, illustrating that for slenderness in the range of 40–120, the AISC equations are very similar to OpenSees analytical predictions for the buckling loads. The very compact members tend to have unconservative estimates of strength when using OpenSees. It is assumed that at these values of slenderness the initial out-of-plane force and displacement may be large compared to the cross-sectional area; however, the overall results are still in good general agreement.

$$F_{CR} = 0.658^{\lambda^2} F_Y \text{ for } \lambda \leq 1.5 \qquad \text{(a)}$$

$$F_{CR} = \frac{0.877}{\lambda^2} F_Y \text{ for } \lambda > 1.5 \qquad \text{(b)} \qquad (7.1)$$

where $$\lambda = \frac{kl}{\pi r}\sqrt{\frac{F_Y}{E}} \text{ and} \qquad \text{(c)}$$

The lengths of the members were chosen using Equation (7.2). In this equation, $S_{D,ELASTIC}$ is the elastic spectral displacement of an equivalent SDOF oscillator with an identical period, R is the stipulated force reduction factor, E is the elastic modulus, and FCR is the estimated buckling load as shown in Equation (7.1). The area for the square cross section used for the buckling members in all of the analysis was determined using Equation (7.3), where S is the slenderness ratio of the element and L is the length of the element (determined by Equation 7.2). The mass for the SDOF oscillator shown in Figure 7.2 is calculated by using Equation (7.4), where T is the targeted fundamental period of the structure, *m* is the entire mass, *L* is the length of the brace [determined by Eq. 7.2), and *A* is the area of the brace (determined by Eq. 7.3), once the length is determined].

$$P_{CR} = \frac{\left(S_{D,ELASTIC}\dfrac{AE}{L}\right)}{R} \qquad \text{(a)} \qquad (7.2)$$

therefore $$L = \frac{\left(S_{D,ELASTIC} E\right)}{RF_{CR}} \qquad \text{(b)}$$

$$S = \frac{kL}{r} = \frac{(1.0)L}{\sqrt{\frac{I}{A}}} \qquad \text{(a)}$$

$$\text{(7.3)}$$

for a square section $$S = \frac{kL}{r} = \frac{(1.0)L}{\sqrt{\frac{(b^4/12)}{b^2}}} = L\sqrt{\frac{12}{A}} \qquad \text{(b)}$$

$$m = \frac{T^2}{4\pi^2}\left(2\frac{AE}{L}\right) \qquad \text{(7.4)}$$

In the numerical parametric studies presented in the remainder of this chapter, it is important to recognize that for a given system mass and frame geometry, and using commercially available member sizes, it may not be possible to develop an actual design having the desired period, slenderness ratio, and strength (R value). The approach outlined above overcomes this limitation, but systems having different slenderness, period, and R values may have different masses, member sizes (A), or geometries (L). This approach gives insight into overall trends, but the results need to be carefully interpreted.

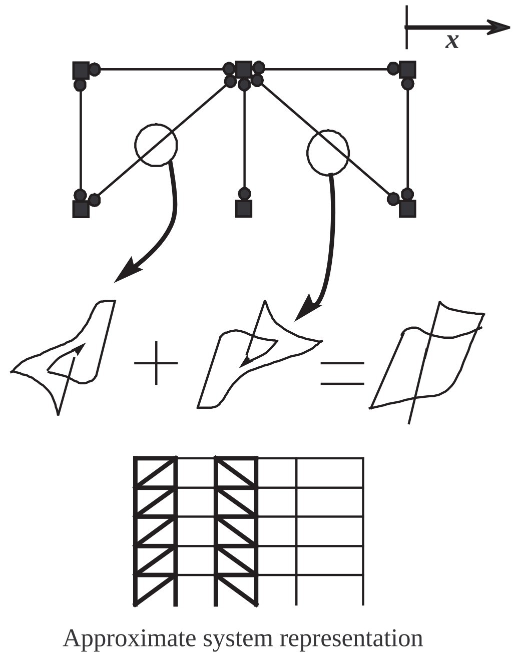

Fig. 7.1 Idealization of SDOF with inclined braces. Axial displacement- axial force hysteresis of braces represented by two, two-dimensional buckling braces assuming axially rigid, pin-ended truss assembly. Potential system that this may be used as an approximation for is shown at bottom of figure.

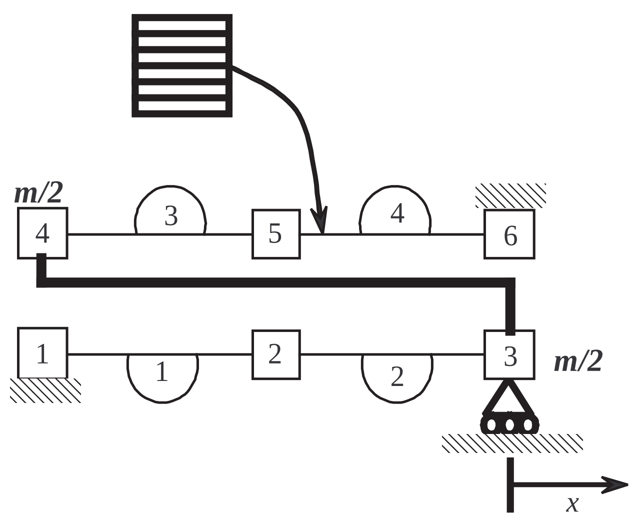

Fig. 7.2 Illustration of SDOF oscillator used in study. Each of four elements is square fiber element with three integration points per element. Lateral translation of nodes three and four are slaved, as shown by thick black line.

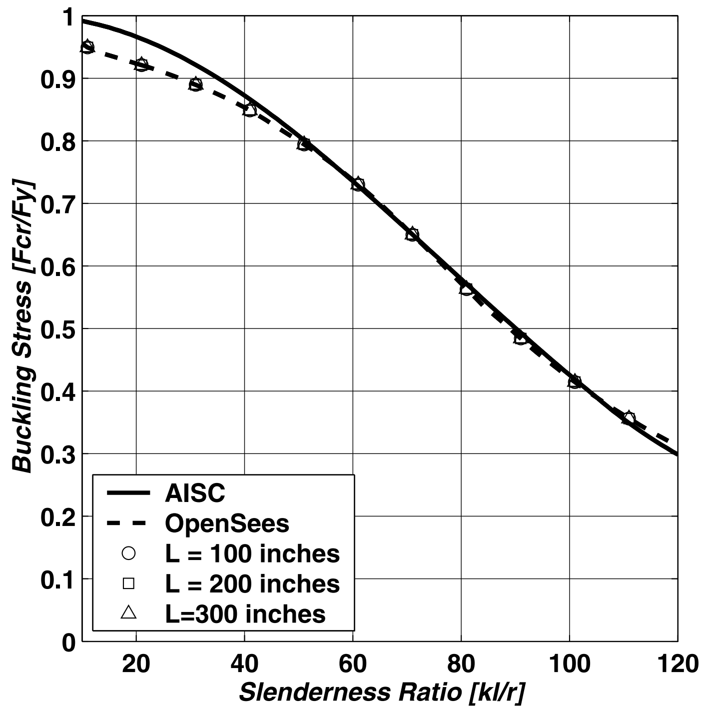

Fig. 7.3 Comparison of AISC buckling stress with OpenSees calculated buckling stress for three different length members. Three different lengths lie on top of each other for OpenSees prediction. OpenSees critical stress is taken as peak buckling load divided by area.

7.2.2 Nonlinear Dynamic Performance of SDOF Subject to Varying Slenderness, Period, and Displacement Ductility

The OpenSees SDOF buckling model was analyzed to determine statistical relationships between system ductility demands and the response modification factor, *R,* for structural systems having different periods and brace slenderness. Well-established iterative methodologies based on nonlinear time-history analysis methods (Miranda and Bertero 1994) were implemented in OpenSees to determine for a particular ground motion record the value of *R* needed for a idealized SDOF system having a particular period and slenderness ratio to develop a targeted displacement ductility value. Here, *R* represents the ratio of the minimum strength of the system required to achieve elastic response to the strength that would result in a specified displacement ductility. In these studies, displacement ductility represents the peak lateral displacement predicted during the analysis divided by the lateral displacement that would initiate buckling in the braces. A tcl script was developed for OpenSees to identify the system strength needed to achieve elastic response and then to iteratively reduce the strength until the target displacement ductility was achieved. This process was repeated for numerous ground motion records, slenderness ratios, elastic structural periods, and target ductility values.

A previous statistical study involving many time-history analysis of ideal elasto-plastic SDOF oscillators led to the derivation of Equations (7.5a–b) (Miranda 1993; Miranda and Bertero 1994). These equations estimate the force reduction factor R for a given target ductility for structures located on stiff soil. Similar studies (using far fewer motions) concluded that for short-period structures the simpler Equation (7.6) would estimate the force reduction factor for a target ductility (Newmark and Hall 1973).

$$R_\mu = \frac{\mu - 1}{\Theta} + 1 \geq 1 \qquad \text{(a)}$$

$$\Theta = 1 + \frac{1}{10T - \mu T} - \frac{1}{2T}\exp\left[-\frac{3}{2}\left(\ln T - \frac{3}{5}\right)^2\right] \qquad \text{(b)} \tag{7.5}$$

$$R_{NH} = \sqrt{2\mu - 1} \tag{7.6}$$

To compare these earlier relations for SDOF systems having bilinear hysteretic characteristics, analyses were initially performed on the OpenSees SDOF buckling model proportioned to represent braced frames having a kL/r value of 60. The R values required for systems having bilinear elasto-plastic characteristics were determined using BiSpec (Hachem 2005). Three target displacement ductilities μ were considered (i.e., μ = 2, 4, and 6). A series of 60 ground motion records previously created for the SAC Steel Joint Venture for the Los Angeles area were used in this investigation (Somerville 1997). These motions were developed to represent hazard levels ranging from frequent to very rare.

The results of this study are shown in Figure 7.4. Two clear trends can be identified here:

1. The bilinear model and the buckling model seem to agree with each other remarkably well for the 60 ground motions selected.
2. Equation (7.5) is a relatively good approximation for required force reduction factor R; however, it does not seem to fit the data as well in the 1–3 sec period range, especially as the value of μ increases.

Possible explanations for the discrepancy noted above include:

1. The ground motions used for the previous study by Miranda (1993) are different than those used in this study.
2. Given the nonlinear nature of the response of an SDOF, there is more than one possible solution for a force reduction factor, *R*,. Figure 7.5 illustrates the ductility demand predictions for various values of *R* obtained for:
   - a randomly chosen earthquake
   - structural period of 1.5 sec
   - elasto-plastic SDOF hysteretic response, and
   - a target lateral displacement ductility of $\mu = 5$

In the case shown, there are three possible solutions for the force reduction factor that will produce a ductility of 5. This situation is very common for earthquakes that have two (or more) predominant pulses, the first one being slightly smaller than the second (and typically of opposite sign). This phenomena has been termed "structural resurrection" in previous literature (Vamvatsikos and Cornell 2002). At larger periods, this effect can be more common. The iteration scheme developed and used with OpenSees does not discriminate between these different feasible *R*-values, it simply iterates until the first feasible solution is found. The initial estimates for *R* are large and a search is performed until any solution is found. This may also lead to the larger R-values than EPP systems at large periods, as shown in Figure 7.4.

To illustrate further the effect of hysteretic characteristics on the design force reduction factor, *R,* additional analyses were done at three specific SDOF periods (T = 0.5, 1.0, and 1.5 sec). Figures 7.6–7.8 show the mean relation between *R* and the targeted displacement ductility obtained for the 60 ground motions considered of the elasto-plastic system and the SDOF buckling system with a brace slenderness ratio of 60. These figures also show the relation for bilinear hysteretic systems predicted using Equation (7.5). Because the statistical study used to develop Equation (7.5) limited the response to a target ductility demand of 6, the plots of Equation (7.5) in Figures 7.6–7.8 are limited to displacement ductilities smaller than 6. Figure 7.6 also shows the simpler relation predicted using Equation (7.6).

These figures illustrate that the response of short-period structures is very sensitive to the hysteretic loop shape and diminishes at longer periods. For example, for a target lateral displacement ductility of 5 and a brace slenderness ratio of 60, the mean value of *R* needed for either a buckling or elasto-plastic system is about 4 for a period of 1.5 and 3.8 for a period of 1.0. For systems having a period of 0.5, the analysis results suggest that the mean required value of R drops to about 3 for the elasto-plastic system and to about 2.75 for the buckling system. This variation of R with period has been noted by many (e.g., Newmark and Hall 1974), and the use of Equation (1.6) with a target displacement ductility of 5 results in a required R of ($\sqrt{2(5)-1}=$) 3, which is the same as predicted numerically for the elasto-plastic systems. In comparison, if an R of 6 is considered, mean displacement ductility demands of about 14 and 18 are developed for the elasto-plastic and buckling systems (kL/r = 60) when the period is 0.5 and about 7.5 and 8 when a period of 1.5 sec is considered.

The scatter in the data used to develop these mean relations is very large, however. Figures 7.9–7.10 show the data for each of the individual records used in developing the mean relationships between R and μ for T = 0.5 sec and the elasto-plastic and buckling systems. It is clear from these two plots that the aleatory uncertainty for ground motions is quite large, and must be considered in the design and the performance-based risk assessment of structures.

To assess the effect of different slenderness ratios on the response of braced frames, the mean force reduction factors were computed again considering the brace slenderness ratios of 40, 60, 80, 100, and 120. The results are shown in Figures 7.11–7.13. It is interesting to note that in a mean sense, the slender brace models perform *better* than the stockier braces in that they have for a given value of R on average a smaller ductility demand for the 60 ground motions considered. This is particularly true in the short-period range. As can be seen in Figure 1.15, brace slenderness has little effect on the required value of R to obtain a target displacement ductility for a structural period of 1.5 sec. When the structural period is 0.5 sec., the mean value of R required for a ductility target of 5 changes from about 2.7 to about 3.5 as the brace slenderness increases from 40 to 120.

This is mainly due to the fact that using current design methods the brace size is controlled by its buckling capacity, and not the structures total collapse load capacity. Referring to Figure 1.2, it can be seen that the buckling capacity of the brace is about 85% of its tensile yield strength when the brace slenderness is 40, but this reduces to 30% when the slenderness increases to 120. As a result, for the same initial brace buckling capacity, the brace tensile capacity will be 0.85 / 0.3 = 2.8 times larger for the more slender brace. In the extreme case, when lateral displacements are increased to the point that the compression brace can carry no load and the tensile capacity of the brace is assumed to be the product of its area and initial yield stress, the strength of the system with the braces with a slenderness ratio of 40 reduces to 59% of its design capacity (taken for simplicity as twice the theoretical strength needed to buckle the compression brace). For a similar system with brace slenderness of 120, the residual strength of the system is 1.6 times larger than the initial design capacity. This high over strength is not normally taken advantage of in design. Additional research is needed to assess the overall consequences of brace slenderness.

7.2.3 Summary and Conclusions

The analytical studies shown in this section demonstrate the usefulness of OpenSees and the OpenSees model described in Chapter 4, and reiterate the known sensitivity of SDOF systems in the short-period range to strength (*R* factor) and hysteresis loop shape. Thus, for a given displacement limit, a braced-frame structure with a period less than around 1 sec should be designed for a *R* value significantly less than the targeted displacement ductility value. This trend is more acute for braces with small slenderness ratios.

It is also very interesting to note from these analyses that slender braces designed for buckling loads during earthquakes will perform relatively better than less slender braces, in an average sense. As noted previously, these results need to be carefully interpreted. Some issues to be considered include:

1. While the overstrength associated with more slender braces might improve dynamic response, it will also result in higher axial (and other) design forces for columns, foundations, beams, and connections, and the out-of-balance force that needs to be considered in the design of beams in V or inverted-V (chevron) configurations will be significantly increased.
2. For the same brace buckling capacity, a more slender brace will need to have a larger cross-sectional area, requiring a heavier and thus more costly brace.
3. However, the larger cross-sectional area will result in a structure with a smaller period. This will normally reduce the elastic spectral displacement for a typical earthquake, but may result in a need to further reduce the value of *R* to achieve a targeted ductility value.
4. Designing of braces with very slender sections may also prove to be useful in terms of the fatigue life of the specimen (Lee and Goel 1987). Slender braces are not likely to yield as much in direct tension and thus will not produce as much plastic strain growth as stockier

braces. Similarly, buckling is initiated in the elastic range and thus the braces may be less susceptible to low-cycle fatigue. These factors contribute to the improved fatigue life.

5. Braces with larger slenderness values will buckle at a smaller displacement than for stockier braces. As a result, the maximum lateral displacement for a braced frame having the same displacement ductility demand will be smaller for the stockier brace than for the more slender brace. This combined with the expected higher ductility capacity and fatigue life of slender braces may permit higher ductility demands to be considered in the design of braced frames having more slender braces.

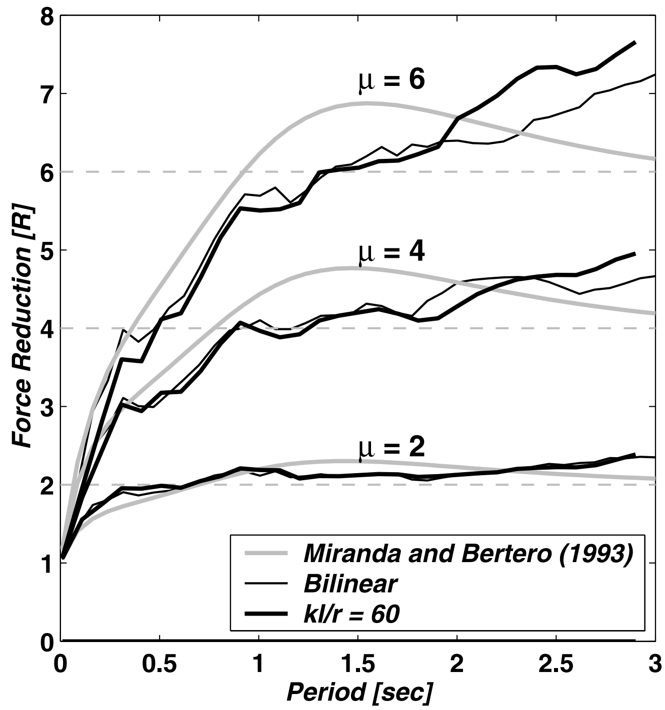

Fig. 7.4 Comparison of statistical model (Miranda and Bertero 1994) with elastic-perfectly-plastic (bilinear) behavior and buckling behavior with slenderness of 60.

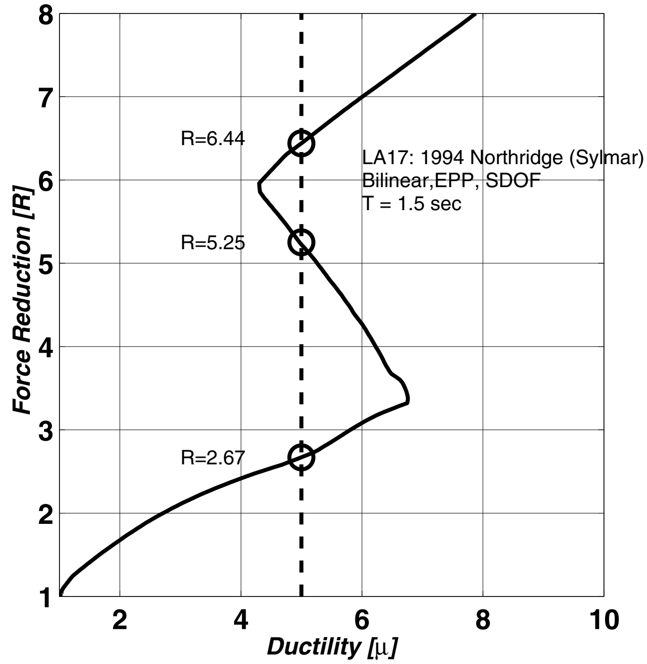

Fig. 7.5 Effect of dynamic resurrection on chosen force reduction factor.

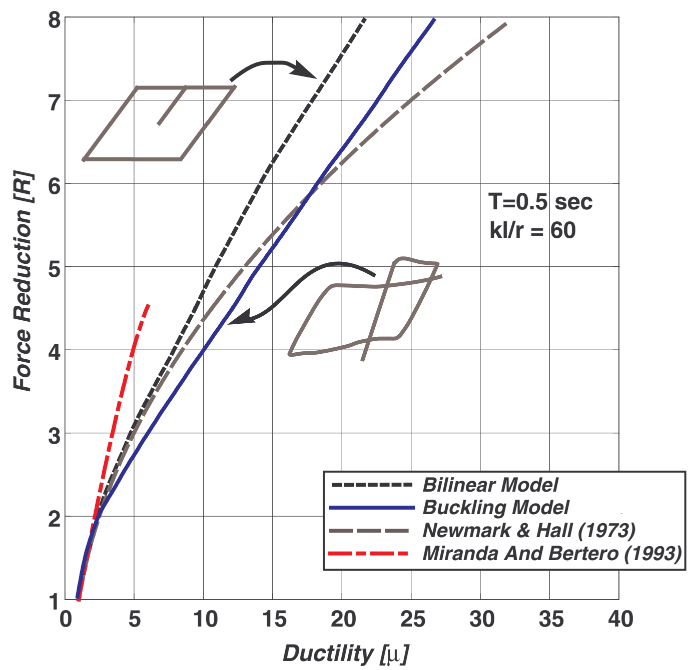

Fig. 7.6 Comparison of statistical model (Miranda and Bertero 1994) and (Newmark and Hall 1973) with elasto-plastic, buckling (kl/r = 60) behavior. All plots shown for T = 0.5 sec.

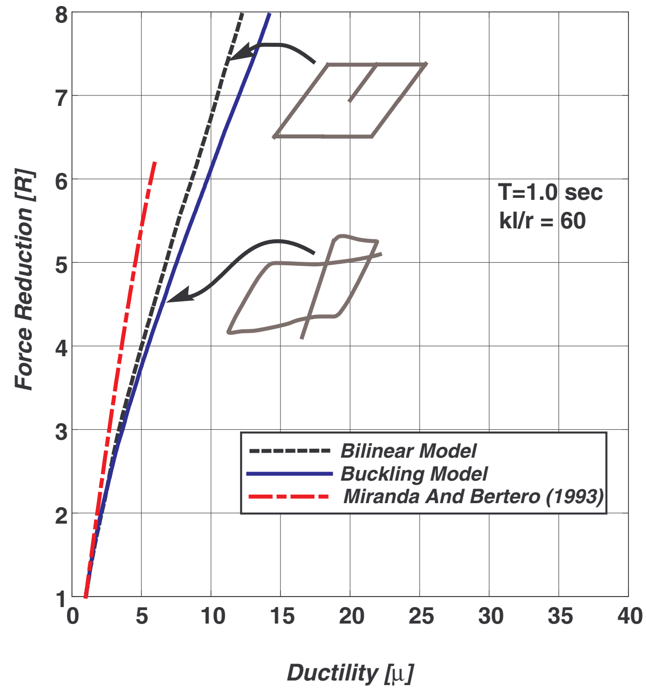

Fig. 7.7 Comparison of statistical model (Miranda and Bertero 1994) with elasto-plastic, buckling (*kl*/*r* = 60) behavior. All plots shown for *T* = 1.0 sec.

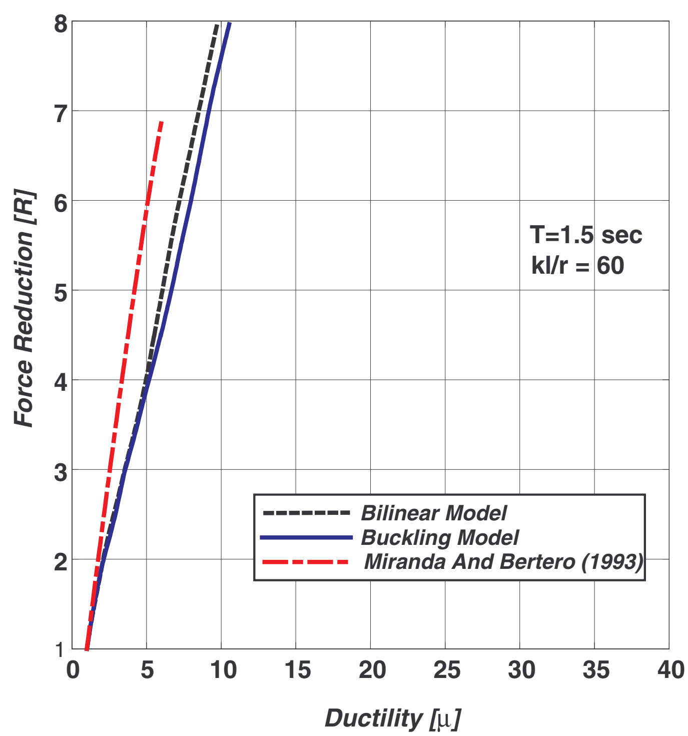

Fig. 7.8 Comparison of statistical model (Miranda and Bertero 1994) with elasto-plastic, buckling (*kl*/*r* = 60) behavior. All plots shown for *T* = 1.5 sec.

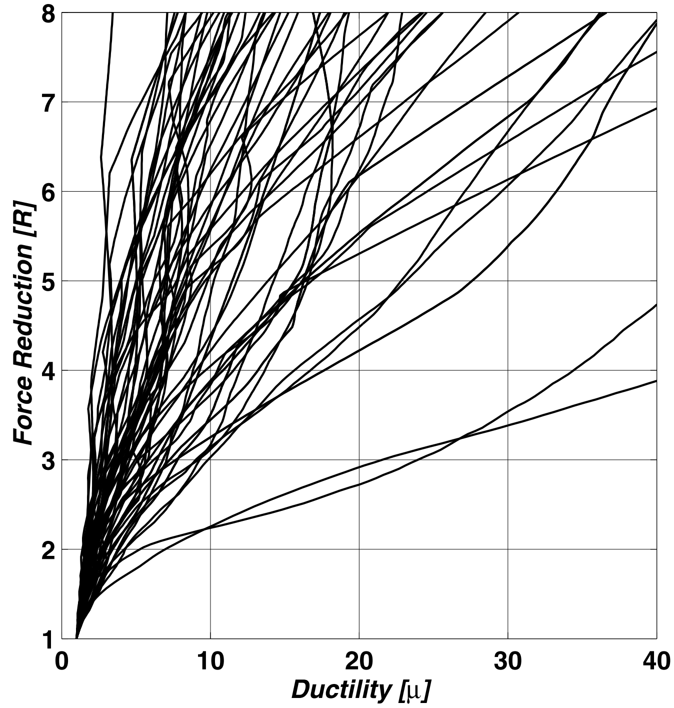

Fig. 7.9 Illustration of scatter in data for elasto-plastic model; T = 0.5 sec.

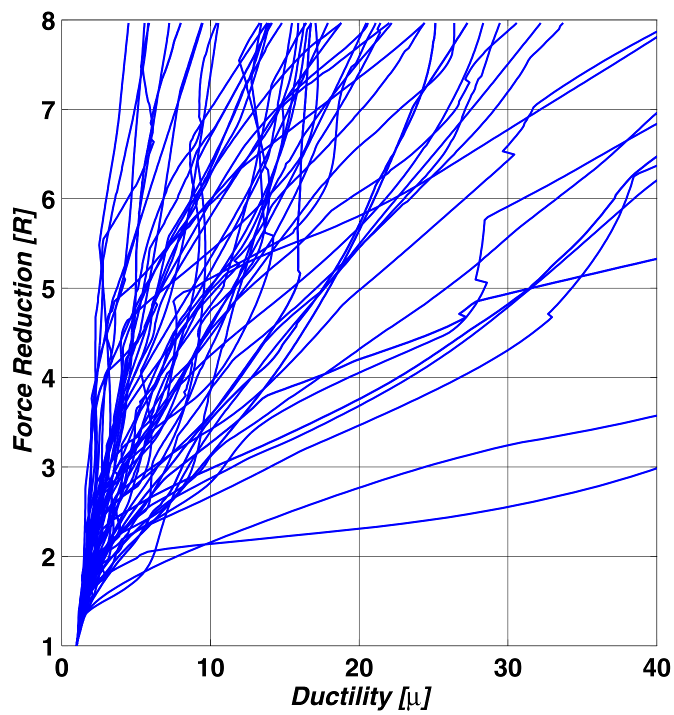

Fig. 7.10 Illustration of scatter in data for buckling model. T = 0.5 sec, and kl / r = 60.

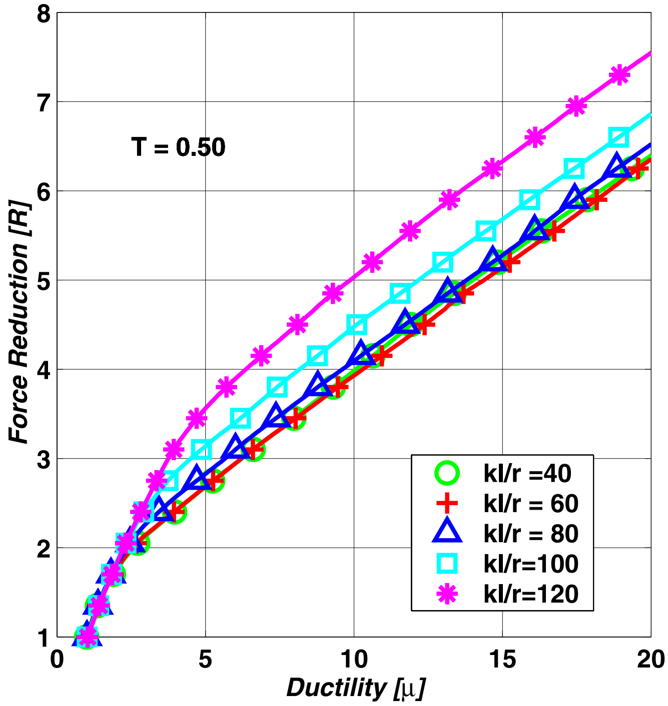

Fig. 7.11 Mean response of 60 ground motions comparing ductility demand and design force reduction factor for Los Angeles area.

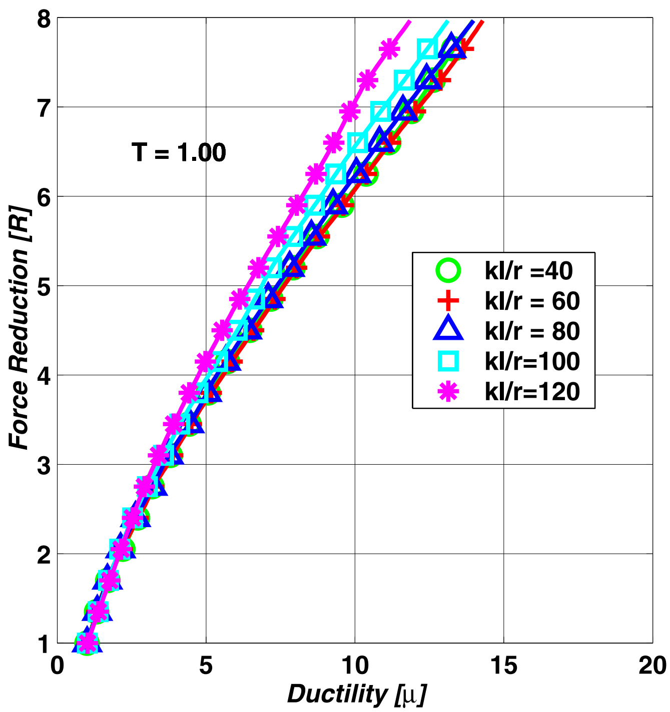

Fig. 7.12 Mean response of 60 ground motions comparing ductility demand and design force reduction factor for Los Angeles area.

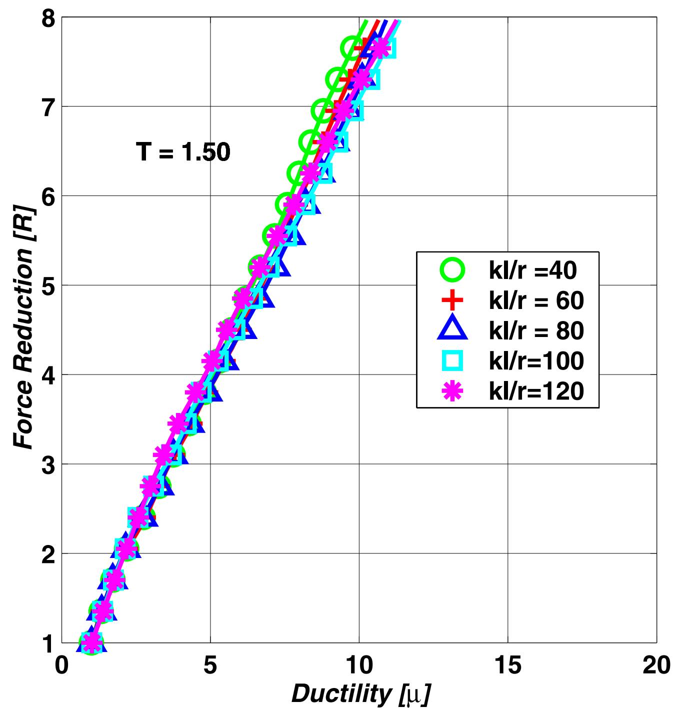

Fig. 7.13 Mean response of 60 ground motions comparing ductility demand and design force reduction factor for Los Angeles area.

7.3 PBEE OF VARIOUS SDOF MODELS

7.3.1 General

The following section provides an example of using PBEE risk analysis for different types of structures to offer a consistent basis for performance comparison. In this section, three different SDOF oscillators are considered: a simple bilinear model, and two models with buckling braces. For the braced systems, slenderness ratios of 60 and 120 are considered. The bilinear system is chosen to have a fundamental period of 1.0 sec, whereas each of the buckling models will have a fundamental period of 0.5 sec. This is thought to be representative values for three-story steel moment frames and braced frames, the shorter period corresponding to the braced frames.

A risk analysis is performed on these structures to determine the probability of exceeding an arbitrarily defined damage measure for a specified seismic hazard level. The ground motions for these records are again chosen as those defined for the SAC Steel Joint Venture corresponding to 50%, 10%, and 2% probabilities of exceedance in 50 years. Therefore, the results will be presented here for these hazard levels.

7.3.2 Design of Models

Typically, design lateral forces for earthquake-resistant structures are based on a hazard associated with a 10% probability of exceedance in 50 years. For this reason, the design-level forces for the buckling SDOFs were taken as the median pseudo-spectral acceleration for the twenty, 5% viscously damped spectra of the 10% in 50 year ground motions for the Los Angeles area. Figure 7.14 shows these spectra, and Figure 7.15 shows the corresponding spectral displacement for these records.

Because the bilinear system is chosen to be representative of a moment-frame system, it was assumed to be governed by drift limits (see Chapter 1). Because only a SDOF analysis will be done, and a prototype three-story frame does not exist, the yield displacement was selected such that the bilinear SDOF structure remained elastic given the median response spectra for the 50% in 50-year event. For the suite of ground motion records used, the ratio of the median value of $S_{D,\ ELASTIC}$ for the 10% in 50-year hazard level and the 50% in 50-year hazard level is 2.2. This corresponds to a feasible effective value of R for a moment-resisting frame controlled by drift.

For this simplified case, the median value of design spectral displacement was used to determine either the buckling load or the yield load for the buckling and bilinear models. Both braced frames have an effective R value of about 6.4 when ϕ factors are considered. Because of the constraint on period and kl/r, the two braced systems have different masses and brace areas and lengths. The normalized hysteresis loops for the braced frames are shown in Figure 7.16. Note that the model with a kl/r of 120 has less inelastic buckling compared to the kl/r of 60 model, and considerable overstrength.

Table 7.1 Median response parameters for varying hazard levels, for buckling models (T = 0.5 sec), and bilinear models (T = 1.0 sec).

Hazard	Model	$S_{D,ELASTIC}$ (in.)	S_A (g)
50% in 50			
	Buckling	1.52	0.60
	Bilinear	3.47	0.35
10% in 50			
	Buckling	2.99	1.18
	Bilinear	7.62	0.77
2% in 50			
	Buckling	4.29	1.69
	Bilinear	13.27	1.34

Table 7.2 Parameters for buckling models.

Model	A (in^2)	L (in)	F_{cr} (ksi)	m ($k*sec^2/in$)
kl/r=60	365	331	44.1	416
kl/r=120	718	928	15.7	292

Table 7.3 Parameters for bilinear models.

Model	K (k/in.)	F_Y (k)	m ($k*sec^2/in$)
Bilinear	475	137	1

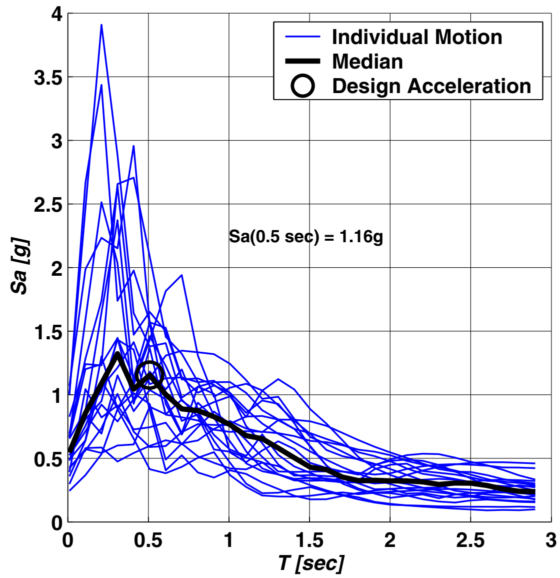

Fig. 7.14 Median pseudo spectral acceleration for Los Angeles area having a 10% probability of exceedance in 50 years. All spectra were computed assuming damping (ξ) was set to 5% of critical.

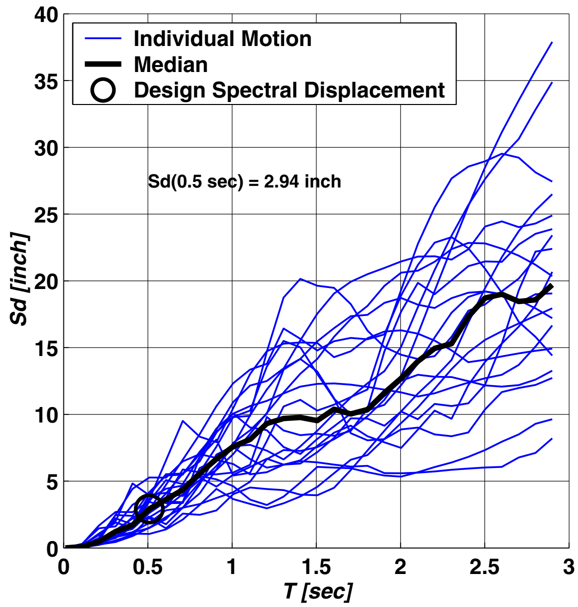

Fig. 7.15 Median pseudo spectral displacement for Los Angeles area having 10% probability of exceedance in 50 years. All spectra were computed assuming damping (ξ) was set to 5% of critical.

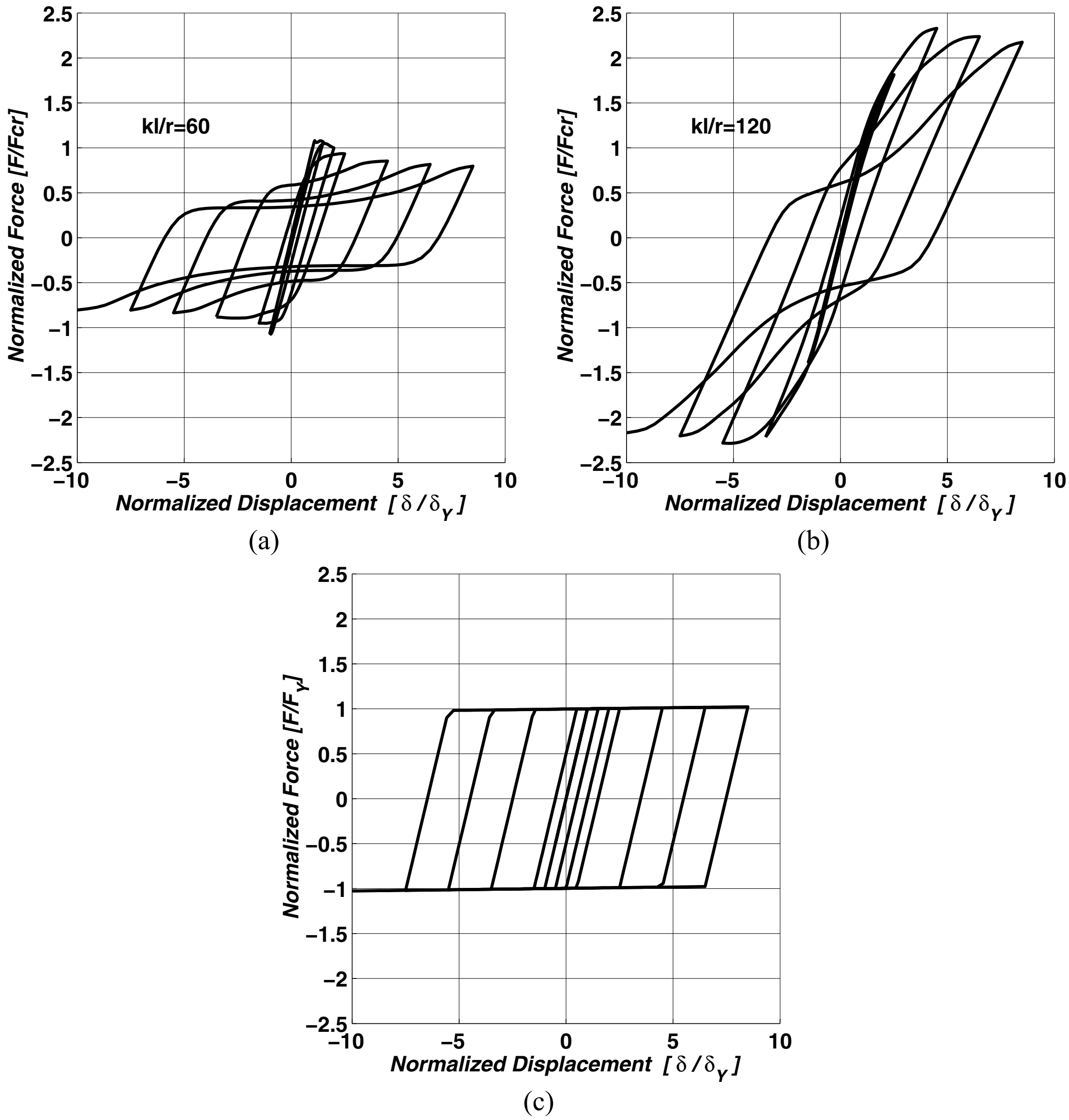

Fig. 7.16 Hysteresis for designed SDOF models: (a) buckling system with *kl/r* = 60; (b) buckling system with *kl/r* = 120; and (c) bilinear model.

7.3.3 Demand Assessment

The three analytical models were subjected to all 60 ground motions representing different hazard levels for the Los Angeles area. For the purpose of this simple example, a single engineering demand parameter EDP was used, corresponding to the displacement ductility demand (μ). This EDP depends not only on peak displacements but also on the yield displacement, which in turn depends on the stiffness and strength of a system. Thus, use of such an EDP requires careful interpretation. How these EDPs were used for this example will be discussed in Section 7.3.4 on damage assessment. Other EDPs can be used, such as interstory drift ratio, member strain, permanent lateral displacements, and so on.

Engineering demand parameters based on peak displacement ductility demands are shown for the three models as a function of ground motion intensity (IM = $S_{D,ELASTIC}$) in Figure 7.17. The estimates of the yield displacements can be made from the SDOF values listed in the tables above. Linear regressions were performed on the data points subject to the constraint of a linear fit through the origin ($S_{D,ELASTIC} = 0$, $\mu = 0$). Equation (7.7) shows this regression, where m is the parameter that minimizes the error between the EDPs ($E\hat{D}P$) and the spectral displacement ($\hat{S}_{D,ELASTIC}$) (Mackie 2004). The data have a considerable scatter about the relation given by this equation, resulting in a significant standard deviation, σ. The parameters m and b, along with σ (in log space) are shown below in Table 7.4. The slope m for the buckling model with a kl/r of 120 is somewhat less than that for kl/r of 60. In addition, the values of b and σ are significantly lower. Similarly, the values of m, b, and σ are all significantly lower for the bilinear (moment-frame) model. Thus, for the same intensity measure ($S_{D,ELASTIC}$), moment frames would be expected to have lower displacement ductility demands. Because of the longer period of the bilinear structure, its value of $S_{D,ELASTIC}$ for a given hazard level would be expected to be higher than for the buckling systems. Thus, moment frames for the same seismic hazard could have higher ductility demands than braced frames, resulting from larger intensity. Similarly, it is important to note that a lower ductility demand does not necessarily mean a lower peak lateral displacement, since the yield displacement of a moment frame may be larger than for a braced frame.

$$\ln(E\hat{D}P) = m \ln(\hat{S}_{D,ELASTIC}) + b \tag{7.7}$$

Table 7.4 Regression values for peak displacement ductility demands for three types of SDOF models.

Model	m	b	σ
Buckling, *kl/r* = 60	1.39	0.94	0.65
Buckling, *kl/r* = 120	1.33	0.79	0.47
Bilinear	0.98	-1.19	0.31

Equation (7.7) can be used to estimate the expected ductility demands for different hazard levels (represented by IM or $S_{D,ELASTIC}$ values). The particular values of $S_{D,ELASTIC}$ for three basic hazard levels considered here for the three systems are shown in Table 7.1.

Because a lognormal distribution of EDPs given an IM is assumed, Equation (7.7) and the parameters in Table 7.4 can also be used to estimate the probability of exceeding a particular value of EDP given an IM (Luco 2002; Mackie 2004). To illustrate this, we will compute the probability of exceeding a ductility of about 4 (i.e., $\mu^* = 4$) for either braced-frame system and 1 (i.e., $\mu^* = 1$) for the moment-resisting frame. These values of μ^* for the braced-frame system ($T = 0.5$ sec) and bilinear system ($T = 1.0$ sec) are thought to be similar drifts for real systems. That is to say, a braced-frame building designed for a reasonable seismic hazard in California would have a yield displacement around 0.25%, whereas a bilinear (e.g., moment-frame) system design for the same hazard is likely to have a yield displacement of about 1%. As such, the two ductilities are thought to cause similar levels of damage to interior nonstructural components, which corresponds to roughly 1% drift in a physical system.

Assuming a lognormal distribution of EDPs for given IMs and using the computed parameters for the regression equation, the probability of exceeding these ductilities for given seismic intensity, $S_{D,ELASTIC}$, is plotted in Figure 7.18.

With these preliminary data, we can now determine the probability of exceeding these displacement ductilities for different target hazard levels (as shown in Table 7.1) for each of the SDOF models. These results are tabulated in Table 7.5. Interestingly, the probabilities of exceeding the μ^* ductility demand for the 10% and 2% in 50-year hazard levels are larger for the bilinear system than for the buckling models. As can be seen in Table 1.1, the value of $S_{D,ELASTIC}$ is much higher for the moment frame than for the braced frames, resulting in the greater probabilities; however, the μ^* ductility demand corresponds to a displacement ductility of 4 for a representative braced frame but only the onset of yielding for a representative moment frame.

Table 7.5 Probabilities of exceeding $\mu = \mu^*$ for various hazards.

Model	μ*	Period (sec)	50 in 50	10 in 50	2 in 50
Buckling, *kl/r* = 60	4	0.5	57%	89%	96%
Buckling, *kl/r* = 120	4	0.5	47%	92%	98%
Bilinear	1	1.0	53%	99%	99.9%

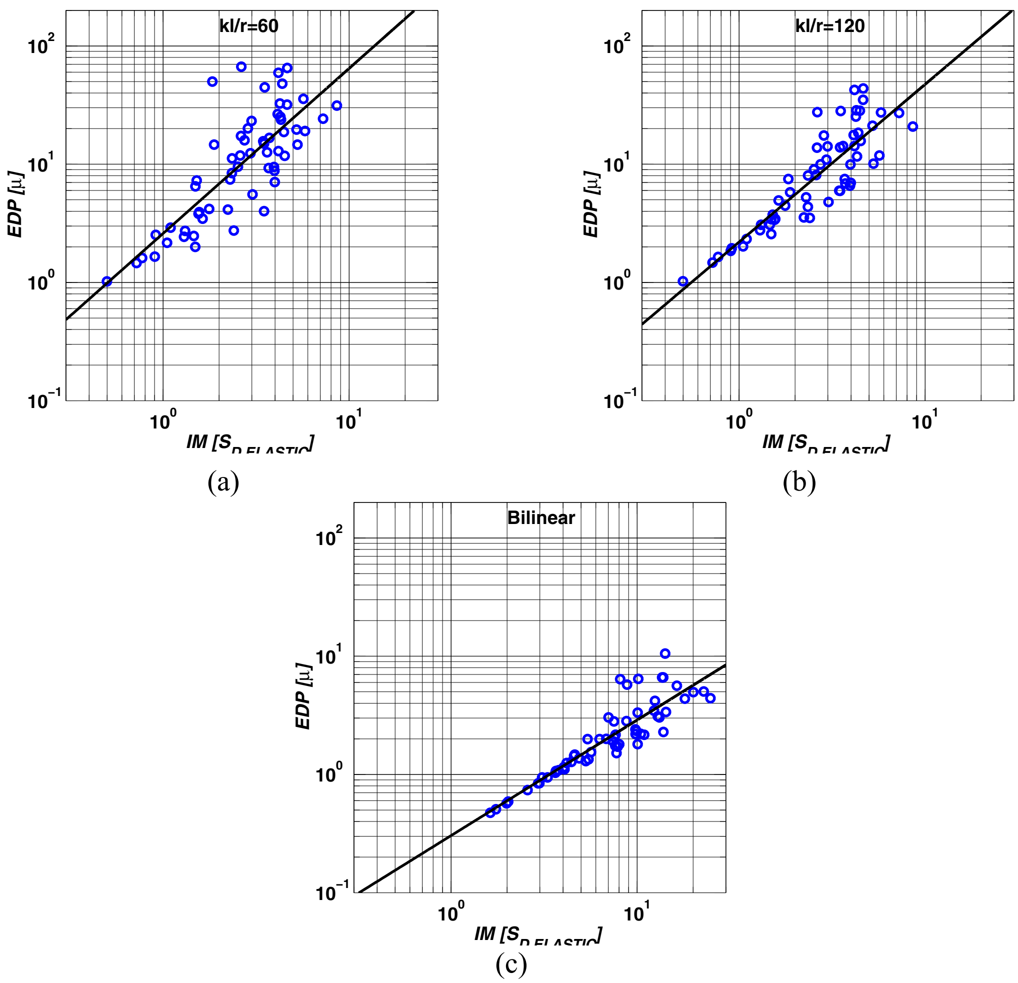

Fig. 7.17 Engineering demand parameters for varying ground motion intensity: (a) buckling element with *kl/r* = 60; (b) *kl/r* = 120; and (c) bilinear model.

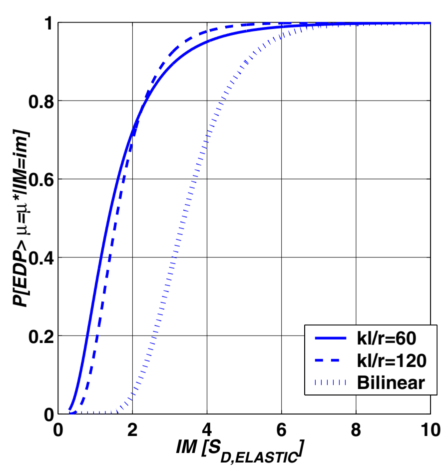

Fig. 7.18 Probability of exceeding $\mu^* = 4$ (SDOF buckling models), and $\mu^* = 1$ (SDOF bilinear model) given ground motion intensity ($S_{D,ELASTIC}$) .

7.3.4 Damage Assessment

Once we determine the parameters that define the expected EDPs given a specific IM, we can assess the likelihood of reaching a particular damage state associated with the selected EDP. To do these computations for this simple example, we will use a direct integration method outlined by (Mackie and Stojadinović 2004). For this example, we will look at the damage condition associated with a post-earthquake need to replace the braces for the braced-frame systems, and with repairing the moment connections in the moment-resisting frame. To simplify this example, we will say that 0.5% drift ($\mu^* = 2$ assuming a yield drift ratio of 0.25%) in a braced structure will trigger the replacement of braces. This is not associated with fracture of the braces, but rather excessive permanent lateral brace displacement. For the moment frame, we will represent the fracture of a pre–Northridge connection or the development of local buckles requiring repair by attaining or exceeding 2% drift ($\mu^* = 2$ assuming a yield drift ratio of 1%). Thus, our damage assessment is Boolean in nature: repair is either triggered or not.

We will assume a lognormal distribution for each of the events that trigger replacement or repair. Because it is more certain that a brace will buckle and retain a permanent sway at a drift of 0.5%, leading to its necessary replacement, the assumed lognormal dispersion defining the aleatory uncertainty is chosen to be a relatively small value (σ = 0.1). Similarly, the phenomena that would trigger fracture of a pre–Northridge beam-

Table 7.6 Lognormal distribution parameters for failure.

Model	*median*	σ
Buckling	ln(2)	0.1
Bilinear	ln(2)	0.4

column connection (or large local buckles in a newer connection) are not as well understood as the brace buckling phenomena; thus, its dispersion is assumed to be much larger (σ = 0.4). The parameters defining the lognormal distribution are shown in Table 7.6 and the cumulative density distributions of each of these are plotted in Figure 7.19.

The following integration was performed to determine the damage fragility for both of the damage states and the SDOF models (Mackie and Stojadinović 2004).

$$P[DM < repair \mid IM = im] = \int_{edp} P[DM < repair \mid EDP = edp] \;\; d\,P[EDP < edp \mid IM = im] \;\, d\,edp \tag{7.8}$$

The first term in the integrand is the cumulative density function of the probability density function shown in Figure 7.19, and the second integrand is the probability density function of the EDP ($\mu = 2$) given the seismic intensity.

This direct integration results in the fragilities for the three models and is shown in Figure 7.20 As noted previously, since the moment-frame and braced-frame structures have different periods, the IM value appropriate for a particular hazard value is different for the two systems (Table 7.1). The specific probabilities of reaching the specified damage states for the three basic hazard levels considered herein are listed in Table 7.7 for the three models. From this we can see that the probability of having to repair either braced-frame system is very high for even a small or moderate hazard level. The simple bilinear model has slightly more than 50% probability of fracturing a pre–Northridge connection (or buckling a new connection) and necessitating repair at the design-level event.

Table 7.7 Probabilities of reaching a state where replacement or repair is necessary.

Model	μ*	*Period (sec)*	*50 in 50*	*10 in 50*	*2 in 50*
Buckling, $kl/r = 60$	2	0.5	90%	99.9%	99.9%
Buckling, $kl/r = 120$	2	0.5	91%	99.9%	99.9%
Bilinear	2	1.0	9.5%	56%	89.6%

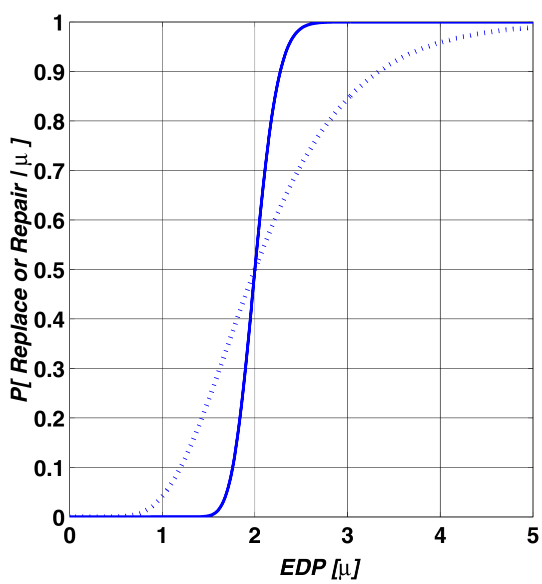

Fig. 7.19 Probability of damage given an engineering demand parameter, μ.

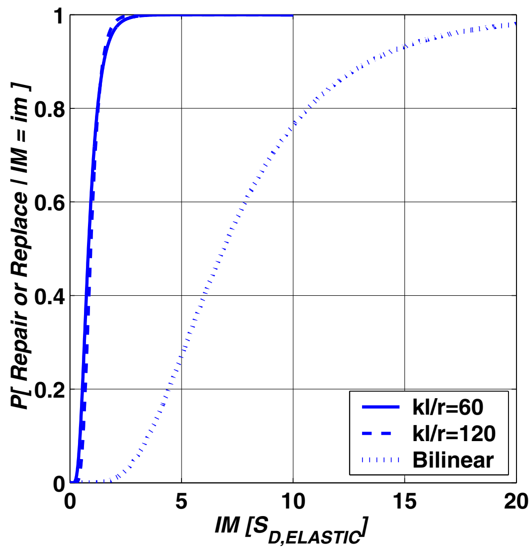

Fig. 7.20 Probability of damage given an seismic intensity measure, $S_{D,ELASTIC.}$

7.4 CONCLUDING REMARKS

From the results in this chapter, it is apparent that PBEE can be used in conjunction with reliable numerical models and probabilistic estimates of earthquake hazard, to gain insight into the various structural parameters that influence response and performance. For example, it is clear that period and brace slenderness may have an important effect on behavior. The shorter periods of low-rise braced-frame structures were demonstrated (as done previously by many investigators) to require higher design forces or lower effective R-values than moment frames of comparable height to achieve a specified displacement ductility value. The R-μ relations for longer-period SDOF moment and braced-frame systems were more similar. These observations suggest the need for more research to assess the desirability of using R-values for braced frames that decrease with decreasing period.

The PBEE methodology also provides a convenient means to compare the performance of different structural systems on a consistent basis. The simple SDOF examples presented demonstrated that the braced-frame systems tend to sustain damage requiring replacement of braces for even low seismic hazard events (i.e., representative of 50% in 50-year probabilities of exceedance). The probability of requiring this level of repair in a moment-resisting frame is not reached until a 2% in 50-year hazard level is considered.

The limitations of the studies presented in this chapter need to be recognized and the presented data carefully interpreted. While the examples reflect structures having periods associated with three-story buildings, only a single-degree-of-freedom numerical model is used in the analyses. Moreover, to achieve the same period, kl/r and other stipulated structural characteristics, the systems analyzed and compared may have different masses, lengths, strengths, and so on, and some of the structures may be infeasible or impractical to actually construct. In the examples presented, the assumptions introduced made it desirable to examine only a few engineering demand parameters and damage measures. Thus, it may be better to carry out such examples on actual multi-degree-of-freedom structures designed to specified criteria and using realistic member sizes. In such systems additional meaningful engineering demand parameters and damage measures can be considered. These issues will be examined in the next two chapters.

8 Performance-Based Earthquake Engineering Analysis of Multi-Story Steel-Braced Frame Structures

8.1 INTRODUCTION

As noted previously, a series of benchmarking studies were carried out following the 1994 Northridge, California, earthquake to assess the performance of steel moment-resisting frames (see FEMA 2000a). Given the current state of uncertainty regarding the likely behavior of conventional concentrically braced frames as discussed in Chapter 2, and the rapid evolution of design guidelines and the increasing availability of new enhanced bracing elements, this methodology was used in Chapter 3 to conduct a preliminary performance-based assessment of several SCBF and BRBF systems. While the results presented were illuminating, they were based on approximate analyses that incorporated many simplifying assumptions. In particular, the results suggested the need to improve modeling of bracing elements, especially with regard to capturing the deterioration or failure associated with member buckling and low-cycle fatigue. The results in Chapters 4–6, introduced an improved fiber-based model and validated its capabilities to predict the behavior of a number of buckling and buckling-restrained braces and braced frames. Chapter 7 examined some of the capabilities and special issues associated with applying PBEE to concentrically braced frames. As such, the groundwork necessary to reconsider the performance-based earthquake engineering assessment undertaken in Chapter 3 has been laid.

This chapter presents a series of extended benchmarking and PBEE studies. These studies focus on improving understanding of the risks associated with low- and mid-rise steel-braced frames having conventional buckling as well as buckling-restrained braces. These studies are limited to 3- and 6-story buildings having braces arranged in a stacked chevron configuration. Quantitative comparisons are made to the performance expected of post-Northridge moment-resisting frames.

In this chapter, the performance of braced steel frames will be assessed using the basic procedure used in Chapter 3 with the following enhancements:

1. A large-displacement beam-column element developed in Chapters 4 and 5 will be used to account for the effects of global brace buckling and the effects low-cycle fatigue for both beam-column elements and for buckling brace elements. It is important to note four key limitations of this model:
    a. The damage mechanics approach used in this element to model low-cycle fatigue does not account for fracture-mechanics-related phenomena. No stress concentrations, initial imperfections, or material toughness properties are assumed. Rather, a damage-mechanics approach is employed where, as an artifact of loosing individual fibers due to low-cycle fatigue, stresses are concentrated over a smaller portion of the cross section, leading to more rapid deterioration of an element.
    b. The beam-column fiber model developed assumes that plane sections remain plane, even at very large inelastic deformations. Thus, the substantial changes in the shape of a cross-section, and the increased local strains, when severe local buckling occurs are not taken into account. As such, the mechanical and fatigue parameters used in the model are calibrated to mimic observed behavior. Given that, it is not likely that all aspects of behavior can be realistically modeled once severe local buckling occurs.
    c. Fatigue calibration has been performed primarily for 6×6x3/8 HSS elements. As such, the modeling parameters previously identified are not strictly applicable to members having other sizes or shapes. Further refinement of input parameters is readily possible by calibrating the model to other data based on braces with different proportions, shapes, and width-thickness ratios on braces filled with various materials and perhaps even on beam-to-column connections. (e.g., Archambault 1995; Celik et al. 2004; Gugerli and Goel 1980a; Lee and Goel 1987; Roeder 1989; Roeder et al. 2005; Shaback and Brown 2003; Stojadinović 2003; Tsai et al. 2004; Zayas et al. 1980a ; Zayas et al. 1980b for previous testing conducted on various shapes and proportions).

d. The modeling of gusset plates and adjacent beam-to-column connection regions can also exhibit complex inelastic behavior modes, including yielding, buckling and rupture. These phenomena have not been explicitly considered in the development of the beam-column fiber element. The experimental results have shown that connection regions can control the ultimate failure modes of a braced-frame structure. As such, caution is needed in interpreting subsequent results, as these modes of failure will be treated only approximately.

2. Large-scale testing of steel-braced frames having buckling-restrained and conventional buckling braces (see Chapter 6) has demonstrated the ability of using these improved models to predict a number of key engineering damage parameters useful for characterization of damage. Thus, the results will be presented below to examine a number of performance measures in addition to collapse prevention.
3. The performance-based assessment methodology used in this chapter will be extended from that used by the SAC/FEMA steel project (see Chapter 3) in keeping with the improvements developed by the Pacific Earthquake Engineering Research Center (e.g., see also Krawinkler 2002) and others. This approach gives the analyst more freedom to choose decision variables that are more important to the stakeholder. A preliminary study based on SDOF systems has been presented using this approach in Chapter 7.

This chapter will assess the following important characteristics of braced-frame building performance:

- As discussed in Chapter 1, structures having relatively short fundamental periods appear to be disproportionately affected by strong ground shaking. For this reason, a series of three- and six-story SCBF and BRBF models will be again examined to explore this behavior in more detail.
- Models of SCBF buildings including the effects of low-cycle fatigue will be compared with identical models that do not account for the effects of fatigue. This will help quantify the importance of considering fatigue life in estimating braced-frame behavior.
- Structures designed with buckling-restrained bracing members using a force reduction factor (R value) of 8 will be analyzed (Sabelli 2000). These structures do not experience the deterioration of stiffness and strength associate with brace buckling and are much more resistant to the effects of low-cycle fatigue. Thus,

comparison of SCBF and BRBF behavior for comparable circumstances will provide insight into the effects of stiffness and strength deterioration.

- Modern detailing practices often omit reinforcement at the reduced net area section that may occur where braces connect with gusset plates. As such, performance assessments will be undertaken below for structures modeled as having and not having reduced neat area region reinforcement. Modeling of the reduced net area region will follow the approximate method developed and calibrated in Chapter 5.
- As discussed in Chapter 2, a number of braced-frame buildings, such as Oviatt Library (WJE 1998), have withstood the effects of severe earthquakes with little damage to the bracing elements, but with evidence of significant vertical displacements at the base. Thus, the effects of base plate uplift (rocking) on a braced-frame structure are considered in an approximate manner in some of the analyses presented below.
- Lastly, the performance of concentrically braced steel structures will be compared against that of similar moment-resisting frames. The moment-frame designs are adopted from the SAC steel project and are representative of typical early post-Northridge designs (FEMA 2000b).

8.2 MODEL BUILDINGS

A total of nine model frames, representative of three- and six-story concentrically braced frames having different lateral-load-resisting systems or different modeling assumptions, were subjected to lateral excitation from 60 ground motions, representing seismic hazard levels ranging from frequent to very rare. Two additional moment-frame systems were considered to provide a frame of reference for assessing performance. A short description of these buildings and their analytical modeling assumptions is provided in Table 8.1–8.2 for the low-rise and mid-rise models, respectively.

Table 8.1 Key analytical assumptions for low-rise buildings.

ID	Number of Stories	Type	Net Section Reinforcement	Fatigue	Rocking Foundation
3VF	3	SCBF	Yes	Yes	No
3VNET	3	SCBF	No	Yes	No
3VNF	3	SCBF	Yes	No	No
3VRCK	3	SCBF	Yes	Yes	Yes
3VB	3	BRBF	Yes	Yes	No
3MRF	3	SMRF	N/A	Yes	No

Table 8.2 Key analytical assumptions for mid-rise buildings.

ID	Number of Stories	Type	Net Section Reinforcement	Fatigue	Rocking Foundation
6VF	6	SCBF	Yes	Yes	No
6VNF	6	SCBF	Yes	No	No
6VRCK	6	SCBF	Yes	Yes	Yes
6VB	6	BRBF	Yes	Yes	No
9MRF	9	SMRF	N/A	Yes	No

8.3 ANALYTICAL MODELING ASSUMPTIONS

For the performance-based analysis presented in this chapter, the model buildings described in Chapter 2 [i.e., those found in Sabelli (2000)] were modeled in OpenSees to include the effect of large displacement in the beam-column members, improved buckling modeling, the effect of reduced net area section reinforcement, the effect of low-cycle fatigue, and the effect of foundation uplift. The models and the ground motions used in the analyses are representative of low- and mid-rise buildings designed for stiff soil in the Los Angeles area. Assumptions about masses, design considerations, and building codes were identical to those employed in Chapter 3.

The beams and columns were modeled to include the effects of fatigue, as calibrated per previous experiments shown in Chapter 5 (Ballio and Castiglioni 1995). The analytical model in Chapter 5 was calibrated to a cantilevered column model using a beam-column element with three integration points. Thus, beams or columns (assumed to be acting in double curvature) were modeled using two nonlinear elements with three integration points per element. To trigger potential lateral buckling in columns, initial imperfections for the columns were introduced by offsetting the node at the midlength of the column transversely by the maximum allowable out-of-straightness permitted by the AISC LRFD (AISC 1993). For the beam and column models, a Menegotto-Pinto material model was again assumed, as described in Chapter 4, with a yield stress value of 55 ksi (i.e., R_yF_y). Each of the column cross sections contained four fibers along the flange depth, four fibers along the flange width, and four fibers along the depth of the web.

The two-dimensional discretization of the column cross section with 16 fibers per flange was done to account for possible out-of-plane buckling of the column between floors. The columns were laterally restrained at the floor levels (to prevent global out-of-plane instability of the structure). The columns and beams were assumed to be rigid torsionally. Because OpenSees does not model section warping and the beams are assumed to be laterally restrained along their top flange by a slab and laterally braced according to AISC requirements, the beam model does account for out-of-plane response. Because beams can rotate between stiffeners and stiffener details may not be able to fully restrain torsional movement, the assumed torsional rigidity of the beams is not necessarily correct as (e.g., see Tsai et al. 2004). The modeling of the beams results in the columns being fixed at the floor levels against rotation about a vertical axis. Gravity columns were linked to the right-most columns shown in Figures 8.4–8.5 utilizing a rigid truss element. While this modeling of column behavior is more refined than done in many other studies, it incorporates several important limitations as noted previously that should be considered in interpreting the results presented.

Conventional buckling braces were all modeled with 20 elements along the length of the brace. At each section, 4 fibers were used along the width of each flange and web, with 4 fibers used through the thickness (i.e., each section was represented by 64 fibers). The material model used was the Menegotto-Pinto material model with expected yield strengths of 60 ksi. Although the nominal brace yield strength is 46 ksi for ASTM A500 grade B, the observed yield strength per the studies by Yang and Mahin (2005) showed yield strengths similar to the 60 ksi value assumed here. The fatigue parameters used were those identified in Chapter 5. Rigid end offsets were taken from the location of the brace gusset plate "fold-line" to the centerline location in the beam-to-column connections. The region of the brace that is welded to the end of the gusset plate was modeled as a bare brace, and did not consider the additional stiffness/strength due to the gusset plates. The section representing the gusset plate fold-line was modeled by 8 fibers across the depth of the gusset plate and 8 fibers across its width, and the Menegotto-Pinto material model with a yield stress of 55 ksi was assumed. This modeling permitted simulation of in-plane frame action and out-of-plane buckling of the braces.

It should be noted that the fatigue parameters used in the brace element model have been successfully calibrated elsewhere to many quasistatic cyclic test results for 6×6×3/8 HSS braces using only two elements. Because of the range of brace sizes and slenderness ratios encountered in these parametric studies and the uncertainty in predicted strains extracted using two elements (see Chapter 5), it was thought that 20 elements per brace would be appropriate for these analyses. In addition, the size of buckling braces in the model buildings are similar to those tested; therefore, the modeling parameters used are felt to be reasonable. Note, however, for larger dimension HSS braces, the fatigue-related parameters used here may not be applicable. Thus, further refinement of brace modeling parameters is desirable in the future.

Except for the models where column base uplift is permitted, the base connections of the columns to the foundations were assumed to be perfectly rigid. Research in this area has led to many design alternatives and options for the design of base plate connections (e.g., see Astaneh-Asl et al. 1992; DeWolf and Bicker 2003; Drake and Elkin 1999; Grauvilardell et al. 2004; Honeck and Westphal 1999; Lee and Goel 2001). Because performance of the base plates during seismic loading for braced frames is still unclear when a combination of high axial loads and flexure are induced (WJE 1998), the models here have simply assumed an ideal rigid connection to remove this variable from the assessment of braced-frame performance.

Gravity columns were modeled as a single continuous leaning column with nodes located at the elevation of each floor. These nodes were rigidly constrained to the lateral displacements at each floor in the braced frame. The properties of the columns were assumed to be the weak-axis bending properties of all tributary "gravity-only" columns, including stiffness and strengths. The leaning column consisted of beam-with-hinges elements with hinge properties based on the dimensions of the gravity-only columns and a 55 ksi yield strength for the steel. The gravity-only columns were modeled with a pinned base.

As with the prior analyses, viscous damping was modeled as being stiffness and mass proportional. Coefficients were selected to achieve viscous damping equal to 4% of critical at the first and third mode. The stiffness proportional term was based on the initial stiffness values.

The same 60 records from the SAC/FEMA joint venture project on steel moment-resisting frames as used in previous analyses were used here. These are described in Section 8.4.

8.3.1 Special Concentrically Braced Frames

A total of seven single-bay analytical models representing special concentrically braced frames utilizing chevron-configuration braces were considered for the analyses. Four represented a three-story structure, while the other three represented six-story structures. Figure 8.1 contains a sketch of the geometry, node numbering convention, and element labeling convention used in the analysis. These conventions will also be used in the BRBF element modeling. The details concerning the models analyzed are presented below:

3VF and **6VF:** These analytical models represent three- and six-story special concentrically chevron-braced-frame structures, respectively. The brace proportions and details are identical to those described in Chapter 2, and are taken directly from Sabelli (2000). The analytical models allow for out-of-plane buckling of the braces and columns and contain fatigue parameters as outlined in Chapter 4 and 5, which were calibrated to the uniaxial and subassemblage tests. It is thought that these brace proportions and details are consistent with modern detailing practices.

3VNET: This analytical model is identical to the 3VF model listed above, except this model assumes no reinforcement of the reduced net area section. The fatigue parameters for the reduced net area sections are those described in Chapter 5.

3VNF and **6VNF:** These models are identical to 3VF and 6VF, except the effects of low-cycle fatigue are not included for the braces or the beams and columns. Lateral buckling of the braces or columns is considered, but rupture due to low-cycle fatigue is not. Thus, these analytical models represent "ideal" behavior of a system having braces with a particular slenderness ratio.

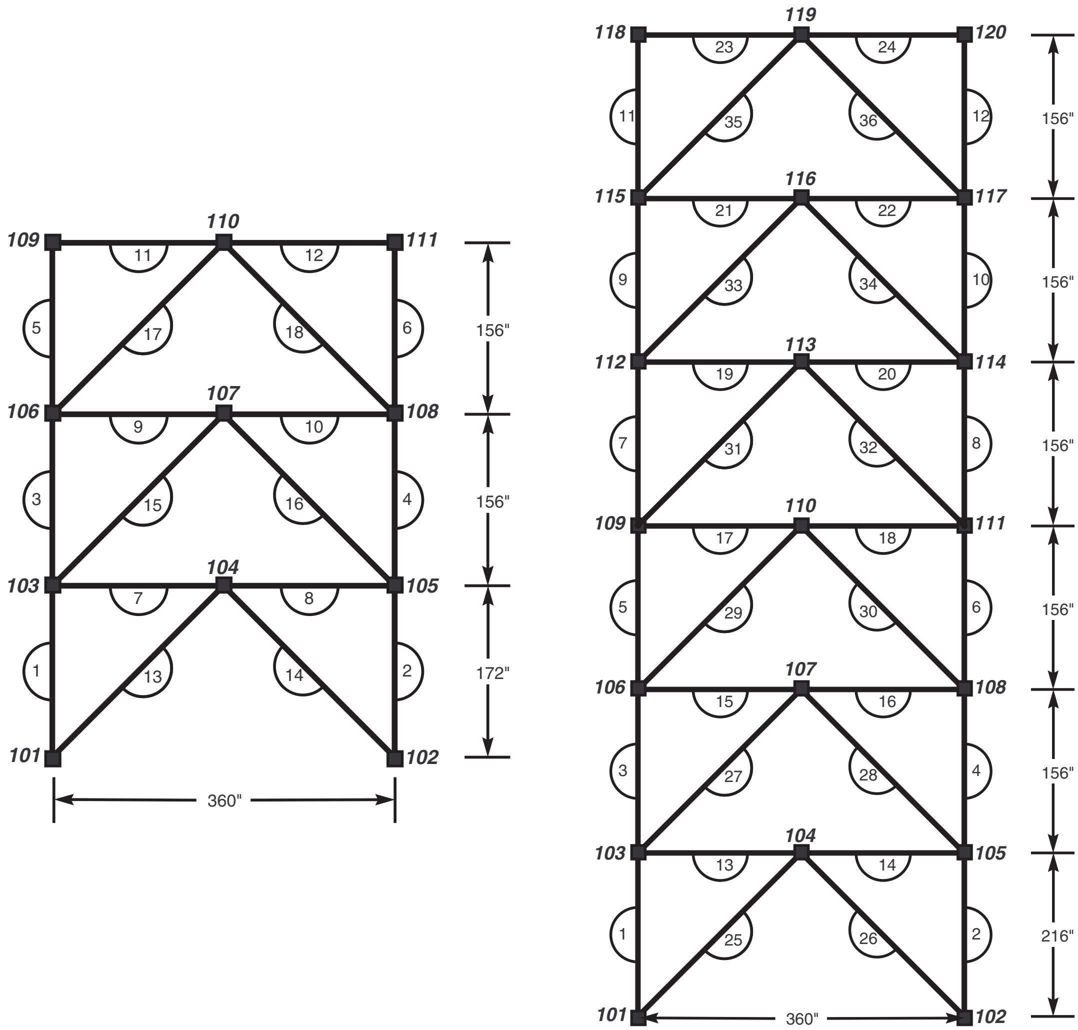

(a) (b)

Fig. 8.1 Elevation of (a) three-story and (b) six-story chevron frames from Sabelli (2000) along with element and node labels. Same configuration, node, and element numbering used for all SCBF and BRBF models.

3VRCK and **6VRCK:** These models represent the effect of column base uplift for SCBF systems otherwise identical to 3VF and 6VF. Figure 8.2 contains a sketch illustrating how the effects of rocking are modeled. A very stiff elastic no-tension spring was modeled as a zero-length element between the bottom column node and the base node. Thus, during uplift, there was no reaction in this spring element, but it acts as a rigid reaction when the gap closes. Lateral forces from the brace and column of the uplifting side of the model was transmitted to the other column (which is assumed to be in contact with the foundation) via a rigid, large-displacement truss. This allowed for the trajectory of motion for the base plate shown in Figure 8.2. The same modeling assumption was applied to both columns.

The lateral restoring force of this system is provided by the gravity loads supported by uplifting columns, and any structural action due to the adjacent beams restraining the uplift in the columns (due to bending and catenary actions). For the system considered, the large number of braced frames used, and the placement of the braced frames on the perimeter of the building, results in relatively small vertical gravity loads on the columns in the braced frames. Thus, they may tend to uplift readily even in small earthquakes. While the uplifting column results in nonlinearity, and possibly significant energy absorption, there are few built-in mechanisms that result in energy dissipation.

In general, the impact of the column with its base should have some energy dissipation associated with it. The elastic (rigid) boundary condition used here may result in more rebound and vertical impact effects than might be found in an actual structure.

Importantly, this structure was not explicitly designed considering the effects of uplift. For example, the increase in axial load in the column that remains in contact with the ground expected when the other column uplifts (and impact forces that may occur when it contacts the base following uplift) are not considered in the design, thereby resulting in possible overload conditions when these events occur. In addition, for new designs, many designers would install energy-dissipation devices in the vertical direction between the bottom of the column and base.

Note that as seen in Figure 8.2, significant lateral displacement of the upper stories of the rocking braced frame can occur with little axial deformation of the braces. Thus, rocking may reduce damage to the braced frame, but not to structural and nonstructural elements in other portions of the building. Damage may also be caused by the vertical uplift at the base plate (in structural, nonstructural, and MEP elements not designed to accommodate these displacement). As can be seen Figure 8.3, uplift will induce increased rotational demands on the connections adjacent to the uplifting frame.

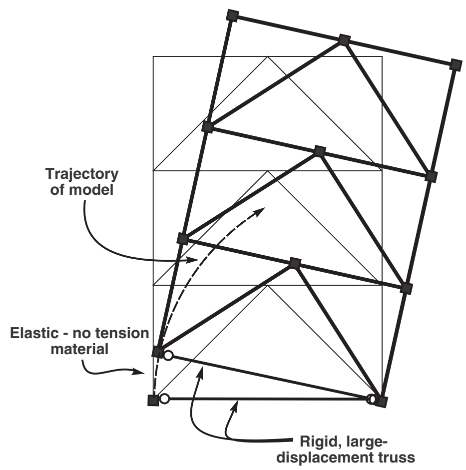

Fig. 8.2 Sketch of rigid body rotation mode of SCBF frame for 3VRCK and 6VRCK models. Shear at lifted column transferred to base via a rigid truss.

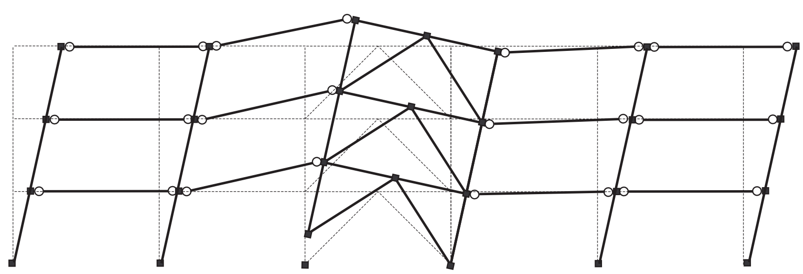

Fig. 8.3 Sketch of lateral displacement of a rocking braced frame. Note that although interstory drift of braced frame is relatively small, interstory drift of other floors remain the same. Also note larger vertical lift and consequential rotation demand of adjacent beams plastic hinges or pin connections.

8.3.2 Buckling-Restrained Braced Frames

The two buckling-restrained models considered are similar to those for the SCBF systems. They are described below:

3VB and **6VB:** These models represent three-story and six-story BRBF planar frames, respectively. They are the same as designed by Sabelli (2000) and analyzed in Chapter 3. The buckling-restrained braced frame models were modeled and calibrated as described in Chapter 3, 4, and 6, and as in Sabelli (2000). Brace yield strengths specified so that the brace design loads were achieved. Rather than using elastic elements to offset the BRBs from the center of the beam-column connections, the relatively small size of this offset compared to those in the BRBF test specimens suggested that a rigid offset would be acceptable. The effective yield length of the BRBs was taken to be 70% of the centerline-to-centerline dimension of the brace. This is representative of fairly typical construction details where the gusset plate, splice, and non-yielding portion of the brace remain elastic, and strains are concentrated in the central reduced area region of the braces. This modeling assumption results in slightly more rigid connections, as observed in Chapter 6; however, this stiffness change is not significant in the observed post-yield behavior of the brace (for more information about design and assumptions see Clark et al. 1999; López and Sabelli 2004; Sabelli 2000). Fatigue parameters for the braces were taken from the single test to failure as identified in Chapter 5.

8.3.3 Moment-Resisting Frame

Two welded steel special moment-resisting frames were modeled and analyzed as a baseline for comparison with the SCBF and BRBF models. The models were taken directly from post-Northridge designs developed by the SAC/FEMA Steel Project. The models are described below.

3MRF and **9MRF:** These three- and nine-story frame models represent low- and mid-rise frames that utilize special moment-resisting frames. These post-Northridge designs were taken from FEMA (2000b). Geometry and element and node conventions for the 3MRF and 9MRF are shown in Figure 8.4 and Figure 8.5, respectively. Fatigue modeling in the beam-column elements was calibrated as described in Chapter 5 for the beam-to-column flexural connections. The models presented here are representative of the M1 (centerline-to-centerline, e.g., no rigid offsets and panel zone modeling) model that can be found in the literature (FEMA 2000b). Fatigue modeling parameters for beam-column members were used for these analyses. It is important to re-iterate that the mechanics of fracture are not included in the fatigue model, and thus the beam-column connections do not include the effects of fracture, other than those that may be associated with low-cycle fatigue.

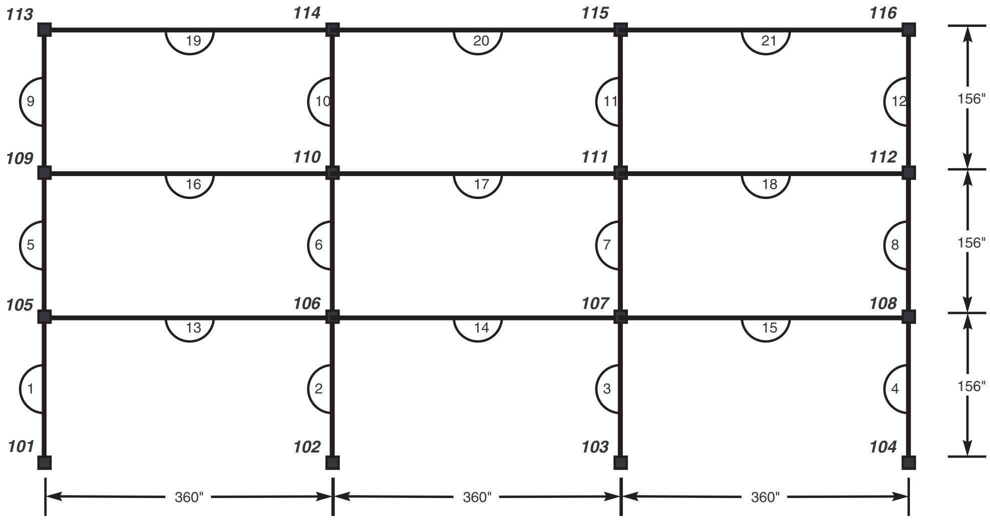

Fig. 8.4 Elevation of 3-story moment-resisting frame (FEMA 2000b).

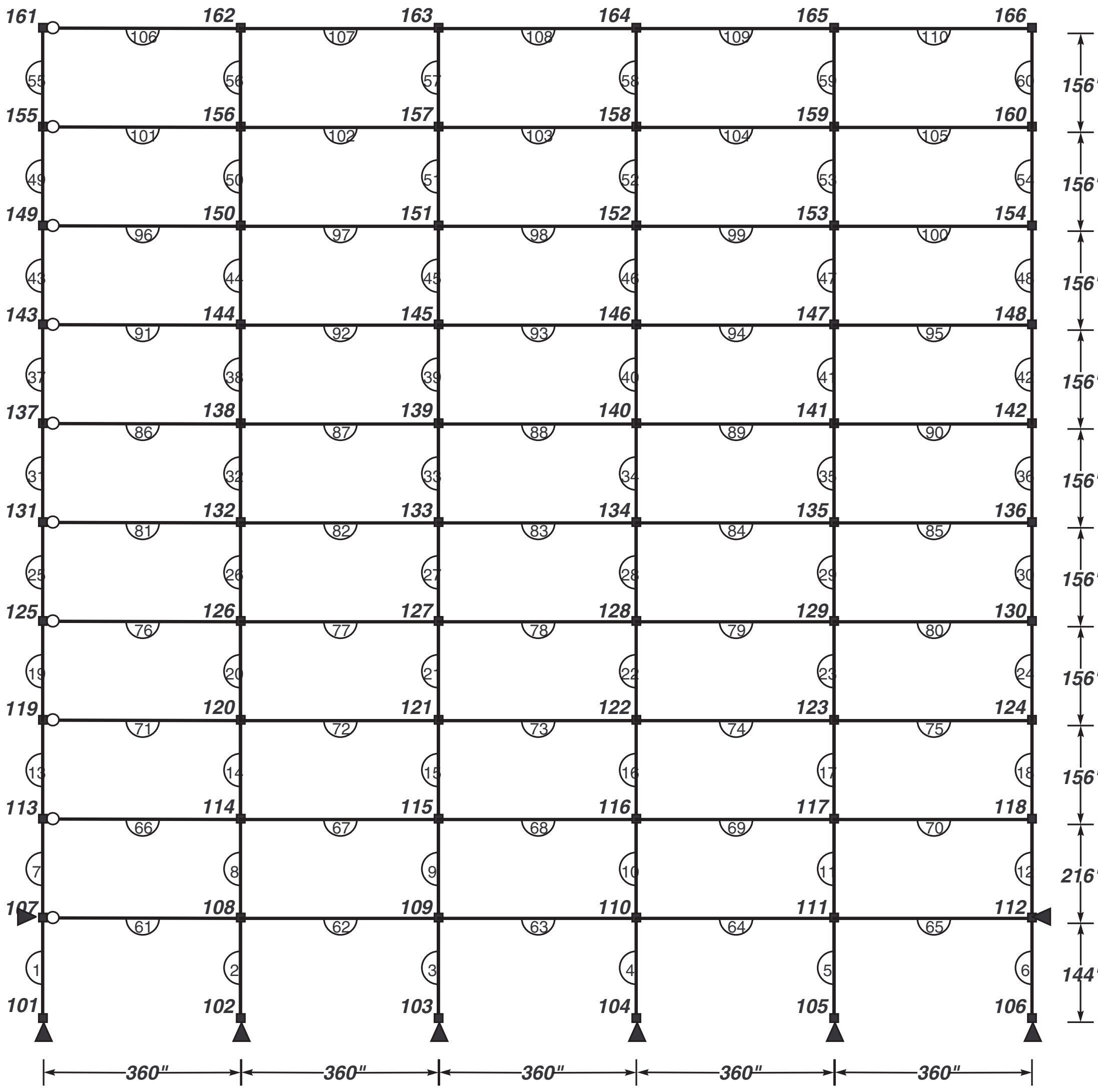

Fig. 8.5. Elevation of 9-story moment-resisting frame (from FEMA 2000b).

8.4 GROUND MOTIONS

The ground motions used to study the performance of concentrically braced steel frames in this study were developed by Somerville (Somerville 1997) and are representative of ground motions for soil type S_D for hazards corresponding to 2%, 10%, and 50% probability of exceedance in 50 years for downtown Los Angeles. Each of these hazard levels contains 10 pairs of ground motions, which have been scaled such that their average response spectrum matched the 1997 NEHRP design spectra of identical soil and hazard. The ground motion pairs were rotated from their original recordings into their fault-normal and fault-parallel components, then rotated 45° to avoid excessive near-fault directivity effects biasing individual analysis. More information about the ground motions used can also be found in Chapter 7 and in Somerville (1997).

8.5 PERFORMANCE OF LOW-RISE STRUCTURES

8.5.1 Case Study Example

In this section, the response results for the three-story structures are described for one of the records corresponding to a hazard of 2% probability of exceedance in 50 years. This record is LA25, which was based on a recording at the Rinaldi receiving station (soil type S_D) during the 1994 Northridge, California, earthquake. This record was scaled by a factor of 1.29 to be consistent with this hazard level (for more information about scaling, the reader is referred to Somerville 1997)

The roof displacement time histories are shown below in Figure 8.6 for all of the low-rise structures. Peak roof drifts and maximum computed interstory drifts are shown in Table 8.3. From this table and Figure 8.7, it is clear that the conventionally braced, fixed-base structures (3VF, 3VNF) have a strong inclination to concentrate damage in one story. For this particular record, the concentration of damage occurred in the lowest story. In contrast, the 3VRCK, 3VB, and 3MRF structures show a very uniform distribution of drift along the height of the structure. Interestingly, The 3VRCK model has the second largest roof displacement of the analytical models shown, but its maximum interstory drift is less than one half that of the conventional braced frames rigidly attached to the foundation (the interstory drift reported is computed with respect to the difference in lateral floor level displacement relative to a vertical reference line, and not with respect to a reference line that rotates relative to the base). This is due primarily to the even distribution of drift along the height of the structure. The rocking mechanism keeps the drifts in all of the floors uniform. As suggested in Figure 8.3, however, this may result in somewhat larger rotational demands for connections in adjacent bays. Also, it is interesting to note from Figure 8.6 that among all of the braced and moment-resisting frames considered, the braced frame permitting foundation uplift had the least residual displacement at the end of the earthquake record.

Table 8.3 Maximum recorded drift indices for models in LA25.

Model	Max. Roof Drift Index,%	Max. Interstory Drift Index, %	Ratio of Max. Interstory to Roof Drift Indices
3VF	3	7.3	2.43
3VNET	5	13.7	2.74
3VNF	2.9	7.1	2.44
3VB	3.2	3.3	1.03
3VRCK	3.5	3.7	1.05
3MRF	4.5	5	1.11

For the LA25 record, Model 3VB achieved the most uniform distribution of drift over its height. The maximum roof drift for Model 3VB is slightly greater than that for Model 3VF, yet the largest interstory drift for Model 3VB is less than one half of the maximum interstory drift of the 3VF model. This concentration of damage in the first story for 3VF can be seen in the displaced shapes that existed at the time when the maximum interstory drift was recorded (see Fig. 8.7). This figure plots the displaced shape with a magnification of 5 times in order to better visualize the displacement pattern and clearly shows the concentration of damage in the bottom story for the conventionally braced structures having a fixed base. It is interesting to note that the senses of the maximum displacements are identical for all of the models, except for the 3VRCK model, where it is reversed.

Figure 8.7 also suggests that the bottom floor beams yield severely for the fixed beam-to-column connection . As noted in Chapter 3, these structures were designed to the 1997 AISC seismic provisions (AISC 1997), which require the beam to be designed to resist the unbalanced forces resulting from the difference in effective tension and compression forces acting in the braces that intersect at the midspan. This computation is based on $0.3\phi_c P_{CR}$ for compression and P_y in tension. The AISC provisions and the beam design in the model buildings were based on the *nominal* yield strength of the specified materials.

The beam in the test specimen was conservatively designed to help avoid lateral or lateral-torsional buckling that would in an actual building be partially restrained by a concrete slab. Although the beam in the SCBF test specimen did not yield significantly during the tests, the post-buckling strength of the braces in the test became considerably smaller than $0.3\varphi P_{CR}$.

In the SNAP-2DX analyses shown in Chapter 3, the nominal yield stress of 46 ksi was used for material strength for the brace, and the predicted post-buckling strength by the brace element was close to the computed value of $0.3\varphi P_{CR}$. For this condition, the beams in the SNAP-2DX models in Chapter 3 did not yield significantly. Furthermore, the larger beam strength will place more tensile demand on the braces, and as mentioned in Chapter 5, the fracture model used in the Goel model is heavily weighted toward the tension excursions. The 2005 AISC seismic provisions use the expected yield strength for the analysis of the braces.

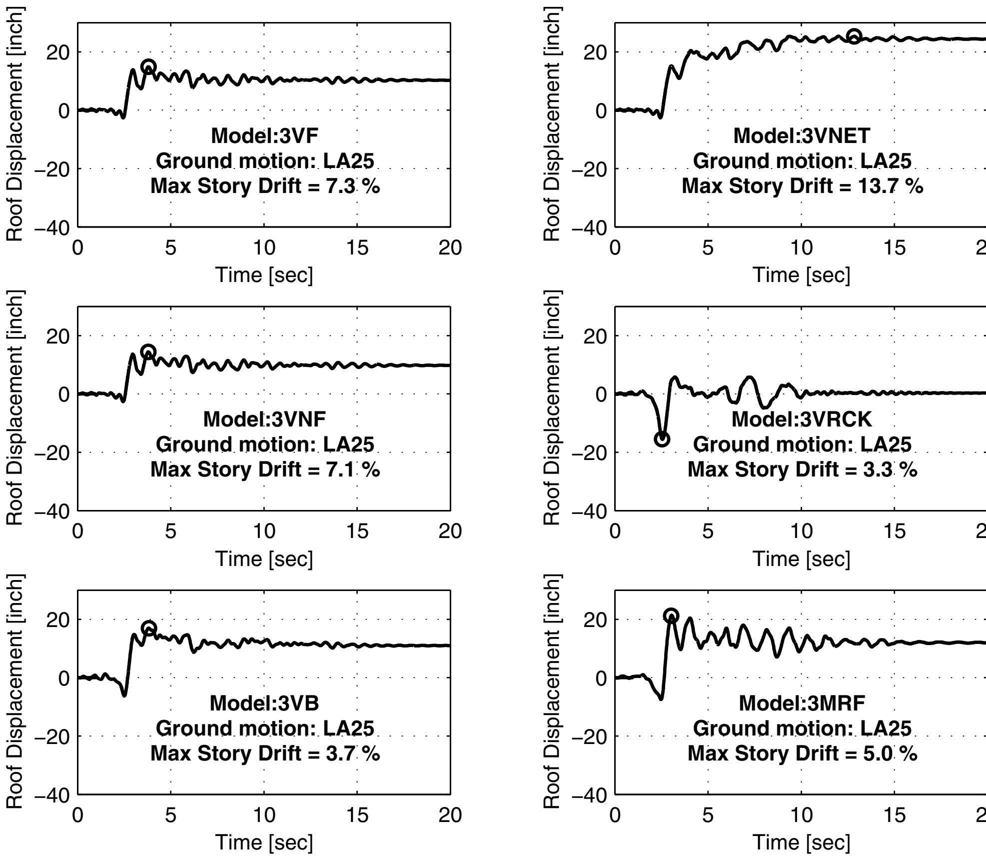

Fig. 8.6 Roof displacement time histories for LA25. Also indicated is time when maximum interstory drift occurs and its corresponding value.

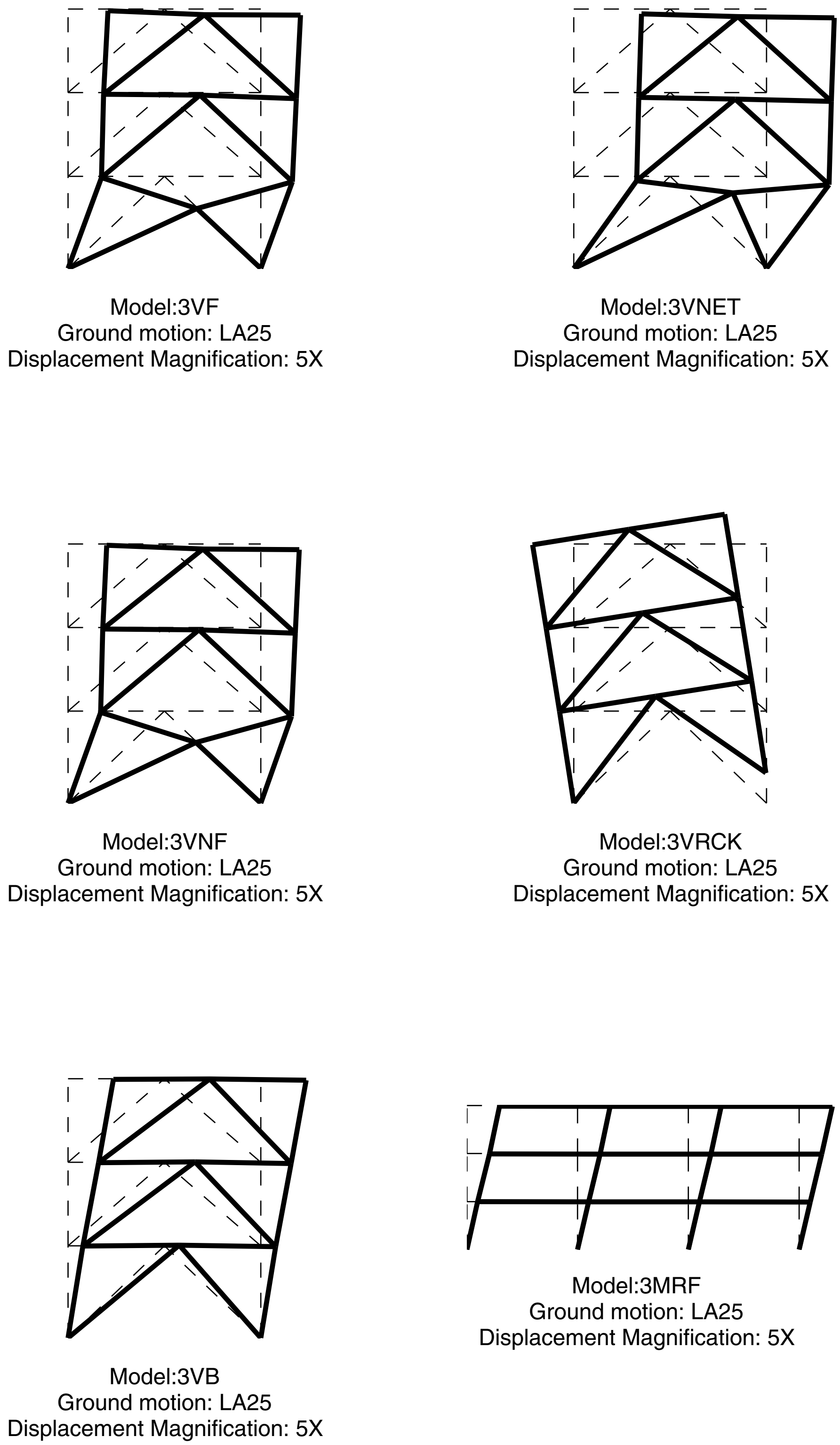

Fig. 8.7 Displaced shapes when maximum interstory drift indices reached for various structures excited by LA25.

For the LA25 record, none of the elements in 3VF model completely reached their low-cycle fatigue life and fractured. However, one of the lower braces in the 3VNET model (element 13 in Fig. 8.1) fractured at the net section, doubling the maximum interstory drift in the first floor. As will be shown later, in many of the cases where brace fractures occurred, collapse also occurred.

The brace hysteretic loops for brace elements 13 and 14 (see Fig. 8.1) are plotted in Figure 8.9 and Figure 8.9, respectively, for all models. Note that for the 3VB model, there is an initial tension yielding cycle in element 14 prior to the compression cycle. This excursion is significant, but does not occur for any of the conventionally braced steel structures. This is due to the vertical displacement of the beams in the conventional braced frame due to the large difference in the tension and compression loads once buckling occurs. The beam is designed to have strength to avoid yielding, but there is no limitation on the beam vertical displacement when the unbalanced brace forces are applied in design. This unbalanced brace force is relatively small in the BRBF, resulting in smaller tension displacements and larger compression displacements in the fixed-base SCBFs. When compared to the conventional models, model 3VB shows an even distribution of demand (one in compression, one in tension) in both of the braces.

Figures 8.8–8.9 also show that the lower-level level braces in Model 3VRCK remained elastic during the response. Thus, the ductility demands on the structural elements are reduced by the rocking action.

When comparing response to the 3MRF structure it is important to re-call that the drift ratio at yield for a typical MRF is roughly 1% (FEMA 2000a). Thus, the drift that is observed in the MRF corresponds roughly to a displacement ductility of 5. For a conventional buckling braced frame, the interstory drift ratio when the braces buckle is about 0.25%, thus the 3VF structure experienced closer to a displacement ductility of 29. For a yield drift of about 0.4% for the BRBF, the displacement ductility of 3VB is about 8. Thus, the increased drift for the SCBF system and its lower yield displacement results in a particularly high displacement ductility demand.

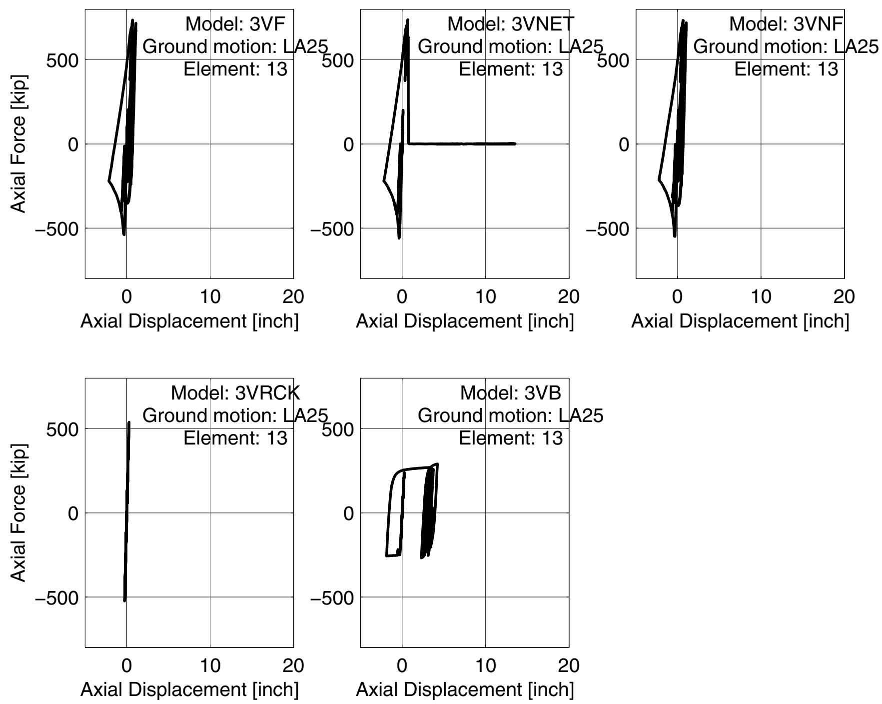

Fig. 8.8 Element 13 axial force–axial displacement relationship for ground motion LA25.

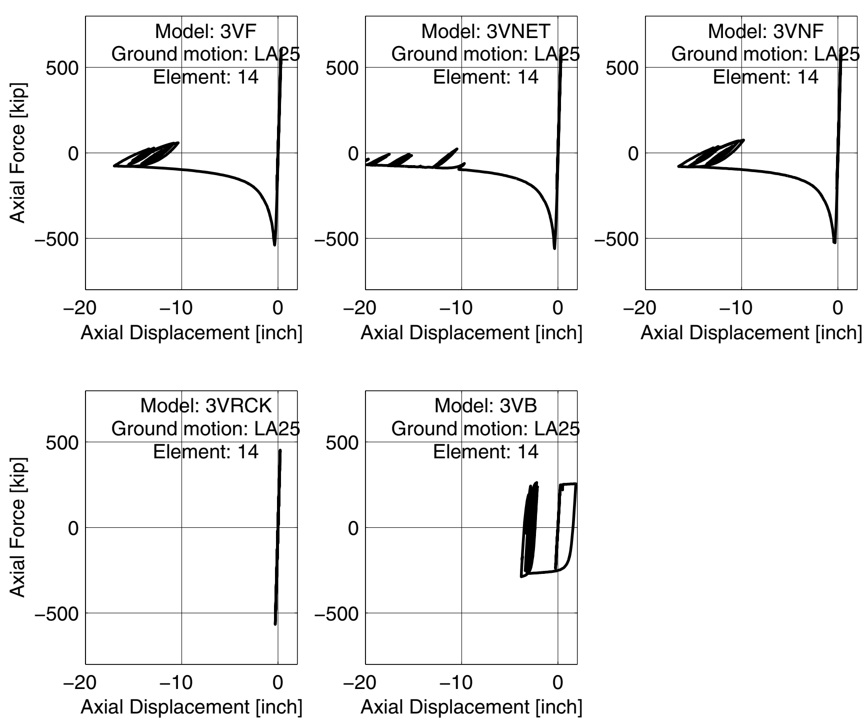

Fig. 8.9 Element 14 axial force - axial displacement relationship for ground motion LA25.

8.5.2 Statistical Evaluation of Seismic Demand

8.5.2.1 Collapse

The large displacement analysis considered in this evaluation allowed for explicitly modeling of global and local instability. For some of the ground motion excitations, OpenSees predicted an instability that led to “collapse.” Because of analytical analysis problems associated with very large displacements, collapse was defined herein as the condition when the vertical interstory distance between any two floors was reduced more than 100 in. Figure 8.10 is an illustration of a typical displaced shape when response is considered to be a collapse. Figure 8.10 shows the response to ground motion LA36. Note that the figure is plotting straight lines from analytical node output; the three-dimensional displaced shape is not captured in this figure.

The definition of collapse is subjective. For instance, a structure where the distance shortens between floors shortens by 100 in. but that remains stable in that configuration may not be considered a true collapse by some. On the other hand, some might consider a structure to have collapsed if the maximum interstory drifts during an earthquake or the permanent lateral drifts following an earthquake exceed 5 or 10%. Similarly, some would suggest that collapse would be defined by the stability of a structure during a reasonably expected aftershock.

Table 8.4 contains a list of the records that produced collapse for either the 3VF or 3VNET structure. While analyses of the other building models indicated the possibility of large lateral displacements, these did not trigger full collapse as defined above. Each of the ground motions that triggered collapse corresponded to a hazard level having a 2% probability of exceedance in 50 years.

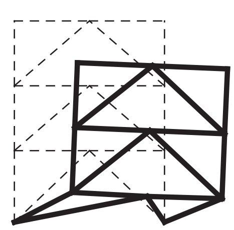

Fig. 8.10 Displaced shape of 3VF collapse due to LA34 ground motion time history.

Table 8.4 Records causing collapse for 3V and 3VNET structures.

Model	Records
3VF	LA21, LA35, LA36
3VNET	LA21, LA26, LA35, LA36, LA37, LA38

A careful examination of Table 8.4 shows that 3 of 20 records (15%) lead to collapse of the 3VF structure at the 2% in 50-year hazard level, and collapse occurs at twice that rate (30%) for the structures without reinforcement of the net reduced area regions. These probabilities are fairly large, but considerably smaller than computed in Chapter 3 using the SAC methodology. For the SAC procedure, collapse was identified by an "excessive" rate of increase in lateral displacement (5 times greater incremental lateral displacements than would be expected for an otherwise comparable elastic system for an increment in the intensity of shaking). Thus, the SAC methodology provides a measure of incipient collapse, whereas the criteria used above identifies only those structures that have actually collapsed.

8.5.3 Non-Collapse Response

A summary of the median (and standard deviation) of analytical response predictions of the models that did not collapse is provided in Table 8.7 below. This table lists the performance of the structures with respect to the following key global performance parameters: residual roof drift, peak interstory drift, and residual lateral capacity (expressed as a percentage of the original capacity), and the number of collapses recorded. For the braces, additional performance parameters are included: maximum out-of-plane displacement, maximum normalized fatigue damage index in any brace, and maximum fractured area as a percentage of initial gross cross-sectional area. These are then further classified by hazard corresponding to 50, 10, and 2% probability of exceedance in 50 years.

The median drift demands for all of the rigid base braced structures for the 50% in 50 year events are in the range of 0.4–0.6%, whereas the drift demands for the 3MRF structure for the corresponding hazard are roughly 1.4% (median demands being roughly elastic). This would be consistent with the design philosophy that stiffer structures would attract less drift demand. As noted previously, however, the yield drifts for the SCBF, BRBF, and MRF systems are on the order of 0.3%, 0.4%, and 1%, respectively, so that even at the 50% in 50-year hazard level, all of the systems are expected to yield slightly.

In the 10% in 50 year events, the drift demands for the braced frames are around 1.5% (not including 3VRCK), which is about a ductility of four to five, depending on the definition of yield displacement (for example, displacement at buckling load versus displacement at tension yield load), and that for the drift demand for 3MRF is roughly 2%, roughly a ductility of two. At this design-level hazard, lower displacements are expected in the braced-frame structure. Because of the sensitivity of the shorter-period braced-frame structure when subjected to ground shaking producing yielding, this relationship changes for the 2% in 50 year events, where the median demands for the conventional bracing members approaches 6% (for 3VF and 3VNF), where the median drift demand is 4.8 for the SMRF structure, and 3.8 for the 3VB structure.

Figure 8.11 further illustrates these trends for the different systems at different hazard levels by plotting the scatter associated with all of the interstory drift demands in all of the structures separated into the three different seismic hazard categories. Figure 8.11 also plots the median, and median plus standard deviation of the interstory drift demands. It is extremely important to note that this table may show misleading information, as the statistical results posted here are computed using the results from only the non-collapsed analysis. Thus, the analyses that predicted collapse are removed from the tabulation for that specific structure only.

Table 8.7 contains median drift demands when considering the collapsed cases for the 3NF and 3VNET cases. The 3VF structure has a smaller median drift compared to the 3VNET case when considering all records. Thus the relationship shown in Table 8.7 may be misleading, as the actual drift demand on a ground motion to ground motion basis is much larger.

Note that in Table 8.7 that the median value of maximum area fractured in any brace in a SCBF model that did not collapse is zero. This is computed by comparing the brace with the maximum fractured area in any brace for each ground motion run. For the non-collapsed cases, over half of the structures did not have a single brace where outer fibers fail. This would imply that there is a strong link between initial fracture of braces and ultimate collapse (similarly for peak and residual drifts). A similar relationship is observed for the 3VNET structure where the median value of the maximum area fractured is also zero. Recall that 6 of the 20 ground motions triggered collapse for these events.

Table 8.5 shows the incidences of complete brace fracture along with the corresponding ground motion excitation, and the number of the element that fractured (see Fig. 8.1 for location of element). Given the chevron bracing configuration used for the model, it is improbable that more than two braces can fracture in any event. As noted previously, the beams are not able to remain entirely elastic in the condition where the compression brace has fractured and the tension brace tries to yield, so that it is unlikely that two braces can fracture in a story except for large lateral displacements or multiple cycles of inelastic buckling. Table 8.5 and the absence of any collapsed instances for the 3VNF model provide a clear indication of the correlation between brace fracture and collapse. Efforts to increase the fracture resistance of braces should have an important impact on collapse resistance. It should be noted from Tables 8.4–8.5 that for 3VF that the structure collapsed completely or at least one brace fractured completely for 5 of the 20 records at the 2% in 50-year hazard level, and for 3VNET this increases to 11 out of 20 records.

Table 8.5 Brace fractures for 3VF and 3VNET showing corresponding non-collapse records (see Fig. 8.1 for element location).

Corresponding Hazard (% in 50 years)	3VF		3VNET	
	Record	Elements fracturing	Record	Elements fracturing
10	--	--	--	--
2	LA22	14	LA22	14
	LA28	13	LA25	13
			LA28	13
			LA32	14
			LA35	13,14

A key aspect of brace buckling in SCBF structures as detailed for these examples is the out-of-plane displacement of the braces. As noted before, this phenomenon can result in large amounts of damage to surrounding nonstructural elements. Median peak residual out-of-plane displacements for the braces (occurring mostly in the bottom story) were on the order of 30 in. for the 2% in 50 year events, and roughly 16 in. for the design hazard level shaking. Even for the 50% in 50 year events, most cases resulted in brace buckling, and the median maximum out-of-plane brace displacement was more than 5 in., certainly requiring brace replacement under serviceability-level events. The 3VRCK model had far less buckling, and thus the out-of-plane displacement demands were far smaller. This would correspond to the observations at CSU Northridge, where very little brace damage was observed, even though interstory drifts may have been very large (WJE 1998).

Figure 8.12 shows the median and standard deviation of interstory displacement demand as a function of height, categorized by hazard level, for the analysis cases that did not collapse. The concentration of damage is largely at the bottom floors for the conventional buckling systems, whereas the demand is more evenly distributed for the 3VRCK, 3VB and 3MRF systems. This is further evidenced by the distribution of damage shown along the heights of the structures in Figure 8.13. The normalized damage is defined as the maximum normalized damage in any cross section of any brace in a floor. The normalized damage is the weighted damage in a given cross section and is evaluated using Equation (8.1):

$$D_{normalized} = \frac{\sum_{i=1}^{N} A_i D_i}{A_{tot}} \tag{8.1}$$

Here, A_i is the area of the fiber i, D_i is the damage in fiber i after the dynamic analysis is complete. D_i ranges from 0 to 1, where a value of zero signifies no damage; a value of D_i equal to 1 signifies the fiber fatigue life is exhausted. A_{tot} is the total area of the cross section.

Table 8.7 indicates that the median maximum normalized damage is 26% for 3VF for the cases that did not collapse (recall that two records caused braces to completely rupture, and three more resulted in collapse) for the records having a 2% in 50-year probability of exceedance. In contrast, for this hazard level, the maximum normalized damage in the buckling-restrained braces in 3BF is 10 times smaller, and no collapse or brace fracture was detected. For the same hazard, the median maximum normalized damage for the 3VNET braces is 18% for all non-collapse records (14 records). As such, this highlights the sensitivity to collapse given a fracture. Thus, the 3VF accumulates damage in the plastic hinge regions during strong ground motions, whereas the Boolean behavior of the 3VNET works or not.

Table 8.6 Counted median values of drift demand of low-rise building response quantities for 3VF and 3VNET (including collapsed records).

ID	Hazard (% in 50 years)	Peak Interstory Drift at Any Floor (%)
3VF	2	5.9
3VNET	2	6.2

Table 8.7 Median (standard deviation) of low-rise building response quantities (non-collapsed runs only).

ID	Hazard (% in 50 year)	Residual Roof Drifts (%)	Peak Interstory Drift at Any Floor (%)	Maximum Residual Out-of-Plane Displacement of Any Brace (in.)	Maximum Normalized Damage in Any Brace Section	Max. Fractured Area In Any Brace (%)	Residual Lateral Capacity (%)	No. of Collapses
3VF	50	0 (0.1)	0.4 (0.7)	5.3 (6.7)	0.01 (0.07)	0 (0)	100 (5)	0
	10	0 (0.2)	1.6 (0.9)	16 (7.2)	0.14 (0.10)	0 (0)	96 (6)	0
	2	0.7 (1.0)	5.7 (2.4)	30 (9.6)	0.26 (0.3)	0 (0.36)	89 (18)	3
3VNET	50	0 (0.1)	0.3 (0.7)	4.7 (7.1)	0.01 (0.08)	0 (0)	97 (4)	0
	10	0.1 (0.2)	1.5 (0.9)	16 (7.2)	0.13 (0.12)	0 (0)	92 (5)	0
	2	0.5 (1.6)	4.0 (3.7)	30 (9.4)	0.18 (0.40)	0 (0.5)	78 (26)	6
3VNF	50	0 /0.2)	0.4 (0.7)	5.0 (6.9)	--	--	100 (2)	0
	10	0 (0.2)	1.5 (0.9)	16 (7.2)	--	--	96 (6)	0
	2	1.1 (1.1)	5.7 (3.0)	35 (10.4)	--	--	90 (6)	0
3VRCK	50	0 (0)	0.7 (0.4)[1]	0.3 (2.0)	0 (0)	0 (0)	100 (0.13)	0
	10	0 (0)	2.6 (0.1)[1]	4.6 (2.6)	0 (0)	0 (0)	100 (0.11)	0
	2	0 (0)	5.1 (3.0)[1]	8.3 (3.5)	0 (0.12)	0 (0.12)	99.7 (0.9)	0
3VB	50	0 (0.1)	0.6 (0.6)	--	0.002 (0.003)	0 (0)	100 (0)	0
	10	0.1 (0.4)	1.3 (0.7)	--	0.006 (0.004)	0 (0)	100 (0)	0
	2	2.1 (2.2)	3.8 (2.1)	--	0.03 (0.02)	0 (0)	100 (0)	0
3MRF	50	0 (0.2)	1.4 (0.8)	--	--	--	100 (0)	0
	10	0.2 (0.4)	2.1 (0.7)	--	--	--	100 (0)	0
	2	1.2 (2.0)	4.8 (2.2)	--	--	--	100 (0)	0

[1]Values of drift with respect to rocking frame are 0.18 (0.11) for 50 in 50, 0.28 (0.09) for 10 in 50, and 0.5 (0.29) for 2 in 50 year events.

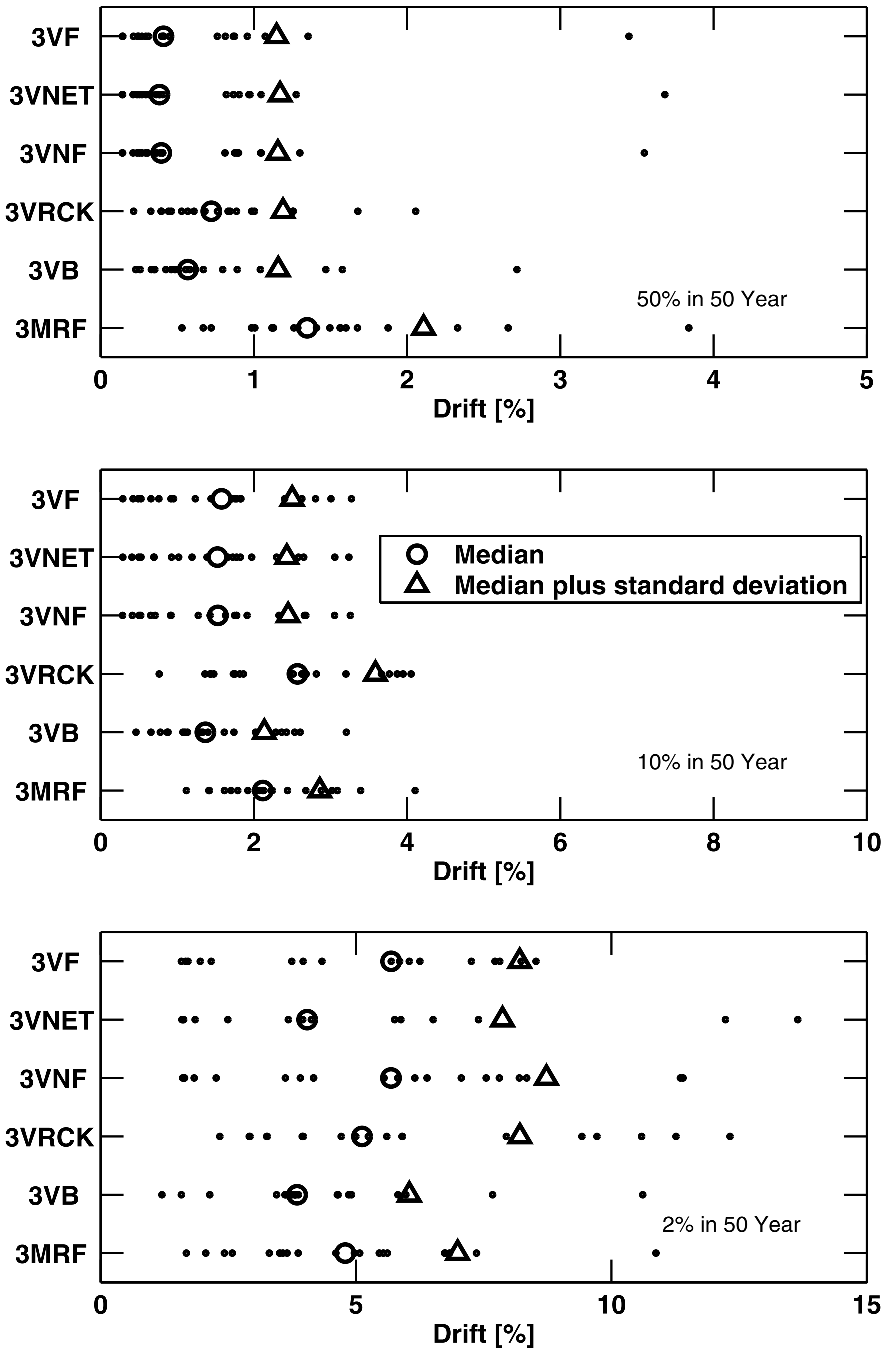

Fig. 8.11 All interstory drift demands for non-collapsed analysis of low-rise structures.

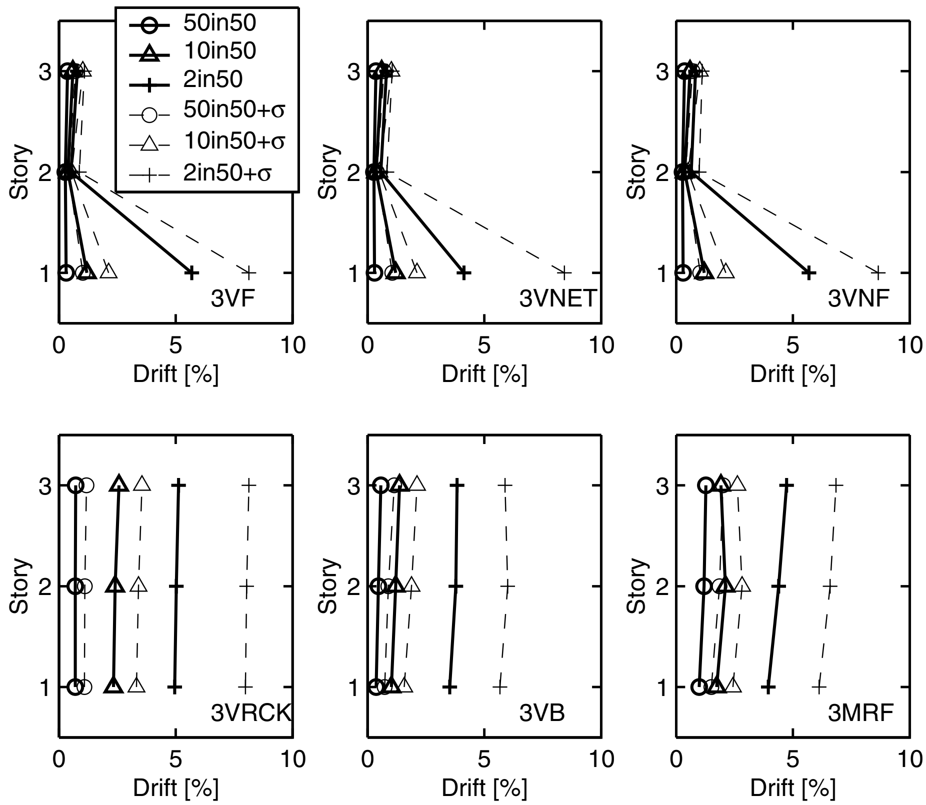

Fig. 8.12 Median and standard deviation of drift demands as function of story height, for analyses not predicting collapse.

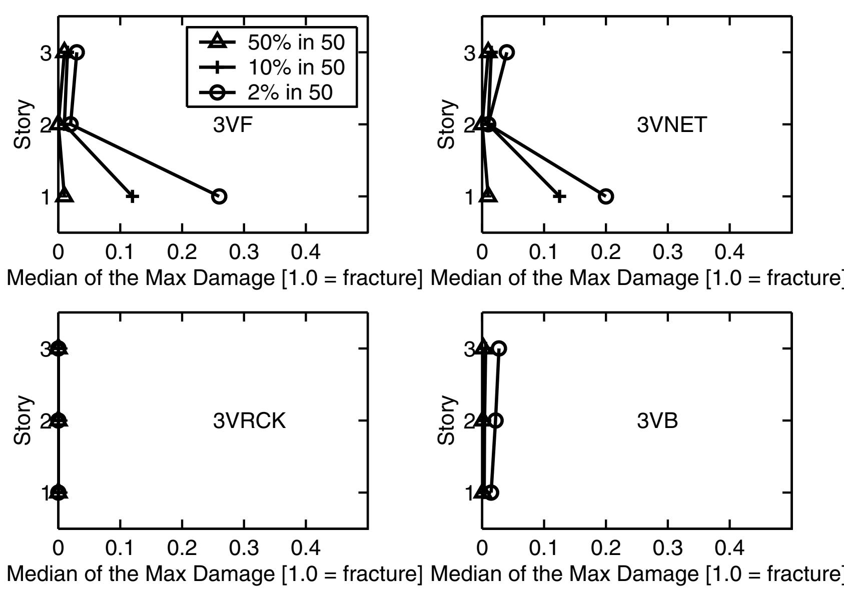

Fig. 8.13 Median values of maximum damage in bracing element.

8.6 MID-RISE STRUCTURES

A similar assessment of mid-rise structures was performed to: (1) compare the effect of longer-period braced frames with the short-period counterpart and (2) the effect of larger column loads and P-Δ effects on these systems. For these mid-rise structures, a model corresponding to net reduced area section failure was not included, as the dire consequence of this type of failure has been aptly demonstrated by the previous results.

8.6.1 Case Study Example

The response of the mid-rise structures was performed again in detail for the LA25 record. Table 8.8 shows the maximum roof drift and the corresponding maximum interstory drift for the mid-rise models. These drifts clearly point to the large concentration of damage on a single floor. A comparison to the low-rise structure's response shows that the drifts for the mid-rise structure are much less than those for the short-period counterparts, with the exception of the 3VB model, which has similar drift demands. In general, for an elastic system one would expect larger roof drifts for a longer-period structure.

Table 8.8 Maximum recorded drift indices for models subjected to LA25.

Model	Max. Roof Drift Ratio, %	Max. Interstory Drift Ratio, %
6VF	1.4	4.4
6VNF	1.4	4.1
6VB	2.2	3.0
6VRCK	1.6	3.4
9MRF	1.9	3.2

Figure 8.14 plots the roof displacement time histories for the mid-rise structures. The rigid base braced structures have only one large cycle of inelastic deformations, whereas the 9MRF model suffers many large cycles of inelastic deformations. The 6VRCK model shows two distinct frequencies of response, one that is very long while the model is rocking, and the other that is shorter when the model is in contact with the ground. The roof drift for the rocking model is slightly larger than the fixed-base 6VF model. While the maximum interstory drift of 6VRCK

is smaller than for 6VF, it is twice as big as the average suggesting that there is a concentration of drift in one story due to localized inelastic action. At this level of excitation, the roof drift of 6VF is 35% larger than for 9MRF, but because of the weak-story behavior of 6VF the maximum interstory drift is 37% bigger than that for 9MRF.

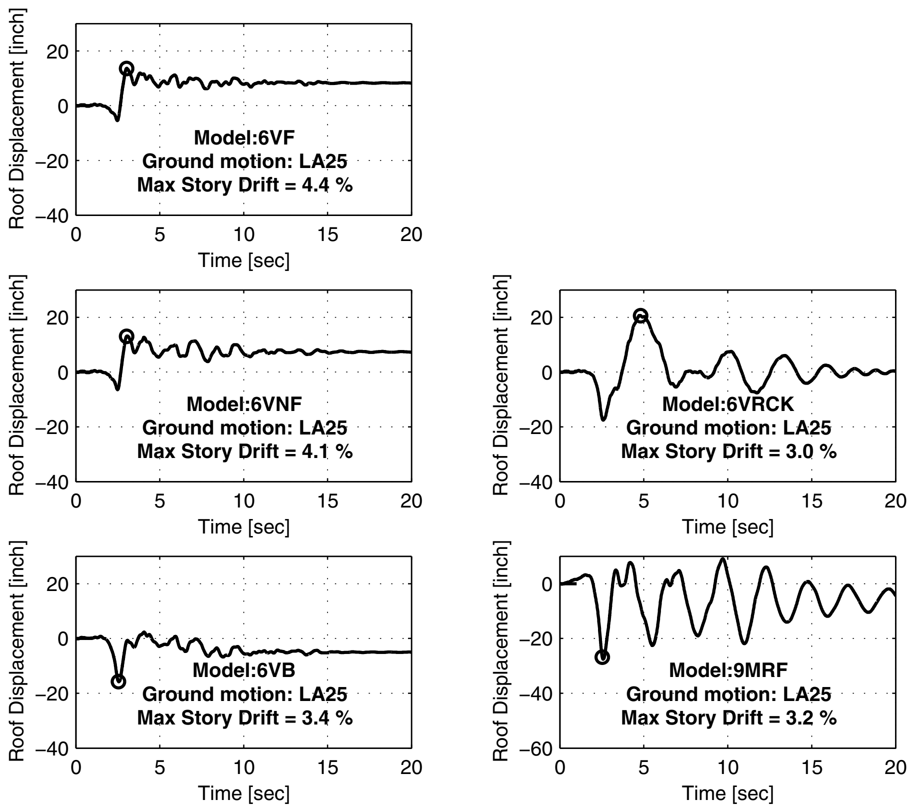

Fig. 8.14 Roof displacement time histories for LA25. Also indicated is time of maximum interstory drift and its corresponding value.

Figure 8.15 shows the displaced shapes of the mid-rise structure when excited by LA25. The displacements are taken from the instant the maximum interstory drift was recorded. The 3VF and 3VNF structures both have clear, non-uniform distribution of drift located in the lower story, and in the upper two stories, the interim floors have relatively small drift demand. The 3VB structure has a relatively even distribution of drift over the first three floors with less drift on the upper floors. The second and third floors of the 9MRF model are showing large drift demand compared to the rest of the structure, which is consistent with the FEMA study (FEMA 2000a).

8.6.2 Collapse

As before, collapse was predicted analytically for only a few of the ground motion excitations at the 2% in 50-year hazard level. For the mid-rise structures, collapse was observed only in the 6VF and 6VRCK structure. For the 6VF structure, six of the twenty records (30%) at this level resulted in more than a 100-in. reduction of story height (i.e., collapse). The location where collapse was triggered was found in not only the lower story, but also in the upper stories. This can be seen in Figure 8.16. The 6VNF model did not collapse for any of the records indicating again the interaction of fracture and collapse. The 6VRCK model collapsed by overturning (Fig. 8.16) for two of the 20 maximum considered level records. Table 8.9 has a list of the ground motions, which triggered collapse for 6VF and 6VRCK structures.

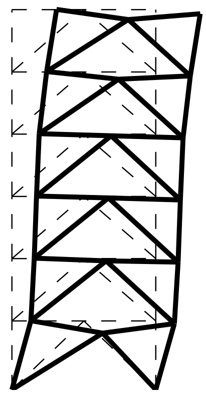

Model:6VF
Ground motion: LA25
Displacement Magnification: 5X

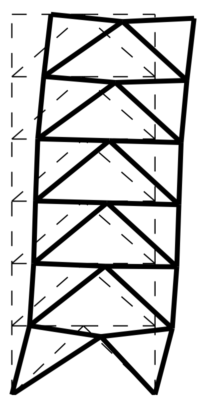

Model:6VNF
Ground motion: LA25
Displacement Magnification: 5X

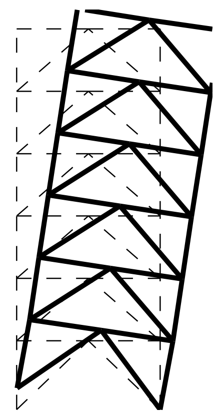

Model:6VRCK
Ground motion: LA25
Displacement Magnification: 5X

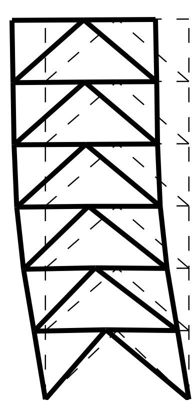

Model:6VB
Ground motion: LA25
Displacement Magnification: 5X

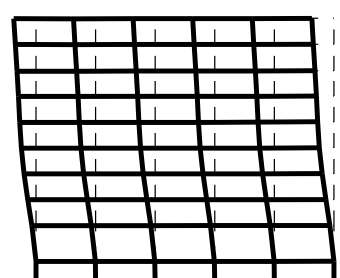

Model:9MRF
Ground motion: LA25
Displacement Magnification: 5X

Fig. 8.15 Displaced shapes for LA25 excitation. Taken at time of maximum interstory drift. Magnification of 5 times.

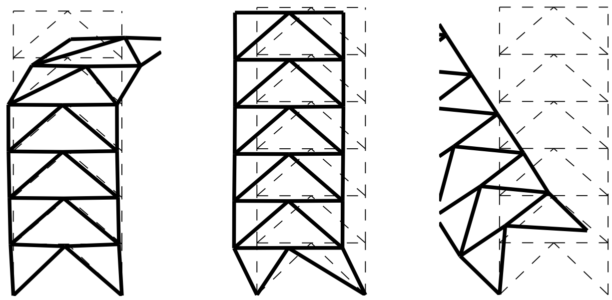

Fig. 8.16 Displaced shapes of "collapsed" records for 6VF and 6VRCK structures prior to numerical collapse.

Table 8.9 Collapse records for 6V and 6VRCK structures.

Model	Records
6VF	LA21,LA31
	LA35,LA36
	LA38,LA40
6VRCK	LA35, LA36
	LA37

8.6.3 Statistical Evaluation of Seismic Demand for Non-Collapsed Records

As before, statistics were prepared for the models that did not collapse, categorized by structure model and hazard level. The results are described below.

Table 8.10 shows the records that resulted in complete brace rupture (not including records where the structure collapsed). Here, it is clear that more instances of fracture are reported compared to the low-rise structures, even though the median drift demand is smaller. For many of the cases where one brace was fractured, the other brace on the same story had over 50% of its fatigue life exhausted. For 6VF, 14 of the 20 records (70%) resulted in either collapse or complete fracture of at least one brace. In the case of 3VF, this ratio was only 25%, and none of the 10% in 50-year events resulted in collapse or fracture. This difference may be attributable to the greater axial loads in columns that may accentuate the P-Δ effect and the longer period of the structure. Had the analyses been run for a 6VNET condition, it may be surmised that even greater instances of brace rupture and system collapse would have been predicted.

Table 8.10 Brace fractures for 6VF and corresponding records (see Fig. 8.1 for element location) for non-collapse records.

Corresponding Hazard (% in 50 years)	Record	Elements fracturing
10	LA07	33
	LA16	36
2	LA22	36
	LA24	26
	LA26	36
	LA28	26
	LA29	35
	LA30	36
	LA32	26,35
	LA33	36

Table 8.12 summarizes, as before, the results from the nonlinear analysis where collapse was not detected. The peak interstory drift indices of the six-story braced-frame structures are smaller than for the 3-story braced frames. Figure 8.17 shows the maximum interstory drift recorded at any floor for all of the models categorized by hazard. As with the low-rise buildings, the braced-frame buildings show smaller drift indices than the moment-frame counterpart, for low-level excitations, but exhibit greater drift indices when the intensity of shaking increases. The median values for residual roof drift indices are the same for 3VF and 6VF for the 2% in 50-year hazard level, but the residual drifts for 6VF are larger for smaller intensities of shaking.

As before, Table 8.11 contains the counted median drift demands for all of the 20 ground motion records (i.e., including the collapsed cases).

In general, damage to braces greater than when compared to the low-rise counterpart, most notable in the 10% hazard level where the median maximum damage in a brace increase significantly from the 3VF model to the 6VF model.

Figure 8.18 shows the median and standard deviation of the maximum story-drift indices recorded over the height of the structure. While the distribution of drift is split between the upper and lower stories for the 6VF and 6VNF models, drifts in the middle portion of the structures are fairly isolated from large drifts. The 6VF model has the second largest drifts on the top floor, where the 6VNF model has substantially less drift demand on the top floor. Interestingly the peak interstory drift for the 6BF and 6VF models are the same, but the distribution is nearly constant over height for the 6BF model, whereas drifts at the intermediate levels are much smaller for the 6VF model. For the 6VB model the trend for slightly large drift demands to occur at the upper levels for smaller hazard levels shifts to larger drift demands near the lower stories for higher seismic hazard levels. This may be a result of the greater number of near-field events (with velocity pulses) for the larger ground motions. In spite of this, the low-cycle fatigue damage to the braces in the 6VB model is very small, in contrast to the 6VF model where the damage was quite high even for the 10% in 50 year hazard level.

As noted for the three-story conventional braced frames, the braces suffer large out-of-plane lateral displacements. The peak and residual displacements for 3VF and 6VF are similar, with 6VF suffering even larger median peak residual out-of-plane lateral displacements than 3VF. For the six-story building, the median peak lateral displacement retained by the conventional buckling braces at the 50% in 50 year (serviceability) level events is greater than 13 in. This will undoubtedly require significant effort to replace the buckled braces and repair nearby nonstructural components, even for serviceability level events. This is not necessary for the buckling-restrained braces until interstory drifts are large enough to cause damage to the nonstructural components or beam-to-column-to-gusset plate connections.

Table 8.11 Counted median values of drift demand of mid-rise building response quantities for 6VF and 6VRCK (including collapsed records) .

ID	Hazard (% in 50 years)	Peak Interstory Drift at Any Floor (%)
6VF	2	5.3
6VRCK	2	3.4

Table 8.12 Median (and standard deviation) of drifts for mid-rise building response quantities for non-collapsed analysis.

ID	Hazard (% in 50 year)	Residual Roof Drift (%)	Peak Interstory Drift at Any Floor (%)	Maximum Residual Out-of-Plane Displacement of Any Brace (in.)	Maximum Normalized Damage in Any Brace Section	Max. Fractured Area in Any Brace (%)	Residual Lateral Capacity (%)	No. of Collapses
6VF	50	0.02(0.1)	0.4(0.3)	13.4(8.3)	0.1(0.1)	0(0)	96(2)	0
	10	0.06(.15)	1.1(0.6)	22.3(5.8)	0.26(0.29)	0(35)	89(11)	0
	2	0.7(1.1)	4.4(2.2)	34.5(7.6)	1.0(0.3)	100(45)	47(25)	6
6VNF	50	0.02(0.05)	0.4(0.3)	11.0(6.9)	--	--	97(4)	0
	10	0.1(0.2)	1.4(0.8)	20.5(5.6)	--	--	89(7)	0
	2	0.7(1.2)	5.1(3.4)	36.5(11.5)	--	--	80(10)	0
6VRCK	50	0(0.01)	0.8(0.4)	0.6(5.3)	0(0)	0(0)	100(0)	0
	10	0(0.01)	2.1(0.14)	3.9(6.4)	0(0)	0(0)	100(0)	0
	2	0.02(0.03)	3.0(0.1)	14.3(7.3)	0(0)	0(0)	100(0)	3
6VB	50	0.08(0.1)	0.4(0.3)	--	0(0)	0(0)	100(0)	0
	10	0.3(0.7)	1.4(0.8)	--	0(0)	0(0)	100(0)	0
	2	1.37(2.2)	4.4(2.5)	--	0.02(0.02)	0(0)	100(0)	0
9MRF	50	0(0.03)	0.9(0.3)	--	--	--	100(0)	0
	10	0.05(0.07)	1.7(0.6)	--	--	--	100(0)	0
	2	0.7(0.9)	3.7(1.9)	--	--	--	100(0)	0

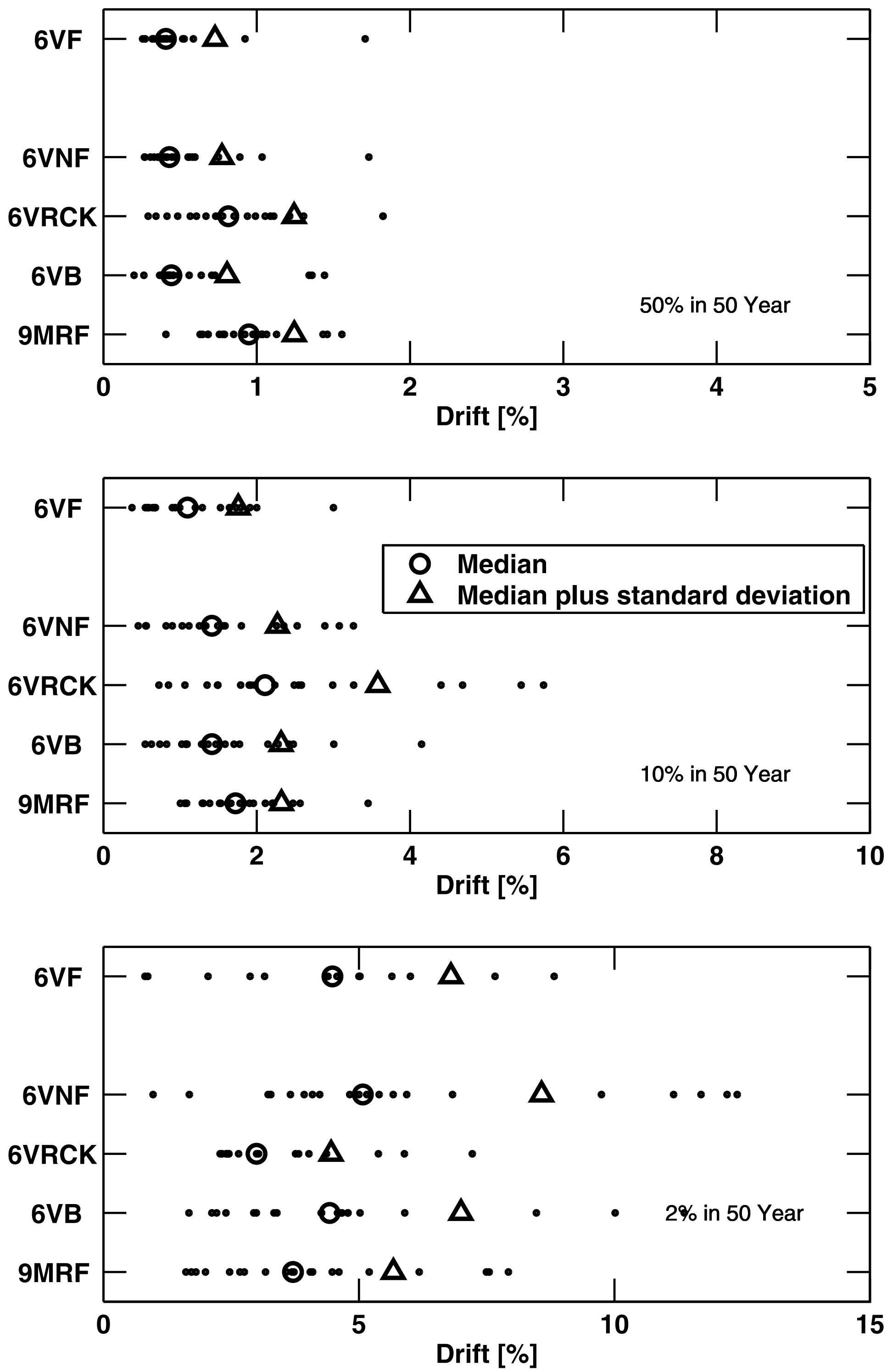

Fig. 8.17 All interstory drift demands for non-collapsed analysis of low-rise structures.

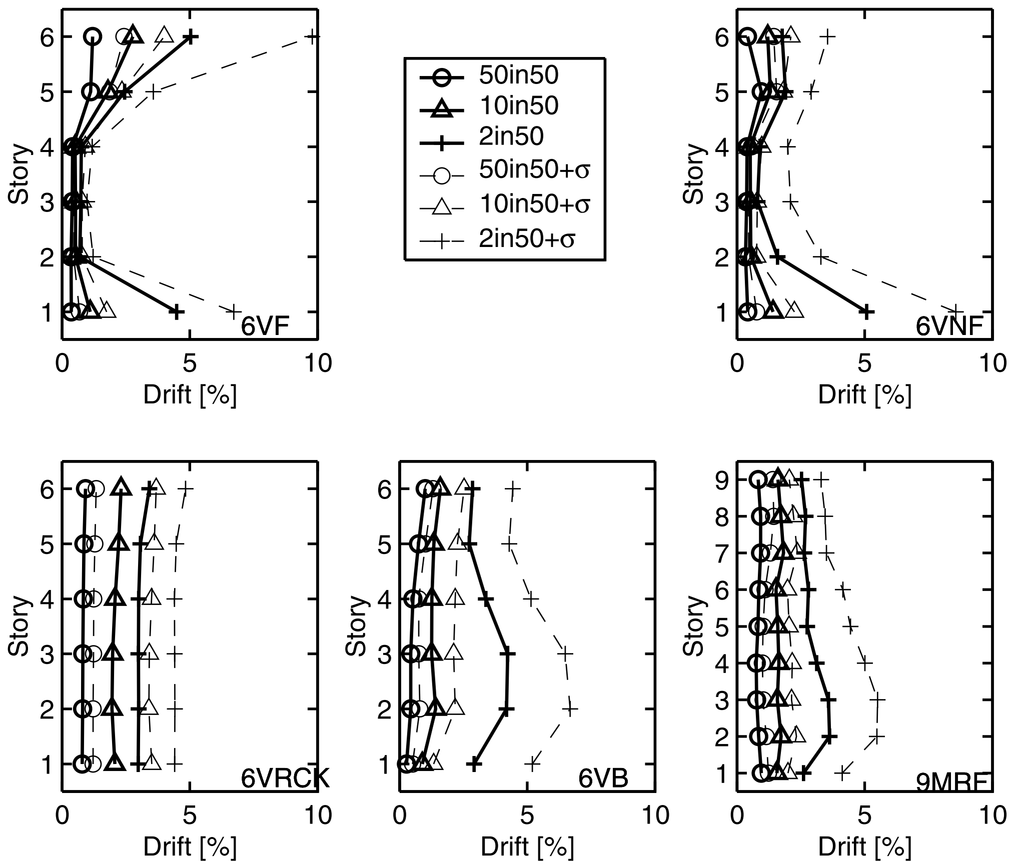

Fig. 8.18 Median and standard deviation of drift demands as a function of story height, for non-collapsed analysis of mid-rise structures.

8.7 CONCLUDING REMARKS

A performance-based assessment of low- and mid-rise systems proportioned and designed in conformance with the 1997 NEHRP provisions were made through a series of nonlinear dynamic analysis of test-calibrated numerical models that included the effects of buckling, low-cycle fatigue, and large displacements. The nonlinear dynamic time-history analyses considered suites of records scaled to hazard levels ranging from frequent to very rare. The following points summarize the key observations made:

- Low-rise conventional concentrically braced structures with rigid connections to the foundations performed poorly in several respects.
  - For the 50% in 50-year hazard level (serviceability) interstory drifts were small relatively small (0.4%) compared to comparable BRBF and MRF systems. However, this drift corresponds to a displacement ductility of about 1.5 to 2, and resulted in a

median maximum residual lateral displacement of at least one brace greater than 5.7 in. This suggests that while conventional braced frames can help limit damage during frequent events to displacement sensitive elements located in regions of the structure away from the braced bent, the braced bend may require significant work to replace some braces and repair damage to surrounding nonstructural elements. Caution should be used in placing conventional braces in locations adjacent to stairs, elevators and safety related utilities.

  - For the 10% and 2% in 50-year hazard levels, interstory drifts typically concentrated in the first story, resulting in peak interstory drifts considerably (2–4 times) larger than the average value based on the median roof displacement normalized by the building height. For example, for the 10% and 2% in 50-year events, the median peak interstory drift indices were 1.6% and in excess of 5.7%, respectively.
  - While none of the records resulted in collapse or even complete brace rupture for the 10% in 50-year design hazard level, 3 records at the 2% in 50-year hazard level caused collapse of the 3VF model, in addition to 2 more records causing complete fracture in at least one brace.
  - In the structures that did not collapse for one of the 2% in 50-year hazard level events, the median maximum residual brace lateral displacement exceeded 30 in., and median residual strength was reduced by 11 from its initial value.
- The performance of the six-story (mid-rise) special concentrically braced frame models with footings restrained from uplifting was in many respects even poorer. For example,
  - For the serviceability level events, the peak drifts are similar to those for the three-story models, but the maximum residual displacement of the braces increases 150% to 13.4 in.
  - For the design-level events, the computed damage index for the braces nearly doubled and two completely fractured a brace.
  - For the 2% in 50 year event, the median peak interstory drift index exceeded 4.4%, and 6 records resulted in collapse of 6VF and an additional 8 records resulted in complete fracture of at least one brace. The median residual strength of 6VF following exposure to the 2% in 50-year events was only 47% of its pre-earthquake capacity.

- While the behavior of SCBF frames in past earthquakes has been far from superior, the number of collapses appear at first glance to be less than suggested by the previous findings. However, it has been noted in many concentrically braced frames that the foundation conditions were not rigid and considerable uplift and sliding occurred at the base of the frame. Model 3VRCK and 6VRCK illustrate that uplift of the base of a concentrically braced frame could explain in large measure the lack of severe damage observed in past earthquakes. While the 3- and 6-story models had roof drifts similar to those with fixed bases, the drifts were uniformly distributed over the height of the structure. This "rigid body" rocking mode of behavior resulted in very little damage to the braces, no concentration of damage in one level more than another, and almost no residual lateral displacement of the structure. Thus, this system would generally result in damage in nonstructural elements due to the large lateral displacements, and to structural and nonstructural elements near the uplifting columns. However, there would be very little damage to the braces and adjacent structural elements. Because the models considered herein were not designed to accommodate the rocking behavior, 3 of the 2% in 50-year hazard level records resulted in complete collapse of 6VRCK, and some localized brace buckling and column yielding was experienced for other rare events (though generally smaller than for the fixed-base structure). None of the records caused the three-story model with uplifting columns to collapse, and the median damage to braces was far less than for any of the other 3-story conventional braced frames.
- Out of 20 records for the 3VF and 6VF models, 3 and 6 resulted in instability where "collapse" was triggered. For the low-rise structure, the non-collapsed cases did not have many fractured braces, resulting in a nearly Boolean performance of the structure (stable or unstable) with regards to brace performance.
- None of the records considered resulted in collapse of the 3VNF model. In contrast, the SCBF systems having unreinforced net reduced area regions where the gusset plate connects saw significantly higher rates of collapse and brace fracture than noted above. For example, the 3VNET system was unstable for 6 of the 20 records. This rate of collapse was twice as high as for 3VF having reinforced net reduced area regions. The analyses indicate that an additional 5 records result in fracture at the net reduced area regions in at least one brace in the 3VNET, whereas only 2 records not producing collapse caused fracture of the central plastic hinge regions in 3VF. These observations

reinforce the need for proper detailing, and illustrate the deleterious influence of brace fracture, even in severely degraded braces, on global structural stability. The reader should be reminded that reinforcement of the net reduced area region is often omitted in common braced frame construction.

- The buckling-restrained systems exhibited superior performance when compared to the conventional bracing systems.
  - For the serviceability level events, the median peak interstory drift indices for the buckling-restrained braces were the same as or slightly smaller than their conventionally braced counterparts. Since the yield drift index for the buckling-restrained braces was larger, this corresponded to smaller displacement ductility demands. Unlike the conventional braces, no permanent lateral displacement occurred with the buckling-restrained braces, reducing the need for costly replacement and repair.
  - For the records corresponding to the 10% and 2% in 50-year hazard levels, the median peak interstory drifts were generally smaller than for the conventionally braced structures. This is in large part due to the reduced tendency of 3VB and 6VB to concentrate damage in a few levels.
  - No incidence of collapse was found for any of the buckling-restrained braced-frame systems.
  - Unlike the conventionally braced frames, none of the braces in the buckling-restrained braced frames fractured. In fact, the computed damage indices for the buckling-restrained braced frames were quite small, suggesting that even for the rare events the braces were far from rupturing, and likely to withstand several more repetitions of the same events. Unlike the conventionally braced frames, there was no reduction of lateral load capacity even for the 2% in 50-year hazard level events.
- No pronounced effects of P-delta were observed in the analysis of the braced-frame systems with rigid foundations. These effects did play a role undoubtedly for the fixed-base SCBF cases where large concentrated drifts occurred in one story and the structures collapsed.
- The analyses of the fixed-base SCBF and BRBF systems for ground motions at the 2% in 50-year hazard level have drifts that are greater than 4%. The ability of gusset plated beam-to-column connections to maintain their integrity at drifts greater than 2% might be

questioned on the basis of the tests of SCBF and BRBF specimens reported in Chapter 5. Since the analytical models used in this chapter only approximated this behavior, performance under rare events may be unconservatively estimated in this chapter.

9 Conclusions and Recommendations

Characterization of the seismic performance of concentrically braced steel-frame structures utilizing modern proportioning and detailing practices is a challenge. Uncertainty in predicting performance is not only a fundamental issue given the complex behavior of bracing elements and connections, but it is also enhanced by the wide range of performance observed in past earthquakes, lack of understanding of system behavior (specifically at large displacements and extreme loadings), and use of typical details which have not been adequately tested.

9.1 BASIC PROCEDURE

The performance-based earthquake engineering techniques used herein are an extension and refinement of other previously developed methodologies applied to concentrically braced steel-frame structures. The research presented herein adopted the Pacific Earthquake Engineering Research (PEER) Center methodology as a basis for characterizing the hazards associated with braced steel buildings. Significant improvements to the existing body of knowledge have been reported in this document, which enhance the existing methodology, as it applies to concentrically braced steel frames:

- Performance of concentrically braced steel buildings in past earthquakes and subsequent discoveries regarding detailing and proportioning have been documented, and where appropriate, conclusions regarding detailing inadequacies have been made.
- A comprehensive study of current literature regarding steel-braced-frame research has been conducted, and key aspects of the lack of knowledge with respect to braced framed performance have been identified.
- A preliminary hazard assessment of braced steel buildings was conducted, identifying important issues regarding the extension of the SAC methodology to a more modern PEER-type methodology for concentrically braced steel structures.

- A rigorous fiber-based beam-column model was formulated and implemented in the computer framework OpenSees to consider the effects of large displacements and combined axial and flexural demand. This model allows for accurate modeling of global buckling and bidirectional bending. Parametric studies were conducted to assess its usefulness in the performance analysis framework.
- A method to increment and accumulate damage was developed to consider the effects of low-cycle fatigue for uniaxial material models. The model was also implemented in OpenSees and calibrated to a wide variety of steel components. These range from beams, conventional HSS braces, buckling-restrained braces and reinforcing bars. The model can be easily calibrated to accumulate damage for other components, materials and situations.
- Several large-scale experiments, ranging from brace tests to subassemblage tests have been conducted that (1) illustrated potential design issues with conventional modeling of concentrically braced steel structures and (2) validated computer models regarding global brace buckling and modeling the effects of low-cycle fatigue.
- A performance-based study has illustrated the interrelationship of strength, brace slenderness ratios, period, and ductility demand considering a simplified but representative single-degree-of-freedom system model.
- Key damage measures for concentrically braced steel frames have been identified, along with a quantifiable description of the significance of damage in braced buildings. These descriptions were based on current research discussed here, past performance of braced steel buildings in earthquakes, and computational analysis of steel buildings.
- A performance-based hazard assessment of short- and medium-rise concentrically braced steel structures has been conducted comparing the influence of (1) low-cycle fatigue, (2) period, (3) brace technology, and (4) detailing. These were compared with "representative" moment-frame structures.

9.2 IMPROVED MODELING TECHNIQUES

The improved physics-based fiber model incorporates a range of new features which provide a computationally efficient method to be used with braced steel structures during seismic excitation. While the modeling approach proposed is applicable to beam-column elements in general, application of this concept has focused herein primarily on bracing members or struts.

Correlation of the numerical results with available experimental evidence demonstrates the ability of the proposed model to represent realistically the buckling strength, the post-buckling behavior, the tensile strength, out-of-plane deformations, and overall hysteretic behavior of steel struts with various types of compact cross-section.

9.3 MODELING THE EFFECTS OF FATIGUE

A general model was incorporated to include the effects of fatigue in OpenSees (Chapter 5). Damage during each cycle was based on Coffin-Manson curves, so that large plastic excursions cause relatively more damage than smaller excursions. A modified rainflow cycle counting technique was used to extract the number and amplitudes of strain cycles developed during the response. Damage from each cycle was linearly accumulated using Minor's rule. This model was successfully calibrated with several uniaxial tests of similar specimens subjected to different loading histories.

Although a fiber model element does not account for the effects of fracture mechanics, cannot model changes in section geometry associated with local buckling, and disregards strain concentrations due to crack opening and stress concentrations, the model proved to be very robust in modeling the global behavior of 6×6×3/8 HSS members when subjected to cyclic hysteresis to failure. With proper empirical data, this method can easily be applied to other members and situations. Because some aspects of the observed behavior (e.g., local buckling, fracture, stress concentrations) may not scale in proportion to size, caution must be exercised in use of the model and identified parameters with other size members and boundary conditions. Also, the generality assumed in the derivation of the fatigue model makes it feasible to account for the effects of fatigue in non-fiber elements, such as zero length elements (e.g., beam-to-column hinge connections).

9.4 EXPERIMENTAL RESULTS

The experimental testing of large-scale testing of BRBF and SCBF specimens was unique in that the specimens were companion experiments, such that the performance of each of the systems can be directly compared against one another in a meaningful fashion. Although certain laboratory constraints prevented testing conditions from being identical, the resulting specimens were reasonable representations of existing building practices.

For all loading histories the BRBF structure (see Chapter 6) exhibited reliable, stable, hysteretic performance with the exception of the fracture of the gusset plate at the free end of the gusset plate, near the beam, at the end of the third test. Damage was distributed throughout the entire first story of the BRBF specimen, including plastic hinging in the beams and columns, column web yielding in shear, panel zone yielding, and brace yielding. At the end of the third test, the northern beam-to-column connection fractured. However, the frame had undergone several cycles near 2% interstory drift prior to this failure.

The SCBF structure (see Chapter 6) was subjected to an identical loading history. In this case, damage was concentrated in the braces in the lower story, although both stories had an equivalent capacity. The resultant distribution of damage was unfavorable, putting significant demands on the braces, and on the columns and beam-column joints in the lower story.

Comparison of the test and numerical results for these SCBF and BRBF tests indicates that the numerical modeling techniques developed adequately model nonlinear behavior, including failure. Thus, it is believed that the expected demands predicted from analysis the analyses presented herein are reasonable approximations of what may be expected. It is important to note that the tests conducted were for reasonably small brace sizes. Typical braces in a building may be two or more times larger than those tested. Because of local and lateral buckling phenomena, it is possible that the strains in large members may lead to fracture earlier than those tested. Interestingly, all of the previous studies on fatigue life of struts have not included brace sizes larger than those tested here. Thus, this is a major consideration for the analysis of larger specimens.

9.4.1 Hazard Analysis

It should be clear from the results presented that the expected performance of conventional concentrically braced frame systems is far worse as that exhibited by comparable buckling-restrained braced frames or moment frames during design and maximum considered level seismic events. It is unfortunate that the severe loss of capacity due to brace fracture plays a significant role in this conclusion, as the loss of braces due to low-cycle fatigue was not only possible but very likely during such levels of shaking. The performance of conventionally braced-frame structures may perform reasonably well when compared to moment frames under small and moderate excitation; however, under more intense shaking, the behavior is marked with a “Boolean” performance, good or bad. This is a result of the sudden loss of strength and concentration of damage when braces fracture.

This research has illustrated that for a specific case with a force-reduction factor , *R,* of six, the brace performance is poor for very rare seismic events. Decreasing the *R*-value may result in better performance of these types of structures; however, the sudden transition from good to bad performance of these systems leads to large uncertainties in predicting behavior at collapse prevention levels of shaking.

9.5 FUTURE RESEARCH DIRECTIONS

The research presented herein, although broad in scope, contains only a fraction of the effort needed to understand fully the multitude of factors influencing the behavior of concentrically braced frames and to develop guidelines for evaluation and design. Moreover the work presented herein has focused on a limited number of configurations, proportions, and details that, while consistent with typical detailing practices, cover only a small portion of the range commonly used in construction. Thus, considerable research is needed to improve computational modeling of concentrically braced frames, quantify the sensitivity of response to various structural and ground motion characteristics, and devise reliable and cost-effective means of achieving targeted performance goals in design. The large lateral displacements of both BRBF and SCBF systems under rare earthquake excitations, the uncertain adequacy of common frame details to develop these drifts in SCBF or BRBF systems, and the large number of brace ruptures and structural collapses predicted for several SCBF systems under these excitations and designed consistent with current code provisions suggest that research on concentrically braced frames is of high priority. Some directions for future research identified in these studies include the following.

Additional research is needed to characterize the hysteretic behavior of braces having sizes and shapes representative of those used in practice. In particular, tests of the type that can be used to refine and calibrate low-cycle fatigue models are critically needed considering the sensitivity of collapse to brace rupture indentified in this research. The uncertain applicability of current fatigue models to members of different sizes and shapes suggests a need to tests larger members and ones with annular, wide flange, and other shapes. Parallel efforts are needed to assess and improve the ability of analytical models to predict the full range of hysteretic behavior of braces, up to and including rupture. While fiber models like those used herein are practicable for the analysis of large structural systems, they do not explicitly account for local buckling and stress concentrations associated with local details. As such, further work is needed to develop and refine finite element analyses methods capable of accurately predicting the effects of yielding, buckling, low-cycle fatigue and fracture. Such analysis when validated can supplement available test data, and address critical detailing issues.

While the behavior of individual braces is the key to the behavior of braced frames, the tests of SCBF and BRBF specimens illustrated that there were important aspects of the performance that were controlled by the connections of the braces to the supporting frame, and by the frame itself. In the tests reported, beam-column-gusset regions developed large inelastic deformations and, at interstory drifts exceeding roughly 2%, ruptured suddenly with a dramatic loss in capacity. Thus, more research is needed to develop connection design procedures and details capable of developing the load path associated with the desired strength of the systems and providing adequate stability the braces and other members attached to the connection through lateral displacement demands consistent with the structural design and seismic hazard. As such, a combination of experiments on idealized connections and subassemblages is needed along with corroborating analyses.

Performance-based design concepts have been demonstrated to be a useful and powerful new approach to assessing and comparing the behavior of structural systems, including concentrically braced frames. However, several needed refinements have been noted, and in the form presented herein, the analyst is provided with information on many aspects of response, and it is difficult to interpret this information. Thus, on one hand, application of formal sensitivity analysis and optimization methods are quite useful to identify design parameters that have the most impact on response, and the ideal values for those design parameters to optimize a performance or cost objective. On the other hand, further use of the PEER PBEE methodology would permit integration of information on individual EDPs and DMs explored herein to provide scalar performance indices based on cost of repair, down time and casualties and injuries. Both of these approaches are logical next steps in research on the performance of concentrically braced steel frames.

Similarly, additional effort is needed to define the targeted performance of a concentrically braced frame. As seen in this report, there are several ways of defining collapse.

On one side, the onset of collapse can be defined by the rate at which interstory drifts increase with increasing intensity of the ground motion, and on the other by actual shortening of a story (as done in Chapter 9, where 100 in. of story height reduction is used). Similarly, one could use the loss of a certain percentage of the lateral story shear capacity, as might be triggered by rupture of the one or more braces, or rupture of the frame connections. Lastly, one could assess safety by whether the building is occupyable following an earthquake, either in terms of the residual damage or its ability to withstand aftershocks. In the cases of well-designed SCBFs important questions related to performance under serviceability-level events could be examined. The studies presented herein show that the braces in the SCBF systems analyzed would likely buckle significantly under these frequent events and require repair of adjacent nonstructural components and replacement of the buckled braces. If these braces are adjacent to emergency egress or fire water supply lines, this behavior could be a safety issue.

The studies presented demonstrated the relative superior performance of a representative buckling braced frame to comparable special concentrically braced frames where both are designed according to the requirements of the 1997 NEHRP provisions. However, both systems are likely to develop quite large interstory drifts for earthquake ground motions consistent with a 2% in 50-year probability of exceedance hazard level. Thus, to improve behavior two approaches suggest themselves.

- In the first approach, such large drift demands are accepted, and research can focus on identifying members and connections capable of achieving collapse prevention at 4% to 7% interstory drift. While buckling-restrained braces appear to have adequate ductility for these rare events from the analyses presented, the supporting steel frame and connections may require additional research to identify details consistent with these drifts. SCBF systems require similar efforts related to framing behavior, but also require research to improve the ductility and fatigue resistance of individual braces. This may be achieved by investigating other shapes such as pipe, circular HSS, wide flange and various stitched sections, braces more resistant to local buckling (stockier sections (i.e., lower b/t ratios), and sections locally restrained from local buckling (i.e., reinforcing plates, concrete fill, external sleeves, etc.).
- Alternatively, research can focus on reliable and cost-effective methods for reducing drift demands on braced-frame structures. Several approaches suggest themselves based on this research.

- Reduce the tendency of SCBF (and to a lesser extent BRBF) systems to concentrate damage in one story. The average interstory drift demand is often much less than the maximum interstory drift in any story.
- Permitting foundations to uplift was shown to be highly effective in reducing damage to braces. This approach may not reduce overall lateral displacement of the system, but it may be able to prevent collapse. The collapse of the braced frames that were permitted to uplift on their foundations appears to be associated with overloading of the single column and brace that carried the lateral and vertical loads on the brace during the uplift at large lateral displacements. Thus, research on appropriate methods to harden these areas may be fruitful. Since many braced frames are lightly loaded, and the numerical models used herein considered rigid impact, additional studies considering various means of post-tensioning the braced frame to the ground or of providing energy-dissipating devices across the uplift plane should be integral components of such studies.
- Formal displacement-based design strategies should be followed. For example, for structures that might be characterized as being in Newmark's energy-preserved range of behavior (Newmark and Hall 1973), significant reductions in displacement might be attained by increasing the strength of the structure. In Chapter 7, it was shown for a single-degree-of-freedom SCBF system that to achieve a brace ductility of about 5, an R factor in the range of 2.5–3.5 could be used. This would be consistent with an interstory drift of around 1.5%. The same study showed that this improvement could also be achieved by using a more slender brace (the increased tensile capacity of the brace provides greater total lateral resistance of the structure (and more slender braces tend to be more ductile). For BRBF systems, the braces are more ductile than conventional buckling braces, so larger values of R could be used to limit displacement. For structures that behave according to Newmark's "displacement preserved" rules, strength will not reduce displacement demands. In this case greater stiffness is required. For braced frames this will result from greater area, which is likely to produce greater strength as well. Thus, more studies are needed to explore the relation of system interstory drift to brace hysteretic properties, strength, stiffness, and fatigue life for various ground motion characteristics and structural period ranges.

- Use more slender braces. This will increase the contribution of the tensile strength of the braces to the overall resistance of the structure. However, beams in chevron and other configurations, columns, connections and foundations will need to be designed to carry more load.

Strengthening and stiffening of braced frames may be effective in reducing drift demands. However, this may increase the accelerations that can develop in the system and increase the forces that individual beams, columns, connections, and foundations will need to resist. Thus, the implications of these alternatives on performance (e.g., falling hazards, bracing requirements for nonstructural components, etc.) and cost should be carefully evaluated. On the other hand, from the limited research herein, it appears that if interstory drifts are limited to about 2%, current connection detailing practices may be adequate.

The studies shown herein have focused on single-bay, stacked chevron configurations. While it is not expected that other configurations like X- or double-story X-configurations will result in improved performance, there may be other advantages in achieving improved details or lower costs. However, there may be some advantages that can be achieved by examining multi-bay braced-frame configurations.

Another situation not examined in this report is the case of braced frames intersecting at a common column. This is common in cases where braced frames are located around elevator, stair, and utility cores. The effect of axial load and bending moments from two frames acting on a single column should be investigated.

This report has focused on structures located in regions of high seismicity. Similar studies should be performed related to concentrically braced frames located in regions of moderate and low seismic hazard. For these areas, ordinary braced frames are permitted with low *R* values and simplified connection details. The adequacy of these combinations should be assessed using numerical methods capable of capturing the yielding, lateral and local buckling of braces, and low-cycle fatigue and fracture of braces, beams, columns, and connections. Similarly, ordinary and similar braced frames are increasingly used in regions of higher seismic risk under restricted applications. The likely performance of these systems should be investigated for ground motions realistically representing the relevant seismic hazard.

All of these studies need to be evaluated and interpreted to form a simple and reliable design method that can be used in engineering practice. As such, a number of trade-offs need to be made relative to various performance expectations (drift, accelerations, damage, definition of collapse, etc.). Thus, it is important in any research study to maintain close collaboration with design practitioners, fabricators/erectors, regulatory officials, and public policy decision makers.

9.6 FINAL REMARKS

It is clear that while concentrically braced frames provide an efficient and economical means of resisting earthquake load effects and current approaches can achieve very good behavior in most cases for frequent events, for larger events, current design approaches can result in a wide range of behavior. Generally, the high ductility of buckling-restrained braces results in very small probability of collapse, and negligible loss in lateral load capacity, even for very rare events. The results suggest that the behavior of SCBF systems is highly variable, but that modest changes in design methods and details can achieve more uniformly reliable behavior.

REFERENCES

Abrahamson, N. A., and Silva, W. J. (1997). "Empirical Response Spectral Attenuation Relations for Shallow Crustal Earthquakes." *Seismological Research Letters*, 68(1).

AIJ. (1995). *Reconnaissance report on damage to steel building structures observed from the 1995 Hyogoken-Nanbu (Hanshin/Awaji) earthquake*, Architectural Institute of Japan, Steel Committee of Kinki Branch, Tokyo, Japan.

Aiken, I. D., and Kelly, J. M. "Cyclic Dynamic Testing of Fluid Viscous Dampers." *Proceedings, Caltrans Fourth Seismic Research Workshop*, Sacramento, California.

AISC. (1993). "Load and Resistance Factor Design LRFD." American Institute of Steel Construction AISC, Chicago, Illinois 60601.

AISC. (1997). "Seismic Provisions for Structural Steel Buildings." American Institute of Steel Construction {AISC}, Chicago, Illinois 60601.

Amzallag, C., Gerey, J. P., Robert, J. L., and Bahuaud, J. (1994). "Standardization of the rainflow counting method for fatigue analysis." *Internation Journal of Fatigue*, 16, 287–293.

Anthes, R. J. (1997). "Modified rainflow counting keeping the load sequence." *Internation Journal of Fatigue*, 19(7), 529–535.

Archambault, M.-H. (1995). « Étude du comportement séismique des contreventements ductiles en X avec profiles tubulaires en acier. » *EPM/GCS-1995-09*, Department of Civil Engineering, École Polytechnique, Montréal, Que.

Astaneh-Asl, A. (1998). "Seismic Design And Behavior of Gusset Plates." Structural Steel And Education Council {Steel Tips}, 209 Vernal Drive, Alamo, California 94507.

Astaneh-Asl, A., Bergsma, G., and Shen, J. H. "Behavior and design of base plates for gravity, wind and seismic loads." *Proceedings, National Steel Construction Conf.*, Las Vegas.

Astaneh-Asl, A., Goel, S., and Hanson, R. D. (1985). "Cyclic out-of-plane buckling of double-angle bracing." *ASCE Journal of Structural Engineering*, 111(5), 1135–1153.

ASTM. (2003). "ASTM E 1049 - 85 : Standard Practices for Cycle Counting in Fatigue Analysis." West Conshohocken, PA.

Ballio, G., and Castiglioni, C. A. (1995). "A Unified Approach for the Design of Steel Structures under Low and/or High Cycle Fatigue." *Journal of Constructional Steel Research*, 34, 75–101.

Ballio, G., and Perotti, F. (1987). "Cyclic Behavior of Axially Loaded Members: Numerical Simulation and Experimental Verification." *Journal of Constructional Steel Research*, 7, 3–41.

Bathe, K.-J. (1995). *Finite Element Procedures.*, Prentice Hall, New York.

Bertero, V. V., and Popov, E. P. (1965). "Effect of Large Alternating Strains of Steel Beams." *Journal of the Structural Division: Proceedings of the American Society of Civil Engineers*, 91(ST1), 1–12.

Bertero, V. V., Uang, C.-M., Llopiz, C., and Igarashi, K. (1989). "Earthquake Simulator Testing of Concentric Braced Dual System." *ASCE Journal of Structural Engineering*, 115(8), 1877–1894.

Black, C., Makris, N., and Aiken, I. (2002). "Component testing, stability analysis and characterization of buckling-restrained Unbonded Braces ™." Earthquake Engineering Research Center, University of California, Berkeley, California.

Black, C., Makris, N., and Aiken, I. D. (2004). "Component Testing, Seismic Evaluation
and Characterization of Buckling-Restrained Braces." *ASCE Journal of Structural Engineering*, 130(6), pp. 880-894.

Black, G. R., Wenger, B. A., and Popov, E. P. (1980). "Inelastic Buckling of Steel Struts Under Cyclic Load Reversals." *UCB/EERC-80/40*, Earthquake Engineering Research Center, Berkeley, CA.

Bonneville, D., and Bartoletti, S. (1996). "Case Study 2.3: Concentric Braced Frame, Lankershim Boulevard, North Hollywood." 1994 Northridge Earthquake; Building Case Studies Project; Proposition 122: Product 3.2, SSC 94–06, Seismic Safety Commission State of California, pages 305–324.

Brown, J., and Kunnath, S. K. (2000). " Low-cycle fatigue Behavior of Longitudinal Reinforcement in Reinforced Concrete Bridge Columns." *MCEER-00-0007*.

Bruneau, M., and Mahin, S. A. (1991). "Full-Scale Tests of Butt-Welded Splices in Heavy-Rolled Steel Sections Subjected to Primary Tensile Stresses." *Engineering Journal, AISC*, 1–17.

Celik, O., C., Berman, J. W., and Bruneau, M. (2004). "Cyclic testing of braces laterally restrained by steel studs to enhance performance during earthquakes." *MCEER-04-0003*, Multidisciplinary Center for Earthquake Engineering Research, Buffalo, New York.

Chai, Y. H., Romstad, K. M., and Bird, S. (1995). "Energy Based Linear Damage Model for High-Intensity Seismic Loading." *ASCE Journal of Structural Engineering*(5), pp. 857–864.

Chambers, J. J., and Ernst, C. J. (2005). "Brace Frame Gusset Plate Research: Phase 1 Literature Review." The University of Utah, Salt Lake City, Utah.

Chen, C.-C., and Lu, L.-W. "Development and experimental investigation of a ductile CBF system,." *Fourth U.S. National Conference on Earthquake Engineering, Proceedings*, El Cerrito, California, pp 575–584.

Chopra, A. K. (1995). *Dynamics of Structures: Theory and Applications to Earthquake Engineering*, Prentice Hall, Upper Saddle River, New Jersey 07458.

Clark, P., Aiken, I., Kasai, K., Ko, E., and Kimura, I. (1999). "Design Procedures for Buildings Incorporating Hysteretic Damping Devices." Proceedings of the 68th Annual Convention, Structural Engineers Association of California, Sacramento.

Crisfield, M. A. (1991). Non-linear finite element analysis of solids and structures, John Wiley & Sons, West Sussex.

de Souza, R. M. (2000). "Force-based Finite Element for Large Displacement Inelastic Analysis of Frames," Ph.D., University of California, Berkeley.

DeWolf, J. T., and Bicker, D. T. (2003). "Column Base Plates." AISC Steel Design Guide Series, American Institute of Steel Construction, 60 pages.

Downing, S. D., and Socie, D. F. (1982). "Simple rainflow counting algorithms." *Internation Journal of Fatigue*, 31–40.

Drake, R. M., and Elkin, S. J. (1999). "Beam-Column Base Plate Design." *Engineering Journal*, 36(1), 29–38.

El-Tayem, A. A., and Goel, S. C. (1985). "Cyclic Behavior of angle X-bracing with welded connections." *UMCE 85-4*, University of Michigan, Department of Civil Engineering, Ann Arbor, Michigan.

FEMA. (1997a). "FEMA 273: NEHRP Guidelines for the Seismic Rehabilitation of Buildings." Federal Emergency Management Agency, Washington, DC.

FEMA. (1997b). FEMA 302: NEHRP Recommended Provisions for seismic regulations for new buildings and other structures, Building Seismic Safety Council, Washington D.C.

FEMA. (1997c). FEMA 303: Commentary to NEHRP Recommended Provisions for seismic regulations for new buildings and other structures, Building Seismic Safety Council, Washington D.C.

FEMA. (2000a). "FEMA 351: Recommended Seismic Evaluation and Upgrade Criteria for Existing Welded Steel Moment Frame Buildings." Federal Emergency Management Agency, Washington, DC.

FEMA. (2000b). "FEMA 355C: State of the Art Report on Systems Performance of Steel Moment Frames Subject to Earthquake Ground Motion Shaking." H. Krawinkler, ed., Federal Emergency Management Agency, Washington, D.C.

FEMA. (2000c). "FEMA 355F: State of the Art Report on Performance Prediction and Evaluation of Steel Moment-Frame Buildings." D. A. Foutch, ed., Federal Emergency Management Agency, Washington, D.C.

FEMA. (2000d). "FEMA 356: Prestandard and Commentary for the Seismic Rehabilitation of Buildings." Federal Emergency Management Agency, Washington, D.C.

Ferch, R. (2004). Berkeley, CA, Personal Communication.

Field, C. "Simulation of full-scale seismic-resistant structural frame tests using LS-DYNA 960 Implicit Solver." *4th European LS-Dyna Users Conference*, Ulm, Germany.

Filiatrault, A., and Cherry, S. (1987). "Performance evaluation of friction damped braced steel frames under simulated earthquake loads." *Earthquake Spectra*, 3(1), pp 57–78.

Filippou, F. C., and Fenves, G. L. (2004). "Earthquake Engineering: From Engineering Seismology to Performance-Based Engineering." Chapter 6: Methods of Analysis for Earthquake-Resistant Structures, Y. Bozorgnia and V. V. Bertero, eds., CRC Press.

Finely, M. M. "Disaster Planning for Libraries: Lessons from California State University, Northridge." *Federal Depository Library Conference*, Bethesda, Maryland.

Fisher, J. W., Kulak, G. L., and Smith, I. F. C. (1997). "A Fatigue Primer For Structural Engineers." *97-11*, Advanced Technologies for Large Structural Systems (ATLSS), Lehigh University; Bethlehem, Pennsylvania, USA.

Fukuta, T., Nishiyama, I., Yamanouchi, H., and Kato, B. (1989). "Seismic Performance of Steel Frames with Inverted V Braces." *ASCE Journal of Structural Engineering*, 115(8), 2016–2028.

Gates, W. E., Marshall, P. W., and Mahin, S. A. "Analytical Methods for Determining the Ultimate Earthquake Resistance of Fixed Offshore Structures." *Offshore Technology Conference, OTC 2751,*.

Ghanaat, Y. (1980). "Study of X-Braced Steel Frame Structures Under Earthquake Simulation." *UCB/EERC-80/08*, University of California, Berkeley, Berkeley, California.

Ghanaat, Y., and Clough, R. W. (1982). “Shaking Table Tests of A Tubular Steel Frame Model.” *UCB/EERC-82/02*, University of California, Berkeley, Berkeley, California.

Giberson, M. F. (1967). “The Response of Nonlinear Multistory Structures Subjected to Earthquake Excitation,” Ph.D. Dissertation, California Institute of Technology, Pasadena.

Glinka, G., and Kam, J. C. P. (1987). “Rainflow counting algorithm for very long stress histories.” *Internation Journal of Fatigue*, 9(3), 223–228.

Goel, S. C., and Tang, X. (1987). “Brace Failures in Dual Bracing Systems.” Proceedings of the sessions at Structures Congress ’87 related to Buildings, American Society of Civil Engineers, 84–99.

Grauvilardell, J., Lee, D., Hajjar, J. F., and Dexter, R. J. (2004). “Synthesis of Design, Testing, and Analysis Research on Steel Column Base Plate Connections in High Seismic Zones.” Structural Engineering Report No. ST-04-02, Department of Civil Engineering, University of Minnesota, Minneapolis, Minnesota, 171 pp.

Gugerli, H., and Goel, S. “Large scale tests for the hysteresis behavior of inclined bracing members.” *Seventh World Conference on Earthquake Engineering*, Istanbul, Turkey, 87–94.

Gugerli, H., and Goel, S. C. (1980b). “Large Scale Tests for the Hysteresis Behavior of Inclined Bracing Members.” Proceedings of the Seventh World Conference on Earthquake Engineering, Turkish National Committee on Earthquake Engineering et al., pages 87–94.

Gupta, A., and Krawinkler, H. (2000). “Dynamic P-delta effects for flexible inelastic steel structures.” *ASCE Journal of Structural Engineering*, 126(1), pp. 145–154.

Hachem, M. (2005). “BiSpec 1.53.” Berkeley, CA, http://www.ce.berkeley.edu/~hachem/bispec/index.html.

Hall, J., and Challa, M. V. R. (1995). “Beam-Column Modeling.” *Journal Of Engineering Mechanics*, 121(12), 1277.

Hamburger, R. O. (2003). “A Vision for the ATC-58 Project: Development of Performance-Based Seismic Design Guidelines.” Applied Technology Council, Sacramento, California.

Hamburger, R. O., Foutch, D. A., and Cornell, A. (2003). “Translating Research to Practice. FEMA/SAC Performance-Based Design Procedures.” *Earthquake Spectra*, 19(2).

Hanson, R. D. (1989). “Editorial.” *ASCE Journal of Structural Engineering*, 115(8), 1835–1836.

Hanson, R. D. (1993). « Passive energy dissipation. » *Earthquake Spectra*, 9(no. 3), pp 319–641.

Hanson, R. D., and Martin, H. W. (1987). “Performance of Steel Structures in the September 19 and 20, 1985 Mexico Earthquakes.” *Earthquake Spectra*, 3(2), 329–346.

Hassan, O. F., and Goel, S. C. (1991). “Modeling of Bracing Members and Seismic Concentrically Braced Frames.” *UMCE 91-1*, University of Michigan, College of Engineering, Ann Arbor, MI 48109-2125.

Higginbotham, A. B. (1973). “The Inelastic Cyclic Behavior of Axially-Loaded Steel Members.” University of Michigan, Department of Civil Engineering, Ann Arbor.

HKS. (2002). *ABAQUS/Standard User’s Manual*, Hibbitt, Karlsson & Sorensen, Rhode Island.

Honeck, W. C., and Westphal, D. (1999). “Practical Design and Detailing of Steel Column Base Plates.” AISC Steel Tips, American Institute of Steel Construction, 19 pages.

Hooper, J. (2003). “Evaluating and Upgrading Welded Steel Moment Frame Buildings Using FEMA 351.” *Earthquake Spectra*, 19(2).

Huckelbridge, A., and Clough, R. (1977a). “Earthquake simulation tests of a nine story steel frame with columns allowed to uplift.” *Earthquake Engineering Research Center, UCB/EERC-77/23*, UC Berkeley, Berkeley, CA.

Huckelbridge, A., and Clough, R. (1977b). “Preliminary experimental study of seismic uplift of a steel frame.” *Earthquake Engineering Research Center, UCB/EERC-77/22*, University of California, Berkeley, Berkeley, CA.

ICBO. (1997). “Uniform Building Code (UBC).” International Conference of Building Officials, Whittier, California.

ICC. (2003). “International Building Code.” I. C. Council, ed., Whittier, California, 656 pages.

Ikeda, K., and Mahin, S. A. (1984). “A refined physical theory model for predicting the seismic behavior of braced steel frames.” University of California, Berkeley, Berkeley, CA.

Ikeda, K., and Mahin, S. A. (1986). “Cyclic response of steel braces.” *Journal of Structural Engineering, ASCE*, 112(2), 342-361.

Ikeda, K., Mahin, S. A., and Dermitzakis, S. N. (1984). “Phenomenological Modeling of Steel Braces Under Cyclic Loading.” *UCB/EERC-84/09*, Earthquake Engineering Research Center, Berkeley, CA.

Jain, A. K., and Goel, S. (1978). “Hysteresis Models For Steel Members Subjected to Cyclic Buckling or Cyclic End Moments and Buckling—Users Guide for DRAIN-2D:EL9 AND EL10.” *UMEE 78R6*, University of Michigan, College of Engineering, Ann Arbor, MI 48109-2125.

Jain, A. K., and Goel, S. (1979). “Seismic Response of Eccentric and Concentric Braced Frames With Different Proportions.” *UMEE 79R1*, University of Michigan, College of Engineering, Ann Arbor, MI 48109-2125.

Jin, J., and El-Tawil, S. (2003). “Inelastic Cyclic Model for Steel Braces.” *Journal of Engineering Mechanics, ASCE*, 129(5), 548–557.

Kahn, L. F., and Hanson, R. D. (1976). “Inelastic Cycles of Axially Loaded Steel Members.” *ASCE Journal of the Structural Division*, 102.

Kamura, H. “Energy dissipation characteristics of hysteretic dampers with low yield strength steel.” *Proceedings, U.S.-Japan Joint Meeting for Advanced Steel Structures*, Tokyo.

Kato, B., Tanaka, H., and Yamanouchi, H. “Field Work Investigation of Steel Building Damage due to the 1978 Miyagiken-oki Earthquake.” *Proceedings of the Seventh World Conference on Earthquake Engineering*, Istanbul, Turkey, 479–486.

Kelly, D. J., Bonneville, D. R., and Bartoletti, S. J. (2000). “1994 Northridge earthquake: damage to a four-story steel braced frame building and its subsequent upgrade.” 12th World Conference on Earthquake Engineering, New Zealand Society for Earthquake Engineering, Upper Hutt, New Zealand.

Khatib, F., Mahin, S. A., and Pister, K. S. (1988). “Seismic behavior of concentrically braced steel frames.” *UCB/EERC-88/01*, Earthquake Engineering Research Center, University of California, Berkeley, CA.

Khatib, I., and Mahin, S. “Dynamic inelastic behavior of chevron braced steel frames.” *Fifth Canadian Conference on Earthquake Engineering*, Balkema, Rotterdam, pages 211–220.

Krawinkler, H. (2002). “Seismic Demand Analysis.” Pacific Earthquake Engineering Research Center, Berkeley, California.

Krawinkler, H., Zohrei, M., Lashkari-Irvani, B., Cofie, N., and Hadidi-Tamjed, H. (1983). “Recommendations for experimental studies on the seismic behavior of steel components and materials.” *Report No. 061*, John A. Blume Earthquake Engineering Center, Stanford University, Stanford, California.

Kullmann, H. G., and Cherry, S. “Full-scale testing of concentrically braced on friction-damped braced steel frames under simulated seismic loading, Eleventh World Conference on Earthquake Engineering, Pergamon, Elsevier Science,1996.” *Eleventh World Conference on Earthquake Engineering*, Acapulco, Mexico.

Lee, D., and Goel, S. (2001). “Seismic Behavior of Column Base Plate Connection Bending About Weak Axis.” *UMCEE 01-09*, University of Michigan, College of Engineering, Ann Arbor, MI 48109-2125.

Lee, K., and Bruneau, M. (2005). “Energy Dissipation of Compression Members in Concentrically Braced Frames: Review of Experimental Data.” *ASCE Journal of Structural Engineering*, 131(4), 552-559.

Lee, K., and Foutch, D. A. (2000). “Performance Prediction and Evaluation of Steel Special Moment Frames for Seismic Loads.” *SAC/BD-00/25*, SAC Joint Venture.

Lee, S., and Goel, S. C. (1987). “Seismic Behaviour of Hollow and Concrete Filled Square Tubular Bracing Members.” *UMCE87-11*, University of Michigan, College of Engineering, Ann Arbor, MI 48109-2125.

Lee, S.-J., and Lu, L.-W. (1989). “Quasi-Static Tests of Scaled Model Building.” *ASCE Journal of Structural Engineering*, 115(8), 1895–1916.

Lehman, D. (1998). “Seismic Performance of Confined Concrete Bridge Columns,” Ph.D. Thesis, University of California, Berkeley, Berkeley.

Liu, Z., and Goel, S. (1988). “Cyclic load behavior of concrete-filled tubular braces.” *Journal of Structural Engineering*, 114(7), 1488–1506.

López, W. A., Gwie, D. S., Lauck, T. W., and Saunders, M. (2004). “UC Berkeley Stanley Hall—Structural Design and Experimental Verification of a Buckling-Restrained Braced Frame System.” *AISC Engineering Journal*(4th Quarter, 2004).

López, W. A., and Sabelli, R. (2004). “Seismic Design of Buckling-Restrained Braced Frames.” Steel Tips: Technical Information and Product Service, Structural Steel Education Council, 78 pages.

LSTC. (1999). *LS-DYNA Keyword User’s Manual (Nonlinear Analysis of Structures)*, Livermore Software Technology Corporation (LSTC), Livermore, CA.

Luco, N. (2002). “Probabilistic Seismic Demand Analysis, SMRF connection Fractures, and Near-Source Effects,” Doctoral Thesis, Stanford University, Palo Alto, California.

Mackie, K., and Stojadinović, B. “Residual Displacement and Post Earthquake Capacity of Highway bridges.” *13th World Conference on Earthquake Engineering*, Vancouver, B.C., Canada, Paper No. 1550.

Mackie, K. R. (2004). “Fragility-based Seismic Decision Making for Highway Overpass Bridges,” Ph.D. Dissertation, University of California, Berkeley, Berkeley, California.

MacRae, G. A. (1994). “P-delta effects on single-degree-of-freedom structures in earthquakes.” *Earthquake Spectra*, 10(3), pp. 539–568.

MacRae, G. A. (1999). “Parametric Study on the Effect of Ground Motion Intensity and Dynamic Characteristics on Seismic Demands in Steel Moment Resisting Frames.” SAC Background Document, SAC/BD-99/01, SAC Joint Venture., Sacramento, CA.

Mahin, S. A., Malley, J. O., Hamburger, R. O., and Mahoney, M. (2003). “Overview of the U.S. program for reduction of earthquake hazards in steel moment-frame structures.” *Earthquake Spectra*, 19(2).

Martinez-Romero. “Damage Assessment and Seismic Behavior of Steel Buildings in Mexico City.” *Proceedings of the International Conference on the Mexico Earthquakes - 1985*, Mexico City, Mexico.

McKenna, F. (1997). “Object Oriented Finite Element Programming: Frameworks for Analysis, Algorithms and Parallel Computing,” University of California, Berkeley, Berkeley, CA 94720.

Menegotto, M., and Pinto, P. E. “Method of Analysis for Cyclically Loaded Reinforced Concrete Plane Frames Including Changes in Geometry and Non-Elastic Behavior of Elements under Combined Normal Force and Bending.” *Proceedings, IABSE Symposium on Resistance and Ultimate Deformability of Structures Acted on by Well Defined Repeated Loads*, Lisbon, Portugal, pp. 15–22.

Merrit, S., Uang, C.-M., and Benzoni, G. (2003). “Subassemblage Testing of Corebrace Buckling-Restrained Braces.” *Report no. TR-2003/01*, University of California, San Diego, La Jolla, California.

Miranda, E. (1993). “Site-Dependent Strength Reduction Factors.” *ASCE Journal of Structural Engineering*, 119(12).

Miranda, E., and Bertero, V. V. (1994). “Evaluation of Strength Reduction Factors for Earthquake-Resistant Design.” *Earthquake Spectra*, 10(2), 357–379.

Miranda, E., and Ruiz-Garcia, J. (2002). “Evaluation of approximate methods to estimate maximum inelastic displacement demands.” *Earthquake Engineering and Structural Dynamics*, 31, 539–560.

Moehle, J. P. “A Framework for Performance-Based Earthquake Engineering.” Applied Technology Council: Tenth U.S.-Japan Workshop on Improvement of Building Seismic Design and Construction Practices; Report ATC-15-9, Redwood City, CA.

Moehle, J. P., Stojadinović, B., Der Kiureghian, A., and Yang, T. (2005). "An Application of PEER Performance-Based Earthquake Engineering Methodology." Research Digest 2005-1, Pacific Earthquake Engineering Research Center, Berkeley, CA.

Naeim, F. (1997). *Performance of Extensively Instrumented Buildings During the January 19, 1994 Northridge Earthquake*, John A Martin And Associates, Research and Development Department, Los Angeles, CA 90015.

Naeim, F. (1998). "Performance of 20 Extensively Instrumented Buildings During the 1994 Northridge Earthquake." *The Structural Design of Tall Buildings*, 7(3), 179–215.

Nagode, M., and Hack, M. (2004). "An online algorithm for temperature influenced fatigue life estimation: stress-life approach." *Internation Journal of Fatigue*, 26, 163–171.

Newmark, N. M., and Hall, W. J. (1973). "Seismic Design Criteria for Nuclear Reactor Facilities." *Report No. 46*, Building Practices for Disaster Mitigation, National Bureau of Standards, U.S. Department of Commerce.

Ohi, K., Shimawaki, Y., Lee, S., and Otsuka, H. (2001). "Pseudodynamic tests on pseudo-elastic bracing system made from shape memory alloy,." *Bulletin of Earthquake Resistant Structure Research Center*, No. 34., pages 21–28.

Osteraas, J., and Krawinkler, H. (1989). "The Mexico Earthquake of September 19, 1985 -- Behavior of Steel Buildings." *Earthquake Spectra*, 5(1), 51–88.

Popov, E. P., and Pinkey, R. B. (1969). "Cyclic Yield Reversal in Steel Building Connections." *Journal of the Structural Division: Proceedings of the American Society of Civil Engineers*, 95(ST 3), 327–353.

Popov, E. P., Takanashi, K., and Roeder, C. W. (1976). "Structural Steel Bracing Systems: Behavior Under Cyclic Loading." *EERC 76-17*, Earthquake Engineering Research Center, Berkeley, CA.

Powell, G. H., and Campbell, S. (1994). "DRAIN-3DX: Element Description and User Guide for Element Type 01, Type 04, Type 05, Type 08, Type 09, Type 15 and Type 17 Version 1.10." *UCB/SEMM-1994/08*, Dept. of Civil Engineering, University of California, Berkeley, Berkeley, CA.

Rai, D. C., Goel, S. C., and Firmansjah, J. (1996a). "User's Guide Structural Nonlinear Analysis Program (SNAP)." Department of Civil and Environmental Engineering; University of Michigan; College of Engineering, Ann Arbor, Michigan.

Rai, D. C., Goel, S. C., and Firmansjah, J. (1996b). "User's Guide: Structural Nonlinear Analysis Program (SNAP)." Department of Civil and Environmental Engineering; University of Michigan; College of Engineering, Ann Arbor, Michigan 48109-2125.

Riahi, A., Powell, G. H., and Mondkar, D. P. (1979). "3D beam-column element (type 2 - parallel element theory) for the ANSR-II program." *UCB/EERC-79/31*, University of California Berkeley,, Berkeley, CA.

Roeder, C. (1989). "Seismic Behavior of Concentrically Braced Frame." *American Society of Civil Engineers: Journal of Structural Engineering*, 115(8), 1837–1856.

Roeder, C. W., Lehman, D. E., Christopolus, A., Gunnarson, I., Johnson, S., and Yoo, J. H. "Seismic design of braced frame gusset plate connections,." *Earthquake Resistant Engineering Structures V , 5th Int. Conf. on Earthquake Resistant Engineering Structures*, Skiathos; Greece, pp. 105–113.

Sabelli, R. (2000). "Research on Improving the Design and Analysis of Earthquake Resistant Steel Braced Frames." FEMA / EERI.

Sabelli, R., Mahin, S. A., and Chang, C. (2003). "Seismic demands on steel braced frame buildings with buckling-restrained braces." *Engineering Structures*, 25(5), 655–666.

Saunders, M. (2003). "Design For Steel Moment Frames for New Buildings." *Earthquake Spectra*, 19(2).

SEAOC. (1995). "Vision 2000: Performance Based Seismic Engineering of Buildings." Structural Engineers Association of California, Sacramento, CA.

Shaback, B., and Brown, T. (2003). "Behaviour of square hollow structural steel braces with end connections under reversed cyclic axial loading." *Canadian Journal of Civil Engineering*, 30, 745–753.

Sherman, D. R. (1976). "Application of Steel Tubing and Pipe." American Iron and Steel Institute, 1000 16th Street, Washington, DC 20036.

Sherman, D. R. (1977). "Tentative Criteria for Structural Applications of Steel Tubing and Pipe." American Iron and Steel Institute, Washington, DC.

Shing, P.-S. B., and Mahin, S. A. (1984). "Pseudodynamic Test Method for Seismic Performance Evaluation: Theory and Implementation." *UCB/EERC-84/01*, Earthquake Engineering Research Center, Berkeley.

Somerville, P. G. (1997). “Development of ground motion time histories for phase 2 of the FEMA /SAC Steel Project.” *SAC BD/97-04*, SAC Steel Joint Venture, Sacramento California.

Spacone, E., Filippou, F. C., and Taucer, F. F. (1996). “Fiber Beam-Column Model for Nonlinear Analysis of RC Frames: I: Formulation.” *Earthquake Engineering and Structural Dynamics*, 25(7), pp. 711–725.

StarSeismic. (2005). “PowerCat Buckling Restrained Brace.” Star Seismic, http://www.starseismic.net.

Stojadinović, B. (2003). “Stability and Low-Cycle Fatigue Limits of Moment Connection Rotation Capacity.” *Engineering Structures*, 25(5), 691–700.

Sweeney, S. C., and Hayes, J. R., Jr. “Shape memory alloy dampers for seismic rehabilitation of existing buildings, PWRI 3387.” *Wind and Seismic Effects, 27th Joint Meeting of the U.S.-Japan Cooperative Program*, Tsukuba, Japan, pp 317–332.

Tang, X. (1987). “Seismic analysis and design considerations of braced steel structures,” Ph.D. Thesis, University of Michigan, Ann Arbor.

Tang, X., and Goel, S. (1989). “Brace Fractures and Analysis of Phase I Structure.” *ASCE Journal of Structural Engineering*, 115(8), 1960-1976.

Tremblay, R. (2002). “Inelastic seismic response of steel bracing members.” *Journal of Constructional Steel Research*, 58, pp. 665–701.

Tremblay, R., and al., e. (1995). “Performance of steel structures during the 1994 Northridge earthquake.” *Canadian Journal of Civil Engineering*, 22(2), 338–360.

Tremblay, R., Archambault, M.-H., and A., F. (2003). “Seismic Response of Concentrically Braced Steel Frames Made with Rectangular Hollow Bracing Members.” *American Society of Civil Engineers: Journal of Structural Engineering*, 129(12), 1626–1636.

Tremblay, R., Archambault, M.-H., and Filiatrault, A. “Seismic Behavior of Ductile Concentric Steel X-Bracings.” *7th Canadian Conference on Earthquake Engineering*, Montreal, Canada, 549–556.

Tremblay, R., and Filiatrault, A. (1996). “Seismic Impact Loading in Inelastic Tension-Only Concentrically Braced Steel Frames: Myth or Reality?” *Earthquake Engineering and Structural Dynamics*, 25(12), 1373–1389.

Tsai, K.-C., Weng, Y.-T., Lin, S.-L., and Goel, S. "Pseudo-Dynamic Test of a Full-Scale CFT/BRB Frame: Part 1 - Performance Based Specimen Design." *13th World Conference on Earthquake Engineering*, Vancouver, B.C., Canada.

Uang, C. M., and Nakashima, M. (2003). "Steel buckling-restrained frames." in Earthquake Engineering: Recent Advances and Application, Chapter 16, Y. Bozorgnia and V. V. Bertero, eds., CRC Press.

Uriz, P., and Dreger, D. "Comparison of Amplitude Scaling versus Source Scaling for Use in Incremental Dynamic Analysis." *Structural Engineers Association of California 2003 Convention*, Squaw Creek, California.

Uriz, P., and Mahin, S. A. (2003). "Seismic Vulnerability of Special Concentrically Braced Steel Frames." Proceedings of the SEAOC 72nd Annual Convention., Structural Engineers Association of California, Squaw Creek, California.

Uriz, P., and Mahin, S. A. (2004). "Seismic Vulnerability Assessment of Concentrically Braced Steel Frames." *International Journal of Steel Structures*, 4(4), 239–248.

Vamvatsikos, D., and Cornell, A. C. (2002). "Incremental Dynamic Analysis." *Earthquake Engineering \& Structural Dynamics,*, 31(3), 491–514.

Wada, A., Saeki, E., Takeuchi, T., and Watanabe, A. (1998). "Development of Unbonded Brace." Nippon Steel's Unbonded Braces (promotional document), Nippon Steel Corporation: Building Construction and Urban Development Division, Tokyo, Japan, pp. 1–16.

Wakabayashi, M., Matsui, C., and Mitani, I. "Cyclic Behavior of a Restrained Steel Brace Under Axial Loading." *6th World conference on Earthquake Engineering*, New Delhi, India, 189–194.

Wakabayashi, M., Nonaka, T., Nakamura, O., and Yamamoto, N. (1971). "An Experiment on the Behavior of Steel Bar Under Repeated Axial Loading." Kyoto University, Kyoto, Japan.

Wakabayashi, M., Nonaka, T., Nakamura, T., Morino, S., and Yoshida, N. (1973). "Experimental Studies on the behavior of Steel Bars Under Repeated Axial Loading, Part-1." Kyoto University, Kyoto, Japan.

Wallace, B., and Krawinkler, H. (1989). "Small-Scale Model Tests of Structural Steel Assemblies." *ASCE Journal of Structural Engineering*, 115(8), 1999–2015.

Watanabe, A. "Properties of brace encased in buckling-restraining concrete and steel tube." *Ninth World Conference on Earthquake Engineering*, Tokyo, 719–724.

Watanabe, A., Hitomi, Y., Saeki, E., Wada, A., and Fujimoto, M. " Properties of Brace Encased in Buckling-Restraining Concrete and Steel Tube." *Proceedings of Ninth World Conference on Earthquake Engineering*, Tokyo-Kyoto, Japan, Paper No. 6-7-4, pp.719–724.

Weng, Y.-T., Lin, M.-L., Tsai, C.-Y., and Tsai, K.-C. "Analytical Assessment of a 2-Story BRBF for Full-Scale 3D Sub-Structural Pseudo-Dynamic Testing." *The First International Conference on Advances in Experimental Structural Engineering AESE 2005*, Nagoya, Japan.

WJE. (1998). "Oviatt Library, East and West Wings Investigation of Base Plate Damage Caused by the Northridge Earthquake." Wiss, Janey, Elstner Associates Inc., Emeryville, CA.

Yang, F., and Mahin, S. A. (2005). "Limiting Net Section Failure in Slotted HSS Braces (in preparation)." Structural Steel Education Council, Moraga, CA.

Zayas, V. A., Mahin, S. A., and Popov, E. P. (1980a). "Cyclic Inelastic Behavior of Steel Offshore Structures." *UCB/EERC-80/27*, University of California, Berkeley, Berkeley, California.

Zayas, V. A., Popov, E. P., and Mahin, S. A. (1980b). "Cyclic Inelastic Buckling of Tubular Steel Braces." *UCB/EERC-80/16*, University of California, Berkeley, Berkeley, California.

Appendix A: OpenSees Fatigue Code

```
/******************************************************************* **
**    OpenSees - Open System for Earthquake Engineering Simulation  **
**          Pacific Earthquake Engineering Research Center          **
**                                                                   **
**                                                                   **
** (C) Copyright 1999, The Regents of the University of California  **
** All Rights Reserved.                                              **
**                                                                   **
** Commercial use of this program without express permission of the **
** University of California, Berkeley, is strictly prohibited.  See **
** file 'COPYRIGHT'  in main directory for information on usage and **
** redistribution,  and for a DISCLAIMER OF ALL WARRANTIES.         **
**                                                                   **
** Developed by:                                                     **
**   Frank McKenna (fmckenna@ce.berkeley.edu)                       **
**   Gregory L. Fenves (fenves@ce.berkeley.edu)                     **
**   Filip C. Filippou (filippou@ce.berkeley.edu)                   **
**                                                                   **
** ******************************************************************
*/

// $Revision: 1.1 $
// $Date: 2003/08/14 20:23:50 $
// $Source:
/usr/local/cvs/OpenSees/SRC/material/uniaxial/FatigueMaterial.cpp,v $

// Written: Patxi
// Created: Aug 2003
//
// Description: This file contains the class definition for
// FatigueMaterial.  FatigueMaterial wraps a UniaxialMaterial
// and imposes fatigue limits.

#include <stdlib.h>

#include <FatigueMaterial.h>
#include <ID.h>
#include <Channel.h>
#include <FEM_ObjectBroker.h>

#include <OPS_Globals.h>

FatigueMaterial::FatigueMaterial(int tag, UniaxialMaterial &material,
                                double dmax, double E_0, double
slope_m,
                                double epsmin, double epsmax )
  :UniaxialMaterial(tag,MAT_TAG_Fatigue), theMaterial(0),
   Cfailed(false), trialStrain(0)
{
  DI  = 0; //Damage index
  X   = 0; //Range in consideration
```

```
  Y   = 0; //Previous Adjacent Range
  A   = 0; //Peak or valley 1
  B   = 0; //Peak or valley 2
  C   = 0; //Peak or valley 2
  D   = 0; //Peak or valley 4
  PCC = 0; /*Previous Cycle counter flag if >1 then previous
'n'
           cycles did not flag a complete cycle */
  R1F = 0; //Flag for first  peak count
  R2F = 0; //Flag for second peak count
  CS  = 0; //Current Slope
  PS  = 0; //Previous slope
  EP  = 0; //Previous Strain
  SF  = 0; /*Start Flag = 0 if very first strain, (i.e. when
initializing)
            = 1 otherwise */
  DL  = 0; //Damage if current strain was last peak.

  if ( dmax > 1.0 || dmax < 0.0 ) {
    opserr << "FatigueMaterial::FatigueMaterial - Dmax must be
between 0 and 1, assuming Dmax = 1\n";
    Dmax = 1;
  } else
    Dmax      = dmax;

  E0        = E_0;
  m         = slope_m;
  minStrain = epsmin;
  maxStrain = epsmax;

  theMaterial = material.getCopy();

  if (theMaterial == 0) {
    opserr <<  "FatigueMaterial::FatigueMaterial -- failed to
get copy of material\n";
    exit(-1);
  }
}

FatigueMaterial::FatigueMaterial()
  :UniaxialMaterial(0,MAT_TAG_Fatigue), theMaterial(0),
   Cfailed(false), trialStrain(0)
{
  DI  = 0; //Damage index
  X   = 0; //Range in consideration
  Y   = 0; //Previous Adjacent Range
  A   = 0; //Peak or valley 1
  B   = 0; //Peak or valley 2
  C   = 0; //Peak or valley 2
```

```
  D   = 0; //Peak or valley 4
```

```
  PCC = 0; /*Previous Cycle counter flag if >1 then previous 'n'
             cycles did not flag a complete cycle */
  R1F = 0; //Flag for first  peak count
  R2F = 0; //Flag for second peak count
  CS  = 0; //Current Slope
  PS  = 0; //Previous slope
  EP  = 0; //Previous Strain
  SF  = 0; /*Start Flag = 0 if very first strain, (i.e. when
initializing)
             = 1 otherwise */
  DL  = 0; //Damage if current strain was last peak.

  Dmax    = 0;
  E0      = 0;
  m       = 0;
  minStrain    = 0;
  maxStrain    = 0;
}

FatigueMaterial::~FatigueMaterial()
{
  if (theMaterial)
    delete theMaterial;
}

static int sign(double a) {
  if (a < 0)
    return -1;
  else if (a == 0)
    return 0;
  else
    return 1;
}

int
FatigueMaterial::setTrialStrain(double strain, double strainRate)
{
  if (Cfailed) {
    trialStrain = strain;
    // return 0;
    return theMaterial->setTrialStrain(strain, strainRate)*1.0e-3;
  } else {
    Cfailed = false;
    trialStrain = strain;
    return theMaterial->setTrialStrain(strain, strainRate);
  }
}

double
```

```
FatigueMaterial::getStress(void)
{
  double modifier = 1.0;
  double damageloc = 1.0-Dmax+DL;
  if (Cfailed)
    // Reduce stress to 0.0
    //return 0.0;
    return theMaterial->getStress()*1.0e-3;
  /*
    else if ( damageloc <= 0.9 )
    modifier = 1.0-725.0/2937.0*pow(damageloc,2);
    else
    modifier = 8.0*(1.0-damageloc);

    if (modifier <= 0)
    //modifier = 1.0e-8;
    modifier = 1.0e-3;
  */
  else
    return theMaterial->getStress()*modifier;
}

double
FatigueMaterial::getTangent(void)
{
  double modifier = 1.0;
  double damageloc = 1.0-Dmax+DL;
  if (Cfailed)
    // Reduce tangent to 0.0
    // return 1.0e-8*theMaterial->getInitialTangent();
    return 1.0e-3*theMaterial->getInitialTangent();
  /*
     else if ( damageloc <= 0.9 )
     modifier = 1.0-725.0/2937.0*pow(damageloc,2);
     else
     modifier = 8.0*(1.0-damageloc);

     if (modifier <= 0)
     // modifier = 1.0e-8;
     modifier = 1.0e-3;
  */
  else
    return theMaterial->getTangent()*modifier;
}

double
FatigueMaterial::getDampTangent(void)
{
  if (Cfailed)
    return 0.0;
  else
    return theMaterial->getDampTangent();
```

```
}



double
FatigueMaterial::getStrain(void)
{
  return theMaterial->getStrain();
}

double
FatigueMaterial::getStrainRate(void)
{
  return theMaterial->getStrainRate();
}

int
FatigueMaterial::commitState(void)
{

  // No need to continue if the uniaxial material copy
  // has already failed.
  if (Cfailed) {
    return 0;
  }

  //Simple check to see if we reached max strain capacities
  if (trialStrain >= maxStrain || trialStrain <= minStrain) {
      Cfailed = true;
      opserr << "FatigueMaterial: material tag " << this->getTag() <<
" failed from excessive strain\n";
      DI = Dmax;
      DL = Dmax;
      return 0;
  }

  //Initialize the fatigue parameters if they have
  // not been initialized yet
  if (SF == 0) {

    A   = trialStrain;
    SF  = 1  ;
    EP  = trialStrain;
    // Initialize other params if not done so already
    PCC = 0;
    B   = 0;
    C   = 0;
    D   = 0;

  }

  /* Now we need to determine if we are at a peak or not
     If we are, then we need to do some calcs to determine
     the amount of damage suffered. If we are not at a peak,
we need to
     pretend like we are at a peak, so that we can calculate
the damage
     as if it WERE a peak.
  */

  // Determine the slope of the strain hysteresis
  if ( EP == trialStrain ) {
    CS = PS;          // No real slope here....
  } else {
    CS = trialStrain - EP;   // Determine Current Slope
  }


  // If we are at a peak or a valley, then check for damage
  if (sign(PS) != sign(CS) && sign(PS) != 0 ) {

    if ( R1F == 0 )  {    // mark second peak

      B = EP;
      Y = fabs(B-A);
      R1F = 1;

    } else {   // start at least the third peak

      // begin modified Rainflow cycle counting
      if (PCC == 1) {

       D = EP;
       X = fabs(D-C);

      } else {

       C = EP;
       X = fabs(C-B);

      }

      if (X < Y) {

       PCC = PCC + 1;

       if (PCC == 1) {
         Y = fabs(C-B);
       } else if (PCC == 2 ) {
         // Count X = |D-C| as a 1.0 cycle
         DI = DI + 1.0 / fabs(pow( (X/E0) , 1/m )) ;
         // Reset parameters
         D = 0;
         C = 0;
```

```
        Y = fabs(B-A);
        PCC = 0;
      }

    } else {

      if (PCC == 1 ) {

        // Count Y = |C-B| as a 1.0 cycle
        DI = DI + 1.0 / fabs(pow( (Y/E0) , 1/m ));
        // Reser parameters
        B = D;
        C = 0;
        D = 0;
        Y = fabs(B-A);
        PCC = 0;

      } else {

        // Count Y = |A-B| as a 0.5 cycle
        DI = DI + 0.5 / fabs(pow( (Y/E0), 1/m ));
        // Reset parameters
        A = B;
        B = C;
        C = 0;
        D = 0;
        Y = X;
        PCC = 0;

      }

    }

  }

  // Flag failure if we have reached that point
  if (DI >= Dmax )  {
    // Most likely will not fail at this point, more
    // likely at the psuedo peak. But this step is
    // is important for accumulating damage
    Cfailed = true;
    opserr << "FatigueMaterial: material tag " << this->getTag() <<
" failed at peak\n";
    DL=DI;
  } else {
    Cfailed = false;
    DL=DI;
  }

} else {

  // Now check for damage, although we are not at a peak at all.
```

```
  // Store temporary damage only as if it were the last
peak: DL
  // Commit to DI only if failure occurs.
  if (B == 0 && C == 0 &&  D == 0) {

    // If we have not yet found the second peak
    X = fabs(trialStrain - A);

    if (fabs(X) < 1e-10) {
      DL = DI ;
    } else {
      DL = DI +  0.5 / fabs(pow( (X/E0), 1/m ));
    }

  } else if (B != 0 && C == 0 &&  D == 0) {

    // On our way to find point C. Range Y defined, no X yet
    X = fabs(trialStrain - B);

    if (fabs(X) < 1e-10) {
      DL = DI;
    } else {
      DL = DI +  0.5 / fabs(pow( (X/E0) , 1/m ));
    }

    if (fabs(Y) < 1e-10) {
      DL = DL;
    } else {
      DL = DL +  0.5 / fabs(pow( (Y/E0) , 1/m ));
    }

  } else if (B != 0 && C != 0 &&  D == 0) {

    // Two ranges stored, but no cycles for either stored
    //   Make sure we get the potential |D-A| range.
    X = fabs(trialStrain-A);

    if (fabs(Y) < 1e-10) {
      DL = DI;
    } else {
      DL = DI +  1.0 / fabs(pow( (Y/E0) , 1/m ));
    }

    if (fabs(X) < 1e-10) {
      DL = DL;
    } else {
      DL = DL +  0.5 / fabs(pow( (X/E0) , 1/m ));
    }

  }

  // Did we fail before a peak?
```

```
    double mStress = theMaterial->getStress();
    if (DL > Dmax && mStress > 0.0 ) {
      DI = DL;
      Cfailed = true;
      opserr << "FatigueMaterial: material tag " << this->getTag() <<
" failed at pseudo peak\n";
    } else {
      Cfailed = false;
    }
  }

  PS = CS;             // Previous Slope
  EP = trialStrain;    // Keep track of previous strain

  // Check if failed at current step
  if (Cfailed) {
    return 0;
  }
  else
    return theMaterial->commitState();

}


int
FatigueMaterial::revertToLastCommit(void)
{
  // Check if failed at last step
  if (Cfailed)
    return 0;
  else
    return theMaterial->revertToLastCommit();
}

int
FatigueMaterial::revertToStart(void)
{
  Cfailed = false;
  DI  = 0; //Damage index
  X   = 0; //Range in consideration
  Y   = 0; //Previous Adjacent Range
  A   = 0; //Peak or valley 1
  B   = 0; //Peak or valley 2
  C   = 0; //Peak or valley 2
  D   = 0; //Peak or valley 4
  PCC = 0; /*Previous Cycle counter flag if >1 then previous 'n'
             cycles did not flag a complete cycle */
  R1F = 0; //Flag for first  peak count
  R2F = 0; //Flag for second peak count
  CS  = 0; //Current Slope
  PS  = 0; //Previous slope
  EP  = 0; //Previous Strain
```

```
  SF  = 0; /*Start Flag = 0 if very first strain, (i.e. when
initializing)
             = 1 otherwise */
  DL  = 0; //Damage if current strain was last peak.

  Dmax    = 0;
  E0      = 0;
  m       = 0;
  minStrain    = 0;
  maxStrain    = 0;

  return theMaterial->revertToStart();
}

UniaxialMaterial *
FatigueMaterial::getCopy(void)
{
  FatigueMaterial *theCopy =
    new FatigueMaterial(this->getTag(), *theMaterial, Dmax,
E0, m ,minStrain, maxStrain);

  theCopy->Cfailed = Cfailed;
  theCopy->trialStrain = trialStrain;

  return theCopy;
}

int
FatigueMaterial::sendSelf(int cTag, Channel &theChannel)
{
    int dbTag = this->getDbTag();

  static ID dataID(3);
  dataID(0) = this->getTag();
  dataID(1) = theMaterial->getClassTag();
  int matDbTag = theMaterial->getDbTag();
  if ( matDbTag == 0) {
    matDbTag = theChannel.getDbTag();
    theMaterial->setDbTag(matDbTag);
  }
  dataID(2) = matDbTag;
  if (theChannel.sendID(dbTag, cTag, dataID) < 0) {
    opserr << "FatigueMaterial::sendSelf() - failed to send
the ID\n";
    return -1;
  }

  static Vector dataVec(21);
  dataVec(0)  = DI;
  dataVec(1)  = X;
  dataVec(2)  = Y;
  dataVec(3)  = A;
```

```
  dataVec(4)  = B;
  dataVec(5)  = C;
  dataVec(6)  = D;
  dataVec(7)  = PCC;
  dataVec(8)  = R1F;
  dataVec(9)  = R2F;
  dataVec(10) = CS;
  dataVec(11) = PS;
  dataVec(12) = EP;
  dataVec(13) = SF;
  dataVec(14) = DL;
  dataVec(15) = Dmax;
  dataVec(16) = E0;
  dataVec(17) = m;
  dataVec(18) = minStrain;
  dataVec(19) = maxStrain;

  if (Cfailed == true)
    dataVec(20) = 1.0;
  else
    dataVec(20) = 0.0;

  if (theChannel.sendVector(dbTag, cTag, dataVec) < 0) {
    opserr << "FatigueMaterial::sendSelf() - failed to send the
Vector\n";
    return -2;
  }

  if (theMaterial->sendSelf(cTag, theChannel) < 0) {
    opserr << "FatigueMaterial::sendSelf() - failed to send the
Material\n";
    return -3;
  }

  return 0;
}

int
FatigueMaterial::recvSelf(int cTag, Channel &theChannel,
                          FEM_ObjectBroker &theBroker)
{
  int dbTag = this->getDbTag();

  static ID dataID(3);
  if (theChannel.recvID(dbTag, cTag, dataID) < 0) {
    opserr << "FatigueMaterial::recvSelf() - failed to get the ID\n";
    return -1;
  }
  this->setTag(int(dataID(0)));

  // as no way to change material, don't have to check classTag of the
material
```

```
  if (theMaterial == 0) {
    int matClassTag = int(dataID(1));
    theMaterial =
theBroker.getNewUniaxialMaterial(matClassTag);
    if (theMaterial == 0) {
      opserr << "FatigueMaterial::recvSelf() - failed to
create Material with classTag "
           << dataID(0) << endln;
      return -2;
    }
  }
  theMaterial->setDbTag(dataID(2));

  static Vector dataVec(21);
  if (theChannel.recvVector(dbTag, cTag, dataVec) < 0) {
    opserr << "FatigueMaterial::recvSelf() - failed to get the
Vector\n";
    return -3;
  }

  DI   = dataVec(0);
  X    = dataVec(1);
  Y    = dataVec(2);
  A    = dataVec(3);
  B    = dataVec(4);
  C    = dataVec(5);
  D    = dataVec(6);
  PCC  = int(dataVec(7));
  R1F  = int(dataVec(8));
  R2F  = int(dataVec(9));
  CS   = dataVec(10);
  PS   = dataVec(11);
  EP   = dataVec(12);
  SF   = int(dataVec(13));
  DL   = dataVec(14);
  Dmax = dataVec(15);
  E0   = dataVec(16);
  m    = dataVec(17);
  minStrain = dataVec(18);
  maxStrain = dataVec(19);

  if (dataVec(20) == 1.0)
    Cfailed = true;
  else
    Cfailed = false;

  if (theMaterial->recvSelf(cTag, theChannel, theBroker) < 0)
{
    opserr << "FatigueMaterial::recvSelf() - failed to get the
Material\n";
    return -4;
  }
```

```
  return 0;
}

void
FatigueMaterial::Print(OPS_Stream &s, int flag)
{
  if (flag == 100) {
    s << DL << endln;
  } else {
    s << "FatigueMaterial tag: " << this->getTag() << endln;
    s << "\tMaterial: " << theMaterial->getTag() << endln;
    s << "\tDI: " << DI << " Dmax: " << Dmax << endln;
    s << "\tE0: " << E0 <<  " m: " << m  << endln;
    s << "\tDL: " << DL << endln;

  }
}
```

Appendix B: Specimen SCBF-1 Drawings

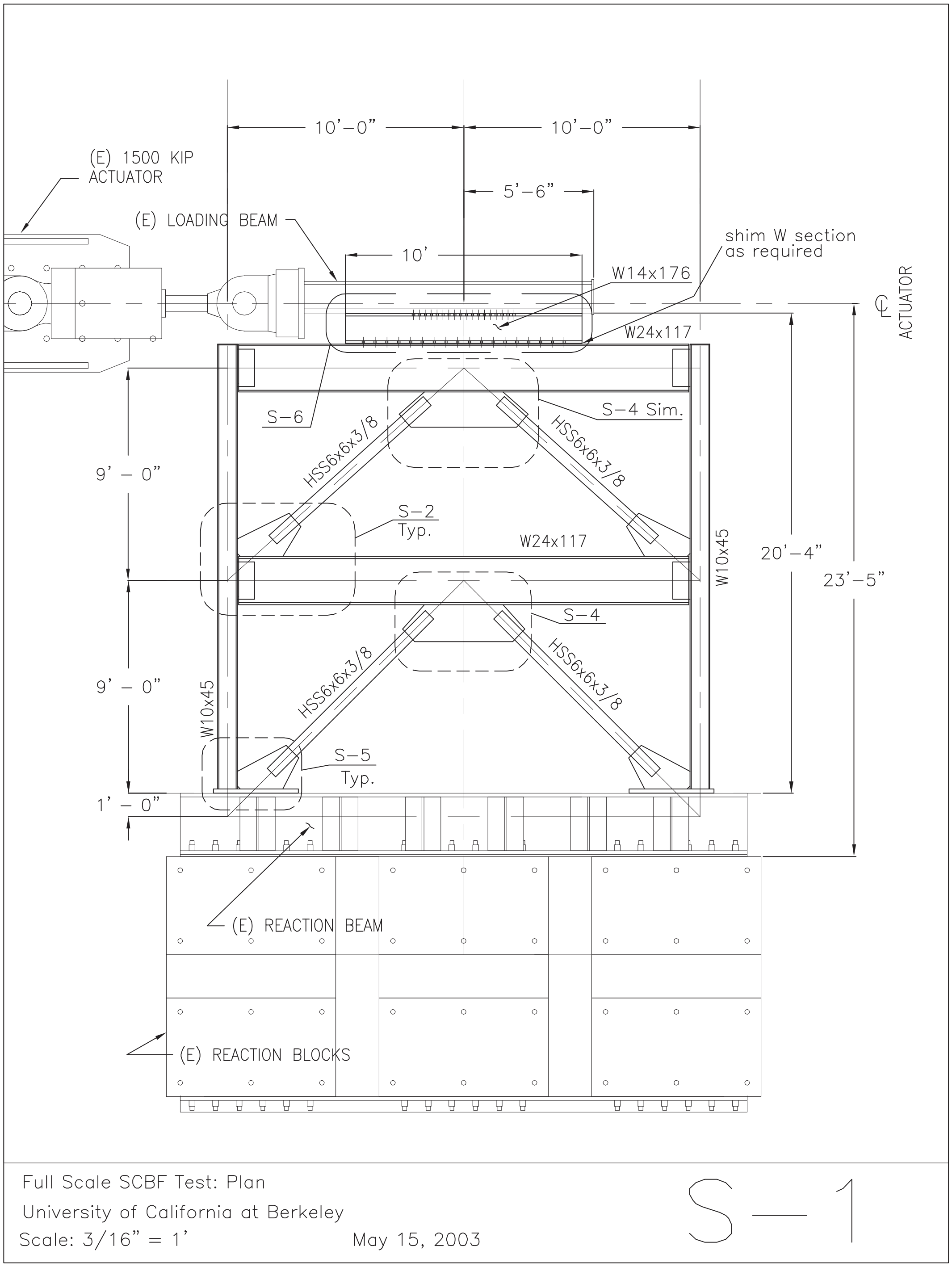

(Fit to page: not to scale shown above.)

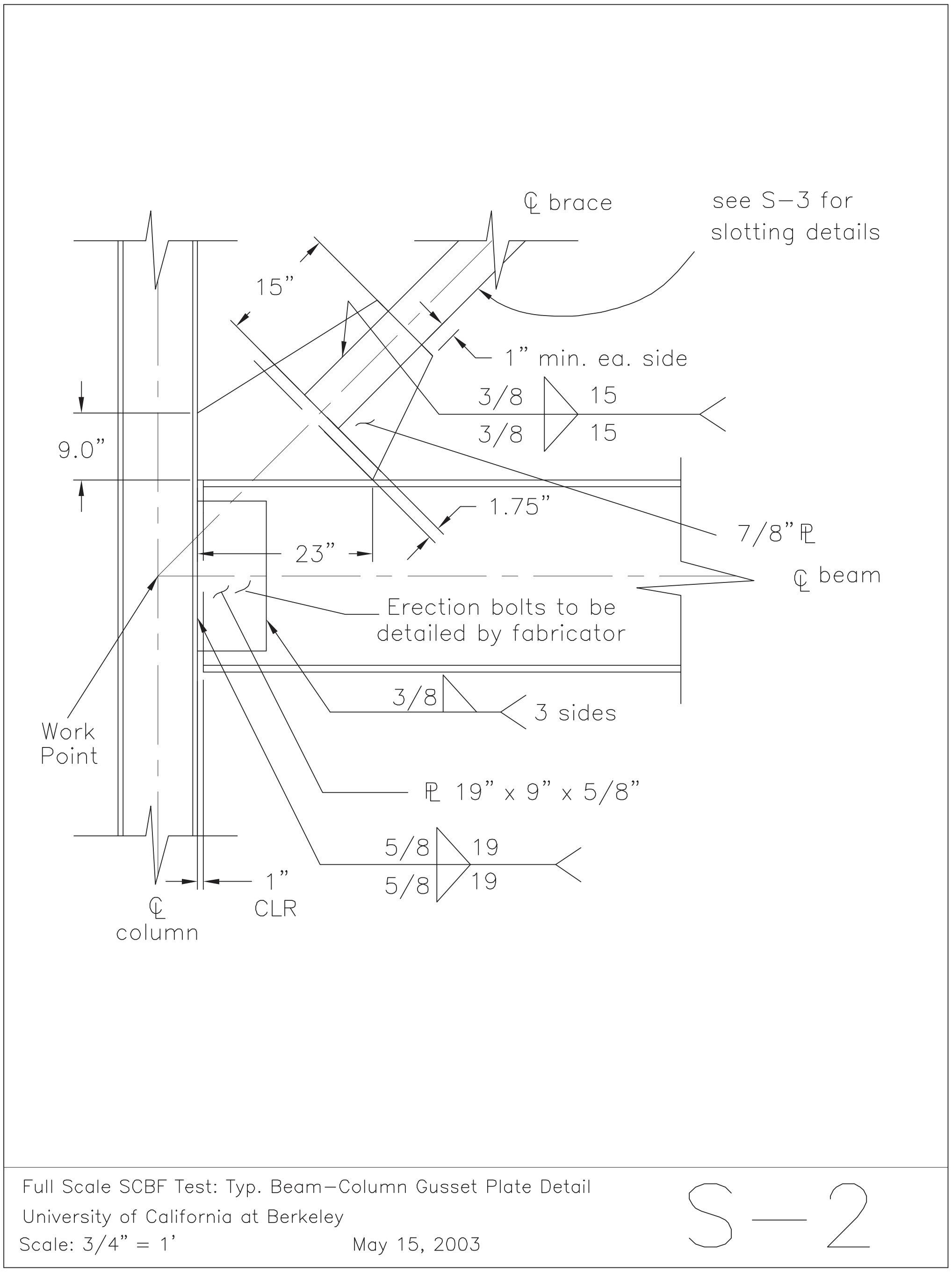

(Fit to page: not to scale shown above.)

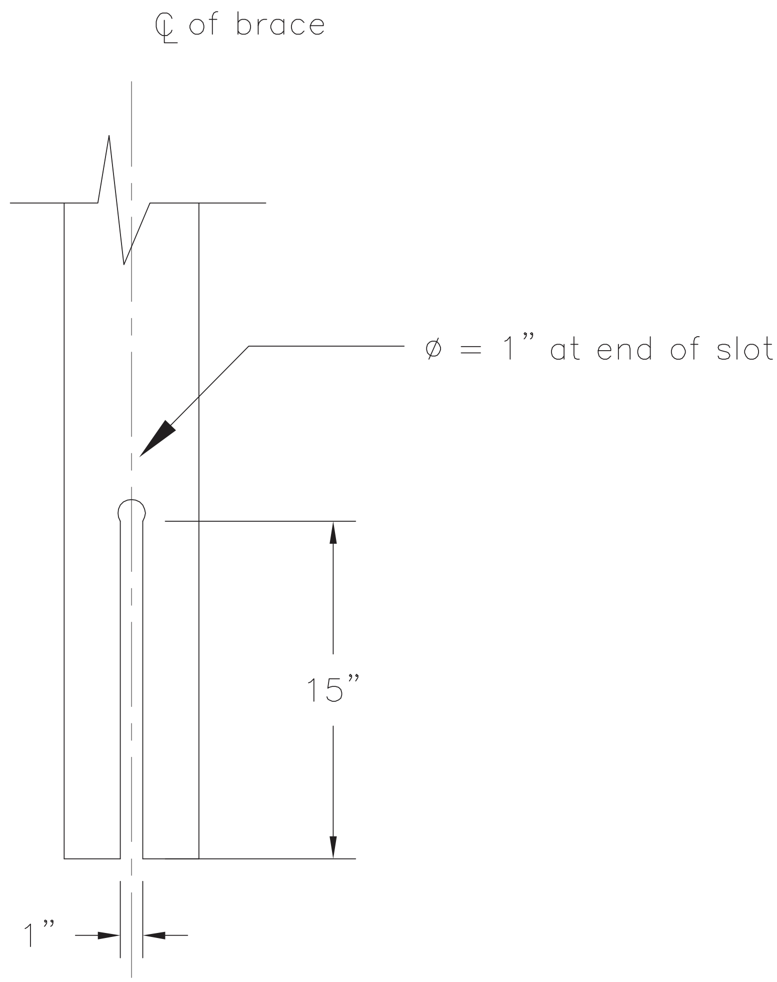

Full Scale SCBF Test: Typ. Brace Slotting Detail
University of California at Berkeley
Scale: 1 1/2" = 1'   May 15, 2003

S—3

(Fit to page: not to scale shown above.)

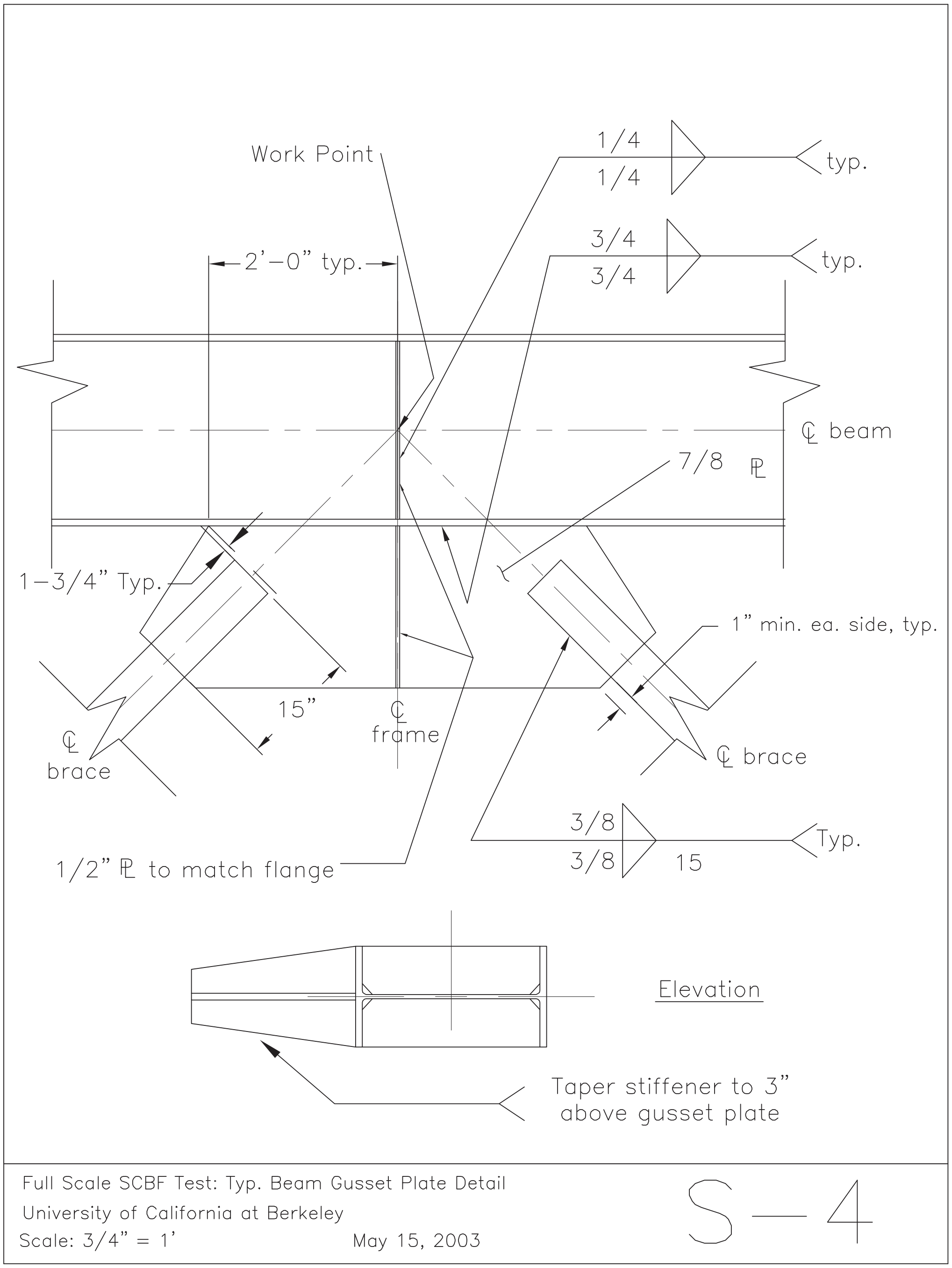

(Fit to page: not to scale shown above.)

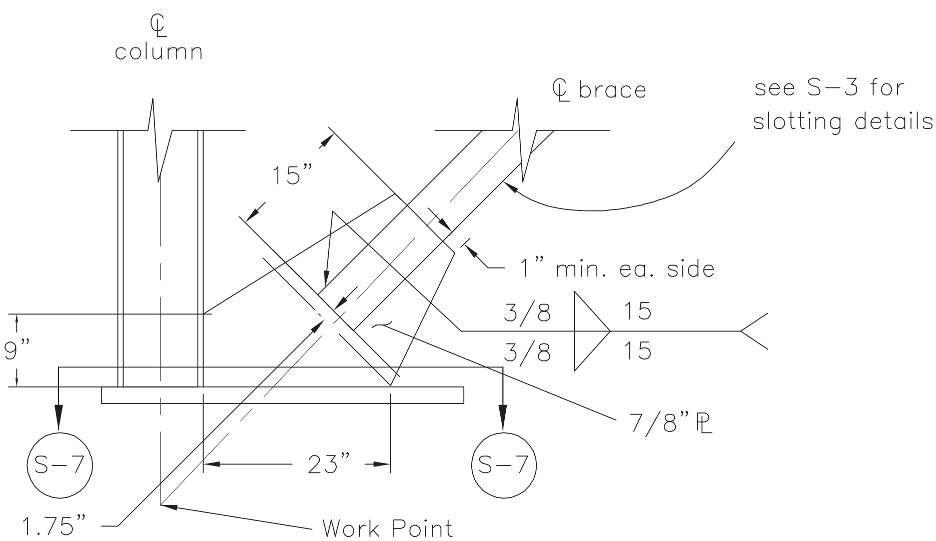

Full Scale SCBF Test: Base Plate Connection Detail
University of California at Berkeley
Scale: 3/4" = 1'   May 15, 2003

S-5

(Fit to fit page: not to scale shown above.)

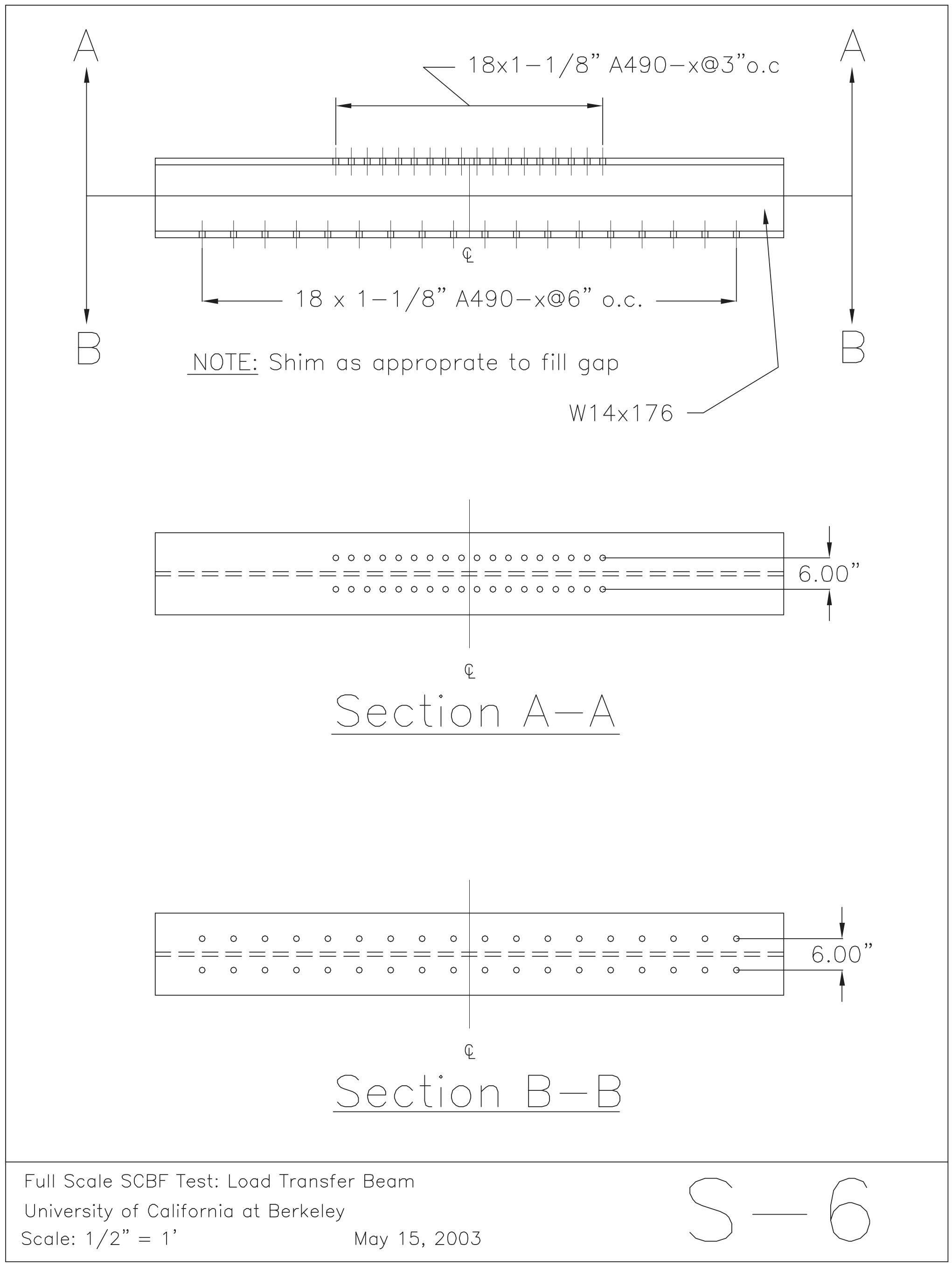

(Fit to page: not to scale shown above.)

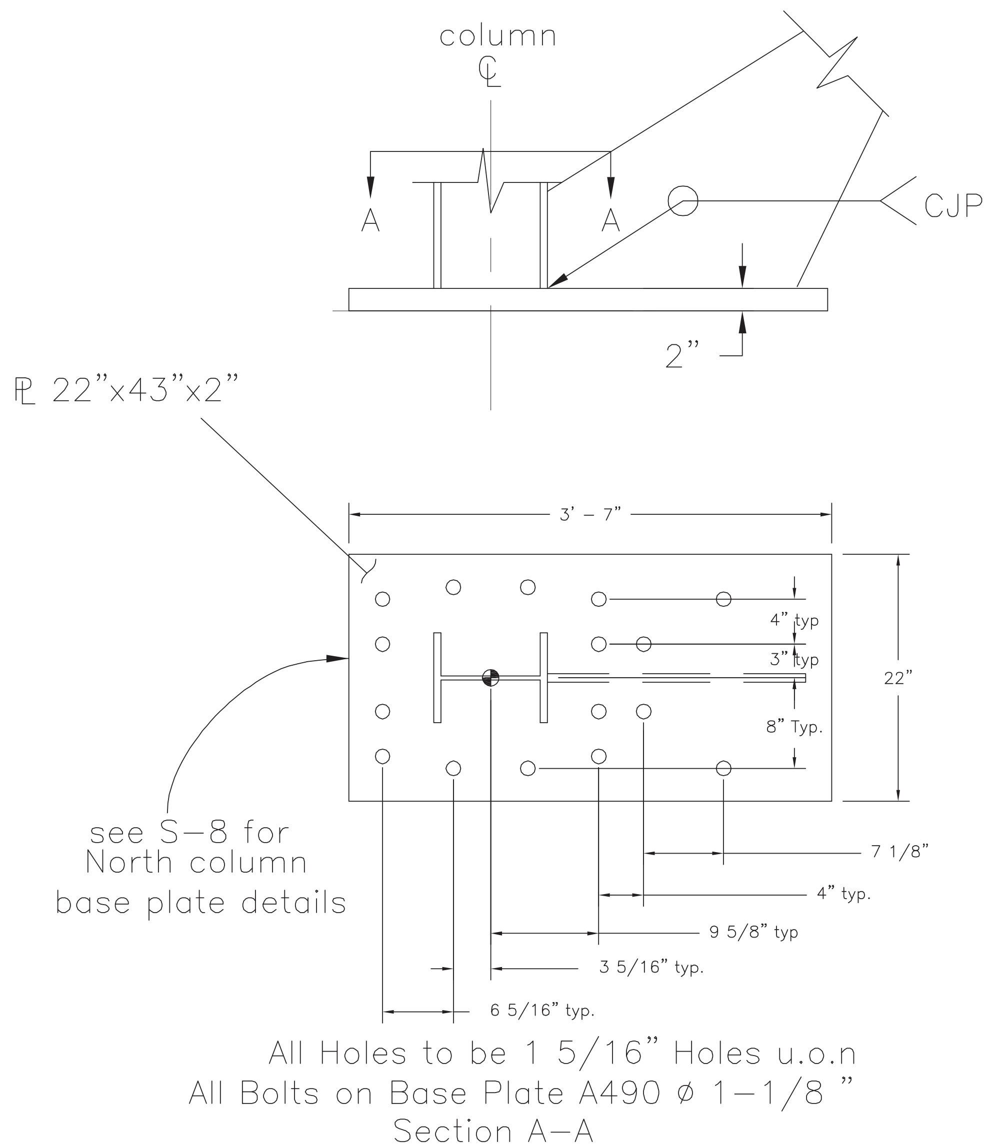

Full Scale SCBF Test: South Column Base Detail
University of California at Berkeley
Scale: 1" = 1' May 15, 2003

S–7

(Fit to page: not to scale shown above.)

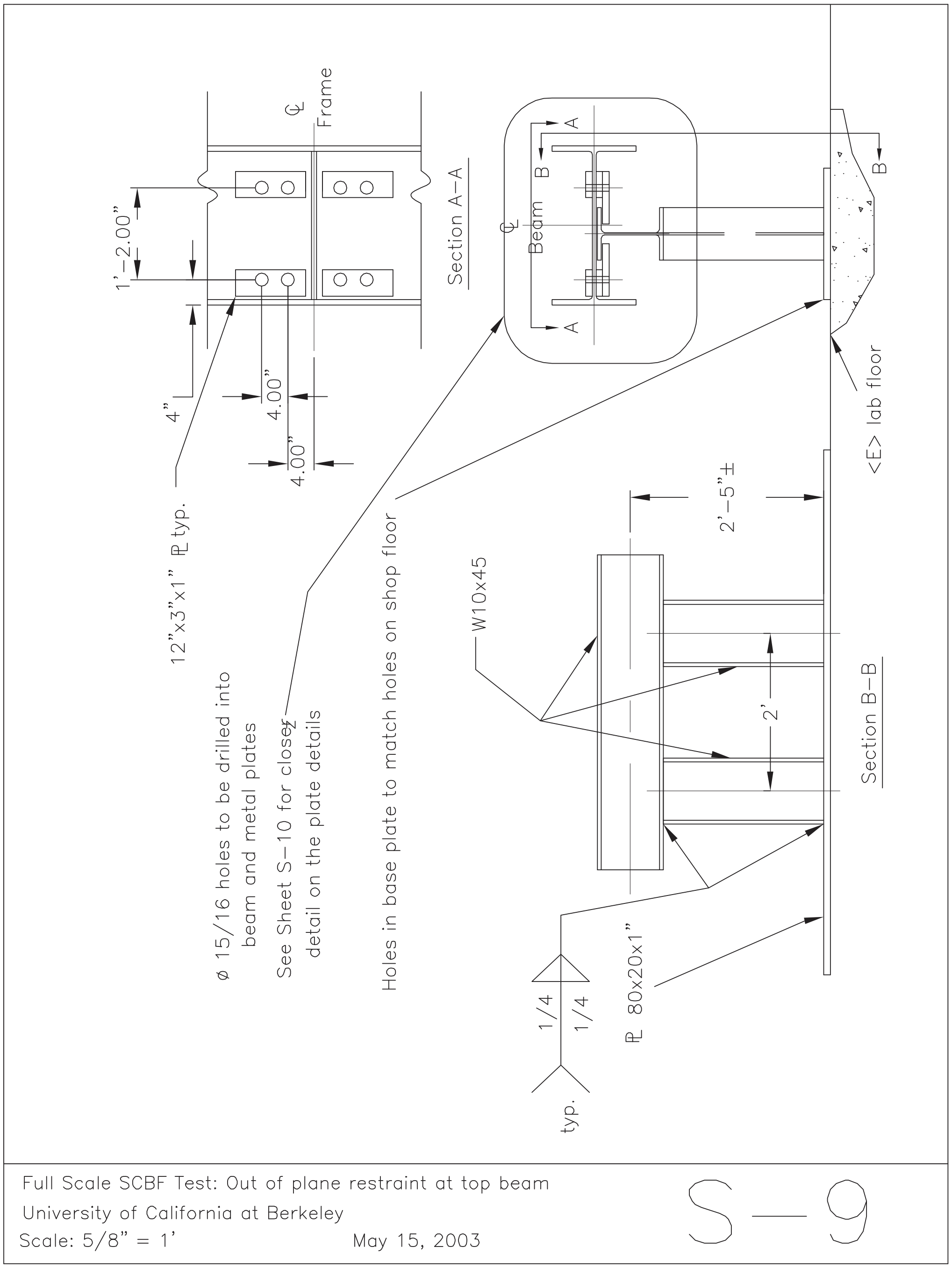

(Fit to page: not to scale shown above.)

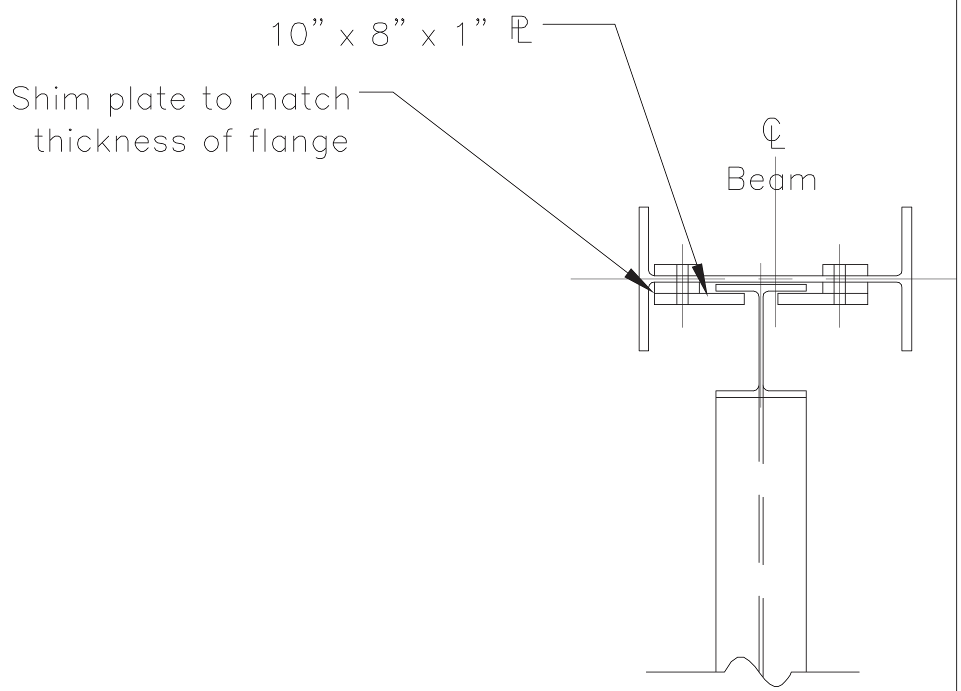

Full Scale SCBF Test: Close up of out–of–plane bracing detail
University of California at Berkeley
Scale: 1" = 1'　　May 15, 2003

S–10

(Fit to page: not to scale shown above.)

Appendix C: Channel Locations for Specimen SCBF-1

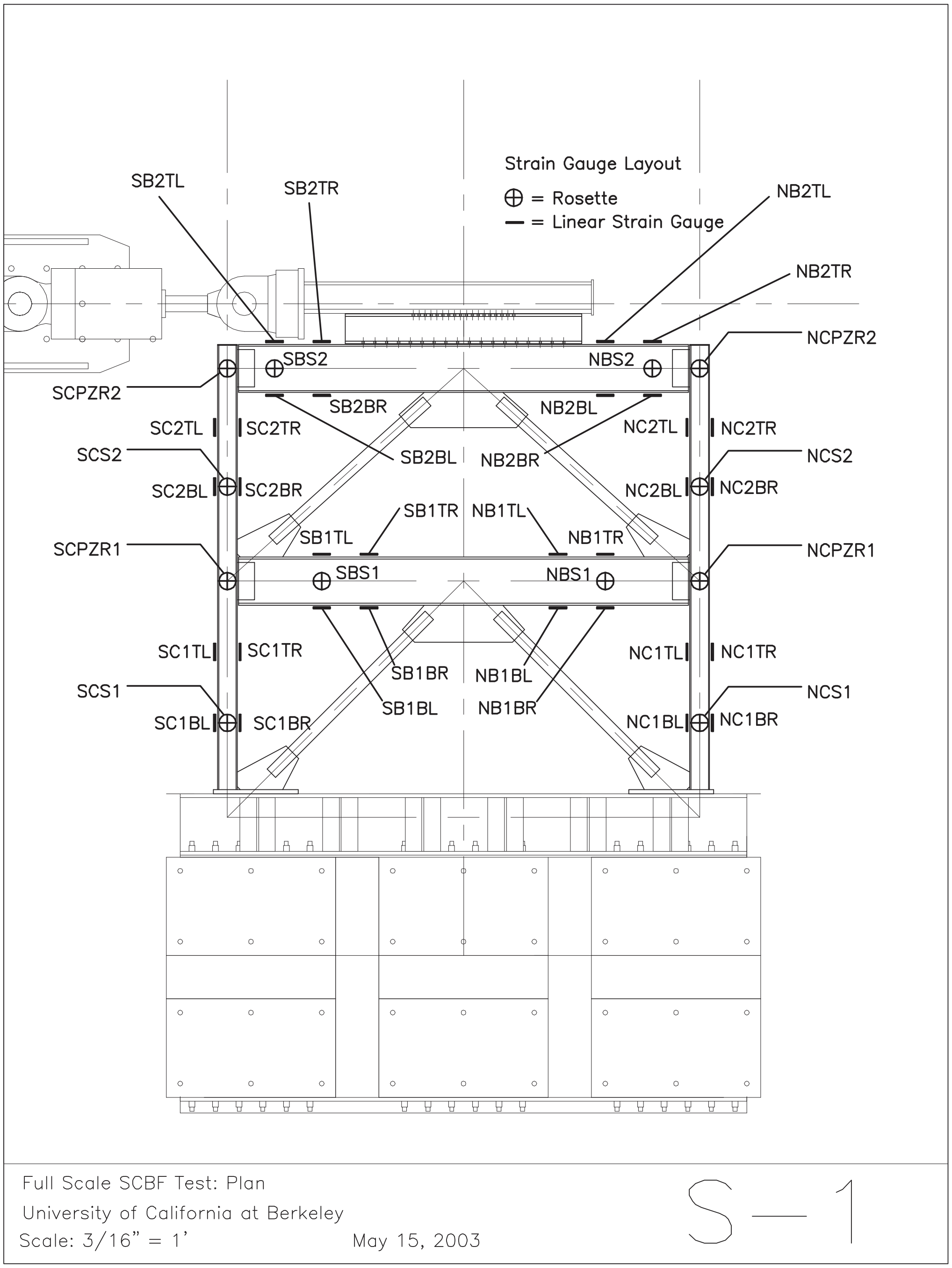

Strain-gage labels.

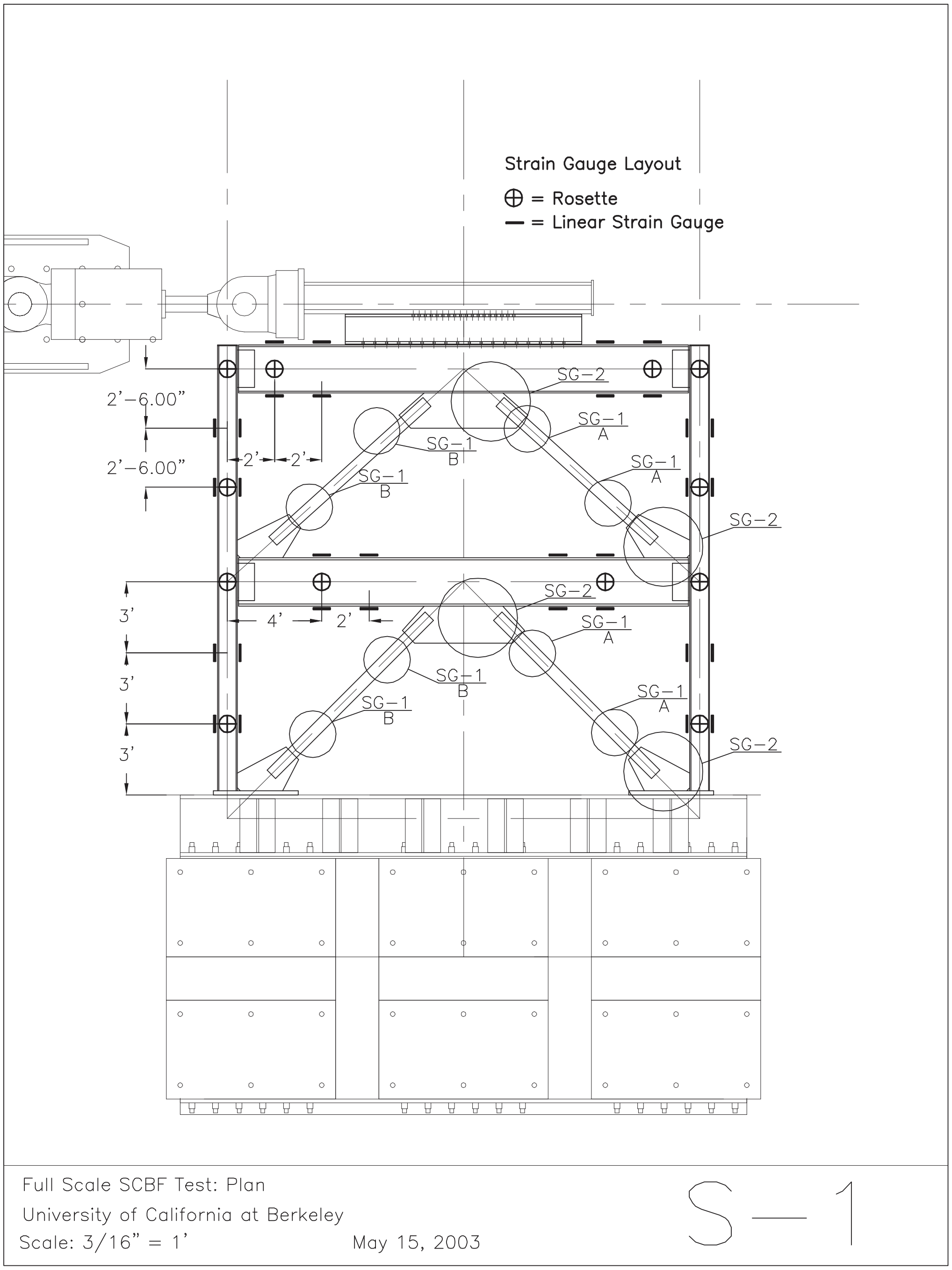

Strain-gage locations.

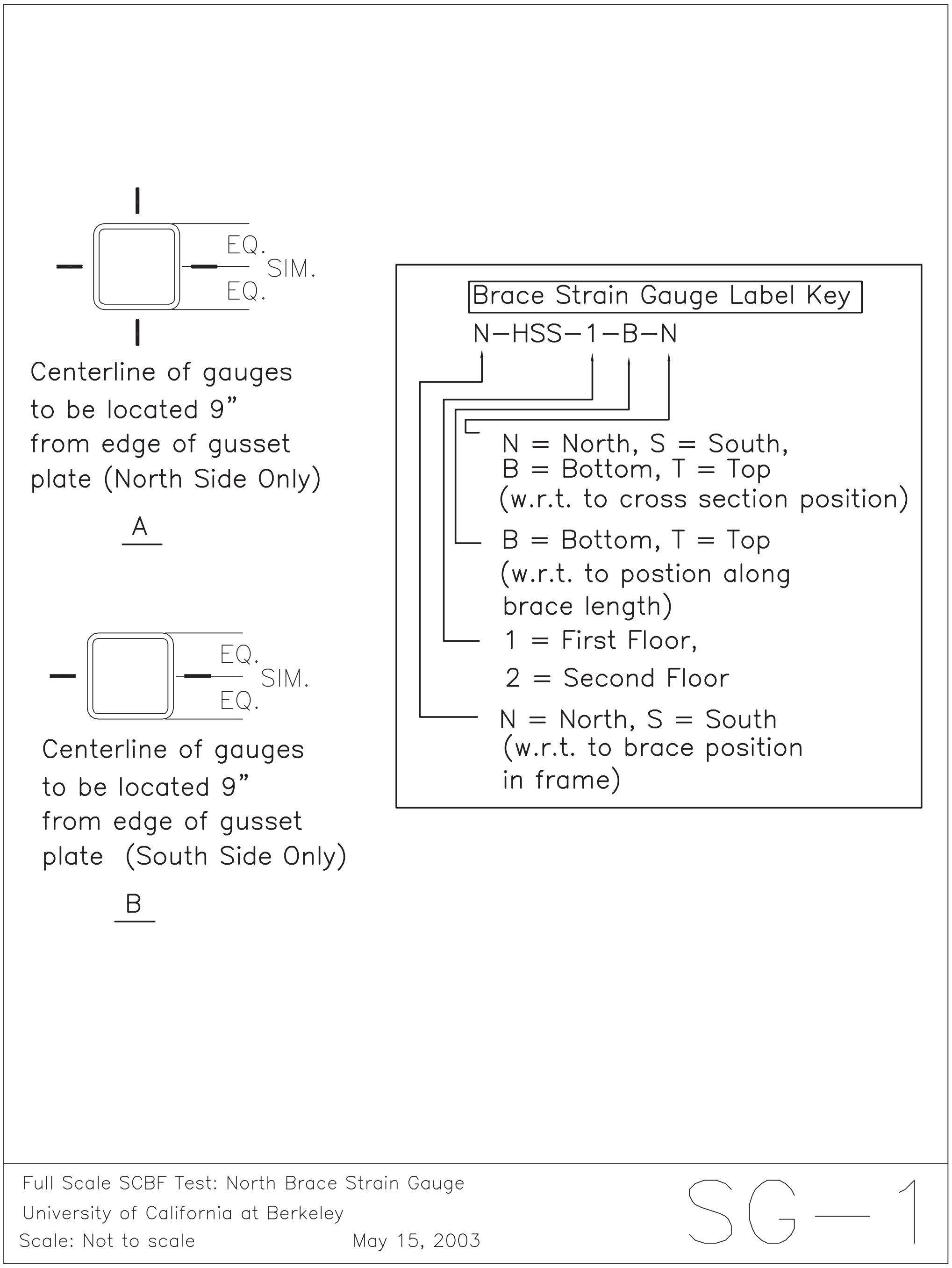

Strain-gage labels and locations.

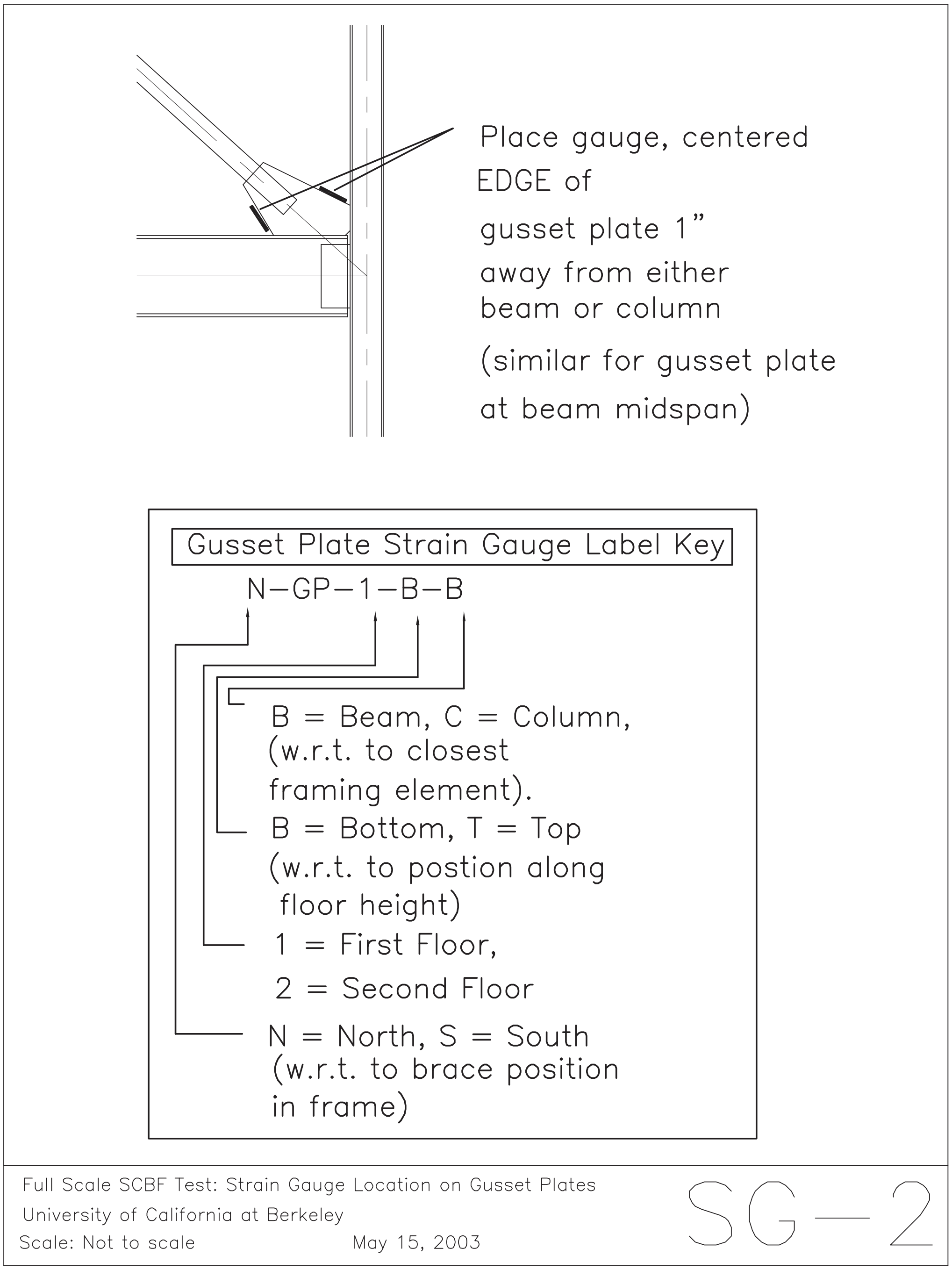

Strain-gage labels and locations.

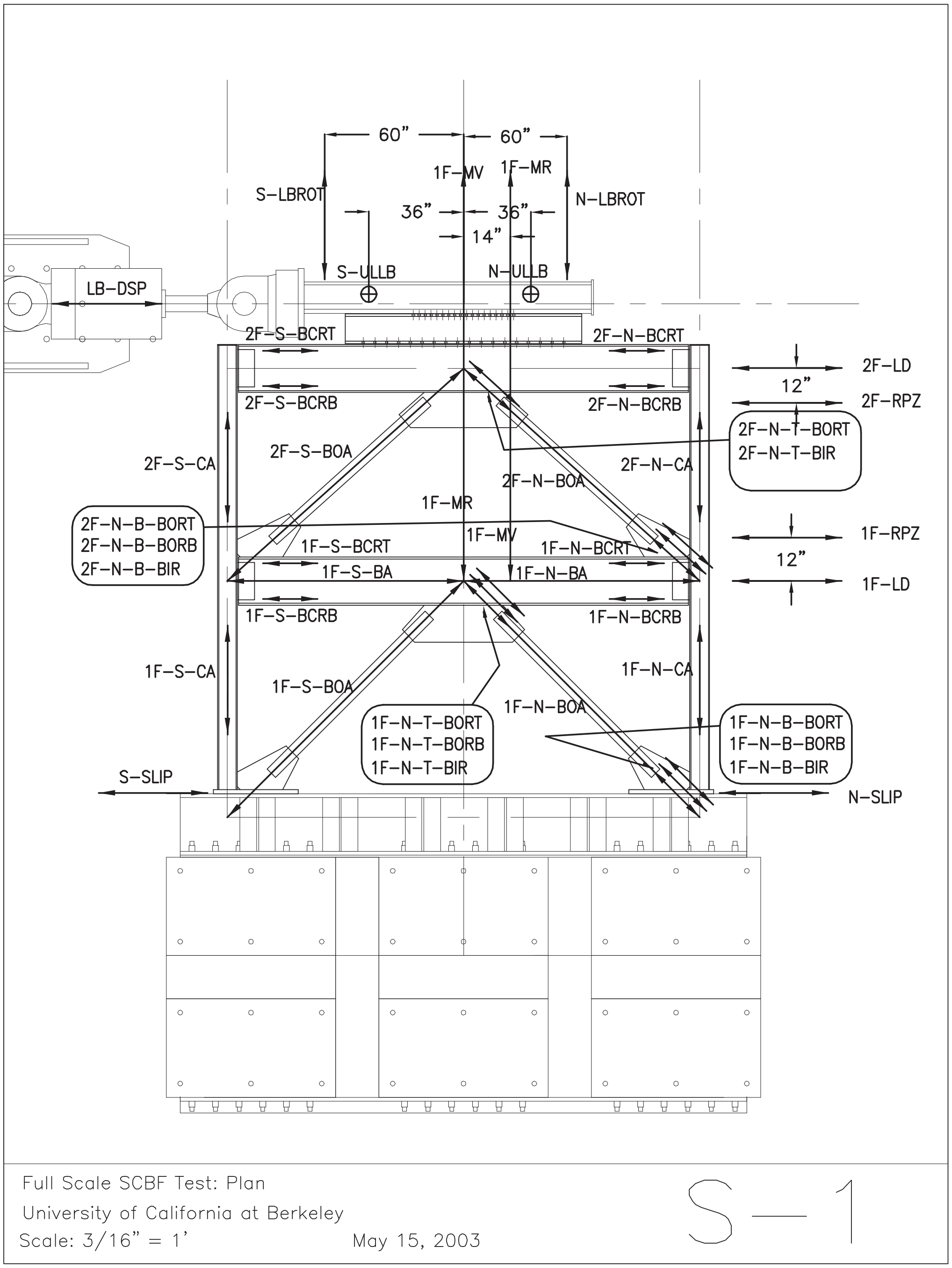

Displacement instrumentation labels.

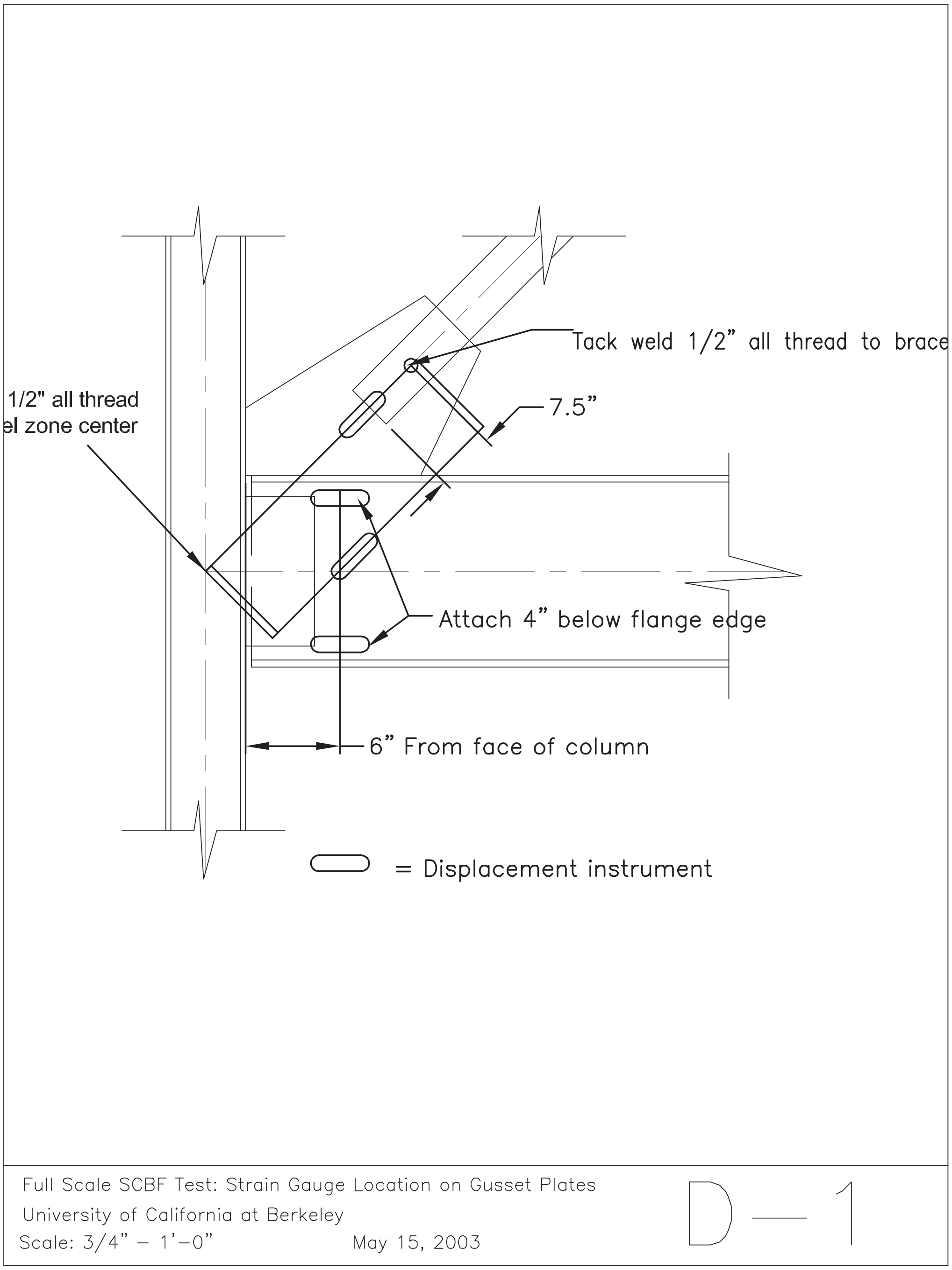

Displacement instrumentation locations.

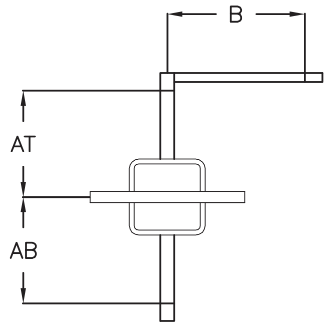

For the top story,

Brace End Displacement Dimensions				
Floor	Position	AT	AB	B
1	Top	17.25”	16.75”	12”
1	Bottom	13.0”	13.5”	12”
2	Top	12.5”	N/A	12”
2	Bottom	12.0”	13.75	12”

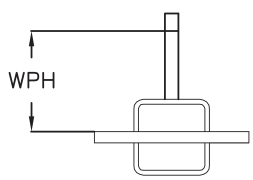

Brace Axial Elongation Dimensions				
Floor	Position	WPH		
1	North	19.0”		
1	South	19.0”		
2	North	16.25”		
2	South	13.5”		

Distance from wire pot to:
Gusset plate or beam web

Full Scale SCBF Test: Strain Gauge Location on Gusset Plates
University of California at Berkeley
Scale: 3/4” – 1’–0”   May 15, 2003

D — 2

Instrumentation location on brace.

Appendix D: Channel List for Specimen SCBF-1

Channel Box # 1; Actuator/Load Cell

channel	Count #	label	Device	description	Input
1	1	LC	Load cell	Actuator for drift	
2	2				
3	3				
4	4				
5	5				
6	6				
7	7				
8	8				
9	9				
10	10				
11	11	tmp	Temposonic	36" temposonic	
12	12				
13	13				
14	14				
15	15				
16	16		trafo	Power supply	2.56V

Channel Box # 2; Strain Gages and Rosettes

channel	Count #	label	Device	Description	Input
17	1	SC1BL	linear	South Col., 1st flr, bottom left	2V
18	2	SC1BR	linear	South Col., 1st flr, bottom right	2V
19	3	SCS1a	2 gauge rosette	South Col., 1st flr, shear	2V
20	4	SCS1b	2 gage rosette	South Col., 1st flr, shear	2V
21	5	SC1TL	linear	South Col., 1st flr, top left	2V
22	6	SC1TR	linear	South Col., 1st flr, top right	2V
23	7	S-HSS-1-B-N	linear	South Brace, 1st flr, bottom, north facing	2V
24	8	S-HSS-1-B-S	linear	South Brace, 1st flr, bottom, south facing	2V
25	9	S-HSS-1-T-N	linear	South Brace, 1st flr, top, north facing	2V
26	10	S-HSS-1-T-S	linear	South Brace, 1st flr, top, south facing	2V
27	11	SB1BL	linear	South Beam, 1st flr, bottom left	2V
28	12	SB1BR	linear	South Beam, 1st flr, bottom right	2V
29	13	SCPZR1a	3 gage rosette	South Col., 1st flr, panel zone rosette	2V
30	14	SCPZR1b	3 gage rosette	South Col., 1st flr, panel zone rosette	2V
31	15	SCPZR1c	3 gage rosette	South Col., 1st flr, panel zone rosette	2V
32	16		Trafo	Power supply	2.56V

Channel Box # 3; Strain Gages and Rosettes

channel	Count #	label	Device	Description	Input
33	1	SC2BL	linear	South Col., 2nd flr, bottom left	2V
34	2	SC2BR	linear	South Col., 2nd flr, bottom right	2V
35	3	SCS2a	2 gage rosette	South Col.,2nd flr, shear	2V
36	4	SCS2b	2 gage rosette	South Col., 2nd flr, shear	2V
37	5	SC2TL	linear	South Col., 2nd flr, top left	2V
38	6	SC2TR	linear	South Col., 2nd flr, top right	2V
39	7	SCPZR2a	3 gage rosette	South Col., 2nd flr, panel zone rosette	2V
40	8	SCPZR2b	3 gage rosette	South Col., 2nd flr, panel zone rosette	2V
41	9	SCPZR2c	3 gage rosette	South Col., 2nd flr, panel zone rosette	2V
42	10	SB2BL	linear	South Beam, 2nd flr, bottom left	2V
43	11	SB2BR	linear	South Beam, 2nd flr, bottom right	2V
44	12	SB2TL	linear	South Beam, 2nd flr, top left	2V
45	13	SB2TR	linear	South Beam, 2nd flr, top right	2V
46	14	SBS2a	2 gage rosette	South Beam, 2nd flr, shear	2V
47	15	SBS2b	2 gage rosette	South Beam, 2nd flr, shear	2V
48	16		trafo	Power supply	2V

Channel Box # 4; Strain Gages and Rosettes

channel	Count #	label	Device	Description	Input
49	1	SBS1a	2 gage rosette	South Beam, 1st flr, shear	2V
50	2	SBS1b	2 gage rosette	South Beam, 1st flr, shear	2V
51	3	SB1TL	linear	South Beam, 1st flr, top left	2V
52	4	SB1TR	linear	South Beam, 1st flr, top right	2V
53	5	S-HSS-2-B-N	linear	South Brace, 2nd flr, bottom, north facing	2V
54	6	S-HSS-2-B-S	linear	South Brace, 2nd flr, bottom, south facing	2V
55	7	S-HSS-2-T-N	linear	South Brace, 2nd flr, top, north facing	2V
56	8	S-HSS-2-T-S	linear	South Brace, 2nd flr, top, south facing	2V
57	9	N-HSS-2-T-N	linear	North Brace, 2nd flr, top, north facing	2V
58	10	N-HSS-2-T-S	linear	North Brace, 2nd flr, top, south facing	2V
59	11	N-HSS-2-T-B	linear	North Brace, 2nd flr, top, bottom facing	2V
60	12	N-HSS-2-T-T	linear	North Brace, 2nd flr, top, top facing	2V
61	13	N-GP-2-T-B	linear	North gusset, 2nd flr, top, next to beam	2V
62	14	NB1TL	linear	North Beam,1st flr, top leftr	2V
63	15	NB1TR	linear	North Beam, 1st flr, top right	2V
64	16		trafo	Power supply	2V

Channel Box # 5; Strain Gages and Rosettes

channel	Count #	label	Device	Description	Input
65	1	NC2BL	linear	North Col., 2^{nd} flr, bottom left	2V
66	2	NC2BR	linear	North Col., 2^{nd} flr, bottom right	2V
67	3	NCS2a	2 gage rosette	North Col.,2^{nd} flr, shear	2V
68	4	NCS2b	2 gage rosette	North Col., 2^{nd} flr, shear	2V
69	5	NC2TL	linear	North Col., 2^{nd} flr, top left	2V
70	6	NC2TR	linear	North Col., 2^{nd} flr, top right	2V
		:::Empty:::	:::Empty:::		
		:::Empty:::	:::Empty:::		
		:::Empty:::	:::Empty:::		
74	10	NB2BL	linear	North Beam, 2^{nd} flr, bottom left	2V
75	11	NB2BR	linear	North Beam, 2^{nd} flr, bottom right	2V
76	12	NB2TL	linear	North Beam, 2^{nd} flr, top left	2V
77	13	NB2TR	linear	North Beam, 2^{nd} flr, top right	2V
78	14	NBS2a	2 gage rosette	North Beam, 2^{nd} flr, shear	2V
79	15	NBS2b	2 gage rosette	North Beam, 2^{nd} flr, shear	2V
80	16		trafo	Power supply	2V

Channel Box # 6; Strain Gages and Rosettes

channel	Count #	label	Device	Description	Input
81	1	NC1TL	linear	North Col., 1^{st} flr, top left	2V
82	2	NC1TR	linear	North Col., 1^{st} flr, top right	2V
83	3	NB1BL	linear	North Beam, 1^{st} flr, bottom left	2V
84	4	NB1BR	linear	North Beam, 1^{st} flr, bottom right	2V
85	5	NBS1a	2 gage rosette	North Beam, 1^{st} flr, shear	2V
86	6	NBS1b	2 gage rosette	North Beam, 1^{st} flr, shear	2V
		:::Empty:::	:::Empty:::		
		:::Empty:::	:::Empty:::		
		:::Empty:::	:::Empty:::		
90	10	N-GP-2-B-B	linear	North gusset, 2^{nd} flr, bottom, next to bm	2V
91	11	N-GP-2-B-C	linear	North gusset, 2^{nd} flr, bottom, next to col	2V
92	12	N-HSS-2-B-N	linear	North Brace, 2^{nd} flr, btm, north facing	2V
93	13	N-HSS-2-B-S	linear	North Brace, 2^{nd} flr, btm, south facing	2V
94	14	N-HSS-2-B-B	linear	North Brace, 2^{nd} flr, btm, bottom facing	2V
95	15	N-HSS-2-B-T	linear	North Brace, 2^{nd} flr, btm, top facing	2V
96	16		trafo	Power supply	2V

Channel Box # 7; Strain Gages and Rosettes

channel	Count #	label	Device	Description	Input
97	1	NC1BL	linear	North Col., 1st flr, bottom left	2V
98	2	NC1BR	linear	North Col., 1st flr, bottom right	2V
99	3	NCS1a	2 gage rosette	North Col., 1st flr, shear	2V
100	4	NCS1b	2 gage rosette	North Col., 1st flr, shear	2V
101	5	N-GP-1-B-B	linear	North gusset, 1st flr, bottom, next to bm	2V
102	6	N-GP-1-B-C	linear	North gusset, 1st flr, bottom, next to col	2V
103	7	N-HSS-1-B-N	linear	North Brace, 1st flr, btm, north facing	2V
104	8	N-HSS-1-B-S	linear	North Brace, 1st flr, btm, south facing	2V
105	9	N-HSS-1-B-B	linear	North Brace, 1st flr, btm, bottom facing	2V
106	10	N-HSS-1-B-T	linear	North Brace, 1st flr, btm, top facing	2V
107	11	N-HSS-1-T-N	linear	North Brace, 1st flr, top, north facing	2V
108	12	N-HSS-1-T-S	linear	North Brace, 1st flr, top, south facing	2V
109	13	N-HSS-1-T-B	linear	North Brace, 1st flr, top, bottom facing	2V
110	14	N-HSS-1-T-T	linear	North Brace, 1st flr, top, top facing	2V
111	15	N-GP-1-T-B	linear	North gusset, 1st flr, top, next to bm	2V
112	16		Trafo	Power supply	2.56V

Channel Box # 8; EMPTY

channel	Count #	Label	device	description	Input
113	1				2V
114	2				2V
115	3				2V
116	4				2V
117	5				2V
118	6				2V
119	7				2V
120	8				2V
121	9				2V
122	10				2V
123	11				2V
124	12				2V
125	13				2V
126	14				2V
127	15				2V
128	16		trafo	Power supply	2V

Channel Box #9; Local Deflections /Pots

channel	count #	Label	device	description	Input
129	1	ASLP	1"stick	Slip of Actuator	5V
130	2	2F-N-BA	1" stick	2nd Floor- North- Beam Axial	5V
131	3	S-ULLB	1"stick	South - Uplift of Loading Beam	5V
132	4	N-ULLB	1"stick	North - Uplift of Loading Beam	5V
133	5	S-LBROT	2"stick	South - Loading Beam - Rotation	5V
134	6	N-LBROT	2"stick	North - Loading Beam - Rotation	5V
135	7	1F-N-BO	15"wire	1st Floor - North Brace, Out-of-Plane displacement	5V
136	8	2F-S-BCRT	1" stick	2nd Floor - South - Beam Column Rotation Top	5V
137	9	2F-S-BCRB	1" stick	2nd Floor - South - Beam Column Rotation Bottom	5V
138	10	2F-S-CA	1" stick	2nd Floor - South - Column Axial	5V
139	11	2F-S-BOA	7" wire	2nd Floor -South - Brace Overall Axial	5V
140	12	1F-MV	2" stick	1st Floor –Midspan Vertical (E-W motion)	5V
141	13	1F-MR	2" stick	1st Floor –Midspan Rotation	5V
142	14	2F-N-T-BORT	6 " stick	2nd Floor - North - Top – Brace OUT-Plane Rot. Top	5V
143	15	2F-S-BA	1" stick	2nd Floor – South – Beam Axial	5V
144	16		Trafo	Power supply	

Channel Box # 10; Local Deflections /Pots

channel	Count #	Label	Device	Description	Input
145	1	2F-LD	15" wire	2nd Floor Lateral Displacement	5V
146	2	2F-RPZ	15" wire	2nd Floor Rotation Panel Zone	5V
147	3	2F-N-T-BIR	6" stick	2nd Floor - North - Top – Brace IN-Plane Rot.	5V
148	4	2F-N-BOA	7" wire	2nd Floor -North - Brace Overall Axial	5V
149	5	2F-N-BCRT	2" stick	2nd Floor - North - Beam Column Rot Top	5V
150	6	2F-N-BCRB	2" stick	2nd Floor - North - Beam Column Rot Bottom	5V
151	7	2F-N-CA	1" stick	2nd Floor - North - Column Axial	5V
152	8	1F-LD	15" wire	1st Floor - Lateral Displacement	5V
153	9	1F-RPZ	15" wire	1st Floor - Rotation Panel Zone	5V
154	10	1F-N-BA	1"stick	1st Floor - North - Beam Axial	5V
155	11	1F-N-BCRT	1" stick	1st Floor - North - Beam Column Rotation Top	5V
156	12	1F-N-BCRB	1" stick	1st Floor - North - Beam Column Rotation Bottom	5V
157	13	2F-N-B-BORT	6"stick	2nd Floor - North - Bottom - Brace OUT-Plane Rot. Top	5V
158	14	2F-N-B-BORB	6"stick	2nd Floor - North - Bottom - Brace OUT-Plane Rot. Bottom	5V
159	15	2F-N-B-BIR	6"stick	2nd Floor - North - Bottom - Brace IN-Plane Rot.	5V
160	16		Trafo	Power supply	5V

Channel Box # 11; Deflection/Pot

Channel	count #	Label	Device	Description	Input
161	1	1F-N-CA	1"stick	1st Floor - North - Column Axial	5V
162	2	N-SLIP	1" stick	North Base Slip	5V
163	3	1F-N-B-BORT	6"stick	1st Floor - North - Bottom - Brace OUT-Plane Rot. Top	5V
164	4	1F-N-B-BORB	6"stick	1st Floor - North - Bottom - Brace OUT-Plane Rot. Bottom	5V
165	5	1F-N-B-BIR	6"stick	1st Floor - North - Bottom - Brace IN-Plane Rot.	5V
166	6	1F-N-BOA	7" wire	1st Floor -North - Brace Overall Axial	5V
167	7	1F-N-T-BORT	6"stick	1st Floor - North - Top - Brace OUT-Plane Rot. Top	5V
168	8	1F-N-T-BORB	6"stick	1st Floor - North - Top - Brace OUT-Plane Rot. Bottom	5V
169	9	1F-N-T-BIR	6"stick	1st Floor - North - Top - Brace IN-Plane Rot.	5V
170	10	1F-S-BOA	7" wire	1st Floor -South - Brace Overall Axial	5V
171	11	1F-S-BA	1"stick	1st Floor - South - Beam Axial	5V
172	12	1F-S-CA	1"stick	1st Floor - South - Column Axial	5V
173	13	1F-S-BCRT	1" stick	1st Floor - South - Beam Column Rotation Top	5V
174	14	1F-S-BCRB	1" stick	1st Floor - South - Beam Column Rotation Bottom	5V
175	15	S-SLIP	1"stick	South Base Slip	5V
176	16		Trafo	Power supply	5V

PEER REPORTS

PEER reports are available from the National Information Service for Earthquake Engineering (NISEE). To order PEER reports, please contact the Pacific Earthquake Engineering Research Center, 1301 South 46th Street, Richmond, California 94804-4698. Tel.: (510) 665-3405; Fax: (510) 665-3420.

PEER 2008/08 *Toward Earthquake-Resistant Design of Concentrically Braced Steel-Frame Structures.* Patxi Uriz and Stephen A. Mahin. November 2008.

PEER 2008/07 *Using OpenSees for Performance-Based Evaluation of Bridges on Liquefiable Soils.* Stephen L. Kramer, Pedro Arduino, and HyungSuk Shin. November 2008.

PEER 2008/06 *Shaking Table Tests and Numerical Investigation of Self-Centering Reinforced Concrete Bridge Columns.* Hyung IL Jeong, Junichi Sakai, and Stephen A. Mahin. September 2008.

PEER 2008/05 *Performance-Based Earthquake Engineering Design Evaluation Procedure for Bridge Foundations Undergoing Liquefaction-Induced Lateral Ground Displacement.* Christian A. Ledezma and Jonathan D. Bray. August 2008.

PEER 2008/04 *Benchmarking of Nonlinear Geotechnical Ground Response Analysis Procedures.* Jonathan P. Stewart, Annie On-Lei Kwok, Youssef M. A. Hashash, Neven Matasovic, Robert Pyke, Zhiliang Wang, and Zhaohui Yang. August 2008.

PEER 2008/03 *Guidelines for Nonlinear Analysis of Bridge Structures in California.* Ady Aviram, Kevin R. Mackie, and Božidar Stojadinović. August 2008.

PEER 2008/02 *Treatment of Uncertainties in Seismic-Risk Analysis of Transportation Systems.* Evangelos Stergiou and Anne S. Kiremidjian. July 2008.

PEER 2008/01 *Seismic Performance Objectives for Tall Buildings.* William T. Holmes, Charles Kircher, William Petak, and Nabih Youssef. August 2008.

PEER 2007/12 *An Assessment to Benchmark the Seismic Performance of a Code-Conforming Reinforced Concrete Moment-Frame Building.* Curt Haselton, Christine A. Goulet, Judith Mitrani-Reiser, James L. Beck, Gregory G. Deierlein, Keith A. Porter, Jonathan P. Stewart, and Ertugrul Taciroglu. August 2008.

PEER 2007/11 *Bar Buckling in Reinforced Concrete Bridge Columns.* Wayne A. Brown, Dawn E. Lehman, and John F. Stanton. February 2008.

PEER 2007/10 *Computational Modeling of Progressive Collapse in Reinforced Concrete Frame Structures.* Mohamed M. Talaat and Khalid M. Mosalam. May 2008.

PEER 2007/09 *Integrated Probabilistic Performance-Based Evaluation of Benchmark Reinforced Concrete Bridges.* Kevin R. Mackie, John-Michael Wong, and Božidar Stojadinović. January 2008.

PEER 2007/08 *Assessing Seismic Collapse Safety of Modern Reinforced Concrete Moment-Frame Buildings.* Curt B. Haselton and Gregory G. Deierlein. February 2008.

PEER 2007/07 *Performance Modeling Strategies for Modern Reinforced Concrete Bridge Columns.* Michael P. Berry and Marc O. Eberhard. April 2008.

PEER 2007/06 *Development of Improved Procedures for Seismic Design of Buried and Partially Buried Structures.* Linda Al Atik and Nicholas Sitar. June 2007.

PEER 2007/05 *Uncertainty and Correlation in Seismic Risk Assessment of Transportation Systems.* Renee G. Lee and Anne S. Kiremidjian. July 2007.

PEER 2007/04 *Numerical Models for Analysis and Performance-Based Design of Shallow Foundations Subjected to Seismic Loading.* Sivapalan Gajan, Tara C. Hutchinson, Bruce L. Kutter, Prishati Raychowdhury, José A. Ugalde, and Jonathan P. Stewart. May 2008.

PEER 2007/03 *Beam-Column Element Model Calibrated for Predicting Flexural Response Leading to Global Collapse of RC Frame Buildings.* Curt B. Haselton, Abbie B. Liel, Sarah Taylor Lange, and Gregory g. Deierlein. May 2008.

PEER 2007/02 *Campbell-Bozorgnia NGA Ground Motion Relations for the Geometric Mean Horizontal Component of Peak and Spectral Ground Motion Parameters.* Kenneth W. Campbell and Yousef Bozorgnia. May 2007.

PEER 2007/01 *Boore-Atkinson NGA Ground Motion Relations for the Geometric Mean Horizontal Component of Peak and Spectral Ground Motion Parameters.* David M. Boore and Gail M. Atkinson. May. May 2007.

PEER 2006/12 *Societal Implications of Performance-Based Earthquake Engineering.* Peter J. May. May 2007.

PEER 2006/11 *Probabilistic Seismic Demand Analysis Using Advanced Ground Motion Intensity Measures, Attenuation Relationships, and Near-Fault Effects.* Polsak Tothong and C. Allin Cornell. March 2007.

PEER 2006/10 *Application of the PEER PBEE Methodology to the I-880 Viaduct.* Sashi Kunnath. February 2007.

PEER 2006/09 *Quantifying Economic Losses from Travel Forgone Following a Large Metropolitan Earthquake.* James Moore, Sungbin Cho, Yue Yue Fan, and Stuart Werner. November 2006.

PEER 2006/08 *Vector-Valued Ground Motion Intensity Measures for Probabilistic Seismic Demand Analysis*. Jack W. Baker and C. Allin Cornell. October 2006.

PEER 2006/07 *Analytical Modeling of Reinforced Concrete Walls for Predicting Flexural and Coupled–Shear-Flexural Responses.* Kutay Orakcal, Leonardo M. Massone, and John W. Wallace. October 2006.

PEER 2006/06 *Nonlinear Analysis of a Soil-Drilled Pier System under Static and Dynamic Axial Loading.* Gang Wang and Nicholas Sitar. November 2006.

PEER 2006/05 *Advanced Seismic Assessment Guidelines.* Paolo Bazzurro, C. Allin Cornell, Charles Menun, Maziar Motahari, and Nicolas Luco. September 2006.

PEER 2006/04 *Probabilistic Seismic Evaluation of Reinforced Concrete Structural Components and Systems.* Tae Hyung Lee and Khalid M. Mosalam. August 2006.

PEER 2006/03 *Performance of Lifelines Subjected to Lateral Spreading.* Scott A. Ashford and Teerawut Juirnarongrit. July 2006.

PEER 2006/02 *Pacific Earthquake Engineering Research Center Highway Demonstration Project.* Anne Kiremidjian, James Moore, Yue Yue Fan, Nesrin Basoz, Ozgur Yazali, and Meredith Williams. April 2006.

PEER 2006/01 *Bracing Berkeley. A Guide to Seismic Safety on the UC Berkeley Campus.* Mary C. Comerio, Stephen Tobriner, and Ariane Fehrenkamp. January 2006.

PEER 2005/16 *Seismic Response and Reliability of Electrical Substation Equipment and Systems.* Junho Song, Armen Der Kiureghian, and Jerome L. Sackman. April 2006.

PEER 2005/15 *CPT-Based Probabilistic Assessment of Seismic Soil Liquefaction Initiation.* R. E. S. Moss, R. B. Seed, R. E. Kayen, J. P. Stewart, and A. Der Kiureghian. April 2006.

PEER 2005/14 *Workshop on Modeling of Nonlinear Cyclic Load-Deformation Behavior of Shallow Foundations.* Bruce L. Kutter, Geoffrey Martin, Tara Hutchinson, Chad Harden, Sivapalan Gajan, and Justin Phalen. March 2006.

PEER 2005/13 *Stochastic Characterization and Decision Bases under Time-Dependent Aftershock Risk in Performance-Based Earthquake Engineering.* Gee Liek Yeo and C. Allin Cornell. July 2005.

PEER 2005/12 *PEER Testbed Study on a Laboratory Building: Exercising Seismic Performance Assessment.* Mary C. Comerio, editor. November 2005.

PEER 2005/11 *Van Nuys Hotel Building Testbed Report: Exercising Seismic Performance Assessment.* Helmut Krawinkler, editor. October 2005.

PEER 2005/10 *First NEES/E-Defense Workshop on Collapse Simulation of Reinforced Concrete Building Structures.* September 2005.

PEER 2005/09 *Test Applications of Advanced Seismic Assessment Guidelines.* Joe Maffei, Karl Telleen, Danya Mohr, William Holmes, and Yuki Nakayama. August 2006.

PEER 2005/08 *Damage Accumulation in Lightly Confined Reinforced Concrete Bridge Columns.* R. Tyler Ranf, Jared M. Nelson, Zach Price, Marc O. Eberhard, and John F. Stanton. April 2006.

PEER 2005/07 *Experimental and Analytical Studies on the Seismic Response of Freestanding and Anchored Laboratory Equipment.* Dimitrios Konstantinidis and Nicos Makris. January 2005.

PEER 2005/06 *Global Collapse of Frame Structures under Seismic Excitations*. Luis F. Ibarra and Helmut Krawinkler. September 2005.

PEER 2005/05 *Performance Characterization of Bench- and Shelf-Mounted Equipment.* Samit Ray Chaudhuri and Tara C. Hutchinson. May 2006.

PEER 2005/04 *Numerical Modeling of the Nonlinear Cyclic Response of Shallow Foundations.* Chad Harden, Tara Hutchinson, Geoffrey R. Martin, and Bruce L. Kutter. August 2005.

PEER 2005/03 *A Taxonomy of Building Components for Performance-Based Earthquake Engineering.* Keith A. Porter. September 2005.

PEER 2005/02 *Fragility Basis for California Highway Overpass Bridge Seismic Decision Making*. Kevin R. Mackie and Božidar Stojadinović. June 2005.

PEER 2005/01 *Empirical Characterization of Site Conditions on Strong Ground Motion.* Jonathan P. Stewart, Yoojoong Choi, and Robert W. Graves. June 2005.

PEER 2004/09 *Electrical Substation Equipment Interaction: Experimental Rigid Conductor Studies.* Christopher Stearns and André Filiatrault. February 2005.

PEER 2004/08 *Seismic Qualification and Fragility Testing of Line Break 550-kV Disconnect Switches.* Shakhzod M. Takhirov, Gregory L. Fenves, and Eric Fujisaki. January 2005.

PEER 2004/07 *Ground Motions for Earthquake Simulator Qualification of Electrical Substation Equipment.* Shakhzod M. Takhirov, Gregory L. Fenves, Eric Fujisaki, and Don Clyde. January 2005.

PEER 2004/06 *Performance-Based Regulation and Regulatory Regimes.* Peter J. May and Chris Koski. September 2004.

PEER 2004/05 *Performance-Based Seismic Design Concepts and Implementation: Proceedings of an International Workshop.* Peter Fajfar and Helmut Krawinkler, editors. September 2004.

PEER 2004/04 *Seismic Performance of an Instrumented Tilt-up Wall Building.* James C. Anderson and Vitelmo V. Bertero. July 2004.

PEER 2004/03 *Evaluation and Application of Concrete Tilt-up Assessment Methodologies.* Timothy Graf and James O. Malley. October 2004.

PEER 2004/02 *Analytical Investigations of New Methods for Reducing Residual Displacements of Reinforced Concrete Bridge Columns.* Junichi Sakai and Stephen A. Mahin. August 2004.

PEER 2004/01 *Seismic Performance of Masonry Buildings and Design Implications.* Kerri Anne Taeko Tokoro, James C. Anderson, and Vitelmo V. Bertero. February 2004.

PEER 2003/18 *Performance Models for Flexural Damage in Reinforced Concrete Columns.* Michael Berry and Marc Eberhard. August 2003.

PEER 2003/17 *Predicting Earthquake Damage in Older Reinforced Concrete Beam-Column Joints.* Catherine Pagni and Laura Lowes. October 2004.

PEER 2003/16 *Seismic Demands for Performance-Based Design of Bridges.* Kevin Mackie and Božidar Stojadinović. August 2003.

PEER 2003/15 *Seismic Demands for Nondeteriorating Frame Structures and Their Dependence on Ground Motions.* Ricardo Antonio Medina and Helmut Krawinkler. May 2004.

PEER 2003/14 *Finite Element Reliability and Sensitivity Methods for Performance-Based Earthquake Engineering.* Terje Haukaas and Armen Der Kiureghian. April 2004.

PEER 2003/13 *Effects of Connection Hysteretic Degradation on the Seismic Behavior of Steel Moment-Resisting Frames.* Janise E. Rodgers and Stephen A. Mahin. March 2004.

PEER 2003/12 *Implementation Manual for the Seismic Protection of Laboratory Contents: Format and Case Studies.* William T. Holmes and Mary C. Comerio. October 2003.

PEER 2003/11 *Fifth U.S.-Japan Workshop on Performance-Based Earthquake Engineering Methodology for Reinforced Concrete Building Structures.* February 2004.

PEER 2003/10 *A Beam-Column Joint Model for Simulating the Earthquake Response of Reinforced Concrete Frames.* Laura N. Lowes, Nilanjan Mitra, and Arash Altoontash. February 2004.

PEER 2003/09 *Sequencing Repairs after an Earthquake: An Economic Approach.* Marco Casari and Simon J. Wilkie. April 2004.

PEER 2003/08 *A Technical Framework for Probability-Based Demand and Capacity Factor Design (DCFD) Seismic Formats*. Fatemeh Jalayer and C. Allin Cornell. November 2003.

PEER 2003/07 *Uncertainty Specification and Propagation for Loss Estimation Using FOSM Methods.* Jack W. Baker and C. Allin Cornell. September 2003.

PEER 2003/06 *Performance of Circular Reinforced Concrete Bridge Columns under Bidirectional Earthquake Loading*. Mahmoud M. Hachem, Stephen A. Mahin, and Jack P. Moehle. February 2003.

PEER 2003/05 *Response Assessment for Building-Specific Loss Estimation.* Eduardo Miranda and Shahram Taghavi. September 2003.

PEER 2003/04 *Experimental Assessment of Columns with Short Lap Splices Subjected to Cyclic Loads*. Murat Melek, John W. Wallace, and Joel Conte. April 2003.

PEER 2003/03 *Probabilistic Response Assessment for Building-Specific Loss Estimation.* Eduardo Miranda and Hesameddin Aslani. September 2003.

PEER 2003/02 *Software Framework for Collaborative Development of Nonlinear Dynamic Analysis Program.* Jun Peng and Kincho H. Law. September 2003.

PEER 2003/01 *Shake Table Tests and Analytical Studies on the Gravity Load Collapse of Reinforced Concrete Frames.* Kenneth John Elwood and Jack P. Moehle. November 2003.

PEER 2002/24 *Performance of Beam to Column Bridge Joints Subjected to a Large Velocity Pulse.* Natalie Gibson, André Filiatrault, and Scott A. Ashford. April 2002.

PEER 2002/23 *Effects of Large Velocity Pulses on Reinforced Concrete Bridge Columns.* Greg L. Orozco and Scott A. Ashford. April 2002.

PEER 2002/22 *Characterization of Large Velocity Pulses for Laboratory Testing.* Kenneth E. Cox and Scott A. Ashford. April 2002.

PEER 2002/21 *Fourth U.S.-Japan Workshop on Performance-Based Earthquake Engineering Methodology for Reinforced Concrete Building Structures*. December 2002.

PEER 2002/20 *Barriers to Adoption and Implementation of PBEE Innovations.* Peter J. May. August 2002.

PEER 2002/19 *Economic-Engineered Integrated Models for Earthquakes: Socioeconomic Impacts.* Peter Gordon, James E. Moore II, and Harry W. Richardson. July 2002.

PEER 2002/18 *Assessment of Reinforced Concrete Building Exterior Joints with Substandard Details.* Chris P. Pantelides, Jon Hansen, Justin Nadauld, and Lawrence D. Reaveley. May 2002.

PEER 2002/17 *Structural Characterization and Seismic Response Analysis of a Highway Overcrossing Equipped with Elastomeric Bearings and Fluid Dampers: A Case Study.* Nicos Makris and Jian Zhang. November 2002.

PEER 2002/16 *Estimation of Uncertainty in Geotechnical Properties for Performance-Based Earthquake Engineering.* Allen L. Jones, Steven L. Kramer, and Pedro Arduino. December 2002.

PEER 2002/15 *Seismic Behavior of Bridge Columns Subjected to Various Loading Patterns.* Asadollah Esmaeily-Gh. and Yan Xiao. December 2002.

PEER 2002/14 *Inelastic Seismic Response of Extended Pile Shaft Supported Bridge Structures.* T.C. Hutchinson, R.W. Boulanger, Y.H. Chai, and I.M. Idriss. December 2002.

PEER 2002/13 *Probabilistic Models and Fragility Estimates for Bridge Components and Systems.* Paolo Gardoni, Armen Der Kiureghian, and Khalid M. Mosalam. June 2002.

PEER 2002/12 *Effects of Fault Dip and Slip Rake on Near-Source Ground Motions: Why Chi-Chi Was a Relatively Mild M7.6 Earthquake.* Brad T. Aagaard, John F. Hall, and Thomas H. Heaton. December 2002.

PEER 2002/11 *Analytical and Experimental Study of Fiber-Reinforced Strip Isolators*. James M. Kelly and Shakhzod M. Takhirov. September 2002.

PEER 2002/10 *Centrifuge Modeling of Settlement and Lateral Spreading with Comparisons to Numerical Analyses***.** Sivapalan Gajan and Bruce L. Kutter. January 2003.

PEER 2002/09 *Documentation and Analysis of Field Case Histories of Seismic Compression during the 1994 Northridge, California, Earthquake.* Jonathan P. Stewart, Patrick M. Smith, Daniel H. Whang, and Jonathan D. Bray. October 2002.

PEER 2002/08 *Component Testing, Stability Analysis and Characterization of Buckling-Restrained Unbonded Braces™.* Cameron Black, Nicos Makris, and Ian Aiken. September 2002.

PEER 2002/07 *Seismic Performance of Pile-Wharf Connections.* Charles W. Roeder, Robert Graff, Jennifer Soderstrom, and Jun Han Yoo. December 2001.

PEER 2002/06 *The Use of Benefit-Cost Analysis for Evaluation of Performance-Based Earthquake Engineering Decisions.* Richard O. Zerbe and Anthony Falit-Baiamonte. September 2001.

PEER 2002/05 *Guidelines, Specifications, and Seismic Performance Characterization of Nonstructural Building Components and Equipment*. André Filiatrault, Constantin Christopoulos, and Christopher Stearns. September 2001.

PEER 2002/04 *Consortium of Organizations for Strong-Motion Observation Systems and the Pacific Earthquake Engineering Research Center Lifelines Program: Invited Workshop on Archiving and Web Dissemination of Geotechnical Data, 4–5 October 2001*. September 2002.

PEER 2002/03 *Investigation of Sensitivity of Building Loss Estimates to Major Uncertain Variables for the Van Nuys Testbed.* Keith A. Porter, James L. Beck, and Rustem V. Shaikhutdinov. August 2002.

PEER 2002/02 *The Third U.S.-Japan Workshop on Performance-Based Earthquake Engineering Methodology for Reinforced Concrete Building Structures*. July 2002.

PEER 2002/01 *Nonstructural Loss Estimation: The UC Berkeley Case Study.* Mary C. Comerio and John C. Stallmeyer. December 2001.

PEER 2001/16 *Statistics of SDF-System Estimate of Roof Displacement for Pushover Analysis of Buildings.* Anil K. Chopra, Rakesh K. Goel, and Chatpan Chintanapakdee. December 2001.

PEER 2001/15 *Damage to Bridges during the 2001 Nisqually Earthquake.* R. Tyler Ranf, Marc O. Eberhard, and Michael P. Berry. November 2001.

PEER 2001/14 *Rocking Response of Equipment Anchored to a Base Foundation.* Nicos Makris and Cameron J. Black. September 2001.

PEER 2001/13 *Modeling Soil Liquefaction Hazards for Performance-Based Earthquake Engineering.* Steven L. Kramer and Ahmed-W. Elgamal. February 2001.

PEER 2001/12 *Development of Geotechnical Capabilities in OpenSees.* Boris Jeremi . September 2001.

PEER 2001/11 *Analytical and Experimental Study of Fiber-Reinforced Elastomeric Isolators*. James M. Kelly and Shakhzod M. Takhirov. September 2001.

PEER 2001/10 *Amplification Factors for Spectral Acceleration in Active Regions.* Jonathan P. Stewart, Andrew H. Liu, Yoojoong Choi, and Mehmet B. Baturay. December 2001.

PEER 2001/09 *Ground Motion Evaluation Procedures for Performance-Based Design.* Jonathan P. Stewart, Shyh-Jeng Chiou, Jonathan D. Bray, Robert W. Graves, Paul G. Somerville, and Norman A. Abrahamson. September 2001.

PEER 2001/08 *Experimental and Computational Evaluation of Reinforced Concrete Bridge Beam-Column Connections for Seismic Performance*. Clay J. Naito, Jack P. Moehle, and Khalid M. Mosalam. November 2001.

PEER 2001/07 *The Rocking Spectrum and the Shortcomings of Design Guidelines.* Nicos Makris and Dimitrios Konstantinidis. August 2001.

PEER 2001/06 *Development of an Electrical Substation Equipment Performance Database for Evaluation of Equipment Fragilities*. Thalia Agnanos. April 1999.

PEER 2001/05 *Stiffness Analysis of Fiber-Reinforced Elastomeric Isolators.* Hsiang-Chuan Tsai and James M. Kelly. May 2001.

PEER 2001/04 *Organizational and Societal Considerations for Performance-Based Earthquake Engineering.* Peter J. May. April 2001.

PEER 2001/03 *A Modal Pushover Analysis Procedure to Estimate Seismic Demands for Buildings: Theory and Preliminary Evaluation.* Anil K. Chopra and Rakesh K. Goel. January 2001.

PEER 2001/02 *Seismic Response Analysis of Highway Overcrossings Including Soil-Structure Interaction.* Jian Zhang and Nicos Makris. March 2001.

PEER 2001/01 *Experimental Study of Large Seismic Steel Beam-to-Column Connections.* Egor P. Popov and Shakhzod M. Takhirov. November 2000.

PEER 2000/10 *The Second U.S.-Japan Workshop on Performance-Based Earthquake Engineering Methodology for Reinforced Concrete Building Structures.* March 2000.

PEER 2000/09 *Structural Engineering Reconnaissance of the August 17, 1999 Earthquake: Kocaeli (Izmit), Turkey.* Halil Sezen, Kenneth J. Elwood, Andrew S. Whittaker, Khalid Mosalam, John J. Wallace, and John F. Stanton. December 2000.

PEER 2000/08 *Behavior of Reinforced Concrete Bridge Columns Having Varying Aspect Ratios and Varying Lengths of Confinement.* Anthony J. Calderone, Dawn E. Lehman, and Jack P. Moehle. January 2001.

PEER 2000/07 *Cover-Plate and Flange-Plate Reinforced Steel Moment-Resisting Connections.* Taejin Kim, Andrew S. Whittaker, Amir S. Gilani, Vitelmo V. Bertero, and Shakhzod M. Takhirov. September 2000.

PEER 2000/06 *Seismic Evaluation and Analysis of 230-kV Disconnect Switches.* Amir S. J. Gilani, Andrew S. Whittaker, Gregory L. Fenves, Chun-Hao Chen, Henry Ho, and Eric Fujisaki. July 2000.

PEER 2000/05 *Performance-Based Evaluation of Exterior Reinforced Concrete Building Joints for Seismic Excitation.* Chandra Clyde, Chris P. Pantelides, and Lawrence D. Reaveley. July 2000.

PEER 2000/04 *An Evaluation of Seismic Energy Demand: An Attenuation Approach.* Chung-Che Chou and Chia-Ming Uang. July 1999.

PEER 2000/03 *Framing Earthquake Retrofitting Decisions: The Case of Hillside Homes in Los Angeles.* Detlof von Winterfeldt, Nels Roselund, and Alicia Kitsuse. March 2000.

PEER 2000/02 *U.S.-Japan Workshop on the Effects of Near-Field Earthquake Shaking.* Andrew Whittaker, ed. July 2000.

PEER 2000/01 *Further Studies on Seismic Interaction in Interconnected Electrical Substation Equipment.* Armen Der Kiureghian, Kee-Jeung Hong, and Jerome L. Sackman. November 1999.

PEER 1999/14 *Seismic Evaluation and Retrofit of 230-kV Porcelain Transformer Bushings*. Amir S. Gilani, Andrew S. Whittaker, Gregory L. Fenves, and Eric Fujisaki. December 1999.

PEER 1999/13 *Building Vulnerability Studies: Modeling and Evaluation of Tilt-up and Steel Reinforced Concrete Buildings.* John W. Wallace, Jonathan P. Stewart, and Andrew S. Whittaker, editors. December 1999.

PEER 1999/12 *Rehabilitation of Nonductile RC Frame Building Using Encasement Plates and Energy-Dissipating Devices.* Mehrdad Sasani, Vitelmo V. Bertero, James C. Anderson. December 1999.

PEER 1999/11 *Performance Evaluation Database for Concrete Bridge Components and Systems under Simulated Seismic Loads.* Yael D. Hose and Frieder Seible. November 1999.

PEER 1999/10 *U.S.-Japan Workshop on Performance-Based Earthquake Engineering Methodology for Reinforced Concrete Building Structures.* December 1999.

PEER 1999/09 *Performance Improvement of Long Period Building Structures Subjected to Severe Pulse-Type Ground Motions*. James C. Anderson, Vitelmo V. Bertero, and Raul Bertero. October 1999.

PEER 1999/08 *Envelopes for Seismic Response Vectors.* Charles Menun and Armen Der Kiureghian. July 1999.

PEER 1999/07 *Documentation of Strengths and Weaknesses of Current Computer Analysis Methods for Seismic Performance of Reinforced Concrete Members.* William F. Cofer. November 1999.

PEER 1999/06 *Rocking Response and Overturning of Anchored Equipment under Seismic Excitations.* Nicos Makris and Jian Zhang. November 1999.

PEER 1999/05 *Seismic Evaluation of 550 kV Porcelain Transformer Bushings.* Amir S. Gilani, Andrew S. Whittaker, Gregory L. Fenves, and Eric Fujisaki. October 1999.

PEER 1999/04 *Adoption and Enforcement of Earthquake Risk-Reduction Measures.* Peter J. May, Raymond J. Burby, T. Jens Feeley, and Robert Wood.

PEER 1999/03 *Task 3 Characterization of Site Response General Site Categories*. Adrian Rodriguez-Marek, Jonathan D. Bray, and Norman Abrahamson. February 1999.

PEER 1999/02 *Capacity-Demand-Diagram Methods for Estimating Seismic Deformation of Inelastic Structures: SDF Systems*. Anil K. Chopra and Rakesh Goel. April 1999.

PEER 1999/01 *Interaction in Interconnected Electrical Substation Equipment Subjected to Earthquake Ground Motions.* Armen Der Kiureghian, Jerome L. Sackman, and Kee-Jeung Hong. February 1999.

PEER 1998/08 *Behavior and Failure Analysis of a Multiple-Frame Highway Bridge in the 1994 Northridge Earthquake.* Gregory L. Fenves and Michael Ellery. December 1998.

PEER 1998/07 *Empirical Evaluation of Inertial Soil-Structure Interaction Effects.* Jonathan P. Stewart, Raymond B. Seed, and Gregory L. Fenves. November 1998.

PEER 1998/06 *Effect of Damping Mechanisms on the Response of Seismic Isolated Structures.* Nicos Makris and Shih-Po Chang. November 1998.

PEER 1998/05 *Rocking Response and Overturning of Equipment under Horizontal Pulse-Type Motions.* Nicos Makris and Yiannis Roussos. October 1998.

PEER 1998/04 *Pacific Earthquake Engineering Research Invitational Workshop Proceedings, May 14–15, 1998: Defining the Links between Planning, Policy Analysis, Economics and Earthquake Engineering.* Mary Comerio and Peter Gordon. September 1998.

PEER 1998/03 *Repair/Upgrade Procedures for Welded Beam to Column Connections.* James C. Anderson and Xiaojing Duan. May 1998.

PEER 1998/02 *Seismic Evaluation of 196 kV Porcelain Transformer Bushings.* Amir S. Gilani, Juan W. Chavez, Gregory L. Fenves, and Andrew S. Whittaker. May 1998.

PEER 1998/01 *Seismic Performance of Well-Confined Concrete Bridge Columns.* Dawn E. Lehman and Jack P. Moehle. December 2000.

ONLINE REPORTS

The following PEER reports are available by Internet only at http://peer.berkeley.edu/publications/peer_reports.html

PEER 2008/101 *Seismic Performance Objectives for Tall Buildings.* William T. Holmes, Charles Kircher, William Petak, and Nabih Youssef. August 2008.

PEER 2007/101 *Generalized Hybrid Simulation Framework for Structural Systems Subjected to Seismic Loading.* Tarek Elkhoraibi and Khalid M. Mosalam. July 2007.

PEER 2007/100 *Seismic Evaluation of Reinforced Concrete Buildings Including Effects of Masonry Infill Walls.* Alidad Hashemi and Khalid M. Mosalam. July 2007.